UNIVERSITY OF SOUTHAMPTON

SULPHIDE ALTERATION AND BIOMINERALISATION IN METALLIFEROUS SEDIMENTS

Submitted by:
Sarah Elizabeth Johanna Glynn B.Sc (Hons)

For the degree of
Doctor of Philosophy Ph.D.

School of Ocean and Earth Science

August 2004

UNIVERSITY OF SOUTHAMPTON

ABSTRACT

FACULTY OF SCIENCE
SCHOOL OF OCEAN AND EARTH SCIENCES
Doctor of Philosophy

SULPHIDE ALTERATION AND BIOMINERALISATION IN METALLIFEROUS SEDIMENTS

By Sarah Elizabeth Johanna Glynn

The fate of sulphide minerals as they age on the seafloor and the processes involved in early diagenesis of near field hydrothermal sediments are largely unknown. This study investigates near field metalliferous sediments from two relict high temperature zones within the Trans Atlantic Geotraverse (TAG) hydrothermal field at 26°N on the Mid-Atlantic Ridge. The cores were analyzed for bulk mineralogy and geochemistry in order to identify diagenetic alteration processes and their impact on bulk geochemical signatures and the evolution of these deposits in space and time. Specific attention was paid to sulphide-rich layers and sulphur isotopes and SEM imaging were used to unravel the complex paragenetic sequence. Microbial interactions were investigated by geochemical, textural and strontium isotope analysis of Fe oxide filaments and associated gypsum.

The downcore mineralogy and geochemistry of cores CD102/58 & 60 indicate deposition from a complex mix of sources. The sulphide layer of CD102/58 represents mass wasting of high temperature chimney and upper mound debris. The sulphide layer of CD102/60 represents mass wasting of an inner mound pyrite-quartz breccia. Downcore metal distributions reflect mineralogical variability and the relative proportions of sulphide and oxide as well as remobilisation due to oxidative dissolution of sulphide (e.g. Cu & Cr), secondary mineralisation (e.g. atacamite), redox cycling (e.g. Mn), precipitation from low temperature diffuse fluids (e.g. opaline silica) and scavenging from seawater (V & P).

CD102/58 has $\delta^{34}S$ values ranging from +4.7-+14.7‰. The heaviest values are associated with primary sulphide phases and reflect precipitation initially at the mound surface followed by high temperature precipitation (>250°C) in the subsurface where the isotopic composition is controlled by partial reduction of seawater sulphate. CD102/60 has $\delta^{34}S$ values ranging from +3.4-+13.0‰. The $\delta^{34}S$ values of primary sulphides reflect reaction of hydrothermal fluid with pre-existing anhydrite sulphate in the stockwork zone. The sulphur isotopic composition of secondary sulphides is controlled by mixing of hydrothermal fluid and reduced seawater sulphate and reaction with previously precipitated sulphides. These new data have extended the range of $\delta^{34}S$ at the TAG hydrothermal site from +4.4-+10.3‰ to +3.4-+14.7‰. The upper end of this range is substantially heavier than values of $\delta^{34}S$ from other sediment free mid ocean ridge hydrothermal sites and suggests that sulphur contributions from reduction of seawater sulphate are much more important than previously recognised.

Sulphide alteration is driven by oxidative dissolution and acid leaching. The mechanisms of sulphide alteration resemble sub-aerial supergene processes. However, submarine supergene processes within the sediment pile are dominated by locally important grain-scale remineralisation and secondary enrichment, as opposed to the much larger scale, downward migrating zones of oxidation and secondary enrichment observed in sub-aerial deposits.

Based on morphological similarities with structures formed by Fe oxidising bacteria a biogenic origin is invoked for Fe oxide filaments from CD102/58. The biogenicity of these structures is supported by the geochemistry and isotopic composition of associated gypsum which for the first time has directly linked these structures to sulphide oxidation. These filament morphologies can therefore be used as biomarkers for bacteriogenic Fe oxide precipitation. However, Fe oxide filaments make up only a minor percentage of the total volume of Fe oxide and are restricted to oxic layers in the upper portion of the core where circumneutral pH conditions are inferred and there are steep redox gradients. Thus, biogenic Fe oxide precipitation is only locally important and abiogenic precipitation dominates.

This study has contributed to our understanding of sediment formation and diagenesis in hydrothermal metalliferous sediments, in particular the fate of sulphide minerals during early seafloor alteration.

Graduate School of the Southampton Oceanography Centre

This Ph.D. dissertation by

Sarah Elizabeth Johanna Glynn B.Sc (Hons)

Has been produced under the supervision of the following persons

Supervisors

Rachel A. Mills
Damon A. H. Teagle

Chair of Advisory Panel

Peter Statham

Members of Advisory Panel

Rachel A. Mills
Damon A. H. Teagle
Peter Statham

Contents

List of Figures

Chapter 1

Chapter 2

Chapter 3

Chapter 4

Chapter 5

Chapter 6

List of Tables

Chapter 1 **Page**

Chapter 2

Chapter 3

Chapter 4

Chapter 5

Chapter 6

ACKNOWLEDGEMENTS

"Another damned, thick, square book!"
Duke of Gloucester 1743-1805

There are many people without whom this thesis could not have been written. Firstly I wish to thank my supervisors Rachel Mills and Damon Teagle and NERC for funding this work. Special thanks must go to Rachel for her constant enthusiasm, guidance and support throughout this project. Also for sending me to the Caribbean - helping me to avoid the cold and WET of my first Southampton winter, for making a mean aubergine curry and for countless cups of coffee. Thanks also to Adrian Boyce and all the technical staff in the stable isotope unit at SUERC for funding and invaluable help with the collection and interpretation of the S isotope data. I am indebted to Matt Cooper, Tina and Posey Boella for their help with sample preparation and chemical analysis. Matt and Tina, and Rachel Dunk, are also thanked for helping to bring this humble geologist up to speed with the scary chemistry. My gratitude must also go to Ross Williams for help with XRD and for letting me take over his lab on a regular basis, thanks for the coffee and fag breaks, the trips to the pub and for introducing me to all the usual suspects, you've helped to make some of the tough times more fun. Bob Jones and John Ford - what can I say guys, thanks for all the help with sample prep, the fun at the barbeques, and the coffee and support. Richard Pearce is thanked for help with the preparation of samples for, and the running of samples on the SEM and Darryl Green is thanked for help with the running of the ICP-AES samples.

I would like to thank my geology teacher from school, Mrs Graham, and my lecturers during undergrad at Leeds, particularly Profs Jane Francis and Joe Cann. Without the encouragement of these people and their love of the subject I would not be here today.

Thanks to all the Bugle St Crew for being my surrogate family, putting up with all my idiosyncrasies, for good company, good food and good wine. The south isn't so bad after all. Thanks also to Jules, Jenny, Roz, Nev, Simon, Clive, Jamie, Rachel D, Michelle, Sophie, Naiose, Andy, Mike, and the rest of the wild bunch for keeping me entertained, and for your encouragement and support. Big thanks must go to my best mate from Leeds, Adam. You have been a constant in my sometimes mad and hectic life at SOC. Huge thanks also go to Phil who has known me for longer than either of us cares to remember. Thanks for keeping me sane; especially during writing up, the next pint of Black Sheep is on me!

Jules and Frank, thanks for the interesting work break in Jan and Feb. Organising a wedding and making all the dresses in 6 weeks was an interesting challenge, well they say a change is as good as a rest. To the pink lady, thank you for welcoming me home, sorry about the slide down the pecking order, but mostly thanks for making me laugh. Just think it'll be quiet when I'm gone.

Mum and Dad there just aren't the words to thank you enough. You have always shown great faith in me and understanding. Along with all the time and money you have invested in me you have also given me great friendship and love. THANK YOU from the bottom of my heart, and I promise to get a real job soon! Grandma, again, you have given me more than I shall ever be able to repay, without your help I would not have been able to do any of this, thank you.

"Felix qui potuit rerum cognoscere causas"
VIRGIL 70-19BC

Chapter 1:

Introduction

Polymetallic massive sulphide deposits are observed throughout the geological record. Many of these deposits are associated with ophiolite sequences, e.g. the Troodos ophiolite in Cyprus, and are inferred to have formed on the seafloor during hydrothermal circulation through the ocean crust (e.g. Constantinou and Govett, 1973; Zierenberg et al., 1988; Hall et al., 1989). These deposits typically consist of massive or layered sulphides which are underlain by an extensive mineralised stockwork zone. Mineralogical zoning and secondary metal enrichment are common to such deposits and are inferred to result from reworking by reaction with hydrothermal fluids and sub-aerial supergene weathering processes (e.g. Constantinou and Govett, 1973; Large, 1977; Lydon, 1984; Zierenberg et al., 1988).

Another characteristic feature of these deposits are the extensive umbers and ochres which form a metal-rich sedimentary apron around the massive sulphide body (e.g. Constantinou and Govett, 1973; Fleet and Robertson, 1980; Robertson and Boyle, 1983). The ochre deposits, which are predominantly composed of goethite with some hematite, limonite, jarosite and magnetite, are widely regarded as the products of submarine weathering and oxidation of massive sulphide on the seafloor (e.g. Constantinou and Govett, 1973; Fleet and Robertson, 1980). However, gossanous deposits can also be formed as a result of terrestrial weathering processes (c.f. Lydon, 1984).

Similar massive sulphide deposits and metal-rich, gossanous sediments are also common to seafloor hydrothermal vent sites and these have been identified as the modern analogue of terrestrial massive sulphide and umber and ochre deposits (e.g. Hannington et al., 1988; Thompson et al., 1988; Herzig et al., 1991; Goulding et al., 1998). The mechanisms and reactions involved in seafloor oxidation of sulphides and gossan production are not well understood. Despite the intense investigation of metalliferous sediments from the TAG site important questions regarding post depositional diagenetic processes remain. This thesis considers both the bulk geochemistry and mineralogy of two metalliferous sediment cores from the TAG field in order to investigate diagenetic mineral alteration processes and their impact on bulk geochemical signatures and the evolution of these deposits in space and time, specific attention is paid to sulphide-rich layers.

1.1 Historical Context

Deep-sea metalliferous sediments were first documented in 1891 on the eastern flank of the East Pacific Rise (EPR) during the *RV Challenger* expedition to traverse the world's oceans sampling sediment en route (Murray and Renard, 1891). However, metalliferous sediments received very little attention until the late 1960's when work by Boström et al. (1969) revealed a direct correlation between the occurrence of such sediments and the active mid-ocean ridge system; metalliferous sediments are characterised by high (Al+Fe+Mn)/Al ratios, markedly higher than average detrital material of continental origin, the distribution of

Al-poor sediments (high ratios) effectively delineating the ocean ridges (Figure 1.1). It was initially suggested that these sediments were the products of co-precipitation of Mn from seawater with Fe and Pb from ridge basalts (Bender et al., 1971). With the discovery of low temperature venting on the Galapagos Rift in 1976 (Corliss, 1979) and high temperature 'black smoker' style venting on the EPR in 1979 (Edmond et al., 1979a; Edmond et al., 1979b) hydrothermal vents and material derived from the fallout of hydrothermal plumes were finally identified as the source of metal enrichment.

Marine hydrothermal systems occur in a range of tectonic environments (German et al., 1995), although they are mostly confined to actively spreading ridges. 42% of all known vent sites occur on fast spreading ridges (Fouquet, 1997) primarily in the Pacific Ocean on the EPR (Baker et al., 1995), however, the Trans-Atlantic Geotraverse (TAG) hydrothermal field at 26°N on the eastern side of the median valley of the Mid Atlantic Ridge (MAR) (e.g. Rona, 1985) is perhaps the most documented site. Hydrothermal fluid flow is restricted to areas of high permeability (e.g. faulting and fracture zones) and high volcanic activity (Zierenberg et al., 1993). The almost continuous faulting and fracturing of crust adjacent to fast spreading ridges, as a result of near continuous magmatic intrusion, constantly creates conduits for fluid flow and therefore the discharge of hydrothermal fluids (Fouquet, 1997; Rohr, 1994; McClain et al., 1993). Slow spreading ridges, in contrast, are characterised by discontinuous magma intrusion from localised volcanic centres and less frequent faulting and fracturing (e.g. Kong et al., 1992; Eberhart et al., 1988). However, the tectonic and magmatic events associated with slow spreading ridges are larger and more localised than those occurring in fast spreading systems, these condition lead to deeply penetrating faults providing long-term, sustainable, focused conduits for hydrothermal fluid flow which result in larger more mature hydrothermal deposits (e.g. Rona, 1988; Hannington et al., 1995a; Fouquet, 1997). Hydrothermal circulation is important for our understanding for oceanic geochemical processes since seafloor hydrothermal circulation is now known to be the principle agent of energy and mass transfer between the crust and the oceans (e.g. Elderfield and Schultz, 1996).

1.2 Hydrothermal Heat and Water Fluxes

Early models of the thermal evolution of the lithosphere (e.g. McKenzie, 1967) consistently predicted greater heat flow for crust <70Ma than was observed (e.g. Stein and Stein, 1994). This difference between predicted heat loss from cooling plates as they move away from ridge axes and the observed conductive heat flow (the global heat flow anomaly, or 'missing heat') can be attributed to advection of heat by hydrothermal circulation (e.g. Stein and Stein, 1994) (Figure 1.2). Despite the fact that known active hydrothermal discharge only covers a minimal percentage of the ridge axis crust (Baker et al., 1995) estimates by Stein and Stein (1994), using global seafloor heat flow datasets, suggest that 34% (11×10^6MW) of the total oceanic heat flux (32×10^6MW) occurs by hydrothermal circulation. Of this 30% (3.3×10^6MW) occurs on crust <1Ma however, this is an upper limit since the observed conductive heat flow may be depressed (Stein and Stein, 1994). Taking this into account Elderfield and Schultz (1996) suggest a heat flux of $2.6\pm0.5\times10^6$MW for crust <1Ma. The other 70% occurs over crust up to 65±10Ma. This age, often referred to as the oceanic crust 'sealing age', is remarkably consistent on all oceanic crust, independent of spreading rate, and is in agreement with the 'missing heat' age predicted by modelling. Uncertainties however, remain in determining the role of hydrothermal heat fluxes on a global scale as the relative importance of axial vs. off axis flow, and high

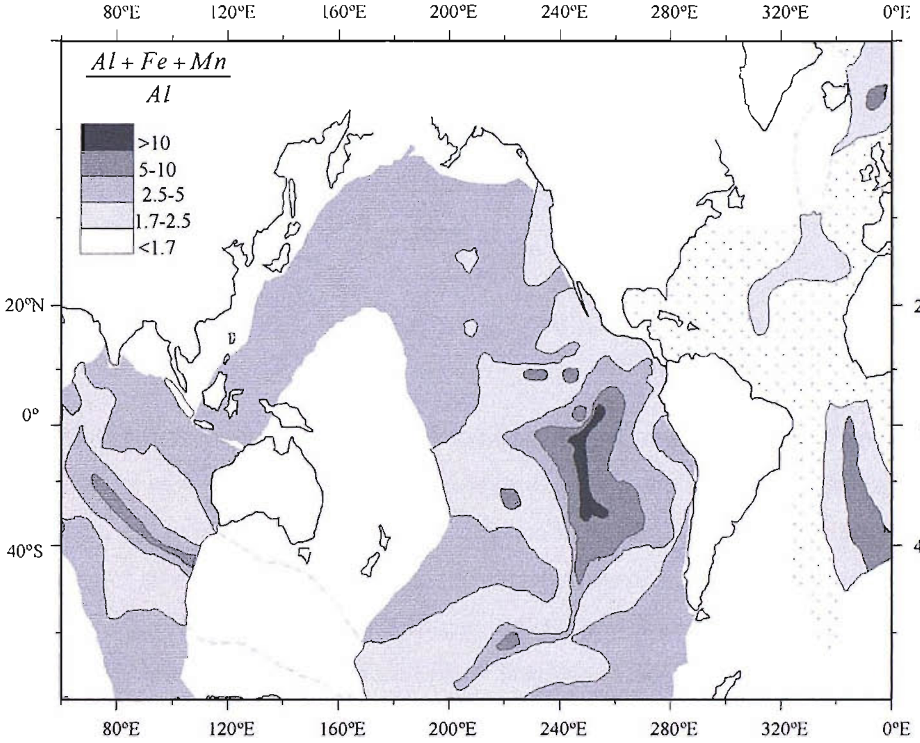

Figure 1.1: (Al+Fe+Mn)/Al ratio of surface sediment. High ratios delineate the ocean ridge system . Adapted from Bostrom et al. (1969).

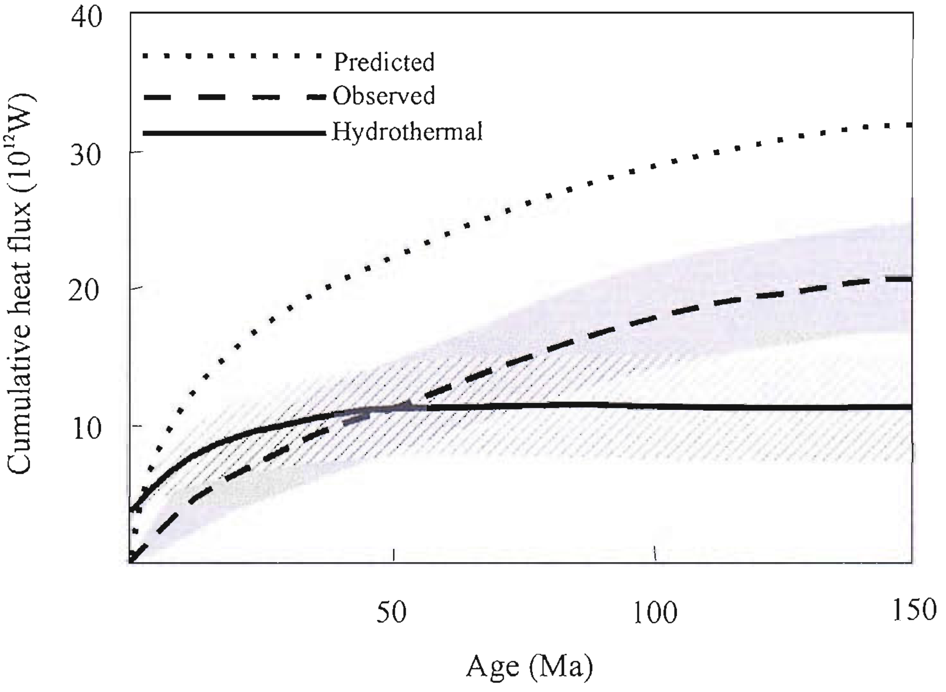

Figure 1.2: Cumulative heat flux vs. Age partionaed into observed (conductive) and hydrothermal 'missing heat' (predicted-observed). Grey shaded area indicates error in the observed value; grey dashed area indicates error in hydrothermal value. Adapted from Elderfield and Schultz, (1996).

temperature 'black smoker' style venting vs. low temperature diffuse flow are not constrained (e.g. Mottl and Wheat, 1994).

The global hydrothermal water flux (WF) can be estimated from the heat flux (HF), the water temperature anomaly (ΔT) and the specific heat capacity of seawater (C_p):

$$WF = \frac{HF}{(\Delta T.Cp)} \qquad (1.1)$$

Assuming that the entire hydrothermal water flux is due to high temperature (~350°C) black smoker fluids with a specific heat capacity of =~5.8J/g°K at 350bars the hydrothermal water flux lies in the range of 3-6x10^{13}kg/year (Elderfield and Schultz, 1996). However, this assumption is an extreme over simplification, although the partitioning of axial flow into high and low temperature is not well constrained on a global scale, at individual vent sites the heat flux associated with diffuse and low temperature flow may exceed that from high temperature flow. For example estimates of the diffuse heat flux at the TAG hydrothermal mound (26°N MAR) are an order of magnitude greater than the heat flux from black smoker style venting (Rudnicki and Elderfield, 1993; Schultz et al., 1996). Taking this into account, recalculation of the hydrothermal water flux based on partitioning 10% of the flow to high temperature fluids (350°C; C_p=~5.8J/g°K) and 90% to low temperature flow at 5°C with a specific heat capacity of ~4J/g°K yields an estimated water flux which is increased by two orders of magnitude to 280-560x10^{13}kg/year (Elderfield and Schultz, 1996). In addition, off axis flow is also important, since 70% of the hydrothermal heat flux occurs on crust >1Ma off-axis diffuse and low temperature flow must also be considered in any calculation of the hydrothermal water flux. Assuming an off-axis heat flux of 7x10^{6}MW and a temperature range of 5-15°C Elderfield and Schultz (1996) calculate the off-axis water flux to be 370-1100x10^{13}kg/year.

Given the water fluxes calculated above and a total water volume for the oceans of 1.37x10^{21}kg (Kadko, 1993) the cycling time for ocean water through high temperature axial flow is in the order of 10 million years, and the cycling time for off-axis flow is in the order of 100-400 thousand years (Elderfield and Schultz, 1996). This is about 3 and 1 orders of magnitude, respectively, smaller than the riverine water flux calculated from the strontium isotope budget (Palmer and Edmond, 1989).

1.3 Generation of Hydrothermal Fluids

As ambient seawater penetrates the ocean crust through faults and fractures, heat is transferred to the downward permeating fluid and extensive interaction and chemical exchange occurs between the superheated seawater and basalt resulting in fluxes of elements to and from basalt and the downwelling fluid (e.g. Edmond et al., 1982; Seyfried and Janecky, 1985; Von Damm, 1988). Experimental and theoretical modeling of seawater recharge and circulation in the upper crust has shown that as down-welling seawater is heated to temperatures of ~150-200°C, sulphate, Ca and Sr are removed from the fluid due to anhydrite precipitation (Shanks et al., 1981; Janecky and Shanks, 1988; Alt et al., 1989; Bowers, 1989). At these temperatures Mg is also removed from the fluid due to subsurface saponite precipitation (e.g. Mottl and Wheat, 1994; Alt et al., 1996). At temperatures >150°C all remaining Mg is removed from solution as Mg undergoes mole for mole exchange with basaltic Ca (Von Damm, 1990; Mottl, 1983) which is released to the superheated fluid (Blount and Dickson, 1969). Due to the quantitative removal of Mg from the downwelling fluid, end member hydrothermal fluid compositions are commonly extrapolated to [Mg] =0 which allows for comparison in fluid compositions at different vent sites.

Si is also precipitated at depth during high temperature subsurface circulation. Thermodynamic calculations suggest that this Si is in equilibrium with quartz (Bowers, 1989); the prevalence of quartz in hydrothermally altered oceanic crust is consistent with this (e.g. Alt et al., 1986; Alt et al., 1996). Based on the temperature variation of Si-Qtz equilibrium the Si content of some end-member hydrothermal fluids has been used to infer the depth of reaction assuming the temperature from the alteration assemblage (e.g. Von Damm, 1990).

As the downwelling fluid approaches temperatures in excess of ~250°C any remaining seawater sulphate is reduced to H_2S as a consequence of the oxidation of ferrous Fe in pyroxene or olivine, or via conversion of basaltic pyrrhotite (FeS) to secondary pyrite (FeS_2) (Shanks et al., 1981; Ohmoto and Lasage, 1982; Shanks and Seyfried, 1987). Whilst seawater SO_4^{2-} is fixed in the crust as anhydrite the sulphide component in basalt, which is highly soluble at high temperature, is leached from the basaltic wallrock (e.g. Shanks et al., 1981; Shanks and Seyfried, 1987; Alt et al., 1989; Bowers, 1989). Direct leaching of basaltic sulphur in this way produces $\delta^{34}S$ values in the fluid close to 0‰ (Seyfried and Janecky, 1985). At the simplest level the observed range of $\delta^{34}S$ values in modern seafloor hydrothermal deposits and vent fluids (~-5.6‰ - +7.3‰) can be attributed to variable mixing of basaltic ($\delta^{34}S$ = +0.1‰: Sakai et al., 1984), and seawater ($\delta^{34}S$ = +20.9‰: Rees et al., 1978) sulphur as up-welling hydrothermal fluids with basalt dominated $\delta^{34}S$, are modified in the shallow subsurface around vent sites and within individual chimneys, as entrained ambient seawater undergoes sulphate reduction (Bowers, 1989; Janecky and Shanks, 1988).

At high temperature metals including: Fe, Cu, Zn and Pb are also leached from basalt and become enriched in the fluid phase. Since these metals are typically carried by chloride complexes, which are extremely temperature dependant, their content in end member fluids is also strongly temperature dependant, e.g. rapid increases in Zn contents occur at temperatures ≥310°C and in Cu and Fe at ≥320°C (Scott, 1997). Figure 1.3 shows a schematic model of common processes in the generation of hydrothermal fluids.

Whilst the seawater entering the crust is slightly alkaline (pH~7.8) all sampled vent fluids are acidic (e.g. Edmond et al., 1982; Von Damm, 1990; Gamo et al., 1996). This change in acidity is due to subsurface mineral-formation during chemical exchange between the basaltic wallrock and the downwelling seawater. This can be demonstrated by consideration of epidote formation; epidote is a common alteration product in hydrothermally altered basalts (e.g. Alt et al., 1986; Alt et al., 1996). Subsurface precipitation of epidote removes Ca, Fe, Al and Si from the fluid and produces 13 moles of H^+ for every mole of epidote (Equation 1.2). Subsurface sulphide precipitation also generates acidity (e.g. Equation 1.3; this is an overall reaction however, pyrite precipitation proceeds via a FeS precursor) (Seewald and Seyfried, 1990).

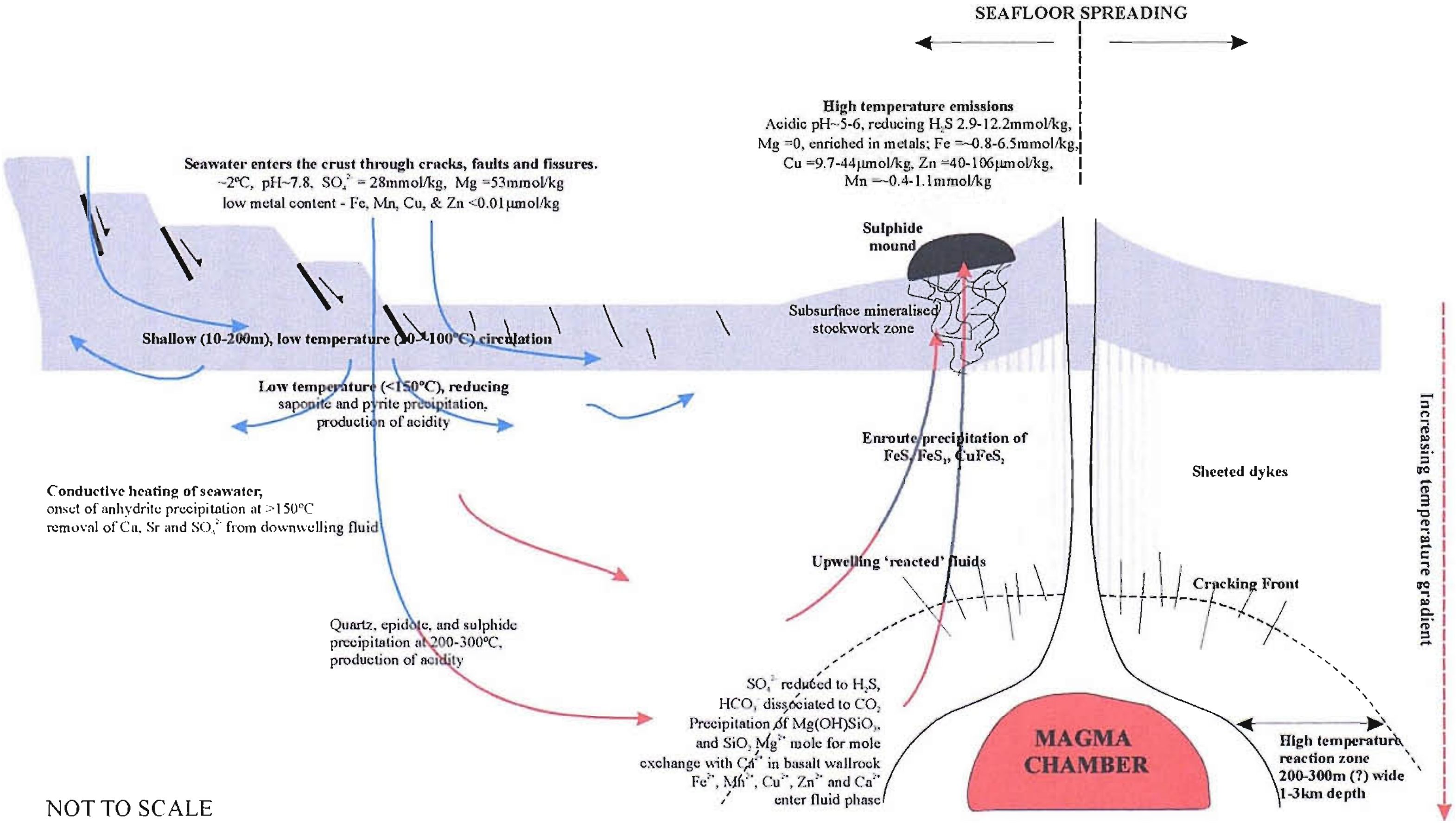

Figure 1.3: Schematic representation of the principal reactions and processes involved in the genesis of hydrothermal fluids.

$$2Ca^{2+} + Fe^{3+} + 2Al^{3+} + 3SiO_{2(aq)} + 7H_2O \Rightarrow \underbrace{Ca_2FeAl_2Si_3O_{12}(OH)}_{Epidote} + 13H^+ \qquad (1.2)$$

$$Fe^{2+} + 2H_2S \Rightarrow \underbrace{FeS_2}_{Pyrite} + 4H^+ \qquad (1.3)$$

Although the concentration of salts and metals in the hydrothermal fluids are largely controlled by the composition of the source-rocks, e.g. the abundance of Ba (which is readily leachable from basalt under hydrothermal conditions) at the Explorer ridge can be directly linked to high Ba contents in basalt at this site (Scott et al., 1990), depending on the temperatures and pressures experienced by the fluid, phase separation may take place and this can also affect the final composition (Von Damm, 1995). Large variations in measured vent fluid salinities suggest that phase separation is a common phenomenon in seafloor hydrothermal systems (e.g. Von Damm, 1990; Von Damm, 1988). For seawater with 3.2wt% NaCl, at 2-3km depth (the depth of most vent systems on MORs) the temperature of the two phase boundary is between 385-405°C (Bischoff and Pitzer, 1985), fluids with temperatures below this are unlikely to undergo phase separation. The temperatures experienced by some vent fluids however, do exceed the temperatures required for phase separation e.g. vent fluids from the Endeavour Ridge are at ~420°C (Delaney et al., 1984), in addition, some fluids with venting temperatures below 385°C may have experienced higher temperature conditions at depth in the reaction zone.

Phase separation of hydrothermal solutions results in the production of a more saline fluid and a low salinity, vapor-rich fluid, at higher temperatures and pressures phase separation leads to conjugate fluids with increasingly different salinities (Bischoff and Rosenbauer, 1984; Bischoff and Pitzer, 1985). Experimental studies have shown that the high salinity brines which are produced during phase separation have an impact on the overall metal carrying potential of the fluid since these brines are enriched in the chloride species required for metal complexation (Bischoff and Rosenbauer, 1987). However, for the effects of phase separation to be observed in hydrothermal fluids venting at the seafloor physical separation of the individual phases is required. Although MacGregor et al. (2001) show that a high salinity fluid phase may be retained in the crust due to its greater density, at the pressure conditions of most hydrothermal systems density differences between the brine and the vapor-rich fluid are small, and physical separation due to density differences is unlikely (Bischoff and Pitzer, 1985). An alternative method of physical separation based on the relative permeability of fluid barriers has been proposed by Fox (1990) who suggested that the saline phase is confined to flow conduits but the low salinity vapor-rich phase flows diffusively through the surrounding rock. Recombination of the separated fluids, at varying mixing proportions, at lower temperature could produce the range of salinities observed (Fox, 1990).

At shallower depths near to the seafloor, and at vent sites on shallow parts of the MOR system, phase separation and subsurface boiling have been observed (e.g. Reykjanes Ridge: German et al., 1994). The production of the gas phase in these cases requires that the partial pressure of gases in the hydrothermal fluid exceeds that of the water column. Boiling of the hydrothermal fluid raises the E_h and pH by removal of CO_2, H_2S and H_2 this in turn leads to sulphide precipitation and the formation of an extensive subsurface mineralized stockwork with a depth range related to the depth of boiling (Drummond and Ohmoto, 1985).

The hydrothermal fluid rises back to the seafloor when supercritical density is approached. The resultant hydrothermal discharge has a temperature of ~250-400°C and is acidic, reducing and enriched in sulphide and ore forming metals scavenged from the basalt (e.g. Seyfried and Janecky, 1985) (Table 1.1). Hydrothermal fluids can re-enter the ocean in several ways e.g. high temperature (black smoker style) focused flow through mineralised chimneys or cracks and fissures; low temperature (white smoker style) focused flow; and diffuse flow through sediment piles (e.g. Edmond et al., 1982; Hannington et al., 1995a; Tivey et al., 1995). As the hydrothermal fluid debouches onto the seafloor mixing with cold bottom waters occurs and ore-forming metals precipitated in response to changes in temperature and composition forming chimney structures and sulphide and oxide deposits in close proximity of the vents (e.g. Styrt et al., 1981; Janecky and Seyfried, 1984; Haymon, 1983).

1.4 Chimney Formation

The mineralogical composition of hydrothermal chimneys indicates complex growth histories with often multiple stages of precipitation and replacement driven by changes in the temperature and chemical composition of the fluids (e.g. Haymon and Kastner, 1981; Styrt et al., 1981; Haymon, 1983; Janecky and Seyfried, 1984; Zierenberg et al., 1984; Woodruff and Shanks, 1988). Despite this, paragenetic sequences in high temperature vents from both Atlantic and Pacific sites, are broadly similar suggesting that chimney formation processes are also more or less comparable.

1.4.1 Black Smoker Chimneys

As high temperature hydrothermal fluids vent onto the seafloor mixing with ambient seawater causes precipitation of anhydrite ($CaSO_4$) (e.g. Spiess et al., 1980; Goldfarb et al., 1983; Haymon, 1983). The Ca^{2+} in this anhydrite is largely derived from the high temperature fluid however, isotopic evidence indicates that the SO_4^{2-} component is derived from seawater (e.g. Spiess et al., 1980; Styrt et al., 1981; Kusakabe et al., 1982). During this initial anhydrite formation minor Zn-sulphide (e.g. Equation 1.4) and pyrite (Equation 1.5) and/or FeS (Equation 1.6) are also precipitated (e.g. Haymon, 1983; Goldfarb et al., 1983).

$$Zn^{2+} + H_2S + Ca^{2+} + SO_4{}^{2-} \Rightarrow \underbrace{ZnS}_{Sphalerite/\,wurtzite} + CaSO_4 = 2H^{+} \tag{1.4}$$

$$Fe^{2+} + H_2S_2 \Rightarrow FeS_2 + 2H^{+} \tag{1.5}$$

$$Fe^{2+} + H_2S \Rightarrow FeS + 2H^{+} \tag{1.6}$$

The existence of both sphalerite and wurtzite in the early growth stages of chimneys requires explanation since sphalerite is the low temperature (up to ~250°C; cubic habit) Zn sulphide polymorph, and wurtzite is the high temperature (250-350°C; hexagonal habit) polymorph. Several possibilities for their coexistence have been suggested: the first relates to the presence of impurities, including Mn, Cd or ZnO, within the crystal. These elements are more soluble in wurtzite than in sphalerite such that an impurity content >10 mole% may favour metastable wurtzite precipitation at temperatures below 250°C (Barton and Skinner, 1979; Haymon and Kastner, 1981). The second possibility is the occurrence of non-stoichiometric conditions, i.e. S/Zn+Fe <1 under these conditions and with low fS_2 stable formation of wurtzite may occur (e.g. Scott and Barnes, 1972;

Element	Concentration in hydrothermal fluid	Concentration in seawater
mmol/kg		
Ca	10.5-55	10.2
H_2S	2.9-12.2	<0.001nm
Mg	0	53
μmol/kg		
Fe	750-6470	~0.5nm
Zn	40-106	0.01
Cu	9.7-44	0.007
Mn	360-1140	~0.37nm
Ba	>8->42.6	0.14
Li	411-1322	26
CH_4	25-100	<0.001nm
nmol/kg		
Pb	9-359	0.01
Co	22-227	0.03
As	30-452	27
Ag	26-38	0.02

Table 1.1: **Comparison of the concentrations of the principal chemical species in hydrothermal fluids with their concentrations in seawater. Adapted from Elderfield and Schultz, (1996).**

Haymon and Kastner, 1981). Alternatively, the co-existence of sphalerite and wurtzite may represent conditions of ZnS supersaturation where rapid precipitation of disordered hexagonal wurtzite is kinetically favoured over precipitation of ordered cubic sphalerite (e.g. Haymon and Kastner, 1981).

Given that most chimneys are in equilibrium with respect to pyrite, the co-existence of pyrite and pyrrhotite in some chimneys (e.g. at 21°N EPR: Haymon and Kastner, 1981; Snake pit MAR: Hannington et al., 1991) also requires explanation. Haymon and Kastner (1981) suggest that pyrrhotite could precipitate as a metastable phase, as a result of rapid crystallisation, as emerging hydrothermal fluids mix with ambient seawater; the dramatic changes in temperature and E_h-pH conditions that occur during mixing may kinetically favour pyrrhotite formation. This is consistent with precipitation experiments which show that simple cooling of hydrothermal fluid results in preferential precipitation of pyrrhotite over pyrite (Equation 1.6) (e.g. Murowchick and Barnes, 1986; Graham et al., 1988). Pyrrhotite however, is unstable in oxidizing conditions and over time may be converted to more stable phases (e.g. pyrite) or will dissolve and return to the fluid (e.g. Haymon, 1983; Goldfarb et al., 1983).

The initial anhydrite chimneys then act as a substrate for further sulphide and sulphate precipitation. As the chimney becomes consolidated vent fluids are insulated, seawater mixing is restricted and the interior temperature rises this leads to precipitation of high temperature Cu-Fe-sulphides, e.g. chalcopyrite and cubanite, either by replacement of the outer anhydrite-Zn sulphide wall or by direct precipitation from the fluid. The central chimney orifice typically becomes lined with chalcopyrite whilst the exterior remains anhydrite-rich (e.g. Goldfarb et al., 1983; Haymon, 1983).

Chalcopyrite formation is more complex than pyrite precipitation. This is because precipitation of chalcopyrite requires an oxidising agent to convert Cu^+ to Cu^{2+}. This role may be carried out by O_2 produced by water dissociation (Equation 1.7 & 1.8) which reaction modelling has shown to be a major control on the redox state of vent fluids (Janecky and Seyfried, 1984).

$$H_2O_{(l)} \Rightarrow 0.5O_{2(g)} + H_{2(g)} \qquad (1.7)$$

$$Cu^+ + Fe^{2+} + 2H_2S + 0.5O_2 \Rightarrow \underbrace{CuFeS_2}_{chalcopyrite} + 3H^+ + 0.5H_2O \qquad (1.8)$$

SO_4^{2-} from seawater could also act as the oxidising agent however, the location of chalcopyrite precipitation at the inner chimney wall, where seawater mixing is restricted, means that this is much less likely (e.g. Woodruff and Shanks, 1988).

Chalcopyrite can also form by the replacement of pre-existing anhydrite and sphalerite or wurtzite (Equation 1.9). In this case the anhydrite sulphate acts as the oxidising agent and the acidity to drive the reaction comes either from the fluid itself or from sulphide precipitation reactions (e.g. Equations 1.5 & 1.6) (e.g. Graham et al., 1988; Woodruff and Shanks, 1988).

$$15ZnS + CaSO_4 + 8Cu^+ + 8Fe^{2+} + 8H^+ \Rightarrow 8CuFeS_2 + 15Zn^{2+} + Ca^{2+} + H_2O \qquad (1.9)$$

Where extensive growth of Cu and Fe sulphides in the chimney interior prevents any further reaction of the venting fluid with anhydrite, chalcopyrite may precipitate by reaction of Cu and Fe-bearing hydrothermal fluids with pyrite and sphalerite, using dissociated water as the oxidising agent (e.g. Graham et al., 1988) (Equation 1.10).

$$2Cu^{+} + Fe^{2+} + 2ZnS + FeS_2 \Rightarrow 2CuFeS_2 + 2Zn^{2+} \qquad (1.10)$$

Since fluids in equilibrium with chalcopyrite typically move towards the stability fields of other Cu-sulphides during cooling (Ohmoto et al., 1983) replacement of chalcopyrite by bornite (Cu_5FeS_4)-chalcocite (Cu_2S) solid solution at the transition to the outer anhydrite-sphalerite wall is common (e.g. Goldfarb et al., 1983; Haymon, 1983; Graham et al., 1988; Woodruff and Shanks, 1988). This is a response to the steep temperature, E_h and pH gradients across the chimney wall (e.g. Tivey and McDuff, 1990; Graham et al., 1988).

As the chimney structure matures, the inner wall grows inwards as Cu and Fe sulphide are deposited, and the outer wall grows upwards and outwards as anhydrite precipitation continues due to conductive heating (above 150°C) of locally entrained seawater (e.g. Haymon and Kastner, 1981; Woodruff and Shanks, 1988; Hannington et al., 1995a). Other sulphates including Mg-hydroxysulphate-hydrate (MHSH) and barite, have also been reported from the outer zones of black smoker chimneys and are similarly attributed to conductive heating of seawater (e.g. Haymon and Kastner, 1981; Tivey and Delaney, 1986; Koski et al., 1994). Minor or trace amounts of marcasite, Fe-oxide and amorphous silica may also be present in a black smoker chimney and these occurrences are controlled largely by the composition and temperature of the vent fluid, the porosity and permeability of the chimney wall and its capacity for seawater entrainment (e.g. Haymon and Kastner, 1981; Tivey and Delaney, 1986; Graham et al., 1988; Woodruff and Shanks, 1988; Koski et al., 1994).

Mature chimneys commonly exhibit mineralogical zonation (Figure 1.4) this is largely due to variations in dissolved metal contents and changes in the temperature, E_h and pH of venting fluids during the growth of a black smoker chimney which produce the varying physiochemical conditions required for the precipitation of a range of sulphide phases and their alteration over time.

1.4.2 White Smoker Chimneys

White smoker chimneys, so called because of the white particles of silica, anhydrite and barite which precipitate as the fluids are quenched by cold seawater, are at lower temperatures (100-300°C) than black smokers and have distinctly different fluid chemistries (e.g. Hannington and Scott, 1988; Koski et al., 1994; Edmond et al., 1995; Tivey et al., 1995). The fluids responsible for white smoker construction are produced from end-member, high temperature fluids which have undergone modification in the subsurface due to conductive cooling and/or local mixing with entrained seawater (e.g. Janecky and Seyfried, 1984; Koski et al., 1994; Tivey et al., 1995). Subsurface cooling of end-member fluids results in precipitation of metals and sulphur within the vent complex and this leads to a drop in fluid pH (e.g. Equation 1.5, 1.6 & 1.8) (e.g. Tivey et al., 1995). This acidity causes the remobilisation of pH sensitive metals, in particular Zn which is abundant in white smoker chimneys and fluids (e.g. Koski et al., 1984; Thompson et al., 1988; Koski et al., 1994; Edmond et al., 1995; Tivey et al., 1995). Conductive cooling is also important for precipitation of silica, since

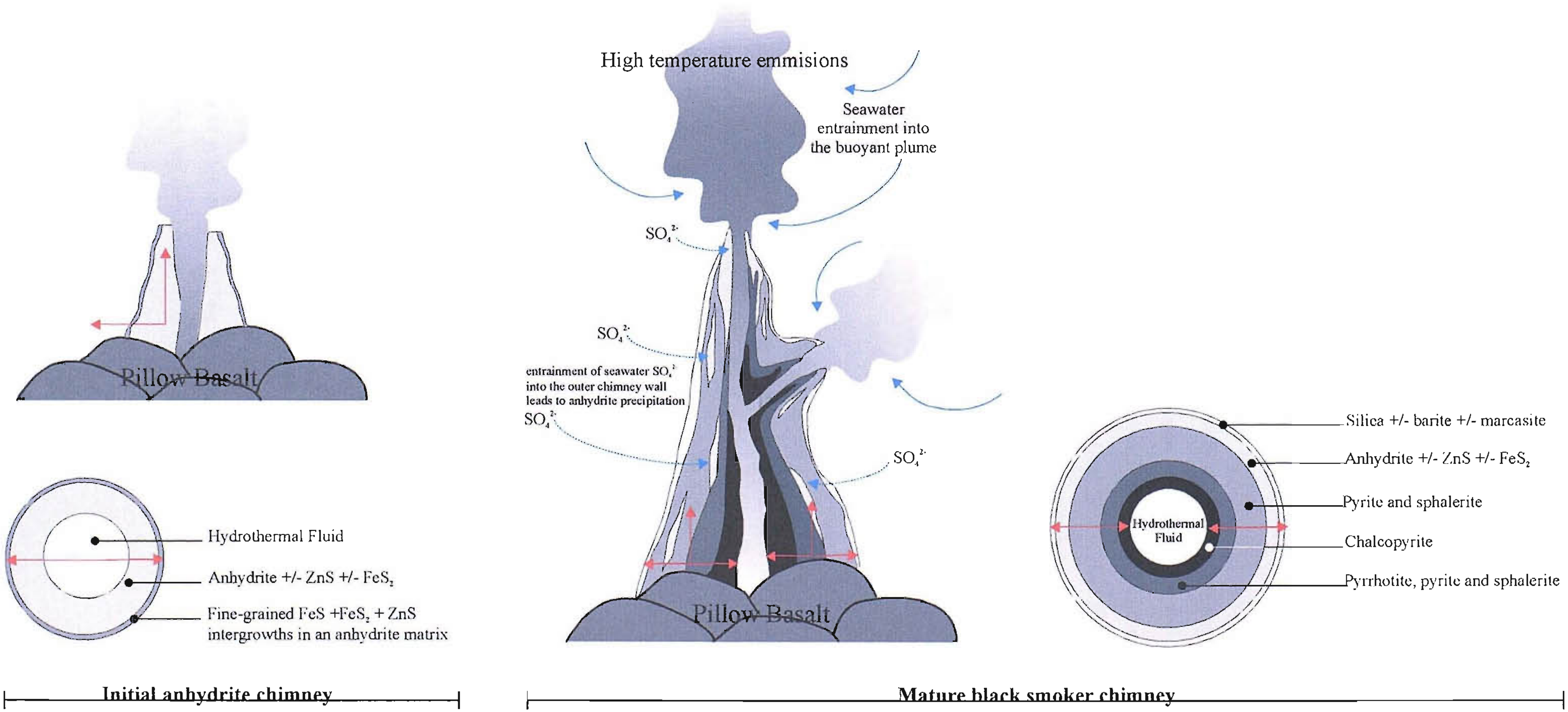

Figure 1.4: Schematic diagram of black smoker chimney growth. The initial growth is dominated by anhydrite precipitation with minor Zn-sulphide +/- minor pyrrhotite or pyrite precipitation as the hydrothermal fluid is rapidly cooled. The initial anhydrite chimney then acts as insulation for the emanating hydrothermal fluids and high temperature Cu-Fe sulphides begin to form. Pyrrhotite within the chimney is converted to more stable pyrite or removed by dissolution. Minor silicate phases are precipitated at the outer chimney walls as hydrothermal fluids are conductively cooled. Further anhydrite precipitation within the chimney wall occurs as entrained seawater is heated to temperatures in excess of 150°C. Red arrows indicate direction of chimney growth. (Adapted from Haymon, 1983).

silica is undersaturated in mixtures of hydrothermal fluid and seawater (Janecky and Seyfried, 1984; Tivey et al., 1995). The white smoker fluids which result from subsurface modification of end-member hydrothermal fluids are typically Si-, SO_4^{2-}- and Zn- rich, 200-300°C, with low H_2S and low pH (~3-4) (e.g. Edmond et al., 1982; Tivey and Delaney, 1986; Hannington and Scott, 1988; Edmond et al., 1995; Tivey et al., 1995; Edmonds et al., 1996; James and Elderfield, 1996a).

Initially white smoker chimneys are constructed of amorphous silica (SiO_2) ± barite ($BaSO_4$), which are precipitated largely in response to conductive cooling (e.g. Koski et al., 1984; Hannington and Scott, 1988; Paradis et al., 1988; Koski et al., 1994). Whilst silica is ubiquitous in all seafloor sites barite is not. The presence of barite at some hydrothermal sites, particularly at sites on the Juan de Fuca Ridge (JdFR) (e.g. Explorer Ridge: Scott et al., 1990; Axial Seamount: Hannington and Scott, 1988) and its absence elsewhere can be directly related to the Ba content of the source rock at depth (e.g. Scott et al., 1990). Although anhydrite precipitation begins at ~150°C (Figure 1.5), it is not commonly a major constituent of white smoker chimneys as it usually precipitates at much higher temperatures and is more typically associated with black smoker chimneys (Janecky and Seyfried, 1984). The initial silica-barite structure is stable since both minerals are insoluble in ambient seawater (Blount, 1977; Chen and Marshall, 1982; Williams et al., 1985). The stability of silica and barite has led the formation of white smoker structures on the JdFR which are several tens of meters high (e.g. Tivey and Delaney, 1986; Hannington and Scott, 1988).

As the silica-barite chimneys grow they insulate the venting fluid and sulphide minerals begin to form. Analyses of fluid inclusions and direct sampling of white smoker fluids indicates that the earliest sulphide formation occurs at temperatures of ~150-200°C (e.g. Koski et al., 1984; Hannington and Scott, 1988; Koski et al., 1994). Marcasite (a pyrite polymorph) is typically the first sulphide to form and is co-precipitated with amorphous silica and barite contributing to the growth of the outer chimney wall, as the interior temperature rises pyrite-marcasite and sphalerite are precipitated (e.g. Koski et al., 1994; Hannington et al., 1995a; Tivey et al., 1995). The walls of the chimneys are often porous (up to ~70%) and this allows entrainment of seawater into the structure where mixing with the venting fluid occurs, this results in temperature and chemical gradients across the wall leading to mineralogical zoning (e.g. Tivey et al., 1995) and the replacement of early formed minerals by sulphides (e.g. Koski et al., 1994).

Mature white smoker chimneys are dominated by low-Fe sphalerite with minor marcasite, pyrite and chalcopyrite (e.g. Paradis et al., 1988; Koski et al., 1994; Tivey et al., 1995). They also contain trace minerals such as galena (PbS) and show significant enrichments in Cd, Pb, Ag, Au, As and Sb, and are lacking the significant Co, Mo and Ni contents which are associated with high temperature black smoker fluids (e.g. Koski et al., 1984; Hannington and Scott, 1988; Paradis et al., 1988; Koski et al., 1994; Tivey et al., 1995). Finally, in the waning stages of white smoker venting, late stage, colloidal deposition of amorphous and opaline silica takes place cementing the chimney structure and filling any remaining pore space (e.g. Koski et al., 1994; Tivey et al., 1995).

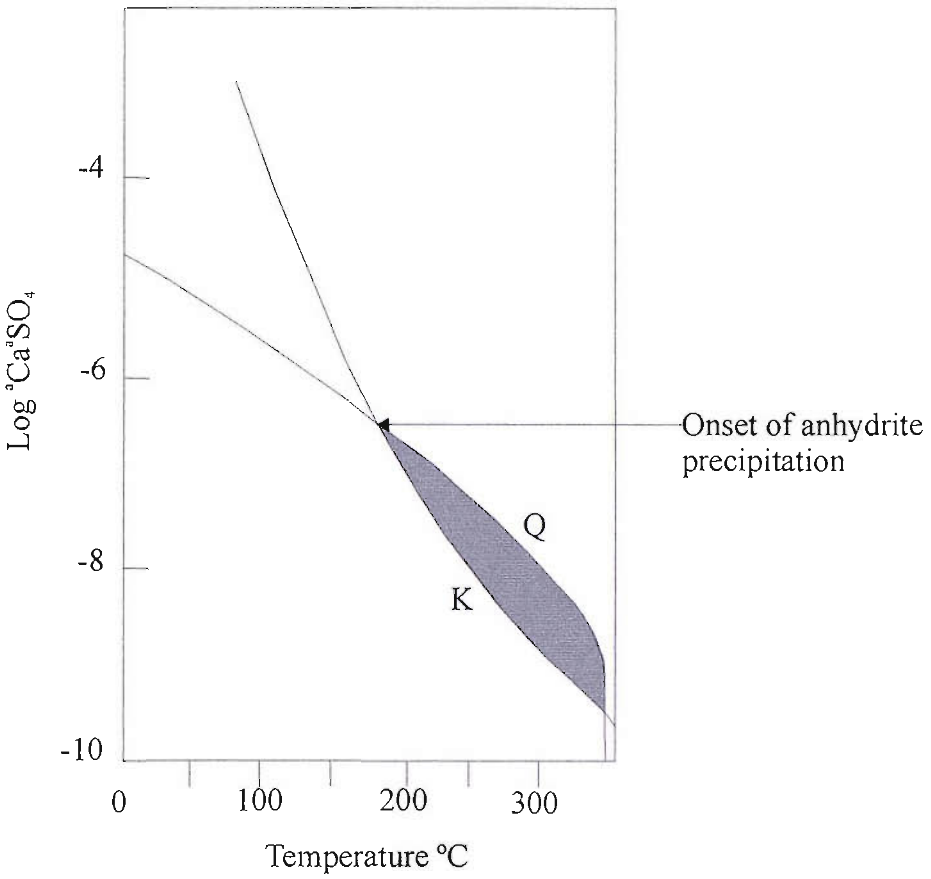

Figure 1.5: **Solubility of anhydrite: anhydrite solubility in a 21°N EP-type end member hydrothermal fluid for conservative mixing with seawater. K= equilibrium constant; Q= actual concentration ratio in the hydrothermal fluid. After Tivey and Delaney, (1986).**

1.5 Growth of Large Sulphide Deposits

1.5.1 Mound Formation

When a black smoker becomes inactive, either because of changes in the underlying plumbing system as old conduits are filled by mineral precipitates, or as hydrothermal activity wanes, collapse of the chimney is facilitated by the dissolution of the supporting anhydrite structure in cold seawater owing to its retrograde solubility (Bischoff and Seyfried, 1978) (Figure 1.5). The resultant chimney debris contributes to the growth of a sulphide talus (e.g. Humphris and Kleinrock, 1996; Hannington et al., 1995a). New chimneys develop at the outer surface of the talus deposit and may eventually overgrow and cement the sulphide debris destroying the primary mineralogical associations, concurrent cementation of the debris by silica-rich diffuse fluids results in the formation of a sulphide mound (e.g. Lydon, 1988; Hannington et al., 1995a; Hannington et al., 1998) (Figure 1.6).

Following ODP drilling of the active TAG mound (detail is discussed in Chapter 2) it was suggested that seafloor hydrothermal deposits grow largely as in situ breccia piles (e.g. Humphris et al., 1995; Humphris and Kleinrock, 1996; Hannington et al., 1998; Honnorez et al., 1998; Knott et al., 1998). Indeed, in many cases the largest seafloor deposits contain debris of older sulphide structures (e.g. Scott et al., 1990; Thompson et al., 1985) or appear to have formed via coalescence of adjacent chimney and mound deposits (e.g. Emberly et al., 1988). However, subsurface sulphide-sulphate and silica precipitation is also important for mound growth and occurs due to convective cooling of ascending hydrothermal fluids and mixing with seawater. At some sites this is aided by the presence of impermeable caps which inhibit the escape of hydrothermal fluids which instead circulate within the deposit recrystallising and redistributing primary mineral phases (e.g. TAG: Humphris et al., 1995; Lau Basin: Fouquet et al., 1993a; Lucky Strike: Langmuir et al., 1997). As the sulphide mound accumulates seawater is entrained into the structure where conductive heating produces the conditions required for anhydrite precipitation (e.g. Janecky and Seyfried, 1984; Janecky and Shanks, 1988; Tivey et al., 1995) and this causes inflation of the deposit (e.g. Hannington et al., 1998). This anhydrite may be cumulatively replaced by quartz (e.g. Knott et al., 1998; Honnorez et al., 1998) or in long lived systems with intermittent high temperature activity it will dissolve as a result of retrograde solubility during periods of hydrothermal quiescence (e.g. Bischoff and Seyfried, 1978) creating new pore space and permeability. The growth of large mounds in this manner and subsurface circulation and remineralisation processes are important in the development of mineralogical zoning in seafloor deposits (e.g. TAG: Tivey et al., 1995; Honnorez et al., 1998; Snake Pit: Detrick et al., 1986; Fouquet et al., 1993b; Galapagos mounds: Emberly et al., 1988; Escanaba Trough: Zierenberg et al., 1993). Mature mounds typically have a Cu-rich interior dominated by a high temperature assemblage of chalcopyrite and pyrite, and a Zn-rich exterior dominated by sphalerite, pyrite and marcasite, overlying a mineralised Cu-Fe stockwork in the hydrothermal upflow zone (e.g. Fouquet et al., 1993b; Honnorez et al., 1998). This pattern of mineralogical zonation resulting from hydrothermal reworking is also common to terrestrial ancient massive sulphide deposits associated with ophiolite sequences (e.g. Constantinou and Govett, 1973; Lydon, 1988). Large complex deposits develop where numerous episodes of venting lead to several stages of sulphide precipitation and overprinting earlier mineral assemblages. The importance of multiple episodes of high temperature activity at any one site is supported by modelling experiments (e.g. Lowell and Rona, 1985). The proposed model for the generation of

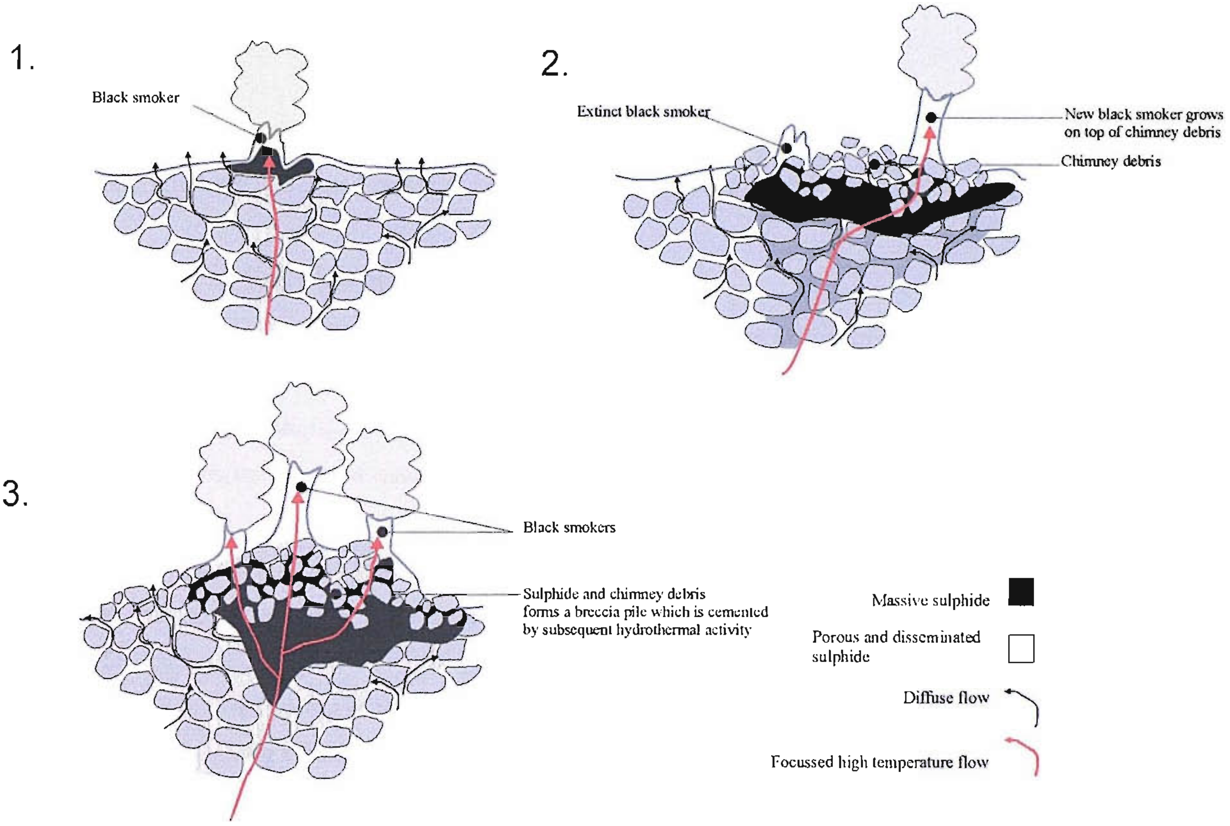

Figure 1.6: Schematic model of the initial stages of mound growth. 1.) Early chimney growth and diffuse venting; 2.) High temperature venting from mature black smoker chimneys on top of sulphide debris from the collapse of earlier chimneys, growth of a sulphide talus and breccia mound with subsurface precipitatio of massive sulphide +/- quartz and anhydrite; 3.) Mature mound deposit, coalescence of earliar vent debris, cementation of breccia pile, focussed high temperature venting.

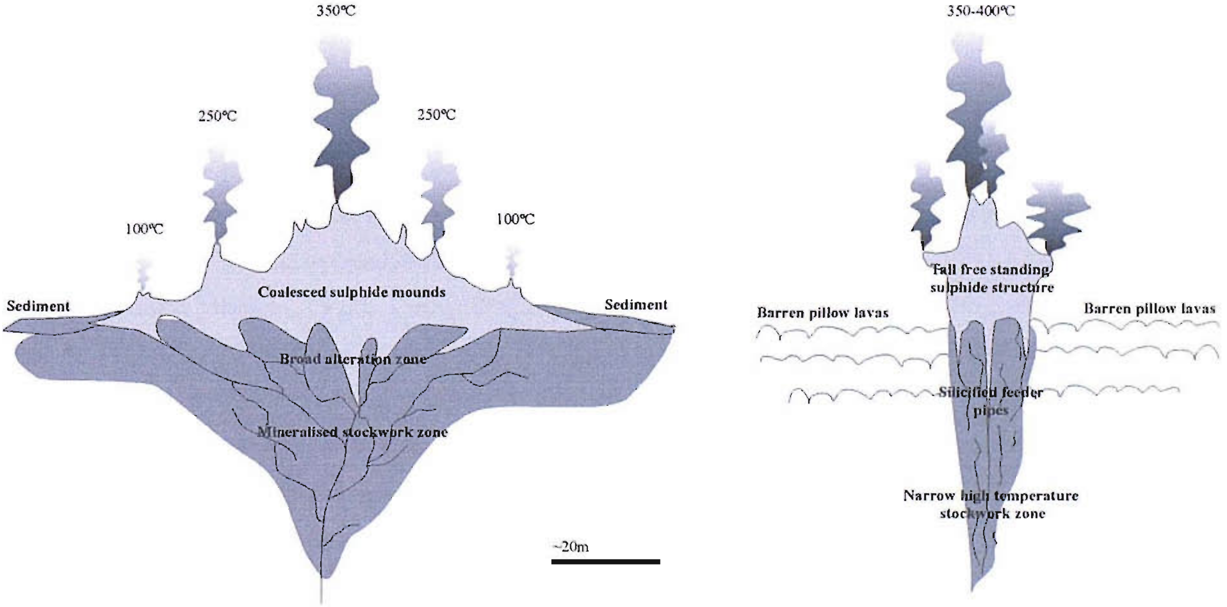

A.) Galapagos-type coalesced sulphide mounds

B.) Endeavour-type free standing sulphide structure

Figure 1.7: Comparison of sulphide deposits from the Galapagos Rift and the Endeavour Ridge. Contrasting seafloor morphologies and venting styles which are controlled by the subsurface permeability. (Adapted from Hannington et al., 1995).

seafloor massive sulphide deposits by Lowell and Rona (1985) suggests that large (>3Mt) deposits are formed from composites of sulphide lenses and pods formed by multiple episodes of high temperature activity.

1.5.2 Morphologies of Seafloor Sulphide Deposits

The morphology of a seafloor deposit appears to be chiefly controlled by the nature of the hydrothermal discharge zone. The effect of sub-seafloor permeability and the development of broad alteration zones on the morphology seafloor deposits can be demonstrated by comparison of the Galapagos mounds and the Endeavour vent field. The upflow zone beneath the Galapagos mounds is up to 100m wide with several focussed fluid conduits and a large sub-seafloor stockwork zone where there is evidence for extensive shallow seawater entrainment (Emberly et al., 1988). The upflow zones of the Endeavour vent field however, are steep and narrow and the chemistry of the venting fluids implies that almost no mixing with seawater is occurring (e.g. Delaney et al., 1984; Butterfield et al., 1994). In contrast to the many coalesced, large diameter, low relief sulphide mounds of the Galapagos deposit, the Endeavour vent field is characterised by tall (up to ~45m), free standing chimney structures venting ≥350°C fluids (Emberly et al., 1988; Hannington et al., 1995a; Fouquet, 1997; Robigou et al., 1993) (Figure 1.7).

The eventual size and the stability of a seafloor massive sulphide deposit is ultimately controlled by the supply of hydrothermal fluids, this is turn is controlled by the stability of fluid conduits and local permeability, the longevity of the heat source and the style of venting at a particular site (e.g. Lowell and Rona, 1985; Krasnov et al., 1995; Fouquet, 1997) (Figure 1.8). Deeply penetrating faults that provide long term conduits for focussed hydrothermal flow, broad sub-seafloor alteration zones, extensive seawater entrainment and a wide variety of venting styles characterise the largest deposits such as TAG, Explorer Ridge and the Galapagos mounds (e.g. Hannington et al., 1998; Scott et al., 1990; Emberly et al., 1988).

1.6 Hydrothermal Plumes

1.6.1 Origin and Dispersal in the Water Column

As hydrothermal fluids discharge on to the seafloor they rise up above their source as a buoyant plume dominated by Fe oxide and oxyhydroxide particles (e.g. Edmond et al., 1982; Feely et al., 1990; Campbell, 1991; Rudnicki and Elderfield, 1993). During discharge hydrothermal fluids are rapidly diluted with ambient seawater by a factor of 10^4 to 10^5 (e.g. Baker et al., 1995; Lupton, 1995) as shear flow at the boundary between the buoyant hydrothermal fluid and bottom waters produces eddies causing turbulent entrainment of large quantities of cold, alkaline, well-oxygenated seawater into the ascending plume (e.g. Kadko, 1993; Lupton, 1995). The emanating plume will continue to rise until neutral buoyancy (or density equilibrium) is achieved typically 200-350m above the vent site, at which point, in the absence of topographic constraints, the plume is dispersed laterally as a hydrographic and chemical anomaly with a spatial scale of tens to thousands of kilometers (e.g. German et al., 1991; Lupton, 1995; Baker et al., 1995). Plumes originating from sites on the EPR, which has a shallow rift (Figure 1.9) can be traced as far as 2000km off-axis by ^{3}He and Mn anomalies (e.g. Lupton and Craig, 1981; Klinkhammer and Hudson, 1986). However, the height of plumes originating on the MAR is well below the steep sides of the deep median valley (Figure 1.9) as a result plume

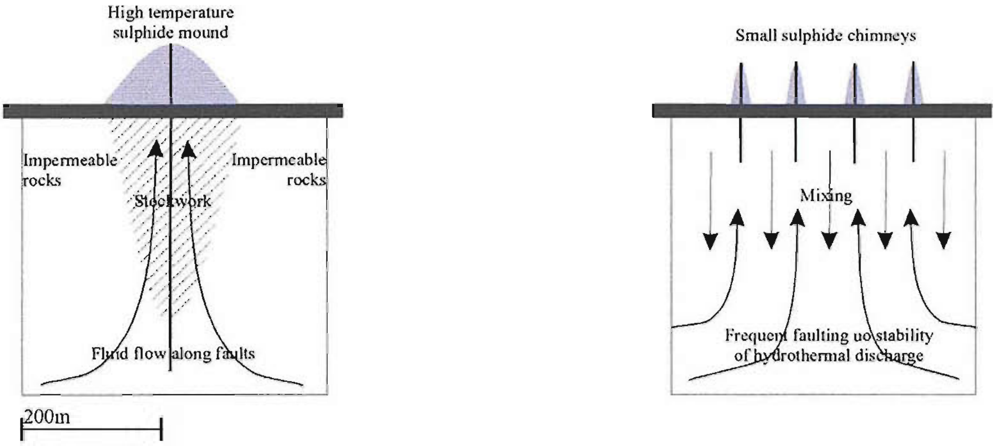

1. Focussed discharge:
significant fluid flow is only achieved along major faults. Large deposits occur where the convective cell is stable for long periods of time.
Examples: TAG & Snake Pit (MAR); off axial seamount (EPR).

2. Tectonic stage on fast spreading ridge:
High permeablity from frequent faulting and fracturing gives numerous fluid conduits. Mixing in the shallow subsurface occurs and both high and low temperature flow is observed. Deposits are numerous but very small due to perturbation in fluid flow from frequent tectonic activity.
Examples: 13°N EPR & the Southern EPR.

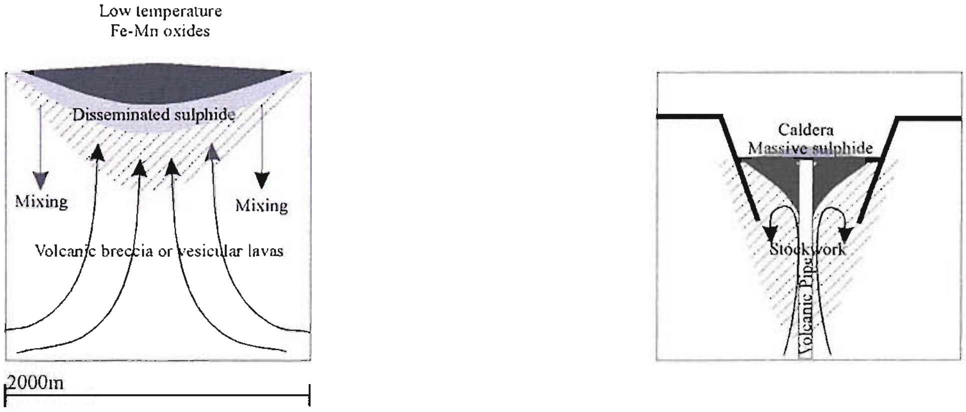

3. Diffuse discharge in permeable volcanic sequences:
Hydrothermal flow is not focussed due to high permeability of the upper crust. This situation is common in felsic volcanic environments. There are few faults at the surface but hydrothermal fluids mix with seawater trapped in the volcanic sequence. The result is low temperature Fe/Mn or Si deposits at the seafloor and disseminated sulphide in the subsurface.
Examples: Southern Lau back-arc basin.

4. Focussed flow associated with a Caldera:
Calderas are areas of high heat flow and intense fracturing providing a heat source and fluid conduit for hydrothermal discharge. Flow of this kind produces large deposits which are lens shaped.
Examples: Lucky Strike (MAR).

Figure 1.8: Factors controlling the size, morphology and stability of seafloor hydrothermal systems. 1) Focussed high temperature discharge, highly stable systems; 2) High temperature diffuse discharge and intermittent focussed discharge occuring during the tectonic stage on fast spreading ridge segments, unstable system; 3) Diffuse discharge in permeable rocks, relatively stable system but no high temperature discharge at the seafloor, massivesulphide is deposited in the subsurface; 4) Focussed high temperature flow associated with calderas, stable system. (Adapted from Fouquet, 1997).

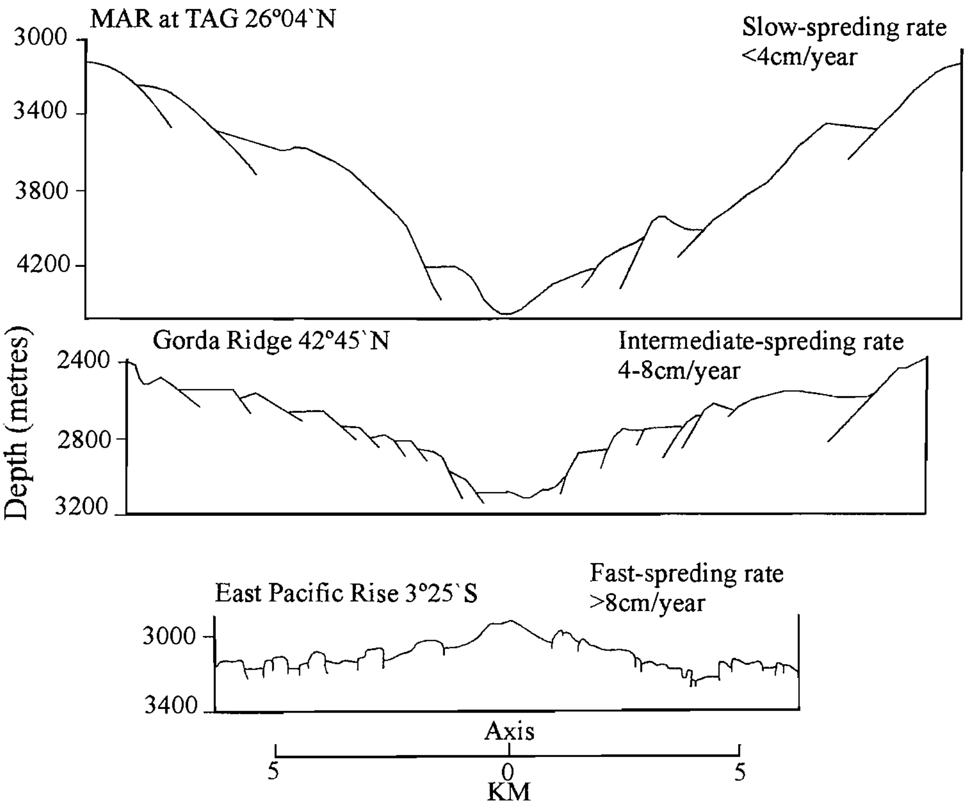

Figure 1.9: **Bathymetric profiles of slow-, intermediate-, and fast-spreading oceanic ridges. Vertical exaggeration 4:1. After Mills (1995).**

material is not dispersed throughout the Atlantic Ocean but is generally confined to the rift valley (e.g. Trefry et al., 1985; Klinkhammer et al., 1986; Trocine and Trefry, 1988; German et al., 1990).

1.6.2 Geochemistry of Hydrothermal Plumes

Plume fluids are chemically complex representing a highly diluted mixture of fluids from several different sources: the initial vent fluid; ambient seawater at the depth of neutral buoyancy; and deeper water incorporated by turbulent entrainment during plume rise (e.g. Mottl and McConachy, 1990; Rudnicki and Elderfield, 1993; Lupton, 1995). In addition, the water entrained during plume ascent is not derived from a single depth, but consists of seawater from all water column depths between the source of the fluid and the depth of neutral buoyancy (e.g. Klinkhammer et al., 1983; Feely et al., 1991; Rudnicki and Elderfield, 1993).

Whilst approximately 50% of the Fe^{2+} component in hydrothermal fluids is deposited as sulphides within the first 8m of plume rise (Feely et al., 1990; Mottl and McConachy, 1990) the remaining Fe^{2+} is rapidly oxidised and precipitated as Fe oxyhydroxide particles, which with Mn oxides and oxyhydroxides are the dominant plume phases (e.g. Campbell, 1991; Rudnicki and Elderfield, 1993). In the near field environment Fe precipitation strongly predominates over Mn precipitation. This is because Mn oxidation kinetics, and thus Mn oxide/oxyhydroxide formation, are considerably slower than Fe, as a result Mn remains in solution and is dispersed in the hydrothermal plume (e.g. Feely et al., 1990; Mottl and McConachy, 1990). These Fe and Mn oxide and oxyhydroxide particles are sites for chemical interaction and exchange with dissolved species in seawater. Uptake of dissolved trace elements by adsorption or co-precipitation with particulate hydrothermal Fe and Mn results in removal of numerous elements, including V, P, As, REE, Th, and Pb from seawater (e.g. Trefry et al., 1985; Trocine and Trefry, 1988; Trefry and Metz, 1989; Mottl and McConachy, 1990; Kadko, 1993; Rudnicki and Elderfield, 1993; James and Elderfield, 1996b). Trace element vs. particulate Fe plots indicate that there are three dominant styles of chemical behaviour in buoyant and neutrally buoyant plumes (e.g. Trocine and Trefry, 1988; Feely et al., 1990; German et al., 1991). Oxyanions such as P, V, and As all behave conservatively during co-precipitation and adsorption onto Fe oxyhydroxide particles during plume rise and dilution and show linear relationships to particulate Fe contents (e.g. Trefry and Metz, 1989; Feely et al., 1990; German et al., 1991). V, As and Cr typically exist as large oxyanions which do not readily undergo adsorption to Fe oxyhydroxides. The rapid initial uptake of these phases during early plume rise most probably reflects changes in the surface charge of Fe oxyhydroxides, in the buoyant plume. At $pH <6.7$ FeOOH has a positive surface charge (Strumm and Morgan, 1981) and as such is an efficient scavenger of anions (Ludford et al., 1996), however, as the vent fluid is diluted by seawater the pH rises ($pH \sim 7.8$), the surface charge becomes negative, and the Fe oxyhydroxides scavenge cations instead (e.g. Ludford et al., 1996). Uptake of P, V, and As by plume particles is an important removal mechanism in the marine geochemical cycles of these elements. For example, V concentrations in plume particles from both the Atlantic and Pacific suggest that hydrothermal Fe oxyhydroxides remove 10-60% of the riverine input of V to the oceans (Trefry and Metz, 1989) and P concentrations suggest that 10-30% of the riverine P input is removed (Feely et al., 1990).

More particle reactive elements including REE, and Th have element particulate Fe ratios that increase with distance from the site of active venting and exhibit non-conservative behaviour with a positive departure from simple linear correlation (e.g. German et al., 1990; German et al., 1991; Kadko, 1993; Ludford et al., 1996). The continuous uptake of these elements from seawater reflects long term adsorption and absorption processes occurring during plume rise, dilution and settling from the neutrally buoyant plume (e.g. German et al., 1990; German et al., 1991). Although the net removal of these elements during plume scavenging is not yet fully quantified it is likely to be important in oceanic geochemical cycles (e.g. Olivarez and Owen, 1989; German et al., 1990; Mottl and McConachy, 1990; Kadko, 1993).

The chalcophile elements, e.g. Cu, Zn, Co and Pb which are enriched in vent fluids, show negative deviations from simple linear correlation with particulate Fe reflecting the precipitation of these elements as sulphide phases which are then deposited in close vicinity to the vent orifice or which undergo oxidative dissolution (e.g. German et al., 1991; Rudnicki and Elderfield, 1993; Ludford et al., 1996). Plume processes are summarized in Figure 1.10.

1.6.3 Global Significance of Trace Element Scavenging

Although the cycling time for ocean water through the oceanic crust is ~3 orders of magnitude slower than the renewal time for ocean water through riverine input (e.g. Elderfield and Schultz, 1996; Palmer and Edmond, 1989) the ability of hydrothermal plumes to entrain large quantities of seawater means that hydrothermal scavenging maybe significant in the geochemical budgets of plume reactive elements (e.g. Trocine and Trefry, 1988; Olivarez and Owen, 1989; Trefry and Metz, 1989; Feely et al., 1990; German et al., 1990; Mottl and McConachy, 1990; German et al., 1991). Because each gram of plume material is associated with an effective scavenging volume (SVF), the net flux of material from a vent field can be equated to the volume of seawater with which the effluent material can interact (Kadko, 1993). Since this flux is dependant upon the scavenging efficiency for different chemical species, elements that behave conservatively in the plume will have zero effective flux, whereas elements which display non-conservative behaviour will have a large flux (Kadko, 1993). Using the SVF of the Endeavour Ridge hydrothermal site Kadko (1993) estimates a global scavenging flux of 5.7×10^{12}l/year. Given an ocean volume of 1.37×10^{12}l, and a global scavenging flux of 5.7×10^{12}l/year the entire volume of the oceans is chemically processed by hydrothermal plumes approximately every 2.4×10^{5}years (Kadko, 1993). This is ~1 order of magnitude smaller than the riverine water flux calculated from the strontium isotope budget (Palmer and Edmond, 1989).

Elderfield and Schultz (1996) however, estimate a much shorter time scale, 4-8×10^{3} years, for the cycling of ocean water through hydrothermal plumes. In this case the flux is calculated from a seawater entrainment ratio of 10^{4} at the height of neutral buoyancy. The flux estimated by Elderfield and Schultz (1996) is ~1 order of magnitude larger than the riverine flux (3-4×10^{4} years: Palmer and Edmond, 1989). This implies that the removal of large quantities of reactive trace elements during plume scavenging will have a significant effect on the geochemical cycles of these elements, and settling of plume particles and their incorporation into the underlying sediments means that these sediments act as sinks for these elements not sources (e.g. Trefry and Metz, 1989; Feely et al., 1990; Kadko, 1993; Elderfield and Schultz, 1996).

The magnitude of chemical fluxes associated with seafloor massive sulphide deposits are much less well known. For example, mineral precipitation rates calculated as a function of the heat flux at the TAG active

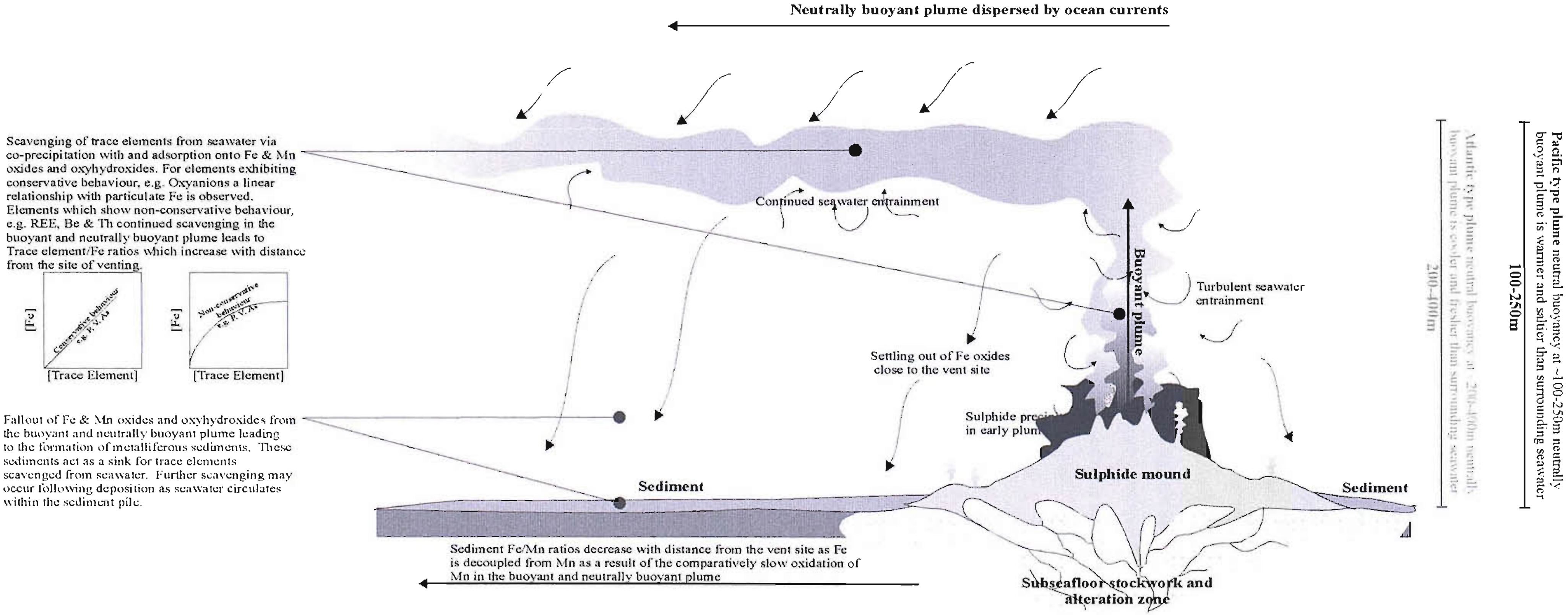

Scavenging of trace elements from seawater via co-precipitation with and adsorption onto Fe & Mn oxides and oxyhydroxides. For elements exhibiting conservative behaviour, e.g. Oxyanions a linear relationship with particulate Fe is observed. Elements which show non-conservative behaviour, e.g. REE, Be & Th continued scavenging in the buoyant and neutrally buoyant plume leads to Trace element/Fe ratios which increase with distance from the site of venting.

Fallout of Fe & Mn oxides and oxyhydroxides from the buoyant and neutrally buoyant plume leading to the formation of metalliferous sediments. These sediments act as a sink for trace elements scavenged from seawater. Further scavenging may occur following deposition as seawater circulates within the sediment pile.

Sediment Fe/Mn ratios decrease with distance from the vent site as Fe is decoupled from Mn as a result of the comparatively slow oxidation of Mn in the buoyant and neutrally buoyant plume

Figure 1.10: Schematic representation summarising basic plume processes. Note that diagram is not to scale.

mound are of the order of 10^6-10^7 kg/year for sulphide and silica and 5-15x10^7 kg/year for anhydrite (James and Elderfield, 1996a). Estimates of the mineral inventory from ODP drilling suggest that all TAG anhydrite is contemporary with the present episode of high temperature venting (<50yr: Lalou et al., 1993; Lalou et al., 1995;James and Elderfield, 1996a). This supports the interpretation that anhydrite dissolves during hydrothermally inactive periods (Humphris and Kleinrock, 1996; Hannington et al., 1998). The dissolution of anhydrite in high temperature mounds means that it is unlikely to be a significant sink for Sr, Ca and SO_4^{2-} from seawater (James and Elderfield, 1996a). In contrast, comparison of sulphide and silica precipitation rates and the mineral inventory indicates that these phases are not contemporary but represent 300-3000 years of accumulation (James and Elderfield, 1996a). The recrystallisation and redistribution of primary sulphide and silica phases during high temperature activity, and mass wasting, reworking and oxidation during periods of hydrothermal quiescence undoubtedly leads to chemical fluxes from the hydrothermal mound to seawater and to the surrounding sediment. However, because the mechanisms and reactions involved in recrystallisation, reworking and oxidation are not fully understood the magnitude of mound fluxes remain unconstrained.

1.7 Metalliferous Sediments

Metalliferous sediments comprise a complex mixture of sources. The fine-grained particulates within the buoyant and neutrally buoyant plume settle out, forming sediments dominated by Fe oxyhydroxides (e.g. Olivarez and Owen, 1989; Mills and Elderfield, 1995a; Cave et al., 2002). These sediments are the ultimate repository for many hydrothermal derived elements and the associated plume particulate scavenged sink (e.g. Trefry and Metz, 1989; Feely et al., 1990; Mills and Elderfield, 1995a). The hydrothermal component of plume derived sediments is diluted by biogenic and detrital components (e.g. Mills et al., 1993) this may be illustrated by a decrease in the (Al+Fe+Mn)/Al ratio with distance from active vents (Bostrom, 1969) (Figure 1.1). Since hydrothermal plumes may be dispersed over thousands of kilometres (e.g. Lupton and Craig, 1981; Klinkhammer and Hudson, 1986) metal enriched sediments also extend long distances off axis (Bostrom, 1969).

Erosion, mass wasting and re-sedimentation of fresh and weathered sulphides and Fe oxides from the surface of active and relict hydrothermal mounds produces metalliferous sediments around a vent complex and is a significant component of near field sediments(e.g. Metz et al., 1988; Mills et al., 1993; German et al., 1999; Severmann, 2000). Slumping and mass wasting of mound material is facilitated by mass gravitational sediment transport, fault activation and micro-earthquakes related to seafloor spreading and magma emplacement in the ocean crust (e.g. Hannington et al., 1988; Thompson et al., 1988; Mills et al., 1993; Severmann, 2000). The bulk geochemistry of these sediments is largely controlled by the mineral input and compositions (e.g. Metz et al., 1988; German et al., 1999).

Geochemical tracers allow identification of different sources, e.g. Pb and Nd isotopes have been used to trace mixing of the MORB signatures of sulphide debris with detrital sources (e.g. Dymond et al., 1973; Barrett et al., 1987; Godfrey et al., 1994; Mills and Elderfield, 1995b; German et al., 1999) and ^{230}Th and the REE have been utilised to assess the extent of seawater interaction and the contribution from hydrothermal plumes (e.g. Barrett and Jarvis, 1988; Olivarez and Owen, 1989; Mills and Elderfield, 1995b). A number of studies have utilised these and other geochemical tracers (e.g. Metz et al., 1988; Shimmield and Price, 1988; Mills et al.,

1993) to identify and quantify plume vs. mass wasting vs. pelagic and detrital inputs to metalliferous sediments (Figure 1.11). For example, Dymond (1981) proposed a five component model to explain sources of material to metal-rich sediments from the southeast Pacific Ocean. This multi-variant analysis estimates the percentages of the following components: detrital aluminosilicates; hydrothermal precipitates; biogenic tests; hydrogenous ferromanganese precipitates; and the insoluble residue of organisms (Dymond, 1981). Various elements were chosen as indicators of end member inputs, e.g. Fe was assigned to a hydrothermal source. This approach was also utilised for sediments from the Galapagos Rift and the EPR (Walter and Stoffers, 1985). However, identification of the sources to sediments by this type of analysis requires a large dataset with good spatial coverage.

A simpler three component mixing model for identification of sources to a metalliferous sediment core from the TAG field was designed by Metz et al. (1988). In this case the proposed components are biogenic ($CaCO_3$%), detrital (10xAl%) and a hydrothermal component calculated by difference. The excellent linear correlation of this independently calculated hydrothermal component and Fe contents (r^2=0.92) in the Metz et al. (1988) core justifies the use of this mixing model as an index of hydrothermal sedimentary inputs (Metz et al., 1988; Mills et al., 1993). Figure 1.11 summaries sources to deep-sea metalliferous sediments.

1.8 Post Depositional Processes in Near Field Sediments

Detailed investigations of the metalliferous sediments surrounding vent sites have revealed that primary phases are subject to physical and chemical change over time (e.g. Barrett et al., 1987; Metz et al., 1988; Hannington, 1993; Mills et al., 1996; German et al., 1999; Severmann, 2000; Severmann et al., 2004; Severmann et al., in review). Physical changes include dissolution of primary phases and secondary mineralisation. Chemical changes include alteration of sulphide material which leads to remobilisation of metals and fluxes of material both to and from seawater.

Near field sediments are enriched in the chalcophile elements since these elements are precipitated as sulphides within the first few meters of plume rise and are therefore deposited in close proximity to vent sites (e.g. Haymon and Kastner, 1981; Haymon, 1983; Barrett et al., 1987; Metz et al., 1988; German et al., 1993; Zierenberg et al., 1993; German et al., 1999). For example, samples of near field sediments from the TAG field have Fe contents up to ~40%, Cu contents typically ~0.5-3.5% and Zn contents of ~350-20000ppm (e.g. Metz et al., 1988; Mills et al., 1993; Severmann, 2000). Samples of near field sediments from 19°S on the EPR show a similar trend of enrichment: Fe 25-39%, Cu 0.1-0.5%, and Zn 500-1000ppm (e.g. Barrett et al., 1987). Whilst near field metal concentrations are largely controlled by the sulphide mineralogy, re-mobilisation of base metals during diagenesis accounts for some of this enrichment (Barrett et al., 1987; Hannington et al., 1988; Hannington et al., 1995b; Severmann, 2000; Severmann et al., in review). Diagenetic re-mobilisation appears to be particularly important for base metals which are redox and pH sensitive. For example, Zn and Pb in a core from the TAG area show diffusion out of sulphide-rich, mass wasted layers, whereas Cu is retained in the sulphide layers, presumably as a result of pH gradients which are driven by the acidity produced during oxidative dissolution of sulphide phases (e.g. Severmann et al., in review).

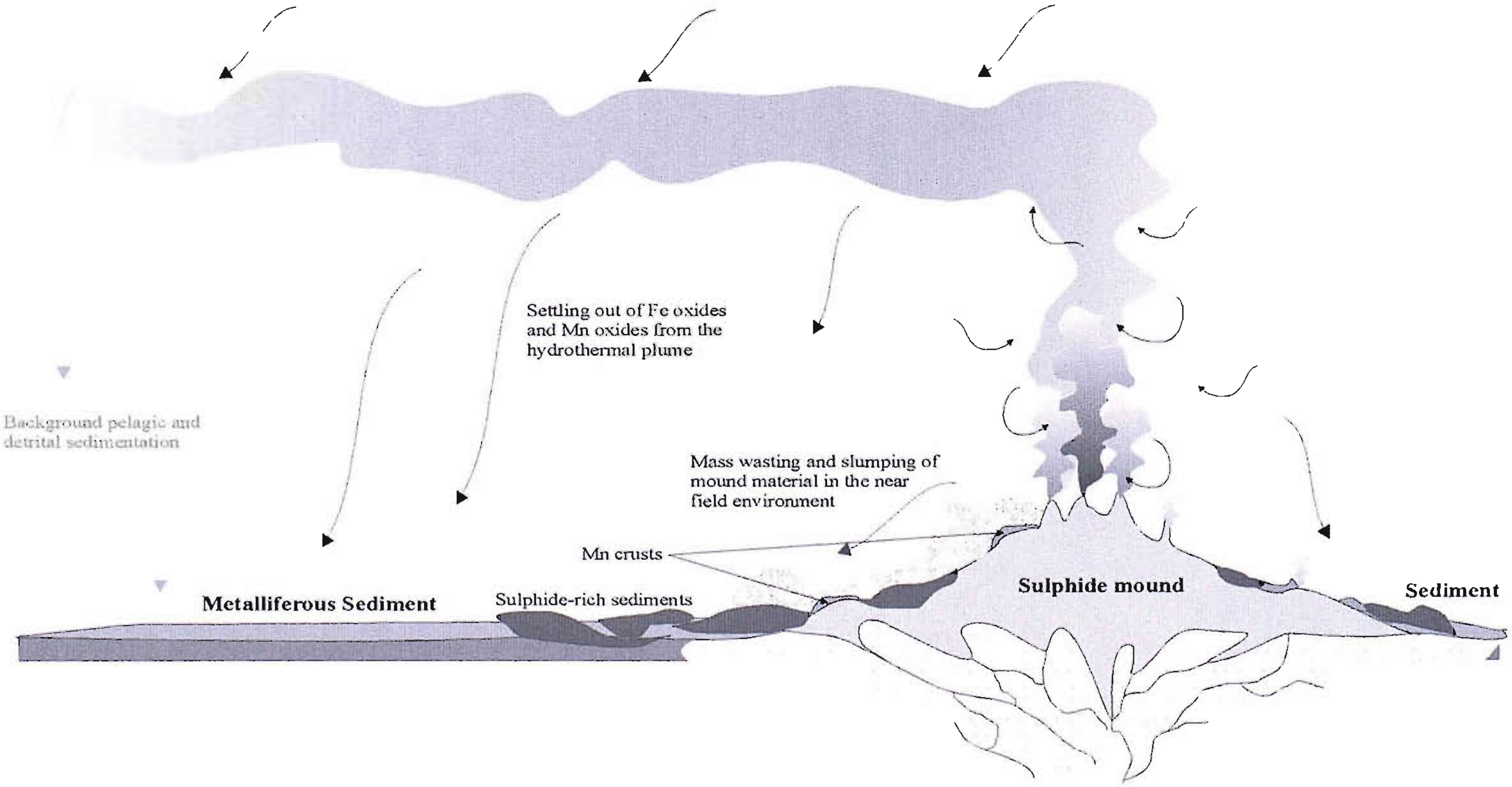

Figure 1.11: Schematic summary of the principal sources to hydrothermal metalliferous sediments. Note that diagram is not to scale.

1.8.1 Sulphide Alteration

Mound models suggest that the initial alteration of primary phases is contemporaneous with high temperature venting as seawater entrained into the mound mixes with hydrothermal fluid and circulates recrystallising and redistributing primary mineral phases (e.g. Humphris et al., 1995; Fouquet et al., 1993a; Langmuir et al., 1997). For example, ODP drilling of the active TAG mound showed zones of enrichment in Cu, Zn and Au which can be attributed to zone refining processes driven by subsurface circulation of mixed fluids and variable pH and E_h conditions within time and space (e.g. Edmond et al., 1995; Tivey et al., 1995; Hannington et al., 1998; Knott et al., 1998). During hydrothermally inactive periods, modification of primary material continues as circulation of seawater and low temperature fluids within sulphide mounds and near field sediments persists (e.g. Hannington and Jonasson, 1992; Humphris et al., 1995; Tivey et al., 1995; Humphris and Kleinrock, 1996; Mills et al., 1996; Severmann et al., 2004).

The dissolution of primary sulphide phases, which are thermodynamically unstable in oxidising seawater, in general terms can be written as:

$$MS + 4H_2O \leftrightarrow M^{2+} + SO_4^{\ 2-} + 8H^+ + 8e^- \qquad (1.11)$$

where MS denotes any metal sulphide. The metal ions released will then form complexes with anions including SO_4^{2-}, Cl^-, F^-, HCO_3^- (minor at low pH) (Thornber, 1985). Since pyrite is the most abundant sulphide in these deposits the dissolution of primary sulphide is dominated by the oxidation of pyrite to Fe oxyhydroxide with the overall reaction:

$$4FeS_2 + 15O_2 + 10H_2O \leftrightarrow \underbrace{\underset{goethite}{4FeO(OH)}}_{+/-hematite(Fe_2O_3)} + 8SO_4^{\ 2-} + 16H^+ \qquad (1.12)$$

This leads to the production of acidic pore fluids which are important in the remineralisation of primary Cu and Zn phases (e.g. Thornber, 1985; Hannington et al., 1988; Mills et al., 1996; Severmann et al., in review;). For example, the Cu^{2+} ions released during dissolution of primary chalcopyrite form cuprous chloride complexes such as $CuCl_3^{2-}$ (e.g. Rose, 1976; Thornber, 1985; Hannington, 1993). Where the solutions carrying such complexes are exposed to ambient seawater, basic Cu salts such as atacamite are precipitated (e.g. Emberly et al., 1988; Hannington, 1993). Remobilisation and enrichment of other metals including Au, Ag, Sb, Pb, Cd may also be attributed to the generation of acidic pore fluids (e.g. Hannington et al., 1988; Herzig et al., 1991; Tivey et al., 1995).

During mass wasting events primary, partially altered and secondary phases are transported to the near field sediments and are intermixed with material derived from plume fallout and background pelagic sedimentation. The above processes of oxidative decay of sulphide, and the remobilisation and remineralisation of base metals, continues within the sediment pile. Over time this may lead to complete oxidation to Fe oxide. Several authors have likened sulphide alteration within metalliferous sediments to sub-aerial supergene processes (e.g. Hannington et al., 1988; Herzig et al., 1991) However, sulphide alteration processes and the ultimate fate of the chalcophile elements in these deposits are largely unknown. Whilst sulphide dissolution in sub-marine and sub-aerial systems is likely to be similar, secondary mineralisation and alteration processes may be significantly different. Sulphide alteration mechanisms, secondary mineralisation in the sediment pile and the validity of comparisons of seafloor processes with terrestrial supergene processes are discussed in detail in Chapter 4: Sulphide Mineralogy and Alteration.

1.8.2 Interaction with Low Temperature Fluids

Diffuse low temperature venting and fluid flow through hydrothermal sediments plays an important role in the heat and chemical fluxes of a hydrothermal system. Indeed diffuse and low temperature flow commonly accounts for more of the heat flux at a vent site than focussed high temperature venting (e.g. Rona and Trivett, 1992; Rudnicki and Elderfield, 1993; Schultz et al., 1996). The low temperature of these fluids, typically <10-50°C, means that they are not able to transport significant concentrations of dissolved metals and sulphur, however they may be responsible for a considerable proportion of amorphous Fe oxyhydroxide, Fe oxide, Mn oxide, authigenic clay and amorphous silica precipitation (e.g. Alt, 1988b; Hannington and Jonasson, 1992). These low temperature fluids are inferred to be cooled mixtures of end member hydrothermal fluid and seawater (e.g. Edmond et al., 1979a; Alt, 1988b; Hannington and Jonasson, 1992; Mills et al., 1996; Severmann et al., 2004). For example, mass balance calculations from pore water compositions suggest that end member hydrothermal fluids contribute 15-18% to the diffuse fluids at the active TAG mound (Mills et al., 1996). Depending on the rate of mixing, the proportion of hydrothermal fluid to seawater and the Fe/H_2S ratio the resultant, mixed low temperature fluid will be rich in either some or all of the following; Si, Mn and Fe. Subsurface precipitation of Si and Fe during mixing in the mineralised stockwork zone has an effect on the chemistry of the low temperature fluid (e.g. Alt, 1988b; Mills et al., 1996). For example, for end member hydrothermal fluids with Fe/H_2S ratios <1 Fe is essentially quantitatively removed from the fluid as sulphide during subsurface mixing; this produces evolved fluids which are Mn-rich (Edmond et al., 1979a; Alt, 1988b). However, if the Fe/H_2S ratio of the end member hydrothermal fluid is >1, excess Fe remains in solution following subsurface sulphide precipitation; this produces evolved fluids which are Fe-rich or both Fe- & Mn-rich (Edmond et al., 1979a; Alt, 1988b).

The precipitation in near field sediments of various phases from these low temperature fluids, principally Si, Fe and Mn oxides and oxyhydroxides and authigenic clays, (most commonly nontronite: e.g. Alt, 1988b; Thompson et al., 1985; Hekinian et al., 1993; Severmann et al., 2004) is dependant upon the prevalent redox conditions. For example, nontronite forms by reaction of poorly crystalline Fe oxyhydroxide in low E_h conditions where Fe^{2+} and Si are in solution (Harder, 1976). Where E_h is higher and Fe^{3+} is in solution goethite will form instead (Singer and Stoffers, 1987). Because Fe can be precipitated in slightly reducing conditions it is decoupled from Mn, the Mn is then either transported further in the fluid phase, or is deposited in the more oxic conditions at the sediment surface forming Mn crusts (e.g. Alt, 1988b; Thompson et al., 1985; Goulding et al., 1998). The Mn concentration of seawater is ~037nM; Mn concentrations of vent fluids however, fall in the range of 360-1140µmol/kg (Table 1.1) (Elderfield and Schultz, 1996). Whilst the vast majority of hydrothermal Mn is deposited in distal sediments, at the TAG site there is also evidence for near field hydrothermal Mn precipitation. This near field Mn precipitation is related to low temperature venting and diffuse flow away from the locus of high temperature activity (e.g. Thompson et al., 1985; Mills et al., 2001).

Whilst some Si is removed from the low temperature fluid during nontronite precipitation there is also evidence, at some sites, for late stage amorphous Si precipitation and silicification of Fe-rich metalliferous sediments (e.g. Alt, 1988b; Hannington and Jonasson, 1992; Magenheim and Gieskes, 1992; Mills and Elderfield, 1995a). For example, silicification of Fe-rich metalliferous sediments at the TAG site has produced distinctive red cherts (Hannington and Jonasson, 1992) and at the Guaymas Basin site authigenic, amorphous, hydrothermal Si phases are precipitated in the sediment pile (Magenheim and Gieskes, 1992). At the Guaymas Basin, the precipitation of amorphous Si is the ultimate control on the permeability of the sediments during low temperature flow (Magenheim and Gieskes, 1992). Most near field hydrothermal sediments contain a mixture of nontronite, Fe and Mn oxides and oxyhydroxides and Si phases and Mn-oxide-Fe-oxide-nontronite assemblages are widely observed (e.g. Barrett and Friedrichsen, 1982; Singer et al., 1984; Mills et al., 1996; Goulding et al., 1998). These sequences reflect (a) precipitation of nontronite and amorphous phases under slightly reducing conditions within the sediment pile; (b) Fe and Mn oxide precipitation in more oxic conditions typically close to or at the surface of the sediments; and (c) changes in porosity and redox conditions in space and time.

1.8.3 The role of micro-organisms

Seafloor hydrothermal environments are host to unique ecosystems where primary biomass is dominated by chemolithoautotrophic micro-organisms (e.g. Jannasch and Mottl, 1985; Edwards et al., 2003a). The large enrichment of transition metals and the existence of sharp redox, pH and temperature gradients observed in near field hydrothermal sediments, provides the conditions required for microbial activity which is thought to play a role in the formation of hydrothermal Fe-oxide deposits and in the production of seafloor gossans (e.g. Alt et al., 1987; Juniper and Fouquet, 1988; Hannington and Jonasson, 1992; Juniper and Sarrazin, 1995; Emerson and Moyer, 2002; Edwards et al., 2003a; Edwards et al., 2003b; Edwards et al., 2003c). While microbial populations are ubiquitous in deep-sea sediments (Parkes et al., 2000) their in situ metabolic activity and their influence on reaction mechanisms are poorly constrained (e.g. D'Hondt et al., 2002; Edwards et al., 2003b; Edwards et al., 2003c). In most deep-sea sediments organic carbon is the main electron donor (e.g. Sorensen et al., 1981) however, experimental evidence suggests that some Fe oxidising bacteria utilise CO_2 instead (e.g. Walsh and Mitchell, 1972; Balashova et al., 1974; Ehrlich, 1981). In near field sediments reduced sulphur compounds, Fe^{2+}, Mn^{2+}, H_2 and CH_4 are also available and may be utilised as electron donors with metal oxides acting as electron acceptors (e.g. Jannasch and Mottl, 1985; McCollom and Shock, 1997). To date, most microbial studies at vent sites have focussed on chemosynthetic bacteria which gain energy from these reduced, dissolved chemical species (e.g. Jannasch and Mottl, 1985; Wirsen et al., 1986; McCollom and Shock, 1997) however, a few studies have investigated microbial utilisation of the abundant metal sulphides and oxides in hydrothermal deposits as a metabolic substrate (e.g. Wirsen et al., 1993; Emerson and Moyer, 2002; Edwards et al., 2003b).

Fe-oxidising microbes are capable of influencing the growth and dissolution of a number of minerals by exerting controls over reaction kinetics and pathways and as such maybe important in sulphide oxidation and Fe^{3+} precipitation. Extensive sampling of hydrothermal vent sites over the last few decades has led to many observations of Fe oxide and silicified filamentous textures in low temperature Fe oxide-rich deposits adjacent to high temperature vent sites, a significant number of these are from seamounts where diffuse low temperature flow is the dominant venting style (e.g. Alt, 1988b; Juniper and Fouquet, 1988; Al-Hanbali and Holm, 2002; Kohler et al., 1994; Edwards et al., 2003b). These textures are very similar to structures formed by neutrophilic Fe-oxidising bacteria including *Gallionella ferruginea* which grows Fe encrusted stalks (e.g. Hanert, 1973; Hanert, 2002) and *Leptothrix ochracea* which forms Fe oxide sheaths (e.g. Emerson and Revsbech, 1994), although neither of these taxa have been conclusively identified (by culture or molecular analysis) from marine hydrothermal Fe oxide deposits.

In addition to enzymatic metabolic interactions, templating of microbes through passive and/or active sorption of inorganic ions to the cell surface, promoting mineral nucleation, appears to be important for preservation of microbial structures at seafloor hydrothermal sites. Templating arises from passive or active uptake of inorganic ion species into or onto the cell which are then converted to oxides and salts for cellular protection (e.g. Ehrlich, 1996b). Once Fe oxides have formed they provide nucleation sites for further precipitation (e.g. Ghiorse, 1984; Ehrlich, 1996b). In addition to Fe oxides, microbial templating by Si and clay phases may occur. Most hydrothermal Fe oxide deposits are intermixed with clay minerals such as nontronite which form in the suboxic conditions associated with sulphide weathering (e.g. Singer et al., 1984; Alt, 1988b; Severmann et al., 2004). The nontronite is often intimately associated with Fe oxide filaments (e.g. Alt, 1988b), and nontronite filaments, tubes and sheaths have been observed in white smoker chimneys (e.g. Kohler et al., 1994). This bio-mineralisation is inferred to arise from templating of the clays around the biogenic structure (Kohler et al., 1994). In addition, oxygen isotope thermometry on separated nontronites suggests formation temperatures of ~50-92°C, which coincide with the optimum temperatures for meso and thermophilic bacteria (Severmann et al., 2004; Severmann et al., in review).

The extent to which precipitation and mediation of iron, silica and clay minerals is the result of the metabolic activity of the bacteria, or a more passive process where the functional groups on the bacterial surfaces react with positively charged ions is unclear (e.g. Banfield et al., 2000; Glasauer et al., 2001; Emerson and Moyer, 2002; Kennedy et al., 2003a; Kennedy et al., 2003b; Kennedy et al., 2003c). In addition, the role of microbes in Fe oxidation and other diagenetic processes at vent sites has not been quantified. Although several studies have suggested that microbes play an important role in Fe oxide production and sulphide dissolution (e.g. Alt et al., 1987; Juniper and Fouquet, 1988; Hannington and Jonasson, 1992; Wirsen et al., 1993; Emerson and Moyer, 2002; Edwards et al., 2003a), filamentous Fe oxides make up only a small percentage of Fe oxide at any particular site (e.g. Little et al., 2004). In addition, a recent study by Severmann et al. (in review) suggests that the role of bacteria in the weathering of seafloor deposits is only important in the upper portions of these deposits that are directly exposed to circumneutral pH conditions and seawater. Whilst Bach and Edwards (2003) estimate that the oxidation of Fe^{2+} and sulphide in the oceanic crust could sustain a bacterial population of up to 48×10^{10}g cellular carbon/year, the findings of Severmann et al. (in review) suggest that this number is over estimated as Fe^{2+} oxidation is likely to restrict chemolithoautotrophic biomass to the upper ocean crust where the circulating fluids are at circumneutral pH. Fe oxidation and bio-mineralisation processes in near field hydrothermal sediments are investigated in detail in Chapter 6: Fe oxidation and bio-mineralisation in metalliferous sediments from the *Alvin* relict high temperature zone.

1.9 Aims and Objectives of this Thesis

This study focuses on two metalliferous sediment cores from the *Alvin* and *Mir* relict high temperature zones of the TAG hydrothermal field. Previous studies at the TAG site have focused on growth of the active mound (e.g. ODP drilling leg 158 Scientific results; Tivey et al., 1995; Humphris and Kleinrock, 1996); the production of sulphide sediments (e.g. Thompson et al., 1985; Metz et al., 1988; Mills, 1995); plume derived sedimentation and the impact of seawater scavenging at this site (e.g. German et al., 1991; German et al., 1993; Mills et al., 1993); and quantification of various sources to the sediments (e.g. Metz et al., 1988; Mills et al., 1993). Other research has considered sulphide alteration and supergene enrichment (e.g. Hannington et al., 1988; Herzig et al., 1991; Hannington, 1993); the interaction of bacteria with, and their role in modification of metal-rich sediments (e.g. Wirsen et al., 1993; Severmann et al., in review); and the importance of low temperature diffuse fluids in the alteration of metal-rich deposits (e.g. Mills et al., 1996; Severmann et al., 2004). In addition, comparisons have been made between the TAG deposits and terrestrial ophiolite sequences e.g. the Troodos Ophiolite (e.g. Herzig et al., 1991; Goulding et al., 1998; Hannington et al., 1998).

Although post-depositional and post-venting, diagenetic processes associated with low temperature fluid flow have been investigated (e.g. Mills et al., 1996; Severmann, 2000; Severmann et al., 2004; Severmann et al., in review) almost without exception the work on TAG sediments has focused on the bulk geochemistry (e.g. Metz et al., 1988; German et al., 1993). Whilst a few studies have considered the impact of diagenetic alteration with respect to some specific mineral phases (e.g. clays: e.g. Severmann et al., 2004; Fe-Mn oxides: e.g. Thompson et al., 1985; Mills et al., 2001; atacamite: Hannington, 1993) there has been little investigation of full mineral assemblages in conjunction with bulk geochemistry. Since the bulk geochemistry of near field sediments is largely controlled by the mineral composition (e.g. Metz et al., 1988; German et al., 1999) a full understanding of sediment genesis and evolution can only be achieved by combined petrological and geochemical studies. This study is the first to systematically investigate the mineralogy of hydrothermal metalliferous sediment cores from the TAG hydrothermal field.

The specific objectives of this study are:

1. To identify mineral sources to near field sediments and to relate the bulk geochemistry to the mineralogical assemblage
2. To identify the sequence of sulphide paragenesis, mineral scale alteration processes and the fate of sulphide material during seafloor weathering
3. To assess the role of microbes in Fe oxidation and to estimate the physiochemical conditions under which this alteration occurs
4. To evaluate the validity of comparisons of seafloor alteration and enrichment mechanisms with terrestrial supergene processes

Chapter 2: Geological Setting and sampling the TAG hydrothermal field

This chapter describes, in detail, the geology of the TAG hydrothermal field and the nature of hydrothermal fluid flow and venting at this site. The sampling strategy and the core locations for this study are given and set in the context of previous sediment studies at this site.

Chapter 3: General Sediment Geochemistry and Mineralogy

This chapter outlines sediment formation and diagenetic alteration processes identified from synthesis of geochemical and petrological data.

Chapter 4: Sulphide Mineralogy and Alteration

Although several authors liken sulphide alteration and metal enrichment in hydrothermal deposits to terrestrial supergene processes (e.g. Hannington et al., 1988; Herzig et al., 1991; Hannington, 1993) there has been no systematic study of sulphide alteration within near field sediments. This chapter focuses on the sulphide-rich layer of each core and identifies paragenetic sequences, formation and sediment emplacement histories, alteration processes and reaction pathways during diagenesis, the validity of comparisons of seafloor processes with terrestrial supergene processes are then evaluated.

Chapter 5: S Isotope Variation of Sulphide-Rich Sediments from the Alvin and Mir Relict High Temperature Zones.

Sulphur isotope systematics have been shown to be a useful tool in the understanding of the complex paragenetic sequences of sulphide precipitation and alteration at hydrothermal sites (e.g. Alt, 1988a; Woodruff and Shanks, 1988; Herzig et al., 1998a; Knott et al., 1998). This chapter investigates mineral scale S isotope variation of diagenetically altered, mass wasted sulphide, from the relict *Alvin* and *Mir* zones and compares S isotope variations with paragenetic sequences identified in Chapter 4 in order to identify sulphide precipitation and dissolution mechanisms during the evolution of the deposit.

Chapter 6: Fe oxidation and bio-mineralisation in metalliferous sediments from the Alvin relict high temperature zone.

This chapter investigates Fe-oxide filaments and associated minerals in hydrothermal sediments from the *Alvin* relict high temperature zone at TAG and examines their relationship to, and impact on sediment diagenesis with an aim to discriminate between abiogenic and biogenic formation processes.

Chapter 7: Conclusions

This chapter syntheses the findings of chapters 3-6 and considers the wider implications of these findings for future studies of near field hydrothermal sediments.

Chapter 2:

Geological Setting and Sampling: The TAG Hydrothermal Field

The TAG system is one of the largest known active hydrothermal fields on the seafloor. Since the first discovery of hydrothermal activity at 26°N on the Mid-Atlantic Ridge (MAR) during the early 1970's by the NOAA Trans-Atlantic Geotraverse (TAG) project the active TAG system has been the subject of extensive multidisciplinary studies and is perhaps the most documented seafloor hydrothermal site and is also the most similar to the cuprous deposits associated with ophiolite VMS deposits. As a result processes occurring in the active mound are reasonably well understood (e.g. Tivey et al., 1995; Humphris and Kleinrock, 1996; Herzig et al., 1998b; Fouquet et al., 1998; Knott et al., 1998); the chemistry and temperatures of the currently venting fluids at the active TAG mound have been well characterised (e.g. Elderfield et al., 1993; Edmond et al., 1995; Edmonds et al., 1996; Gamo et al., 1996; James and Elderfield, 1996a); and the deposition and alteration of near-vent sediments have been extensively documented (e.g. Shearme et al., 1983; German et al., 1993; Thompson et al., 1988; Mills et al., 1996; Goulding et al., 1997; Severmann et al., 2004).

The TAG field occupies an area of ~25km^2 ~2.5km east of the ridge axis at 26°N, in the centre of a 40km long segment trending north-north-east bounded by non-transform discontinuities on the eastern wall of the rift valley (Rona et al., 1986; Purdy et al., 1990). The segment is spreading asymmetrically at half rates of 1.1cm yr^{-1} to the west and 1.3cm yr^{-1} to the east (McGregor et al., 1977). Assuming linear spreading rates the TAG field lies on crust which is ~190Ka. The TAG field comprises an active high temperature sulphide mound at 26°08'N in a water depth of ~3620m (Rona et al., 1986), and two relict high temperature zones that occur between 3400 and 3500m water depth and 2 to 3km north and northeast of the active mound: the *Alvin* and *Mir* zones respectively (Rona et al., 1986; Rona et al., 1993a; Rona et al., 1993b) (Figure 2.1). A region of low temperature hydrothermal Mn + Fe oxide and nontronite mineralisation occurs near the base of the eastern rift valley wall 3.7km upslope of the active mound (Rona et al., 1993b). Chemical and physical parameters indicate that diffuse low temperature flow occurs in this area (e.g. Scott et al., 1974; Rona et al., 1975; Jenkins et al., 1980; Thompson et al., 1985) and the formation of Mn crusts can be attributed to a combination of direct precipitation from these low temperature diffuse fluids and contributions from Mn-rich plume particles (Scott et al., 1974; Mills et al., 2001).

2.1 The Active TAG mound

The presently active TAG mound is situated ~1.5-2km east of the ridge axis close to the juncture between the rift valley floor and the eastern wall, (Rona et al., 1986) at the edge of a volcanic dome ~500m in diameter (Rona et al., 1993b). This region is cross cut by ridge parallel (NNE) and obliquely oriented (ENE) faults and fissures that are interpreted to provide the pathways for focussed hydrothermal upflow (Kleinrock and Humphris, 1996). The mound is a roughly circular feature ~200m in diameter and 50m high, composed of

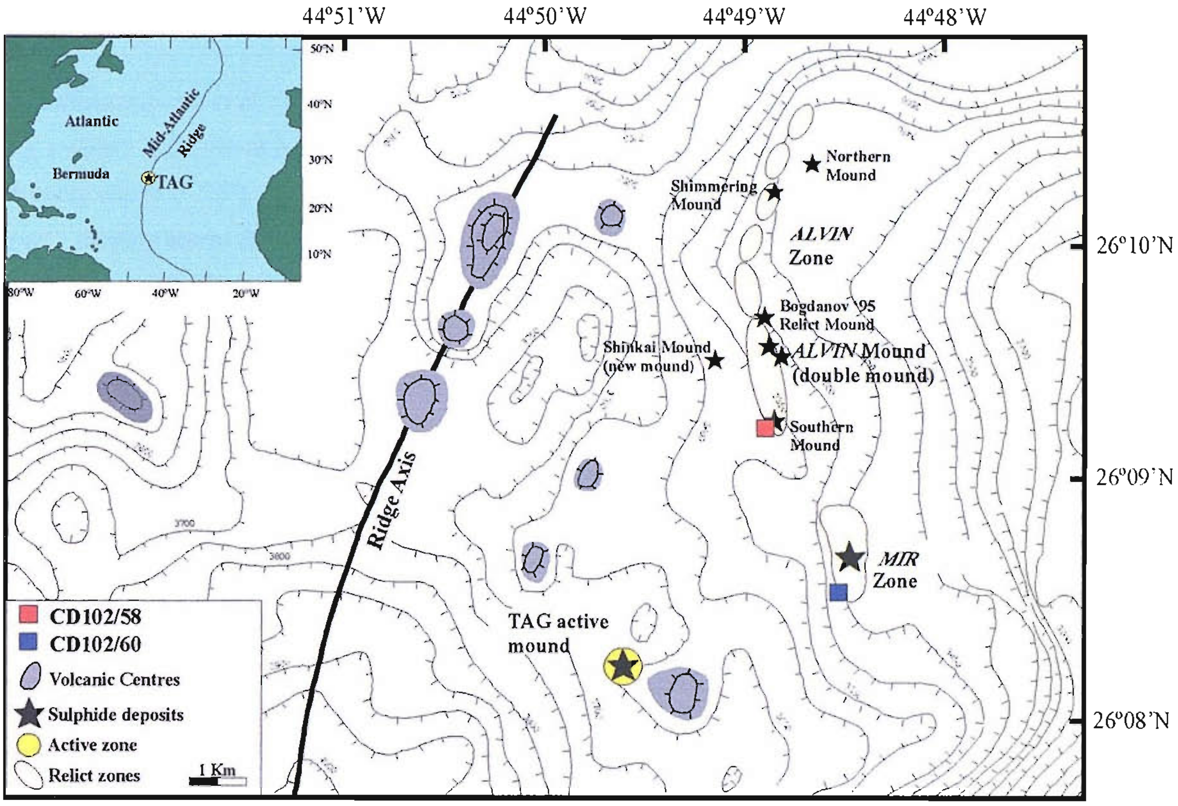

Figure 2.1: SeaBeam bathymetry of the TAG hydrothermal field showing the locations of the active high temperature mound and the *Alvin* and *Mir* relict high temperature zones . Adapted from Rona et al. (1993) and White et al. (1998).

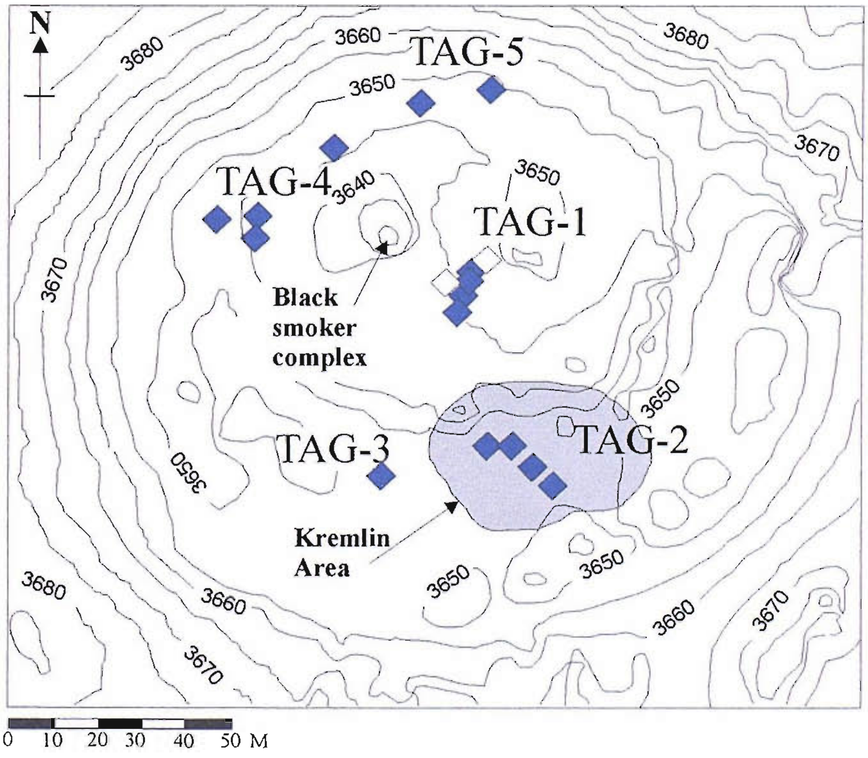

Figure 2.2: High resolution bathymetry of the active TAG mound (5 m isobaths). Diamonds indicate locations of drill holes from five areas referred to as TAG-1 through to TAG-5: solid diamonds denote holes with successful recovery; hollow diamonds indicate holes with no recovery. Grey shading marks the extent of the Kremlin Area, where white smoker fluids are discharged. Adapted from Knott et al. (1998).

two distinct platforms (Rona et al., 1986; Humphris and Kleinrock, 1996). The lower platform is ~150m in diameter; the southern and eastern edges lie at ~3670m water depth and are characterised by moderate to shallowly dipping scarps (< 25°), the northern and western sides lie at ≥ 3680m water depth and are typified by more steeply dipping scarps (35-45°) (Humphris and Kleinrock, 1996). The change in seafloor depth is interpreted to be the result of sub-surface faulting beneath the mound (Humphris and Kleinrock, 1996). This is supported by gravity data that show the thickness of massive sulphide decreasing from 50m in the northern portion of the mound to ~10m in the southern portion (Evans, 1996). The upper platform, ~90m in diameter at ~3650m water depth, is asymmetrically superimposed on the NNW portion of the lower platform. Whilst the transition between the platforms on the northern side is obscured by a steep scarp that extends from 3700-3650m water depth, the transition at the southern side is delineated by 5m high scarps.

U-series dating suggests that hydrothermal activity began ~50Kya (Lalou et al., 1995). Subsequent activity at the TAG mound has been sporadic with high temperature events approximately every 5Ka, the current episode of high temperature venting commenced ~80 years ago after a hiatus of about 4Ka (Lalou et al., 1990; Lalou et al., 1993; You and Bickle, 1998).

There are three principal venting styles at the TAG mound: high temperature black smokers, white smokers and diffuse low temperature flow (Figure 2.3). Although diffuse low temperature (<50°C) fluids emanate from both platforms and percolate through the sides of the mound as well as through the surrounding talus and sediments (e.g. Humphris and Kleinrock, 1996; Tivey et al., 1995), high temperature activity is highly localised. High temperature fluids (363 ±3°C) (Edmond et al., 1995) are vigorously discharged through a cluster of pyrite-chalcopyrite-anhydrite chimneys (up to 15m high: Tivey et al., 1995) situated on a cone structure (20-30m diameter by 10-15m high) located 25m NW of the centre of the upper platform: the black smoker complex (BSC) (Figure 2.2) (Rona et al., 1986; Thompson et al., 1988; Tivey et al., 1995; Humphris and Kleinrock, 1996). These high temperature fluids are acidic (~pH 3.3) and have high H_2S (3 ±0.5mmol/l) and base metal concentrations (Fe ~5500µmol/l; Cu ~150µmol/l; Zn ~45µmol/l) (Edmond et al., 1995; Edmonds et al., 1996; Gamo et al., 1996). As the hydrothermal fluid is vented, mixing with ambient seawater occurs and sulphides are precipitated, contributing to a particle laden, buoyant plume that obscures the summit of the BSC (Humphris and Kleinrock, 1996).

Lower temperature fluids (260-300°C: Edmond et al., 1995) are discharged from smaller (1-2m high), white smoker, sphalerite-rich chimneys with minor amorphous silica and marcasite or pyrite (Thompson et al., 1988; Tivey et al., 1995) located in the SE portion of the lower platform (Humphris and Kleinrock, 1996): the Kremlin Area (e.g. Thompson et al., 1988). The white smoker fluids are also acidic (~pH 3) but are severely depleted with respect to H_2S (~0.5mmol/l), Fe (~3800µmol/l) and Cu (~3µmol/l). Zn (300-400µmol/l) concentrations however, are greatly increased (Edmond et al., 1995; Edmonds et al., 1996; Gamo et al., 1996). Differences in the fluid chemistries of the black and white smokers reflect the evolution of the end member hydrothermal fluid by conductive cooling and mixing with locally entrained seawater and concomitant mineral precipitation. The temperature and Mg values of white smoker fluids indicate addition of 15-20% seawater. Entrainment of seawater and precipitation of Fe sulphide within the mound causes a drop in temperature and pH promoting large-scale remobilisation of Zn. This results in an order of magnitude

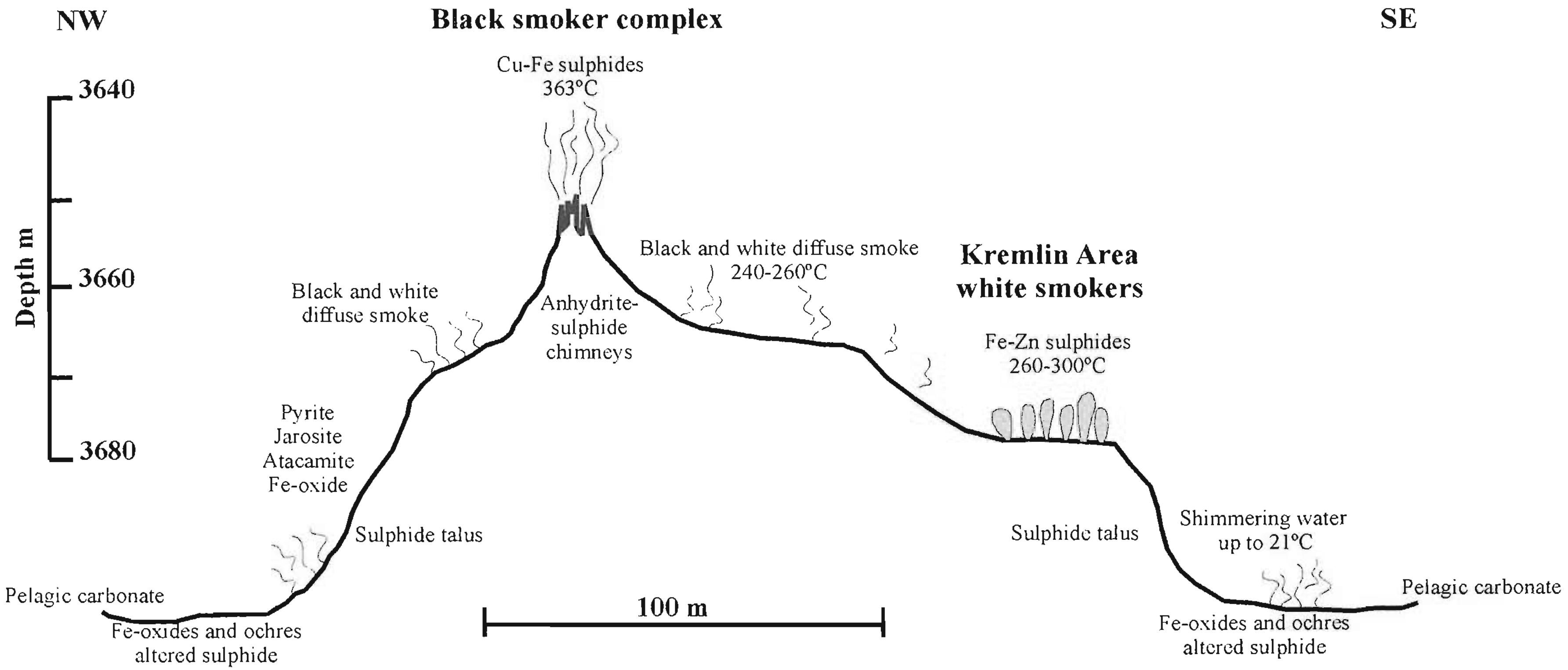

Figure 2.3: Schematic cross section through the TAG mound showing venting and deposit styles (adapted from Mills, 1995). High temperature black smoker fluids are vigorously discharged through a cone structure in the north-west of the upper platform. Lower temperature white smoker fluids are vented through small (1-2 m high) bulbous dome shaped structures in the south-east of the lower platform. Diffuse low temperature fluids percolate and are discharged through both platforms, the sides of the mound and through the surrounding talus. The mound is surrounded by an apron (~100 m in diameter) of sulphide talus, metalliferous sediment and pelagic carbonate.

increase in Zn concentrations in white smoker fluids over black smoker fluids (Tivey et al., 1995; Edmond et al., 1995; Edmonds et al., 1996).

Diffuse fluids at the TAG mound are also produced by mixing of hydrothermal fluids with seawater; deviations from ideal mixing lines can be attributed to mineral precipitation and dissolution within the mound (e.g. James and Elderfield, 1996a). These fluids play an important role in low temperature supergene alteration of sulphide and basalt, which leads to precipitation of secondary minerals at the mound surface. Diffuse flow also forms a significant proportion of the heat flux at the TAG mound. Estimates of the diffuse heat flux are in the order of 2000MW (Schultz et al., 1996). This greatly exceeds the heat flux from black smoker style venting at TAG estimated to be ~940MW (Rudnicki and Elderfield, 1993).

2.1.1 Internal structure of the TAG mound

The active TAG mound was drilled in 1994 during ODP leg 158. Cores were recovered from fifteen drill holes concentrated in five areas of the mound: TAG-1 through to –5 (Figure 2.2). Drilling revealed a complex composite structure dominated by breccias of various types, and constrained the lateral extent of the mineralised upflow zone and associated intense crustal alteration to ~80m (Humphris et al., 1995). The mound is estimated to contain ~4 million tonnes of sulphide with a bulk copper content of 30-60,000 tonnes (Humphris et al., 1995), comparable in size to average Cyprus-type deposits (Strens and Cann, 1986).

Based on the samples recovered during drilling, the mound can be lithologically divided into four major zones (Humphris et al., 1995) (Figure 2.4). The upper 10-20m of the mound at TAG-1 through to -5 are dominated by clast supported massive pyrite (typically >75% volume) breccias. These are composed of compact, granular pyrite clasts a few millimetres to > 5cm in size within a matrix of fine- to medium-grained pyrite, with minor chalcopyrite and anhydrite (*zone 1*) (Humphris et al., 1995; Knott et al., 1998). Underlying this at TAG-1 and –5 are anhydrite-rich breccias (*zone 2*). These breccias can be further subdivided into two types. The upper 10m (down to 30 meters below seafloor (m.b.s.f)) are matrix supported pyrite-anhydrite breccias; below this, to a depth of ~45m.b.s.f, are pyrite-silica-anhydrite breccias (Humphris et al., 1995). Both breccia types are composed of compact granular pyrite clasts. These are cemented by either anhydrite, containing 5-50% fine-grained disseminated pyrite and chalcopyrite, or anhydrite and silica (Knott et al., 1998). Extensive anhydrite veining occurs in this zone as multi-stage fracture fillings and cavity linings with vein widths of < 1mm to > 40cm (Humphris et al., 1995). Pyrite and chalcopyrite mineralisation associated with the anhydrite veining is a minor component within the veins and is seen as localised bands, clots and in rare cases as disseminated sulphide. Sulphide mineralisation at vein edges is much more common, here pyrite and chalcopyrite selvages range in thickness from 1-10mm (Knott et al., 1998). Beneath the anhydrite rich zone, intensely silicified wall rock breccias mark the upper portion of the hydrothermal stockwork (*zone 3*) (Humphris et al., 1995). This zone shows considerable heterogeneity. The upper part is dominated by pyrite-quartz breccia with clasts of silicified, paragonitic basalt 0.1-70mm in size (Honnorez et al., 1998). With depth, the abundance of basalt fragments increases whilst the pyrite content decreases. The degree of silicification also becomes less intense with depth and the breccia is cut by quartz and pyrite veins (Knott et al., 1998; Honnorez et al., 1998). The quartz-paragonite wall rock breccia grades into chloritised basalt and weakly mineralised basalt fragments below ~100m.b.s.f, (*zone 4*) (Humphris et al., 1995; Knott et al., 1998;

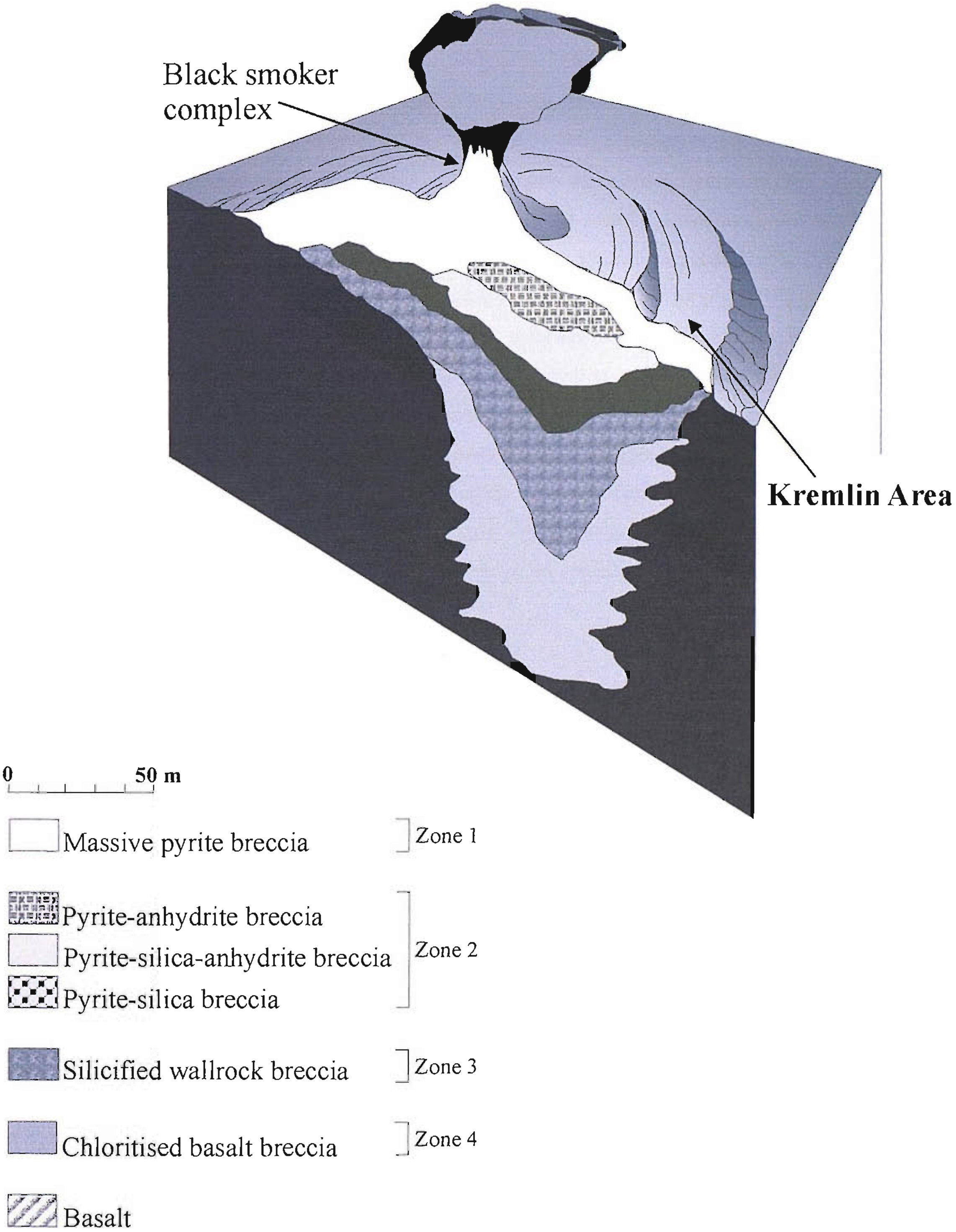

Figure 2.4: Schematic cross section through the TAG mound showing lithological zonation inferred from ODP drilling results (adapted from Humphris et al. 1995).

Honnorez et al., 1998). This is the deepest part of the stockwork and consists of at least 15m of chloritised basalt (Honnorez et al., 1998) cut by pyrite and quartz veins (Humphris et al., 1995; Knott et al., 1998).

2.1.2 Mound growth

The complexities of mineralogical and lithological relationships revealed during drilling of the active TAG mound (e.g. Humphris et al., 1995; Honnorez et al., 1998; Knott et al., 1998) indicate that it has undergone multiple stages of development. The growth of the TAG mound can be attributed to hydrothermal replacement and mineralisation in the stockwork zone coupled with mass wasting and cementation of material precipitated at the surface of the mound (Humphris and Kleinrock, 1996; Hannington et al., 1998) (Figure 2.5). In the initial stages of mound growth, hydrothermal fluids venting at the seafloor precipitate sulphide minerals and form chimney structures. As sulphide accumulates, seawater is entrained into the chimney walls where conductive heating produces the conditions for anhydrite precipitation, causing inflation of the mound (Hannington et al., 1998). At the seafloor, collapse of chimneys and mass wasting and faulting events contribute to the growth of a sulphide talus. Whilst Humphris et al. (1995) suggest that the TAG mound has grown largely as an in situ breccia pile; subsurface precipitation is also important and occurs due to convective cooling of ascending hydrothermal fluids and mixing with seawater. Cementation and replacement of the sulphide talus by silica rich solutions, and sulphide and sulphate, results in the formation of complex sulphide-anhydrite-silica breccias.

Whilst anhydrite precipitation had been predicted prior to drilling (e.g. Edmond et al., 1995; Tivey et al., 1995) its abundance was not. The anhydrite mineral inventory estimated from drilling results is ~3×10^8kg (Humphris et al., 1995). Precipitation of anhydrite occurs by conductive heating of seawater that is entrained into the mound (e.g. Janecky and Seyfried, 1984; Janecky and Shanks, 1988). A range of $^{87}Sr/^{86}Sr$ values between ~0.70630 and 0.70912 (Mills et al., 1998) for TAG anhydrites, indicates significant seawater entrainment into the subsurface around the site of venting (Teagle et al., 1998a; Chiba et al., 1998; Mills and Tivey, 1999). Permeability within the active mound is enhanced by the dissolution of anhydrite owing to its retrograde solubility. During periods of quiescence, continued seawater entrainment causes temperatures to drop below 150°C resulting in the dissolution of anhydrite and the creation of pore space and collapse breccias (Humphris et al., 1995). Estimates of anhydrite formation rates (which lie in the range of $5\text{-}15 \times 10^7$kg/yr) and the mineral inventory suggest that the anhydrite sampled from Leg 158 drill cores is all contemporary (James and Elderfield, 1996a). This supports the interpretation that anhydrite dissolves during hydrothermally inactive periods. Renewed activity channels fluid through collapse breccias re-cementing earlier sulphides with a new generation of anhydrite which is then cumulatively replaced by quartz (e.g. Humphris et al., 1995; You and Bickle, 1998; Hannington et al., 1998).

The transient and episodic nature of high temperature venting at the TAG site contributes to the protracted and complex evolution of the massive sulphide mound. The importance of multiple episodes of high temperature activity in the formation of large sulphide deposits is supported by Lowell and Rona (1985) who modelled the generation of seafloor massive sulphides and suggested that large (>3Mt) massive sulphide deposits, like the TAG mound, formed by multiple episodes of high temperature hydrothermal activity.

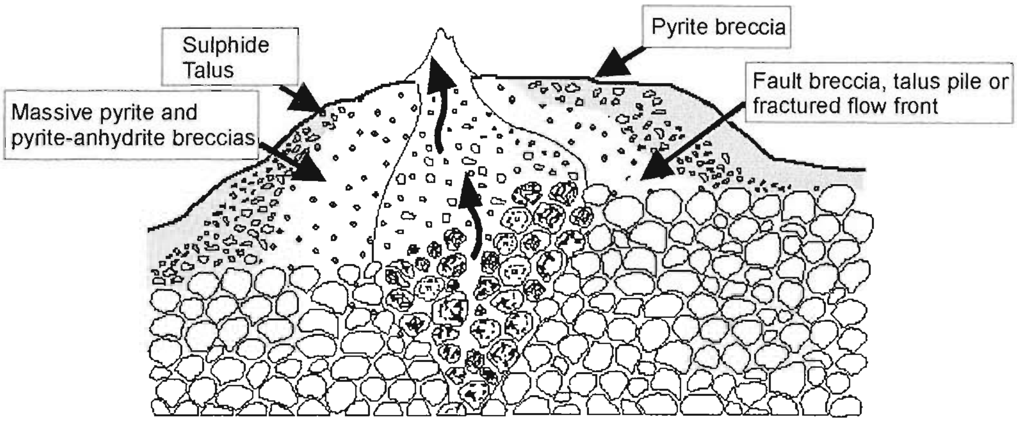

1.) Initial High temperature upflow and growth of large mound-like sulphide deposit

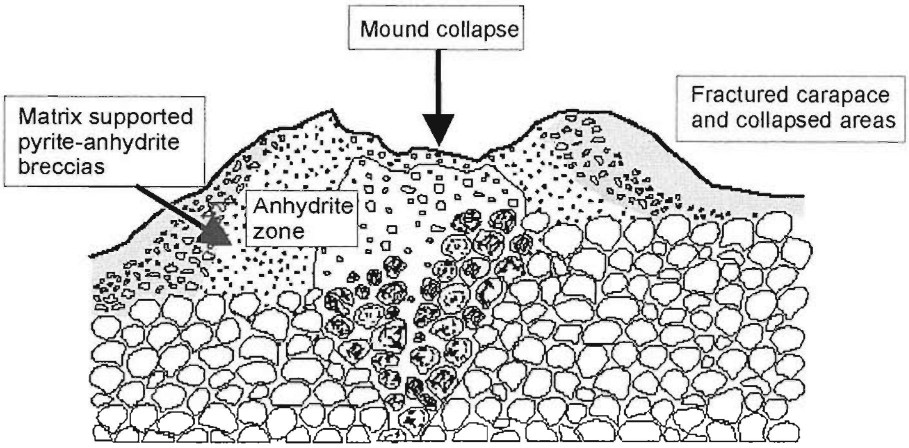

2.) Periodic collapse of anhydrite-supported breccias during periods of hydrothermal inactivity

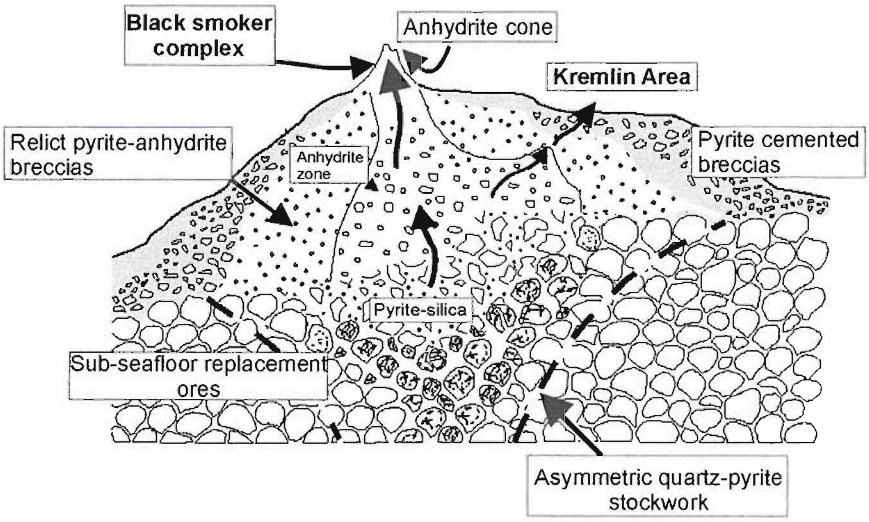

3.) Renewed venting: hydrothermal fluid focussed through collapse features and development of new fluid pathways, formation of composite sulphide mound and stockwork complex (present state of the active TAG mound).

Figure 2.5: Model for the development of the TAG mound based on drilling observations Adapted from Hannington et al. (1998).

2.1.3 Fluid flow within the TAG mound

Fluid flow regimes within the active mound are complex. Seawater entrainment is controlled by both the subsurface permeability and highly focussed high temperature fluid flow. The clustering of black smoker chimneys in one area reflects a structural control on fluid flow within the TAG mound. This highly focussed fluid flow causes entrainment of seawater in the main portion of the mound below ~3650m water depth by producing a pressure differential (Tivey et al., 1995). Mixing of entrained seawater with the ascending hydrothermal fluid and conductive heating results in the precipitation of sulphides and anhydrite (Janecky and Seyfried, 1984; Janecky and Shanks, 1988). Several studies have used the Sr isotope systematics of hydrothermal anhydrite to trace fluid mixing during mound formation (e.g. Mills et al., 1998; Teagle et al., 1998a; Mills and Tivey, 1999). The range of $^{87}Sr/^{86}Sr$ values for TAG anhydrites (~0.7063-0.70912) allows identification of seawater recharge zones (values close to 0.70916) and areas where seawater entrainment is restricted (values close to 0.7063) (Mills et al., 1998) (Figure 2.6).

A range of sulphide $\delta^{34}S$ values between +5.5-+10‰ (e.g. Gemmell and Sharpe, 1998; Herzig et al., 1998b; Chiba et al., 1998; Knott et al., 1998) interpreted to be the result of mixing of seawater sulphate ($\delta^{34}S$ +21‰: Rees et al., 1978) and MORB derived sulphur ($\delta^{34}S$ ~0-+1‰: Sakai et al., 1984) also allow identification of mixing processes. According to deep subsurface processes outlined by Alt (1995) and Shanks et al (1995), initial fluids entering the TAG system at depth should have $\delta^{34}S$ values of MORB. Mixing of this fluid with partially reduced, locally entrained seawater sulphate in the upper parts of the subseafloor stockwork produces a modified fluid with a heavier $\delta^{34}S$ value of +6-+7‰. Sulphides precipitated within the stockwork zone have the same $\delta^{34}S$ value as the modified fluid. As this fluid approaches the seawater interface further mixing with cold seawater occurs and massive sulphides are deposited with $\delta^{34}S$ values of +6-+8‰ (Gemmell and Sharpe, 1998).

Oxygen isotopes indicate that basalt chloritisation at depth occurred at temperatures of ~250-350°C and water/rock ratios of ≥ 300 by variable mixtures of seawater and hydrothermal fluid (Alt and Teagle, 1998). Oxygen isotope studies of stockwork quartz indicate that it formed in equilibrium conditions with the hydrothermal fluid (Teagle et al., 1998b; Alt and Teagle, 1998). $\delta^{18}O$ values of quartz from the mound are generally higher than those from the stockwork and result from precipitation during seawater mixing and cooling (Alt and Teagle, 1998). Variations in $\delta^{18}O$ values reflect differences in water/rock and seawater/ hydrothermal fluid mixing ratios throughout the mound.

The occurrence of silica indicates conductive cooling of hydrothermal fluids during transport since it is undersaturated in mixtures of hydrothermal fluid and seawater (Janecky and Seyfried, 1984; Tivey et al., 1995). Surficial silica occurrence is inferred to be a result of percolation of Fe-Si low temperature hydrothermal fluids across the mound (e.g. Tivey et al., 1995; Humphris et al., 1995). Amorphous silica precipitation in porous sulphide near the surface of the mound creates an impermeable cap. This silica cap enhances conductive cooling and restricts seawater mixing by trapping the fluid in the near surface (Fouquet et al., 1998). This in turn enhances the efficiency of silica precipitation. A lack of abundant quartz within the massive sulphide at depth, suggests that cooling by seawater mixing is dominant over conductive cooling.

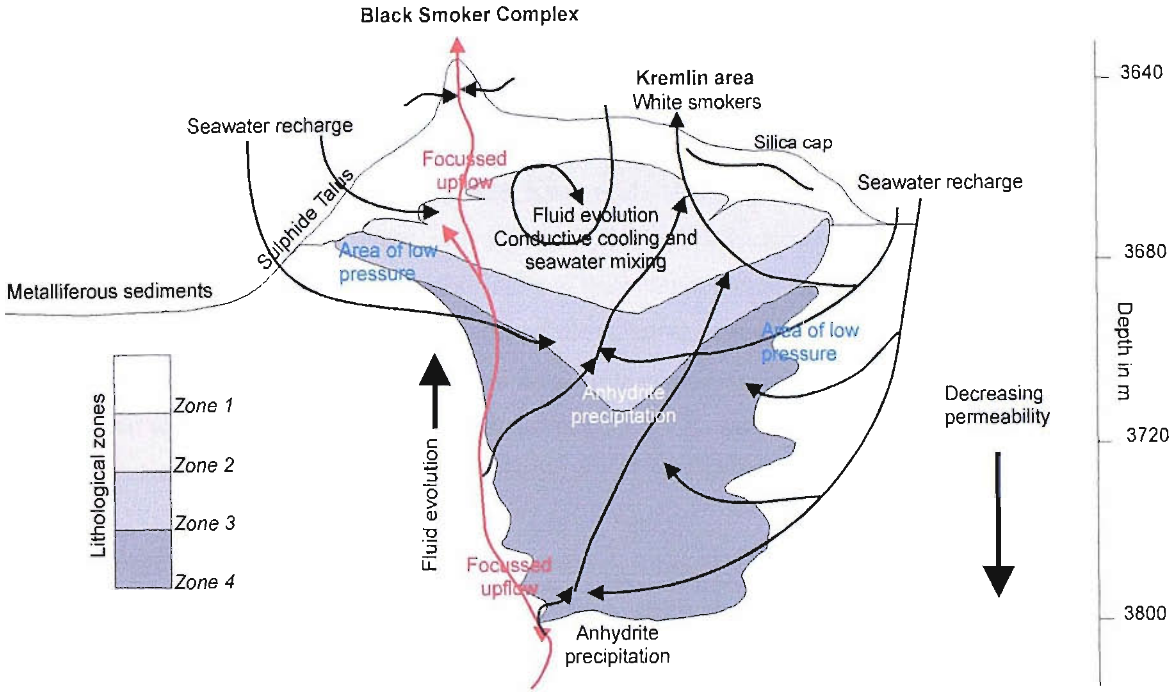

Figure 2.6: Schematic cross section of circulation within the TAG mound, Arrows demonstrate the path of ascending high temperature hydrothermal fluid, seawater recharge, fluid circulation and areas of focussed venting. Lithology as for Figure 2.4 Adapted from Mills et al. (1998).

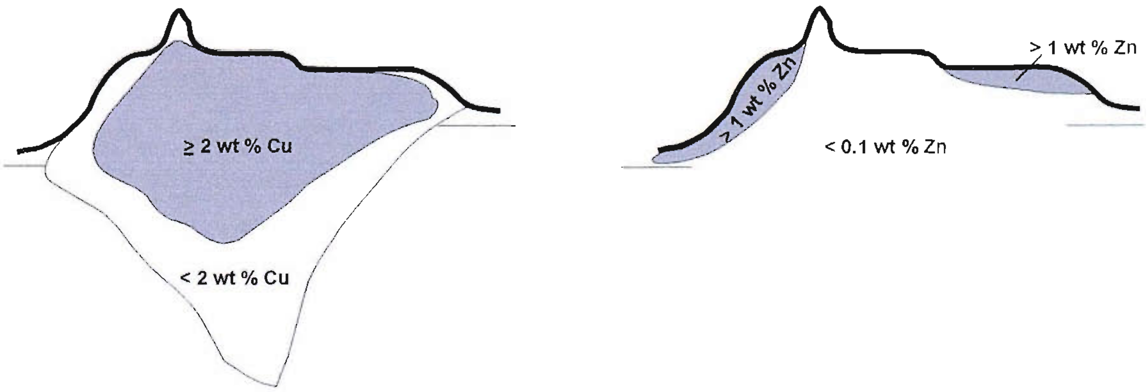

Figure 2.7: Schematic representation of Cu and Zn zonation within the TAG mound. During metal mobilisation, Cu is retained in the mound interior and Zn is concentrated at the seawater interface (adapted from Hannington et al. 1998).

2.1.4 Zone refining and oxide formation

Cementation of the various breccias within the mound inhibits the escape of hydrothermal fluids, which instead circulate within the mound recrystallising and redistributing primary mineral phases (e.g. Hannington et al., 1988; Humphris et al., 1995; Honnorez et al., 1998; Knott et al., 1998; You and Bickle, 1998; Hannington et al., 1998). Precipitation of pyrite, anhydrite and silica within the mound decreases the pH of the circulating hydrothermal fluid and causes remobilisation of base metals including Zn, Cu, Au, Ag, Pb, and Cd. This produces distinctive zoning of metals, in particular the effective separation of Cu and Zn (Figure 2.7). Whilst Cu is retained with Fe in the mound interior Zn is stripped and concentrated at the seawater interface (e.g. Edmond et al., 1995; Tivey et al., 1995; Knott et al., 1998 Hannington et al., 1998): surficial bulk Cu/Cu+Zn ratios are <0.5, ratios from the mound interior are ~1 (Hannington et al., 1998).

Remobilisation of metals also occurs at the surface of the mound as exposed sulphide debris undergoes extreme oxidative weathering (e.g. Herzig et al., 1991; Hannington, 1993; Hannington et al., 1998). Reprecipitation of metals during secondary mineralisation occurs within the sediment pile and at the seawater interface as crusts and coatings including hematite, jarosite, covellite and atacamite (e.g. Herzig et al., 1991; Hannington, 1993; Hannington et al., 1998). Whilst initial alteration of primary phases is contemporaneous with high temperature venting, modification continues during hydrothermally inactive periods, as circulation of seawater and low temperature fluids persists. During mass wasting events primary, partially altered and secondary phases are transported to the surrounding sulphide talus and near field sediments where they are intermixed with material derived from plume fallout and background pelagic sedimentation. Oxidative decay, metal remobilisation and secondary mineralisation continue within the sediment pile. Over time, this may lead to complete oxidation to Fe-oxide.

2.2 The *Mir* Zone

The *Mir* zone is situated ~2km east of the active TAG mound and covers an area ~1km in diameter, on the lower east wall of the rift valley, between 3430 and 3575m water depth (Rona et al., 1993a; Rona et al., 1993b; Stepanova et al., 1996) (Figure 2.1). The *Mir* zone is flanked on the southeast and northwest sides by volcanic centres, and is cut by axis-parallel and obliquely oriented normal faults and fissures (Rona et al., 1996). Heat flow across this zone is variable; the highest values (8.9–13.3W/m^2) are recorded from the northwest quadrant, close to the western volcanic centre, whilst measurements from the southeast quadrant, furthest from the volcanic centre, record background values (~0.3W/m^2) (Rona et al., 1996). Photo-profiling of the *Mir* zone indicates that it is dominated by a large mound ~400m in diameter and up to 70m high (Rona et al., 1986; Stepanova et al., 1996) predominantly composed of sulphide deposits with Fe-oxides, silica and red metalliferous sediments interspersed with carbonate lutite (Rona et al., 1993a; Rona et al., 1993b). The summit is covered by toppled and standing inactive chimneys of various sizes, and sulphide blocks some of which are covered by a thin cover of metalliferous sediment (Rona et al., 1993a; Rona et al., 1993b; Stepanova et al., 1996).

The *Mir* zone can be divided into three sub-zones based on the mineralogy and morphology of the deposits (Rona et al., 1993a; Rona et al., 1993b) (Figure 2.8):

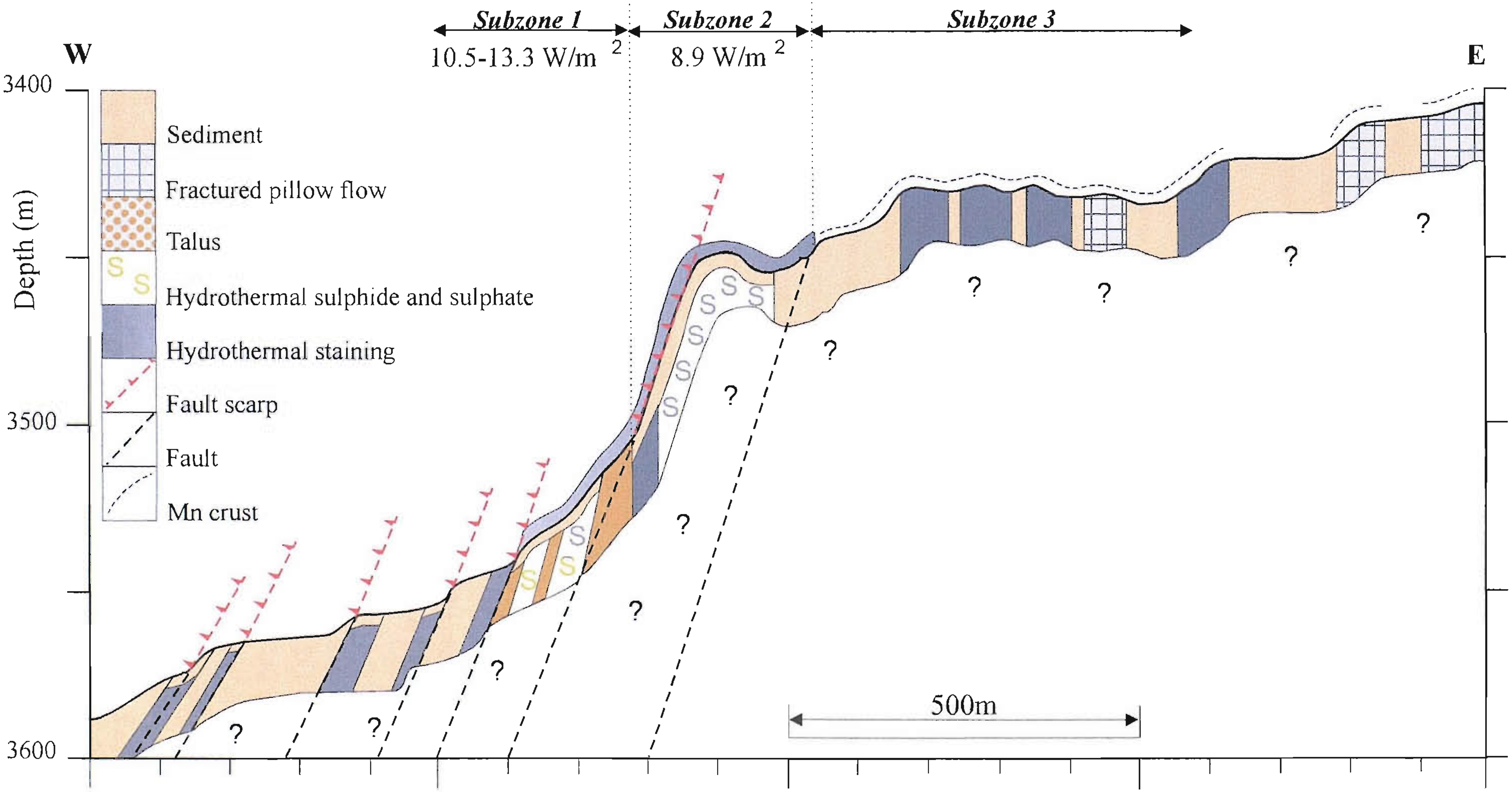

Figure 2.8: Cross section (east-west) through the northern end of the *Mir* zone showing three subzones, geological features, lithology and conductive heat flow values measured during DSV Alvin dives to the TAG hydrothermal field during 1993. Adapted from Rona et al (1993).

Subzone 1: An area ~200m wide with a mean slope of 30°, at the western margin of the *Mir* zone close to the western volcanic centre, between 3500–3575m water depth. This subzone comprises mixed hydrothermal deposits and basaltic breccias. Weathered and altered sulphides and metalliferous sediment are derived from mass wasting of massive sulphide at the top of the subzone and basaltic breccias exposed by normal faulting (Rona et al., 1993b). Radiometric dating of massive sulphide fragments indicates that there have been at least 3 episodes of sulphide precipitation: ~100kya; ~50kya and ~20kya (Lalou et al., 1995).

Subzone 2: Comprises semi-continuous sulphide outcrop in an area ~400m wide (E-W) by 700m long (N-S) with a mean slope of 8°. Subzone 2, lies to the east of subzone 1 in water depths of 3450–3500m (Rona et al., 1993a). It is characterised by numerous standing and toppled inactive chimneys up to 25m in length and 3m in diameter, many of which appear to have grown on top of a pre-existing sulphide talus. Oxidative alteration is most pervasive in the southern and central areas of the subzone. In the northern portion, sulphides are silicified and oxidation is more limited (Rona et al., 1993a).

Subzone 3: A series of small mounds ~5m in diameter by 2m high extending ~200m east of *subzone 2*, between 3420–3460m water depth. The mounds are composed of black and yellow low temperature hydrothermal material that is similar to Fe-oxyhydroxide and nontronite deposits from the low temperature zone, higher up on the eastern wall of the rift valley. These mounds are variously covered by thin deposits of low temperature hydrothermal material intermixed with pelagic carbonate. Mn crusts and coatings up to several centimetres thick occur on exposed pillows, hydrothermal talus and at the surface of the sediment (Rona et al., 1993a; Rona et al., 1993b).

2.2.1 Mineralogical zonation of the *Mir* mound: implications for formation

Several different types of chimney and massive sulphide mineral assemblages have been identified from the *Mir* zone, these are summarised in Table 2.1. The distribution of the various mineral assemblages, and deposit types at the *Mir* mound shows a well-defined zonation. The NE quadrant of the mound is enriched in Cu and is dominated by Cp-Py and Bn-Cp-Op assemblages showing granular and relict colloform textures (Stepanova et al., 1996). High Zn and Si contents, related to Sp-Py-Op and Sp-Cp-Py-Op assemblages are located in the centre of the mound (Stepanova et al., 1996; Rona et al., 1993b). Siliceous rocks are predominantly seen at the periphery of the mound and in the southern quadrant. These are variously quartz, recrystallised opal, (in the west) and opal (in the east) (Stepanova et al., 1996).

Models for mound growth inferred from mineralogical studies are very similar to those for the active mound. The early stages of formation are dominated by precipitation of opaline silica (which is later transformed to quartz and replaced by sulphide) from low temperature pre-ore fluids. In the early stages of sulphide deposition and high temperature activity massive pyrite and pyrite and marcasite dendrites are precipitated. This is followed by deposition of chalcopyrite and recrystallisation of early pyrite. As high temperature activity waned, temperatures within the mound dropped and metal remobilisation occurred resulting in the deposition of Py-Sp-Op and Sp-Op assemblages. Cu-rich assemblages are found in the northern portion of the mound, Zn-rich assemblages are most developed in the central portion and siliceous formations are dominant in the south (Stepanova et al., 1996). The occurrence of several breccia types, a large sulphide talus and metal

	Major mineral assemblage	**Textural and geochemical associations**
CHIMNEYS		
20cm diameter	Py-Cp	Granular or layered Cp and Py in central parts of the chimneys is overgrown by Mc-Py dendrites. Cu, Si and Au, concentrations are enriched compared to similar chimneys from the active TAG mound, whereas Fe + Ag are depleted and Pb, Co and Cd are severely depleted.
5-25m long up to 3m diameter	Py-Mc	Py-Mc chimneys are silicified and have low Cu (<3.2wt%), Se (<3 ppm) and Cd (<5 ppm) contents, and high Si (~25wt%) and Co (370ppm).
2m high	Py-Sp	Massive and colloform Py and Sp, bulbous shaped chimneys similar to those from the Kremlin area at the active TAG mound. High Zn (18 wt%), Ag (200 ppm) and Pb (350 ppm)
10-20m high	Cp-Sp	Moderately high Cu (~14 wt%) and Zn (10 wt%), low Pb (26 ppm) and Co (11 ppm).
10 cm diameter	Sp-Op	Cu minerals are replacing the opaline matrix. Colloform Sp is found in the centre of the chimneys. Enriched in Ag, Au, Cd, Ga, Hg, Sb and Pb.
	Bn-Cp-Op	Composed of friable aggregates. Covellite and chalcocite are also present.
MASSIVE SULPHIDE		
	Cp-Py	Py forms course-grained aggregates with relict colloform textures. Hydrothermal reworking and replacement is evident. Grain sizes of 1-2 mm. Anhedral Cp replaces Py. Trace element depleted.
	Mc-Py-Op	Dendritic structures are dominant and are replaced by Py. Late Py and Si form veinlets.
	Sp-Py-Op	Porous assemblage showing considerable heterogeneity and irregular layering. Colloform Sp is associated with Si fills. Py is locally replaced by Mc. Enriched in Ag, Au, Cd, Ga, Hg, Sb and Pb.
	Sp-Cp-Py-Op	Distribution of individual minerals is extremely variable. Py is extensively recrystallised to euhedral crystals or fine-grained aggregates. Sp has a colloform texture. Late Py forms rims, veinlets and cavity fills. Cp forms interlayers up to 5 mm thick separating pyrite generations.

Table 2.1: Summary of major chimney and massive sulphide types recorded from the *Mir* mound. Minerals: Py –pyrite; Cp-chalcopyrite; Sp-sphalerite; Op-opal; Bn-bornite; Mc-marcasite. Sources: Stepanova et al., 1996; Rona et al., 1993a; Rona et al., 1993b; Thompson et al., 1985; Hannington et al., 1988.

zonation, in particular the separation of Cu and Zn, suggest that, like the active mound, the *Mir* mound has grown largely as an in situ breccia pile which has undergone extensive hydrothermal reworking, zone refining and subsurface precipitation.

2.3 The *Alvin* Zone

The *Alvin* zone is a discontinuous, elongate group of several inactive sulphide mounds approximately 2km in length (NE-SW) by 1km width (NW-SE), and is located 2-4km NNE of the active TAG mound at water depths of 3400–3600m (Rona et al., 1986; Rona et al., 1993b). The *Alvin* zone is flanked on its east and west sides by pillow lava domes. The pillow lavas to the west extend over an area ~400m in diameter and 15m high and contain glassy flows. Those to the east are fractured and coated by manganese oxide (Rona et al., 1993b). The southern most mound, the *Alvin* mound, is ~200m in diameter and 28m high (Tivey et al., 1996), similar in size to the active TAG mound. Radiometric dating of massive sulphides from the *Alvin* mound gives a uniform age of ~50ka (Lalou et al., 1993). Heat flow across the mound is at background levels (Rona et al., 1996). A zone of low magnetisation occurs below the mound similar to anomalies measured at the active TAG mound suggesting the presence of a hydrothermal upflow zone (Tivey et al., 1996).

The mounds are covered by standing and toppled chimneys, layered hydrothermal crusts and metalliferous sediments intermixed with carbonate lutite. Samples from the mound tops and flanks consist of coarse-grained pyrite with minor chalcopyrite and trace amounts of sphalerite (Rona et al., 1996). The interiors of the sulphides are protected from oxidation by a thin covering of Fe-oxide (Lisitsyn et al., 1989). The presence of atacamite coatings and crusts indicates leaching of Cu from the underlying sulphides (Hannington, 1993; Rona et al., 1996). The mounds are currently undergoing extensive erosion, mass wasting and dissection by faulting and are now heterogeneously covered, and surrounded by deposits of Fe-oxyhydroxides and oxides (Rona et al., 1993a) and capped with pelagic carbonate (Severmann, 2000). A gravity core from the southern periphery of the *Alvin* zone contained two distinct layers of sulphide debris intercalated with metalliferous sediment and pelagic carbonate. Radiometric dating of these sulphidic layers indicates slumping events at 8.5ka and 6ka B.P. (Metz et al., 1988).

2.4 Sampling

2.4.1 Core locations

The sediment samples for this study were collected by *RV Charles Darwin* during cruise CD102 in 1996 (Palmer and scientific party, 1996). Table 2.2 gives brief descriptions and locations of cores recovered during CD102. Two gravity cores were selected for this investigation: CD102/60 (26°08.48'N; 44°48.50'W) from the south-western margin of the *Mir* zone; and CD102/58 (26°09.26'N; 44°48.90'W) from the southern periphery of the *Alvin* southern mound (Figure 2.9). There have been several studies of metalliferous sediments from the TAG hydrothermal field (e.g. Scott et al., 1974; Shearme et al., 1983; Metz et al., 1988; Mills et al., 1993; German et al., 1993; Severmann, 2000). These studies have characterised the major and trace element geochemistry of these deposits (e.g. German et al., 1993); rare earth element signatures (e.g. Mills et al., 1993; Mills and Elderfield, 1995b); clay mineralogy (e.g. Severmann et al., 2004); isotopic tracers used to characterise the various inputs to these sediments and age relationships, including U-series, Pb, Sr and

Station No.	Latitude (N)	Longitude (W)	Core type	Recovery (cm)	Action*	Comments
10	29°23.55	43°25.00	Gravity	221	P	Carbonate ooze
11	29°23.44	43°24.92	Multi	30	P	Carbonate ooze
13	29°23.64	43°24.92	Box	36	P	Carbonate ooze
17	26°08.65	44°48.39	Gravity	65	A	Fe-stained carbonate
18	26°08.53	44°48.38	Gravity	221	P	Carbonate ooze grading into Fe-oxide rubble.
19	26°08.59	44°48.22	Box	33	P	Fe-stained carbonate ooze, some Mn-oxide staining, filamentous organisms on surface
24	26°08.63	44°48.32	Gravity	26	A	Fe- stained carbonate ooze
25	26°08.61	44°48.42	Multi	15	P	Carbonate ooze grading into Fe-oxide rubble, Mn-oxide crusts on surface
27	26°08.51	44°48.45	Gravity	120	A	Fe-oxide rubble, some chimney fragments.
31	26°08.47	44°48.47	Gravity	20	A	Sulphide debris
32	26°08.49	44°48.49	Gravity	142	A	Fe-oxide rubble – 14 sections.
37	26°08.56	44°48.42	Gravity	205	P	Carbonate ooze grading into Fe-oxide rubble.
41	26°09.20	44°48.93	Gravity	120	A	Carbonate ooze grading into Fe-oxide rubble – 4 sections.
42	26°09.26	44°48.95	Gravity	150	A	Carbonate ooze grading into Fe-oxide rubble, some sulphide layers? – 5 sections.
43	26°09.26	44°48.90	Gravity	228	P	Carbonate ooze grading into Fe-oxide rubble
52	26°09.28	44°48.92	Gravity	229	A	Carbonate ooze grading into Fe-oxide rubble – 3 sections.
53	26°09.26	44°48.93	Multi	25	P	Fe-stained carbonate ooze, nontronite (?) layer, some Fe-oxide rubble
55	26°08.48	44°48.48	Gravity	79	A	Fe-oxide rubble
56	26°08.59	44°48.39	Box	35	P	Carbonate ooze grading into Fe-oxide rubble, weathered chimney fragments with filamentous organism on the surface, some atacamite
57	26°08.54	44°48.44	Gravity	140	A	Carbonate ooze grading into Fe-oxide rubble and nontronite (?) at base
58	26°09.26	44°48.90	Gravity	200	A	Carbonate ooze grading into Fe-oxide rubble –2 sections
60	26°08.48	44°48.50	Gravity	112	A	Carbonate ooze grading into Fe-oxide rubble with sulphides.
66	26°08.51	44°48.47	Multi	4	P	Fe-oxide rubble

*** P = processed on board, A = archived**

Table 2.2: Core locations and brief description of cores recovered during cruise CD102

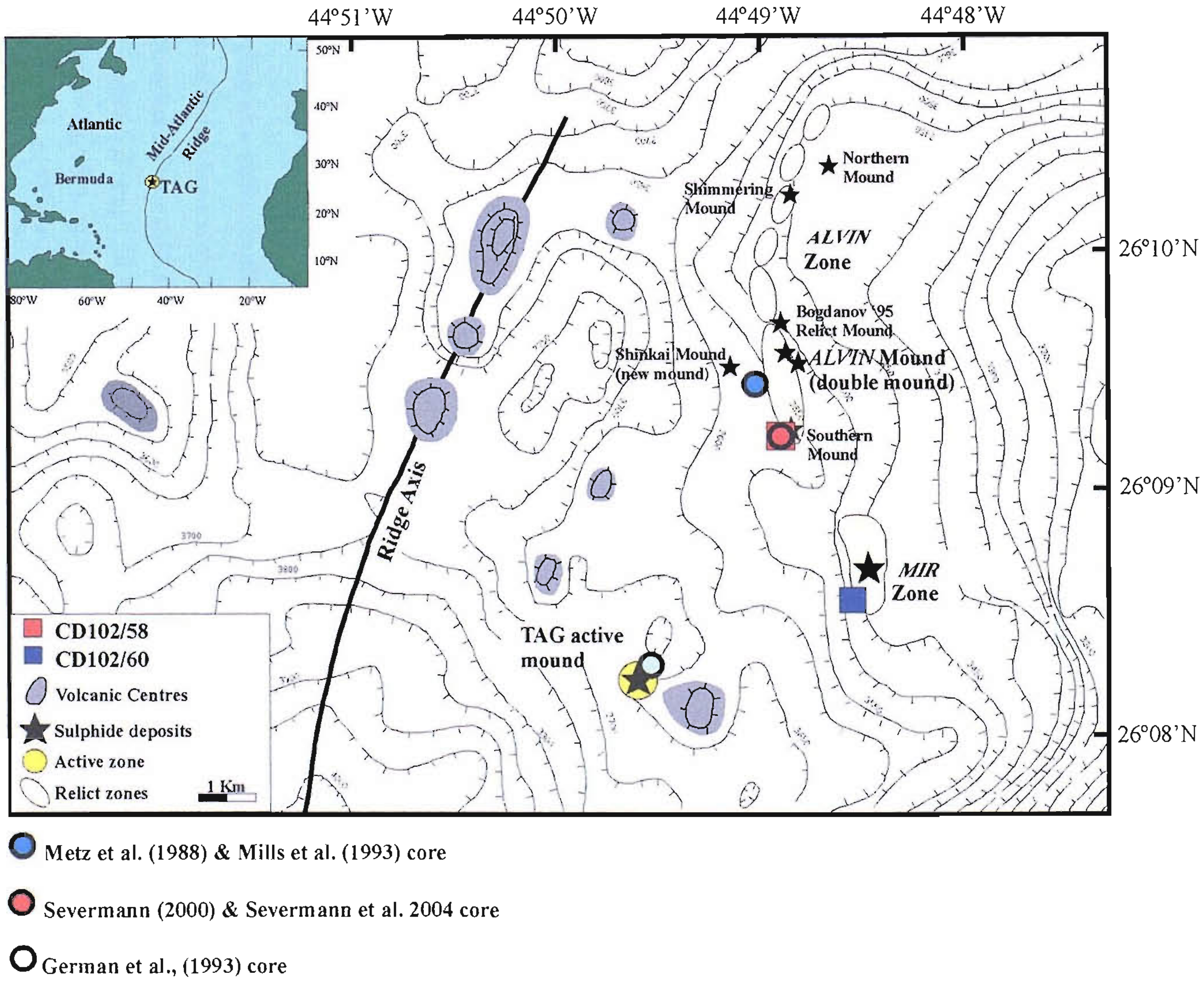

Figure 2.9: SeaBeam bathymetry of the TAG hydrothermal field showing the locations of cores CD102/58 and CD102/60 investigated in this study (shaded squares) the locations of three other metalliferous sediment cores of interest in this study (shaded circles).

Nd (e.g. Mills et al., 1993; Severmann et al., 2004; German et al., 1993; Lalou et al., 1993); and biological interactions during diagenesis (e.g. Severmann et al., 1998; Wirsen et al., 1993). In addition, comparisons have been made between oxic metalliferous sediments from the TAG hydrothermal field and the umber and ochre deposits associated with ophiolite sequences (e.g. Goulding, 1998).

The Severmann (2000) and Severmann et al. (2004) studies of core CD102/43 are of particular interest with regards to the present study, since core CD102/43 was also collected during the CD102 cruise and its recovery location was adjacent to CD102/58 (Figure 2.9). The Metz et al. (1988) core was also collected close to the Southern *Alvin* mound NNE of CD102/58 (Figure 2.9). Both the Metz et al. (1988) core, which was also the subject of the Mills et al. (1993) study, and CD102/43 consist of sulphide-rich layers, predominantly pyrite, intercalated with Fe oxides and oxyhydroxides capped by pelagic calcium carbonate. These different layers record periods of intense hydrothermal input from mass wasting events (sulphide-rich layers) interspersed with periods of hydrothermal quiescence during which sulphidic material has undergone oxidation and reworking, and pelagic background sedimentation dominates. In addition, there is geochemical evidence for diffuse evolved low temperature fluid flow through these sediments which is responsible for some Fe oxide and amorphous silica precipitation (e.g. Severmann, 2000), and for the formation of low temperature hydrothermal clays (e.g. $^{87}Sr/^{86}Sr$ ratios: Severmann et al., 2004), as well as the redistribution of redox sensitive metals (e.g. Mn: Metz et al., 1988; Severmann, 2000; and U: Mills et al., 1993) and the immobilisation of seawater sourced elements due to adsorption onto and co-precipitation with Fe oxide and oxyhydroxide phases (e.g. Ni, V and Cr: Metz et al., 1988; REE: Mills et al., 1993).

Cores CD102/58 and CD102/60 investigated in the present study share many of the geochemical and sedimentalogical features of CD102/43 and the Metz et al. (1988) core however, despite the fact that cores 58 and 60 were collected in relatively close proximity to these previously described sediments they are significantly less altered. The similarities and differences between cores 58 and 60, and previously studied metalliferous sediments from the TAG site are dealt with in the following chapters of this thesis.

2.4.2 Core logging and sub sampling

The cores were stored in their liners at 4°C, initially at the University of Bristol before being transferred to Southampton Oceanography Centre (SOC) where sub-sampling was undertaken. The cores were sectioned longitudinally, lithologically (Figure 2.10 & 2.11) and petrophysically logged (see appendix A), and photographed before 10-20g sub-samples were taken at 1-3cm depth intervals downcore, the sub-samples were then dried in an oven at 55°C for a period of five days. Following drying, the sub-samples were stored in glass bottles ready for chemical analysis. The preparation of polished blocks and thin sections for mineralogical and isotopic analyses is dealt with in Chapter 3 and 5.

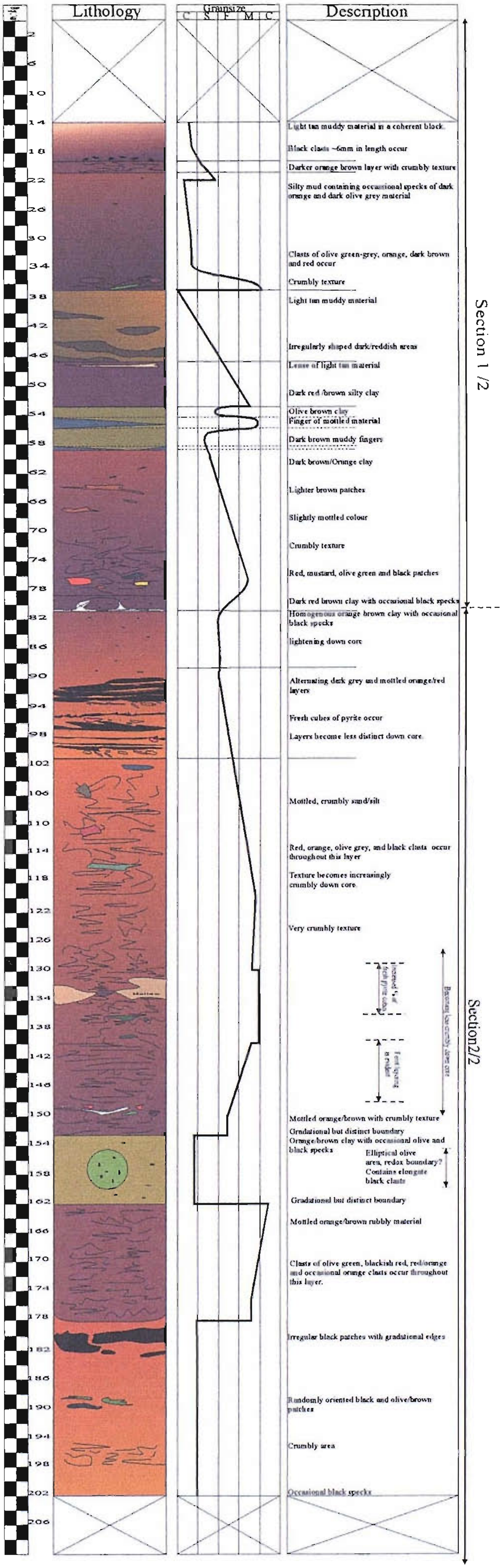

Figure 2.10: Lithological log of CD102/58. Log was recorded immediately following splitting of the core

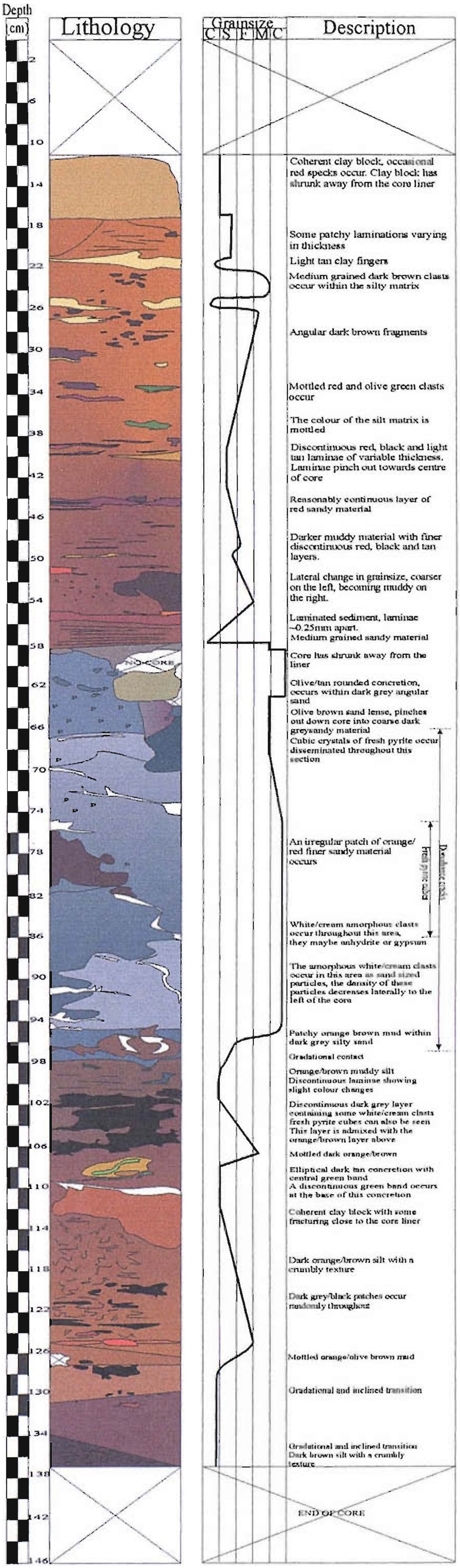

Figure 2.11: Lithological log of CD102/60. Log was recorded immediately following splitting of the core

Chapter 3:

General Sediment Geochemistry and Mineralogy

3.1 Introduction

Geochemical analyses have shown that hydrothermal metalliferous sediments comprise a complex mixture of sources (e.g. Hodkinson et al., 1986; Metz et al., 1988; Mills et al., 1993; German et al., 1993) (Studies from key locations are summarized in Table 3.1). The fine grained particulates within the buoyant and neutrally buoyant plume settle out, forming metalliferous sediments dominated by Fe-oxyhydroxides. These sediments are the ultimate repository for many hydrothermally derived elements and the associated plume particulate scavenged sink (e.g. German et al., 1991; Mills and Elderfield, 1995b; Cave et al., 2002). The hydrothermal component of plume derived sediments is diluted by biogenic and detrital sediment, this is illustrated by a decrease in the (Al+Fe+Mn)/Al ratio with distance from active vents (Bostrom, 1969). Debris from mass wasting of hydrothermal mounds is a significant component of metalliferous sediments close to vent sites (e.g. Metz et al., 1988; Mills et al., 1993). Slumping and mass wasting is facilitated by mass gravitational sediment transport, fault activation and micro-earthquakes related seafloor spreading and magma emplacement in the ocean crust. During mass wasting events primary, partially altered and secondary phases are transported to near field sediments where they are intermixed with material derived from plume fallout and background pelagic sedimentation. During weathering and oxidation of the hydrothermal material at the seafloor low temperature mixed hydrothermal and seawater fluids may circulate within the sediment pile and this leads to modification of primary phases and results in remobilization of some elements and secondary mineralisation. This chapter summarizes the general geochemistry and mineralogy of cores CD102/58 and CD102/60, and identifies the principal sources to the sediment, and sediment formation processes.

3.2 Materials and Methods

Down core general geochemistry and bulk mineralogy of cores CD102/58 and CD102/60 were obtained from investigation of selected sub-samples.

3.2.1 Inductively Coupled Plasma–Atomic Emission Spectroscopy (ICP-AES)

Sample preparation

Prior to chemical treatment all samples were dried at ~55°C and ground to a homogeneous fine powder in tungsten carbide TEMA vessels. Total dissolution of 0.2g of bulk sediment using HNO_3-HF-HCl and Aqua Regia was performed in Teflon beakers. Samples were reacted for 30 minutes with 15 drops of concentrated HNO_3 following which 3ml of HF was added and the beakers sealed and refluxed at ~125°C for 24 hours. The solutions were then evaporated to dryness and treated with 3ml of Aqua Regia to ensure complete digestion of sulphide phases. Once all sulphide was dissolved the samples were evaporated to dryness and

Location	Sulphide and chimneys: mound formation	Near field sediments	Far field sediments
East Pacific Rise (EPR)	Haymon and Kastner, 1981; Oudin et al., 1981; Styrt et al., 1981; Vidal and Clauer, 1981; Bischoff et al., 1983; Goldfarb et al., 1983; Zierenberg et al., 1984; Woodruff and Shanks, 1988; Graham et al., 1988; Marchig et al., 1990	Dill et al., 1994; German et al., 1999; Alt et al., 1987	Bender et al., 1971; Dymond et al., 1973; Dymond and Veeh, 1975; Marchig et al., 1982; Barrett et al., 1987; Barrett and Jarvis, 1988; Barrett et al., 1988; Hekinian et al., 1993
South West Pacific: Lau Basin	Von Stackelberg, 1985; Hawkins and Helu, 1986; Herzig et al., 1998a	Von Stackelberg, 1985	Bertine and Keene, 1975; Cronan, 1983; Cronan et al., 1986; Hodkinson et al., 1986; Reich and Marchig, 1990; Hodkinson and Cronan, 1991
The Endeavour Segment: Juan de Fuca Ridge and Middle Valley	Bischoff et al., 1983; Tivey and Delaney, 1986; Koski et al., 1984; Hannington and Scott, 1988; Goodfellow and Franklin, 1993; Koski et al., 1994; Duckworth et al., 1994; Stuart et al., 1994	Brett et al., 1987; Goodfellow and Blaise, 1988; Ballu et al., 1998	German et al., 1997
Escanaba Trough, Southern Gorda Ridge	Morton et al., 1987; Zierenberg et al., 1993	Koski et al., 1988; Zierenberg and Schiffman, 1990; Hoyt, 1992; Zierenberg et al., 1993	
Galapagos	Corliss, 1979; Edmond et al., 1979b; Emberly et al., 1988; Herzig et al., 1988; Lalou et al., 1989; Knott et al., 1995		Edmond et al., 1979b; Walter and Stoffers, 1985
TAG	Rona, 1985; Thompson et al., 1988; Rona et al., 1993b; Rona et al., 1993a; Humphris et al., 1995; Humphris and Kleinrock, 1996; Chiba et al., 1998; Fouquet et al., 1998; Goulding et al., 1998; Hannington et al., 1998; Herzig et al., 1998b; Honnorez et al., 1998; Knott et al., 1998 Tivey et al., 1995; Teagle et al., 1998a; Teagle et al., 1998c; Mills and Tivey, 1999	Shearme et al., 1983; Thompson et al., 1985; Hannington et al., 1988; Metz et al., 1988; Lalou et al., 1989; Lalou et al., 1990; German et al., 1993; Hannington, 1993; Mills et al., 1993; Mills et al., 1994; Hannington et al., 1995b; Mills, 1995; Mills and Elderfield, 1995b; Mills et al., 1996; Goulding et al., 1997; Goulding et al., 1998; Severmann, 2000; Severmann et al., 2004	Mills and Elderfield, 1995a; Thompson et al., 1985; Bogdanov et al., 1998; Mills et al., 2001
Snake Pit	Detrick et al., 1986; Thompson et al., 1988;	Detrick et al., 1986; Gillis et al., 1990; Lalou et al., 1993	
Lucky Strike	Langmuir et al., 1997; Von Damm et al., 1998		
Rainbow	Fouquet, 1997	Bogdanov, 1999	German et al., 1996; Cave et al., 2002
Broken Spur	Duckworth et al., 1995; Butler et al., 1998	Duckworth et al., 1995	

Table 3.1: Key references and locations of massive sulphide and associated metalliferous sediment studies in the Pacific and Atlantic Oceans. Near field sediments are those collected close to sulphide mounds and which contain a significant percent of reduced sulphur species, far field sediments are principally composed of Fe oxide and are related to sedimentation from overlying hydrothermal plumes and distal low temperature diffuse fluids.

converted to chloride by addition of 6M HCl. 5ml aliquots of these solutions were diluted 10-fold in Milli-Q water.

Analysis

The resulting, 0.6M HCl solutions and reagent blanks were then analyzed for Na, Mg, Al, P, S, K, Ca, Ti, V, Cr, Mn, Fe, Co, Ni, Cu, Zn, Sr and Ba by ICP-AES on a Perkin Elmer Optima 4300DV at Southampton Oceanography Centre (SOC). All ICP-AES measurements were calibrated using matrix-matched, multi element solutions of appropriate dilutions of standards of known concentration (standard concentrations are listed in appendix A). The analytical accuracy was monitored by simultaneous analysis of these standard solutions; the full standard set was run at the beginning of the analysis with standard solution 3 run as every tenth measurement as a drift monitor (the samples and standards running list is shown in appendix B), and from the measurement of standard three, a drift correction was applied. Analytical precision, expressed as a coefficient of variation, was <1% (1σ) for Fe, Cu, Zn, Ca, Mg, Na, Mn, Al, K, Sr, Ba, V, Ni, Cr and Co and 1-1.4% (1σ) for S, P and Ti. Downcore elemental concentrations determined by ICP-AES are listed in Table 3.2a (CD102/58) and b (CD102/60).

3.2.2 X-Ray Diffraction (XRD)

3.2.3.1 Bulk Mineralogy

An overview of the bulk mineralogy downcore for CD102/58 and CD102/60 was obtained from X-ray diffraction patterns of selected samples on a Philips PW 1730 automated powder diffractometer using Co-K_α radiation. Samples were ground to a fine powder using a ceramic pestle and mortar. Dry powder mounts were then scanned between 2-60° at 0.2° 2θ/min. The detection limit is dependant on the crystallinity of individual minerals and typically ranges between 1-5%.

3.2.3.2 Clay Separations

Prior to chemical treatment all samples were dried at ~55°C and ground to a homogeneous fine powder in tungsten carbide TEMA vessels.

Removal of Carbonate Phase

4g of bulk sediment were treated with ~50ml of 10% acetic acid, agitated in an ultra sonic bath for ~3 minutes and left to settle overnight. When the reaction was complete the overlying acetic acid was carefully decanted and replaced with distilled water and left to settle overnight. Samples were washed with distilled water until the smell of acetic acid was gone and the sample thoroughly washed.

Removal of amorphous Fe-oxide phases

Samples were then treated with sodium citrate-bicarbonate dithionite buffer solution (CBD) following the method of Mehra and Jackson (1960). CBD was prepared by mixing eight parts of 0.3M sodium citrate solution (Tri-basic sodium citrate – $Na_3C_6H_5O_7.1H_2O$) with one part 1M bicarbonate solution ($NaHCO_3$). 180ml of the mixed reagent was added to the wetted sediments and incubated in a water bath at ~75°C for 15 minutes. During the incubation three 4g aliquots of sodium-dithionate were carefully added at 5 minute intervals and the solution stirred constantly for 1 minute and intermittently for the further 4 minutes between

Depth (cm)	Fe (%)	Cu (%)	Zn (%)	Ca (%)	Mg (%)	Na (%)	Mn (%)	Al (%)	P (%)	K (%)	Ti (ppm)	Sr (ppm)	Ba (ppm)	V (ppm)	Ni (ppm)	Cr (ppm)	Co (ppm)
1.5	11.2	0.27	0.05	24.0	0.59	1.01	0.18	0.95	0.20	0.25	660	1442	48.1	263	20.4	18.2	35.1
19	38.6	0.10	0.09	11.5	1.20	4.04	0.73	0.38	0.31	0.39	226	722	123	279	26.9	6.48	16.8
31	23.0	0.33	0.18	11.5	1.07	3.86	0.84	0.63	0.18	0.43	359	650	179	152	34.8	16.0	42.7
38	42.7	0.85	0.60	0.5	0.73	1.22	0.11	0.11	0.34	0.16	44.2	170	32.6	165	11.7	40.0	19.3
52	21.8	0.74	0.50	11.4	0.94	1.67	1.17	1.23	0.20	0.52	768	626	388	198	25.3	25.3	60.1
60	39.7	0.85	0.52	0.82	0.95	2.64	0.25	0.23	0.24	0.39	128	174	100	132	5.04	13.7	11.2
66.25	42.8	0.65	0.93	0.61	1.06	1.88	0.10	0.55	0.37	0.38	361	153	140	230	10.7	27.9	13.3
74.5	43.2	0.22	2.69	0.37	0.69	1.36	0.05	0.34	0.49	0.25	171	96.6	232	306	13.5	30.1	24.6
78.5	29.9	12.02	9.87	0.14	0.29	0.63	0.02	0.12	0.08	0.10	27.3	27.0	24.2	198	8.89	19.1	72.5
82	30.1	6.66	11.90	0.10	0.44	0.83	0.02	0.10	0.06	0.18	15.7	28.2	28.6	177	10.3	14.3	98.3
83	32.6	5.95	13.79	0.12	0.41	0.84	0.03	0.11	0.06	0.17	27.3	33.0	101	205	9.56	15.3	118
84.25	34.9	4.11	9.62	0.15	0.36	0.78	0.02	0.12	0.08	0.16	31.2	34.0	24.4	183	7.77	15.0	100
85.75	33.9	5.57	14.72	0.11	0.32	0.80	0.02	0.08	0.05	0.19	14.3	52.0	309	181	10.5	10.5	61.5
87.25	38.2	1.75	3.79	0.20	0.65	1.38	0.03	0.11	0.23	0.30	40.2	53.0	45.2	180	10.2	23.5	124
101	37.5	0.67	1.40	0.21	0.90	1.39	0.04	0.04	0.15	0.46	17.3	53.6	76.8	95.5	6.95	5.41	21.7
105	41.5	0.59	1.29	0.22	1.08	1.60	0.04	0.05	0.18	0.53	19.2	60.8	20.2	140	5.69	9.17	17.3
111	36.2	0.91	1.18	0.27	1.11	2.44	0.04	0.04	0.13	0.60	14.2	83.5	5.46	84.4	6.08	4.51	25.7
117.5	39.1	0.94	2.60	0.14	0.85	1.28	0.04	0.04	0.13	0.46	10.3	42.2	4.04	98.3	7.04	5.09	29.4
127	34.7	0.06	1.12	0.29	1.14	2.15	0.05	0.70	0.27	0.82	423	82.0	250	186	8.78	17.7	12.3
143	34.7	0.06	1.24	0.34	1.25	3.21	0.04	0.69	0.25	1.00	408	91.8	252	181	9.89	17.8	9.41
147	32.5	0.43	5.99	0.15	0.89	1.39	0.04	0.02	0.08	0.54	9.15	37.5	4.15	85.8	6.32	4.52	25.0
154	41.7	0.05	0.76	0.24	1.09	1.62	0.07	0.03	0.20	0.66	14.3	66.3	35.3	89.5	2.60	3.42	10.8
162	38.4	0.06	0.64	0.19	0.96	1.24	0.06	0.02	0.17	0.54	8.69	56.2	28.6	93.1	1.85	4.43	19.1
172	37.1	3.49	0.89	0.60	0.50	1.46	0.02	0.85	0.30	0.11	9.13	229	14.1	212	3.76	25.5	5.85
182	35.0	0.28	0.26	0.20	0.94	1.63	0.07	0.04	0.26	0.61	8.87	68.5	230	125	1.37	12.6	6.46
186	41.6	0.43	0.30	0.27	1.12	1.66	0.09	0.11	0.32	0.50	50.2	76.2	48.8	116	83.2	15.9	8.51
Precision % (1σ)	0.64	0.50	0.71	0.70	0.49	0.46	0.59	0.45	1.05	0.56	1.40	0.55	0.56	0.95	0.62	0.67	0.81

Table 3.2a: Major and minor element concentrations, determined by ICP-AES, in core CD102/58.

Depth (cm)	Fe (%)	Cu (%)	Zn (%)	Ca (%)	Mg (%)	Na (%)	Mn (%)	Al (%)	P (%)	K (%)	Ti (ppm)	Sr (ppm)	Ba (ppm)	V (ppm)	Ni (ppm)	Cr (ppm)	Co (ppm)
1.5	14.3	0.62	0.17	22.2	0.79	1.41	0.22	1.05	0.22	0.26	725	1183	47.0	303	25.7	24.0	20.3
16	23.1	0.80	0.47	11.5	1.41	2.48	1.64	0.53	0.27	0.44	304	710	130	229	137	14.6	10.6
30	39.3	4.04	0.97	0.95	1.66	1.28	0.03	0.31	0.44	0.16	64.0	320	24.3	153	4.13	41.4	22.7
38	23.7	0.73	0.87	1.87	1.22	2.66	0.12	0.50	0.40	0.14	33.1	214	16.1	303	13.6	56.5	6.67
46	37.9	0.04	0.33	0.23	1.30	2.21	0.05	0.02	0.23	1.17	12.0	59.2	15.4	74.3	1.11	1.33	5.35
49	44.2	1.78	0.82	0.22	0.30	0.82	0.02	0.51	0.06	0.05	9.18	49.8	3.77	159	28.3	8.54	114
57	18.9	4.40	1.40	0.25	1.28	0.57	0.01	0.22	0.08	0.04	26.7	11.1	1.49	85.1	15.2	7.52	24.8
64	20.6	4.23	1.37	0.50	1.37	0.79	0.02	2.28	0.04	0.05	1858	17.7	3.88	158	42.0	97.3	64.3
72	21.6	0.83	2.07	1.88	2.91	1.37	0.04	5.68	0.06	0.08	5018	48.1	10.9	261	101	253	60.6
78	11.9	0.33	3.17	4.04	4.01	2.07	0.05	9.39	0.09	0.10	7967	136	25.9	263	119	420	48.2
86	35.3	8.21	0.72	0.12	0.48	0.89	0.02	0.79	0.11	0.13	85.0	17.1	3.68	307	10.5	25.1	20.2
92.5	23.7	12.1	0.40	0.12	0.49	0.99	0.01	0.89	0.05	0.14	162	15.0	5.45	395	11.7	30.2	21.4
97	26.5	0.56	0.72	0.48	2.80	3.58	0.05	2.66	0.19	0.98	1899	62.8	57.4	173	21.8	58.5	36.4
101	36.5	0.27	0.69	0.97	1.36	3.15	0.05	1.04	0.29	0.45	373	69.3	33.6	313	8.79	26.8	9.28
111	37.1	0.17	0.63	0.31	1.42	3.34	0.05	0.82	0.27	0.52	152	78.1	13.5	196	5.51	15.4	2.21
117.5	37.4	4.04	0.77	0.26	0.85	1.44	0.05	1.00	0.32	0.24	217	34.3	11.5	304	6.06	28.1	7.29
122	45.8	1.30	0.34	0.93	0.74	1.63	0.08	0.80	0.44	0.15	146	32.4	10.2	614	6.45	38.7	5.61
Precision % (1σ)	0.64	0.50	0.71	0.70	0.49	0.46	0.59	0.45	1.05	0.56	1.40	0.55	0.56	0.95	0.62	0.67	0.81

Table 3.2b: Major and minor element concentrations, determined by ICP-AES, in core CD102/60.

each addition. Following this ~10ml of saturated NaCl solution was added and the mixture centrifuged at 3000rpm for 3 minutes and the supernatant carefully discarded. To ensure complete removal of amorphous Fe-oxide the treatment was repeated with 90ml CBD and three aliquots of 2g sodium-dithionate. After the second treatment the sediments were washed with 100ml of Milli-Q water to which 5ml of saturated NaCl solution was added.

Removal of amorphous silica phases

Following removal of amorphous Fe-oxides the samples were resuspended in 200ml of 2% sodium bicarbonate solution and heated to ~85°C in a water bath for 45 minutes. The mixture was then centrifuged at 3000rpm and the supernatant discarded. The sediments were then washed with 100ml of Milli-Q water to which 5ml saturated NaCl solution was added and centrifuged for a further 3 minutes.

Separation of the <2μm fraction

The wetted sediments were re-suspended in 80ml of a 1% sodium hexa-metaphosphate solution (Calgon®) to aid dispersion, and ultra sonically agitated for 30 minutes. Immediately upon removal from the ultra sonic bath samples were centrifuged at 750rpm for 3 minutes. The supernatant was carefully discarded and the residue washed with 80ml of Milli-Q water and re-centrifuged at 3000rpm for 3 minutes. The wash stage was then repeated. Smear slides of the clay residue were then prepared for XRD analysis and air dried for 24 hours and the remaining sample dried at ~50°C after which the samples were ground to a fine powder in an agate pestle and mortar then weighted to calculate the percent of clay in the bulk sediment (Table 3.4).

XRD Analysis

X-ray diffraction patterns of the air dried, clay smear slides were obtained on a Philips PW 1730 automated powder diffractometer using Co-K_α radiation. The air dried slides were scanned between 1-17° at 0.2° 2θ/min. The slides were then heated in a dessicator with ethyl glycol overnight at ~55°C. This replaces interlayer water with ethyl glycol and allows identification of swelling clays e.g. smectite. The slides were scanned between 2-40° at 0.2° 2θ/min. Following this the slides were heated in an oven at 375°C overnight, to drive off loosely bound and interlayer water, removed individually and scanned between 2-17° at 0.2° 2θ/min. Finally the slides were heated in an oven at 550°C overnight to drive off all remaining water, removed individually and scanned between 2-17° at 0.2° 2θ/min.

3.2.3 XRF

Since Si and S cannot be analysed by ICP-AES, Si and S, as well as other major element (Ti, Al, Fe, Mn, Mg, Ca, K, Na, P, Co, and Cu) concentrations were measured on a Philips MAGIX-PRO fully automated sequential, wavelength dispersive XRF (WD-XRF). 1 gram samples of bulk sediment were ignited at 980°C in ceramic crucibles to remove volatiles prior to preparation of fused beads. Samples were fused at 1200°C in platinum crucibles with a lithium tetraborate flux (Spectroflux® 100) at a dilution of 1:20. Final concentrations were corrected for loss on ignition (LOI). Accuracy for the analysis was monitored by simultaneous analysis of standard reference material of known concentration. Analytical accuracy and precision of the measurements was poor, ±6.9-34% (1σ). The poor accuracy and precision of the XRF data can be related principally to homogenisation and liberation difficulties. Although attempts were made to solve and/or minimize these problems, e.g. addition of a non-wetting agent to the melt, and increasing the flux to sample ratio, satisfactory data could not be obtained. As such, the XRF data set is excluded from the following discussion of the general sediment geochemistry.

3.2.4 Optical Microscopy

Three polished thin sections of a resin impregnated section from 76 to 87cm depth, in CD102/58, were examined and photographed in both transmitted and reflected light on a binocular polarizing microscope.

3.3 Results and Discussion

3.3.1 Bulk Mineralogical Composition and Stratigraphy

Mineralogical data for cores CD102/58 and CD102/60 are summarised in Figure 3.1 and 3.2. Both cores are capped by a carbonate layer with varying amounts of iron staining underlain by poorly consolidated fine-medium grained Fe-oxyhydroxide-rich sediment. Underlying the Fe-oxyhydroxide-rich layers are medium-coarse grained, sulphide-rich layers dominated by pyrite and sphalerite with lesser amounts of chalcopyrite and covellite in Core 58 and pyrite with minor chalcopyrite and sphalerite and trace covellite in Core 60. The sulphide layer, in both cases, is underlain by a further Fe-oxyhydroxide layer and below this in Core 60 is a Fe-oxide layer. Plume inputs to both cores are low; these are near-field hydrothermal sediments. Both cores are extremely heterogeneous in nature with a wide range in grain size (<2μm - ~1cm) and composition.

3.3.1.1 CD102/58

Although the stratigraphic relationships within this core are complex and reflect inputs from several different sources the core can be divided into four mineralogically distinct units (Figure 3.1):

1. **0-33cm Carbonate Cap.** Dominated by calcite-rich, fine-grained, pelagic sediments intermixed with goethite of hydrothermal origin. The $CaCO_3$ content was calculated from bulk Ca content assuming that Ca is held as $CaCO_3$, this assumption is justified by XRD analyses which indicate that calcite is the only Ca bearing mineral phase, and by clay contents which are <1% in this part of the core indicating minimal detrital inputs. Calcium carbonate concentrations range from ~60-29wt%, with the lowest values occurring towards the base of this layer and corresponding to an increase in the abundance of hydrothermally sourced goethite downcore. This range in carbonate contents is consistent with the range reported for other metalliferous sediment cores collected nearby; CD102/43 $CaCO_3$% =~1-62.5 (Severmann et al., 2004); Metz et al. (1988) core $CaCO_3$% =~4-64. A further lens, ~0.5cm thick, of carbonate (28.5wt% of the bulk sediment) occurs at 52cm.
2. **33-76cm Fe-oxyhydroxide rubble layer 1.** Dominated by goethite and quartz, gypsum occurs as a minor phase below ~68cm depth downcore. Alignment of elongate clasts and minor layering indicate deposition via a mass flow event. Quartz may have been transported to the sediment from the nearby mound during the mass flow event; alternatively it may represent in situ precipitation from a low temperature Si-rich fluid; or contributions from both. The origin and evolution of Si phases is discussed in detail in Section 3.3.3. This layer is the product of sulphide oxidation; element distributions (Section 3.3.4 and 3.3.5) indicate that contributions of Fe-oxide and oxyhydroxide phases from plume fallout are minimal.

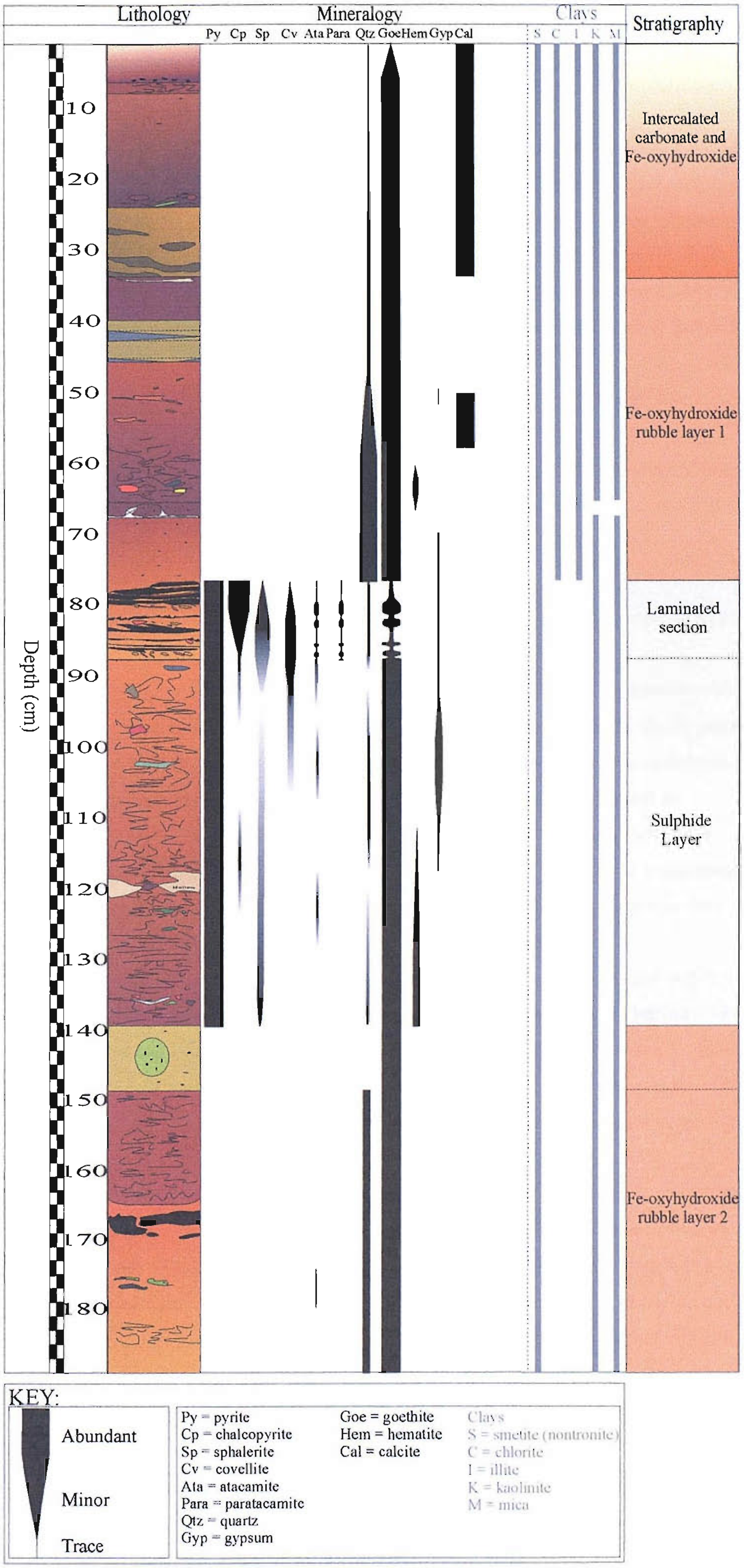

Figure 3.1: Mineralogical occurrence and adundancies downcore CD102/58 determined from XRD and optical microscopy. Stratigraphic subdivisions are based on the dominant mineralogy and sedimentary relationships.

3. **76-138.5cm Sulphide layer.** Dominated by pyrite and sphalerite with minor chalcopyrite and covellite. Goethite is also abundant. Between 76-87cm the sediment is laminated with alternating black, sulphide-rich and orange, goethite-rich layers typically about 0.7cm thick. The sulphide layers in the laminated section are graded suggesting sedimentation via turbidity flows. Gypsum is present as a minor phase down to ~117cm downcore. Secondary Cu salts, atacamite and paratacamite, are also present. The genesis and alteration history of the Core 58 sulphide layer is discussed in detail in Chapter 4: Sulphide Mineralogy and Alteration.
4. **138.5-188cm (base) Fe-oxyhydroxide rubble layer 2.** Goethite is the principle phase with minor quartz and trace atacamite. This layer is mineralogically and sedimentalogically very similar to Fe-oxyhydroxide layer 1 and is also inferred to be the product of sulphide oxidation and alteration of primary mound material following transport from the *Alvin* mound to the surrounding sediments.

3.3.1.2 CD102/60

Stratigraphic relationships within this core are also complex reflecting inputs from several sources. The core can be divided into five mineralogically distinct units (Figure 3.2):

1. **0-33cm Carbonate Cap.** Dominated by calcite-rich, fine-grained, pelagic sediments intermixed with goethite of hydrothermal origin and intercalated with elongate lenses of Fe-oxide, and to a lesser extent atacamite. Major quartz and minor opal (an amorphous variety of quartz) occur throughout this layer. Calcium carbonate concentrations (calculated from ICP-AES data assuming all Ca is present as carbonate) range from 55.5wt% at the top of the core to ~2.5wt% at the base of this layer where the abundance of goethite and hematite increase. The range in carbonate contents for Core 60 is comparable to Core 58 and to CD102/43 (Severmann et al., 2004) and the Metz et al. (1988) core. The boundary with the Fe-oxide and Fe-oxyhydroxide layer underlying the carbonate cap is gradational.
2. **33-47cm Fe-oxide and oxyhydroxide rubble layer 1.** Dominated by goethite, hematite and quartz with minor cristobalite (a quartz polymorph). The sediment is medium-coarse grained, except between 44-47cm where it is fine-grained and laminated. Throughout this layer bands and elongate lenses of fine-grained Fe-oxide-rich material occur within the dominant, medium-grained, Fe-oxyhydroxide material. These laminae are the result of sediment transport and are not related to alteration processes occurring in situ.
3. **47-96cm Sulphide layer.** Dominated by pyrite with chalcopyrite, minor sphalerite and trace covellite. Minor quartz, opal and cristobalite occur throughout. Plagioclase and chlorite occur between ~64-96cm depth downcore. The presence of plagioclase feldspars and chlorite indicate inclusion of partially altered basalt fragments. This is consistent with the paragenesis model (Chapter 4: Section 4.4.3) of formation of the sulphide layer from an inner mound pyrite-quartz breccia transported to the surrounding sediments during a faulting event. Normal faulting within the Mir zone, which has exposed apparent, hydrothermal, basaltic breccias, has previously been invoked to account for basalt supply to surrounding sediments (Rona et al., 1993b; Rona et al., 1993a). The genesis and alteration history of the Core 60 sulphide layer is discussed in detail in Chapter 4: Sulphide Mineralogy and Alteration.

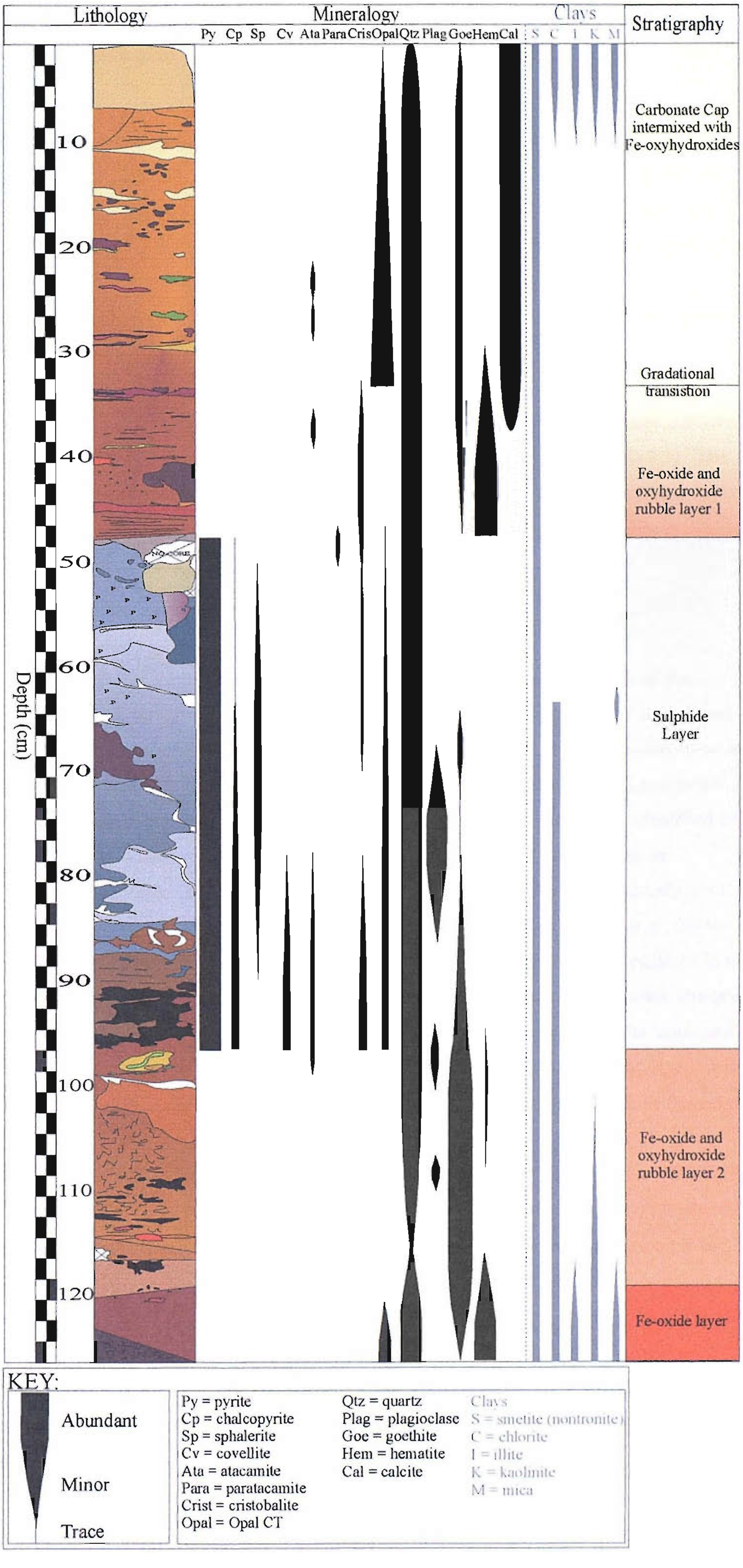

Figure 3.2: Mineralogical occurrence and adundancies downcore CD102/60 determined from XRD and optical microscopy. Stratigraphic subdivisions are based on the dominant mineralogy and sedimentary relationships.

4. **96-119cm Fe-oxide and oxyhydroxide rubble layer 2.** Principally goethite and quartz with minor plagioclase and hematite of hydrothermal origin. The material is fine-medium grained sandy silt with patches of dark brown or grey/black material randomly occurring throughout. The base of this layer is inclined at ~25° suggesting that the core was recovered from the edge of an infilling basin or local hollow, or as drape cover over a faulted block.
5. **119-126cm (base) Fe-oxide layer.** Dominated by fine-grained hematite and quartz with minor goethite and opal.

The major mineralogical compositions of CD102/58 and CD102/60 compare well with previously published data for metalliferous sediments from hydrothermal sites in both the Atlantic and Pacific (Table 3.3). The most striking difference between cores 58 and 60, and those of previous studies, is the predominance of clay phases other than nontronite. In Core 58 kaolinite and micas dominate whilst in Core 60, chlorite is important.

3.3.2 Clay Mineralogy

Clay mineralogy and wt% recovery from bulk sediments are shown in Table 3.4. XRD spectra of clay separates from Core 58 and Core 60 show well defined peaks indicating that the clays are well crystallised. There is no indication of amorphous phases, i.e. no raised backgrounds, confirming their successful removal during chemical treatment (Figure 3.3). Both cores contain a mixture of detrital, hydrothermal and basaltic clays. Smectite is present in all samples analysed. Although the variety of smectite cannot be identified from XRD spectra it is most likely to be nontronite since nontronite is the most common clay mineral in hydrothermal deposits (e.g. Alt, 1988a; Thompson et al., 1985; Hekinian et al., 1993). More specifically the clay mineralogy of an adjacent core, CD102/43, is almost exclusively nontronite (Severmann et al., 2004). Clay contributions from detrital sources, with a typical assemblage of kaolinite and illite, are restricted to the carbonate cap and upper Fe-oxyhydroxide rubble layers in both cores. Chlorite, a product of basalt alteration (e.g. Alt, 1995 Honnorez et al., 1998) (Section 3.3.3.3), is present between 0-~90cm (base of the laminated section of the sulphide layer) in Core 58, and throughout Core 60, except at a depth of 37-39cm, where it is typically associated with plagioclase occurrence relating to the inclusion of partially altered basalt fragments.

Calculated clay recoveries (Table 3.4) range from 0.54-18.1% of the bulk sediment in Core 58 and from 0.69-5.5% of the bulk sediment in Core 60. The highest clay contents in both cores are found in Fe-oxyhydroxide and Fe-oxide rich sediment below the sulphide layers. These recoveries, except for basal clays from Core 58 (154cm: 18.1wt% clay; and 182cm: 11.4wt% clay) are significantly less than the <2μm fraction reported for sediments from the surface of the TAG mound (20-43wt% clay), surficial carbonate sediments from the TAG area (11-14wt% clay) and buried Fe-oxysilicates from the *Alvin* Zone (34-64wt% clay) (Severmann et al., 2004). The lower clay wt% values in this study compared to previously published data from the TAG area reflect the lesser extent of oxidation of sulphide material in these cores, especially Core 60, and may also indicate that the low temperature diffuse fluids and the E_h conditions required for the in situ precipitation of hydrothermal clays, e.g. nontronite, are less extensive in these sediments. The nontronitic clays from Core 43 were all precipitated during authigenic alteration and re-crystallization of primary detrital material and have

	Reference: **Core number/ Location**	**This study CD102/58 Alvin mound**	**This study CD102/60 Mir mound**	Severmann (2000) CD102/43 Alvin Mound	Metz et al (1988) Alvin Zone	German et al (1993) ~120m NE of active BS complex TAG	Goulding (1998) SW of Kremlin area TAG	Zierenberg et al (1993) Escanaba Trough
Mineral	**General Formula**							
Pyrite	FeS_2	**X**	**X**	X	X	X	X	X
Marcasite	FeS_2							
Pyrrhotite	FeS							X
Sphalerite	ZnS	**X**	**X**	X	X		X	X
Chalcopyrite	$CuFeS_2$	**X**	**X**	X	X		X	X
Covellite	CuS	**X**	**X**	X				
Atacamite	$Cu_2Cl(OH)_3$	**X**	**X**	X	X		X	
Paratacamite	$Cu_2Cl(OH)_3$	**X**	**X**		X		X	
Quartz	SiO_2	**X**	**X**	X	X	X	X	
Cristobalite	SiO_2		**X**					
Opal	SiO_2		**X**	X			X	
Amorphous Si			**X**			X		
Amorphous Fe-oxide/ oxyhydroxide		**X**	**X**	X	X	X		X
Goethite	FeO(OH)	**X**	**X**	X	X		X	
Hematite	Fe_2O_3	**X**	**X**	X	X		X	
Pyrolusite	MnO_2				X		X	
Birsenite				X	X		X	
Calcite	$CaCO_3$	**X**	**X**	X	X	X	X	X
Gypsum	$CaSO_4.nH_2O$	**X**						
Barite	$BaSO_4$	**X**						
Plagioclase	$(Na,Al)Si_3O_8$ – $(Ca,Al)Si_3O_8$		**X**	X		X		X
Nontronite	$NaFe_2$ $(Si,Al)_4$ $O_{10}(OH)_2.H_2O$	**X**	**X**	X	X			
Other clays		**X**	**X**	X			X	
	Reference:	Hékinian et al (1993) EPR						
	Core number/ Location	Society Region 18°S	Pitcairn Region 25°S	Austral Region 29°S	21°N	12°N	11°N	Hess Deep
Mineral	**General Formula**							
Pyrite	FeS_2				X	X		
Marcasite	FeS_2							
Pyrrhotite	FeS							
Sphalerite	ZnS				X			
Chalcopyrite	$CuFeS_2$					X		
Covellite	CuS							
Atacamite	$Cu_2Cl(OH)_3$							
Paratacamite	$Cu_2Cl(OH)_3$							
Quartz	SiO_2				X			
Cristobalite	SiO_2							
Opal	SiO_2	X				X	X	
Amorphous Si								
Amorphous Fe-oxide/ oxyhydroxide		X	X	X	X	X	X	X
Goethite	FeO(OH)	X	X	X	X	X	X	X
Hematite	Fe_2O_3							
Pyrolusite	MnO_2							
Birsenite								
Calcite	$CaCO_3$							
Gypsum	$CaSO_4.nH_2O$							
Barite	$BaSO_4$				X	X	X	
Plagioclase	$(Na,Al)Si_3O_8$ – $(Ca,Al)Si_3O_8$							
Nontronite	$NaFe_2$ $(Si,Al)_4$ $O_{10}(OH)_2.H_2O$							
Other clays					X	X		X

Table 3.3: Mineral occurrences in CD102/58 and CD102/60. Mineral occurrences in metalliferous sediments from Atlantic and Pacific sites are shown for comparison.

Sample ID	Depth (cm)	Clay content (wt%)§	Bulk Sediment Al wt%	Clay mineralogy	Description of bulk sediment
Alvin Mound - This study CD102/58					
14-17	0-3	0.84	0.95	Sm, Chl, Kao, Ill, Qtz, trace Plag and Mica	Carbonate ooze
46-47	32-33	1.01	~	Sm, Chl, Kao, Ill, Qtz, trace Plag and Mica	Carbonate ooze intermixed with Fe-oxyhydroxide
65-67	51-53	7.99	1.23	Sm, Chl, Kao, Ill, Qtz, trace Plag and Mica	Fe-oxyhydroxide and quartz with minor carbonate
79-81.5	65-67.5	6.43	0.55	Sm, Chl, minor Qtz and Kao	Sulphide debris admixed with Fe-oxyhydroxides
87.5-89.5	73.5-75.5	0.54	0.34	Sm, Chl, Kao, Ill, Qtz, trace Plag and Mica	
102-104	88-90	9.62	~	Sm minor Ill and Mica	
118-120	104-106	8.51	0.05	Sm minor Ill and Mica	
130.5-132.5	116.5-118.5	8.53	0.04	Sm minor Ill and Mica	
167-169	153-155	18.05	0.03	Sm minor Ill and Mica	Fe-oxyhydroxide
195-197	181-183	11.41	0.04	Sm minor Ill and Mica	
Mir Mound - This Study CD102/60					
11-14	0-3	0.69	1.05	Sm, Chl, Kao, Ill, Qtz, minor Plag and Mica	Carbonate ooze
48-50	37-39	1.52	0.5	Sm minor Qtz, Ill and Mica	Fe-oxyhydroxide
74-76	63-65	2.51	2.28	Sm, Chl, Kao, minor Qtz, Plag and Mica	Sulphide and Quartz breccia
96-98	82-84	3.51	~	Sm and Chl	Sulphide and Quartz breccia with Fe-oxyhydroxide
111-113	100-102	4.24	1.04	Sm, trace Chl	Clastic Fe-oxyhydroxide
132-134	121-123	5.5	0.8	Sm, Crist, Qtz, minor Chl	
Alvin Zone CD102/43					
43-5	20-25	14	1.0	Sm, Kao, Qtz, Plag minor Ill	Fe-oxyhydroxide-rich carbonate ooze
43-8	35-40	11	0.9		
43-15	70-75	39	0.7		Fe-oxysillicate layer between sulphide debris from nearby mound
43-21	100-105	52	0.2		
43-25	120-125	38	0.0		
43-32	155-160	64	0.5	Sm	
TAG Active mound					
2598	0-4	38	0.1		Surficial Atacamite crust from area of diffuse flow
2897-1	0-4	43	0.0	Sm minor Qtz	Sulphide debris
2897-2	4-8	35	0.0		Carbonate ooze
2901-1	0-3	19	0.3		Sulphide debris and Fe-oxides
2901-2	3-6	20	0.2		
~50km west of MAR - Background core CD102/10					
10-3	3-8	2	0.6		Carbonate ooze
10-5	13-18	4	~	Ill, Kao, Qtz, Plag	Carbonate ooze
10-25	113-118	3	0.9		Carbonate ooze
10-38	178-183	2	0.9		Carbonate ooze

§ Minimum clay % based on physical recovery following clay separation
Al for CD102/58 and CD102/60 analyzed by ICP-AES (this study), Al for CD10243; CD102/10 and TAG Active mound samples analyzed by XRF (Severmann pers. comm.). Clay recoveries and sample descriptions for CD102/43; CD102/10 and TAG Active mound from Severmann et al. (2003).
Mineral abbreviations: Sm=smectite; Chl=chlorite; Kao=kaolinite, Ill=illite; Qtz=quartz; Plag=plagioclase.

Table 3.4: Location of clay separates and bulk sediment descriptions. Data from the TAG Active Mound, a previous study of the Alvin zone and background sediments from the Mid-Atlantic are shown for comparison.

Scan A:

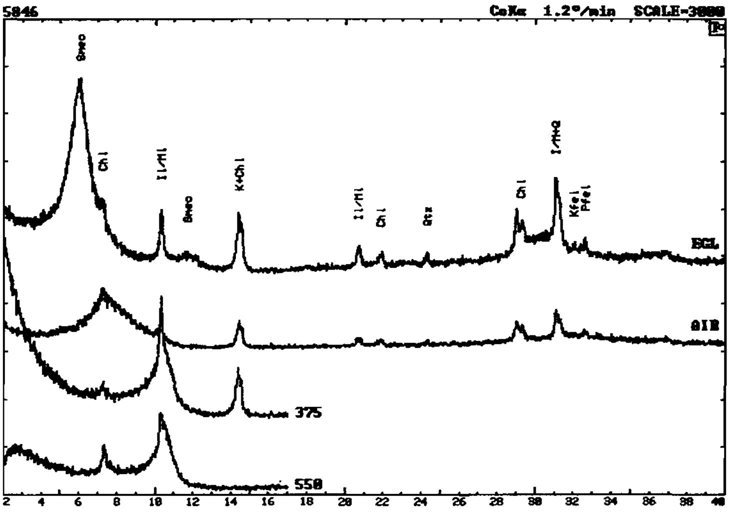

Scan B:

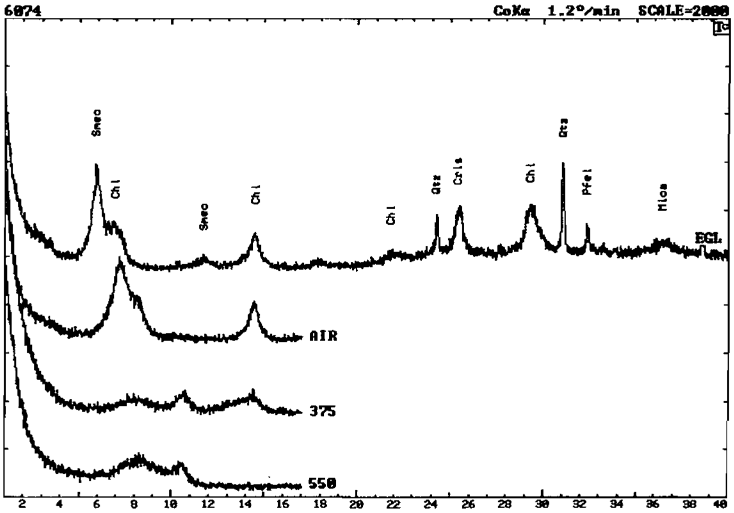

Figure 3.3: Typical XRD clay scans from this study: scan A = core CD102/58 from a depth of 32-33cm (sampling depth of 46-47cm); scan B = core CD102/60 from a depth of 63-65cm (sampling depth of 74-76cm).

inferred formation temperatures of 54-96°C (Severmann et al., 2004). However, despite the close proximity of Core 58 to Core 43 the alteration of Core 58 sediments is much less extensive.

3.3.3 Sources to the Sediment: Calculation of the Hydrothermal Component

Previous studies of metalliferous sediment cores from the TAG hydrothermal field (Metz et al., 1988; Mills et al., 1993) have invoked a three component mixing model to explain the distribution of biogenic, detrital and hydrothermal material in these sediments. The biogenic component is calculated as wt% $CaCO_3$ since organic carbon and biogenic opaline silica contributions combined account for <2% of the sediment in this area (Broecker and Peng, 1982). The detrital component is calculated as 10 times the Al concentration, based on typical values for North Atlantic clays (Lambert et al., 1984). The hydrothermal component is then calculated by difference. Figures 3.4a-f and Table 3.5 show the downcore variation in these components calculated using the data from this study.

3.3.3.1 Correlation to Fe Concentration

In contrast to data from the Metz et al (1988) TAG core, which showed a strong linear relationship between sediment Fe concentrations and the independently determined hydrothermal component (r^2=0.92) (Metz et al., 1988; Mills et al., 1993), the correlation between sediment Fe concentrations and the independently determined hydrothermal component from this study is very poor; Core 58 r^2=0.598 and Core 60 r^2=0.481. The poor correlations for the *Alvin* and *Mir* cores appear to be related to the abundance of pyrite. If only data from non pyrite bearing depths are considered, the linear correlation for Core 58 improves to r^2=0.77 and Core 60 improves to r^2=0.67. The correlation is poorest for both cores where pyrite is abundant; r^2 for Fe concentration vs. hydrothermal component in the sulphide layers is 0.01 for Core 58 and 0.39 for Core 60. These data are consistent with r^2 values calculated for pyrite bearing depths (23-46cm) in the Metz et al. (1988) TAG core where r^2=0.16. The lack of correlation in the pyrite bearing layers of Cores 58 and 60 reflects less Fe in these layers than expected. Metz et al. (1988) predict Fe concentrations of 44% for a 100% hydrothermal component and >35% for samples with a hydrothermal component in excess of 80%. Whilst the calculations of this study indicate a mean hydrothermal component of 98.2% in the sulphide layer of Core 58, and a mean of 67.3% in the sulphide layer of Core 60, Fe concentrations in the sulphide layers are low compared to the Metz et al (1988) prediction, ranging from 29.9-41.5% in Core 58, and 11.9-44.2% in Core 60.

The discrepancy between predicted and measured Fe concentrations can be explained by consideration of mineral chemistry. The best correlations between sediment Fe concentration and the independently determined hydrothermal component, for all three cores, occur where the dominant Fe bearing phase is an oxide or oxyhydroxide, the most common of which are goethite (FeO(OH)) and hematite (Fe_2O_3). The Metz et al. (1988) predictions for Fe% at variable hydrothermal component are based on Fe occurring predominantly as oxide or oxyhydroxide. The problem in the sulphide layers of Cores 58 and 60 is that Fe is present principally as pyrite (FeS_2) and, mole for mole, pyrite contains 16.3 and 23.4% less Fe than goethite and hematite respectively. This suggests that overtime the oxidation of the sulphide layers, and conversion of pyrite to goethite and hematite, should improve the correlation between sediment Fe concentrations and the independently determined hydrothermal component. Although the good overall correlation (r^2=0.98) between

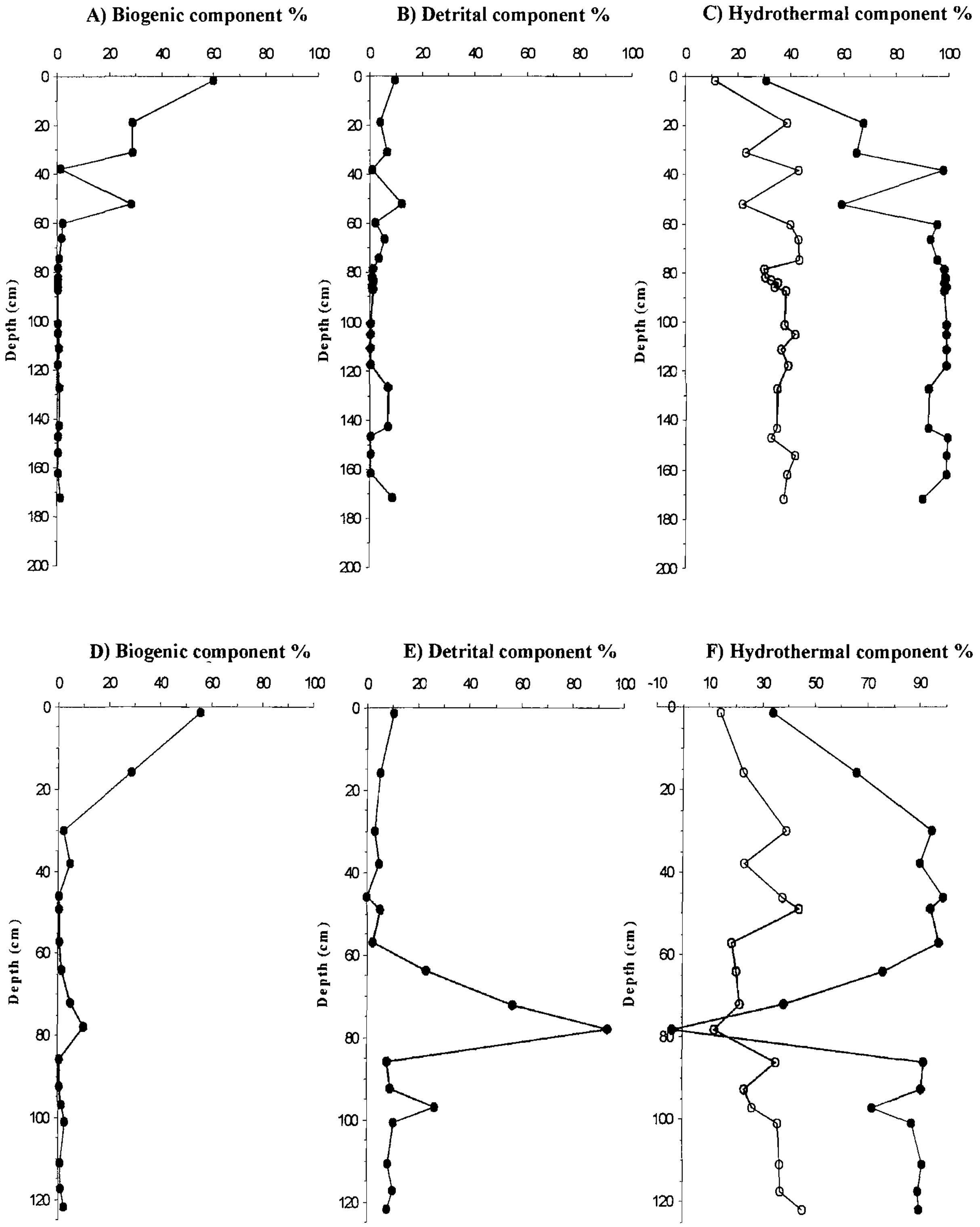

Figure 3.4: Downcore variation in calculated components for Core 58: A) biogenic; B) detrital; and C) hydrothermal; and Core 60 D) biogenic; E) detrital; and F) hydrothermal. For comparison downcore Fe wt%(open circles) is plotted with the hydrothermal component (solid circles). Shaded areas denote the extent of each sulphide layer identified from mineralogical studies

Depth (cm)	Biogenic component %	Detrital component %	Hydrothermal component %	Fe (%)
CD102/58				
1.5	59.9	9.5	30.6	11.2
19	28.7	3.8	67.5	38.6
31	28.7	6.3	64.9	23.0
38	1.2	1.1	97.7	42.7
52	28.5	12.3	59.2	21.8
60	2.0	2.3	95.7	39.7
66.25	1.5	5.6	92.9	42.8
74.5	0.9	3.4	95.7	43.2
78.5	0.4	1.2	98.5	29.9
82	0.3	1.0	98.7	30.1
83	0.3	1.1	98.6	32.6
84.25	0.4	1.2	98.4	34.9
85.75	0.3	0.8	98.9	33.9
87.25	0.5	1.1	98.4	38.2
101	0.5	0.4	99.0	37.5
105	0.5	0.5	98.9	41.5
111	0.7	0.4	98.9	36.2
117.5	0.4	0.4	99.3	39.1
127	0.7	7.0	92.3	34.7
143	0.9	6.9	92.2	34.7
147	0.4	0.2	99.4	32.5
154	0.6	0.3	99.1	41.7
162	0.5	0.2	99.3	38.4
172	1.5	8.5	90.0	37.1
Mean	6.2	3.0	90.8	35.1

Depth (cm)	Biogenic component %	Detrital component %	Hydrothermal component %	Fe (%)
CD102/60				
1.5	55.5	10.5	34.0	14.3
16	28.8	5.3	65.8	23.1
30	2.4	3.1	94.6	39.3
38	4.7	5.0	90.4	23.7
46	0.6	0.2	99.2	37.9
49	0.5	5.1	94.4	44.2
57	0.6	2.2	97.2	18.9
64	1.3	22.8	76.0	20.6
72	4.7	56.8	38.5	21.6
78	10.1	93.9	-4.0	11.9
86	0.3	8.0	91.8	35.3
92.5	0.3	8.9	90.7	23.7
97	1.2	26.6	72.2	26.5
101	2.4	10.4	87.2	36.5
111	0.8	8.2	91.0	37.1
117.5	0.7	10.0	89.3	37.4
122	2.3	8.0	89.7	45.8
Mean	6.9	16.8	7.6	17.8

Table 3.5: Downcore distribution of calculated biogenic, detrital and hydrothermal components, and Fe wt% in CD102/58 and CD102/60.

sediment Fe concentration and the calculated hydrothermal component in the Metz et al. (1988) TAG core justifies its use as an index of hydrothermal activity, the sulphide-rich nature of CD102/58 and CD102/60 mean that it is not appropriate in this study.

3.3.3.2 The Use of Al as a Proxy for Detrital Inputs

The use of the Al content of bulk hydrothermal sediments as an index of detrital input (e.g. Metz et al., 1988; Shimmield and Price, 1988; Mills et al., 1993) assumes that all Al in these sediments has a detrital origin, and that the sedimentary accumulation of Al depends on the extent of dilution by hydrothermal phases. Since the Al content of North Atlantic clays is typically ~9.5% (e.g. Thomson et al., 1984) detrital input is calculated as 10 times the Al% of bulk sediments. Al contents from the TAG area are generally <1% (e.g. Metz et al., 1988; Thompson et al., 1985; German et al., 1993) this is because background detrital input to the Mid-Atlantic is low; clay recovery from CD102/10 (29°N), a background core, was <4% (Severmann et al., 2004). Good agreement between sediment mineralogy, Fe content and detrital inputs calculated from the Al content for the Metz et al. (1988) TAG core and Core 58 justify the use of the Al detrital proxy, in these cases. However, the assumptions used to calculate the detrital component of bulk hydrothermal sediments from Al content are not valid for Core 60.

3.3.3.3 Additional Non-Detrital Al in CD102/60

The downcore Al content of Core 60 ranges from 0.02-9.39% with the highest values (2.28-9.39%) occurring within the sulphide layer (64-78cm depth). Calculation of the detrital component using the method described above gives a detrital input of <1% to ~94%, the highest values, when combined with the biogenic component are >100% which is clearly incorrect. In addition, where Al content is highest sulphide minerals, quartz and plagioclase dominate the bulk mineralogy and smectite (nontronite?) and chlorite the clay mineralogy, the common assemblage of illite and kaolinite for North Atlantic clays is not observed. This suggests that there is an additional, non detrital, source of Al to Core 60.

There are two potential sources for the additional Al in Core 60. The first possibility to consider is contributions from non-detrital clay phases. Although the clay content of Core 60, which ranges from <1%-5.5%, is consistent with that expected from detrital inputs (background core clay contents range from 2-4%: Severmann et al., 2004) the clay mineralogy is dominated by the hydrothermal phases smectite and chlorite, rather than illite and kaolinite which are the dominant phases in North Atlantic clays (Table 3.4). Since nontronite ($NaFe_2(Si,Al)_4O_{10}(OH)_2.H_2O$), from the smectite clay group, is the most common clay mineral in hydrothermal deposits (e.g. Alt, 1988a; Hekinian et al., 1993; Severmann et al., 2004) and the clay separates are deep green in colour, implying a significant Fe(II) component, the smectite from Core 60 is inferred to be nontronitic. Collomorphic textures and layering of nontronite in these sediments indicates precipitation occurred in situ, during sulphide alteration; nontronite precipitates from low temperature hydrothermal fluids under low E_h conditions where Fe^{2+} and Si are present in solution (Harder, 1976). In contrast, chlorite ($(Mg,Al,Fe^{2+})_{12}\,[(Si,Al)_8O_{20}]\,(OH)_8$), a common alteration product of basalt at temperatures in excess of ~200°C (e.g. Alt, 1995; Honnorez et al., 1998), is not precipitated in situ but is transported to the sediment during mass wasting events and its presence reflects the inner mound origin of the Core 60 sulphide layer (Chapter 4; Section 4.4.3).

Whilst both nontronite and chlorite can accommodate Al in their crystal structure their presence cannot explain the high Al contents of the bulk sediments. Published chemical data show that nontronite from the TAG Active mound and the *Alvin* zone is extremely Al-poor, including several samples containing Al below detection limits (Severmann et al., 2004). Assuming that this trend applies to all nontronite from the TAG hydrothermal field, the nontronite in Core 60 is also likely to have low Al contents. While chlorite can contain a maximum Al content of ~54% mass balance considerations indicate that even an Al-rich chlorite cannot account for the high Al content of the bulk sediment: the relative percentages of each clay phase are not known, but if it is assumed that Al-rich chlorite accounts for 100% of the clays recovered from Core 60, the maximum clay content of 5.5% could account for 2.97wt% Al in the bulk phase which is significantly less than the maximum bulk Al content of 9.4%. In addition, if the non-detrital clays were the source of the additional Al one would expect the Al and clay contents to correlate such that the highest Al% would be expected to be associated with the highest clay content, however, Al wt% and Clay wt% do not show any correlation.

The second potential source of the additional non-detrital Al is plagioclase. Optical inspection and XRD analyses of bulk sediments show that plagioclase occurs as a major mineral constituent between depths of 64-~80cm and at 97cm, and as a minor phase between depths of 94-~110cm. The occurrence of plagioclase coincides with high Al content; the highest Al contents occurring where plagioclase is a major mineral phase. Plagioclase feldspars form a solid solution series of pure anorthite (An) ($CaAl_2Si_2O_8$) and pure albite (Ab) ($NaAlSi_3O_8$); as such they exhibit a range of chemical compositions. Since plagioclase is the only major Ca-bearing mineral observed in the samples with high Al (i.e. no $CaCO_3$) it can be assumed that the bulk sediment Ca content is solely derived from plagioclase. From the Ca content of the bulk sediments the Al contribution from plagioclase can be calculated for different mixtures of anorthite and albite. The validity of the resultant predictions of the maximum contribution of Al from plagioclase to the bulk sediment can be checked by comparison of known and calculated Na wt% (Figure 3.5 and Table 3.6).

These calculations suggest that where plagioclase is a major mineral phase it accounts for a maximum of ~70-85% of the Al in bulk sediment samples. The remaining 30-15% of Al that is not accounted for by plagioclase contributions constitutes 0.68-1.54% of the bulk sediment. Bulk Al contents, minus the plagioclase contribution, are comparable to other sediments from the TAG area where bulk sediment Al contents are generally ≤1% (e.g. Metz et al., 1988; Thompson et al., 1985; German et al., 1993; Severmann et al., 2004). This significant source of non-detrital Al in Core 60 means that the use of the bulk sediment Al content, as an index of detrital input, from which the hydrothermal input is then computed, is not justifiable in this case. This also suggests that the methods described above for calculation of the major sources to near-field hydrothermal sediments should be used with caution.

3.3.4 Silica Occurrence

Large areas of the active TAG mound exhibit low temperature diffuse flow. These low temperature fluids are a mixture of conductively heated seawater, and hydrothermal fluids which have undergone extensive conductive cooling during circulation within the mound (Tivey et al., 1995). As the temperature of these modified mixed fluids drops, they become supersaturated with respect to silica (e.g. Janecky and Seyfried,

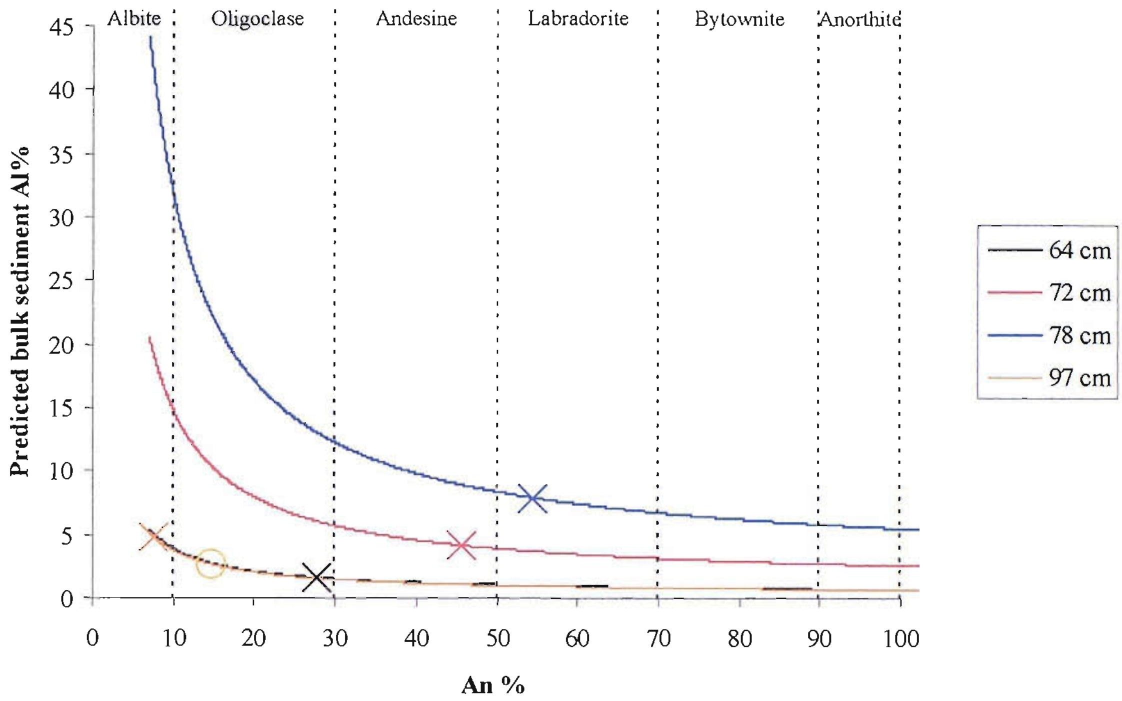

Figure 3.5: Predicted Al% in bulk sediment, based on known Ca% content, for varying mixtures of anorthite and albite. Crosses indicate the variety of plagioclase based on anorthite % and maximum Al contribution assuming all Ca and Na are derived solely from plagioclase. The open circle indicates a revised An% for sample depth 97cm as significant Na contributions to the bulk sediment from halite result in the prediction of Al% exceeding that measured.

Sample depth (cm)	Measured Ca%	Measured Na%	Calculated An%	Predicted bulk sediment Al%	Measured bulk sediment Al %	
64	0.5	0.79	27.8	1.6	2.28	×
72	1.88	1.37	45.6	4.14	5.68	×
78	4.04	2.07	54.4	7.87	9.39	×
97	0.48	3.58	7.6	4.85	2.66	×

Calculation of Al and Na in 97 revised as initial prediction contains too much Al

This is because of high Na contents due to contributions from halite in the bulk sediments

Sample depth (cm)	Measured Ca%	Measured Al%	Calculated An%	Predicted bulk sediment Na%	
97	0.48	2.66	14.6	1.72	○

Anorthite (An) = $CaAl_2Si_2O_8$
Albite (Ab) = $NaAlSi_3O_8$

Table 3.6: Comparison of calculated bulk Al% from plagioclase with measured bulk sediment Al%. These data indicate that plagioclase could account for a maximum of ~70-85% of the measured bulk sediment Al content.

1984; Tivey et al., 1995). Consequently, silica occurs with abundance in a variety of hydrothermal samples from TAG (e.g. Humphris et al., 1995; Mills et al., 1996; Hopkinson et al., 1999; see Chapter 2). Amorphous silica and a range of crystalline quartz polymorphs have been reported from the TAG area, several studies suggest that hydrothermal crystalline silica is secondary to an amorphous precursor (e.g. Koski et al., 1994; Hopkinson et al., 1998). The inferred transformation path for conversion of amorphous silica at TAG is:

Silica gel/siliceous solution →chalcedony →granular microquartz →macroquartz.

During hydrothermal synthesis of amorphous silica by Bettermann and Liebau (1975), several alternative transformation paths were observed:

Amorphous silica →cristobalite →keatite →quartz;

Amorphous silica →cristobalite →quartz and amorphous silica →keatite →quartz.

The transformation path of amorphous silica to quartz is dependent upon pressure and temperatures constraints (Bettermann and Liebau, 1975).

Diffuse low temperature flow and abundant silica are also common to the *Alvin* and *Mir* relict high temperature zones (e.g. Rona et al., 1993b; Stepanova et al., 1996). Quartz and opal occur in both Core 58 and Core 60. Cristobalite, a high temperature polymorph of quartz, is also present in Core 60 and is consistent with a high temperature inner mound origin of the sulphide layer of this Core. The presence of both quartz and cristobalite in Core 60 may be related to the 'sluggishness' of the reconstructive transformation paths described above, these transformations require considerable energy and consequently several quartz phases can co-exist metastably for long periods (e.g. Bettermann and Liebau, 1975). Mineralogical textures and associations of quartz and silica in the laminated section at the top of the sulphide layer in Core 58 indicate authigenic precipitation. Here the quartz and silica act as a cement and preservation casing for filamentous Fe-oxides and Fe-oxyhydroxides (Filaments Fe phases are discussed in detail in Chapter 6: Fe-oxidation and bio-mineralisation).

3.3.5 Metal Distributions

Concentrations of the most abundant metals in CD102/58 and CD102/60 are listed in Table 3.2a & b, comparison of average metal contents in Core 58 and Core 60 with metal rich sediments from other hydrothermal sites are given in Table 3.7. Downcore variations in Fe, Cu and Zn are shown in Figure 3.6a-d; variations in Mn, Cr, Co and Ni are shown in Figure 3.7a-f.

3.3.5.1 CD102/58

Iron, Copper and Zinc

Fe concentrations are uniformly high downcore ranging from 11.2-43.2%. Cu and Zn concentrations are also high (mean values of 1.85 and 3.34% respectively) with the highest values found within the sulphide layer (76-138.5cm) where Cu increases to a maximum of 12% and Zn increases to a maximum of 14.7%. The mineralogical data suggest that these high metal contents are due to the presence of Cu and Zn principally as

Location	Fe (wt%)	Cu (wt%)	Zn (wt%)	Ca (wt%)	Al (wt%)	Mg (wt%)	Mn (ppm)	Cr (ppm)	Co (ppm)	Ni (ppm)	Reference
OBS vent field core 1636	24.40	17.30	9.00	0.20	0.10	1.90	182.00		321.00		German et al 1999
EPR SO 12/A	26.87				0.50	1.37		34.55			Marchig et al 1982
Bauer Deep SO 12/B	12.92				2.05	1.86		6.84			Marchig et al 1982
DSDP 92	32.70	0.10	0.10	2.60	0.80	0.80	95930.0		148.00	658.00	Barrett et al 1987
Juan de Fuca Ridge core GC88-6	8.20	0.00	0.00		7.10		4800.00				German et al 1997
TAG core 2182	31.00	4.00	0.20	6.10	0.70	0.50	1244.00				German et al 1993
TAG	31.50	1.89	0.23				1940.00	23.10		18.50	Metz et al 1988
TAG (Metz et al core)	29.24	1.76	0.29				1737.85				Mills and Elderfield 1993
ALVIN CD102/58	**35.11**	**1.85**	**3.34**	**2.49**	**0.30**	**0.83**	**1600.44**	**15.45**	**38.05**	**13.42**	**This study**
MIR CD102/60	**29.29**	**2.61**	**0.94**	**2.76**	**1.68**	**1.43**	**1463.94**	**67.48**	**28.22**	**32.83**	**This study**
Average marine sediment	4.10	0.00	0.01				770.00	72.00		52.00	Bowen 1979

Table 3.7: Comparison of mean concentrations of the most abundant metals in CD102/58 and CD102/60 with metalliferous sediments from hydrothermal sites in the Atlantic and Pacific. Mean values for average marine sediments are also shown for comparison, note that the hydrothermal derived metals (Fe, Cu & Zn) are always enriched over average marine sediments and that seawater derived Cr and Ni are typically depleted in near-field metalliferous sediments compared to average marine sediments.

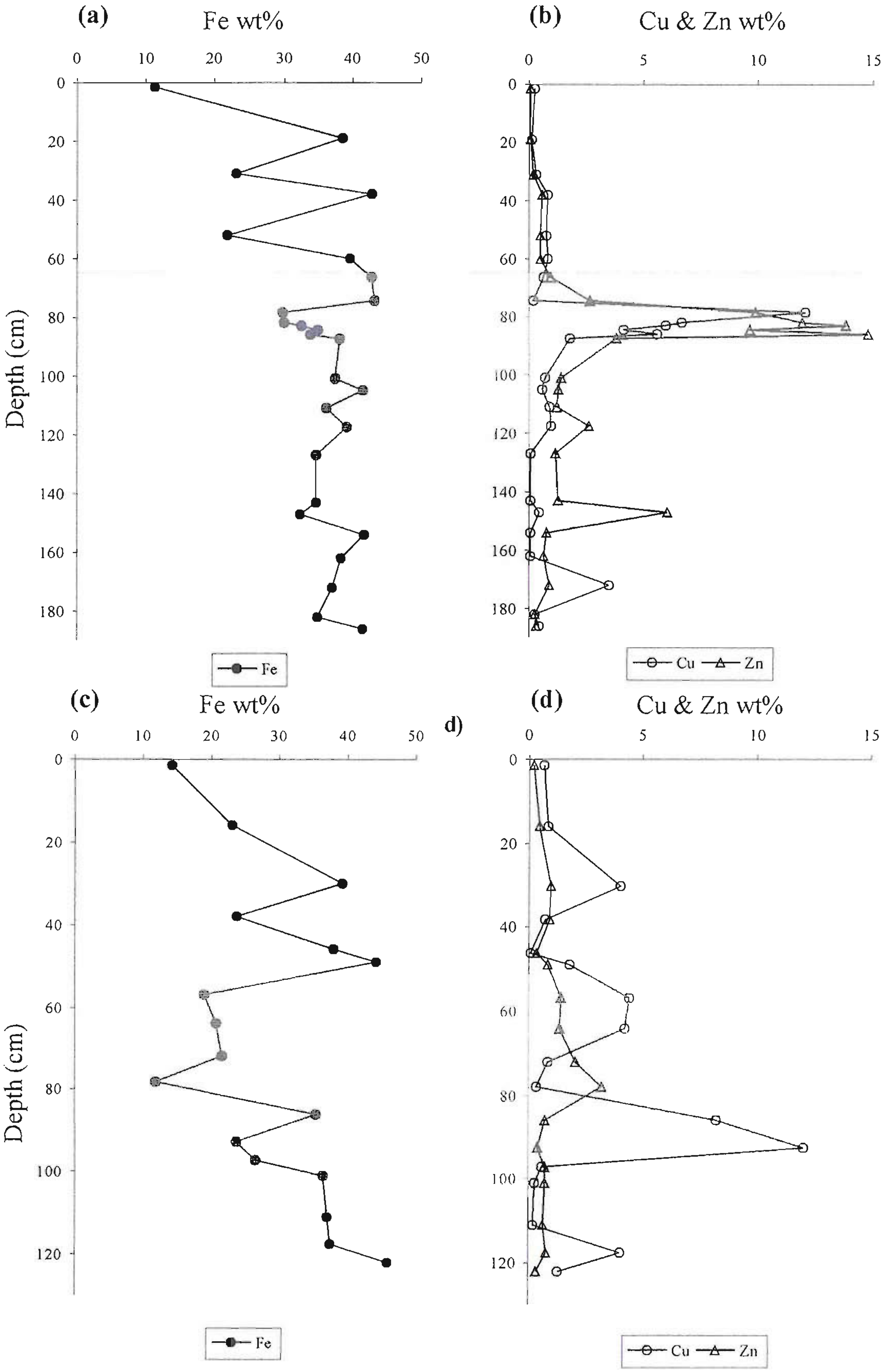

Figure 3.6: Downcore profiles of (a) Fe, (b) Cu and Zn in CD102/58, and (c) Fe, (d) Cu and Zn in CD102/60. Shaded area denotes location of the sulphide layer in each core.

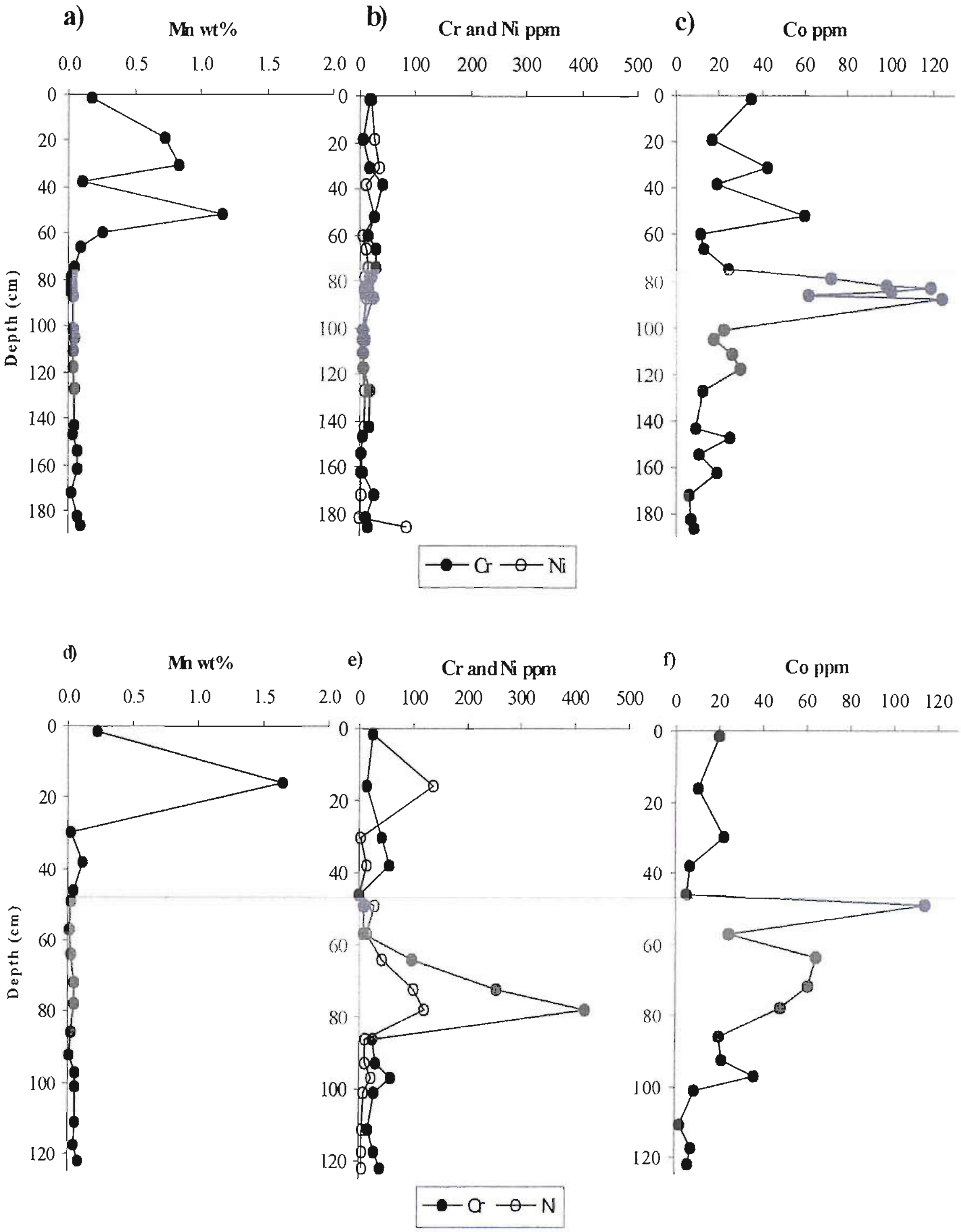

Figure 3.7: Downcore profiles of (a) Mn, (b) Cr and Ni and (c) Co in CD102/58 and (d) Mn, (e) Cr and Ni and (f) Co in CD102/60.

sulphide phases; no other major Zn bearing phase is identified and Cu contributions from secondary Cu salts are only minor. Neither Cu nor Zn correlated with Fe; Figure 3.8a-e illustrates all correlations with r values $\geq$0.60. In a previous study of metalliferous sediment core from the TAG area the lack of correlation between Fe, Cu and Zn was attributed to the mineralogical variability of mass wasted deposits (German et al., 1993), the distributions of these metals in Core 58 reflects similar variability. Even where no sulphides are reported Cu and Zn contents throughout the core are typically two orders of magnitude greater than average marine sediments. This enrichment reflects the presence of secondary Cu salts, i.e. atacamite and paratacamite, and Cu and Zn-rich secondary Fe-oxides and oxyhydroxides resulting from the oxidation of primary sulphide phases, which are common in similar sediments from the TAG area (e.g. Metz et al., 1988; Thompson et al., 1985).

Cu/Fe molar ratios in Core 58 have a mean value of 0.05; this is approximately twice those measured in black smoker vent fluids at the active TAG mound (Cu/Fe = 0.027: Edmond et al., 1995) but similar to Cu/Fe ratios of near field sediments at TAG (Cu/Fe = ~0.09: e.g. Metz et al., 1988; German et al., 1993) In contrast, mean Zn/Fe ratios of 0.09 are ~10 times higher than Zn/Fe in TAG black smoker fluids and 15 times greater than Zn/Fe of near field sediments (Zn/Fe = ~0.006: e.g. Metz et al., 1988; German et al., 1993). However, they are identical to Zn/Fe of white smoker fluids at TAG (Zn/Fe = 0.09: Edmond et al., 1995). The differences in Cu/Fe and Zn/Fe ratios reflect the different physiochemical regimes of Cu and Zn precipitation and the juxtaposition of material derived from high temperature black smoker fluids and lower temperature white smoker fluids in these sediments. This is in agreement with sulphide mineralogy textures within the sulphide layer which indicate a mix of high temperature black smoker and lower temperature white smoker assemblages (Chapter 4). The relative enrichment of Cu in Core 58 sediments compared with previous sediment studies within the TAG field (e.g. Metz et al., 1988; German et al., 1993) is a reflection of the lesser extent of alteration in this core, the persistence of primary chalcopyrite and the presence of secondary Cu minerals including covellite and atacamite.

Manganese and Fe/Mn ratios

Mn contents range from 0.02-1.17% with the highest values occurring near the core top. Two peaks in Mn content are observed downcore, the first occurs at 31cm depth, where Mn content is 0.84% and the second at 52cm depth and coincides with the occurrence of carbonate lense, here Mn reaches a maximum of 1.17%. Below 65cm Mn accounts for <0.1% of the bulk sediment. The range in Mn content in Core 58 is comparable with reported Mn contents for adjacent cores (Severmann, 2000; Metz et al., 1988). The upper Mn peak most likely marks the transition from Mn^{2+} to MnO_2 where Mn-bearing, reducing fluids encounter the more oxidising conditions of the carbonate cap. The origin of the second peak at 52cm depth is more problematic. Since the core was recovered from a location in close proximity to manganese oxide deposits inferred to result from low temperature diffuse flow (e.g. Rona et al., 1993b) and inputs from Mn-rich water from low temperature seeps during periods of hydrothermal quiescence one possible source for this secondary peak is input from a laterally flowing, diffuse, low temperature, Mn-rich fluid precipitating Mn-oxides. However, given the oxic nature of the upper Fe-oxyhydroxide rubble layer enrichment via remobilisation within the sediment column is unlikely. The most probable cause of the secondary Mn peak is a change in fluid fluxes and mixing as a result of non-steady state processes.

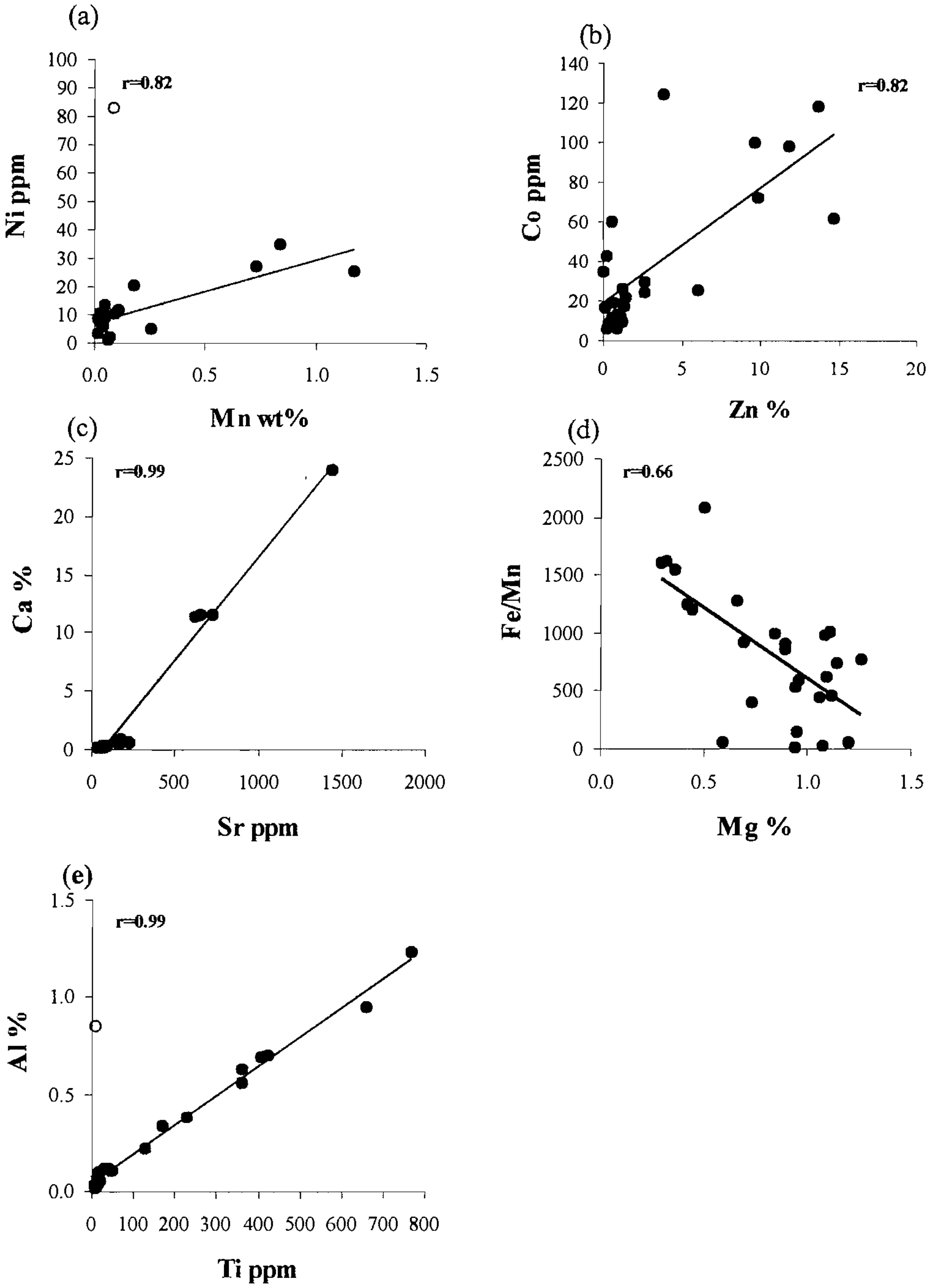

Figure 3.8a-e: Scatterplots of element pairs from CD102/58 which show correlation coefficients where r is >0.6. Note the open circle in plot (a) Ni vs. Mn, denotes data from the base of the core at 186cm depth which is not included in the calulation of the r value; the open circle in plot (e) Ti vs. Al, denotes data from 172cm depth which is excluded from the r value, if this data point is included r=0.89.

Hydrothermal Fe is almost completely removed from solution by precipitation, either as sulphide or Fe-oxide/oxyhydroxide, close to the site of venting, Mn oxidation and precipitation, however, are considerably slower than Fe, as a result Mn remains in solution and is dispersed in the hydrothermal plume, this is reflected in the high Fe/Mn ratio of near field sediments (e.g. Feely et al., 1990; Mottl and McConachy, 1990). The Fe/Mn ratio of the bulk sediment is variable, mean Fe/Mn ratios are 48 in the carbonate cap, 388 in the upper Fe-oxyhydroxide rubble layer, 1195 in the sulphide layer and 815 in the lower Fe-oxyhydroxide rubble layer. The lowest Fe/Mn ratios in the carbonate cap reflect the mobility of Mn in suboxic conditions and immobilisation in oxic conditions rather than dilution of hydrothermal phases by background pelagic sedimentation. The high Fe/Mn ratios below the carbonate cap reflect the near field hydrothermal provenance of this core.

Nickel

Ni concentrations range from 1.37-83.2ppm with the highest values occurring at the base of the core. With the exception of the highest value, Ni has a mean concentration of 34.8ppm, this is considerably lower than Ni in average marine carbonate sediments (mean = 52ppm: Bowen, 1979) and reflects low detrital inputs and only limited scavenging from seawater. Ni shows no correlation with Fe, Cu or Zn which is consistent with a detrital rather than hydrothermal origin. With the exception of the high Ni content of the basal sample (186cm depth) an association with Mn is observed, r=0.82 (Figure 3.8a). A similar relationship between Ni and Mn is reported for the Metz at al. (1988) core.

Chromium

Cr contents range from 3.42-40ppm with a mean value of 15.5ppm. Again, these values are considerably lower than those for average marine sediments (mean = 72ppm: Bowen, 1979). Similar Cr contents in the Metz et al., (1988) TAG core were attributed to adsorption of Cr from seawater onto hydrothermal Fe-oxides and oxyhydroxides, this hypothesis was supported by a correlation between Cr and Fe (r=0.84). However, Cr and Fe in Core 58 do not show a correlation and in this core and the Cr content cannot be chiefly attributed to scavenging of Cr from seawater. An alternative source for Cr in these sediments might be detrital input however, the lack of any correlation with other detritally derived elements (e.g. Al, Ti, Mg, and K) suggests that this if this is the case, the lack of correlation may reflect hydrothermal reworking since Cr is mobile under hydrothermal conditions (e.g. Marchig et al., 1982).

Cobalt

Co ranges from 38.1-124ppm with a mean value of 5.85. The highest Co contents are observed in the sulphide layer (76-138.5cm mean Co = ~61.9ppm), here the mean Co content is 3 times that elsewhere in the core (0-76cm and 138.6-188cm mean Co = 20.6ppm). The downcore distribution of Co and a correlation with Zn content (r=0.74) (Figure 3.8b) suggests that Co concentrations are related to the occurrence of sphalerite within the high temperature hydrothermally derived sediment. Indeed Co is an indicator of high temperature processes and sedimentary enrichment is symptomatic of a high temperature chimney source (e.g. Tivey et al., 1995).

Calcium, Magnesium and Strontium

Ca concentrations within the carbonate cap (0-33cm) are high ranging from 11.5-24%. Below this Ca accounts for <1% of the bulk sediment except at 52cm depth (11.4%) where a thin, <0.5cm thick, lens of pelagics are observed. Below the Carbonate cap Ca contents are significantly lower, typically ~<1%, this reflects the absence of a major Ca-bearing mineral phase within the hydrothermally derived material. Gypsum, which is only present in minor to trace amounts, is the only Ca-bearing mineral observed in the hydrothermally derived material below 33cm depth.

Sr shows an excellent correlation with Ca (r=0.99) (Figure 3.8c), this reflects the ability of Sr to substitute for Ca in the $CaCO_3$ and $CaSO_4.nH_2O$ crystal lattices. Mg can also substitute for Ca in the crystal lattice however, no correlation between Ca and Mg is observed. Bulk sediment Mg contents are generally ~1%, since Mg concentration in vent fluids is effectively zero (e.g. Elderfield and Schultz, 1996) all of this Mg must be sourced from seawater or detrital inputs. Since Mg does not correlate with Al a detrital origin is unlikely. Another potential process for transport of Mg from seawater to the sediment is scavenging of Mg by Fe and Mn oxides during early plume rise; a moderate correlation between Fe/Mn and Mg (r=0.66) (Figure 3.8d) suggests that adsorption of Mg from seawater onto Fe and Mn oxide and oxyhydroxides maybe important. In addition low temperature clay phases in which Mg is a common interlayer cation are likely to be another important source for Mg in this core.

Titanium

Excepting one sample with relatively high Al at 172cm depth, Ti shows an excellent correlation with Al (r=0.99) (Figure 3.8e). Ti and Al are both relatively immobile elements and are detrital in origin.

Vanadium and the V/Fe ratio

Vanadium contents range from 84.4-306ppm with a mean value of 168ppm. The downcore distribution of V is highly variable but is consistent with previously published V concentrations for sediment from the TAG area (Metz et al., 1988). Several studies indicates that V is scavenged from seawater by co-precipitation with plume particles (e.g. Trefry and Metz, 1989; Rudnicki and Elderfield, 1993; Kadko, 1993) The V distribution in the Metz et al. (1988) core is controlled by the efficiency of V scavenging from seawater onto ferric hydroxide plume phases prior to sedimentation. However, V in this core does not correlate with either Fe or Mn. This may indicate that V originally supplied to the sediment via seawater scavenging onto ferric hydroxides is re-mobilised and redistributed during diagenesis. In addition scavenging of V may continue in the sediment pile via diffusion of seawater into the sediment or adsorption from seawater rich alteration fluids. V/Fe ratios suggest that unmodified plume input to this core is minimal. V/Fe ratios of the TAG plume range from 0.004 to 0.0078 whilst V/Fe ratios of Core 58 sediments are an order of magnitude less with a mean value of 0.0006. This is consistent with comparison of Core 58 and TAG plume P/Fe ratios which are also an order of magnitude lower (Section 3.3.6).

3.3.5.2 CD102/60

Iron, Copper and Zinc

Fe concentrations are uniformly high downcore ranging from 11.9-45.8%. Cu and Zn concentrations are also high (mean values of 2.61 and 0.94% respectively) with the highest values found within the sulphide layer (47-96cm) where Cu increases to a maximum of 12.1% and Zn increases to a maximum of 3.17% (Figure 3.6c & d). The mineralogical data suggest that these high metal contents are due to the presence of Fe, Cu and Zn principally as sulphide phases. The mineralogical data indicate that goethite and hematite are only present at trace or minor amounts if at all. Sphalerite is the only major Zn bearing phase identified. Non-sulphide Cu-bearing minerals, e.g. atacamite (precipitated as a result of chalcopyrite and covellite oxidative dissolution (Chapter 4)) are present but only at minor levels. Neither Cu nor Zn correlated with Fe, this is attributed to the mineralogical variability of the deposit; Figure 3.9a-m illustrates all correlations with r values ≥ 0.60. Where no sulphides are reported, Cu contents are consistently 2 to 3 orders of magnitude greater than average marine sediment values, and Zn contents are typically two orders of magnitude greater than average marine sediments. This enrichment is similar to that observed in Core 58, and again most likely reflects the presence of Cu and Zn-rich secondary Fe-oxides and oxyhydroxides resulting from oxidation of primary sulphide phases, which are common in similar sediments from the TAG area (e.g. Thompson et al., 1985; Metz et al., 1988).

Cu/Fe molar ratios in Core 60 have a mean value of 0.1; this is approximately 3 times those measured in black smoker vent fluids at the active TAG mound (Cu/Fe = 0.027: Edmond et al., 1995) but is comparable with Cu/Fe ratios of near field sediments at TAG (Cu/Fe = ~0.09: e.g. Metz et al., 1988; German et al., 1993). Mean Zn/Fe ratios of 0.04 are 4 times those measured in TAG black smoker fluids (Zn/Fe = 0.01), about half those measured from white smoker fluids at TAG (Zn/Fe = 0.09: Edmond et al., 1995) and ~6.5 times the Zn/Fe ratio of previous studies of near field sediments (e.g. Metz et al., 1988; German et al., 1993). The differences in Cu/Fe and Zn/Fe ratios reflect the different physiochemical regimes of Cu and Zn precipitation and hydrothermal reworking which ultimately results in the separation of Cu and Zn. The greater Cu/Fe ratio in Core 60 compared to Core 58 reflects the principally high temperature origin of this material characterised by the greater abundance of Cu bearing sulphides, and the less extensive weathering and oxidation of this core. Lower Zn/Fe ratios in Core 60 compared to Core 58 reflects lower inputs from lower temperature (possibly white smoker) assemblages.

Manganese and Fe/Mn ratios

Mn contents show a mean value of 0.15%, the highest values occur in the carbonate cap in the top 33cm of the core. A peak in Mn content of 1.64% is observed at 16cm depth. Below the carbonate cap Mn typically accounts for <0.1% of the bulk sediment. The peak in Mn content marks the transition from Mn^{2+} to MnO_2 where Mn-bearing, reducing fluids encounter the more oxidising conditions of the carbonate cap

The Fe/Mn ratio of the bulk sediment is variable, mean Fe/Mn ratios are 511 in the carbonate cap, 475 in the upper Fe-oxyhydroxide rubble layer, 1240 in the sulphide layer, 674 in the lower Fe-oxyhydroxide rubble layer and 550 in the Fe-oxide layer. The moderately Fe enriched Fe/Mn ratios in the carbonate cap result from mixing of pelagic sediment with Fe-oxides and oxyhydroxides of hydrothermal origin. The high Fe/Mn ratios

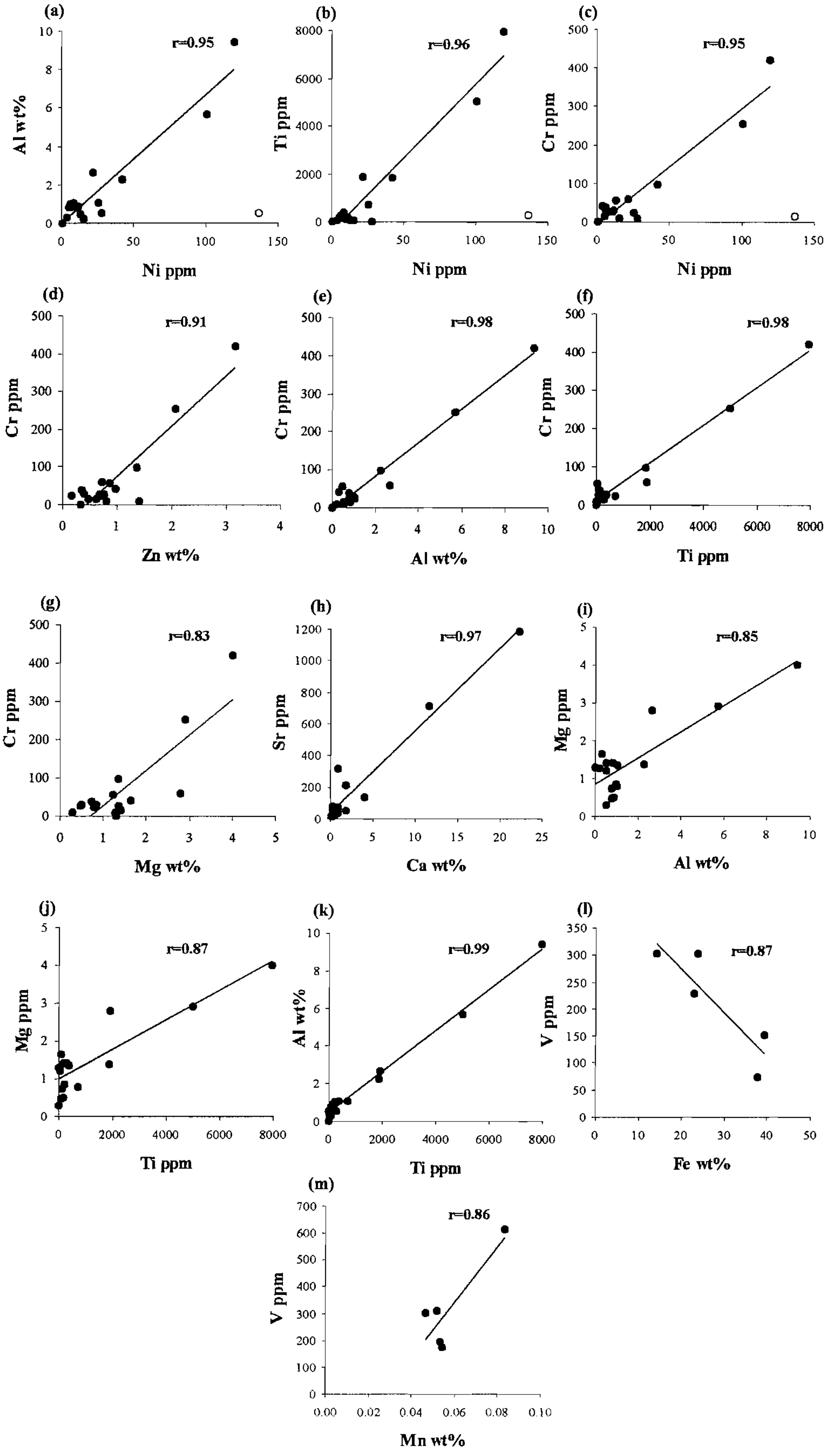

Figure 3.9: Scatterplots of elemental pairs from CD102/60 which show correlation coefficients where r is >0.6. Plot l) shows the correlation between V and Fe above the sulphide layer and plot m) shows V and Fe below the sulphide layer. Note the open circle in plots a), b), and c) this denotes data from 16cm where Ni is at a maximum value of 137ppm.

of the sulphide layer confirm the near field hydrothermal provenance of this layer which was formed as an inner mound pyrite-quartz breccia similar to those reported following ODP drilling of the active TAG mound (Chapter 4).

Nickel

Ni concentrations range from 1.11-137ppm. The highest value occurs within the carbonate cap and corresponds to the Mn peak which marks the transition between low oxygen, reducing conditions present within the hydrothermally derived material and the more oxic conditions present in the carbonate cap. Mean Ni contents of 32.8ppm are considerably lower than Ni contents in average marine sediments (mean = 52ppm: Bowen, 1979) reflecting low detrital inputs. With the exception of the maximum Ni content of 136.79ppm at 16cm depth, Ni shows excellent linear correlations to Al (r=0.95), Ti (r=0.96) and Cr (r=0.95) (Figure3.9a-c) but no correlation with Fe, Cu or Zn. This suggests that Ni in this core has a detrital, rather than hydrothermal origin. The high Ni contents (>100ppm) at 72 and 78cm depth within the sulphide layer correspond to a decrease in the Fe/Mn ratio. This enrichment may reflect hydrothermal reworking and redistribution of Ni or scavenging and absorption from mixed low temperature hydrothermal fluids and seawater circulating within the sediment during diagenesis. An association of Ni with Mn rather than Fe was also reported for the Metz et al. (1988) core.

Chromium

Cr contents range from 1.33-420ppm with a mean value of 67.5ppm. Whilst the mean value is comparable to Cr in average marine sediments (mean = 72ppm: Bowen, 1979), values >72ppm indicate enrichment of Cr. Samples which show enrichment are restricted to the sulphide layer at depths of 64-78cm. Linear correlation between Cr and Zn (r=0.91) (Figure 3.9d), in the sulphide layer suggests that this layer may include Cr spinel and suggests that Cr enrichment is due to inclusion of hydrothermal/basaltic sourced Cr. Excellent correlations of Cr with Al (r=0.98) and Ti (r=0.98) and a correlation with Mg (r=0.83) (3.9e-g) indicates that elsewhere in the core Cr is related to detrital inputs. The lack of correlation with other detritally derived elements (e.g. K) suggests that at least some hydrothermal reworking of Cr has taken place. No correlation is observed between Cr and Fe, therefore, in contrast to the Metz et al. (1988) TAG core, contributions from scavenging of Cr from seawater onto hydrothermal Fe-oxides and oxyhydroxides must be minimal.

Cobalt

Co ranges from 2.21-114ppm with a mean value of 28.2. Similar to Core 58, the highest Co contents are observed in the sulphide layer (47-96cm mean Co = 50.5ppm), here the mean Co content is 4 times that elsewhere in the core (0-47cm and 96-126cm mean Co = 12.6ppm). Whilst Co contents do not show a correlation with any of the measured elements, the downcore distribution of Co suggests that it is associated with sulphide minerals, and is therefore, hydrothermal in origin but may have been redistributed during zone refining processes.

Calcium, Magnesium and Strontium

Ca concentrations in the carbonate cap at the top of the core are high with a maximum value of 22.2%. Steadily decreasing Ca downcore in the carbonate cap reflects the extent of admixed Fe-oxides and oxyhydroxides present. Below the carbonate cap Ca contents have a mean value of 0.87% however Ca contents as high as 4.04% are observed. The high Ca contents below the carbonate cap do not reflect an increased biogenic component but the present of calcic plagioclase (anorthite). The presence of plagioclase (a mineral component of basalt) and chlorite (a basalt alteration product) are indicative of a basaltic input to these sediments, this is in agreement with paragenesis as a pyrite-quartz breccia in the inner *Mir* mound close to the upper hydrothermal stockwork zone (Chapter 4).

Sr shows an excellent correlation with Ca (r=0.97) (Figure 3.9h), this reflects the ability of Sr to substitute for Ca in the $CaCO_3$ and anorthite crystal lattice. Mg can also substitute for Ca in the crystal lattice however, no correlation between Ca and Mg is observed. Bulk sediment Mg contents have a mean value of 1.43%, since Mg concentration in vent fluids is effectively zero (e.g. Elderfield and Schultz, 1996) all of this Mg must be sourced from seawater or detrital inputs. Mg shows a correlation with Al (r=0.85), Ti (r=0.87) (Figure 3.9i and j) and Cr (r=0.83) (Figure 3.9g) all of which are derived from detrital inputs; this suggests that Mg is also principally detrital in origin and is most probably associated with the detrital clays as an interlayer cation.

Titanium

Ti concentrations range from 9.18-7967ppm. A general decrease in Ti content is observed downcore. Ti shows an excellent correlation with Al (r=0.99) (Figure 3.9k) and is inferred to be associated largely with detrital inputs and the plagioclase phase.

Vanadium and the V/Fe ratio

Vanadium contents range from 74.3-614ppm with a mean value of 252.ppm. The distribution of V is variable but shows a general trend to increasing contents downcore. The concentration of V in this core is consistent with previously published V concentrations for sediment from the TAG area (Metz et al., 1988). The distribution of V is controlled by adsorption of V from seawater onto freshly precipitated Fe/Mn-oxyhydroxides. When data from the sulphide layer are excluded V contents above the sulphide layer (0-47cm) show a negative correlation with Fe, r=0.89 but no relationship to Mn, and V contents below the sulphide layer (96-126cm) show a correlation with Mn, r=0.86 but no relationship to Fe (Figure 3.9l and m). Thus the V content of the sediment is controlled by the availability of Fe/Mn-oxyhydroxides and efficiency of seawater scavenging prior to sedimentation. Plume input to these sediments is relatively low; V/Fe ratios of bulk sediments in Core 60 are consistently less than plume ratios, low plume input is also consistent with P/Fe ratios for Core 60.

3.3.6 Distribution of Non-Metallic Elements

Concentrations of Ba, P, K in Core 58 and Core 60 are listed in Table 3.2a & b. Downcore variations in Ba, P, and K are shown in Figure 3.10a-d. Figure 3.11a-e illustrates all correlations with r values ≥0.60.

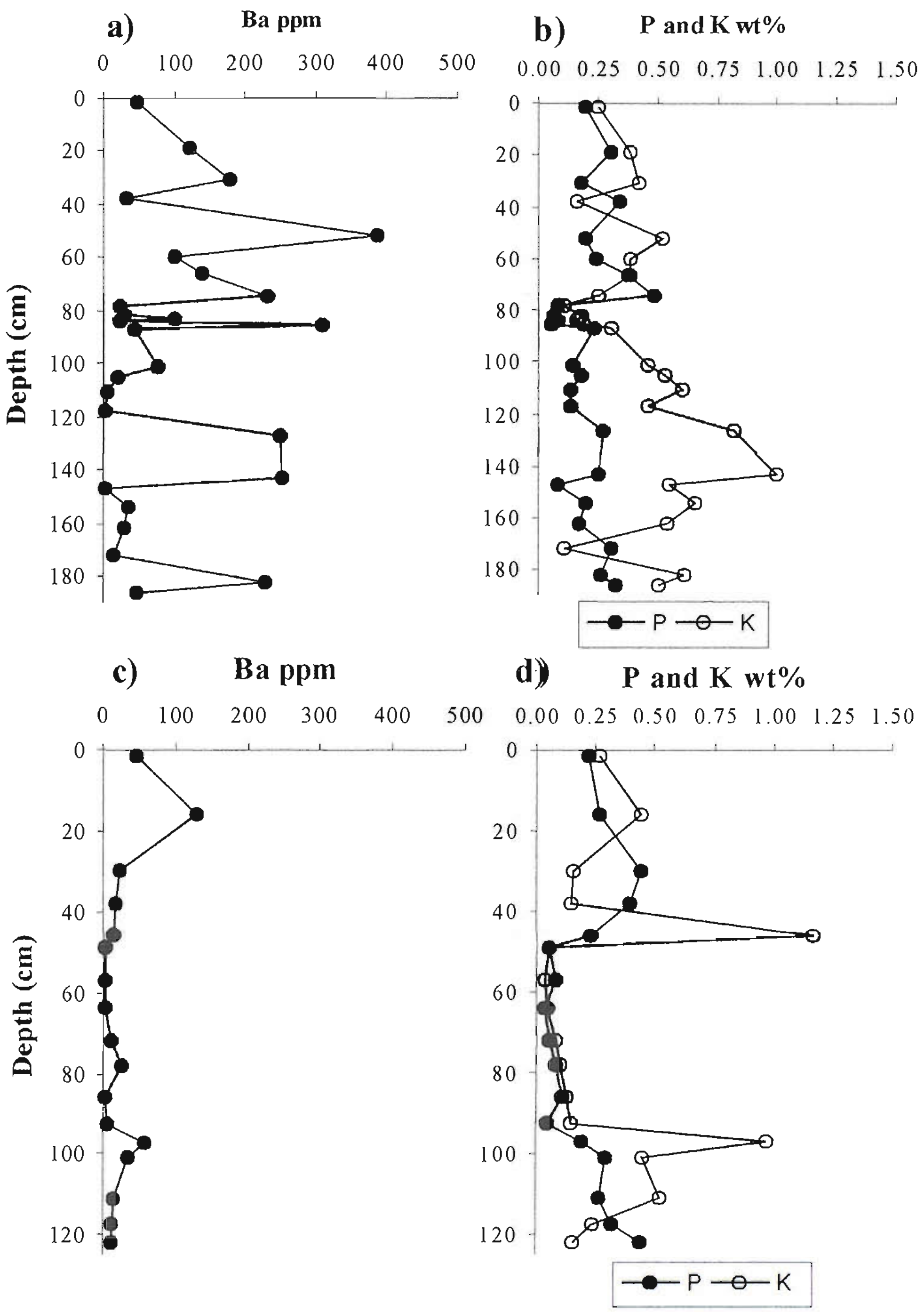

Figure 3.10: Downcore profiles of (a) Ba, (b) P and K in CD102/58, and (d) Ba, (e) P and K, in CD102/60. Shaded area denotes location of sulphide layer in each core.

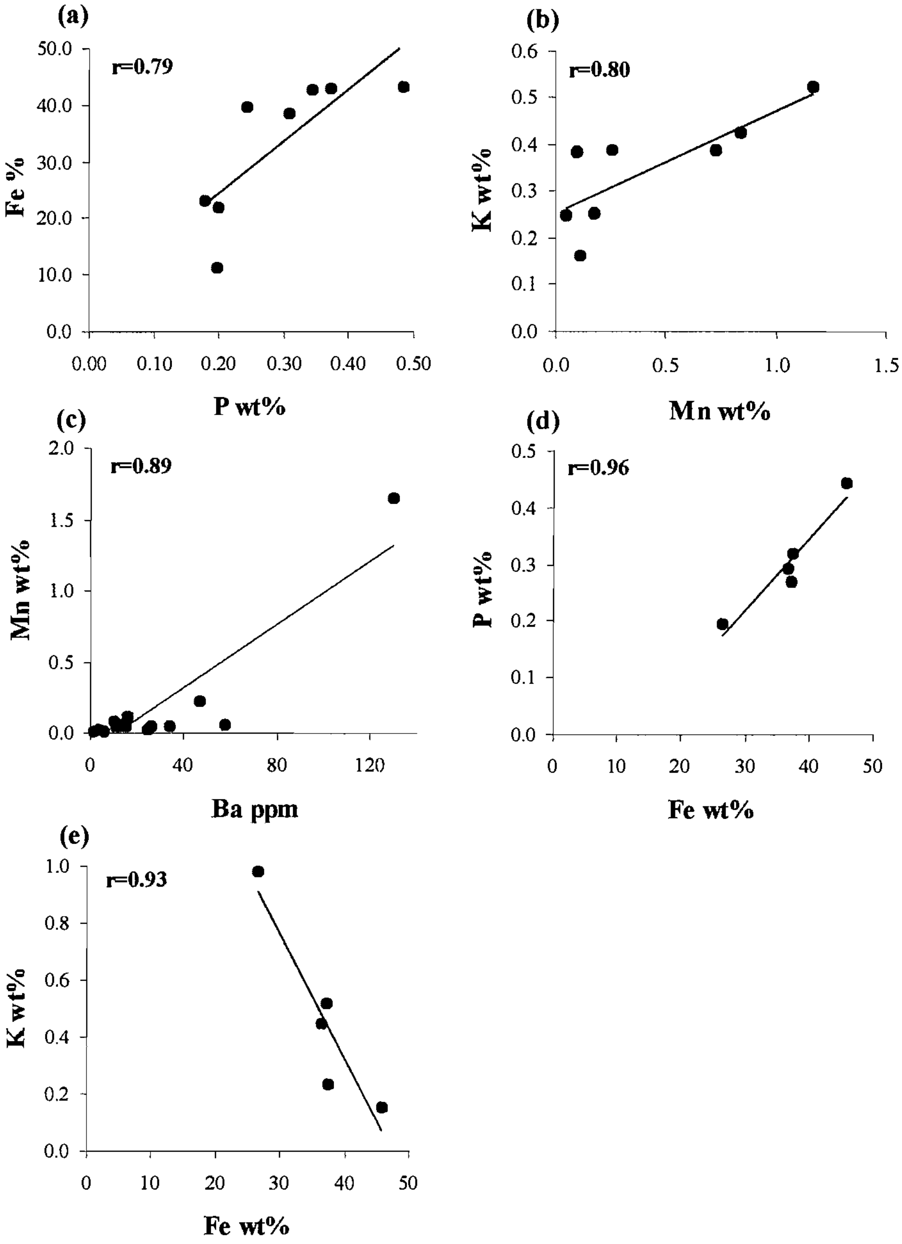

Figure 3.11a-e: Scatterplots of elemental pairs from CD102/58 and CD102/60 which show correlation coeffiecients where r is >0.6. Plot (a) shows the correlation between P and Fe above the sulphide in core 58; (b) shows the correlation betweent K and Mn above the sulphide layer in core 58; (c) is Mn vs. Ba in core 60; Plots (d) and (e) show P and K vs. Fe below the sulphide layer in core 60.

3.3.6.1 CD102/58

Barium

Ba concentrations are highly variable and range from 4.04-388ppm with a mean value of 106ppm. Ba does not correlate with any other element measured.

Phosphorus and the P/Fe ratio

P contents range from 0.05-0.49% with a mean value of 0.21%. The lowest values are associated with the laminated section of the sulphide layer. The distribution of P above the sulphide layer (0-76cm) correlates with Fe, r=0.79 (Figure 3.11a), and is inferred to be controlled by co-precipitation and adsorption to ferric oxides and oxyhydroxides in the hydrothermal plume and from pore fluids within the sediment. However, contributions from unmodified plume material to these sediments are low. P/Fe ratios in Core 58 are at least an order of magnitude lower than those of the TAG plume (P/Fe ratio = 0.137: Feely et al., 1991).

Potassium

K contents range from 0.1-1.0% with a mean value of 0.41. A general trend of increasing concentration with depth is observed. The lowest values are again observed in the laminated section at the top of the sulphide layer. This is consistent with the hydrothermal origin of the laminated section as K is sourced from seawater. Above the sulphide layer K correlates with Mn, r=0.77 (Figure 3.11b). This suggests that K distribution in the upper 76cm of the core is controlled by adsorption to Mn oxides and hydroxides. Interestingly P and K do not show a correlation with each other or the other detritally sourced elements (e.g. Al and Ti).

3.3.6.2 CD102/60

Barium

Ba concentrations are range from 1.49-130ppm with a mean value of 24.3ppm. Three peaks in Ba content are observed. The largest peak occurs at 16cm depth where Ba contents are 130ppm, two smaller increases occur at 78cm and 97cm depth where Ba contents are 25.9ppm and 57.4ppm respectively. Ba shows a good correlation to Mn, r=0.89 (Figure 3.11c). This suggests that Ba and Mn are associated in the solid phase and may be sourced from low temperature hydrothermal fluids percolating through the sediment pile during diagenesis.

Phosphorus and the P/Fe ratio

P contents are low throughout the core reflecting minimal plume input to these sediments and they are almost identical to data from Core 58; P/Fe ratios in Core 60 are also at least an order of magnitude lower than TAG plume values. P wt% ranges from 0.04-0.44% with a mean value of 0.21%. The lowest values are associated with the sulphide layer. Below the sulphide layer (96-126cm) P shows an excellent correlation to Fe, r=0.96 (Figure 3.11d), and is inferred to be controlled by co-precipitation and adsorption to ferric oxides and oxyhydroxides in the hydrothermal plume and from pore fluids within the sediment. Above 96cm depth no correlation between Fe and P is observed.

Potassium

K contents are low throughout the core and range from 0.04-1.17% with a mean value of 0.3. There are two distinct peaks in K content downcore, these peaks occur at the upper and lower limits of the sulphide layer (47-96cm). The first peak at 46cm depth shows an increase from ~0.15% to 1.17%, the second peak at 97cm depth shows an increase from contents of <0.15% within the sulphide layer to 0.98%. The lowest values, observed in the sulphide layer, are consistent with the inner mound origin of this layer since K is sourced from seawater. Below 96cm depth K shows a negative correlation to Fe, r=-0.93 (Figure 3.11e), this suggests that the seawater source of K is diluted by Fe-rich hydrothermal inputs. Above 96cm K does not correlate with any of the other elements measured in this study.

3.3.7 Sediment Formation and Diagenesis

The bulk mineralogy and downcore elemental variations of metalliferous sediments from the *Alvin* (CD102/58) and *Mir* (CD102/60) relict high temperature zones indicate deposition from a complex mixture of sources and physical and chemical alteration of the sediment pile over time. Physical changes include dissolution of primary phases and secondary mineralisation; chemical changes include alteration of sulphide material which leads to remobilisation of metals and ultimately fluxes of material both to and from seawater.

Downcore Ca contents indicate that both cores 58 and 60 are capped by ~30cm of carbonate of pelagic origin. These carbonate caps becoming increasingly admixed with Fe-oxyhydroxides towards their bases. This can be seen from increasing Fe contents and the occurrence of goethite with orange staining in Core 58, and hematite and goethite with red staining in Core 60. This goethite and hematite is sourced from oxidised material transported from the *Alvin* and *Mir* mounds during mass wasting and plume fallout.

Increases in Mn towards the base of the carbonate layers mark the locus of Mn^{2+}/MnO_2 transition where Mn-rich reducing fluids diffusing upwards encounter the increasingly oxic conditions of the carbonate caps resulting in precipitation of Mn-oxides. The depth and magnitude of the Mn-redox transition at ~30cm in Core 58 (the upper Mn peak) is consistent with the downcore Mn profile of adjacent cores (Metz et al., 1988; Severmann, 2000). The depth of the Mn peak in Core 60 is also comparable with published data however, Mn is enriched~2-fold in Core 60 compared to Core 43 and the Metz et al. (1988) core (Metz et al., 1988; Severmann, 2000) (Figure 3.12). The secondary Mn peak in Core 58 is interesting as it coincides with a thin carbonate lens. If the carbonate cap is undergoing acidic dissolution, a process which has been inferred for the carbonate cap of the adjacent Core 43 (Severmann, 2000) then this secondary Mn peak and carbonate occurrence may represent the original depth of the Core 58 carbonate layer where the basal carbonate lens has been protected from dissolution. It might also represent non steady state processes, where there are changes in the Mn flux when Mn is not only sourced by release from sulphide layers at depth in the sediments, following reduction and dissolution of oxidised species, but also from evolved low temperature alteration fluids. Local changes in redox conditions during diagenesis will also have an impact. This is consistent with the extreme heterogeneity in Mn transport and reaction across the TAG field where surficial enrichments are common (e.g. Scott et al., 1974; Metz et al., 1988; Mills et al., 2001; Shearme et al., 1983; Severmann, 2000) and Mn enrichments in the upper tens of centimetres of sediments, up to 15% have been reported (Goulding, 1998; Goulding et al., 1998). Interestingly, in Core 58 Ni and Mn show a linear correlation, r=0.82, and in Core 60

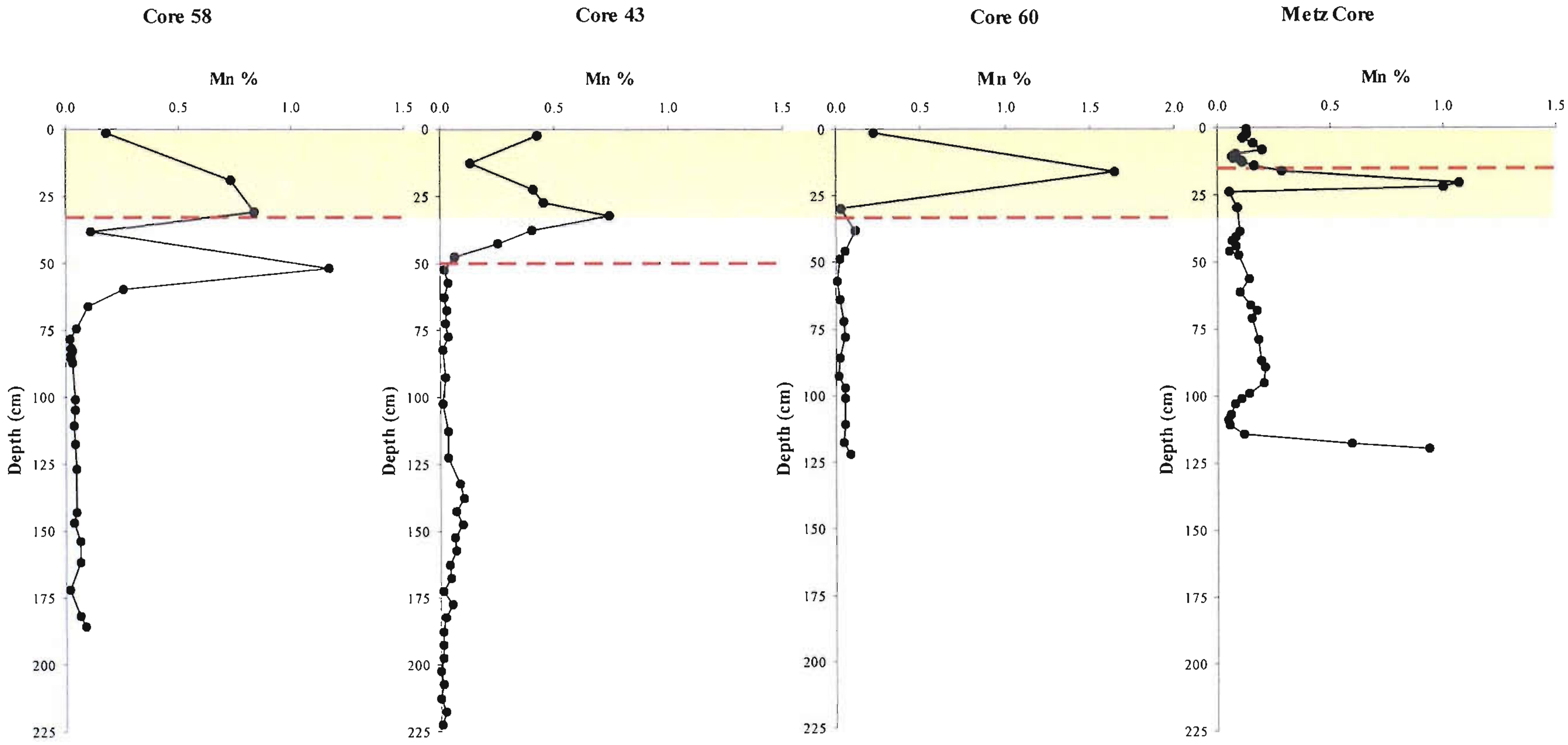

Figure 3.12: Comparison of downcore Mn profiles in cores 58 and 60 with core 43 (Severmann, 2000) and the Metz et al. (1988) core. The dashed red line in all plots denotes the base of the carbonate cap identified from mineralogy and $CaCO_3$ contents. The shaded area denotes the carbonate cap of core 58 and 60; the shaded area at 52cm depth Core 58 marks the location of the secondary carbonate lens in this core.

outside of the sulphide layer Mn and Ni also show an excellent linear correlation (r =0.99), this suggests that accumulation of Ni is also controlled by the bulk redox conditions.

The carbonate caps are underlain by Fe-oxyhydroxide rubble. Sedimentary layering and alignment of elongate clasts indicates deposition as a mass flow event. High metal concentrations and the mineralogy indicate that these layers are the weathering products of sulphidic mound material rather than material from plume fallout. The presence of quartz and opal in the upper Fe oxide layers of cores 58 and 60 suggest that sulphide oxidation is not the only source of Fe oxide and oxyhydroxide in these cores and that some of maybe precipitating from low temperature Fe-Si-rich fluids (e.g. Alt, 1988b; Hannington and Jonasson, 1992) . The collomorphic textures of Fe oxides in these layers support an authigenic origin (Figure 3.13), in addition precipitation of dissolved Fe(II) from low-temperature fluids rather than oxidation of sulphides or contribution from the overlying hydrothermal plume has been invoked for similar Fe oxide-rich layers in other sediments from the TAG field (e.g. Mills and Elderfield, 1995b; Mills et al., 1996; Severmann et al., 2004). The occurrence of atacamite in the upper Fe oxide/oxyhydroxide of Core 60 suggests upward diffusion of Cu bearing fluids from the underlying sulphide layer. Cu is soluble under oxidising conditions and low pH (e.g. Large et al., 1989) precipitation may be related to neutralisation of the Cu bearing fluid via dissolution of carbonate material resulting locally important changes in E_h and pH.

Following cessation of high temperature venting, chimneys on the top of sulphide mounds collapse and disintegrate producing sulphide debris. Subsequent slumping of this material is facilitated by mass gravitational transport, fault activation and related micro-earthquakes. The occurrence of sulphides in distinct layers is interpreted to be the result of episodic transport of sulphide debris from the *Alvin* and *Mir* relict mounds. Similar sulphide layers reported from this area have also been attributed to mass-flow events (e.g. Metz et al., 1988; German et al., 1993; Severmann, 2000). The sulphide layers of both cores are enriched in the chalcophile elements.

The sulphide layer of Core 58 has been subject to extensive oxidation and alteration. The secondary mineralogy of this core suggests that supergene processes have been important in the modification of this material (for a full discussion of supergene processes see Chapter 4). Both Cu and Zn remain high throughout this layer however, peak enrichments which are two orders of magnitude greater than for other TAG cores (e.g. Metz et al., 1988; German et al., 1993) are associated with the laminated section. Here Cu and Zn peak at ~12 and 15wt% respectively, the peak Co contents are coincident with the Cu and Zn peaks and all three enrichments are related to inclusion of high temperature chimney material (Tivey et al., 1995). The mineralogy shows that the Core 58 sulphide layer has undergone oxidative alteration; despite a high percentage of sulphide minerals, Fe oxides are the dominant mineral phase. These Fe oxides are the result of sulphide oxidation and dissolution which results in the production of acidic pore-fluids. Acidic pore-fluids are then responsible for the redistribution of pH and redox sensitive elements and may explain the varied distribution of Cr and Ni throughout this layer. However, Core 58 is much less altered than adjacent sediments, this can be seen from the clay mineralogy, in contrast to other sediments described from this area, where clay phases are almost exclusively nontronitic, e.g. Core 43 (Severmann, 2000; Severmann et al., 2004), chlorite and kaolinite are also important. In addition, the nontronite from Core 43 is authigenic and

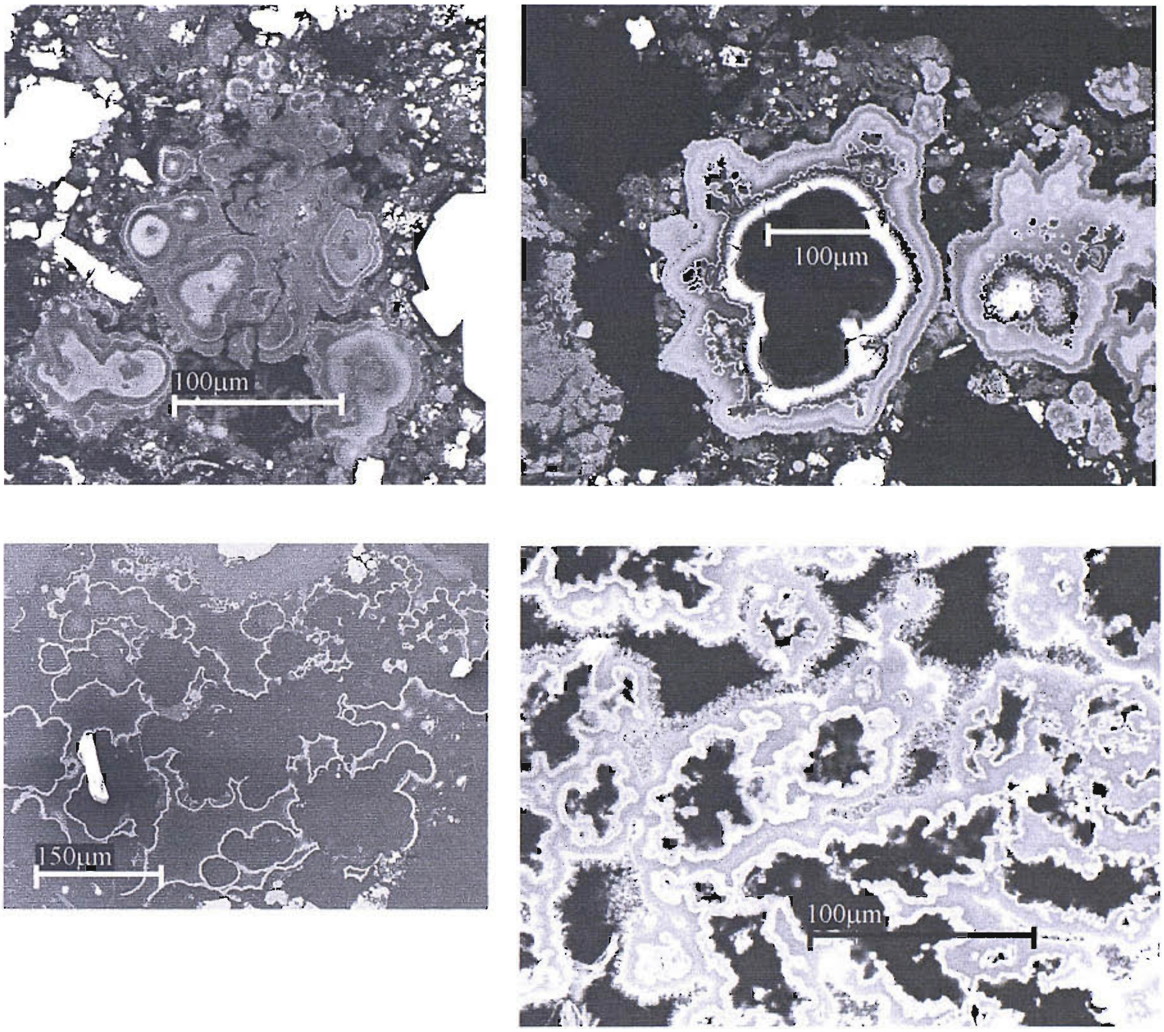

Figure 3.13: SEM images (SEM method is given in Chapter 4) of collomorphic Fe oxides, Fe oxyhydroxides and Fe silicates from the laminated section (76-87cm depth) at the top of the sulphide layer of core 58. Note that all the images show compositional zoning, bright layers are rich in Fe oxide and/or oxyhydroxide, duller layers are rich in Fe oxysilicates.

shows evidence of re-precipitation of earlier phases whereas; the clays in Core 58 are inferred to be allogenic. The presence of some nontronite in Core 58 indicates low E_h and pH conditions and Fe^{2+} and Si in solution (Harder, 1976). The presence of nontronite as only a minor phase suggests that although these conditions may be locally important they are not pervasive and within the sulphide layer and the Fe oxide/ oxyhydroxide layers of Core 58, Fe oxide precipitation appears to dominate over nontronite formation.

The geochemistry and mineralogy of the sulphide layer of Core 60 indicates that the primary assemblage was precipitated within the *Mir* mound, close to the upper hydrothermal stockwork zone which has contributed basaltic material and led to high Al contents (Chapter 4). This sulphide layer is considerably less oxidised than Core 58 and other cores from the TAG site (e.g. Thompson et al., 1985; Metz et al., 1988; Mills et al., 1993; German et al., 1993; Severmann, 2000; Severmann et al., 2004). The mineralogy and Fe and S contents suggest that unlike Core 58, Core 43 and the Metz et al. (1988) core Fe-sulphides predominate over Fe-oxides and oxyhydroxides. Whilst Co contents are less than the enrichments (up to 470ppm) observed in TAG mound sulphides and Core 43 (~200-500ppm: Severmann, 2000) they are up to 6 times higher than elsewhere in Core 60 and are indicative of a high temperature source (e.g. Tivey et al., 1995). High Cu contents with mean values of 2.6wt% are comparable to Cu contents of similar cores from the TAG area (e.g. Metz et al., 1988; German et al., 1993), however, the most enriched value of 12.08wt% is approximately twice that of previous studies. This reflects the fact that chalcopyrite is the predominant Cu host in Core 60 whereas in other cores Cu is primarily held in secondary Cu salts, e.g. atacamite or is associated with Fe oxides following oxidation and dissolution of primary Cu sulphides (e.g. Metz et al., 1988; German et al., 1993; Mills et al., 1996). High Cu contents (up to ~4wt%) elsewhere in Core 60 reflect remobilisation of Cu during diagenesis as a result of the acidic conditions produced during pyrite oxidation. Zn concentrations in the sulphide layer of Core 60 are consistently higher (~1.4wt%) than in other TAG sediments which typically have Zn contents <0.5wt% (e.g. Metz et al., 1988; German et al., 1993; Severmann, 2000), these are related to Zn sulphides rather than adsorption to Fe oxide (Metz et al., 1988).

Fe-oxyhydroxide and Fe-oxide layers at the base of both cores are very similar to the upper Fe-oxyhydroxide layers. These are also attributed to oxidation and alteration of primary sulphide material during diagenesis and authigenic precipitation from Fe-Si-rich low temperature fluids.

3.4 Conclusions

The downcore mineralogy and geochemistry of both Cores 58 and 60 indicates deposition from a complex mix of sources and subsequent physical and chemical alteration during diagenesis.

- **Core 58** collected from the *Alvin* relict high temperature zone, was emplaced as a result of a mass wasting event and comprises 4 distinct units:
  1. 0-33cm: intercalated carbonate (pelagic) and Fe oxyhydroxide
  2. 33-76cm: Fe oxyhydroxide layer 1 – product of sulphide oxidation and precipitation from diffuse low temperature fluids.
  3. 76-138.5cm: sulphide layer –high temperature sulphide material derived from mass wasting most probably of the nearby Southern *Alvin* mound. Contains enrichment in Cu, Zn, and Co

4. 138.5-188cm (base): Fe oxyhydroxide layer 2 – very similar to the upper Fe oxyhydroxide layer, also the product of sulphide oxidation and precipitation from diffuse low temperature fluids.

- **Core 60** collected from the periphery of the *Mir* mound, dominated by high temperature inner mound material emplaced as a result of mass wasting most likely as a result of movement on the normal faults which dissect the *Mir* mound. Core 60 comprises 5 distinct units:
  1. 0-33cm: intercalated carbonate (pelagic) and Fe oxyhydroxide
  2. 33-47cm: Fe oxyhydroxide layer 1 – product of sulphide oxidation and precipitation from diffuse low temperature fluids. Upwards diffusing Cu-bearing fluids from the sulphide layer below precipitate secondary Cu minerals.
  3. 47-96cm: sulphide layer –high temperature sulphide material derived from mass wasting of the *Mir* mound. Contains enrichment in Cu, Zn, Co, Cr and Ni.
  4. 96-119cm: Fe oxyhydroxide layer 2 – very similar to the upper Fe oxyhydroxide layer, also the product of sulphide oxidation and precipitation from diffuse low temperature fluids. Base of this layer is inclined at ~25° suggesting deposition at the edge of a basin or local hollow, or as drape cover over a faulted block.
  5. 119-126cm (base): Fe oxide layer: hematite and opal rich

Downcore metal distributions reflect mineralogical variability and the relative proportions of oxides and sulphides as well as remobilisation (e.g. Cr and Cu), due to oxidative dissolution of sulphide and secondary remineralisation, (e.g. atacamite), redox cycling (important for redox sensitive elements e.g. Mn, and for Ni which is not redox active but appears to be scavenged by MnO_2), precipitation from diffuse low temperature fluids (e.g. opaline silica, nontronite and gypsum), and scavenging from seawater (V and P). The complex mineralogy and geochemistry of these sediments reflects the extreme heterogeneity in the extent of alteration and preservation of primary features across the TAG site.

Chapter 4:

Sulphide Mineralogy and Alteration

4.1 Introduction

4.1.1 Sulphide mineralogy in seafloor hydrothermal deposits

Sulphide minerals in seafloor hydrothermal deposits are precipitated in the subsurface, and chimney structures, in response to changes in temperature and pH/E_h conditions driven by mixing of hydrothermal fluid with seawater (e.g. Haymon and Kastner, 1981 James and Elderfield, 1996a Janecky and Seyfried, 1984 Styrt et al., 1981 Zierenberg et al., 1984). Basic models for chimney growth suggest that initially the central orifice of a typical black smoker chimney is lined with chalcopyrite with an anhydrite-rich exterior (Haymon and Kastner, 1981). With continued venting, debouching hydrothermal fluids are insulated by the growth of chimney walls, this facilitates precipitation of high temperature Cu-Fe sulphides and results in chimney interiors which are typically dominated by Cu-sulphides and exteriors dominated by lower temperature, Zn-sulphides (e.g. Haymon, 1983 Styrt et al., 1981 Woodruff and Shanks, 1988). In strongly reducing fluids pyrrhotite is an abundant chimney component, however it is unstable in oxidizing conditions and over time may be converted to more stable phases (e.g. pyrite) or will dissolve and return to the fluid (e.g. Haymon, 1983 Goldfarb et al., 1983). Some black smoker chimneys are dominated by Zn-sulphides e.g. hexagonal wurtzite (e.g. Haymon and Kastner, 1981; Styrt et al., 1981; Zierenberg et al., 1984; Tivey and Delaney, 1986). This suggests that some Zn-sulphides are stable at high temperature. Minor or trace amounts of bornite, pyrite, marcasite, Fe-oxide and amorphous silica may also be present in a black smoker chimney. Lower temperature, i.e. white smoker chimneys, in contrast to black smoker chimneys, are commonly dominated by sphalerite with minor amounts of marcasite or pyrite and amorphous silica, with trace amounts of chalcopyrite and Fe-oxide (e.g. Tivey et al., 1995).

At the seafloor, collapse of chimneys and mass wasting and faulting events contribute to the growth of a sulphide talus. Circulation of hydrothermal fluid and mixing with entrained seawater within the sulphide talus and hydrothermal stockwork zone leads to further sulphide precipitation in the subsurface, and cementation and replacement of primary mineralogical features. The primary sulphide mineralogy of seafloor massive sulphide deposits is subsequently modified by hydrothermal diagenetic alteration (e.g. Hannington, 1993; Tivey et al., 1995; Hannington et al., 1998; Knott et al., 1998). Secondary sulphide mineral phases include: pyrite, covellite, bornite, chalcocite, sphalerite and less commonly digenite. A summary of sulphide mineralogy from modern, seafloor massive sulphide deposits, in the Pacific and Atlantic Oceans is given in Table 4.1.

4.1.2 Sulphide alteration in seafloor hydrothermal deposits

Models of mound growth suggest that initial alteration of primary phases is contemporaneous with high temperature venting as seawater entrained into the mound mixes with hydrothermal fluid and circulates

Vent Site	Mineral	Textures and occurrences	Abundance	Reference
Middle Valley NJdFR	Pyrrhotite (Po)	Open, interlocking network of hexagonal platelets; tabular crystals	X	Goodfellow and Franklin. 1993.
	Sphalerite (Sp)	Anhedral; colloform; cubic; hexagonal; commonly interstitial to Po network	X	
	Pyrite (Py)	Cubic aggregates; lacy network commonly replacing Po network	X	
	Marcasite (Mc)	Laths overgrowing Po network	X	
	Chalcopyrite (Cp)	Anhedral cores and overgrowth rims; exsolution lamellae in Iss and Sp	X	
	Isocubanite (Iss)	Central cores in Sp; anhedral crystals	X	
	Covellite (Cv)	Anhedral replacement of Cp	x	
	Galena (Ga)	Cubic and anhedral grains in Po	Trace	
Middle Valley NJdFR	Pyrite	Colloform; euhedral; massive aggregates; some skeletal crystals; some grains are porous	X	Duckworth et al. 1994
	Pyrrhotite	Interlocking laths some with hollow centres commonly overgrown by Py	X	
	Marcasite	Small inclusions within Py; euhedral crystals	x	
	Sphalerite	Variable Fe content; some Cp and Po inclusions	x	
	Chalcopyrite	Replaces Sp and Po	x	
Endeavour Segment 47 °N JdFR	Pyrite	Cubic; anhedral-subhedral clusters intergrown with marcasite; blades; Mc and Wt inclusions are common; rare inclusions of Cp, Iss and Po	X	Tivey and Delaney. 1986
	Marcasite	Anhedral crystals intergrown with Py; colloform aggregates; contains Wt inclusions; some Po inclusions	X	
	Wurtzite	Hexagonal crystals	X	
	Pyrrhotite	Thin tablets; intergrown with Wt; inclusions in Py and Mc	Trace	
	Sphalerite	Dodecahedra within amorphous silica	Trace	
	Chalcopyrite	Anhedral grains; surrounding or surrounded by Wt, Py and/or Mc	x	
	Isocubanite	Interconnected grains; sometimes rimming Py; commonly rimmed by Wt	x	
	Galena	Finegrained anhedral; rimming Wt; occasionally as inclusions in Wt	Trace	
SJdFR	Pyrite	Layers and lenses of globular and columnar forms; colloform bands; disseminated subhedral grains; euhedral cubes; framboids; blebs in Sp and opaline silica	X	Koski et al. 1984
	Marcasite	Aggregates along Py globules; rarely interstitial	x	
	Pyrrhotite	Tabular crystals	Trace	
	Sphalerite	Dendritic; colloform; globular. Occurs as overgrowths on Py and patches in Wt	Trace	
	Wurtzite (Wt)	Euhedral; columnar crystals; infills cavities and is intergrown with Sp	X	
	Chalcopyrite	Subhedral grains associated with Sp and Wt	X	
	Cubanite (Cb)	In cores of Cp grains contains Cp lamellae	X	
	Galena	Subhedral grains rim Sp; radiating and dendritic forms in cores of colloform Sp	X	
	Jordanite (Jd)	Subhedral grains	Trace	
Cyamex EPR	Pyrite		X	Oudin et al. 1981
	Marcasite		X	
	Chalcopyrite		x	
	Wurtzite		X	
	Sphalerite		X	
	Digenite (Dg)		Trace	
	Covellite		Trace	
21°N EPR	Pyrite	Striated cubes; framboids; cryptocrystalline	X	Zierenberg et al. 1984; Haymon and Kastner, 1981
	Wurtzite	Hexagonal platelets	x	
	Sphalerite	Cubes; dodecahedrons; tetrahedrons; rounded and cryptocrystalline grains	X	
	Chalcopyrite	Mamillory and botryoidal masses, tetrahedrons; cryptocrystalline	x	
	Marcasite		Trace	
	Covellite		Trace	
	Cubanite		Trace	
	Pyrrhotite	Hexagonal plates, individual and in radiating clusters	Trace	
	Galena		Trace	

Table 4.1: Mineral textures and occurrences at modern sea floor hydrothermal sites in the Pacific and Atlantic Oceans. X = major constituent; x = minor constituent.

Vent Site	Mineral	Textures and occurrences	Abundance	Reference
Green Seamount EPR	Pyrite		X	Alt 1988
	Marcasite		x	
	Chalcopyrite		x	
	Covellite		Trace	
	Zn sulphide		trace	
Chimneys 21° N EPR	Chalcopyrite	Fine to coarsely crystalline (1-2mm) often intimately associated with anhydrite; exsolution lamellae	X	Styrt at el. 1981
	Wurtzite	Hexagonal crystals; very fine grained crystals associated with Py, Cp and anhydrite; Fe-rich; as coatings on anhydrite; columnar crystals	X	
	Pyrite	Very fined grained associated with Cp, Wt and anhydrite	x	
	Sphalerite		Trace	
	Bornite/chalcocite		Trace	
	Cubanite		Trace	
11° N and 13°N EPR	Pyrite	Subhedral cubes; dendritic; rounded blades; aggregates forming curved bands; colloform structures – relics of original marcasite	X	Graham et al. 1988
	Marcasite	Anhedral crystals; colloform; needles; rounded blades; inclusions in Py, disseminated grains	X	
	Wurtzite	Anhedral crystals; colloform; elongate; hexagonal crystals; inclusions in Py	x	
	Sphalerite	Anhedral and colloform crystals	X	
	Pyrrhotite	Inclusions in Py and Cp cubes; prismatic and fractured crystals	Trace	
	Chalcopyrite	Overgrowths on Py and as Fracture; vug fill; anhedral grains	X	
	Bornite	Blebs within Py; irregular patches on Py grain boundaries, replaced by Cv and Dg	X	
	Digenite	Replaces Bn	Trace	
	Chalcocite		Trace	
	Isocubanite	Contain Cp exsolution lamellae	x	
	Covellite	Replaced Bn	x	
Broken Spur MAR	Pyrrhotite	Found in Diffuser and ledge type sulphides, more rarely in chimneys	X	Butler et al. 1998
	Pyrite	Found in ledge, mature and brecciated sulphide types	X	
	Marcasite	Found in diffuser, ledge and brecciated sulphide	X	
	Chalcopyrite	Found in all sulphide types	X	
	Isocuabnite	Found in diffuser and brecciated sulphide	Trace	
	Bornite (Bn)	In chimney sulphide	x	
	Chalcocite (Cc)	Found in chimney and brecciated sulphide	x	
	Covellite	Found in chimney and brecciated sulphide	Trace	
	Wurtzite	Found in diffuser and ledge sulphides	x	
	Sphalerite	Found in diffuser, ledge and brecciated sulphide also a trace component in chimneys	X	
	Galena	Found only in ledge sulphide	Trace	
Snake Pit MAR	Pyrite	Colloform; cemented by silica; as cores in Sp; dendritic forms encroaching Sp	X	Kase et al. 1990
	Isocubanite	Spherical grains and aggregates; some crystals contain lamellae of Cp; overgrown by Cp; found as core of some Sp crystals; blebs in Sp grains	X	
	Marcasite	Spherical; colloform grains; Po cores; overgrown by Sp	X	
	Chalcopyrite	Forms exsolution lamellae in Iss, some crystals altering to Cv along grain boundaries; rarely contains Iss lamellae,	X	
	Sphalerite	As overgrowths on Mc; Iss cores; cementing composite grains; contain blebs of Iss	x	
	Pyrrhotite	Long prismatic crystals also short forms; in cores of some Iss grains; cemented by silica; found in centre of some Mc spheres; interstitial	x	
	Covellite	As an alteration product along chalcopyrite grain boundaries	x	
TAG mound MAR	Pyrite	Disseminated; euhedral crystals; colloform bands and clots; microcrystalline aggregates; porous grains; veinlets	X	Knott et al. 1998
	Chalcopyrite	Anhedral; disseminated grains; intergrown with Py and Sp; as inclusions in Sp; euhedral blades in vugs; overgrowths on Py; rare veinlets	Trace to x	
	Sphalerite	Anhedral grains disseminated in quartz zones; intergrown with Cp; overgrowths on Cp and quartz; inclusions in Py	Trace	
	Marcasite	Late crusts in vugs; banded aggregates; inclusions intergrowths with Py	Trace	
	Pyrrhotite	Boxwork pseudomorphed by porous Py; bladed crystals; late overgrowths on quartz	Trace	

Table 4.1 cont.

recrystallising and redistributing primary mineral phases (Humphris et al., 1995; Tivey et al., 1995; Scott, 1997; You and Bickle, 1998). In fact, the precipitation of pyrite (pyrite precipitation occurs via a pyrrhotite precursor (Chapter 1) the full reaction is shown in Equation 1.3), anhydrite and silica, during high temperature activity, effectively drives zone refining and alteration by decreasing the pH of the circulating hydrothermal fluid (e.g. Seewald and Seyfried, 1990; Tivey et al., 1995). For example separation of Cu and Zn may be achieved because of the different solubilities of chalcopyrite and sphalerite as a function of pH. Under the low pH conditions sustained within active mounds, as hydrothermal fluid is conductively cooled, Cu solubility is greater than Zn. Where hydrothermal fluid is mixed with entrained seawater, pH increases, and Zn has greater solubility (Figure 4.1) (Large et al., 1989). This is well illustrated in the active TAG mound where ODP drill cores have shown enrichment of Cu in zones 2 and 3, the upper hydrothermal stockwork, and Zn in zone 1 at the seawater crust interface (Chapter 2). The presence of acidic fluids is also important in the remobilisation and remineralised of other metals and enrichment of Au, Ag, Pb and Cd, in addition to Cu and Zn, results from changes in E_h and pH conditions during diagenesis (Hannington et al., 1988; Herzig et al., 1991; Humphris et al., 1995; Tivey et al., 1995; Severmann, 2000).

The presence of quartz and opaline silica in many seafloor deposits is indicative of the variable physical and chemical conditions present during the growth and initial alteration of sulphide mounds since silica is undersaturated in end member hydrothermal fluids and is precipitated from conductively cooled mixtures of hydrothermal fluid and seawater (Janecky and Seyfried, 1984; Tivey et al., 1995). Much of the amorphous silica and quartz in the TAG mound occurs as breccia cement but it is also seen as a replacement of anhydrite and sulphide (e.g. Humphris et al., 1995; Honnorez et al., 1998; Hopkinson et al., 1998; Knott et al., 1998; Hopkinson et al., 1999).

The precipitation of thin oxide crusts on the surface of seafloor massive sulphide deposits is also contemporaneous with high temperature activity. There are two distinct mechanisms by which the precipitation of oxide crusts may occur: the first of these is Fe-oxide precipitation where acidic solutions carrying Fe leached from the underlying sulphide have migrated to the outer surfaces of a deposit, e.g. oxide crusts at the surface of the active TAG mound (Hannington, 1993; Hannington et al., 1988). These surface crusts have REE patterns that are consistent with the formation of Fe oxides via the alteration of sulphides and which show the evolution of the fluid during transport (Mills and Elderfield, 1995b). Alternatively, Fe-oxides maybe precipitated directly from cooled hydrothermal fluid when the Fe/H_2S ratio is greater than one, e.g. Fe-oxide crusts at the Red Seamount, EPR (Edmond et al., 1979a; Alt et al., 1987). These two mechanisms of Fe-oxide precipitation may also occur simultaneously (e.g. Hannington et al., 1988; Hannington and Jonasson, 1992; Mills and Elderfield, 1995b). The resultant Fe-oxide deposits have been compared to the gossanous material overlying ancient massive sulphide deposits now exposed on land (e.g. Alt et al., 1987; Hannington et al., 1988; Herzig et al., 1991; Hannington, 1993; Dill et al., 1994; Goulding, 1998).

During hydrothermally inactive periods, modification continues as circulation of seawater and low temperature fluids persists (e.g. Humphris et al., 1995; Tivey et al., 1995; Humphris and Kleinrock, 1996). The dissolution of primary metal sulphide phases, which are unstable in oxidising seawater, in general

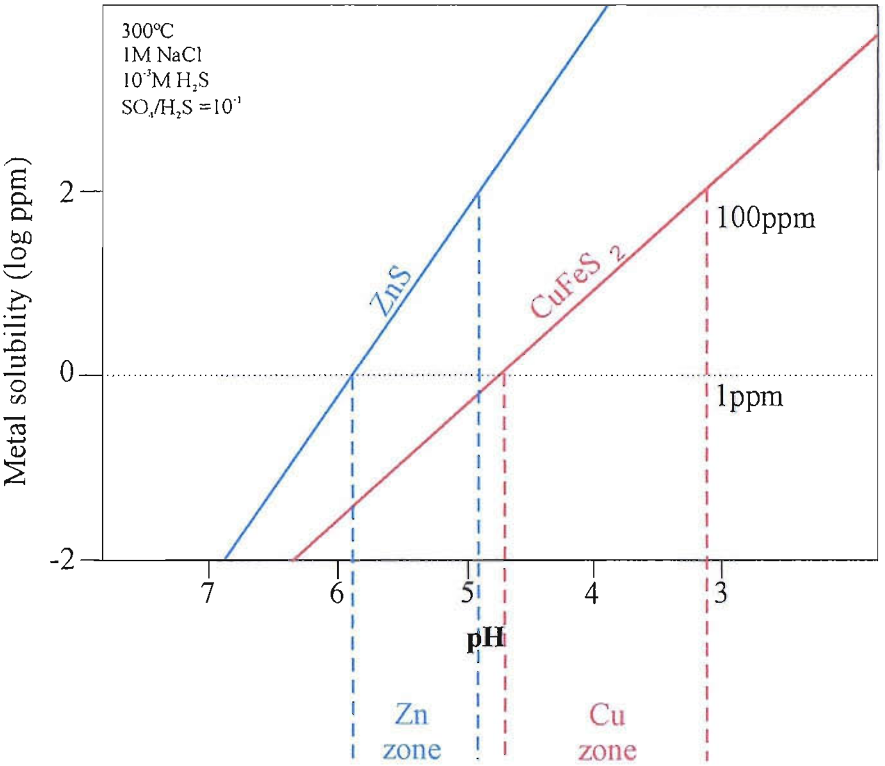

Figure 4.1: Solubilities of sphalerite (ZnS) and chalcopyrite ($CuFeS_2$) as a function of pH. Changing pH conditions allows for the separation of Cu and Zn within an actively forming seafloor massive sulphide deposit. Sustained low pH conditions in the core of a deposit allows for separation of Cu and Zn, if a large increse in pH occurs rapidly sphalerite and chalcopyrite will co-precipitate. (Adapted from Large et al., 1989).

terms, is shown by Equation (1.11). Metal ions released into solution will then form complexes with anions including SO_4^{2-}, Cl^-, F^-, or HCO_3^-(minor at low pH), subsequent precipitation of secondary sulphide minerals may be explained by reduction of oxidising solutions carrying base metals (Thornber, 1985). The dissolution of primary sulphides is most likely dominated by the oxidation of pyrite to Fe-oxyhydroxide and Fe oxide (Equations 1.12 and 4.1: Nordstrom, 1982) via aqueous Fe^{2+} (Equation 4.6).

$$2Fe^{2+} + 0.5O_2 + 5H_2O \Leftrightarrow 2Fe(OH)_3 + 4H^+ \tag{4.1}$$

However, this is not the only potential oxidation pathway, in low oxygen conditions, NO_3^-, MnO_2 (e.g. Equation 4.2: Schippers and Jorgensen, 2001) and Fe(III) (Equation 4.3: e.g. Wiersma and Rimstidt, 1984; McKibben and Barnes, 1986; Schippers and Sand, 1999) may act as electron acceptors.

$$FeS_2 + 7.5MnO_2 + 11H^+ \rightarrow Fe(OH)_3 + 2SO_4^{\ 2-} + 7.5Mn^{2+} + 4H_2O \tag{4.2}$$

$$FeS_2 + 8H_2O + 14Fe^{3+} \rightarrow 15Fe^{2+} + 2SO_4^{\ 2-} + 16H^+ \tag{4.3}$$

In addition, chemical experiments have shown that pyrite oxidation rarely occurs as a straight forward reaction, such as Equation 1.12, and more commonly proceeds via intermediate sulphur and Fe species (e.g. Nordstrom, 1982; Schippers and Sand, 1999; Canfield, 2001a; Habicht and Canfield, 2001; Schippers and Jorgensen, 2001). Equation 4.4 shows a two step oxidation mechanism for pyrite via a thiosulphate intermediate (Schippers and Sand, 1999):

$$\begin{gathered} FeS_{2(S)} + 6Fe^{3+}{}_{(aq)} + 3H_2O \rightarrow S_2O_3^{\ 2-} + 7Fe^{2+}{}_{(aq)} + 6H^+ \\ S_2O_3^{\ 2-} + 8Fe^{3+}{}_{(aq)} + 5H_2O \rightarrow 2SO_4^{\ 2-} + 8Fe^{2+}{}_{(aq)} + 10H^+ \end{gathered} \tag{4.4}$$

Bacterial interaction in pyrite oxidation is well documented and Fe oxidising microbes are capable of influencing the growth and dissolution of a number of minerals by exerting control over reaction kinetics and pathways (e.g. Silverman and Ehrlich, 1964; Lacey and Lawson, 1970; Fowler et al., 1999; Kirby et al., 1999; Schippers and Sand, 1999). In the ambient bottom water conditions present at the seawater TAG sulphide mound interface Fe(II) has a half life of <1 minute and inorganic oxidation of pyrite will proceed rapidly however, in the lower pH (~6) low oxygen (O_2 ~1ml/l) conditions present within massive sulphide deposits, inorganic oxidation proceeds slowly with Fe(II) half lives >5 days ((Millero et al., 1987) this environment potentially provides the conditions for significant biological mediation of Fe(II) oxidation (Emerson and Moyer, 2002). Fe oxidation, bacterial interactions and bio-mineralisation are discussed in detail in Chapter 6.

The oxidation of pyrite via equations 1.12, 4.3 and 4.4 leads to the formation of acidic pore fluids which are important in the remineralisation of primary Cu and Zn phases (Thornber, 1985 Hannington et al., 1988; Large et al., 1989; Tivey et al., 1995). The pH of pore fluids from sulphidic material undergoing oxidation at the TAG mound are reported to range from 3.6 to 5.5 (Hannington, 1993), Chalcopyrite solubility (measured in ppm) at pH 3.6 is 2 orders of magnitude greater than at pH 5 where solubility drops below 1ppm, sphalerite is soluble to higher pH, dropping below 1ppm at ~pH 6 (Figure 4.1) (Large et al., 1989).

Once in solution E_h-pH changes and chloride complexing dominate the geochemical behaviour of Cu at low temperatures. Cu is soluble under oxidising conditions and low pH (e.g. Large et al., 1989), Fe^{2+} is considerably less soluble under these conditions and will either remain in the primary sulphide or will precipitate as hematite and/or goethite as a result of hydrolysis reactions (e.g. Thornber, 1985; Baes and Mesmer, 1976) (e.g. Equation 4.4). This difference in solubility provides an efficient mechanism by which Cu may be fractionated from Fe. Remineralisation of primary chalcopyrite to pyrite with loss of Cu^{2+} ions can be achieved in this manner (e.g. Rose, 1976). Cu^{2+} ions released during the remineralisation of chalcopyrite to pyrite form cuprous chloride complexes such as $CuCl_2^-$ and $CuCl_3^{2-}$ (e.g. Rose, 1976; Hannington, 1993). Since Cu solubility is highest at low pH, where the solutions carrying such chloride complexes are exposed to ambient seawater, basic Cu salts, such as atacamite, which commonly occurs as a product of secondary mineralisation in the weathered portions of sulphide mounds (e.g. Emberly et al., 1988; Hannington, 1993), are precipitated (Detrick et al., 1986; Alt et al., 1987; Hannington et al., 1988). Since atacamite is precipitated in response to pH increases resulting from exposure of the solutions carrying copper chloride complexes to ambient seawater, the presence of atacamite delineates the extent of seawater penetration within a deposit during remobilization of Cu (Hannington, 1993).

Although this mechanism of Cu dissolution and remineralisation is akin to sub-aerial supergene processes (Section 4.1.3) atacamite is rarely observed from terrestrial massive sulphide deposits. This is because under the high Cl^- concentration and pH of ambient seawater atacamite is only slightly soluble however, in fresh waters where the Cl^- concentration and pH are lower atacamite is highly soluble (e.g. Rose, 1976; Hannington, 1993).

During mass wasting events primary, partially altered and secondary phases are transported to near field sediments and are intermixed with material derived from plume fallout and background pelagic sedimentation. Oxidative decay of pyrite and remobilisation and secondary mineralisation of the chalcophile elements continues within the sediment pile. E_h and pH gradients drive remobilisation of metals in the sediment pile and these conditions are analogous to those discussed above relating to mound processes. For example, investigation of a core collected close to CD102/58, the Severmann core (2000) (CD102/43) there is evidence for diffusion of Zn and Pb out of sulphide layers whereas Cu is retained by the pH gradient. Over time, these processes of oxidation and remobilisation may lead to complete oxidation to Fe-oxide. Elevated metal contents in sediments from the FAMOUS hydrothermal site (37° N MAR) can be attributed to diagenetic re-mobilisation of sulphides by low temperature alteration of primary phases and post-depositional circulation of hydrothermal fluids and seawater through the sediment pile (Scott et al., 1979). Similar trends of enrichment have been reported for samples of metalliferous sediments from DSDP Leg 92 from 19° S on the EPR which demonstrate a range of concentrations in the chalcophile elements; Fe 25-39wt%, Cu 1000-2000ppm, Zn and Ni 500-1000ppm and Co 100-150ppm which are attributed to remobilisation of base metals during diagenesis (Barrett et al., 1987). These are significantly higher than for sediments derived from plume fallout e.g. sediments deposited from the Rainbow hydrothermal plume at

36°N MAR have Fe contents of 1-2%, Cu 70-448ppm, Zn 20-33ppm, and Ni $\leq$100ppm (Cave et al., 2002). A comparison of metal contents in metalliferous sediments from the Atlantic and Pacific with material from this study is given in Chapter 3.

4.1.3 Supergene Processes

The term supergene relates to sub-aerial processes of mineral precipitation in which an existing ore body is enriched to a higher grade (Figure 4.2). At the simplest level supergene enrichment can be viewed as a two stage process (e.g. Bear, 1963 Constantinou and Govett, 1973; Boyle, 1979; Thornber, 1985): (1) Sulphides in oxidising parts of the ore body, generally those areas above the water table, undergo oxidation resulting in the production of acidic pore waters which leads to mineral dissolution via chemical leaching of base metals. Since pyrite is typically the most common sulphide, the oxidation of pyrite is fundamental to this process. Fe-oxides and oxyhydroxides are precipitated in the leached zone forming a gossanous cap, whilst metal bearing solutions migrate downwards towards the water table. (2) Below the water table, where conditions are usually reducing, the leached metals are re-precipitated as higher grade minerals. These reactions typically involve replacement of unaltered sulphide by secondary sulphides. A classic example of this is the conversion of chalcopyrite to covellite via Equation 4.5:

$$CuFeS_2 + Cu^{2+} \rightarrow 2CuS + Fe^{2+} \qquad (4.5)$$

Whilst the two stage process described above is a valid summary of supergene processes, in reality, the chemical reactions governing sulphide alteration and which ultimately lead to gossan formation are much more complex (e.g. Boyle, 1979; Nordstrom, 1982; Thornber and Wildman, 1984; Thornber, 1985).

Metal sulphides, of which pyrite is the most abundant, are chemically unstable in oxidising and low pH conditions. Where sulphides are exposed to such conditions spontaneous oxidation will occur, e.g. Equation 4.7, and base metals are solubilised. The solubility of an element and its hydrolysis and complexing behaviour are the most important factors governing its fate during alteration, these in turn are controlled by the prevailing pH and E_h conditions (e.g. Baes and Mesmer, 1976; Nordstrom, 1982; Thornber and Wildman, 1984; Thornber, 1985).

Most metals are transported chiefly in their complexed form, $S_2O_3^{2-}$, SO_4^{2-}, OH^-, Cl^-, F^-, CO_3^{2-} and HCO_3^- are important ligands for metal mobility (e.g. Sillen and Martell, 1964; Sillen and Martell, 1971; Rose, 1976; Mann, 1984; Thornber, 1985; Herzig et al., 1991 Hannington, 1993). For example, in the low pH conditions associated with mineral dissolution in the supergene oxidising zone, Cu will most commonly form complexes with Cl^- (e.g. Rose, 1976), however, it can also form stable complexes with F^-, SO_4^{2-}, CO_3^{2-}, $S_2O_3^{2-}$, and OH^-. In the same conditions Fe(II) and Fe(III) will also form complexes with Cl^-, F^-, SO_4^{2-}, CO_3^{2-}, and OH^- but are most commonly complexed with $S_2O_3^{2-}$ (e.g. Sillen and Martell, 1964; Sillen and Martell, 1971; Pitwell, 1973; Thornber, 1985). Experimental data show that the stability of a metal ion complex in solution is dependant upon its proximity to the weathering sulphide and the extent of dilution as it diffuses to areas of lower concentration (Sillen and Martell, 1964; Sillen and Martell, 1971; Thornber, 1985). Under laboratory conditions $S_2O_3^{2-}$ has been shown to be the dominant ligand close to the surface of

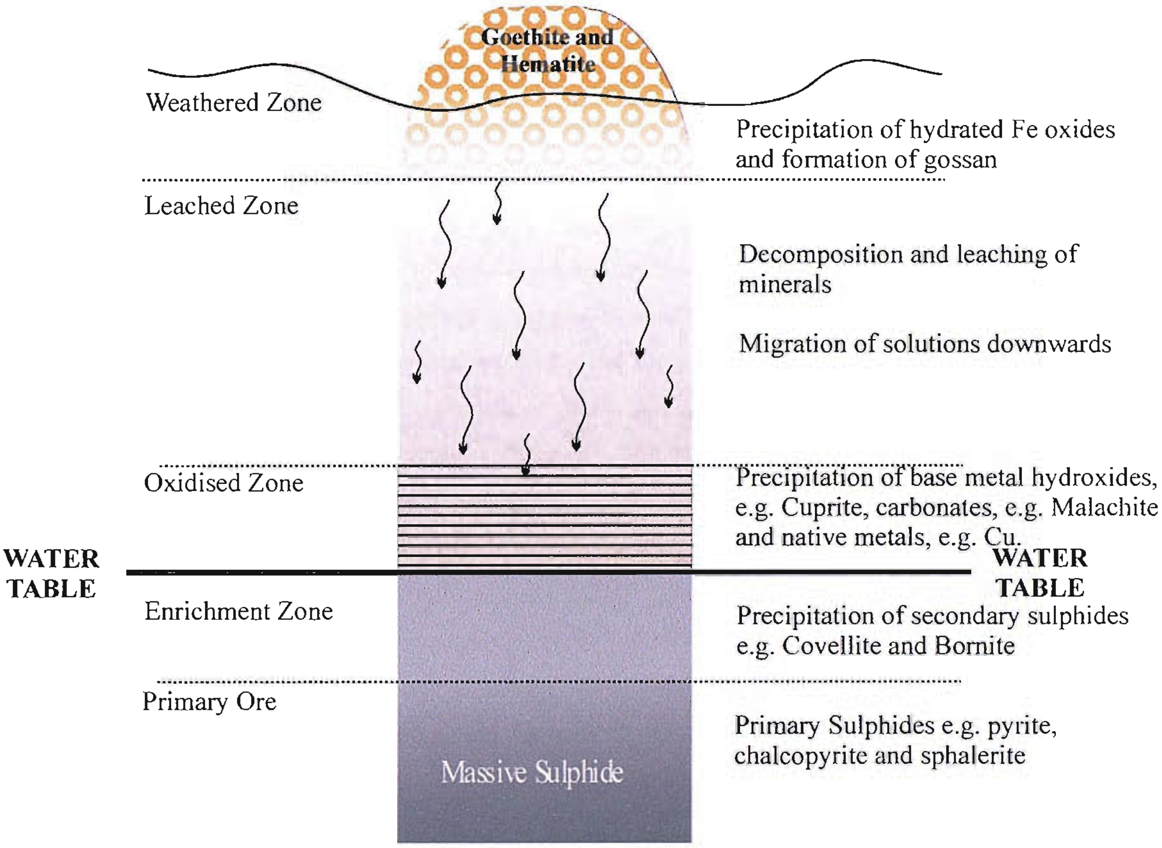

Figure 4.2: Schematic representation of an idealised supergene weathering profile. The extent of oxidation is dependant upon the position of the water table with respect to the primary ore, and complete oxidation will only take place with continued uplift of the massive sulphide.

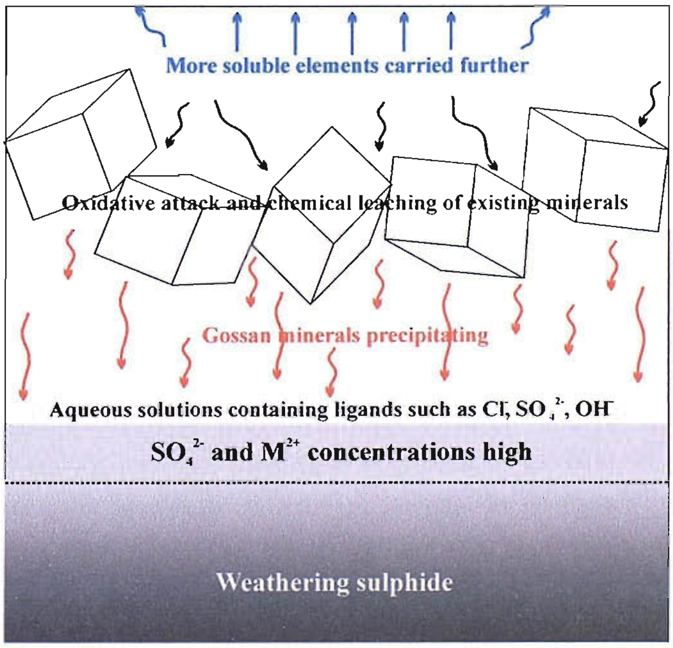

Figure 4.3: Basic representation of the major chemical processes involved in sulphide weathering and initial gossan formation (Adapted from Thornber, 1985).

a weathering sulphide, and hydrolysis reactions, and therefore re-precipitation, under these conditions are inhibited, with dilution, as metals diffuse away from the surface of the weathering sulphide, $SO_4^{2-}$and OH^- complexes, and transport as non complexed aqueous M^{2+} becomes increasingly important and precipitation via hydrolysis may take place (Sillen and Martell, 1964; Sillen and Martell, 1971; Baes and Mesmer, 1976; Thornber and Wildman, 1984; Thornber, 1985).

Re-precipitation and hydrolysis reactions are principally controlled by changes in pH and E_h conditions (Baes and Mesmer, 1976). This is because changes in pH and E_h alter the behaviour of particular ligands which in turn affects the stability of metal bearing complexes and therefore metal solubility. The effect of changing pH and E_h conditions, with respect to the role of gossan forming processes, may be demonstrated by consideration of Fe^{2+}. Below pH6 Fe^{2+} is highly soluble, oxidation by dissolved oxygen and hydrolysis by reaction (4.6) results in precipitation of unstable $Fe(OH)_3$ and produces protons causing a further decrease in pH, this in turn results in the solubilisation of base metals. At higher pH, >7, Fe^{2+} has significantly lower solubility and exists predominantly as $Fe(OH)^+_{(aq)}$ and $Fe(OH)_2$. Whilst further oxidation of $Fe(OH)_2$ by dissolved oxygen also results in precipitation of $Fe(OH)_3$ (reaction 4.7) no acidity is produced and the precipitate remains stable (Thornber and Wildman, 1984; Thornber, 1985). This type of hydrolysis behaviour causes Fe to be concentrated in precipitates formed where there are steep E_h and pH gradients.

$$4Fe^{2+} + O_2 + 10H_2O \rightarrow 4Fe(OH)_3 + 8H^+ \tag{4.6}$$

$$4Fe(OH)_2 + O_2 + 2H_2O \rightarrow 4Fe(OH)_3 \tag{4.7}$$

Where precipitation is rapid, i.e. at sharp E_h-pH gradients, goethite and amorphous Fe oxyhydroxides, e.g. ferrihydrite, are precipitated. Ferrihydrite, however, is not stable and over time will transform to more crystalline phases, commonly hematite (Fe_2O_3) (e.g. Thornber and Wildman, 1984; Cornell and Schwertmann, 1996).

The end product of leaching processes occurring in the oxidising zone, are the Fe-oxide gossans which overlie sub-aerial massive sulphide deposits. Gossans consist of hydrated Fe-oxides, e.g. goethite (FeO(OH), and hydrated Fe sulphates, e.g. jarosite ($KFe_3(SO_4)_2(OH)_6$) and are commonly enriched in elements which have low solubility in the oxidising conditions associated with alteration and leaching processes, e.g. gold, or which have strong adsorption affinities with Fe oxide and oxyhydroxide, e.g. Cu and Pb (e.g. Bear, 1963; Constantinou and Govett, 1973; Boyle, 1979; Thornber and Wildman, 1984; Thornber, 1985; Dold and Fontbote, 2001; Dill et al., 2002). In deposits where the acidic weathering solution has come into contact with carbonates, the gossan will contain base metal carbonates in addition to Fe-oxides: interaction of acidic solutions with alkaline carbonate results in dissolution of the carbonate which neutralizes the acidity causing the pH to increase and base metals to precipitate (e.g. Thornber, 1985; Scott et al., 2001; Dill et al., 2002). Figure 4.3 shows a schematic representation of the major chemical and physical steps involved in gossan formation.

Several authors have likened alteration within submarine massive sulphide deposits and metalliferous sediments to sub-aerial supergene processes (e.g. Hannington et al., 1988; Herzig et al., 1991; Binns et al., 1993; Hannington, 1993). The elevated metal contents in submarine metalliferous sediments are attributed to dissolution of sulphide phases and re-precipitation in the overlying oxide deposits as a result of the steep E_h-pH gradients which exist in these sediments (e.g. Barrett et al., 1987; Hannington et al., 1988; Herzig et al., 1991; Dill et al., 1994; Goulding et al., 1997; Severmann, 2000). However, the mechanisms of sulphide alteration and the ultimate fate of the chalcophile elements in submarine systems are largely unknown. Although classic, sub-aerial supergene processes and sub-marine sulphide alteration and oxide formation are both driven by oxidative dissolution, secondary mineralisation and alteration processes maybe significantly different.

4.1.4 Aims and Objectives

The geochemistry of TAG cores collected in close proximity to those of this study has been studied in detail (e.g. Metz et al., 1988; Mills et al., 1993; Severmann, 2000) and although post-depositional and post-venting, diagenetic processes associated with low temperature fluid flow have been investigated (e.g. Mills et al., 1996; Severmann, 2000; Severmann et al., 2004) alteration within near field, sulphide-rich sediments and the impact of diagenetic oxidation processes on the geochemistry and mineralogy of these deposits remains poorly constrained.

This study investigates sulphide-rich layers within two metalliferous sediment cores from the *Alvin* and *Mir* relict high temperature zones within the TAG field. The objectives of this chapter are to identify: the primary and secondary mineral assemblages; the paragenetic sequence of mineralisation; alteration processes and pathways; and the formation and emplacement history of each sulphide layer, in order to determine the impact of alteration processes on the mineralogy, geochemistry and evolution of near-field sulphide-rich sediments and to evaluate the validity of comparisons of sub-marine sulphide alteration with sub-aerial supergene processes.

4.2 Materials and Methods

Samples for this study were collected from the sulphide layers of cores CD102/58 (*Alvin* zone) at 76 to 138.5cm depth downcore, and CD102/60 (*Mir* mound) at 48 to 96cm depth downcore (Figure 4.4). The downcore bulk mineralogy and geochemistry of both cores are discussed in Chapter 3.

4.2.1 Sample preparation

Polished blocks for reflected light microscopy were prepared by setting hand picked sulphide mineral separates in epoxy resin following which the epoxy blocks were ground and polished. Three sulphide-rich rock nuggets at depths of: 49.5 to 53.5cm; 58 to 63cm; 67.5 to 71.5cm from CD102/60 (the *Mir* core) were also set in polished blocks (Figure 4.5). Three polished thin sections, 30μm thick, were prepared for SEM analysis, reflected and transmitted light microscopy, from a resin impregnated section, 1cm wide by 10cm long, of the laminated section at 76 to 87cm depth within the sulphidic layer of CD102/58 (the *Alvin* core) (Figure 4.6 and 4.7).

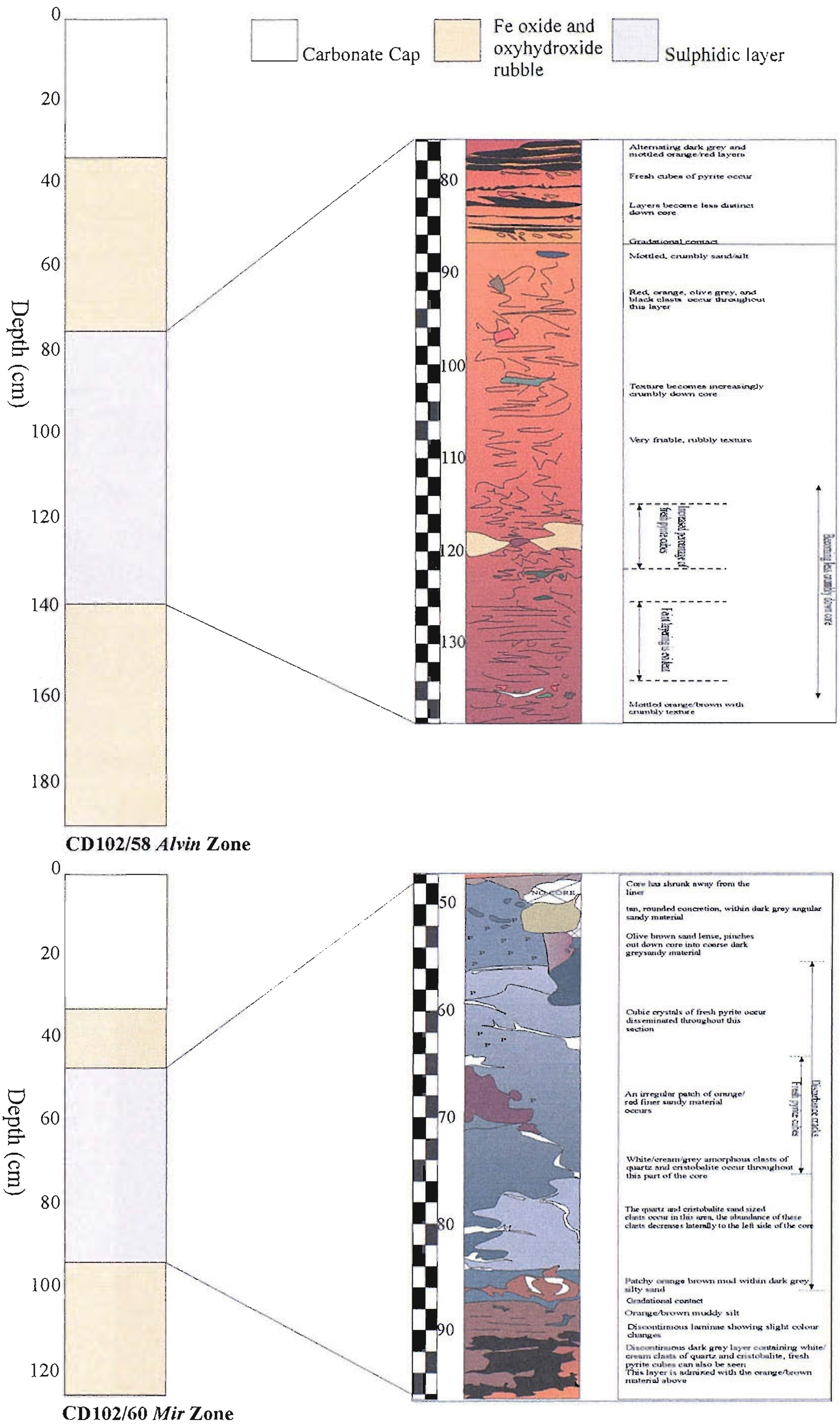

Figure 4.4: Idealised stratigraphic logs showing major lithology downcore for CD102/58, the *Alvin* core, and CD102/60, the *Mir* core. The inset, in both cases, is a detailed log of the sulphide layer of each core. The sulphide layer of CD102/58 occurs between 76 and 138.5 cm depth. The sulphide layer of CD102/60 occurs between 48 and 96 cm depth.

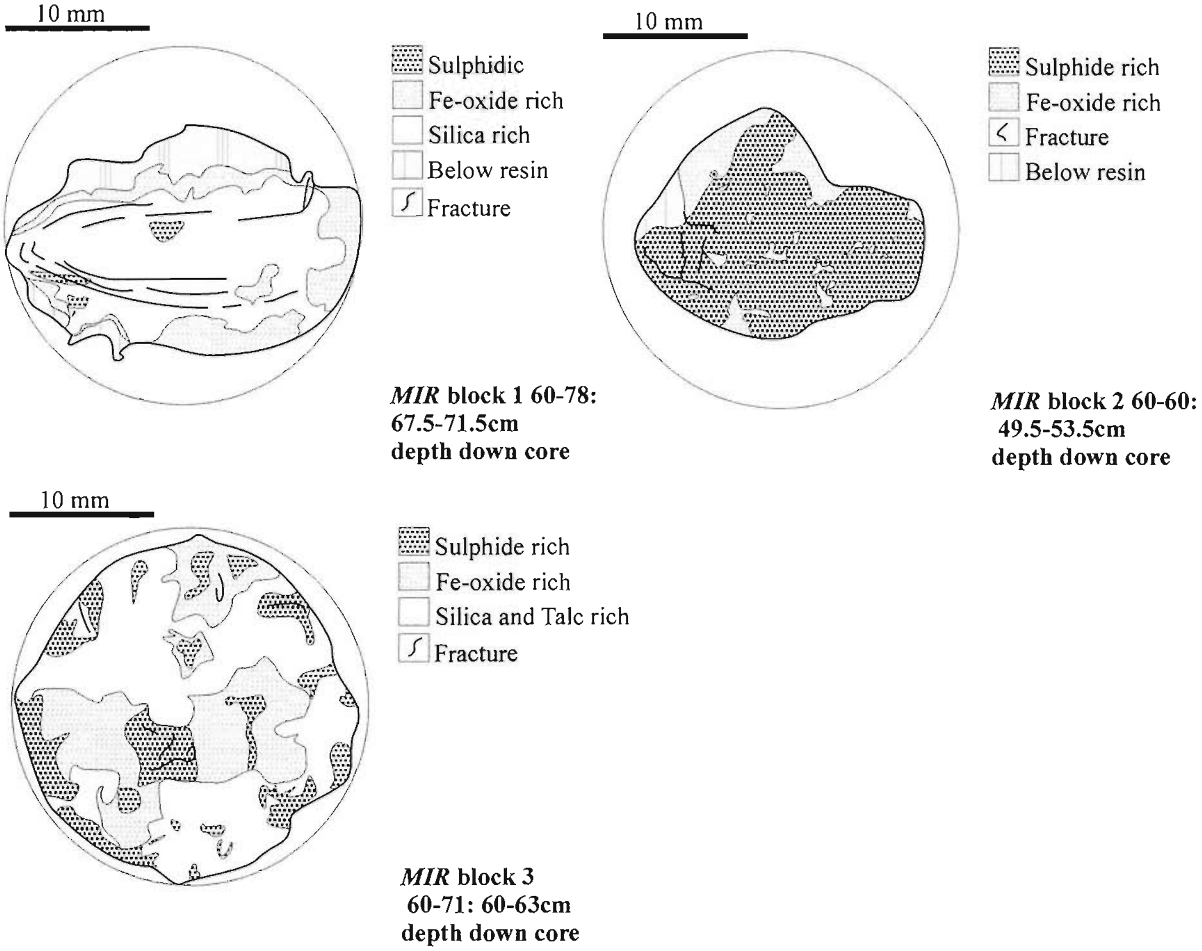

***MIR* block 1 60-78: 67.5-71.5cm depth down core**

***MIR* block 2 60-60: 49.5-53.5cm depth down core**

***MIR* block 3 60-71: 60-63cm depth down core**

Figure 4.5: **Sketch maps of the polished blocks of 3 rock nuggets from the *Mir* core: CD102/60.**

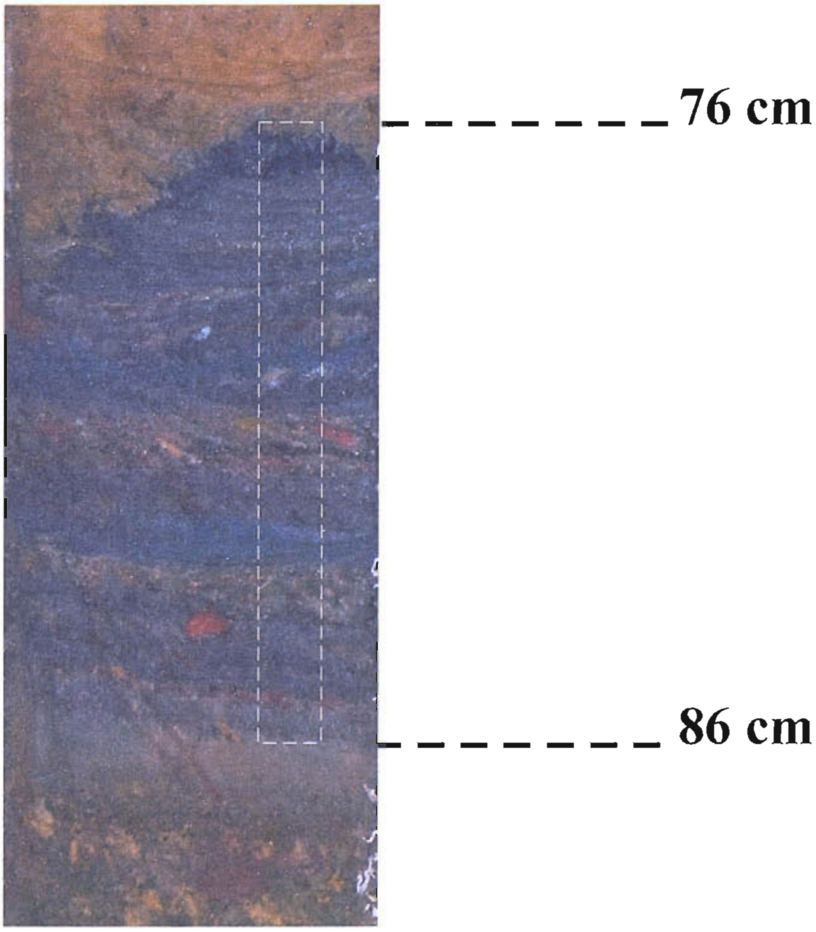

Figure 4.6: **Location of impregnated section from the top of the sulphide layer of core 58 marked by white dashed box. Three 30μm thick, polished thin sections were prepared from this section for SEM and transmitted and reflected light microscopy.**

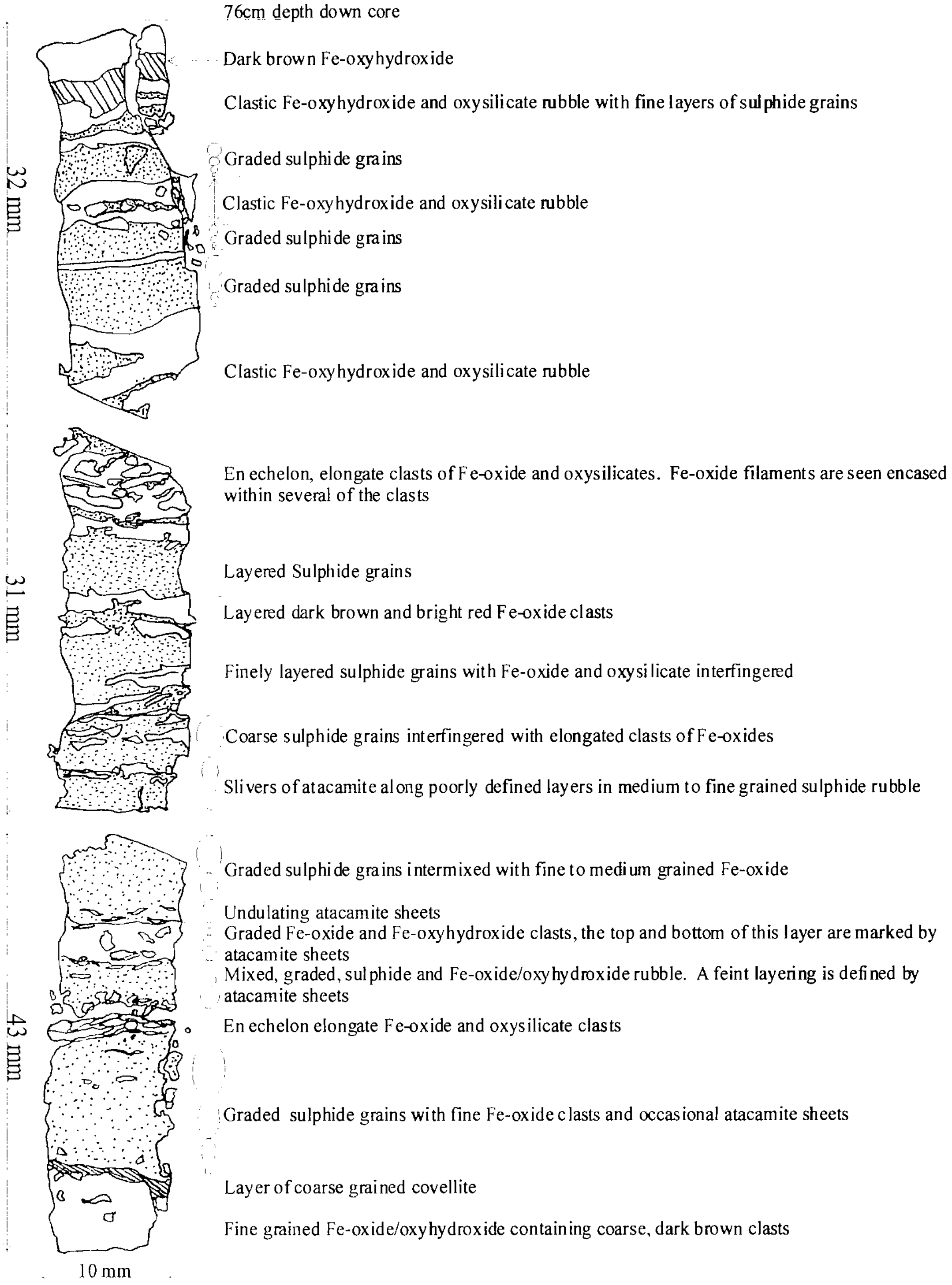

Figure 4.7: Micro-logs of polished thin sections prepared from the impregnated striped section at the top of the sulphidic layer core CD102/58, the *Alvin* core. Graded bedding and alignment and imbrication of Fe-oxide and oxyhydroxide clasts indicate that the alternating layers of sulphidic and Fe-oxide rich material are sedimentary in origin rather than in situ alteration features.

4.2.2 Scanning Electron Microscopy (SEM)

The three polished thin sections from the resin impregnated stripped section at 76-87cm depth at the top of the sulphide layer of Core 58 were examined on a LEO 1450VP, Tungsten Filament SEM at 20kV using a beam current of 80nA and a probe current of 700pA. Qualitative X-Ray microanalyses were performed over 50 second periods using a Princeton Gamma Tec (PGT) microanalysis X-ray spot with a spot size of 2-3μm.

4.2.3 Transmitted and Reflected Light Microscopy

Polished blocks were examined and photographed in reflected light on a binocular polarizing microscope. The polished thin sections were examined and photographed in both transmitted and reflected light on a binocular polarizing microscope.

4.3 Results

The sulphidic portions of both cores show considerable heterogeneity both in mineral distribution and texture. Pyrite is the dominant sulphide phase and is ubiquitous throughout the sulphidic portions of both Core 58 and 60. Lesser amounts of sphalerite and chalcopyrite, with minor covellite occur in Core 58 and chalcopyrite with minor sphalerite and trace covellite in Core 60 (Figure 4.8 and Table 4.2).

4.3.1 The *Alvin* core (CD102/58)

4.3.1.1 *Pyrite, FeS_2*

Pyrite is ubiquitous in the sulphidic portion of this core and locally constitutes up to 75% of a sample. It occurs in the primary mineral assemblage and as a secondary phase associated with alteration. Primary pyrite is most commonly seen as massive fine – medium grained aggregates of euhedral pyrite cubes (Figure 4.9a & e), and less commonly as reworked randomly oriented collomorphic crusts (Figure 4.11d & e) and spheres (Figure 4.9c), medium–coarse singular euhedral cubes (Figure 4.9d, i & j), and as tube structures (sulphidic tube structures are discussed in detail in Chapter 6). Much of this primary pyrite is porous and fractured (Figure 4.9a & b). Primary pyrite cubes are frequently rimmed or overgrown by sphalerite and Fe-oxysilicates (Figure 4.9d, f, i & j; Figure 4.10a, b & e). Oxidative corrosion and dissolution of primary pyrite is illustrated by the presence of irregular grain boundaries (Figure 4.9j; Figure 4.10c), which are enclosed by layered or filamentous Fe-oxide (Chapter 6), and dissolution pits on grain surfaces (Figure 4.10d) which are frequently filled with secondary mineral phases, most commonly Fe-oxides and Fe-oxyhydroxides but also Fe, Cu, Al, Mg silicates. Fe-oxide/oxyhydroxide/and oxysilicate polymorphs of primary pyrite cubes resulting from replacement of primary pyrite are observed and some have cores of relict pyrite. Figures 4.9, 4.10 and 4.11 show photomicrograph and SEM images of primary pyrite textures and mineralogical associations in Core 58.

Secondary pyrite occurs predominantly as medium-coarse grained euhedral cubes and aggregates often with relict chalcopyrite inclusions (Figure 4.10g). It is also commonly seen as collomorphic rims around sphalerite, chalcopyrite and covellite (Figure 4.11a, & b; Figure 4.15b). In addition pristine, cubic grains of secondary pyrite are seen as replacements of highly porous subhedral primary pyrite and chalcopyrite, and as rims on covellite (Figure 4.11c). Secondary pyrite is also associated with co-precipitated secondary sphalerite

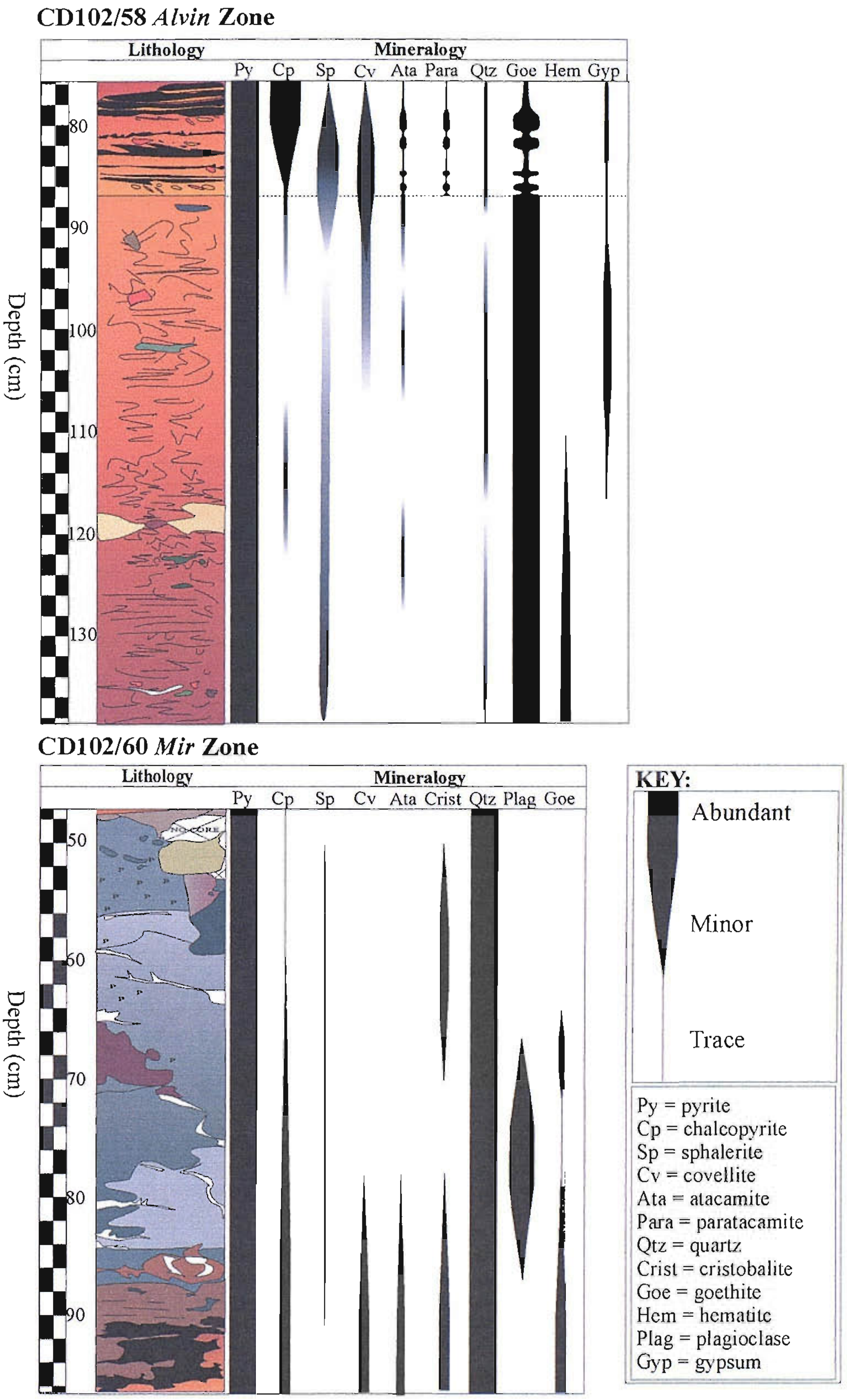

Figure 4.8: Mineralogical occurrences and abundance downcore in the sulphide layers of cores 58 and 60. For both cores pyrite is the dominant sulphide phase and the abundance of Fe oxide and oxyhydroxide increases downcore. Oxide and oxyhydroxide phases are much more abundant in core 58 where oxidation of the sulphide layer is pervasive. Chalcopyrite and sphalerite are spatially separated in both cores. The primary mineral assemblage for core 58 consists of pyrite, chalcopyrite and sphalerite; the secondary assemblage consists of pyrite, covellite, goethite, hematite, atacamite, paratacamite, quartz and gypsum. The primary assemblage of core 60 consists of pyrite, chalcopyrite, quartz and cristobalite, with a secondary assemblage of pyrite, sphalerite, atacamite and goethite.

	Mineral	Textures and occurrences	Abundance	Reference
TAG mound MAR	**Pyrite (Py)**	Disseminated; euhedral crystals; colloform bands and clots; microcrystalline aggregates; porous grains; veinlets	X	Knott et al. 1998
	Chalcopyrite (Cp)	Anhedral; disseminated grains; intergrown with Py and Sp; as inclusions in Sp; euhedral blades in vugs; overgrowths on Py; rare veinlets	Trace to x	
	Sphalerite (Sp)	Anhedral grains disseminated in quartz zones; intergrown with Cp; overgrowths on Cp and quartz; inclusions in Py	Trace	
	Marcasite (Mc)	Late crusts in vugs; banded aggregates; inclusions intergrowths with Py	Trace	
	Pyrrhotite (Po)	Boxwork pseudomorphed by porous Py; bladed crystals; late overgrowths on quartz	Trace	
CD102/58 ***Alvin*** **zone**	**Pyrite (Py)**	Euhedral fine to medium grained aggregates; Euhedral cubes; collomorphic bands and colts; porous and fractured grains; rims on Cp, Sp and Cv; co-precipitated with secondary Sp and Cp	X	This study
	Chalcopyrite (Cp)	Sub-anhdral medium grained crystals; overgrowths on primary pyrite; co-precipitated with secondary pyrite	x	
	Sphalerite (Sp)	Coarse to medium grained; an-subhedral crystals; porous and fractured replacing Py and Cp; collomorphic rims and bands	X	
	Covellite (Cv)	Anhedral and extremely porous replacement of Cp; overgrowth rims on Cp; collomorphic bands and clots; interstitial cement within Cp	x	
CD102/60 ***Mir*** **zone**	**Pyrite (Py)**	Medium to fine grained aggregates; euhedral crystals; collomorphic bands; fine grained disseminated in silica cement; porous and radially fractured; late overgrowths of euhedral cubic crystals on Cp and Sp; co-precipitated with Cp	X	This study
	Chalcopyrite (Cp)	Coarse-grained anhedral crystals; fractured grains; fine-grained disseminated within silica cement; co-precipitated with Py; altered to Cv at grain boundaries.	x	
	Sphalerite (Sp)	An-subhedral rims on Py; fracture fill; replacement of Py	x	
	Covellite (Cv)	Alteration rims at Cp grain boundaries	Trace	

Table 4.2: Comparison of mineral textures and occurrences from the TAG hydrothermal mound with near field sulphide sediments from the adjacent relict hydrothermal zones: *Alvin* (CD102/58) and *Mir* (CD102/60). X = major constituent; x = minor constituent.

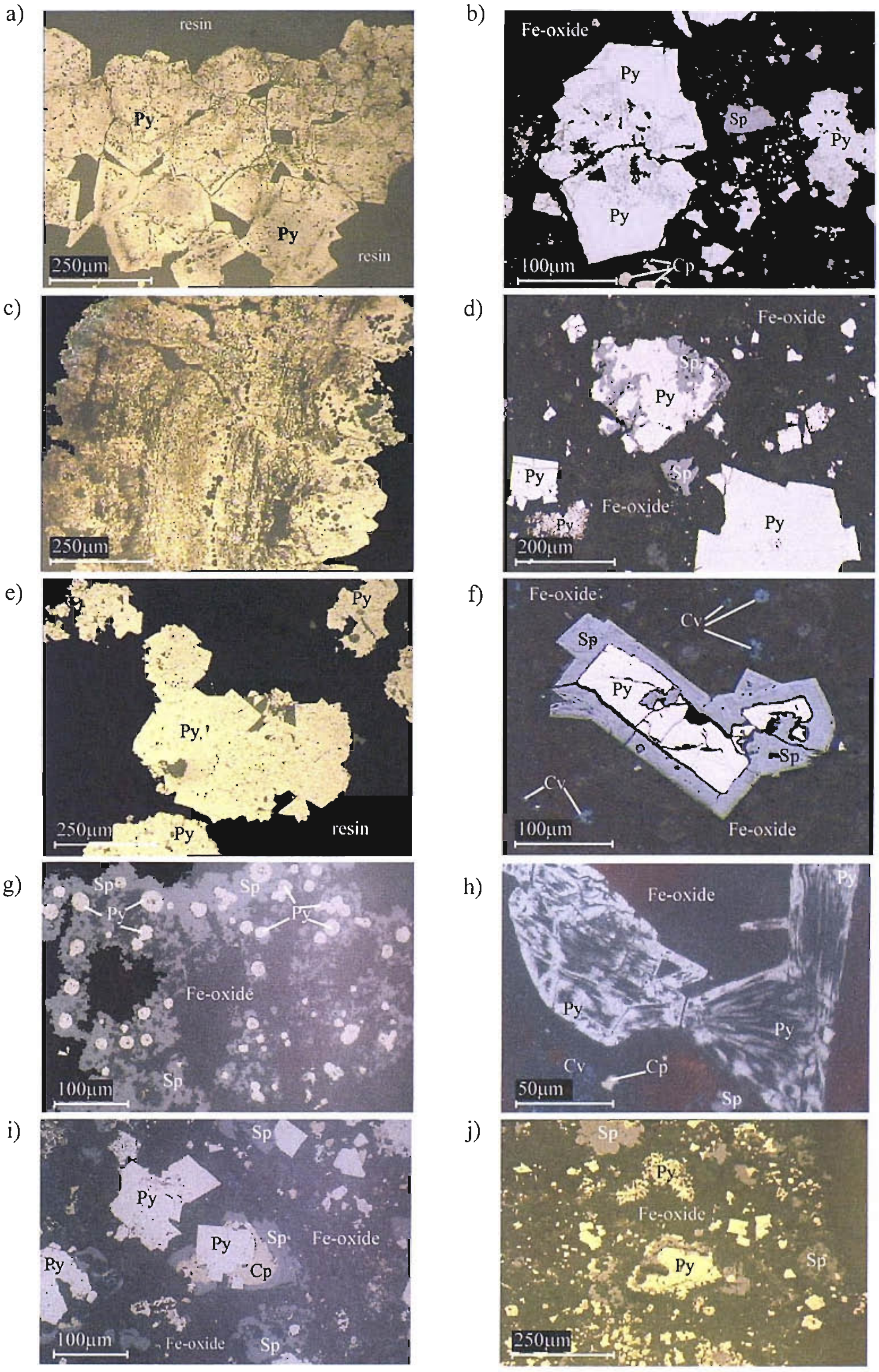

Figure 4.9: Photomicrographs in reflected light of the textures and mineralogical associations of primary pyrite from core 58: a) Aggregate of porous euhedral pyrite cubes; **b)** Subhedral fractured pyrite grain with corrosion pits concentrated along fractures; **c)** Layered, porous, collomorphic pyrite; **d)** Euhedral pyrite grains. Central grain shows replacement by sphalerite along fractures; **e)** Aggregate of euhedral pyrite cubes; **f)** Elongate pyrite grain overgrown by compositionally zoned sphalerite, within an Fe oxide matrix which contains blebs of covellite; **g)** Spherical, colloform pyrite enclosed in anhedral sphalerite; **h)** Skeletal subhedral pyrite grain within Fe oxide; **i)** Euhedral pyrite cubes. Central pyrite cube is partially overgrown by anhedral chalcopyrite which is itself overgrown by anhedral sphalerite; **j)** Fine and medium grained anhedral primary pyrite, and euhedral secondary pyrite, note that much of the primary pyrite is overgrown or sheathed by anhedral sphalerite.

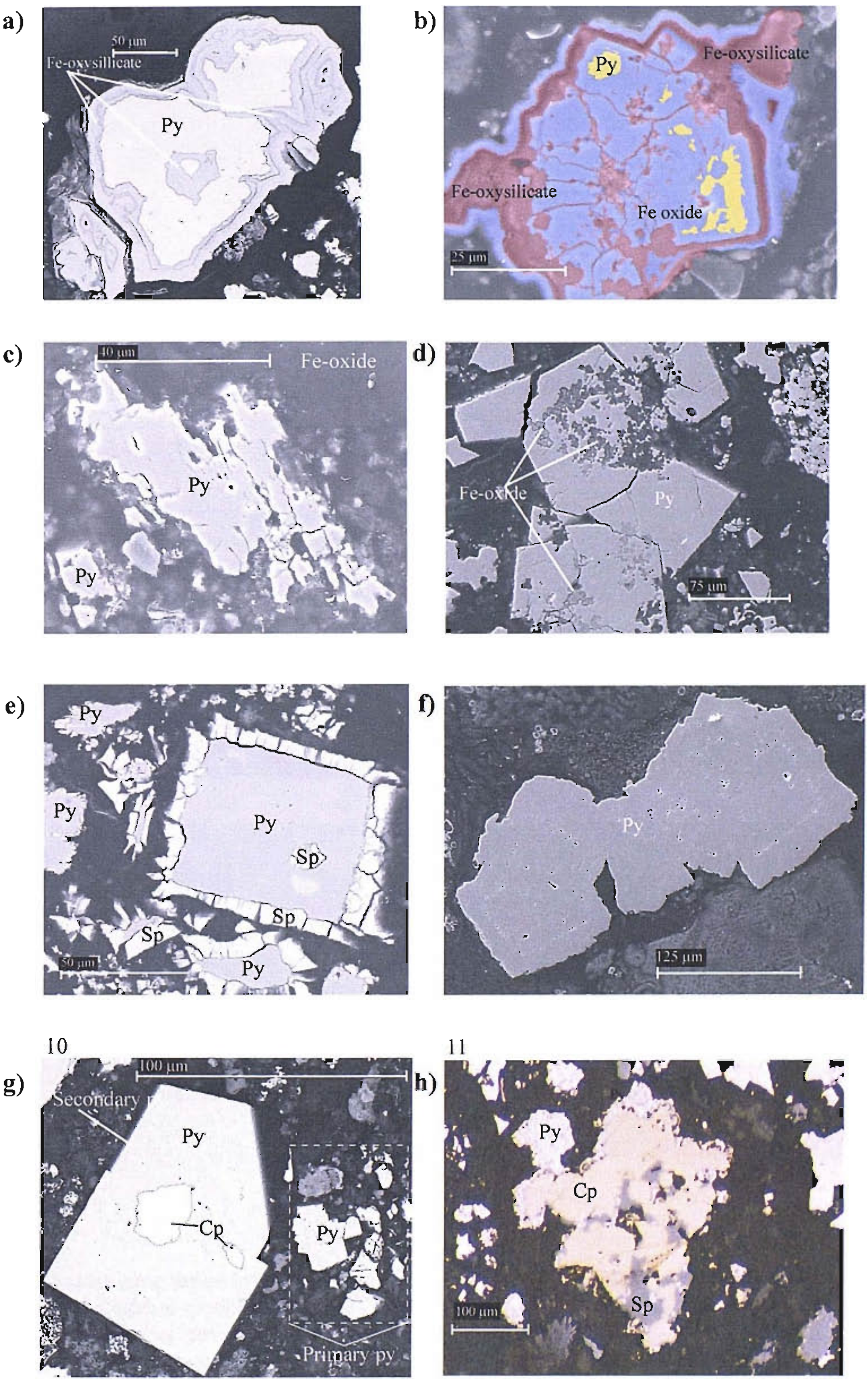

Figure 4.10: Photomicrographs in reflected light (h) and SEM images (a-g) of the textures and mineralogical associations of primary and secondary pyrite from core 58: **a)** Subhedral primary pyrite overgrown by compositionally zoned Fe oxysilicate; **b)** Fe oxide polymorph of fractured pyrite cubes, fractures are cemented by Fe oxysilicate and the polymorph is overgrown by Fe oxysilicate and Fe oxide; **c)** Fractured, subhedral primary pyrite with corroded grain boundaries; **d)** Secondary euhedral pyrite with dissolution pits filled by Fe oxide; **e)** Primary euhedral pyrite with sphalerite overgrowth; **f)** Primary euhedral pyrite overgrown by secondary pyrite; voids mark extent of primary pyrite grains; **g)** Euhedral secondary pyrite cube with core of primary chalcopyrite; fractures subhedral primary pyrite; **h)** Primary anhedral chalcopyrite overgrown by collomorphic secondary pyrite.

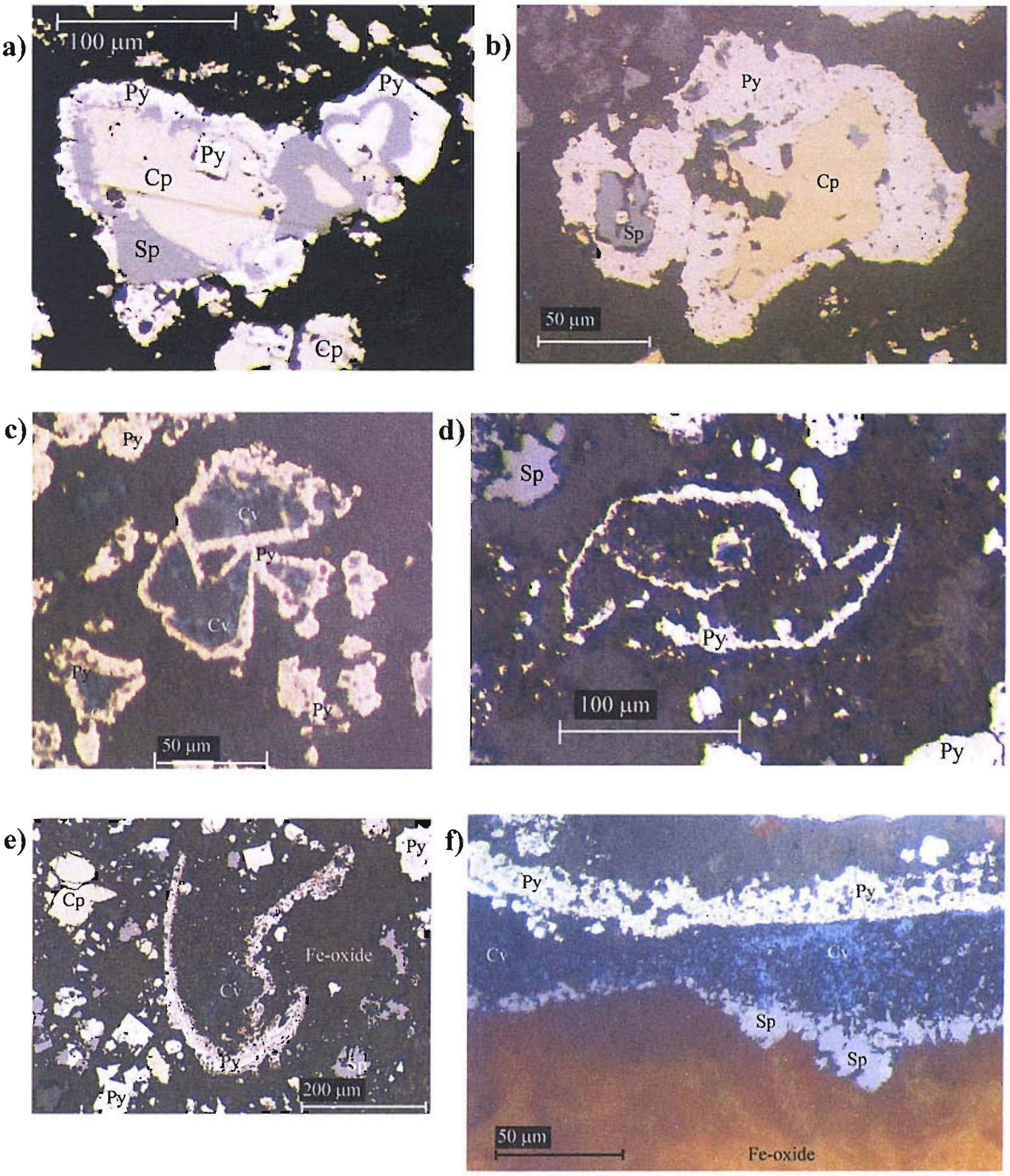

Figure 4.11: Photomicrographs in reflected light of primary and secondary pyrite from core 58: **a)** Collomorphic and euhedral secondary pyrite overgrowing sphalerite which is itself overgrowing chalcopyrite; **b)** Anhedral chalcopyrite and sphalerite encased by sub-euhedral secondary pyrite aggregates; **c)** Extremely porous, subhedral covellite polymorph of primary chalcopyrite containing blebs of relict chalcopyrite, overgrown by rim of secondary pyrite; **d)** Randomly oriented primary collomorphic pyrite crusts; **e)** Randomly oriented collomorphic primary pyrite crust; euhedral secondary pyrite cubes; fractured subhedral chalcopyrite; **f)** Layers of secondary collomorphic pyrite, covellite and sphalerite forming sulphide crust parallel to bedding at the base of the laminated section of the sulphide layer of core 58.

(Figure 4.15c &f) and chalcopyrite (Figure 4.12g). In rare cases secondary pyrite is overgrown by anhedral covellite or subsequent generations of pyrite and sphalerite (Figure 4.15e).

Although primary pyrite crusts have been reworked during sediment transport, and are randomly oriented, crusts of secondary, collomorphic pyrite occur sub-horizontally, parallel to, and between, the alternating layers of sulphide-rich and Fe-oxide-rich material in the top 10cm of the sulphidic layer (Figure 4.11f). The location of these secondary crusts reflects changing redox conditions between sulphide-rich and oxide-rich laminae and/or changes in effective porosity and/or mixing of evolved fluids from above and below the laminated section. The proportion of secondary to primary pyrite increases downcore in the laminated upper 10cm of the sulphide layer. A corresponding coarsening of pyrite grainsize downcore reflects this increase in secondary pyrite. The textures and mineralogical associations of primary and secondary pyrite observed indicate multiple stages of replacement, dissolution, overgrowth and re-precipitation. Figures 4.10 and 4.11 show photomicrograph and SEM images of secondary pyrite textures and mineralogical associations in Core 58.

X-ray microprobe analyses of random pyrite grains showed rare occurrences of arseno-pyrite inclusions and uranium enrichments (for detail the reader is referred to Chapter 6)

4.3.1.2 *Chalcopyrite, $CuFeS_2$*

Chalcopyrite occurrence downcore is considerably more variable than pyrite, where present, constituting only 5 to 20% of the sample, the majority of which is paragenetically early. Most of the chalcopyrite is concentrated in the top 10cm of the sulphidic layer with occurrence becoming increasing sporadic downcore. This observed decrease downcore in the abundance of chalcopyrite corresponds with a downcore increase in the abundance of sphalerite. The change in the abundances of chalcopyrite and sphalerite correspond well with downcore variation in bulk sediment Cu and Zn contents; at the top of the laminated section, Cu accounts for ~12wt% of the bulk sediment; however, Cu contents decrease downcore to ~1.7wt% at the base of the laminated section. In contrast, Zn contents are relatively low at the top of the laminated section accounting for only ~2.7wt% of the bulk sediment increasing to ~14.7wt% at the base of the laminated section (Chapter 3). This suggests that either a) some degree of zone refining, resulting in the separation of Cu and Zn, is taking place during alteration within the sediment, or b) that the laminated section is sourced from higher temperature chalcopyrite-rich mound material and sulphidic material below the laminated section is derived from sphalerite-rich, lower temperature white smoker type material, this is discussed fully in Section 4.4.1.

In general, chalcopyrite occurs as sub-anhedral, medium-grained crystals (Figure 4.12 a-e & h-k), but is also visible as rare sub-euhedral singular grains and aggregates (Figure 4.12f & g; Figure 4.13a & f); these are typically secondary and in many cases indicate co-precipitation with secondary pyrite. In rare cases chalcopyrite is observed as an overgrowth on primary pyrite cubes (Figure 4.12k). All primary chalcopyrite grains show evidence of alteration, this is most frequently seen as corrosion of grain boundaries, dissolution pitting, and replacement by porous covellite (Figure 4.12; 4.13; Figure 4.14b & d). Chalcopyrite grains are frequently seen with covellite rims or with fractures cemented by covellite (Figure 4.12a-e). In addition, replacement by sphalerite and pyrite is relatively common and is observed as partial replacement of, and overgrowth rims on, some chalcopyrite grains (Figure 4.10h; Figure 4.12c, I & j) and as secondary pyrite and sphalerite grains with cores of chalcopyrite (Figure 4.10g). Figure 4.12 shows photomicrographs and Figure 4.13 shows SEM images of chalcopyrite textures and mineralogical associations in Core 58.

4.3.1.3 *Covellite, CuS*

Covellite is not part of the primary mineral assemblage and is the product of chalcopyrite alteration. Although covellite is observed throughout the sulphidic layer of this core, like chalcopyrite, it is most abundant in the upper 10cm of the core and is particularly concentrated at depths downcore of 81-87cm. Covellite most typically occurs as anhedral, extremely porous replacement of chalcopyrite (Figure 4.12d; Figure 4.14b), but is also observed as collomorphic crusts (Figure 4.14a, d, e), planar bands commonly spatially related to sphalerite and pyrite bands as stacked mono-mineralic layers parallel to laminae (Figure 4.11f), as fracture fill and interstitial cement of both sulphides and Fe-oxide (Figure 4.14b & f), and as overgrowth rims around chalcopyrite and some pyrite grains (Figure 4.12a, b & d). In rare cases, covellite itself is overgrown by rims of late pyrite or sphalerite (Figure 4.11c; Figure 4.12c; Figure 4.14c &e). Figure 4.14 shows photomicrographs of covellite textures and mineralogical associations in Core 58.

4.3.1.4 *Sphalerite, ZnS*

Sphalerite is predominantly associated with the secondary mineral assemblage although some an-subhedral primary sphalerite remains. Sphalerite is commonly coarse-grained and subhedral (Figure 4.15a-f), although some rare euhedral examples are visible. The Fe content is variable and typically low with many grains compositionally zoned. In transmitted polarized light sphalerite is translucent with zones of yellowish brown (Fe-poor) and opaque dark brown (Fe-rich) (Figure 4.15a), this is consistent with precipitation in disequilibrium conditions (e.g. (Knott et al., 1998)). Sphalerite occurs both as pristine, unaltered grains (Figure 4.12j; Figure 4.14e; Figure 415b & f) and porous fractured grains (Figure 4.15c, d & e). Pristine sphalerite is generally paragenetically late and is often co-precipitated with pristine secondary pyrite. Anhedral, porous and fractured sphalerite replaces, and frequently contains inclusions of, primary pyrite and chalcopyrite (Figure 4.9f, g, & i; Figure 4.10e; Figure 4.12i). Replacement of other sulphide phases by sphalerite occurs along grain boundaries, fractures and in areas of high porosity (Figure 4.9d & g; Figure 4.13c). Pristine pyrite and chalcopyrite grains which have low to zero porosity tend to be overgrown rather than replaced by sphalerite (Figure 4.9f; Figure 4.10e). Replacement and overgrowth of sphalerite by late pyrite is also evident (Figure 4.11a & b; Figure 4.15b). Figure 4.15 shows photomicrograph images of sphalerite textures and mineralogical associations in Core 58

4.3.1.5 *Non-sulphide phases*

Goethite (FeO(OH)) is the dominant hydrated Fe-oxide phase and is also the principal non-sulphide phase. It is seen in transmitted polarized light as reddish-yellow amorphous and collomorphic masses (Chapter 3; Figure 3.13). It is also seen as zoned collomorphic rims around sulphide grains, as filamentous overgrowths at pyrite grain boundaries, as a replacement of pyrite and as filamentous meshes and clasts of layered filamentous masses cemented by silica. Hematite (Fe_2O_3) occurs as a minor phase and is seen almost exclusively as filamentous masses (Goethite and hematite filamentous material is discussed in detail in

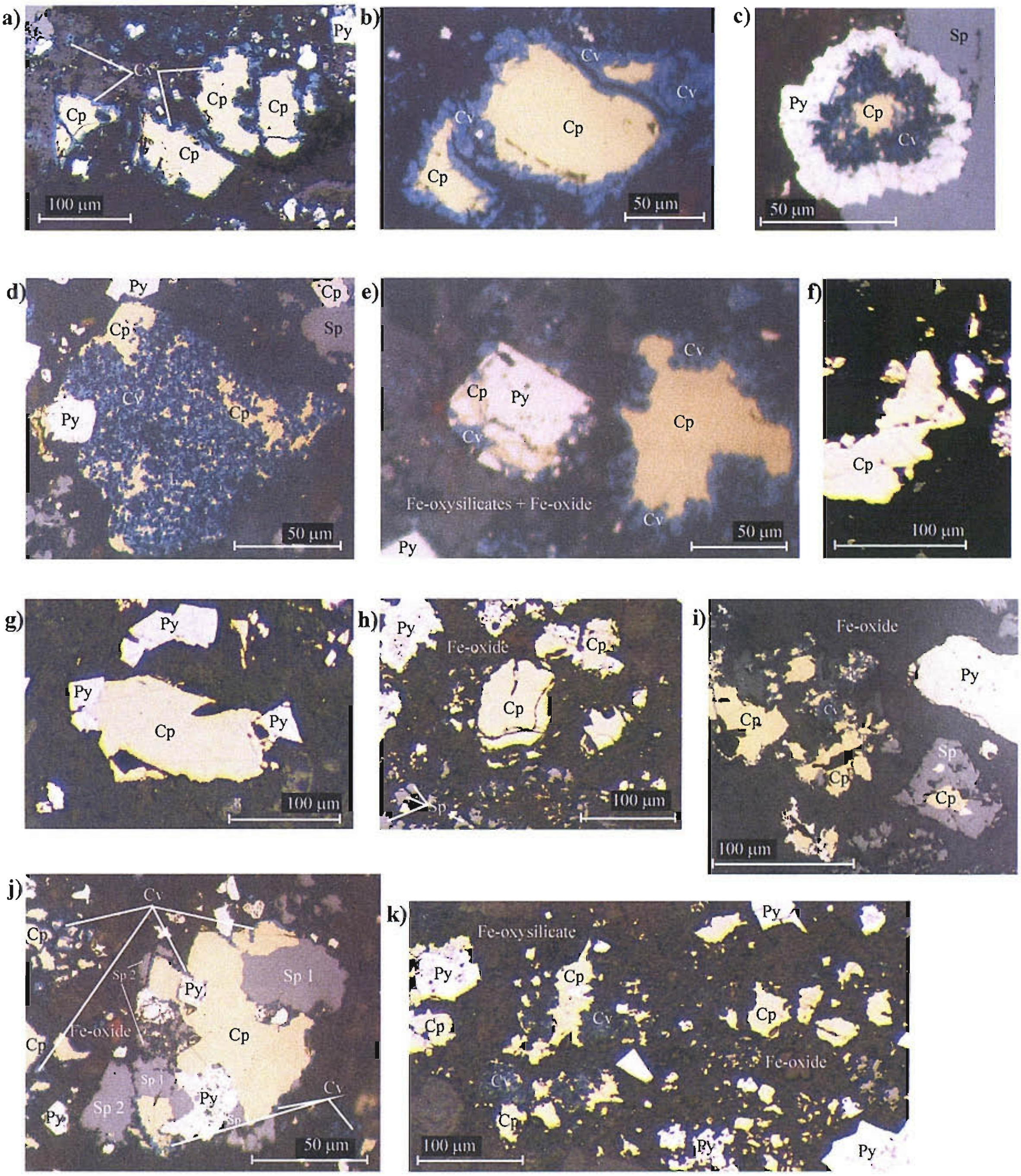

Figure 4.12: Photomicrographs in reflected light of chalco pyrite textures and mineralogical associations from core 58: **a)** Anhedral chalcopyrite with corroded grain boundaries overgrown by covellite; **b)** Anhedral chalcopyrite undergoing replacement to covellite at grain boundaries; **c)** Porous covellite replacing anhedral chalcopyrite, central core of chalcopyrite remains. The covellite is then itself being overgrown by a circular aggregate of euhedral pyrite; **d)** Sub-euhedral porous covellite polymorph of chalcopyrite, note that replacement is incomplete with relict chalcopyrite remaining; **e)** Fractured euhedral primary pyrite cemented by chalcopyrite and rimmed by covellite; covellite replacing chalcopyrite at grain boundaries; **f)** Aggregate of pristine euhedral secondary chalcopyrite; **g)** Secondary , pristine, chalcopyrite with co-precipitated euhedral pyrite; **h)** Subhedral fracture chalcopyrite; **i)** sub-anhedral chalcopyrite with co-precipitated sub-anhedral sphalerite, some alteration of chalcopyrite to covellite is evident along fractures; **j)** Co-precipitated chalcopyrite, primary sphalerite (Sp 1) and pyrite in centre of view. Some alteration of chalcopyrite to covellite is evident at grain boundaries as are overgrowths of secondary sphalerite (Sp 2); **k)** Anhedral chalcopyrite with corroded grain boundaries; euhedral secondary pyrite cubes; primary pitted pyrite cubes with overgrowths of secondary chalcopyrite; fine grained covellite associated with chalcopyrite alteration.

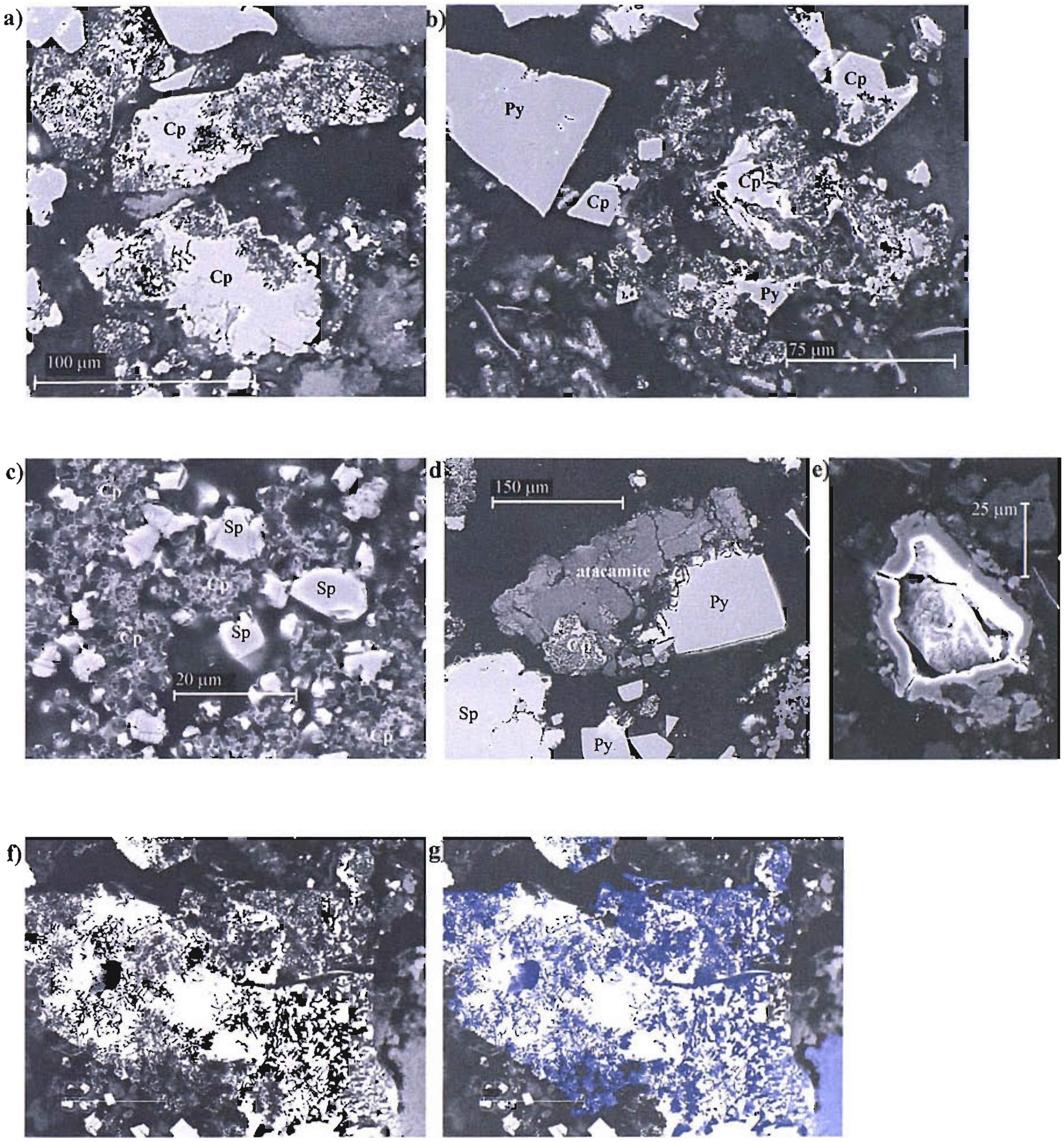

Figure 4.13: SEM images (a, b, d, f & g secondary images: c & e backscatter images of chalcopyrite textures and mineralogical associations from core 58: **a)** Subhedral chalcopyrite showing replacement to porous covellite; **b)** Euhedral chalcopyrite showing onset of covellite replacement; near complete replacement of anhedral chalcopyrite by porous covellite; **c)** Honeycomb textured, porous chalcopyrite with inclusions of sub-anhedral sphalerite, some of which have corroded grain boundaries; **d)** Euhedral pyrite and subhedral chalcopyrite overgrown by an atacamite crust; **e)** Subhedral relatively unaltered chalcopyrite grain encased in Fe oxysilicate; **f)** Subhedral chalcopyrite undergoing replacement to covellite; **g)** Same view as (f) showing covellite highlighted in blue demonstrating the dendritic, tunnel-like style of the covellite replacement.

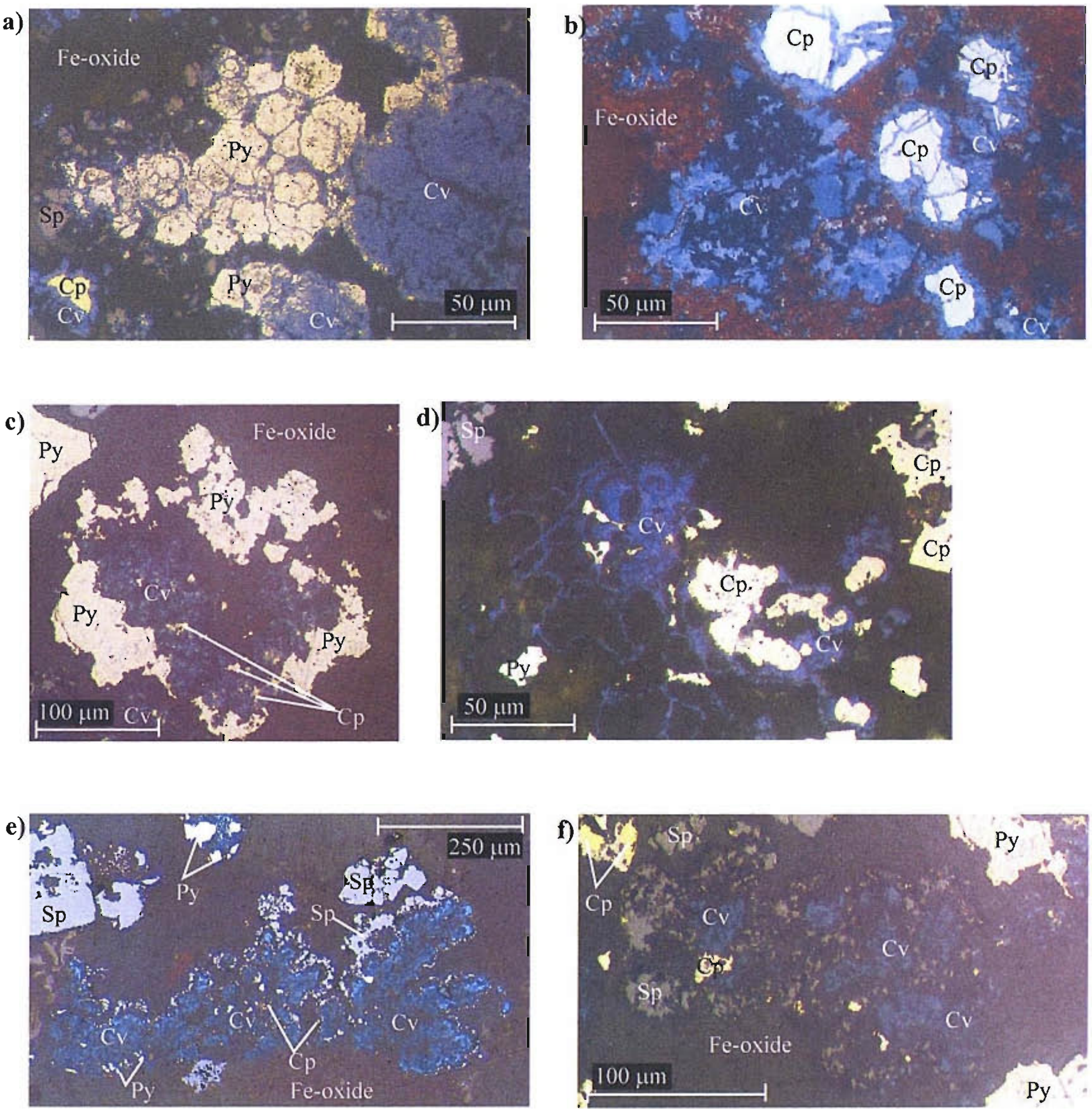

Figure 4.14: Photomicrographs in reflected light (unless otherwise stated) of covellite textures and mineralogical associations from core 58: **a)** Radial porous, collomorphic pyrite replaced and cemented by covellite; **b)** (reflected and transmitted light) Anhedral chalcopyrite partially replaced and cemented by covellite within an Fe oxide matrix; **c)** Near complete replacement of chalcopyrite by porous covellite (note relict inclusions of chalcopyrite), the porous covellite is overgrown by subhedral secondary pyrite; **d)** Anhedral chalcopyrite with corroded grain boundaries, overgrown by covellite; fractures in Fe oxide and chalcopyrite cemented by covellite; collomorphic covellite with relict chalcopyrite inclusions; **e)** (reflected and transmitted light) Dendritic, collomorphic, layer of covellite containing very fine-grained relict chalcopyrite and pyrite inclusions overgrown by layer of porous fractured sphalerite; **f)** porous covellite overgrown by porous sphalerite, note that the covellite conatains some relict chalcopyrite inclusions.

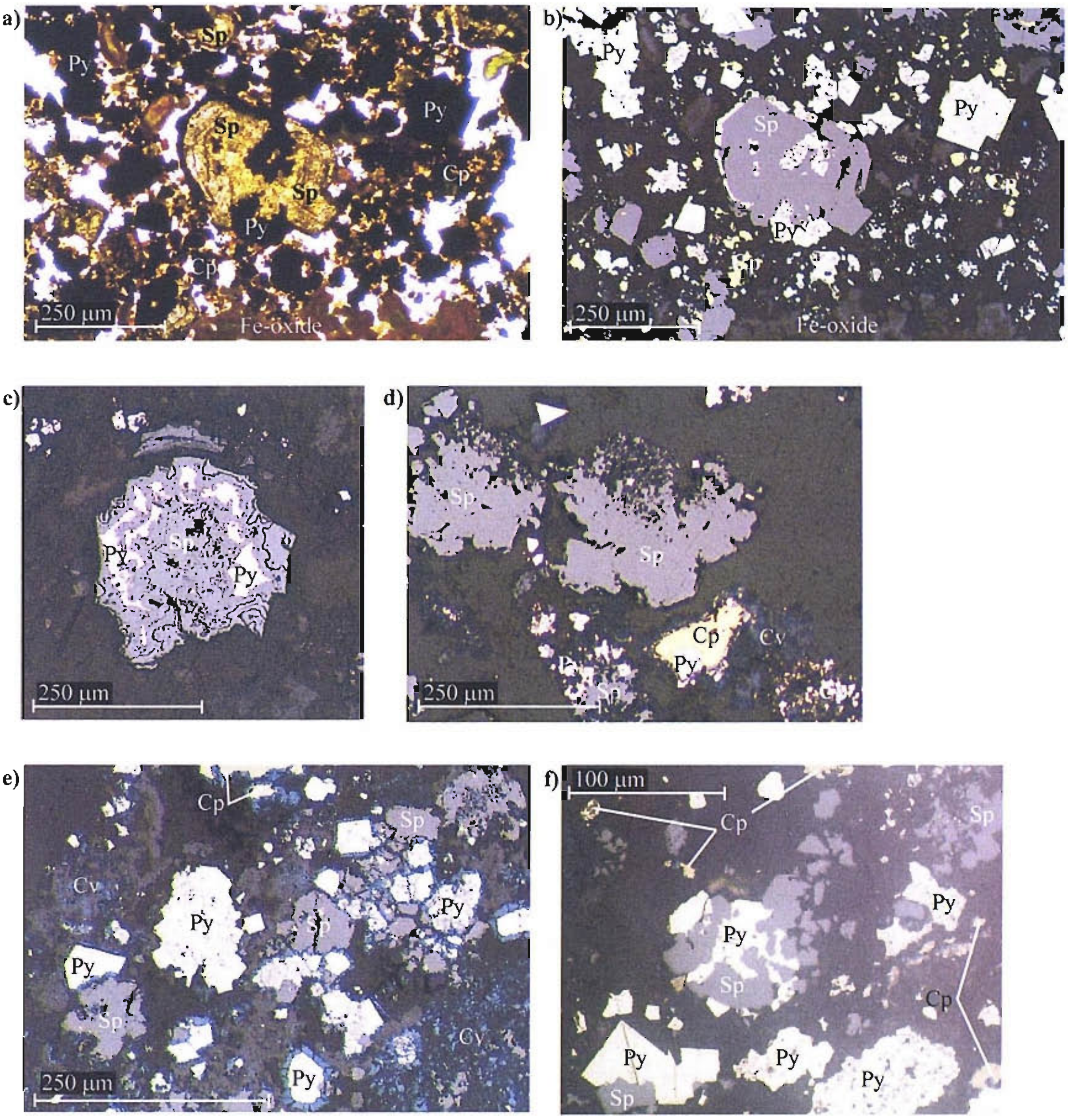

Figure 4.15: Photomicrographs in reflected light (unless otherwise stated) of sphalerite textures and mineralogical associations from core 58: **a)** (transmitted light) Fe poor sphalerite showing compositional zoning, dark brown areas >Fe content than amber areas; **b)** same field of view as (a) (reflected light) Fe poor sphalerite containing pyrite inclusions and overgrown by a rim of collomorphic pyrite; **c)** Secondary, zoned, anhedral sphalerite with co-precipitated pyrite inlcusions; **d)** Subhedral sphalerite with variable porosity; co-precipitated chalcopyrite and pyrite overgrown by covellite; **e)** Fractured, subhedral sphalerite intergrown with fractured pyrite, in some cases the fractures are cemented by covellite; **f)** Co-precipitated pristine secondary pyrite and sphalerite; porous an-subhedral primary pyrite not associated with sphalerite.

Chapter 6). The bulk geochemistry indicates that the presence of goethite and hematite in the sulphidic layer is principally the result of Fe-sulphide oxidation with some precipitation from low temperature Fe-Si-rich fluids and only minor contributions from plume fallout (Chapter 3).

Quartz (SiO_2) and amorphous silica are commonly contaminated by Fe-oxide and oxyhydroxide phases and are present as interstitial cement, suggesting in situ precipitation, and amorphous masses which are interlayered with goethite and Fe-oxysilicates in the upper 10cm of the sulphidic layer. Since seawater is undersaturated with respect to Si the presence of authigenic Si phases suggests circulation of evolved silica rich fluids within the sediment pile, resulting from conductive cooling of mixtures of hydrothermal fluid and seawater. Surficial silica occurrence at the TAG mound is inferred to be a result of percolation of Fe-Si low temperature hydrothermal fluids across the mound (e.g. Tivey et al., 1995; Humphris et al., 1995). Furthermore, authigenic precipitation of Si from low temperature Fe-Si-rich fluids has been invoked for an adjacent core (CD102/43) (Severmann, 2000; Severmann et al., 2004) and for similar sediments from other hydrothermal sites (e.g. Alt, 1988b; Hannington and Jonasson, 1992).

Atacamite ($Cu_2Cl(OH)_3$) and paratacamite (a polymorph of atacamite) are secondary Cu phases and their occurrence mirrors the distribution of chalcopyrite and covellite. They are seen in transmitted light as light pea green to brilliant emerald green, translucent, collomorphic and amorphous masses which are oriented parallel to bedding. These textures are very similar to those reported for atacamite from the surface of the active TAG mound (Hannington, 1993). The morphology and orientation of atacamite and paratacamite parallel to laminae suggests that they were precipitated in situ and not transported during mass wasting. The juxtaposition of oxidised and reduced Fe phases and atacamite at several depths in the top 10cm of the sulphidic layer indicates variations in redox and pH conditions between each laminae.

Gypsum ($CaSO_4.2H_2O$) is the dominant sulphate mineral, it occurs as medium to coarse-grained euhedral crystals with abundant Fe-oxide/oxyhydroxide and pyrite inclusions. The included Fe-oxides and oxyhydroxides have filamentous morphologies; the included pyrite is typically euhedral. Gypsum crystals are a relatively late feature and frequently cross cut silica and goethite layers and clasts (see Chapter 6: Fe-oxidation and biomineralisation).

X-ray microprobe analyses (spot size 2-3μm) reveal the presence of a trace phase composed of Fe, S and O, suggesting a hydrated Fe-sulphate which, in addition to Fe-oxide and goethite, is observed infilling dissolution pits in pyrite grains.

Clay minerals are a minor phase constituting on average only 6.8% of a bulk sample. XRD analyses of clay separations (Chapter 3: Table 3.4) indicate that the clays in the sulphidic layer are almost exclusively smectite with trace amounts of illite. The deep green colour of the clay separates implies a large Fe(II) component. This, and the low Al content, typically <0.5wt% of the bulk sediment, suggest that these clays are unlikely to be detrital in origin and maybe low temperature hydrothermal nontronites ($NaFe_2(Si, Al)_4O_{10}(OH)_2.H_2O$). This is in agreement with published clay mineralogy for the *Alvin* zone (e.g. Severmann et al., 2004).

4.3.2 The *Mir* core (CD102/60)

4.3.2.1 *Pyrite, FeS_2*

Pyrite is the dominant sulphide phase, it is ubiquitous throughout the sulphide layer and locally constitutes up to 75% of a sample. Primary pyrite is most commonly seen as aggregates (Figure 4.16b & d; Figure 4.17e), and individual, medium-grained, euhedral, cubic crystals (Figure 4.17d and g). It also occurs as collomorphic bands typically 30μm thick (Figure 4.16 g & i) and as bands of euhedral cubes typically 200μm thick (Figure 4.16h), and as fine grained disseminated pyrite within the silica cement. In addition spherical pyrite grains with moderate porosity and radial fractures are visible (Figure 4.16f). The onset of silica replacement at grain boundaries, along fractures and within porosity is evident in these spherical pyrites. For some grains, the initial growth is porous and collomorphic, these grains are typically overgrown by later precipitation of secondary euhedral pyrite (Figure 4.17b). Co-precipitation of primary pyrite with primary chalcopyrite is also evident (Figure 4.16a). In rare cases primary pyrite is overgrown by rims of anhedral sphalerite (Figure 4.17j). More commonly anhedral sphalerite is seen replacing primary pyrite along fractures or in areas of high porosity.

Secondary pyrite is visible as pristine or lightly fractured medium-coarse grained euhedral crystals and aggregates (Figure 4.17a & c). It is frequently observed as overgrowths on primary chalcopyrite (Figure 4.17f & g). In contrast to primary pyrite, the grain boundaries of secondary pyrite are sharp and show no signs of corrosion or replacement by sphalerite or silica phases.

4.3.2.2 *Chalcopyrite, $CuFeS_2$*

Chalcopyrite is a primary mineral phase and is not part of the secondary mineral assemblage. Occurrence is variable but typically, where present, it constitutes approximately 15–20% of a sample. Chalcopyrite is principally coarse-grained (~0.25 to 1.5mm), commonly anhedral and moderately fractured (Figure 4.16a, b &c; Figure 4.17d, e, f & g) but is also seen as disseminated fine-grained crystals within the silica cement (Figure 4.16h & i). In the upper 30cm of the sulphide layer chalcopyrite is frequently overgrown by collomorphic silica phases and co-precipitated with primary pyrite (Figure 4.16a & c). In the lower 20cm of the sulphide layer, chalcopyrite grain boundaries show alteration to covellite and/or secondary pyrite overgrowths (Figure 4.17d,e,f & g). An increase in Cuwt% downcore from ~4.5- ~12wt% in the basal 20cm of the sulphide layer is related to covellite occurrence and indicates enrichment of Cu as chalcopyrite alters to covellite (Chapter 3)

4.3.2.3 *Covellite, CuS*

Covellite is a trace phase associated only with the secondary mineral assemblage. It is seen exclusively as alteration rims on chalcopyrite in the lower half of the sulphide layer and is absent in the top 30cm (Figure 4.17d, e, f & g).

4.3.2.4 *Sphalerite, ZnS*

Sphalerite is also solely associated with the secondary mineral assemblage. Whilst rare occurrences are visible in the upper 30cm of the sulphide layer, sphalerite is most commonly observed in the lower 20cm. It

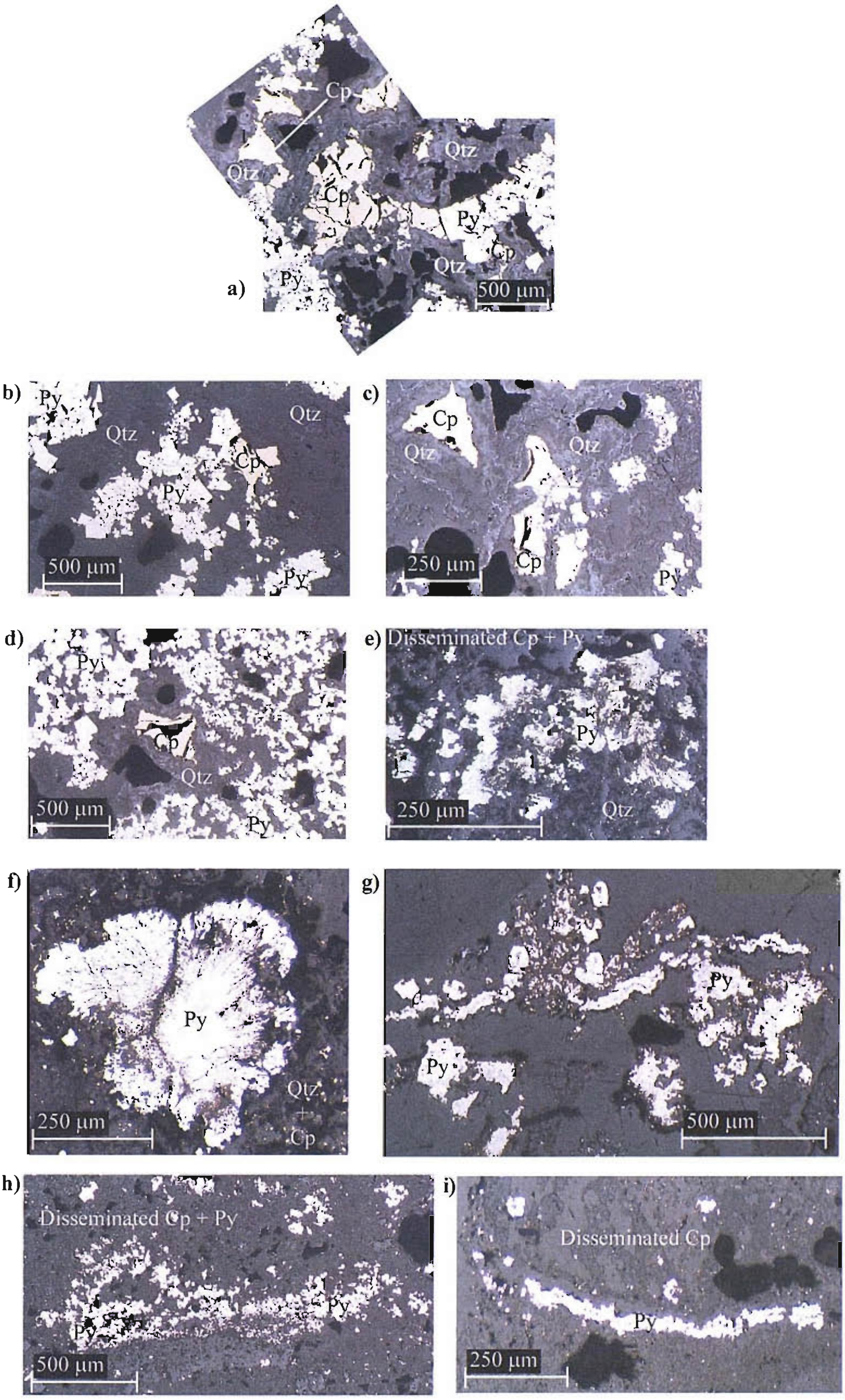

Figure 4.16: Photomicrographs in reflected light textures and mineralogical associations from core 60: **a)** Coarse-grained, primary, fractured anhedral chalcopyrite co-precipitated with coarse-grained primary porous euhedral pyrite. Both chalcopyrite and pyrite are cemented by collomorphic quartz; **b)** Medium-grained anhedral primary chalcopyrite and euhedral primary pyrite cemented by quartz; **c)** Medium-grained, anhedral primary chalcopyrite with euhedral primary pyrite. Chalcopyrite is ovegrown by banded collomorphic quartz cement; **d)** Medium-fine-grained euhedral primary pyrite with anhedral fractured chalcopyrite, both cemented by quartz; **e)** Dendritic, porous pyrite cemented by quartz containing fine-grained disseminated pyrite and chalcopyrite; **f)** Fractured spherical pyrite with radially oriented fractures and porosity voids, within quartz cement conatining fine-grained disseminated chalcopyrite; **g)** Collomorphic banded pyrite and anhedral porous pyrite within quartz cement; **h)** Band of fine-grained euhedral pyrite within quartz cement which contains fine-grained disseminated chalcopyrite and pyrite; **i)** Band of collomorphic pyrite and anhedral porous pyrite cemented by quartz containing fine-grained disseminated chalcopyrite.

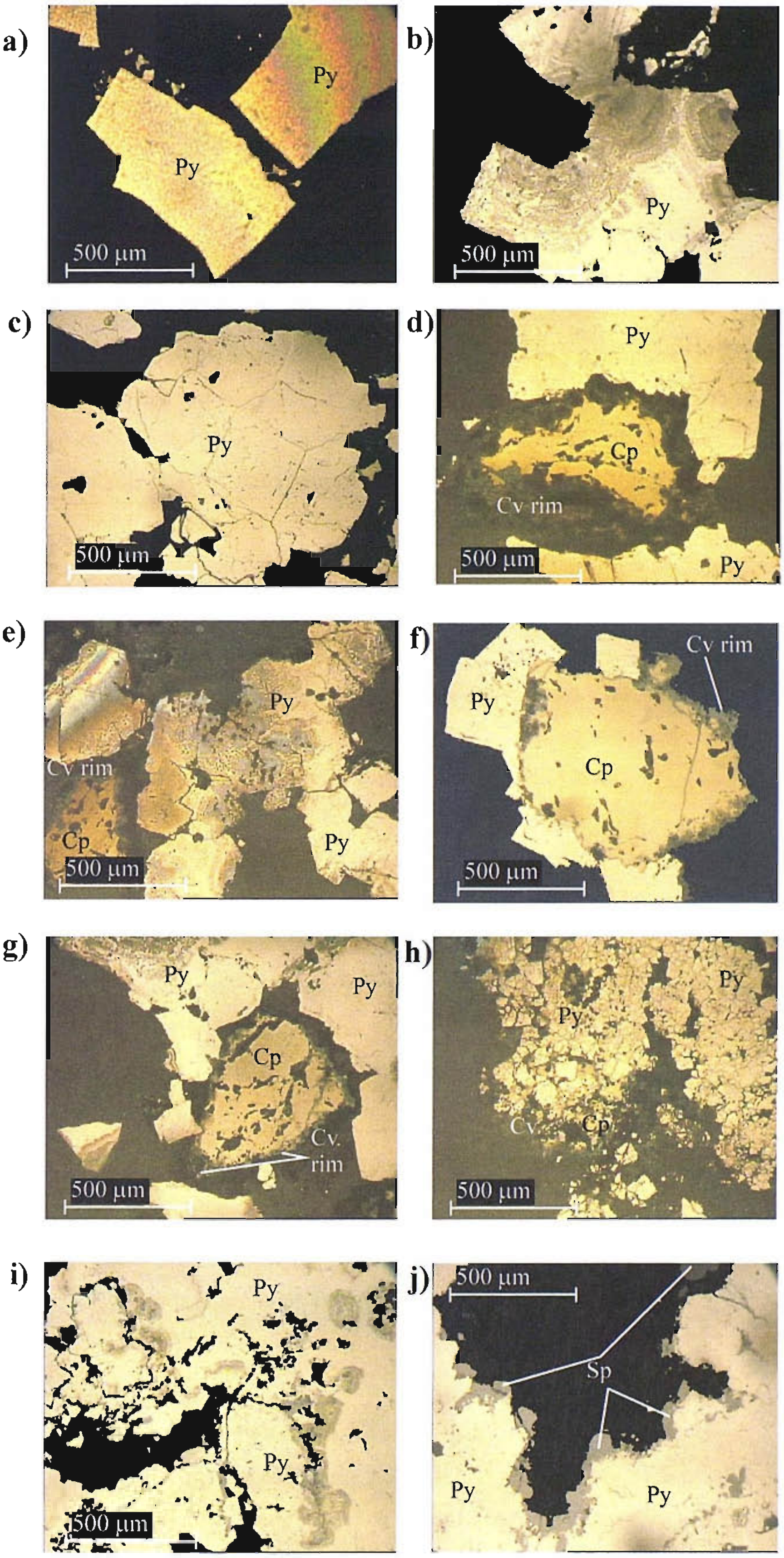

Figure 4.17: Photomicrographs in reflected light textures and mineralogical associations from core 60: **a)** Euhedral coarse-grained, secondary pyrite; **b)** Primary collomorphic pyrite overgrown by coarse-grained euhedral secondary pyrite; **c)** Fractured aggregate of sub-euhedral secondary pyrite; **d)** Anhedral, fractured coarse-grained primary chalcopyrite showing evidence of alteration to covellite at grain boundaries and overgrown by euhedral secondary pyrite; **e)** Anhedral, coarse-grained primary chalcopyrite showing evidence of alteration to covellite at grain boundaries; collomorphic primary pyrite; **f)** Coarse-grained aggregate of subhedral chalcopyrite showing evidence of alteration to covellite at grain boundaries and overgrown by sub-euhedral secondary pyrite; **g)** Fine-medium-grained fractured aggregate of euhedral secondary pyrite overgrowing and replacing anhedral chalcopyrite. Anhedral chalcopyrite also shows evidence of altertion to covellite at grain boudaries not enclosed by pyrite; **h)** Bands of primary, porous, collomorphic pyrite overgrown by subhedral, coarse-grained secondary pyrite; **i)** Subhedral, coarse-grained primary pyrite overgrown by a rim of anhedral sphalerite. Primary pyrite also contains inclusions of sphalerite along fractures and as porosity fill.

occurs as an-subhedral rims and as replacements and overgrowths along fractures and within pore spaces of primary pyrite grains (Figure 4.17j).

4.3.2.5 *Non-sulphide phases*

Quartz and cristobalite (a quartz polymorph identified from XRD scans of bulk sediment: (Chapter 3)) are the principal non-sulphide phases. They are commonly seen as collomorphic, vuggy amorphous masses, rims on primary pyrite and chalcopyrite crystals and as interstitial cement containing fine-grained disseminated sulphide (Figure 4.16a, c, e, h & i). In the upper 30cm of the sulphidic layer the presence of quartz cement has protected the sulphides from oxidative decay. This cemented upper portion of the sulphide layer is similar to the pyrite-silica breccias described from the ODP drilling of the active TAG mound (Chapter 2). The abundance of quartz and cristobalite decreases downcore but locally constitutes as much as 50% of a sample in the uppermost part of the sulphide layer.

Goethite is the dominant hydrated Fe-oxide phase however; it is only reported from the basal 15cm. It is seen as amorphous masses and clasts, fine-grained dustings and crusts on sulphides, compositionally zoned collomorphic bands and as a finely laminated horizon at the base of the sulphide layer.

Atacamite occurs as a trace mineral in the basal 20cm. It appears as collomorphic crusts and bands, often interlayered with collomorphic goethite, and as amorphous clasts disseminated throughout goethite.

Clays are present only at trace levels, constituting on average 3% of a bulk sample. XRD analyses of clay separates (Chapter 3) indicate that smectite is the dominant clay mineral with some chlorite (a product of basalt alteration).

4.4. Discussion: Sulphide paragenesis and alteration

The general paragenetic sequence for sulphides from both the *Alvin* (CD102/58) and *Mir* (CD102/60) cores is: primary pyrite and chalcopyrite, sphalerite, secondary pyrite, covellite, late pyrite and sphalerite. This simple assemblage is typical of sulphide deposits at sediment free mid-ocean ridges (Table 4.1 and references there in).

4.4.1 Sulphide precipitation and alteration in CD102/58: The *Alvin* core

The mineralogical textures and occurrences observed in the sulphide layer of the Core 58 indicate a polyphase hydrothermal history with several cycles of sulphide precipitation, replacement, dissolution and overgrowth, documenting hydrothermal reworking of material from the *Alvin* mound prior to and following mass wasting.

Consideration of metal solubilities suggests that precipitation of the primary sulphide assemblage, of pyrite and chalcopyrite, occurred under high temperature black smoker conditions; precipitation of chalcopyrite from a typical hydrothermal fluid requires temperatures in excess of 250°C (e.g. Haymon, 1983). The observed mineralogical textures are consistent with precipitation from a black smoker fluid. The primary collomorphic pyrite bands observed in this core are consistent with early precipitation from a moderately high temperature fluid between ~250 to 300°C (e.g. Koski et al., 1984; Kase et al., 1990; Duckworth et al., 1994; Knott et al., 1998). These bands insulate and channel fluid flow leading to the precipitation of higher temperature Cu, Fe sulphides. The fine-grained porous aggregates of pyrite with anhedral, locally coarse grained, granular and porous chalcopyrite, which dominate the primary mound derived assemblage, are very similar to textures described for sulphides precipitating into open space at the near surface, under diffuse, high temperature flow close to active chimneys at the TAG mound (e.g. Hannington et al., 1995b; Tivey et al., 1995; Knott et al., 1998).

The secondary mound derived sulphide assemblage of pyrite, sphalerite and minor quartz formed under distinctly different conditions. The change from precipitation of Cu and Fe sulphides to Zn and Fe sulphides and quartz is indicative of modification of the mineralising fluid and a drop in temperature. This suggests precipitation from a conductively cooled, evolved hydrothermal fluid related to mixing and zone refining processes within the *Alvin* mound, this general description could include white smoker fluids. The textural associations of primary chalcopyrite and sphalerite are consistent with precipitation of sphalerite from a later, low temperature fluid. Sphalerite is commonly seen as a replacement of, and overgrowth on primary chalcopyrite, however, there is no evidence here for co-precipitation of these two phases.

The primary and secondary mound sulphides were then transported to near field sediments as a result of mass wasting and slumping events. Sedimentary emplacement of sulphide-rich layers as a result of slumping and mass wasting events is a commonly invoked process in metalliferous sediment cores from the TAG area (e.g. Metz et al., 1988; Mills, 1995; Severmann, 2000). Since the laminated layers are inferred to result from sedimentary processes and not in situ alteration (Chapter 3) the layering of black, graded, sulphide rich beds with orange, Fe-oxide rich beds indicates that the initial oxidation of the mound sulphides occurred prior to mass wasting. Following mass wasting and sedimentary emplacement secondary pyrite, sphalerite and covellite are precipitated. The continued precipitation of sulphide phases within the sediment is facilitated by oxidative dissolution of mound derived sulphides which leads to circulation of metal rich solutions within the sediment and remineralisation from these fluids in response to changes in E_h and pH conditions.

Pervasive low temperature oxidation has affected all parts of the sulphide layer but the continued presence of primary chalcopyrite in the laminated section suggests this is less advanced in the top 10cm; chalcopyrite is a primary phase whose abundance decreases downcore below the laminated section, where the contribution from chalcopyrite alteration products, e.g. atacamite, increases. The alteration of the *Alvin* sulphides is most likely dominated by the oxidation of pyrite to goethite (Equation 1.12). This type of oxidation is well documented in mining and ore processing and may be catalyzed by bacterial interaction. This reaction is consistent with the abundance of goethite in the sulphide layer.

The oxidation of pyrite to goethite produces $2H^+$ for each mole of FeS_2 oxidised. The presence of acidic conditions is important in the remineralisation of primary Cu and Zn phases (Thornber, 1985; Hannington et al., 1988; Tivey et al., 1995). The Cu released during the oxidation of primary chalcopyrite has been re-precipitated as atacamite and paratacamite (a polymorph of atacamite), secondary copper salts. Atacamite commonly occurs as a product of secondary mineralisation in weathered portions of sulphide mounds (e.g.

Emberly et al., 1988; Hannington, 1993). E_h – pH changes and chloride complexing dominate the geochemical behaviour of Cu at low temperatures and Cu^{2+} ions released during the remineralisation of chalcopyrite to pyrite form cuprous chloride complexes such as $CuCl_2^-$ and $CuCl_3^{2-}$ (e.g. Rose, 1976). Where the solutions carrying such chloride complexes are exposed to ambient seawater, basic Cu salts, in this case atacamite and paratacamite, are precipitated (Detrick et al., 1986); Hannington, 1993). Thus the presence of atacamite and paratacamite indicate ingress of ambient seawater into the sediment pile during Cu mobilization.

Free energies of formation for atacamite and paratacamite suggest only trivial differences in the stability fields of the two minerals (Barton and Bethke, 1960). However, Garrels (1986) noted that the rate of crystallization is dependent on the pH of the mineralising solution. Paratacamite is the most likely phase in strongly acidic conditions, whereas atacamite will precipitate in solutions that are more alkaline. The occurrence of both atacamite and paratacamite as elongate bands parallel to bedding in the oxide-rich beds of the upper 10cm of the sulphide layer, suggests diffusion of the alteration fluids carrying Cu vertically through the sediment pile from the sulphide-rich to the oxide-rich layers. This implies steep redox and pH gradients between the: orange, goethite-rich laminae (more oxidizing conditions) and the black, sulphide-rich laminae (more reducing conditions).

The occurrence of atacamite and paratacamite in Core 58 is very similar to the collomorphic masses and crusts of atacamite reported from the TAG mound (Hannington, 1993) and veinlets and fracture fill described from gossanous deposits on the East Pacific Rise (Alt et al., 1987). In both these cases the presence of atacamite has been similarly attributed to the oxidation of Cu sulphides and re-precipitation of the resultant aqueous Cu^{2+} as atacamite on encountering ambient seawater.

Secondary enrichment of Cu is evident from the presence of covellite (covellite contains ~32% more Cu than chalcopyrite). Precipitation of covellite is the result of enrichment processes akin to sub-aerial supergene Cu enrichment and consists of two phases:

1. Oxidative fractionation of Cu from chalcopyrite during remineralisation to pyrite. The Cu^{2+} ions released during remineralisation in the upper 10cm of the sulphide layer migrate downwards in acidic solutions.
2. Where the Cu-bearing solutions encounter reducing conditions in the sulphide-rich laminae at the base of the stripped section covellite is precipitated as a replacement of primary chalcopyrite (Equation 4.6).

Covellite mineralisation as a result of chalcopyrite replacement is clearly seen as overgrowths on chalcopyrite at grain boundaries and along fractures. Covellite has also been precipitated directly from the Cu-bearing solutions. The observed collomorphic masses and the porous band of covellite at the base of the stripped section do not show evidence of a chalcopyrite precursor.

The acidity produced during oxidation of pyrite, which is responsible for the remobilization of Cu, may also result in some degree of separation of Cu and Zn. In contrast to mound derived sphalerite in the upper 10cm of the core which most commonly occurs as individual subhedral pristine crystals showing grading from fine to coarse downcore within individual laminae, indicating precipitation prior to emplacement in sedimentary layers, sphalerite textures below ~90 cm depth downcore typically indicate authigenic precipitation e.g. secondary sphalerite is observed as collomorphic bands, often parallel to bedding, and as interstitial fracture fill. The growth of secondary, authigenic sphalerite maybe accounted for by precipitation from downwelling Zn-rich fluids, sourced from the alteration of mound derived sphalerite at the top of the sulphide layer, and is facilitated by sharp changes in redox and pH as oxidation proceeds. Growth appears to be enhanced by nucleation on pre-existing sulphides and sphalerite overgrowths are typically more coarse-grained than individual sphalerite crystals.

The processes governing dissolution of primary Cu and Zn phases in this core and re-precipitation, particularly the conversion of chalcopyrite to covellite, resemble sub-aerial supergene processes. However, the complex and intimate juxtaposition of contrasting E_h and pH conditions in time and space in Core 58 has resulted in locally important, grain-scale re-mineralisation and secondary enrichment, rather than the much larger scale zones of secondary enrichment observed in sub-aerial deposits (e.g. Hannington et al., 1988; Herzig et al., 1991; Hannington, 1993). The end product of the sulphide alteration processes affecting Core 58 is goethite, the secondary sulphates e.g. jarosite, common in sub-aerial gossans are not present. This because the SO_4^{2-} produced during sub-marine sulphide oxidation is extremely soluble and is dissolved into seawater.

The occurrence of amorphous silica as a cement within the Fe-oxyhydroxide rich laminae in the top 10cm of this sulphide layer suggests that circulation of cooled diffuse hydrothermal fluids, in addition to ambient seawater and acidified pore waters, is sustained following sedimentation. These cooled hydrothermal fluids are likely to be similar to the low temperature, diffuse hydrothermal fluids precipitating Fe-oxide and silica described from the active TAG mound (Mills et al., 1996) and from Red Seamount on the EPR (e.g. Edmond et al., 1979b; Alt et al., 1987).

4.4.2 Generalized paragenetic sequence in CD102/58: The *Alvin* core

The mineralogy and mineral textures of the *Alvin* core sulphide samples suggests two major phases of sulphide precipitation. These sulphides have subsequently undergone alteration and remineralisation due to oxidation and acid leaching:

1. Primary collomorphic pyrite is precipitated under moderately high temperature conditions between 250 to 300°C. This collomorphic pyrite insulates the hydrothermal fluid leading to precipitation of pyrite and chalcopyrite from a high temperature hydrothermal fluid close to an actively venting black smoker at the surface of the mound. The porous texture of primary pyrite and chalcopyrite from the *Alvin* sediment is consistent with the textures described for pyrite and chalcopyrite precipitated recently from diffuse high temperature hydrothermal flow at or near the surface of the TAG mound close to black smoker chimneys (Hannington et al., 1995b; Tivey et al., 1995; Knott et al., 1998).
2. High temperature venting shifts to another area of the mound and lower temperature, Zn-rich fluids circulate in the subsurface. Zone refining takes place and sphalerite is precipitated as Zn is moved to the surface of the mound whilst chalcopyrite is dissolved and the Cu removed to the mound interior. The dissolution of chalcopyrite is incomplete and some of the remaining chalcopyrite is transported to the sediments as a minor component. Oxidation of primary sulphides is initiated prior to sedimentary deposition of the Core 58 sulphide layer and results in precipitation of Fe oxyhydroxide phases e.g. goethite.

3. The mound derived sulphides and the oxidized material at the seawater interface are transported to the sediment during a mass wasting event. Sedimentary settling processes result in deposition of alternating oxide-rich and sulphide-rich laminated layers with graded grainsize.
4. Ingress of ambient seawater into, and the variable oxidation state of, the sediment results in the on set of dissolution of mound derived sulphides followed by remineralisation as secondary sulphides, e.g. covellite and sphalerite, or as other metal bearing alteration minerals e.g. goethite and atacamite. Contemporaneous circulation of Fe^{3+}-Si-rich, diffuse low temperature, evolved hydrothermal fluids, similar to diffuse low temperature fluids precipitating Fe oxide and amorphous silica described from the active TAG mound (Mills et al., 1996) and from Red Seamount on the EPR (e.g. Edmond et al., 1979b; Alt et al., 1987), precipitate amorphous silica and Fe-oxyhydroxides in the laminated section of the sulphide layer.

A schematic representation of the general paragenetic sequence is shown in Figure 4.18.

4.4.3 Sulphide precipitation and alteration in CD102/60: The *Mir* core

Alteration and oxidation of the Core 60 sulphide layer is much less pervasive than that evident in Core 58. The upper 30cm of the Core 60 sulphide layer is moderately well cemented by quartz and cristobalite, this cement has restricted fluid flow through the top section limiting oxidation and alteration of sulphide phases. Consequently, in the upper 30cm the primary, high temperature (>250°C (e.g. Haymon, 1983)) mineral assemblage of pyrite and chalcopyrite dominates and no secondary Cu minerals, and only very minor Fe-oxides/oxyhydroxides are observed. The much more poorly consolidated sulphidic material in the lower 20cm of the sulphide layer, in contrast to the upper portion, does show evidence of oxidative alteration and secondary mineralisation. The secondary mineral assemblage is composed of pyrite, sphalerite, covellite, atacamite and goethite.

The most striking feature of the sulphide layer of Core 60 is its resemblance to the pyrite-quartz breccias described from the upper most parts of the hydrothermal stockwork zone in the TAG mound from ODP drilling. Mineral textures and occurrences, with the exception of anhydrite, are virtually identical; comparisons of petrographic features for the TAG pyrite-quartz breccia and the sulphide layer of Core 60 are given in Table 4.3. These similarities suggest that the processes governing the formation of the Core 60 sulphide layer, prior to mass wasting and sedimentary emplacement, are likely to be comparable to those effecting deposition of pyrite-quartz breccias in the TAG mound at the present.

ODP drilling results indicate that pyrite-quartz breccias develop from modification of pyrite-anhydrite breccias through replacement of the original anhydrite matrix by quartz followed by further sulphide and quartz precipitation (Humphris et al., 1995; Honnorez et al., 1998; Knott et al., 1998). The textures produced are complicated with several generations of pyrite intergrown with quartz (Knott et al., 1998). The pyrite-quartz textures observed in the sulphide layer of Core 60 are consistent with this.

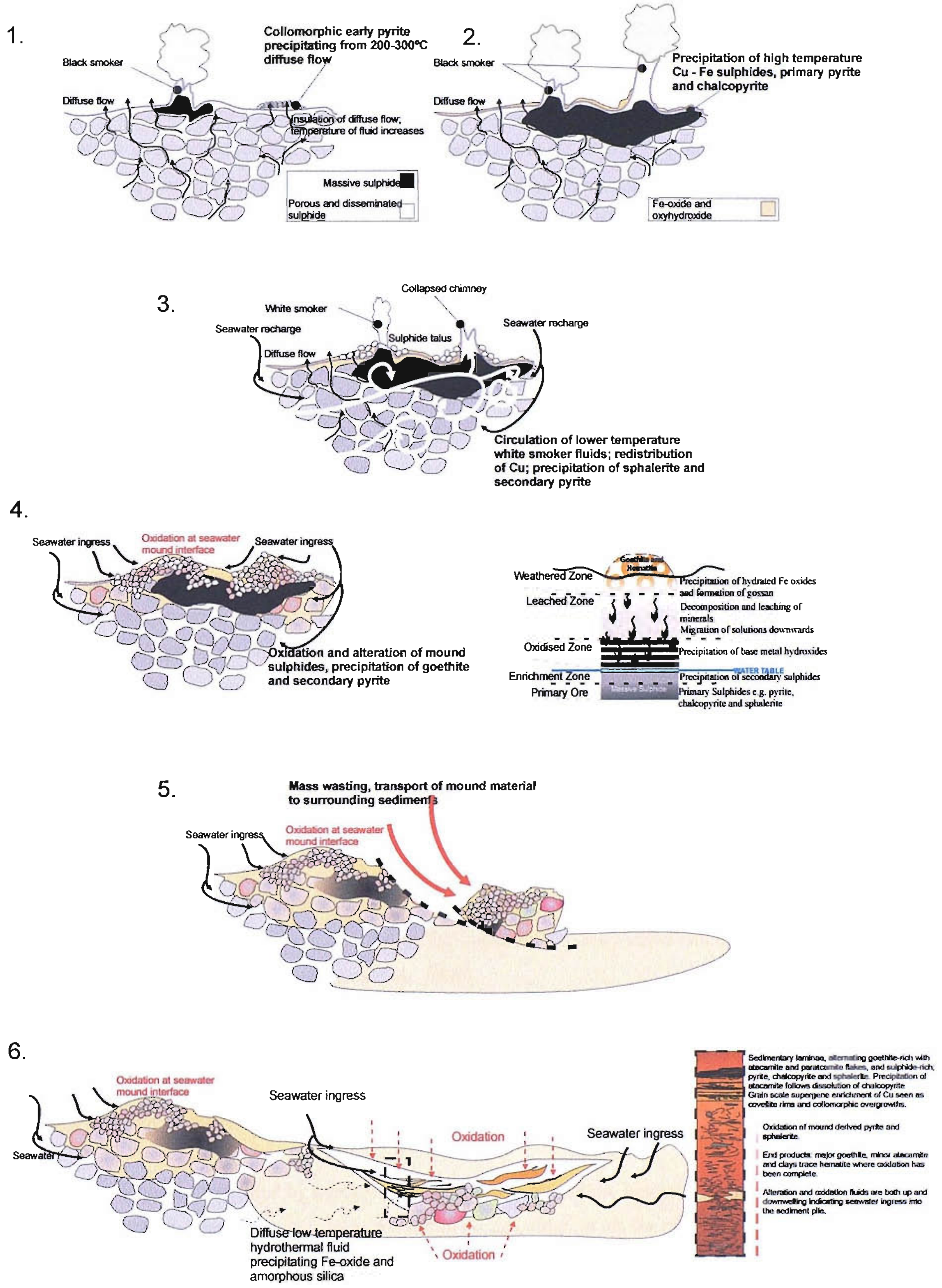

Figure 4.18: Schematic representation of sulphide paragenesis, oxidation and alteration of the *Alvin* core, CD102/58. 1) precipitation of colloform early pyrite crusts; **2)** insulated by pyrite crust high temperature precipitation of chalcopyrite and pyrite commences; **3)** high temperatrure activity switches to another area of the *Alvin* mound and lower temperature fluids circulate precipitating sphalerite, pyrite and quartz, and redistributing copper minerals; **4)** Oxidation at the mound seawater interface and precipitation of Fe-oxides and oxyhydroxides, onset gossanisation, idealistic supergene weathering profile is shown for comparison to sub-aerial supergene weathering processes; **5)** Mass wasting of mound material and transport to the surrounding sediment; **6)** Ingress of seawater and circulation of diffuse low temperature hydrothermal fluids within the sediment; continued oxidation and alteration; remobilization of base metals; precipitation of gossan minerals. **Note diagrams are not to scale.**

Mineralogy	TAG pyrite-quartz breccia	Sulphide layer of *Mir* core, CD102/60
Pyrite (Py)	**20 – 80 %** Euhedral aggregates; Locally fractured polycrystalline aggregates with porous cores; Euhedral grains, corroded; Irregular aggregates; Microcrystalline disseminated in quartz.	**15 – 75 %** Euhedral aggregates; Euhedral grains locally corroded; Irregular aggregates and bands; Microcrystalline disseminated in quartz.
Quartz (Qtz)	**10 – 70 %** Vuggy; Polycrystalline; Collomorphic; Vug linings; Overgrowths on Py.	**~ 50 %** Vuggy; Collomorphic; Overgrowths on Py and Cp.
Chalcopyrite (Cp)	**Trace - 20 %** Anhedral intergrown with Py; Ragged grains; Disseminated in Qtz; Inclusions in Py.	**5 – 15 %** Anhedral intergrown with Py; Ragged fractured grains; Disseminated in Qtz; Inclusions in Py.
Sphalerite (Sp)	**Trace** Inclusions in Py; Late overgrowth on Qtz.	**Trace** Inclusions in Py; Late overgrowths on Qtz and Py.
Fe-oxyhydroxide	**Trace** Very fine-grained; Locally disseminated.	**Trace** Very fine-grained; Amorphous masses; Dustings on sulphides; Locally disseminated.
Clay minerals	**Trace – 5 %** Dusty patches in Qtz; Interstitial; Fibrous aggregates; Vug fill	**Trace – 3 %** Dusty patches in Qtz; Interstitial.
Chlorite	**Trace to 3 %**	**Trace**
Atacamite	**Not reported**	**Trace in lower 20 cm**
Anhydrite	**0 – 30 %**	**Not reported**

Table 4.3: Comparison of mineral textures and occurrences from the TAG pyrite-quartz breccia with the sulphide layer of the *Mir* core (CD102/60).

Pyrite-quartz relationships maybe further complicated over time because the hydrothermal crystalline silica at TAG is secondary to an amorphous silica precursor (e.g. Hopkinson et al., 1998). For example precipitation of silica in locally open pore space and its transformation to quartz results in a volume change and production of collomorphic and vuggy textures. The resultant vugs may then be filled with later sulphides (Knott et al., 1998). The collomorphic and vuggy textures, and the presence of both cristobalite and quartz in Core 60 are consistent with the quartz textures described from the TAG mound and precipitation of quartz via an amorphous silica precursor. The co-existence of the two silica phases may be related to the 'sluggishness' of the transformation path/s which allow several quartz phases to coexist metastably (Chapter 3).

Altered basalt chips are reported from the TAG pyrite-quartz breccia and indicate that this zone was originally basaltic. Whilst no basalt chips have been recovered from the Core 60 sulphide layer the presence of plagioclase and chlorite suggests that prior to alteration basalt was a constituent of this layer.

Sphalerite only occurs in trace amounts and is related to the alteration rather than primary sulphide assemblage. Only trace amounts of sphalerite are reported for the pyrite-quartz breccias at TAG since zone refining processes within the TAG mound result in the removal of Zn from the mound interior and its concentration near the crust-seawater interface (e.g. Edmond et al., 1995; Tivey et al., 1995; Hannington et al., 1998; Knott et al., 1998). The *Mir* mound is comparable in size to the active TAG mound and is composed of several breccia types, a large sulphide talus and shows metal zoning (Rona et al., 1993b; Rona et al., 1993a; Stepanova et al., 1996). The processes and conditions governing zone refining in the *Mir* mound during hydrothermally active periods are almost certainly the same as those operating in the active mound at the present. As such, the absence of a primary Zn-sulphide indicates precipitation of the primary assemblage within the mound interior from a high temperature hydrothermal fluid. Sedimentary emplacement of this inner mound material is most likely due to mass wasting facilitated by the axis parallel and obliquely oriented normal faults which dissect the *Mir* mound (Rona et al., 1996).

Alteration and oxidation of the sulphide layer has been retarded by the presence of quartz cement which has limited the flow of oxidizing fluids through this sediment. The most advanced oxidation is observed in the basal 20cm and is related to decreasing quartz percent and consolidation of the layer.

The alteration assemblage is dominated by goethite. The percentage of goethite increases downcore as quartz and consolidation decrease. Goethite produced as a result of pyrite oxidation via the reaction shown in Equation 1.12. The locally acidic pore fluids generated by this reaction facilitate the disproportionation of Fe and Cu in chalcopyrite (Section 4.5.1.1). Where the released Cu^{2+} ions encounter reducing conditions they have been re-precipitated as covellite as a replacement and overgrowth of primary chalcopyrite. Cu^{2+} is also precipitated as atacamite where fluids carrying dissolved Cu from chalcopyrite decay come into contact with ambient seawater (Detrick et al., 1986; Hannington, 1993).

Clay minerals which are present only in trace amounts are not detrital in origin but are the result of basalt alteration (i.e. chlorite) within the *Mir* mound prior to mass wasting.

Whilst downcore mineralogy suggests that the sulphide layer of Core 60 is restricted to depths of 44.5-96cm, the Fe-oxide and oxyhydroxide-rich layers above and below suggest that size and oxidation of this sulphide-rich, mass wasted section may be more extensive than that apparent from the downcore distribution of sulphide minerals. There are two broad possibilities for the emplacement of the Fe-oxide and oxyhydroxide layers. The first is that they represent sedimentation of oxidized material from two individual mass wasting events, one prior to and one following the deposition of the altered pyrite-quartz breccia (the sulphide layer). The second is that all three layers were deposited in one event. The most plausible explanation is in fact a combination of these two possibilities.

The upper Fe oxide/oxyhydroxide layer has a gradational contact with the overlying carbonate cap and the base shows sedimentary layering and a sharp contact with the underlying sulphide layer (Chapter 3). This layering strongly suggests that this upper Fe oxide/ oxyhydroxide layer was deposited as a separate unit following deposition of the sulphide layer. The gradational contact of the upper oxide layer with the carbonate cap may indicate combined sedimentation of hydrothermally derived Fe oxide and oxyhydroxide with background pelagic material and/or some dissolution of carbonate material as a result of acidic pore fluids generated during sulphide oxidation in the layer below.

However, there is no geochemical or mineralogical evidence here for background pelagic sediment between the lower Fe oxide/ oxyhydroxide layer and the sulphide layer. If these two layers represent distinct mass wasting events then these must have occurred in rapid succession. The juxtaposition of highly oxidized material and the relatively unaltered mound breccia via such rapid mass wasting events with no intervening background sedimentation seems unlikely. Furthermore, the boundary between the sulphide layer and the lower Fe oxide/ oxyhydroxide layer is not sharp (as it is between the sulphide layer and the upper Fe oxide/ oxyhydroxide layer) but is gradational, and plagioclase and chlorite (basalt alteration products) are reported from the lower layer (Chapter 3). This suggests that the sulphide layer and the lower Fe oxide/ oxyhydroxide layer were deposited at the same time, as one unit of pyrite-quartz breccia, and that oxidation of the bottom half of the layer has been much more extensive than that observed in the upper portion where quartz cement appears to have provided at least some protection from oxidative sulphide decay. Whether the extensive oxidative alteration of the lower Fe oxide/ oxyhydroxide layer from the pyrite-quartz breccia precursor occurred predominantly prior to the mass wasting event or following it is unclear.

4.4.4 Generalized paragenetic sequence in CD102/60: The *Mir* core

1. Precipitation of primary pyrite and chalcopyrite during high temperature fluid flow within the mound. The presence of plagioclase and chlorite, remnants of basalt, suggest that this primary sulphide precipitation took place in the upper parts of the hydrothermal stockwork zone.
2. Cementation of primary sulphide clasts by silica precipitated from a conductively cooled mix of end-member hydrothermal fluid and seawater and formation of a pyrite-quartz breccia.
3. Sedimentary emplacement during a mass wasting event is most likely facilitated by movement on the axis parallel and obliquely oriented normal faults which dissect the *Mir* mound (Rona et al., 1996).
4. Oxidation and reworking of the sulphide layer proceeds from lower extreme of the mass wasted layer. The end product of the oxidation is goethite and hematite.

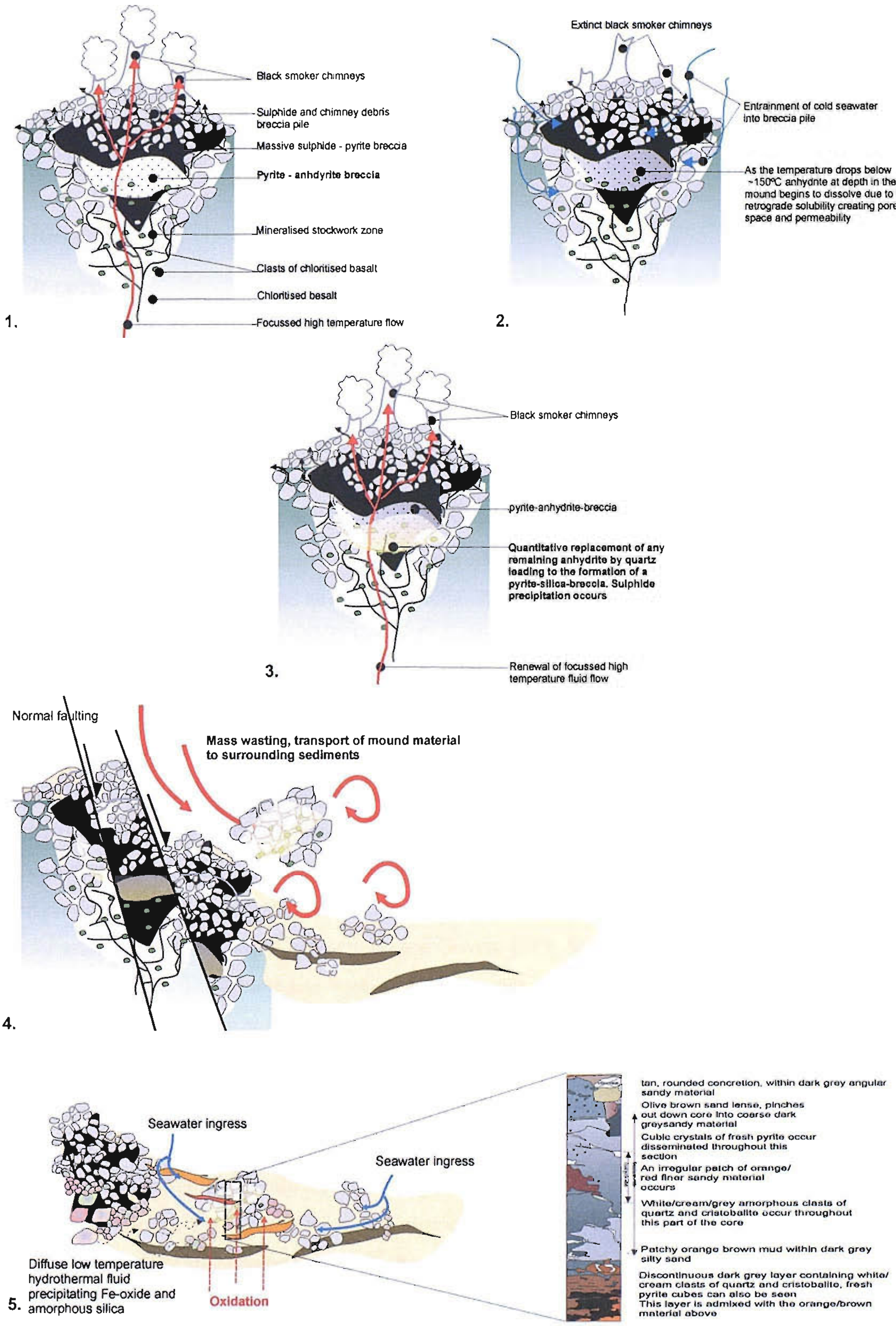

Figure 4.19: Schematic representation of sulphide precipitation, transport to sediment and alteration of the sulphide layer of the *Mir* core, CD102/60. 1.) Precipitation of pyrite and chalcopyrite during high temperature fluid flow and formation of pyrite-anhydrite breccia. Clasts of chloritised basalt are included; **2.)** Hiatus in high temperature activity, on set of anhydrite dissolution; **3.)** Renewal of high temperature flow; partially dissolved anhydrite is cumulatively replaced by quartz - formation of pyrite-silica breccia; and new generation of sulphide precipitation; **4.)** Normal faulting dissects the *Mir* mound exposing the mound interior. Mass wasting and slumping transports cemented hydrothermal blocks from the mound interior to the surrounding sediments; **5.)** Oxidation of mass wasted material and low temperature fluid flow, oxidation proceeds from the base of the mass wasted pyrite-silica breccia block where the cement is less extensive or fractured allowing access for alteration fluids. The quartz and cristobalite cement of the moderately well consolidated material towards the top of the sulphide layer retards fluid flow and oxidation is less advanced in this area. Oxidation leads to remobilisation of base metals and precipitation of gossan minerals, e.g. Goethite. **Note diagrams are not to scale.**

A schematic representation of the general paragenetic sequence is shown in Figure 4.19.

4.5 Conclusions

4.5.1 The *Alvin* core

The primary and secondary mound derived minerals represent a pro-grade assemblage. Initial mineralisation of porous, collomorphic pyrite crusts from diffuse, moderately high temperature hydrothermal fluid leads to insulation and focusing of fluid flow facilitating precipitation of pyrite and chalcopyrite from a high temperature, black smoker style fluid. As high temperature activity waned, the secondary sulphide assemblage of pyrite, sphalerite and quartz was precipitated from a conductively cooled lower temperature, Zn-rich solution. Initial alteration and oxidation of the mound material at the mound seawater interface and within the mound as ambient seawater infiltrated the deposit was contemporaneous with hydrothermal activity. Further substantial and pervasive oxidation and alteration of sulphidic material leading to the formation of goethite, atacamite, gypsum (Chapter 6) and clays (Chapter 3) continued following transport of mound derived material to the surrounding sediment via mass wasting and slumping events.

The precipitation of secondary and late sulphides, including covellite and sphalerite, is a consequence of acid leaching processes which resemble sub-aerial supergene reactions. The results of these submarine supergene processes are locally important, grain-scale re-mineralisation and secondary enrichment, rather than the much larger scale, downward migrating zones of oxidation and secondary enrichment observed in sub-aerial deposits. The end products of alteration in this core are dominated by goethite and are similar to gossans overlying sub-aerial massive sulphides (e.g. Constantinou and Govett, 1973; Scott et al., 2001), and other submarine Fe-oxide rich deposits which have also been compared to sub-aerial gossanous material (e.g. Oudin et al., 1981; Alt et al., 1987; Hannington et al., 1988; Metz et al., 1988; Herzig et al., 1991; Hannington and Jonasson, 1992; Hannington, 1993; Dill et al., 1994; Hannington et al., 1995b; Goulding, 1998).

4.5.2 The *Mir* core

The striking similarity of the *Mir* core sulphide layer to the pyrite–quartz breccias described from the active TAG mound (e.g. Humphris et al., 1995; Humphris and Kleinrock, 1996; Knott et al., 1998) and the presence of plagioclase and chlorite, which are remnants of basalt alteration, confirm that the primary sulphide assemblage was precipitated under high temperature conditions during the formation of a pyrite–quartz breccia at the top of the hydrothermal stockwork zone within the *Mir* mound. Mass wasting of the *Mir* mound and transportation of sulphidic material to the surrounding sediment maybe a consequence of movement on the axis parallel and obliquely oriented normal faults which dissect the *Mir* mound (Rona et al., 1996). Following sedimentary emplacement alteration of primary sulphides due to acid leaching resulted in the precipitation of secondary pyrite and covellite, and oxidation of primary and secondary sulphide resulted in the formation of goethite and hematite with minor atacamite. The presence of quartz and cristobalite cement is inferred to inhibit the flow of oxidising and alteration fluids through the upper parts of the sulphide layer. The most advanced oxidation and alteration is observed below 83cm depth where the modal percent of quartz and consolidation decrease.

Similar to the *Alvin* core sulphide layer, precipitation of the secondary sulphides, covellite and sphalerite, is a consequence of acid leaching of primary sulphide in processes resembling sub-aerial supergene reactions. Secondary sulphide enrichment is locally important, and is typically seen as grain-scale re-mineralisation rather than large scale pervasive oxidation and secondary enrichment. The end products of alteration in this core are dominated by goethite and hematite and are again very similar to the gossanous weathering products which overlying sub-aerial massive sulphides (e.g. Constantinou and Govett, 1973; Scott et al., 2001), and other submarine Fe-oxide rich deposits compared to sub-aerial gossans (e.g. Oudin et al., 1981; Alt et al., 1987; Hannington et al., 1988; Metz et al., 1988; Herzig et al., 1991; Hannington and Jonasson, 1992; Hannington, 1993; Dill et al., 1994; Hannington et al., 1995b; Goulding, 1998).

4.5.3 Wider implications –comparisons with other metalliferous sediment studies.

The sulphide layer of Core 58, although much less altered than, compares well to similar sulphide layers in nearby cores (Metz et al., 1988; Mills et al., 1993; Severmann, 2000). Sulphide layers in core 43 (Severmann, 2000) and the Metz et al. (1988) core (Mills et al., 1993) are also attributed to mass wasting of sulphidic mound material and the geochemistry of these layers is predominantly controlled by the mineralogy rather than dissolution, remobilisation and seawater scavenging processes. The occurrence of Fe oxides and oxyhydroxides in Core 58 and other sulphide dominated sediments from the TAG field can be variously attributed to the oxidation of sulphide phases, which are thermodynamically unstable in ambient seawater, and precipitation from diffuse low temperature fluids circulating within the sediment pile, with only minimal inputs from plume fallout (Thompson et al., 1985; Metz et al., 1988; German et al., 1993; Mills et al., 1993; Severmann, 2000; Severmann et al., 2004). The sulphide layer of Core 60 which represents a relatively large scale mass wasting event, transporting inner mound material to the near field sediments appears to be more unique.

Mound or chimney related sulphide debris is also an important sedimentary component at hydrothermal sites elsewhere on the MAR. However, many of these sulphide bearing sediments do not have distinct sulphide layers, like those reported at TAG, but contain sulphide admixed with Fe oxide and clay minerals suggestive of extensive seawater alteration (e.g. MARK: Cherkashev, 1995, and Snake Pit: Detrick et al., 1986). Studies of metalliferous sediments from the EPR, in contrast to studies from the MAR, have focussed largely on the Fe oxide deposits of the ridge flanks where sulphide is not an important sedimentary component (e.g. Dymond and Veeh, 1975; Dymond, 1981; Barrett et al., 1987; Shimmield and Price, 1988) with very little investigation of near field sediments (e.g. German et al., 1999). The study by German et al. (1999) does identify a relatively fresh sulphidic input to a core from the OBS vent field but again does not identify specific sulphide layers like those reported from TAG.

The sediment thickness near to a vent site depends largely on the crustal age and longevity of hydrothermal activity. It is not surprising therefore, that the TAG field exhibits the most extensive metalliferous sediments in the Atlantic (e.g. Shearme et al., 1983; Metz et al., 1988; German et al., 1993; Mills, 1995). The occurrence of distinct, relatively thick sulphide layers within TAG near field sediments appears to be related to the longevity of high temperature hydrothermal activity at this site. Large, mature sulphide mounds like those of the TAG field, where lots of mass wasting can occur, result in transport of a significant amount of sulphidic material to the surrounding sediments. Thus the occurrence of sulphide dominated near field sediments, which are geochemically and mineralogically distinct from plume derived material and diffuse low temperature deposits at Atlantic hydrothermal sites, and only minimal, often admixed sulphide inputs to sediments at Pacific hydrothermal sites reflects the fact that Pacific sites are typically composed of many small mounds and chimney clusters whereas Atlantic sites commonly comprise much larger massive sulphide mounds which are stable over longer periods. The mineralogy and formation of distinct sulphide layers in cores 58 and 60 can be related to the occurrence of the large, mature, relict mounds of the *Alvin* and *Mir* zones which reflect the longevity and stability of hydrothermal activity at the TAG site. In particular, the pyrite-quartz breccia assemblage of the Core 60 sulphide layer requires a mature mound where there have been multiple episodes of high temperature activity. In this respect, the type of sulphide sediment, and the formation of Core 60 maybe unique to the TAG field.

Chapter 5:

Sulphur Isotope Variation of Sulphide-Rich Sediments from the *Alvin* and *Mir* Relict High Temperature Zones.

5.1 Introduction: Sulphur isotope systematics in seafloor hydrothermal systems

Sulphur isotope systematics in seafloor hydrothermal systems are complex; this is due to the existence of several sulphur sources and sinks, and variable fractionation during sulphur cycling. There are two principal sources of sulphur in modern seafloor hydrothermal systems: seawater, which contains very minor reduced sulphur species and has ~2688ppm sulphate with $\delta^{34}S$ = +20.9‰ (Rees et al., 1978); and Mid-Ocean Ridge Basalt (MORB), with a range of sulphur content between ~600 to ~1600ppm and a mean value of ~810ppm and $\delta^{34}S$ = +0.1 ±0.5‰ (Sakai et al., 1984). Sulphur sinks during high temperature (>150°C) circulation include: anhydrite precipitation during seawater recharge to the hydrothermal system at depth; conversion of basaltic mono-sulphides to poly-sulphides as a result of water rock interactions in the deep hydrothermal reaction zone; and formation of massive, vein and disseminated, mound and chimney sulphides. Variation in the value of $\delta^{34}S$ in high temperature systems can be attributed to mixing of sulphur from the seawater and basalt reservoirs, fractionation during sulphate reduction and transformation of transient sulphur species. However, the causes of variation in $\delta^{34}S$ values in the lower temperature conditions surrounding active vent sites and relict sites, (including supergene alteration conditions), are much more complex. This is mainly due to the action of metal/sulphur oxidizing and reducing bacteria in these systems and the numerous pathways of sulphide oxidation and sulphate reduction possible during biogeochemical cycling of sulphur.

5.1.1 Sulphur isotope systematics in high temperature systems

Experimental and theoretical modelling of seawater recharge and circulation in the upper crust, has shown that as down-welling seawater is heated to temperatures of ~150-200°C sulphate is removed from the fluid due to anhydrite precipitation (Shanks et al., 1981; Janecky and Shanks, 1988; Alt et al., 1989; Bowers, 1989). Since the calcium concentration of seawater is only one third that of sulphate, excess sulphate remains in the hydrothermal seawater, despite addition of Ca leached from the basaltic wall rock (Blount and Dickson, 1969). Deeper in the crust at temperatures ≥250°C inorganic sulphate reduction, as a consequence of the oxidation of ferrous Fe in pyroxene or olivine (Equation 5.1) or via conversion of basaltic pyrrhotite (FeS) to secondary pyrite (FeS_2) (Equation 5.2) becomes important (Shanks et al., 1981; Ohmoto and Lasage, 1982; Shanks and Seyfried, 1987).

$$8Fe^{2+} + 10H^{+} + SO_4^{\;2-} = 8Fe^{3+} + H_2S + 4H_2O \qquad (5.1)$$

$$7FeS + 8H^{+} + SO_4^{\;2-} \rightarrow 4FeS_2 + 4H_2O + 3Fe^{2+} \qquad (5.2)$$

At low water/rock ratios and high temperatures, the inorganic reduction of seawater sulphate is rapid and complete leading to no significant isotopic fractionation i.e. the seawater derived sulphide has $\delta^{34}S$ of the initial sulphate, (+20.9‰), (Shanks et al., 1981; Ohmoto and Lasage, 1982; Shanks and Seyfried, 1987; Alt et al., 1989). Whilst seawater sulphur is fixed in the crust as sulphate and sulphide, igneous sulphur is leached from the basaltic wallrock (e.g. Shanks et al., 1981; Shanks and Seyfried, 1987; Alt et al., 1989; Bowers, 1989). The sulphide component in basalt is highly soluble at high temperature and direct leaching of basaltic sulphur produces $\delta^{34}S$ values in the fluid close to 0‰ (Seyfried and Janecky, 1985).

The observed range of $\delta^{34}S$ values in modern seafloor hydrothermal deposits and vent fluids (Figure 5.1) can be attributed to variable mixing of basaltic ($\delta^{34}S = +0.1$‰), and seawater ($\delta^{34}S = +20.9$‰) sulphur (Sakai et al., 1984; Rees et al., 1978). It has been argued that sulphate reduction at depth in the hydrothermal reaction zone characterizes $\delta^{34}S$ values in vent fluids and associated sulphide deposits (e.g. Shanks and Seyfried, 1987; Bluth and Ohmoto, 1988; Woodruff and Shanks, 1988). However, incremental reaction modelling of vent fluid compositions suggests that up-welling hydrothermal fluids have basalt dominated $\delta^{34}S$, which is modified in the shallow subsurface around vent sites and within individual chimneys, as entrained ambient seawater undergoes inorganic sulphate reduction (Janecky and Shanks, 1988; Bowers, 1989). In reality, the $\delta^{34}S$ values of vent fluids and their associated sulphide deposits are the result of a combination of deep subsurface reactions and shallow, near-surface sulphide-sulphate precipitation and sulphate reduction, with higher $\delta^{34}S$ values indicating a larger reduced seawater sulphate component (e.g. Zierenberg et al., 1984; Janecky and Shanks, 1988; Woodruff and Shanks, 1988; Herzig et al., 1998a).

Since there is very little variation in the basaltic composition of the ocean crust, and therefore the $\delta^{34}S$ value of basalt, large-scale variations in $\delta^{34}S$ between different vent sites reflect differences in the underlying plumbing and permeability structures of each system. For example the Snake Pit (23°N MAR) and Broken Spur (29°N MAR) hydrothermal sites exhibit very similar $\delta^{34}S$ ranges between ~0–+3.0‰ (Kase et al., 1990; Duckworth et al.,1995; Butler et al., 1998). However, the TAG mound (26°N MAR) has a range in $\delta^{34}S$ of ~+5–+9‰ (Chiba et al., 1998; Gemmell and Sharpe, 1998; Herzig et al., 1998b). This difference in the value of $\delta^{34}S$ at the TAG mound, compared to other vent sites nearby on the Mid Atlantic Ridge, is due to a number of factors; notably the much larger size of the TAG mound in which high temperature conditions are maintained, and the longevity and episodic nature of hydrothermal activity at this site (e.g. Chiba et al., 1998; Gemmell and Sharpe, 1998; Knott et al., 1998). Small-scale variations between hydrothermal fluid and coeval sulphide may be explained by in situ processes relating to the permeability structure of chimneys and sulphide mounds, and the extent of shallow seawater entrainment (e.g. Janecky and Shanks, 1988; Ohmoto and Goldhaber, 1997; Chiba et al., 1998).

5.1.2 Sulphur isotope systematics in low temperature conditions

The rate of inorganic sulphate reduction is principally dependent upon the temperature, pH, and fO_2 of the system (e.g. Ohmoto and Rye, 1979). Under hydrothermal conditions where pH and fO_2 are low and temperatures are at or in excess of 200°C inorganic sulphate reduction via equilibrium isotopic exchange is geochemically important (Ohmoto and Lasage, 1982). However under the low temperature, ≤50°C, conditions operating at, and/or near to the surface of active vents sites, relict vent sites, and during alteration of near field

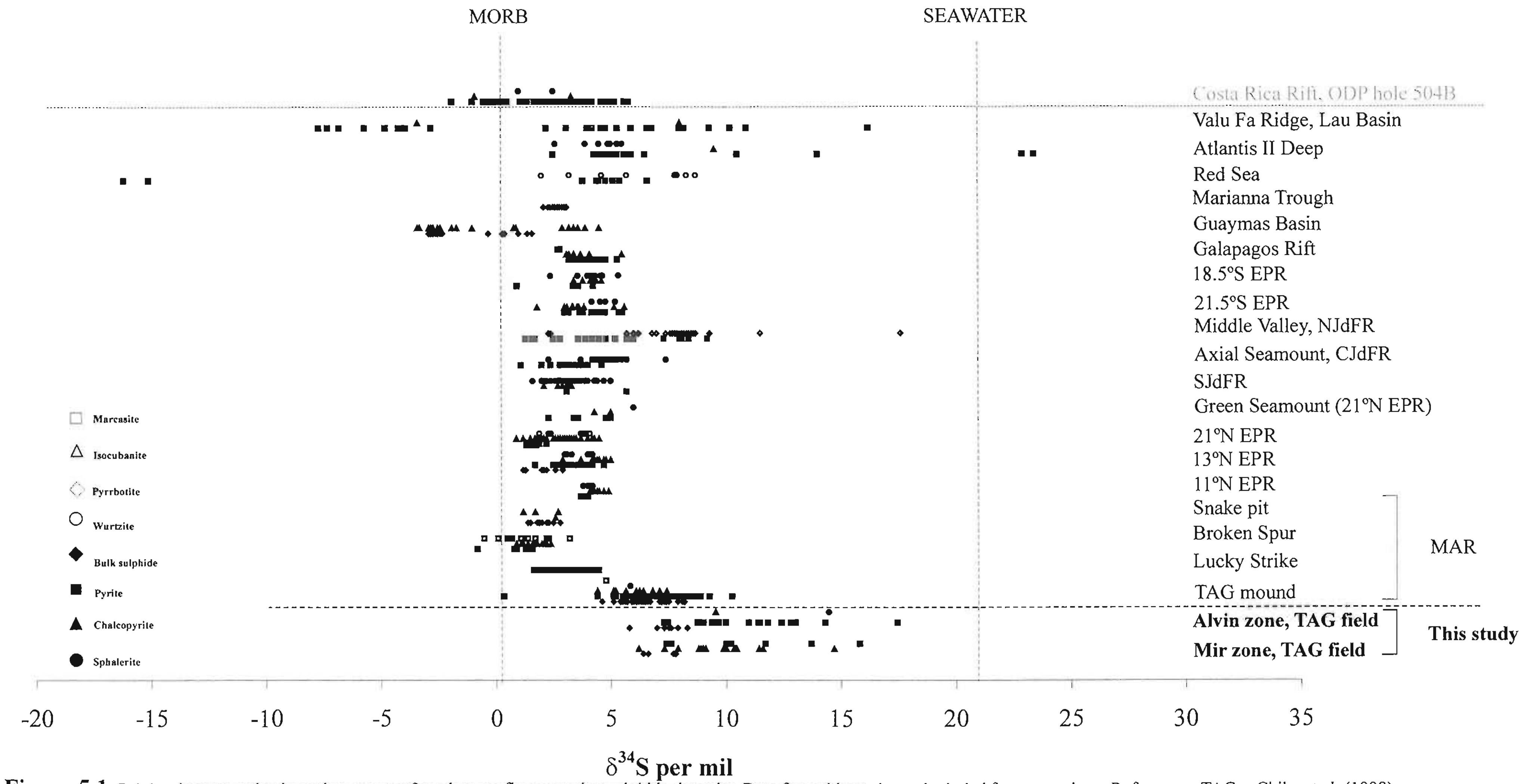

Figure 5.1: Sulphur isotope ratios in various types of modern seafloor massive sulphide deposits. Data from this study are included for comparison. References: TAG = Chiba et al. (1998); Gemmell and Sharpe (1998); Herzig et al. (1998a); Knott et al. (1998); Lucky Strike =Rouxel et al. (2004); Broken Spur = Duckworth et al. (1995); Butler et al. (1998); Snake Pit = Kase et al. (1990); 11°N EPR = Bluth and Ohmoto (1988); 13°N EPR = Bluth and Ohmoto (1988); Stuart et al. (1995); 21°N EPR = Woodruff and Shanks (1988); Zierenberg et al. (1984); Green Seamount = Alt (1988); SJdFR = Shanks and Seyfried (1987); Axial Seamount, CJdFR = Hannington and Scott (1988); Middle Valley, NJdFR = Goodfellow and Blaise (1988); Duckworth et al. (1994); Stuart et al. (1994); Goodfellow and Franklin (1993); 21.5°S EPR = Marchig et al. (1990); 18.5°S EPR = Marchig et al. (1990); Galapagos Rift = Knott et al. (1995); Guaymas Basin = Peter and Shanks (1992); Marianna Trough = Kasakabe et al (1990); Red Sea = Blum and Puchelt (1991); Atlantis II Deep = Zierenberg and Shanks (1988); Valu Fa Ridge, Lau Basin = Herzig et al (1998b).
Costa Rica Rift, ODP hole 504B = Alt et al (1989); Kawahata and Shikizono (1988).. N.B. not seafloor included for comparison.

Abbreviations: EPR = East Pacific Rise; SJdFR = Southern Juan de Fuca Ridge; NJdFR = Northern Juan de Fuca Ridge; CJdFR = Central Juan de Fuca Ridge; MAR = Mid-Atlantic Ridge sulphide-rich sediments kinetically controlled bacterial sulphate reduction dominates (e.g. Ohmoto and Rye, 1979; Canfield, 2001a; Habicht and Canfield, 2001 and references there in).

Hydrothermal vent sites sustain large microbial communities including both heterotrophic and lithotrophic organisms which are able to utilize sulphur species (e.g. Wirsen et al., 1993; Campbell et al., 2001). Isotopic fractionation arises from the fact that the chemical reaction rate is mass dependent and that microbes preferentially utilize the lighter ^{32}S over the heavier ^{34}S because of the lower energy costs.

Assimilatory Sulphate Reduction (ASR)

Sulphur is a fundamental requirement for living cells and is assimilated from the surrounding environment most commonly as sulphate. For incorporation of this sulphate into cellular compounds it must be reduced to sulphide this occurs via ASR. Following uptake of sulphate there are two known pathways by which reduction can occur. The first, known as the adenosine-5'-phosphosulfate (APS) pathway is generally exploited by O_2 producing phototrophic eukaryotes, the second, known as the phosphoadenosine-5'-phophosulfate (PAPS) pathway is favoured by anoxygenic microorganisms (e.g. Canfield, 2001a) (Figure 5.2). The APS pathway leads to the formation of either sulphate esters or reduced sulphur compounds typically HS^-, the PAPS pathway results only in the formation of reduced sulphur compounds (e.g. Canfield, 2001a).

Isotopic fractionation is due to kinetic effects relating to the unidirectional and mass dependent nature of sulphate uptake. Although both pathways include numerous intracellular steps which may result in isotopic fractionations, observed fractionations associated with ASR are relatively small, e.g. measurements of $\Delta\ \delta^{34}S_{\text{sulphate}}$- $\delta^{34}S_{\text{organic sulphur}}$ for E. coli, and some yeast and green alga species range from 0.9–2.8‰ (Kaplan and Rittenberg, 1964). This is a function of the unidirectional nature of ASR reactions; since there is no isotopic exchange with external sulphur reservoirs, following cellular uptake of sulphate, no net fractionation will be observed (e.g. Rees, 1973). It is however, important to note that isotopic fractionation generated in laboratory culture experiments is never as large as the fractionations inferred from field observations. This implies that real systems are much more complex involving multiple reaction steps and stages of mineralisation that have not yet been resolved in laboratory cultures (e.g. Canfield, 2001a; Canfield, 2001b)

Dissimilatory sulphate reduction (DSR).

DSR is carried out by a specialized group of micro-organisms which utilize the energy gained from catalysising exergonic reactions for cell growth, in which either organic carbon or gaseous hydrogen is oxidized as sulphate is reduced (Equations 5.3 and 5.4: Canfield, 2001a).

$$SO_4^{\ 2-} + 2CH_2O \rightarrow H_2S + 2HCO_3^{\ -} \qquad (5.3)$$

$$2H^+ + SO_4^{\ 2-} + 4H_2 \rightarrow H_2S + 4H_2O \qquad (5.4)$$

Although sulphate reducers are phylogenetically diverse and are known from several major lineages within the bacterial domain, within hydrothermal environments DSR is predominantly carried out by heterotrophic

The APS Pathway

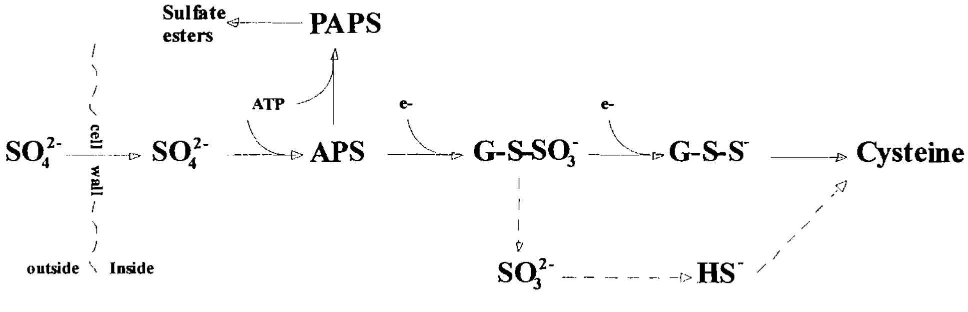

The PAPS Pathway

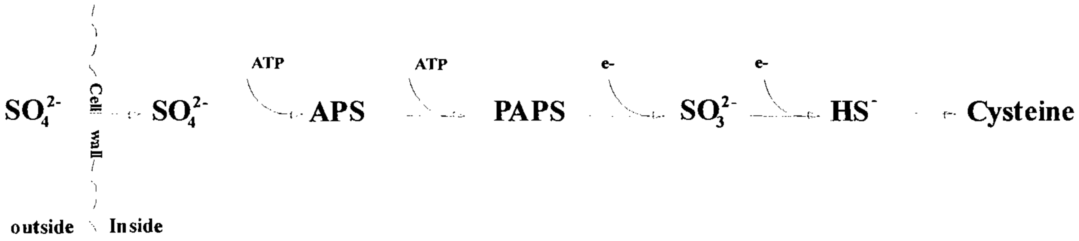

Figure 5.2: The pathways of assimilatory sulphate reduction. In the APS pathway sulphur can either be oxidized to cysteine or converted to sulphate esters. Uptake of sulphate into the cell is a unidirectional process. ATP = adenosine triphosphate (Adapted from: Canfield, 2001a).

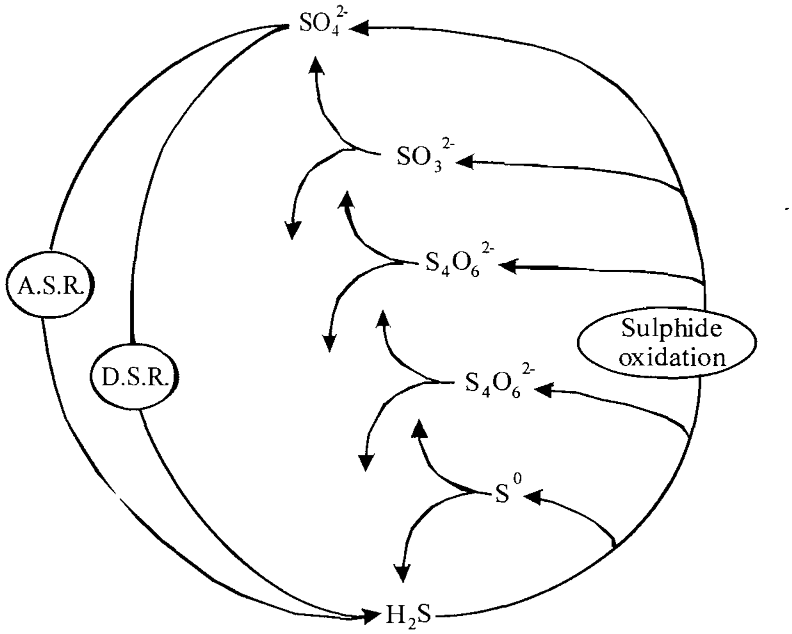

Figure 5.3: Pathways of sulphur transformation of interest in isotope studies in the environment. Note the numerous possible pathways and intermediate species for sulphide oxidation. (Adapted from Canfield, 2001a).

bacterial organisms, principally *Desulfovibrio desulfuricans* which is an obligate anaerobe (e.g. Trudinger et al., 1985; Jorgensen et al., 1992; Campbell et al., 2001).

S isotopic fractionation as a result of DSR can be substantial with published measurements indicating maximum $\Delta\ \delta^{34}S_{sulphate}$- $\delta^{34}S_{sulphide}$ of 40-~50‰ (e.g. Kaplan and Rittenberg, 1964; Chambers et al., 1975; Canfield and Teske, 1996; Canfield et al., 1998). The extent of fractionation during DSR is dependent on a number of factors most notably the rate of sulphate reduction, sulphate concentration, and the variety of electron donor (e.g. Kaplan and Rittenberg, 1964; Kemp and Thode, 1968; Chambers et al., 1975; Ohmoto and Rye, 1979; Habicht and Canfield, 2001). For example, experimental data show that during DSR the kinetic isotope effect increases with a decrease in the rate of reduction, e.g. a reduction rate of $10^{-0.5}$mole SO_4^{2-} /l sec^{-1} results in a fractionation of ~1.5-2.5‰; a slower reduction rate of $10^{-4.5}$mole SO_4^{2-}/l sec^{-1} results in a fractionation of ~6.5‰ (e.g. Ohmoto and Rye, 1979). Where sulphate concentrations are in excess of 1mM S isotopic fractionations of ~46‰ have been observed, where sulphate concentrations are <1mM S isotopic fractionations are considerably smaller, typically <5‰ (e.g. Canfield, 2001b). The type of electron donor also has an effect on the extent of isotopic fractionation. Fractionation of S isotopes in laboratory cultures of *Desulfovibrio desulfuricans* are greater when organic carbon is the electron donor (Equation 5.3) with maximum fractionation of ~45‰, than when H_2 (gas) is the electron donor (Equation 5.4) with fractionation typically <10‰ (Kaplan and Rittenberg, 1964; Chambers et al., 1975). Other factors which influence the degree of isotopic fractionation as a result of DSR include the reaction pathway, the specific bacterial strain involved and the temperature, e.g. the optimum growth temperature for *Thermodesulfobacterium* is 80°C (Stackebrandt et al., 1995) whereas heterotrophic S-reducers have a wide optimum temperature range of 38-68°C (Miroshnichenko et al., 2002).

Sulphide Oxidation

In addition to sulphate reduction, sulphide oxidation is important in effecting the range of $\delta^{34}S$ values possible under low temperature conditions. Although much less is known about the pathways of sulphide oxidation several important mechanisms for the oxidation of sulphide in nature have been identified and include:

1. Biologically mediated oxidation of metal sulphide to elemental sulphur, and elemental sulphur to sulphate affected by specialized bacteria which catalyze certain reactions. The most commonly involved types are mesoacidophilic, chemolithotrophic. Three species dominate studies to date, these are:
   - *Thiobacillus ferrooxidans*, an acidophilic species which can oxidize reduced sulphur compounds to sulphate and Fe(II) to Fe(III).
   - *Thiobacillus thiooxidans*, which is only able to oxidize reduced sulphur compounds
   - *Leptospirillum ferrooxidans*, which is only able to oxidize Fe(II) to Fe(III) (Toran and Harris, 1989; Ehrlich, 1996b; Bosecker, 1997; Schippers and Sand, 1999).
2. Inorganic oxidation of sulphide to sulphate and other intermediate sulphur compounds
3. Disproportionation of sulphur compounds via intermediate oxidation states

The first two oxidation mechanisms can be considered as true oxidation pathways requiring an external electron acceptor; the third mechanism does not require an electron acceptor and instead balances the production of sulphate by the production of sulphide. Only small S isotope fractionations may be expected to arise from simple sulphide oxidation since the oxidation rate is not controlled by metal-sulphur bond rupture as such, the kinetic isotopic effect is negligible (e.g. Ohmoto and Rye, 1979; Canfield, 2001a). However, sulphide oxidation most commonly proceeds via unstable intermediate sulphur species e.g. thiosulphate and polythionates, disproportionation, or further oxidation of these intermediate species can result in S isotope fractionation where sulphate is depleted in ^{34}S and polythionates are enriched (Figure 5.3) (e.g. Toran and Harris, 1989; Jorgensen, 1990; Schippers and Sand, 1999; Bottcher, 2001; Canfield, 2001a).

It should be noted that there are, problems associated with using S isotope signatures to assign oxidation reaction pathways as not all oxidation pathways produce a unique S isotope signature and both in nature and in laboratory experiments sulphide oxidation can occur by several different pathways simultaneously (Figure 5.3).

Disproportionation

Most of the intermediate sulphur compounds formed during sulphide oxidation are unstable and therefore do not accumulate in the environment. Although some of these intermediate species will undergo simple reduction or oxidation to more stable phases others will be disproportionated by bacterial sulphate reducers. Disproportionation of a sulphur intermediate to sulphide and sulphate does not require an external electron donor or acceptor e.g. Equations 5.5; 5.6; and 5.7 (Bak and Pfennig, 1987; Bak and Cypionka, 1987; Canfield et al., 1998; Canfield, 2001a):

$$4S^0 + 4H_2O \rightarrow 3H_2S + SO_4^{2-} + 2H^+ \tag{5.5}$$

$$4SO_3^{2-} + 2H^+ \rightarrow H_2S + 3SO_4^{2-} \tag{5.6}$$

$$S_2O_3^{2-} + H_2O \rightarrow H_2S + SO_4^{2-} \tag{5.7}$$

The fractionation of S isotopes during disproportionation reactions is highly variable. Laboratory investigations of the disproportionation of elemental sulphur (Equation 5.5) show a narrow range in S isotope fractionation with the resulting sulphide depleted in ^{34}S: $\Delta\ \delta^{34}S_{sulphur}$- $\delta^{34}S_{sulphide}$ -6 to -9‰, and sulphate enriched in ^{34}S: $\Delta\ \delta^{34}S_{sulphur}$- $\delta^{34}S_{sulphate}$ ~18‰ (Canfield et al., 1998). Much larger fractionations have been observed during the disproportionation of sulphite (Equation 5.6). Experiments with pure cultures indicate that disproportionation of sulphite results in $\Delta\ \delta^{34}S_{sulphite}$- $\delta^{34}S_{sulphide}$ -37‰ and $\Delta\ \delta^{34}S_{sulphite}$- $\delta^{34}S_{sulphate}$ ~12‰ (Habicht et al., 1998). In this case the 3:1 difference between the fractionation to sulphide and sulphate is related to the stoichiometry of the reaction (Equation 5.6). Laboratory investigations of fractionation during thiosulphate disproportionation in general yield sulphide which is depleted in ^{34}S and sulphate which is enriched in ^{34}S (Cypionka et al., 1998; Habicht et al., 1998).

In the case of thiosulphate, isotope exchange between individual sulphur species is important in determining the extent of fractionation. This is because thiosulphate is composed of sulphonate sulphur ($-SO_3^-$) and sulphane sulphur ($-S^-$). Sulphate resulting from the disproportionation of thiosulphate is derived from the sulphonate sulphur and the sulphide is derived from the sulphane sulphur. The extent of fractionation during disproportionation of thiosulphate is also dependant upon whether the system is open or closed with respect to

H_2S. In systems open to H_2S, where sulphide is constantly removed (e.g. via formation of FeS_2), laboratory experiments with pure cultures indicate that kinetic fractionations are most important and the sulphate produced is isotopically light compared to the original sulphonate (Cypionka et al., 1998). In systems closed to H_2S, e.g. where there is limited availability of metals to form sulphide minerals, and sulphide is allowed to accumulate, differences between sulphane and sulphonate sulphur are related to isotopic exchange of these two species with the thiosulphate pool (Habicht et al., 1998).

5.1.3 Observed $\delta^{34}S$ values and S isotopic fractionation at modern hydrothermal vent sites

Since equilibrium isotopic fractionation between aqueous H_2S and precipitating sulphide is minor at elevated temperatures (≥300°C): $\Delta\ \delta^{34}S_{MeS\text{-}H2S} \leq 0.5‰$ (Ohmoto and Rye, 1979), the observed values of sulphide $\delta^{34}S$ should be a reasonable representation of the $\delta^{34}S$ value of the fluid from which they precipitated, assuming equilibrium conditions. However, the measured ranges of sulphide $\delta^{34}S$ at modern seafloor hydrothermal sites are generally >1.5‰, and in some cases are >10‰ (Figure 5.1). This suggests that some or all of the following maybe occurring:

- Sulphide precipitation is occurring in non-equilibrium conditions.
- ^{34}S enrichment is extremely variable through time and space: at several sites, e.g. TAG and 21° N EPR time series studies of fluid chemistry suggest that water/rock reactions at depth have reached equilibrium (Edmond et al., 1995; Edmonds et al., 1996; Campbell et al., 1988). This implies that any large-scale variation at sites of stable end-member fluid chemistry is due to near surface seawater sulphate reduction. However, near surface inorganic seawater sulphate reduction is not likely for several reasons: firstly, inorganic sulphate reduction requires temperatures ≥200°C, the onset of anhydrite precipitation at lower temperatures (~150°C) resulting in the removal of seawater SO_4^{2-} from the fluid via anhydrite precipitation, limits the availability of sulphate for reduction in the near surface (e.g. Janecky and Seyfried, 1984; Janecky and Shanks, 1988). Secondly, entrainment of, and mixing with, cold (~2°C) seawater should cool the hydrothermal fluid preventing the temperatures required for inorganic sulphate reduction.
- Overprinting of primary 'pristine' sulphide during hydrothermal diagenesis: this results in ^{34}S enrichment as mixing with, and sulphur contributions from, reduction of seawater sulphate increase (Gemmell and Sharpe, 1998).
- Bacterial sulphate reduction contributing isotopically light sulphur either within the massive sulphide deposit at the seafloor or in the subsurface hydrothermal system. Sulphate reducing bacteria have been reported at depths of 500m below seafloor (Parkes et al., 2000) and at temperatures of c.100°C (Jorgensen et al., 1992).
- Leaching of sedimentary sulphides: this is only important for sedimentary-hosted hydrothermal deposits e.g. Guaymas Basin and Middle Valley, and results in a shift to lighter $\delta^{34}S$ values (Peter and Shanks, 1992; Goodfellow and Franklin, 1993).
- Mixing of hydrothermal fluid with basement fluid, or pore waters contributing heavy $\delta^{34}S$, e.g. 21°N EPR (Woodruff and Shanks, 1988), or with magmatic fluids contributing light $\delta^{34}S$, e.g. Valu Fa Ridge, Lau Basin (Herzig et al., 1998a).

The narrow range of reported sulphide $\delta^{34}S$ values (~-1.0‰ to ~+4.0‰) at sediment-free ocean ridge hydrothermal sites (except the TAG site which has a range in $\delta^{34}S$ of +0.35-+10.3‰) reflect precipitation from a fluid where sulphur is sourced principally from basalt with a smaller component derived from reduced seawater sulphate (e.g. Styrt et al., 1981; Zierenberg et al., 1984; Shanks and Seyfried, 1987; Bluth and Ohmoto, 1988; Hannington and Scott, 1988; Woodruff and Shanks, 1988; Duckworth et al., 1995; Knott et al., 1995; Gemmell and Sharpe, 1998). For example, the lightest reported $\delta^{34}S$ values of coeval vent fluids and sulphide phases at 21°N EPR are close to equilibrium fractionation values, shifts in $\delta^{34}S_{H2S}$ of 2-3‰ can be accounted for by the addition of a few percent of reduced seawater sulphate (assuming quantitative sulphate reduction) (Arnold and Sheppard, 1981; Styrt et al., 1981; Zierenberg et al., 1984; Shanks and Seyfried, 1987; Woodruff and Shanks, 1988). Similarly, $\delta^{34}S$ values at the Broken Spur vent site (29°N MAR) which range from -0.5‰-~+3‰, also reflect a predominantly basaltic sulphur source and limited input of reduced seawater sulphate (Duckworth et al., 1995; Butler et al., 1998). The heavier and broader range in $\delta^{34}S$ values reported from the TAG mound are the exception to the general pattern of light $\delta^{34}S$ at sediment free mid ocean ridge hydrothermal sites. Heavier $\delta^{34}S$ values at TAG, which indicate greater seawater influence result, in part from the size, vigour and longevity of hydrothermal activity at this site (Section 5.1.4).

Sulphide $\delta^{34}S$ values in sediment hosted hydrothermal deposits, cover a much larger range: ~-10‰-+15‰, reflecting additional sulphur contributions from sedimentary, bacteriogenic, basement fluid and porewater reservoirs as well as basaltic sulphur and reduced seawater sulphate (e.g. Blum and Puchelt, 1991; Duckworth et al., 1994; Stuart et al., 1994; Peter and Shanks, 1992; Goodfellow and Franklin, 1993). At the Middle Valley vent site (N.JdFR) $\delta^{34}S$ ranges from ~+1.0‰ to +10.0‰ (Goodfellow and Blaise, 1988; Duckworth et al., 1994; Stuart et al., 1994). $\delta^{34}S$ enrichment is almost certainly acquired from seawater sulphate trapped in the overlying turbidite sediments which has been inorganically reduced under hydrothermal conditions by reaction with organic matter (Goodfellow and Blaise, 1988; Duckworth et al., 1994).

The range in $\delta^{34}S$ of ~-4.0‰-+5.0‰ in hydrothermal sulphides from the Guaymas basin reflects mixing of basaltic sulphur, bacteriogenic sulphide, sulphur from the thermal decomposition of organic sulphur bearing compounds and reduced seawater sulphate. Negative $\delta^{34}S$ values, indicate contributions from biogenic hydrogen sulphide from the underlying sediments, and positive values reflect contributions from reduced seawater sulphate (Peter and Shanks, 1992).

The range of $\delta^{34}S$ values (-7.0‰-+13.6‰) at the Kebrit Deep in the Red Sea, also principally reflect contributions from biogenic sulphate reduction and inorganic seawater sulphate reduction. Controls on S isotope fractionation at this site include variable seawater/rock ratios during sulphate reduction, a wide range in temperature and mixing between biogenic H_2S and hydrothermal solutions. Heavy $\delta^{34}S$ values are related to moderate to high temperature sulphides and result from inorganic reduction of seawater sulphate. Lighter $\delta^{34}S$ values are related to biogenic contributions from the sedimentary host rock. In addition bacterial processes are inferred to play an important role in the oxidation of sulphidic material following cessation of smoker activity and this also leads to modification of the S isotopic composition (Blum and Puchelt, 1991).

Negative $\delta^{34}S$ values may also arise via incorporation of sulphur from magmatic volatiles. The significantly light $\delta^{34}S$ values reported from the Valu Fa Ridge hydrothermal site in the Lau Basin may be the result of several processes such as biogenic reduction of sulphate and isotopic fraction of sulphur between reduced and oxidized species, but are most likely the result of direct contributions from ^{32}S enriched magmatic volatile phases (Herzig et al., 1998a).

5.1.4 Sulphur isotopes in the active TAG mound

Prior to ODP drilling of the TAG mound, only 14 $\delta^{34}S$ values, with a range of +4.0 - +6.0‰ (mean =+5.0‰), had been reported from the surface of the TAG mound (Lein et al., 1991). Drilling of the TAG mound provided the first opportunity to study the lateral and vertical S isotope variation in an actively forming massive sulphide deposit. The overall range of measured sulphide $\delta^{34}S$ values from the TAG mound is +0.4 - +10.3‰ with a mean of +7.0‰ (n = 233) (Chiba et al., 1998; Gemmell and Sharpe, 1998; Herzig et al., 1998a; Knott et al., 1998). This is heavier than the mean sulphide $\delta^{34}S$ reported from other sediment-free mid-ocean ridge hydrothermal sites by 3-4‰.

5.1.4.1 Sulphur isotope composition and variation

Despite significant lateral variations in lithology across the mound, mean values and ranges for $\delta^{34}S$ at each drilling site are almost identical:

- **TAG-1:** range +4.4 - +8.9‰, mean = +6.8‰ (n = 114) (Chiba et al., 1998; Gemmell and Sharpe, 1998; Herzig et al., 1998a; Knott et al., 1998).
- **TAG-2**: range +5.4 - +8.5‰ (with the exception of one value at +0.4‰; data outlier), mean = +7.1‰ (n = 31) (Chiba et al., 1998; Gemmell and Sharpe, 1998; Herzig et al., 1998a; Knott et al., 1998).
- **TAG –3:** only one reported $\delta^{34}S$ value = +7.3‰ (Herzig et al., 1998b).
- **TAG-4:** range +4.6 - +9.3‰, mean = +7.1‰ (n = 45) (Gemmell and Sharpe, 1998; Herzig et al., 1998a; Knott et al., 1998).
- **TAG-5:** range +5.4 - +10.3‰, mean = +6.9‰ (n = 42) (Gemmell and Sharpe, 1998; Herzig et al., 1998a; Knott et al., 1998).

The isotopically lightest mineralisation is vein-related; the mean $\delta^{34}S$ of vein-related sulphides is 1.5‰ lighter than the heaviest mean $\delta^{34}S$ associated with altered basalt (Table 5.1). Whilst still minor the largest variations in $\delta^{34}S$ occur between different textural types of sulphide (Table 5.2; Figure 5.4). Porous sulphide is the isotopically lightest textural type with mean $\delta^{34}S$ =+5.74‰. Disseminated sulphide is the isotopically heaviest: mean $\delta^{34}S$ =+7.65‰. In relation to lithology, porous sulphide is most commonly associated with the massive pyrite and pyrite-anhydrite breccias in the upper part of the mound. Disseminated pyrite is largely related to altered basalt from the base of the mound and the underlying stockwork (Gemmell and Sharpe, 1998; Knott et al., 1998).

Existing interpretations of $\delta^{34}S$ values at the TAG mound are somewhat contradictory with some workers inferring significant changes in $\delta^{34}S$ with depth (Knott et al., 1998; Gemmell and Sharpe, 1998), and others stating that there is no significant difference with depth (Chiba et al., 1998; Herzig et al., 1998b). Despite a

Lithology	Min $\delta^{34}S$ ‰	Max $\delta^{34}S$ ‰	Mean $\delta^{34}S$ ‰	Standard deviation	Standard error (1σ)	Number of analyses
Massive pyrite	+0.35	+8.3	+6.5	1.20	0.16	53
Pyrite breccia	+5.1	+7.91	+6.6	0.94	0.24	15
Pyrite-anhydrite breccia	+4.4	+10.27	+6.5	1.02	0.19	29
Pyrite-silica-anhydrite breccia	+5.1	+8.3	+6.4	0.75	0.17	20
Pyrite-silica breccia	+5.7	+9.29	+7.3	0.77	0.10	60
Altered basalt	+6.05	+8.9	+7.6	0.80	0.15	30
Veins	+5.2	+7.51	+6.1	0.65	0.20	11
Total analyses						**218**

Table 5.1: Summary of $\delta^{34}S$ variation with lithology in analyses from ODP drilling of the active TAG mound. Lithological types are listed in descending depth order with the exception of veins, which occur in all depths. For descriptions of the various lithogical types, the reader is referred to Chapter 2 section 2.1.1. There is no significant (95% confidence limit: two sample populations t-test) statistical difference in $\delta^{34}S$ values between different lithological types. Data are compiled from: Chiba et al., 1998; Gemmell and Sharpe, 1998; Herzig et al., 1998a; Knott et al., 1998.

Sulphide Texture	Min $\delta^{34}S$ ‰	Max $\delta^{34}S$ ‰	Mean $\delta^{34}S$ ‰	Standard deviation	Standard error (1σ)	Number of analyses
Porous sulphide	+4.8	+6.6	+5.74	0.76	0.34	5
Massive sulphide	+0.35	+8.3	+6.83	1.15	0.15	55
Vein sulphide	+4.4	+8.41	+6.59	0.88	0.15	34
Crust	+5.1	+6.2	+5.8	0.64	0.37	3
Disseminated sulphide	+5.7	+10.27	+7.65	1.00	0.16	38
Clasts	+5.8	+8.41	+7.24	0.65	0.11	33
Total analyses						**168**

Table 5.2: Summary of $\delta^{34}S$ variation with sulphide texture in analyses from ODP drilling of the active TAG mound. In relation to lithology, porous sulphide is most commonly associated with the massive pyrite and pyrite-anhydrite breccias in the upper part of the mound and disseminated pyrite is largely related to altered basalt from the base of the mound and the underlying stockwork (Gemmell and Sharpe, 1998; Knott et al., 1998). There is no significant (95% confidence limit: two sample populations t-test) statistical difference in $\delta^{34}S$ values between different Textural types. Data are compiled from: Chiba et al., 1998; Gemmell and Sharpe, 1998; Herzig et al., 1998a; Knott et al., 1998.

link between lithological type and depth most interpretations of the data state that no significant variation is observed between different breccia types. Associations between $\delta^{34}S$ and textural types have been made (Gemmell and Sharpe, 1998). Herzig et al (1998) have argued that all data are insignificantly different. Whilst these interpretations may hold true for the individual data sets concerned, if the entire $\delta^{34}S$ dataset from TAG ODP drilling is considered it becomes apparent that there are statistically significant variations in the S isotopic composition at TAG, and that these are related to textural variations and changes in lithological type with depth.

Mean $\delta^{34}S$ values for lithological zones 1 (massive pyrite and pyrite breccias) and 2 (pyrite-anhydrite and pyrite-silica-anhydrite breccias) (Chapter 2) range from +6.4-+6.6‰ and differences between the lithologies are statistically insignificant. However, mean $\delta^{34}S$ values for lithologies from zone 3, pyrite-silica breccias and altered basalt, close to the hydrothermal stockwork at depth in the TAG mound, which are +7.3‰ and +7.6‰ respectively, are statistically, significantly different from those of zones 1 and 2 (Table 5.3 summarizes statistical significance (95% confidence limit; two sample populations t-test) calculations). This supports evidence for a trend to increasing $\delta^{34}S$ with depth (e.g. Knott et al., 1998; Gemmell and Sharpe, 1998), i.e. a temperature control, and can be explained by inorganic reduction of seawater sulphate at depth in the TAG mound with only minor inorganic reduction in the upper parts of the mound. $\delta^{34}S$ variations associated with textural type are more complex. As might be expected, porous sulphide, which is predominantly associated with zone 1 lithologies (e.g. Knott et al., 1998), has the lightest mean $\delta^{34}S$ value of +5.7‰, and disseminated sulphide, which occurs variously throughout all zones but is predominantly associated with zone 3 lithologies, close to the hydrothermal stockwork zone (e.g. Gemmell and Sharpe, 1998; Knott et al., 1998), has the heaviest mean $\delta^{34}S$ value of +7.7‰. $\delta^{34}S$ data for these two textural types are significantly different (95% confidence limit; two sample populations t-test). Interestingly, $\delta^{34}S$ values of sulphide clasts, which occur principally in zone 1 (e.g. Knott et al., 1998; Gemmell and Sharpe, 1998) are significantly different from porous sulphides and sulphide crusts which are also associated predominantly with zone 1 and 2 assemblages. Vein and massive sulphide textures, which are ubiquitous, show varied associations: vein sulphides are only significantly different from the disseminated sulphides of zone 3, whereas massive sulphide is significantly different from both porous sulphide (zone 1) and disseminated sulphide (zone 3). The $\delta^{34}S$ of various textural types and their relationships to lithological zones suggests that different styles of sulphide precipitation (i.e. different sulphide textures) are not responsible for the observed range in $\delta^{34}S$, but they do support the lithogical evidence for a depth control on $\delta^{34}S$ values.

5.1.4.2 Evolution of the sulphur isotope composition

Fluids entering the TAG system at depth should have $\delta^{34}S$ values close to MORB (Mid-Ocean Ridge Basalt) (+0.1 ±0.5‰: Sakai et al., 1984) (Alt et al., 1986; Alt et al., 1989; Shanks et al., 1995). Mixing of this fluid with partially reduced seawater sulphate in the discharge zone produces a modified fluid with a heavier $\delta^{34}S$ value. However, modeling has shown that this process can only increase $\delta^{34}S$ to a maximum of +4.5‰ if the initial end-member fluid has a value close to MORB and a full range of equilibrium and disequilibrium paths occur (Janecky and Shanks, 1988). This is largely due to the fact that addition of seawater lowers the

Lithologies

	Massive pyrite	Pyrite breccia	Pyrite-anhydrite breccia	Pyrite-silica-anhydrite breccia	Pyrite-silica breccia	Altered basalt	Veins
Massive pyrite	~	Same	Same	Same	Different	Different	Same
Pyrite breccia	Same	~	Same	Same	Different	Different	Same
Pyrite-anhydrite breccia	Same	Same	~	Same	Different	Different	Same
Pyrite-silica-anhydrite breccia	Same	Same	Same	~	Different	Different	Same
Pyrite-silica breccia	Different	Different	Different	Different	~	Same	Different
Altered basalt	Different	Different	Different	Different	Same	~	Different
Veins	Same	Same	Same	Same	Different	Different	~

Table 5.3a

Textures

	Porous sulphide	Massive sulphide	Vein sulphide	Sulphide Crusts	Disseminated sulphide	Sulphide clasts
Porous sulphide	~	Different	Same	Same	Different	Different
Massive sulphide	Different	~	Same	Same	Different	Same
Vein sulphide	Same	Same	~	Same	Different	Same
Sulphide Crusts	Same	Same	Same	~	Different	Different
Disseminated sulphide	Different	Different	Different	Different	~	Same
Sulphide clasts	Different	Same	Same	Different	Same	~

Table 5.3b

Table 5.3a and b: Summary tables of statistical significance between $\delta^{34}S$ values for (a) different lithological and (b) different textural types at the active TAG mound: Significance was calculated from a null hypothesis that there is no difference in $\delta^{34}S$ values between each different lithology and textural type. Pairs of data sets which are statistically significantly different (95% confidence limit: two sample populations t-test) are labeled: Different; pairs of data sets which do not show any statistically significant difference are labeled: Same. Lithological types are listed in depth order with massive pyrite from the upper portions of the mound and altered basalt from the basal portions within the hydrothermal stockwork zone; veins are ubiqυιτουσ τηρουγηουτ αλλ λιτηολογιεσ. $\delta^{34}S$ data from the active TAG mound are complied from: Chiba et al., 1998; Gemmell and Sharpe, 1998; Herzig et al., 1998a; Knott et al., 1998.

temperature of the precipitating fluid and causes an increase in E_h such that mixtures of seawater and hydrothermal fluid do not have the capacity to reduce the quantity of sulphate required to increase $\delta^{34}S$ by more than 4.5‰ (Janecky and Shanks, 1988). This is not sufficient to explain the heavy $\delta^{34}S$ values reported from the active TAG mound. Several processes have been suggested to explain heavy $\delta^{34}S$ values at TAG:

- Reaction of the upwelling hydrothermal fluid with previously formed sulphides within the mound and the underlying stockwork leading to a modified fluid slightly enriched in ^{34}S (Gemmell and Sharpe, 1998). However, modelling suggests that under optimum conditions this will only increase $\delta^{34}S$ values by ~2‰ (Janecky and Shanks, 1988).
- Local reduction of seawater sulphate in the shallow subsurface (Herzig et al., 1998b; Knott et al., 1998). The onset of anhydrite precipitation at 150°C means that shallow sulphate reduction is unlikely to result in significant increases in $\delta^{34}S$ since inorganic sulphate reduction required temperatures ≥200°C (see below).
- Thermochemical reduction of pre-existing anhydrite at temperatures exceeding 300°C contributing reduced seawater sulphate to the upwelling hydrothermal fluid (Janecky and Shanks, 1988; Shanks et al., 1995; Herzig et al., 1998b).

The presence of anhydrite to depths of at least 125metres below seafloor (m.b.s.f.) indicates entrainment of seawater into the mound subsurface and maintenance of high temperatures (e.g. Teagle et al., 1998a; Mills and Tivey, 1999). Measurements of anhydrite, sulphate $\delta^{18}O$ indicate precipitation under disequilibrium conditions (Chiba et al., 1998). Since the half-reaction time of oxygen isotope exchange between aqueous sulphate and water under the conditions operating in the TAG mound is calculated to be less than a few minutes (Chiba et al., 1998) the failure to reach equilibrium suggests that anhydrite precipitates rapidly within the anhydrite precipitation zone (Chiba et al., 1998). Additionally, it has been argued that reduction of entrained seawater sulphate would not have a significant effect on the S isotopic composition of the hydrothermal fluid, as seawater sulphate reduction at hydrothermal temperatures is kinetically limited and fluid flow rates are high (e.g. Bluth and Ohmoto, 1988 Woodruff and Shanks, 1988). However, significant contributions from local reduction of entrained seawater sulphate are unlikely since anhydrite precipitation is initiated at ~150°C (removing SO_4^{2-}) and inorganic sulphate reduction requires temperatures in excess of ~200°C, in addition, mixing with cold (~2°C) seawater should result in cooling of the hydrothermal fluid. Despite this, S and O isotopic compositions of anhydrite suggest that at least some sulphate reduction is taking place in the mound (Chiba et al., 1998). $\delta^{34}S$ values of anhydrite from the TAG mound are slightly enriched in heavy $\delta^{34}S$ ($\delta^{34}S$ values up to +23‰: Chiba et al., 1998) compared with seawater (+20.9‰: Rees et al., 1978) which suggests that partial reduction of seawater sulphate has taken place during mixing of the ascending hydrothermal fluid with entrained seawater in the anhydrite precipitation zone. During sulphate reduction at temperatures <380°C isotopically light sulphur is preferentially partitioned into precipitating sulphide and the remaining aqueous sulphate becomes isotopically heavier than the original seawater sulphate (e.g. Ohmoto and Lasage, 1982; Chiba et al., 1998).

An alternative mechanism for generation of heavy $\delta^{34}S$ is sulphate reduction via oxidation of ferrous Fe in basalt, in a shallow circulation system, near the hydrothermal feeder zone at depth (Janecky and Shanks, 1988). However, this effect is insignificant in large, $>10^6$ tonne, deposits as the volume of basalt available for reaction is limited, restricting sulphate reduction in the shallow subsurface, which in turn, leads to homogenisation of the S isotopic composition (Janecky and Shanks, 1988).

The limited potential for sulphate reduction within the TAG mound, and shallow subsurface as a result of anhydrite precipitation, the high fluid flow, temperature constraints and the limited availability of basalt for SO_4^{2-} reduction via oxidation of Fe(II) implies that the heavy $\delta^{34}S$ values must be inherited deep in the hydrothermal upflow zone. Consideration of the lightest $\delta^{34}S$ values within the TAG mound has led Knott et al. (1998) to suggest an end-member fluid with $\delta^{34}S = \sim +5.5‰$. This seems to be a reasonable estimate since the $\delta^{34}S_{H2S}$ of the currently venting fluid at TAG is +6.6-+7.5‰ (Knott et al., 1998; Shanks, 2001). Mixing of a fluid with $\delta^{34}S = \sim +5.5‰$, with reduced sulphate and pre-existing sulphide in the shallow subsurface could explain the heaviest published $\delta^{34}S$ values ($\delta^{34}S$ close to +10‰) reported from the TAG mound.

5.2 Aims and objectives of this study

Whilst the extensive work on S isotope systematics within the TAG mound, following ODP drilling, has provided a general insight in to S isotope systematics in large seafloor hydrothermal deposits, it also demonstrated that investigation of mineral scale S isotope fractionation, related to the complex paragenetic sequence of sulphide precipitation and alteration at such sites, is required for a full understanding of the processes controlling the bulk S isotopic composition. However, due to the difficulties of extracting mineral separates by conventional means, the majority of published data are from bulk sulphide samples or mineral separates where the sample resolution is poor and mixing of phases cannot be ruled out. In addition, classical sampling techniques such as micro-drilling and hand separation greatly exceed the scale of textural and mineralogical variation.

In order to investigate mineral scale S isotope variation of diagenetically altered, mass wasted sulphide, from the relict *Alvin* and *Mir* zones within the TAG hydrothermal field, without the problem of contamination, a novel analytical technique was employed for this study: SO_2 was derived from individual sulphide grains via laser combustion in an oxygenated, vacuum-sealed chamber. The advantage of this technique is that it allows precise measurement of the S isotopic composition between coexisting mineralogical and textural types (for comparison, bulk sulphide samples were also investigated by conventional means). Previous S isotope studies utilizing the in situ laser technique or similar ion microprobe methods (e.g. Deloule et al., 1986; McKibben and Eldridge, 1995; Bawden et al., 2003; McGowan et al., 2003; Peevler et al., 2003) have demonstrated the importance of precise micro-scale analysis, which can provide detailed information about mineralising and alteration processes that cannot be resolved from bulk analyses, in the understanding of the complex fluid and mineral histories associated with sulphide deposits. In most studies the use of in situ S isotope techniques has extended the range in $\delta^{34}S$ previously measured from bulk samples (e.g. Bawden et al., 2003; Peevler et al., 2003) and for some deposits, which had been extensively studied by classical techniques, new results from in situ micro-scale analyses have led to complete revision of paragenetic models (e.g. McGowan et al., 2003).

5.3 Materials and methods

Samples for this study were collected from the sulphide layers of cores: CD102/58, from sediment at the southern periphery of the *Alvin* mound, the sulphide layer occurs between 76-138.5cm depth; and CD102/60, from sediment at the southern extreme of the *Mir* mound, the sulphide layer occurs between 46 - 96cm depth.

5.3.1 Sample preparation

Sulphide mineral separates for S isotope were obtained by hand picking of the >125µm size fraction, under the binocular microscope. The surface of the sulphides were cleaned by ultra sonic agitation in 0.5M HCl for 30 minutes, following which, the samples were washed three times with Milli-Q water and dried overnight at 50°C.

Polished blocks for in situ laser analysis were prepared by setting the mineral separates in epoxy resin following which the epoxy blocks were ground and polished. Three sulphide-rich rock nuggets at depths of: 49.5-53.5cm; 58-63cm; 67.5-71.5cm from Core 60 (the *Mir* core) were set in standard polished blocks (Chapter 4). Sample depths and brief descriptions of the dominant mineralogy are given in Table 5.4.

5.3.2 Conventional S isotope analysis of bulk sulphide separates

5-10mg of sulphide sample were mixed with ~200mg Cu_2O and roasted under vacuum conditions at 1075°C in a furnace for 25 minutes. The resulting SO_2 was then cryogenically purified by vacuum distillation. Isotopic analyses were then carried out on a SIRA II dual inlet mass spectrometer at the Scottish Universities Environmental Research Centre (SUERC), East Kilbride. The S isotope composition is reported as the $^{34}S/^{32}S$ ratio of the sample relative to Canon Diablo Troilite (CDT) ($^{34}S/^{32}S$ = 0.0450045; Ault and Jensen, 1963), expressed by the notation $\delta^{34}S$ defined by Equation 5.8:

$$\delta^{34}S_{sample} = \left[\frac{^{34}S/^{32}S_{sample}}{^{34}S/^{32}S_{CDT}} - 1 \right] \times 1000 \tag{5.8}$$

External precision and accuracy were monitored by simultaneous repeat analyses of internal and international standards: CP-1: chalcopyrite (-4.6‰); NBS-123: sphalerite (+17.1‰); and IAEA-S-3: silver sulphide (-31‰). Analytical uncertainty was generally better than ±0.2‰.

5.3.3 In situ laser combustion S isotope analysis

A polished block containing sulphide grains was placed within the sample chamber of the laser port, under vacuum conditions, and a shot of O_2 introduced. In situ laser extraction of sulphide sulphur was performed following the method of Fallick et al (1992). Typically, laser analyses were carried out on areas of ~200 by 300µm (Figure 5.5). The resulting SO_2 was then cryogenically purified in a vacuum distillation line connected to the laser port, and the purified gas run directly into the mass spectrometer. Isotopic analyses were carried out on a SIRA II dual inlet mass spectrometer. External precision and accuracy were monitored by simultaneous repeat analyses of internal and international standards: CP-1; NBS-123; and IAEA-S-3. Analytical uncertainty was generally better than ±0.3‰. All in situ laser analyses were carried out at SUERC.

Sample	Depth interval down core (cm)	Bulk conventional S isotope analyses	Sphalerite conventional S isotope analyses	In situ laser S isotope analyses	Dominant sulphide mineralogy
CD102 58					
58-90	76.5-78.5	X	X		Py with minor Cp
58-91	77-79		X		Sphalerite separate
58-93	79-80			X	Py & Sp with minor Cv
58-94	80-81	X	X	X	Py with minor Sp, Cp & Cv
58-96	82.5-83.5	X	X		Py
58-98	84-86	X		X	Py & Sp
58-104	90-92		X		Sphalerite separate
58-106	92-94	X			Py with minor Cp & Cv
58-110	96-98	X		X	Py with minor Cp
58-112	98-100			X	Py
58-116	102-105	X		X	Py with minor Sp
58-122	108-110	X		X	Py with minor Sp
58-128	114-116.5	X		X	Py & Cp with minor Cv
58-136	122-124	X		X	Py
CD102/60					
60-59	48-50	X			Py
60-60	49.5-53.5			X	Py & Cp
60-69	58-60	X			Py with minor Cp
60-71	60-63			X	Py & Cp
60-78	67.5-71.5			X	Py
60-84A	73-75			X	Py & Sp
60-84	73-75			X	Py with minor Sp
60-86	75-77	X			Py with minor Sp & Cp
60-90	79-81	X			Py & Sp with minor Cp
60-92	81-83			X	Py & Cp
60-94	83-85			X	Py & Cp with minor Cv
60-98	87-89	X		X	Py with minor Cp

Table 5.4: Summary of all S isotope samples and analyses from cores: CD102/58 and CD102/60. Mineral abbreviations: Py = pyrite; Cp = chalcopyrite; Sp = sphalerite; Cv = covellite.

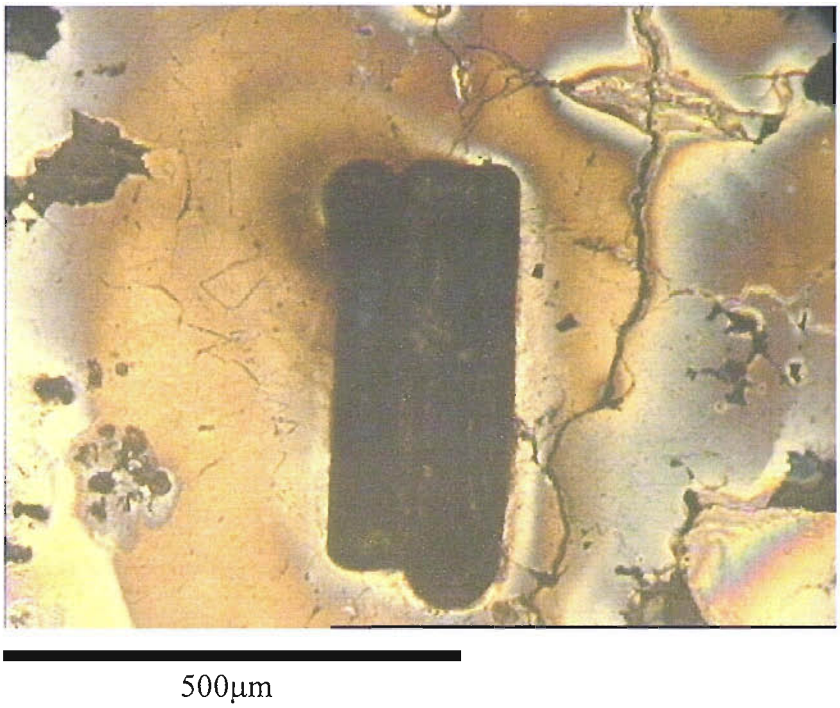

Figure 5.5: The laser combustion S isotope technique removes problems associated with contamination and allows precise targeting of mineral and textural types. Above is an example of a laser track within a fractured pyrite grain from sample 60-84A (Mir zone).

The laser method results in a mineral specific sulphur isotope fractionation between the host mineral and the SO_2 gas produced via combustion (Kelley and Fallick, 1990). Experimentally determined fractionation correction factors are currently available for several sulphide and sulphosalt minerals for the SUERC laboratory (Wagner et al., 2002).

5.4 Results

CD102/58: The Alvin Core

Sulphur isotope ratios were measured for 10 bulk sulphide samples from depths of 76.5 - 124cm and 5 hand picked sphalerite separates from depths of 76.5 - 92cm by conventional means, and for 24 mineral separates from depths of 79.5 - 123cm, by in situ laser combustion (the sulphide layer of CD102/58 occurs at 76 - 138.5cm).

CD102/60: The Mir Core

Sulphur isotope ratios were measured for 5 bulk sulphide samples from depths of 49-88cm by conventional means, and 26 mineral separates from depths of 51.5-88cm by in situ laser combustion (the sulphide layer of CD102/60 occurs at 46-96cm depth).

Conventional S isotope analyses of bulk sulphide samples from both cores are listed in Table 5.5. Sphalerite separates from Core 58 measured by conventional methods are listed in Table 5.6. Results of in situ laser combustion analyses are listed in Table 5.7.

5.4.1 Bulk Sulphide Samples

5.4.1.1 CD102/58: The *Alvin* core

Sulphur isotope ratios were measured by conventional means for 10 bulk sulphide samples from depths of 76.5-124cm (the sulphide layer of CD102/58 occurs at 76-138.5cm). The $\delta^{34}S$ values of the bulk sulphide samples fall within a narrow range: $\delta^{34}S_{\text{bulk sulphide}}$ +6.9-+8.3‰, with a mean value =+7.6‰ ±0.14 (1σ) (n=10). This is within the range of $\delta^{34}S$ values reported from the active TAG mound: +4.4-10.3‰ (mean =+6.9‰ ±0.31 (1σ) (n=233)) (Chiba et al., 1998; Gemmell and Sharpe, 1998; Herzig et al., 1998a; Knott et al., 1998) and $\delta^{34}S_{H2S}$ in black smoker fluids (+6.6-+7.5‰: Knott et al., 1998; Shanks, 2001) from the active TAG mound. This range is 3-4‰ heavier than $\delta^{34}S$ at other sediment free mid-ocean ridge hydrothermal sites (Figure 5.1). Whilst the dominant mineral in Core 58 sulphide sub-samples is pyrite, the assemblage and modal proportions of sphalerite, chalcopyrite and covellite vary from sample to sample. Because the data fall within a narrow range there is little variation in bulk sulphide $\delta^{34}S$ values with mineralogy or depth downcore (Figure 5.6a). However, the lightest values show some association with sphalerite occurrence and the heaviest with covellite.

5.4.1.2 CD102/60: The *Mir* core

Sulphur isotope ratios were measured by conventional means for 5 bulk sulphide samples from depths of 49 - 88cm. The $\delta^{34}S$ values of the bulk sulphide samples, like those for Core 58, have a restricted range of +6.4 -

Sample	Depth (cm)	Dominant Mineralogy	Line Number	Gas Yield %	$\delta^{34}S_{CDT}$ (‰)
CD102/58					
58-90	77.5	Py with minor Cp	SA9329	83	+7.0
58-94	80.5	Py with minor Sp, Cp and trace Cv	SA9359	72	+6.9
58-96	83	Py	SA9332	Off scale	+7.6
58-98	85	Py & Sp	SA9330	89	+7.6
58-106	93	Py with minor Cp & Cv	SA9331	95	+8.3
58-110	97	Py with minor Cp	SA9336	Off scale	+7.9
58-116	103	Py with minor Sp	SA9328	95	+7.3
58-122	109	Py with minor Sp	SA9335	Off scale	+7.9
58-128	114.75	Py & Cp with minor Cv	SA9333	92	+7.9
58-136	123	Py	SA9334	99	+7.3
				Mean	**+7.6 ± 0.14**
CD102/60					
60-59	49	Py	SA9355	72	+6.4
60-69	59	Py with minor Cp	SA9357	80	+7.7
60-86	76	Py with minor Sp & Cp	SA356	89	+7.8
60-90	80	Py & Sp with minor Cp	SA9365	70	+6.7
60-98	88	Py with minor Cp	SA9339	62	+6.6
				Mean	**+7.0 ± 0.29**

Table 5.5: Summary of conventional S isotope analyses of bulk sulphide samples from CD102/58 and CD102/60. Depth is given as the mid depth for the sampling interval. Mean is shown ±1 standard error.

Sample	Depth (cm)	Line Number	$\delta^{34}S_{CDT}$ (‰)
58-90.5	77.5	SA9900	+6.3
58-91	78	SA9898	+9.8
58-94	80.5	SA9897	+5.9
58-96	83	SA9896	+6.2
58-104	91	SA9899	+7.1
		Mean	**+7.1 ±0.71**

Table 5.6: Summary of conventional S isotope analyses of sphalerite separates from CD102/58. Depth is given as the mid depth for the sampling interval. Mean is shown ±1 standard error.

Sample	Depth (cm)	Line number	Min	Description	Sulphide Generation	$\delta^{34}S_{cdt}$ (‰) mineral
58-93	79.5	LS5948	Sp	Anhedral overgrowth on euhedral Py grain	Secondary	+28.4§
		LS5949	Py	Aggregate of sub-euhedral Py cubes	Secondary	+8.9
		LS5950	Py	Pristine euhedral Py cube	Secondary	+9.4
		LS5951	Py	Aggregate of porous sub-euhedral Py cubes	Secondary	+8.9
58-94	80.5	LS5958	Py	Fractured, euhedral cubic Py	Secondary	+10.0
		LS5959	Py	Porous euhedral cubic Py	Primary	+11.0
58-98	85	LS5954	Py	Radial clusters of euhedral Py cubes	Secondary	+11.8
		LS5955	Py	Aggregate of euhedral, porous and fractured Py	Primary	+11.4
58-110	97	LS5938	Py	Aggregate of fractured subhedral Py with corroded cores	Primary	+17.5
		LS5940	Py	Sub-euhedral pitted cubic Py	Primary	+12.4
58-112	99	LS5941	Py	Sub-anhedral pitted Py with radial fractures	Primary	+24.0§
		LS5944	Py	Radial aggregate of euhedral cubic Py	Secondary	+9.4
		LS5945	Py	Pristine anhedral Py	Secondary	+7.3
58-116	103.5	LS5927	Sp	Anhedral 'holely' Sp encroaching anhedral Py	Secondary	+14.5§
		LS5928	Py	Extremely porous anhedral Py	Primary	+12.8
58-122	109	LS5923	Cp	Fractured anhedral Cp with Py rim, altered to Cv along some fractures	Primary	+9.5
		LS5925	Py	Banded, corroded Py	Secondary	+8.8
		LS5926	Py	Pristine subhedral Py	Secondary	+9.4
58-128	114.75	LS5920	Py	Aggregate of pristine, euhedral Py cubes	Secondary	+7.5
		LS5921	Py	Euhedral cubic Py	Secondary	+9.7
		LS5922	Py	Sub-euhedral corroded Py	Primary	+9.0
58-136	123	LS5917	Py	Aggregate of slightly porous euhedral Py cubes	Primary	+13.0
		LS5918	Py	Euhedral cubic Py	Secondary	+8.8
		LS5919	Py	Aggregate of porous sub-euhedral cubic Py, with irregular Cp overgrowths	Primary	+14.3
					Mean§	**+12.0‰ ±1.0**
					Mean	**+10.5‰ ±0.5**

Table 5.7a: Summary of in situ laser combustion S isotope analyses from CD102/58. Mean§ is calculated without samples which may have been contaminated by resin; denoted by §.

Tables 5.7a and b: Summary of in situ laser combustion S isotope analyses. In both cores depth is given as the mid-depth for the sampling interval. Mineral abbreviations: Py=pyrite; Cp=chalcopyrite; Sp=sphalerite; Cv=covellite. Mean values are shown as ±1 standard error. Sulphide generation is assigned from textural studies (Chapter 4).

Sample	Depth (cm)	Line number	Min	Description	Sulphide Generation	$\delta^{34}S_{cdt}$ (‰) mineral
60-60	51.5	LS5775	Py	Euhedral cubic Py slightly pitted	Primary	+7.9
		LS5776	Py	Euhedral cubic Py	Secondary	+9.1
		LS5778	Py	Subhedral slightly corroded Py	Primary	+8.9
60-71	61.5	LS5781	Cp	Subhedral Cp with corroded edges	Primary	+7.6
		LS5782	Cp	Suhedral slightly fractured Cp	Primary	+10.1
		LS5783	Py	Aggregate of subhedral Py	Primary	+10.4
		LS5784	Py	Anhedral Py	Primary	+14.7
		LS5785	Cp	Subhedral Cp	Primary	+10.2
		LS5787	Cp	Subhedral Cp	Primary	+10.0
		LS5788	Cp	Corroded dendritic Cp	Primary	+10.1
		LS5789	Py	Sub-euhedral cubic Py	Secondary	+8.8
		LS5791	Py	Sub-euhedral cubic Py	Secondary	+10.1
		LS5792	Cp	Anhedral Cp with corroded edges	Primary	+7.4
		LS5793	Py	Subhedral Py	Secondary	+8.9
60-78	69.5	LS5786	Py	An-subhedral pitted Py	Primary	+6.2
60-84A	74	LS5929	Py	Slightly fractured subhedral Py encroached by Sp	Secondary	+9.1
60-84	74	LS5931	Py	Porous euhedral Py	Primary	+10.5
		LS5932	Py	Aggregate of porous euhedral cubic Py	Primary	+9.0
60-92	82	LS5961	Cp	Anhedral Cp with Cv overgrowth rimmed on one side by Py	Primary	+11.7
		LS5962	Py	Anhedral corroded Py	Primary	+8.8
60-94	84	LS5933	Cp	Fractured anhedral Cp with Cv overgrowth	Primary	+13.7
		LS5935	Cp	Fractured Cp encroached by Cv	Primary	+15.8
		LS5937	Py	Fracture subhedral Py	Secondary	+7.3
60-98	88	LS5914	Py	Pristine euhedral Py	Secondary	+11.4
		LS5915	Py	Pristine euhedral Py	Secondary	+9.9
		LS5916	Py	Sub-euhedral corroded Py	Primary	+10.3
					Mean	**9.9 ±0.4**

Table 5.7b: **Summary of in situ laser combustion S isotope analyses from CD102/60.**

+7.8‰ with a mean = +7.0‰ ±0.29 (1σ) (n=5). Again this is well within the previously reported range of $\delta^{34}S_{sulphide}$ (Chiba et al., 1998; Gemmell and Sharpe, 1998; Herzig et al., 1998a; Knott et al., 1998) and $\delta^{34}S_{H2S}$ in black smoker fluids (Knott et al., 1998; Shanks, 2001) from the active TAG mound and is heavier than $\delta^{34}S$ reported at other sediment free mid ocean ridge hydrothermal sites. The dominant mineral constituent of all the bulk sulphide samples is pyrite with minor chalcopyrite and trace sphalerite. No overall depth or mineralogical stratigraphy can be seen in the bulk S isotope data downcore (Figure 5.6b).

5.4.2 In Situ Sulphide Laser Separates

5.4.2.1 CD102/58: The *Alvin* core

Sulphur isotope ratios were measured by in situ laser combustion for 24 sulphide mineral separates from depths of 79.5 - 123cm (Table 5.7a). Three data points from in situ laser combustion analyses at depths of 79.5cm ($\delta^{34}S$ =+28.43‰); 99cm ($\delta^{34}S$ =+23.95‰); and 103.5cm ($\delta^{34}S$ =+14.45‰) are discarded from the data set due to distillation problems which are related to resin contamination (see section 5.4.2.3). The $\delta^{34}S$ data from in situ laser analyses are heavier than bulk sulphide samples and show a much wider range: $\delta^{34}S_{sulphide\ separates}$ +7.3 - +17.5‰, with a mean value =+10.5‰ ±0.5 (1σ) (n=21). Some of the $\delta^{34}S$ values reported here are significantly heavier than previously published data for sediment free mid-ocean ridges including data from the TAG mound; the heaviest $\delta^{34}S$ value of +17.5‰ (from primary corroded pyrite) is 7.2‰ heavier than the most ^{34}S enriched value reported from the TAG mound. In contrast to bulk sulphide $\delta^{34}S$, data from in situ laser analyses do show variation with depth downcore (Figure 5.7a). Mean values for individual depths show a gradual increase in the value of $\delta^{34}S$ from +9.0‰ at 79.5cm, close to the top of the sulphide layer (76cm) to +14.9‰ at 97cm depth. Below this there are two further maxima of +12.8‰ and +12.0‰ at depths of 103.5cm and 123cm respectively.

5.4.2.2 CD102/60: The *Mir* core

Sulphur isotope ratios were measured by in situ laser combustion for 26 sulphide mineral separates from depths of 51.5 - 88cm (Table 5.7b). The $\delta^{34}S$ data from in situ laser analyses are again heavier than bulk sulphide samples and show a much wider range: $\delta^{34}S_{sulphide\ separates}$ +6.2 - +15.8‰, with a mean of +9.9‰ ±0.43 (1σ) (n=26). Some of the $\delta^{34}S$ values reported here are significantly heavier than previously published data for sediment free mid-ocean ridges including data from the TAG mound; the heaviest $\delta^{34}S$ value of +15.8‰ (from primary chalcopyrite overgrown by covellite) is 5.5‰ heavier than the most ^{34}S enriched value reported from the TAG mound. In contrast to the bulk sulphide samples, data from in situ laser analyses show variation with depth down core (Figure 5.7b). Mean values for individual depths show a gradual decrease downcore from values at the top of the sulphide layer which are close to or exceeding +10‰, to values <+10‰ towards the base of the sulphide layer. A minimum in $\delta^{34}S$ of +6.2‰ occurs at 82cm. In addition, the area surrounding the second maxima (69.5 - 84cm) corresponds to an increase in the modal percentage of Fe-oxide/oxyhydroxide phases and secondary covellite and atacamite downcore towards the base of the sulphide layer.

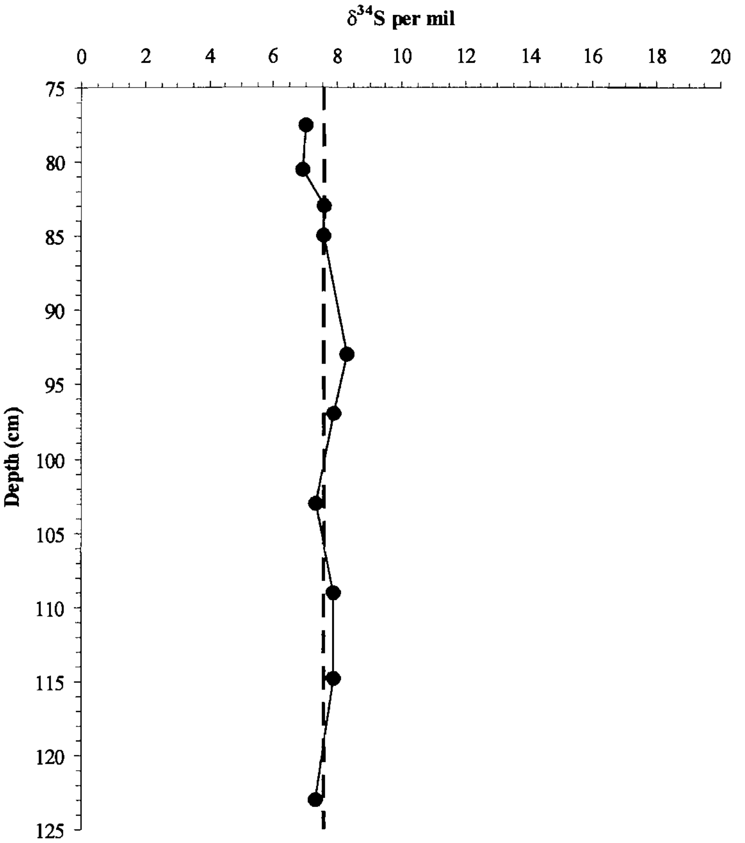

Figure 5.6a: Downcore profile of bulk sulphide δ^{34}S values for CD102/58. Black dashed line indicates the mean δ^{34}S value.

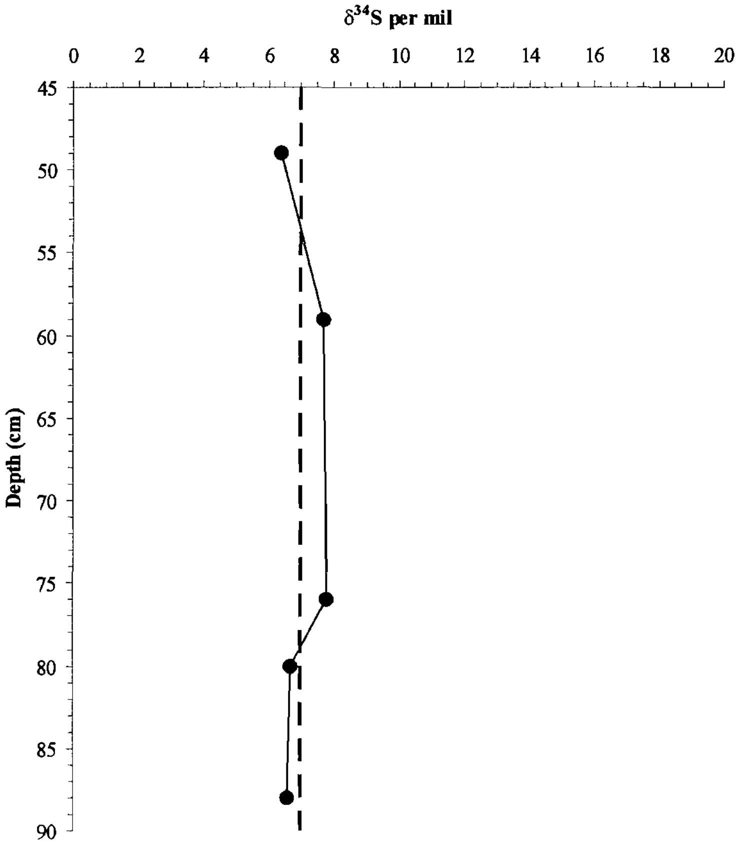

Figure 5.6b: Downcore profile of bulk sulphide δ^{34}S values for CD102/60. Black dashed line indicates the mean δ^{34}S value.

Figure 5.6: Downcore profiles of bulk sulphide δ^{34}S values measured by conventional methods.

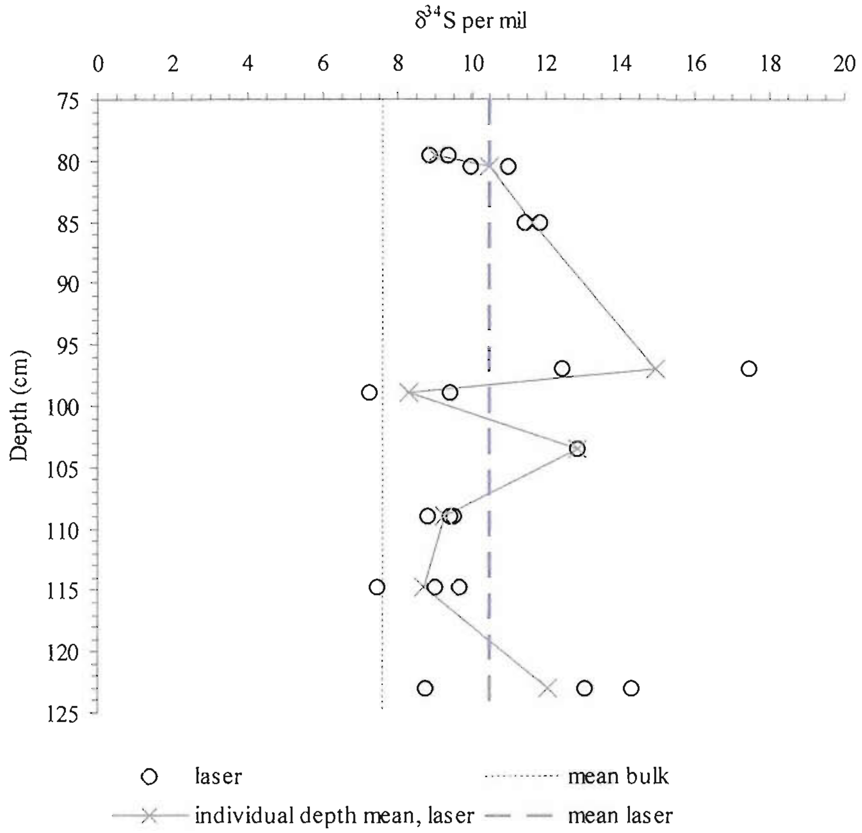

Figure 5.7a: Downcore profile of laser sulphide δ^{34}S values for CD102/58.

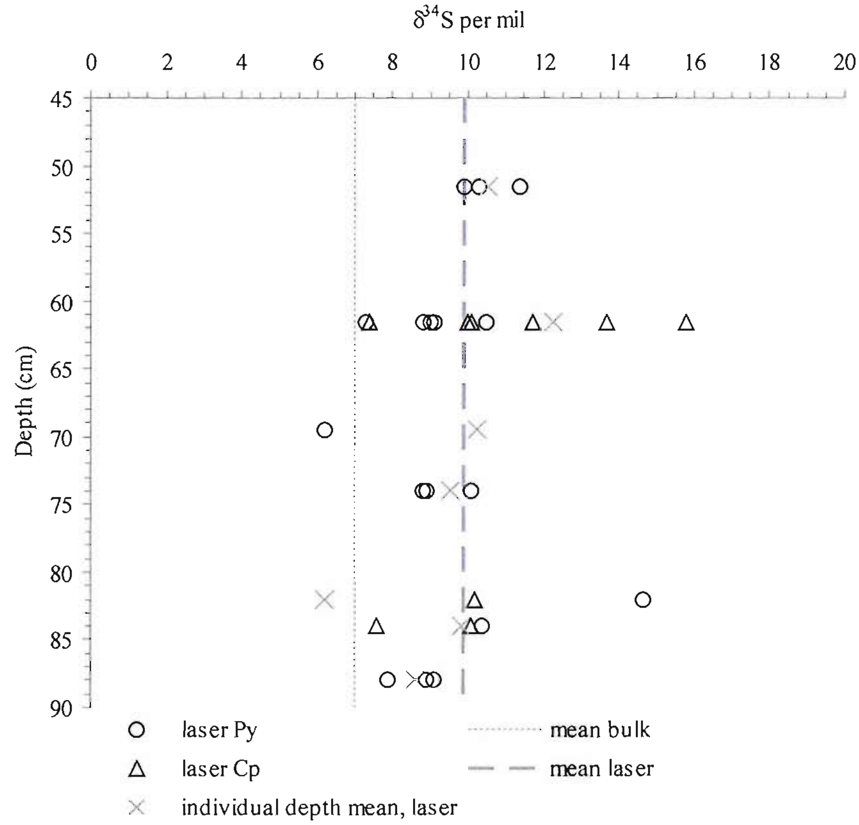

Figure 5.7b: Downcore profile of laser sulphide δ^{34}S values for CD102/60.

Figure 5.7: Downcore profiles of δ^{34}S values of sulphide separates measured by in situ laser combustion. Black dashed line indicates the mean δ^{34}S value of bulk sulphide samples measured by conventional means. The grey dashed line indicates the mean δ^{34}S value of laser sulphide samples. The individual depth mean refers to sample depths where there is more than one data point.

5.4.2.3 Validity of the Laser Sulphur Isotope Data

Discrepancies between the mean $\delta^{34}S$ value of bulk samples measured by the conventional method, and the mean $\delta^{34}S$ value of sulphide separates measured by the laser method, suggest that the novel $\delta^{34}S$ values generated by the laser method require careful consideration and validation. Although there was no analysis of reference sulphide material by the laser technique, the conventional method internal and international standards: CP-1 ($\delta^{34}S$ -4.6‰); NBS-123 ($\delta^{34}S$ +17.1‰); and IAEA-S-3 ($\delta^{34}S$ -31.0‰) were run during the laser analysis to monitor external precision and accuracy. Since the analytical uncertainty for these standard materials was generally better than ±0.2‰ any error in the laser data must be generated during the laser combustion of individual sulphide crystals and/or during the distillation process. There are three major factors which may have affected the laser sulphur isotope values and produced the novel results and the discrepancies between the data collected by laser and conventional means, these are:

1. Distillation problems – related to resin contamination;
2. Induced fractionation generated during the laser combustion step;
3. Sampling bias and artefacts.

Distillation Problems

Distillation problems were encountered during analysis of samples which had small surface areas (typically <100μm^2), and/or where the sulphide crystal was thin. During the combustion of such samples some of the epoxy resin in which the sulphides were set was also volatized, this was seen as an explosive burn. Contamination by organic compounds, e.g. acetone, released by the resin cause the gas evolved to 'stick' to the distillation apparatus and several distillations are then required to produce a gas clean enough to run on the mass spectrometer (A. Boyce. Pers. Comm.). When volatization of resin occurs, the $\delta^{34}S$ value produced is always higher than expected. One way to minimise the problem of resin volatization could be to polish samples with wax involving no resin. However, the samples used in this study were too small for wax polishing and required setting in epoxy resin to hold the samples together. All samples which gave particularly explosive burns during combustion and which required more than one distillation are rejected from the data set. As such sphalerite laser data points from 79.5 and 103.5cm depth (line numbers LS5948 & LS5927, $\delta^{34}S$ = +28.4‰ & +14.5‰ respectively) and one pyrite laser data point from 99cm depth (line number LS5941, $\delta^{34}S$ = +24.0‰) have been discarded from further analysis of the data set and are not shown on subsequent graphical plots.

Laser Induced Fractionation

Fractionation of sulphur isotopes during the laser combustion step is likely to be controlled by crystallographic structure and mineral composition particularly bond strength (Wagner et al. 2002). This can be illustrated by problems encountered during laser analysis of sphalerite from Core 58. Despite sphalerite comprising up to 27.9 wt% of a bulk sample from the Core 58 sulphide layer (calculated assuming all Zn is held as ZnS) analysis by laser combustion was problematical. This is essentially because the majority of sphalerite from the *Alvin* core is Fe-poor (Chapter 4). During laser combustion the S in Fe-poor sphalerites dissociates too rapidly to form SO_2 with the available oxygen (A. Boyce. Pers. Comm.). In such cases, a thin film of elemental sulphur was deposited on the roof of the sample chamber. This suggests that the mineral crystal structure (which is controlled by the mineral composition) is likely to have a major effect on fractionation during laser combustion. Induced isotopic fractionations generated during laser combustion are likely to account for isotopic shifts of ~1‰ (A. Boyce. Pers. Comm.). Table 5.7 shows the data corrected for this fractionation.

The laser sulphide separates data show an average +2.8‰ shift from mean bulk values after correction for fractionation; this suggests two things: 1) the laser results show 'real' heavy data and/or; 2) there is some other fractionation at work which is unaccounted for.

- 'Real' heavy values: this is a distinct possibility. As previously discussed all published laser and ion microprobe sulphur data to date have extended the range of $\delta^{34}S$ to higher values. The difficulty here is that it was not possible to check these data independently by running conventional and laser methods on the same sample.
- Other Fractionation: again this is a real possibility and again, this could not be tested within the scope of this thesis. Investigations into other unknown fractionations will however, be carried out prior to publication of these data.

As these discrepancies are not resolved here, a correction factor of +2.8‰ (this is the difference between the mean bulk $\delta^{34}S$ value and the mean laser $\delta^{34}S$ value) is applied to the laser data (Table 5.8). Following a +2.8‰ correction sulphide separates from Core 58 have a range in $\delta^{34}S$ of +4.5‰-+14.7‰ with a mean of +7.7‰±0.5 (n=21), this is within error of the bulk sulphide mean for this core, $\delta^{34}S_{\text{bulk sulphide}}$ =+7.6‰±0.1 (n=10) (Figure 5.8a), and sulphide separates from Core 60 have a range in $\delta^{34}S$ of +3.4‰-+13.0‰ with a mean of +7.1‰±0.4 (n=26), this is also within error of the bulk sulphide mean for this core, $\delta^{34}S_{\text{bulk sulphide}}$ =+7.0‰±0.3 (n=5) (Figure 5.8b). These corrected laser $\delta^{34}S$ values are used in all further discussion of the laser data.

Sampling bias and artefacts

Differences between the bulk sulphide $\delta^{34}S$ values measured by conventional methods and the laser sulphide $\delta^{34}S$ values may also be related to sampling bias. For Core 58, 21 out of the 24 laser analyses were performed on pyrite grains; 2 on sphalerite and 1 on chalcopyrite. Out of these both the sphalerite analyses and one pyrite analysis have been discarded from the data set due to distillation problems (see above). In the cases of chalcopyrite, many of the grains were too small for analysis, or samples were contaminated either by other mineral phases, or by epoxy resin. In addition, chalcopyrite was only a trace component in the >125µm size fraction used for analysis; much of the chalcopyrite identified by XRD analyses of the same samples must be in the fine fraction (<125µm). The lack of sphalerite laser $\delta^{34}S$ values are due to the difficulties associated with analysis of sphalerite S isotopes by the laser method. In order to investigate sphalerite S isotopes 5 hand picked sphalerite separates were run for S isotopes using the conventional method. The results of these analyses are listed in Table 5.6). $\delta^{34}S$ for the conventionally analysed sphalerites ranges from +5.9-+9.8‰; mean =+7.1‰±0.7 (1σ) (n=5). Although sphalerite $\delta^{34}S$ values follow the general trend of Core 58 bulk sulphide samples to heavier values downcore (Figure 5.9) all sphalerite $\delta^{34}S$values, with the exception of data from 78cm depth ($\delta^{34}S$ =+9.8‰), are lighter than bulk sulphide $\delta^{34}S$ measured by conventional means. Bulk

Sample	Depth (cm)	Line number	Min	Description	Sulphide Generation	$\delta^{34}S$ (‰) Mineral measured	$\delta^{34}S$ (‰) Mineral -2.8‰ fractionation
58-93	79.5	LS5949	Py	Aggregate of sub-euhedral Py cubes	Secondary	+8.7	+5.9
		LS5950	Py	Pristine euhedral Py cube	Secondary	+9.4	+6.6
		LS5951	Py	Aggregate of porous sub-euhedral Py cubes	Secondary	+8.9	+6.1
58-94	80.5	LS5958	Py	Fractured, euhedral cubic Py	Secondary	+10.0	+7.2
		LS5959	Py	Porous euhedral cubic Py	Primary	+11.0	+8.2
58-98	85	LS5954	Py	Radial clusters of euhedral Py cubes	Secondary	+11.8	+9.0
		LS5955	Py	Aggregate of euhedral, porous and fractured Py	Primary	+11.4	+8.6
58-110	97	LS5938	Py	Aggregate of fractured subhedral Py with corroded cores	Primary	+17.5	+14.7
		LS5940	Py	Sub-euhedral pitted cubic Py	Primary	+12.4	+9.6
58-112	99	LS5944	Py	Radial aggregate of euhedral cubic Py	Secondary	+9.4	+6.6
		LS5945	Py	Pristine anhedral Py	Secondary	+7.3	+4.5
58-116	103.5	LS5928	Py	Extremely porous anhedral Py	Primary	+12.8	+10.0
58-122	109	LS5923	Cp	Fractured anhedral Cp with Py rim, altered to Cv along some fractures	Primary	+9.5	+6.7
		LS5925	Py	Banded, corroded Py	Secondary	+8.8	+6.0
		LS5926	Py	Pristine subhedral Py	Secondary	+9.4	+6.6
58-128	114.75	LS5920	Py	Aggregate of pristine, euhedral Py cubes	Secondary	+7.5	+4.7
		LS5921	Py	Euhedral cubic Py	Secondary	+9.7	+6.9
		LS5922	Py	Sub-euhedral corroded Py	Primary	+9.0	+6.2
58-136	123	LS5917	Py	Aggregate of slightly porous euhedral Py cubes	Primary	+13.0	+10.2
		LS5918	Py	Euhedral cubic Py	Secondary	+8.8	+6.0
		LS5919	Py	Aggregate of porous sub-euhedral cubic Py, with irregular Cp overgrowths	Primary	+14.3	+11.5
					Mean	**+10.5‰±0.5**	**+7.7‰±0.5**

Table 5.8a: Summary of in situ laser combustion S isotope analyses from CD102/58 corrected for fractionation during laser combustion.

Tables 5.8a and b: Summary of in situ laser combustion S isotope analyses. In both cores depth is given as the mid-depth for the sampling interval. Mineral abbreviations: Py=pyrite; Cp=chalcopyrite; Sp=sphalerite; Cv=covellite. Mean values are shown as ±1 standard error. Sulphide generation is assigned from textural studies (Chapter 4).

Sample	Depth (cm)	Line number	Min	Description	Sulphide Generation	$\delta^{34}S$ (‰) Mineral measured	-2.8‰ fractionation
60-60	51.5	LS5775	Py	Euhedral cubic Py slightly pitted	Primary	+7.9	+5.1
		LS5776	Py	Euhedral cubic Py	Secondary	+9.1	+6.3
		LS5778	Py	Subhedral slightly corroded Py	Primary	+8.9	+6.1
60-71	61.5	LS5781	Cp	Subhedral Cp with corroded edges	Primary	+7.6	+4.8
		LS5782	Cp	Suhedral slightly fractured Cp	Primary	+10.1	+7.3
		LS5783	Py	Aggregate of subhedral Py	Primary	+10.4	+7.6
		LS5784	Py	Anhedral Py	Primary	+14.7	+11.9
		LS5785	Cp	Subhedral Cp	Primary	+10.2	+7.4
		LS5787	Cp	Subhedral Cp	Primary	+10.0	+7.2
		LS5788	Cp	Corroded dendritic Cp	Primary	+10.1	+7.3
		LS5789	Py	Sub-euhedral cubic Py	Secondary	+8.8	+6.0
		LS5791	Py	Sub-euhedral cubic Py	Secondary	+10.1	+7.3
		LS5792	Cp	Anhedral Cp with corroded edges	Primary	+7.4	+4.6
		LS5793	Py	Subhedral Py	Secondary	+8.9	+6.1
60-78	69.5	LS5786	Py	An-subhedral pitted Py	Primary	+6.2	+3.4
60-84A	74	LS5929	Py	Slightly fractured subhedral Py encroached by Sp	Secondary	+9.1	+6.3
60-84	74	LS5931	Py	Porous euhedral Py	Primary	+10.5	+7.7
		LS5932	Py	Aggregate of porous euhedral cubic Py	Primary	+9.0	+6.2
60-92	82	LS5961	Cp	Anhedral Cp with Cv overgrowth rimmed on one side by Py	Primary	+11.7	+8.9
		LS5962	Py	Anhedral corroded Py	Primary	+8.8	+6.0
60-94	84	LS5933	Cp	Fractured anhedral Cp with Cv overgrowth	Primary	+13.7	+10.9
		LS5935	Cp	Fractured Cp encroached by Cv	Primary	+15.8	+13.0
		LS5937	Py	Fracture subhedral Py	Secondary	+7.3	+4.5
60-98	88	LS5914	Py	Pristine euhedral Py	Secondary	+11.4	+8.6
		LS5915	Py	Pristine euhedral Py	Secondary	+9.9	+7.1
		LS5916	Py	Sub-euhedral corroded Py	Primary	+10.3	+7.5
					Mean	**+9.9‰ ±0.4**	**+7.1‰±0.4**

Table 5.8b: Summary of in situ laser combustion S isotope analyses from CD102/60 corrected for fractionation during laser combustion.

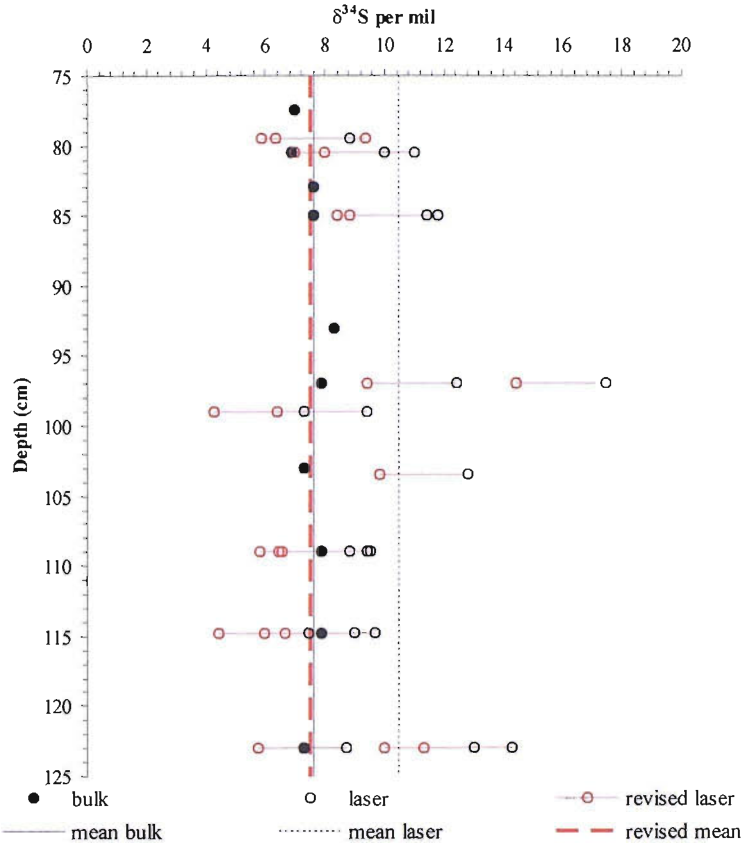

Figure 5.8a: CD102/58

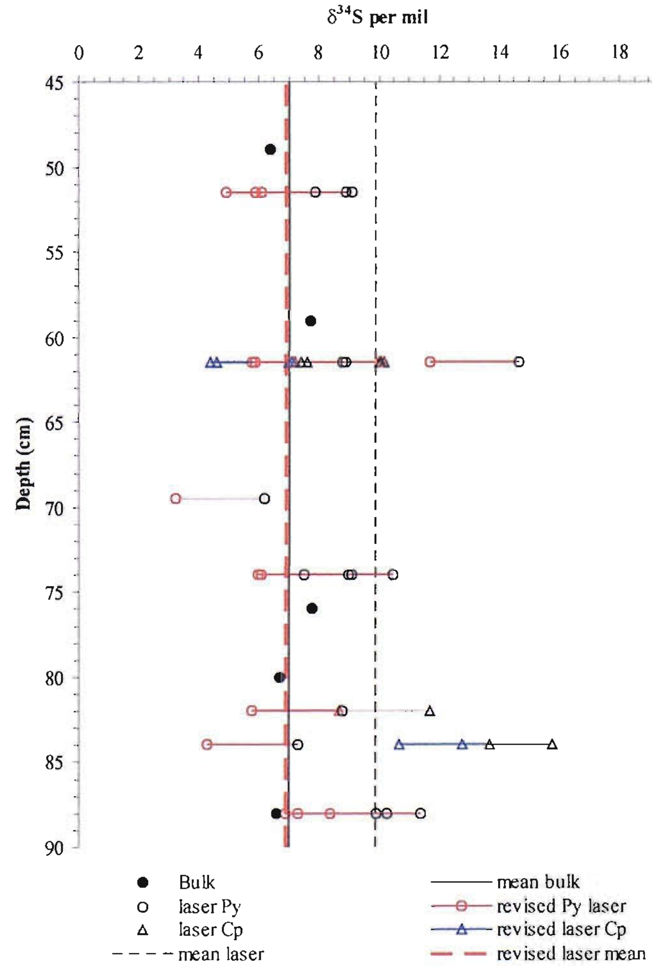

Figure 5.8b: CD102/60

Figure 5.8: Revised downcore profiles, assuming laser induced fractionation of +2.8 per mil, of δ^{34}S values of mineral separates measured by in situ laser combustion for Cores 58 & 60.

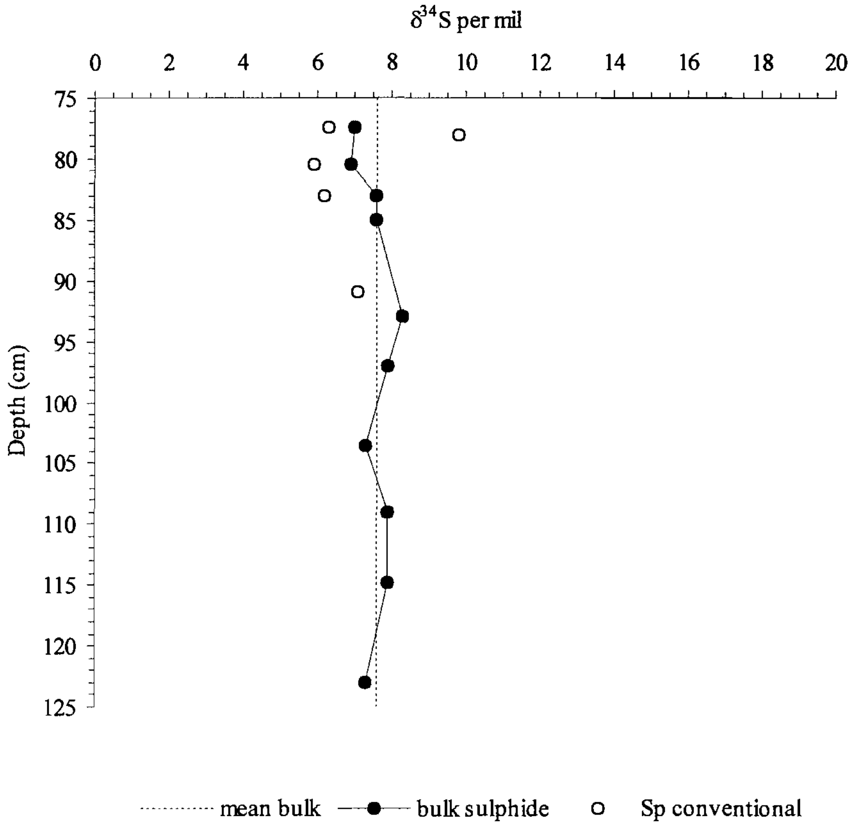

Figure 5.9: Downcore profiles of Core 58 sphalerite and bulk sulphide $\delta^{34}S$ measured by conventional methods.

sulphide $\delta^{34}S$ is 1-~1.5‰ heavier than sphalerite $\delta^{34}S$ values. Some of the discrepancy between the mean bulk sulphide and mean laser sulphide $\delta^{34}S$ values may be accounted for by variable contribution to the bulk samples of the relatively light sphalerite $\delta^{34}S$. The lightest bulk $\delta^{34}S$ values are close to the top of the Core 58 sulphide layer corresponding to depths where sphalerite is a major mineral phase with the trend to heavier bulk sulphide $\delta^{34}S$ values downcore corresponding to a modal decrease in the proportion of sphalerite in the bulk sediment.

For Core 60, 17 out of the 26 laser analyses were performed on pyrite grains; 9 on chalcopyrite grains with no sphalerite analyses. Sphalerite occurs only as a trace mineral in Core 60. Because sphalerite occurs predominantly as a replacement and thin overgrowths along fractures and within pore spaces of primary pyrite grains it was not possible to measure the $\delta^{34}S_{sphalerite}$ values by the laser method. In the upper 30cm of the Core 60 sulphide layer (46 - 96cm) laser chalcopyrite $\delta^{34}S$ values are consistently lighter than laser pyrite $\delta^{34}S$ values from the same depths. However, in the basal 20cm chalcopyrite is consistently heavier than laser pyrite $\delta^{34}S$ values from the same depths. Interestingly the increase to heavier chalcopyrite $\delta^{34}S$ downcore corresponds to an increase in the modal percentage of chalcopyrite (Figure 4.8) which, assuming conservation of the bulk mineral proportions in the conventional bulk sulphide $\delta^{34}S$ sub-samples, should lead to heavier bulk sulphide $\delta^{34}S$. However, this is not the case, Core 60 bulk sulphide $\delta^{34}S$ values measured by conventional methods, although fairly constant downcore, are lighter towards the base of the sulphide layer. This probably reflects a pyrite bias in the conventionally run bulk sulphide samples. It may also reflect sampling artefacts. The heaviest laser chalcopyrite $\delta^{34}S$ values are from chalcopyrite grains with covellite overgrowths, $\delta^{34}S$ ranges from +8.9‰ - +13.0‰; mean =+10.9‰ (n=3). These values must be interpreted with caution since they may represent covellite contamination. If this is the case it would suggest that covellite in Core 60 has heavy $\delta^{34}S$ compared to the measured $\delta^{34}S$ of chalcopyrite and pyrite in this core. Unfortunately it was not possible to measure the $\delta^{34}S$ value of covellite in Core 60 due to resin and chalcopyrite contamination problems and the small surface area of covellite in the samples.

5.4.2.4 Laser $\delta^{34}S$ Textural Associations: The *Alvin* Core

Texturally the lightest $\delta^{34}S$ values are associated with 'pristine' pyrite grains (secondary), i.e. those that show no evidence of corrosion, pitting or fracturing. The range of $\delta^{34}S$ for pristine pyrite is relatively narrow: +4.5 - +7.2‰; mean =+6.0‰ ±0.5 (1σ) (n=6). The heaviest $\delta^{34}S$ values are related to porous, corroded and fractured pyrite grains (primary): $\delta^{34}S$ =+6.0 - +14.7‰; mean =+9.0‰ ±1.0 (1σ) (n=9). This is also the greatest range for a textural type covering 8.7‰. $\delta^{34}S$ values of pyrite aggregates, which are observed in both the primary and secondary assemblages, range from +6.1 - +10.2‰, mean =+8.0‰ ±1.0 (1σ) (n=4) reflecting a mix of heavier primary $\delta^{34}S$ and lighter secondary $\delta^{34}S$ (Figure 5.10; Table 5.9).

The most significant variations in $\delta^{34}S$ are related to the order of sulphide precipitation. Interestingly, the most $\delta^{34}S$ enriched samples are paragenetically early, whilst the lightest $\delta^{34}S$ values are associated with secondary pyrite and sphalerite. Primary pyrites have a range in $\delta^{34}S$ of +6.2 - +14.7‰, mean =+8.5‰ ±0.9 (1σ) (n=9); secondary pyrite and sphalerite are considerably lighter and range from $\delta^{34}S$ =4.5-9.0‰, mean

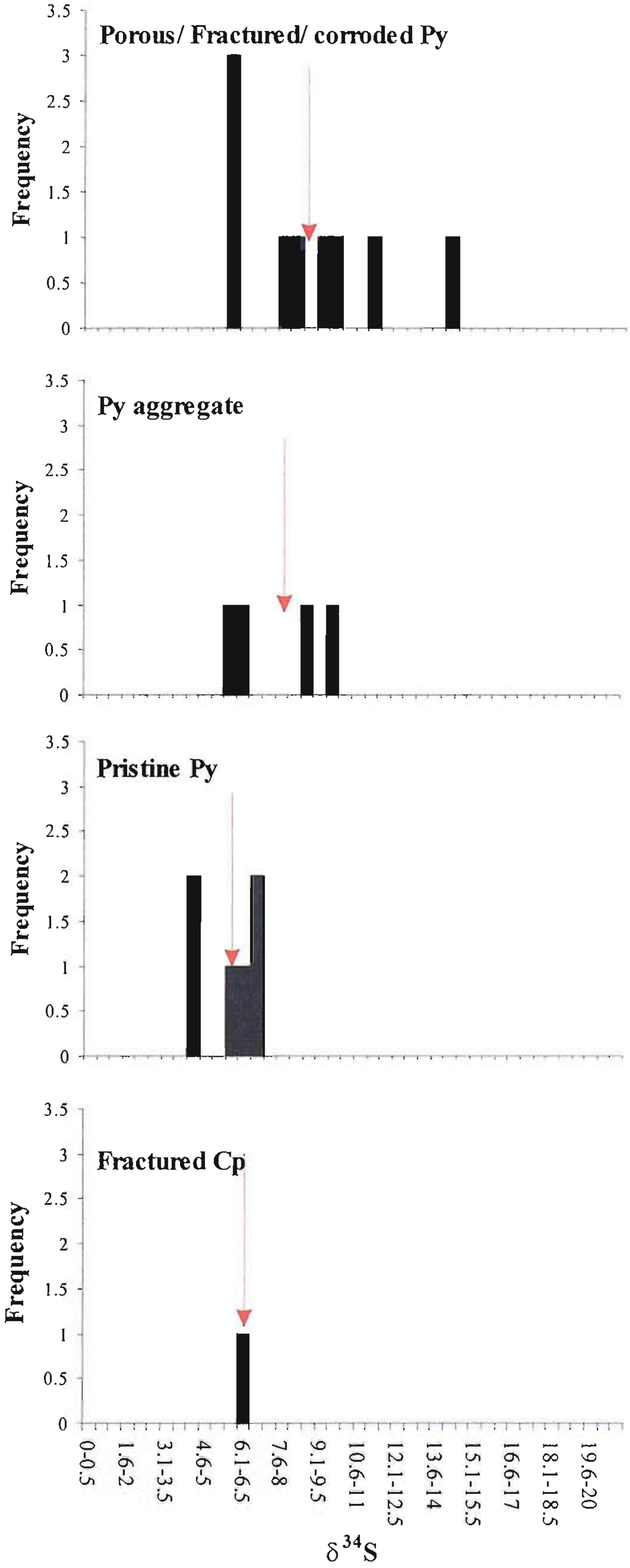

Figure 5.10: Histograms showing variation in $\delta^{34}S$ with textural type in CD102/58. The heaviest $\delta^{34}S$ values are associated with primary porous, pitted and corroded pyrites; the lightest $\delta^{34}S$ values are associated with pristine secondary pyrites. Pyrite aggregates which are both primary and secondary textures are intermediate reflecting a mix of heavier primary and lighter secondary $\delta^{34}S$ values. Red Arrows mark the position of the mean $\delta^{34}S$ value for each textural type. Abbreviations: Py= pyrite; Cp= chalcopyrite.

Sulphide texture	Min $\delta^{34}S$ ‰	Max $\delta^{34}S$ ‰	Average $\delta^{34}S$ ‰	Standard deviation	Standard error	Number of analyses
Pyrite aggregates	+6.1	+1020	+8.0	1.97	0.99	4
Porous/ corroded/ fractured Py	+6.0	+14.7	+6.0	0.96	0.32	9
Pristine pyrite	+4.5	+7.2	+5.9	1.08	0.441	7
Fractured Cp	+6.7	+6.7	/	/	/	1
Total analyses						21

Table 5.9: Summary of $\delta^{34}S$ variation between different textural types for CD102/58

Sulphide Texture	Min $\delta^{34}S$ ‰	Max $\delta^{34}S$ ‰	Average $\delta^{34}S$ ‰	Standard deviation	Standard error	Number of analyses
Pyrite aggregates	+6.1	+7.6	+6.6	0.84	0.49	3
Porous/ corroded/ fractured Py	+3.4	+11.9	+6.7	2.55	0.90	8
Pristine pyrite	+5.1	+8.6	+6.7	1.21	0.50	6
Fractured Cp	+7.2	+7.4	+7.3	0.10	0.06	3
Corroded Cp	+4.6	+7.3	+5.6	1.50	0.87	3
Cp with Cv overgrowths	+8.6	+13.0	+10.9	2.05	1.18	3
Total analyses						26

Table 5.10: Summary of $\delta^{34}S$ variation between different textural types for CD102/60

= +5.7‰ ±0.4 (1σ) (n=17) (Figure 5.11). Comparison of primary and secondary $\delta^{34}S$ values downcore indicates that secondary sulphide is always lighter than primary pyrite, with the exception of data from 85cm (primary=+8.6‰; secondary=+9.0‰) and 114.75cm depth (primary=+6.2‰; secondary=6.9‰) (Figure 5.11). Variation between primary and secondary sulphide $\delta^{34}S$ is significantly different (95% confidence limit: two sample populations t-test). Comparison of the observed $\delta^{34}S$ range for secondary pyrite and sphalerite and bulk sulphide suggests that bulk samples are dominated by $\delta^{34}S$ from secondary sulphides. This is in agreement with optical observations which indicate that oxidative alteration within the sulphidic layer is pervasive and that the secondary mineral assemblage, principally pyrite and goethite, dominates.

5.4.2.5 Laser $\delta^{34}S$ Textural Associations: The *Mir* Core

Texturally, there is very little variation in values of $\delta^{34}S$ (Figure 5.12). The mean $\delta^{34}S$ values for all pyrite textures: pyrite aggregates; porous/ corroded/ fractured pyrite; and pristine pyrite are almost identical: +6.6‰ ±0.5 (1σ) (n=3), +6.7‰ ±0.9 (1σ) (n=8), and +6.7‰ ±0.5 (1σ) (n=6), respectively. This is also very similar to mean $\delta^{34}S$ of fractured chalcopyrite =+7.3‰ ±0.1 (1σ) (n=3). The lightest $\delta^{34}S$ values are associated with corroded chalcopyrite: mean $\delta^{34}S$ =+5.6‰ ±0.9 (1σ) (n=3). The heaviest $\delta^{34}S$ values are from chalcopyrite with covellite overgrowths, mean =+10.9‰ (n=3). This is also the only textural type whose $\delta^{34}S$ values are significantly different (95% confidence limit: two sample populations t-test) from $\delta^{34}S$ of all other textures. However, the high $\delta^{34}S$ values for chalcopyrite with covellite overgrowths must be interpreted with caution since they may represent sampling artefacts relating to covellite contamination.

In contrast to $\delta^{34}S$ data from Core 58, $\delta^{34}S$ values of sulphide separates from Core 60 do not show any large variation relating to primary or secondary sulphide mineralisation (Figure 5.13). Primary pyrite and chalcopyrite cover a larger range (+3.4-+13.0‰) than secondary pyrite (+4.5-+8.6‰). However, unlike secondary sulphides in Core 58, which are consistently lighter than primary pyrites, $\delta^{34}S$ values of secondary sulphides from Core 60 (mean $\delta^{34}S$ = +6.5‰) are within the range for primary pyrites and are within 2 standard errors (1σ) of the mean primary $\delta^{34}S$ value of +7.4‰ (Figure 5.13).

5.5 Discussion

Published $\delta^{34}S$ data for the TAG hydrothermal site are heavier than $\delta^{34}S$ from other sediment free mid-ocean ridge hydrothermal sites and range from ~+4.4-+10.3‰, these data have been attributed to contributions of heavy $\delta^{34}S$ via inorganic reduction of seawater sulphate within the TAG mound (Lein et al., 1991; Chiba et al., 1998; Gemmell and Sharpe, 1998; Herzig et al., 1998b; Knott et al., 1998). The $\delta^{34}S$ of bulk sulphide samples from this study, measured by conventional means fall within this range and can be explained by existing isotope models for the TAG area. However, although the laser data set needs to be interpreted with caution (see section 5.4.2.3) the sampling sensitivity of the in situ laser technique utilized in this study which allows for discrimination between mineralogical and textural types has extended the range of $\delta^{34}S$ at the TAG hydrothermal field from +4.4‰ - +10.3‰ to +3.4‰ - +14.7‰. This is significant because existing models for S isotope behaviour at the TAG site can only account for a maximum $\delta^{34}S$ value of +10‰ assuming an end member fluid with $\delta^{34}S$ =~+5.5‰.

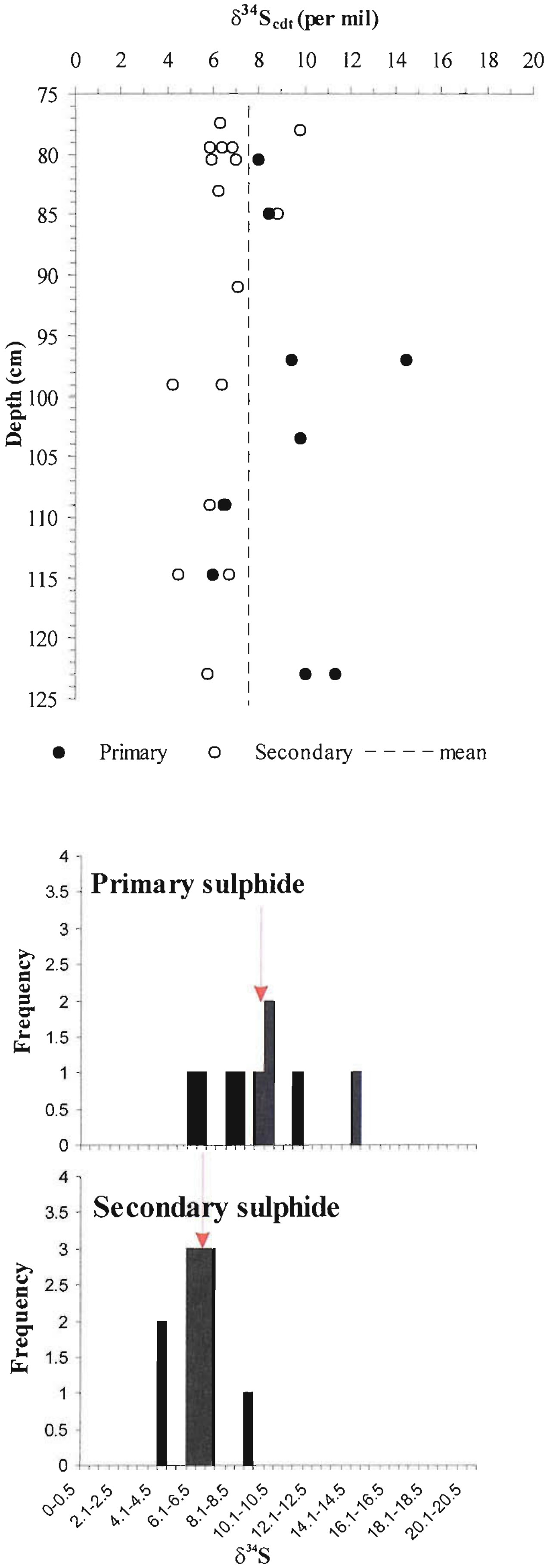

Figure 5.11: CD102/58 laser sulphide separates: a) downcore profile of primary and secondary sulphides. Note that with the exception of data from 85cm and 114.75cm depth the δ^{34}S values of all secondary sulphides are lighter than the associated primary sulphide. b)Histograms of the δ^{34}S distribution between primary and secondary sulphides; red arrows denote mean value in each case.

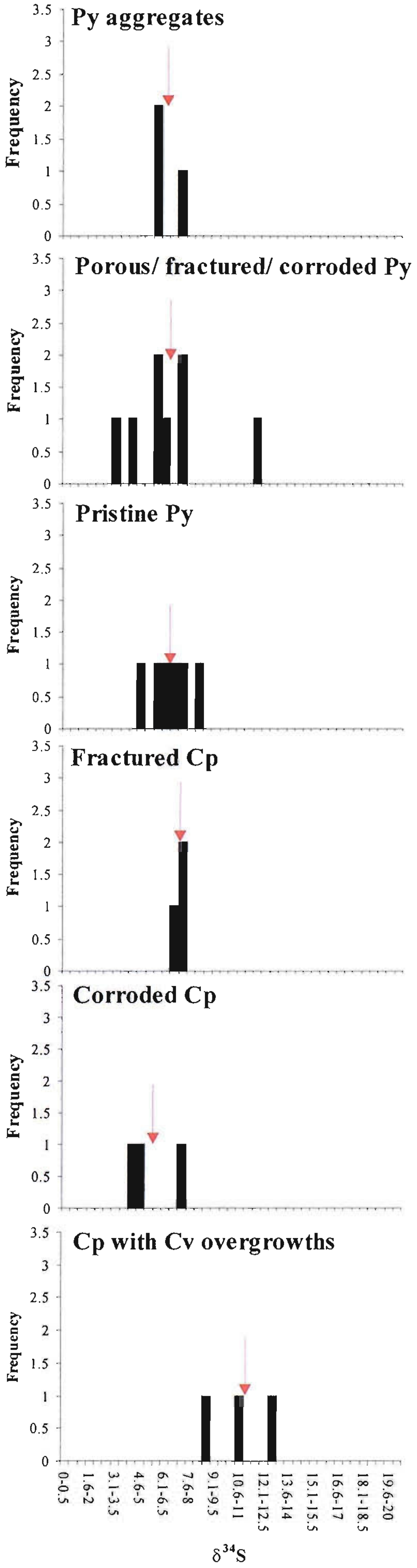

Figure 5.12: Histograms showing variation in $\delta^{34}S$ with textural type in CD102/60. Red Arrows mark the position of the mean $\delta^{34}S$ value for each textural type. Abbreviations: Py= pyrite; Cp= chalcopyrite.

5.5.1 CD102/58: The *Alvin* core

These data are considerably enriched in heavy $\delta^{34}S$ compared to other sediment free mid-ocean ridge hydrothermal sites, including the existing $\delta^{34}S$ data set from the TAG mound. Whilst heavy $\delta^{34}S$ values up to ~+10‰, at the active TAG mound, can be explained by mixing of inorganically reduced seawater sulphate and an end-member fluid with $\delta^{34}S$ =+5.5‰ (Knott et al., 1998; Shanks, 2001), assuming a maximum increase in $\delta^{34}S$ of 4.5‰ (Janecky and Shanks, 1988) this cannot directly explain the heavy values ($\delta^{34}S$ >+10‰) observed in laser samples from Core 58 ($\delta^{34}S$ +14.7‰ and +11.5‰). If the $\delta^{34}S$ value of the parent hydrothermal fluid at the *Alvin* mound was the same as $\delta^{34}S_{H2S}$ of currently venting fluids at the TAG mound ($\delta^{34}S_{H2S}$ =+6.6-+7.5‰: Knott et al., 1998; Shanks, 2001) the heaviest $\delta^{34}S$ value (+14.7‰) from this study requires a seawater contribution of ~52-56%. Assuming simple mixing, such a high seawater contribution would result in fluid temperatures of ~162-176°C and increases in pH, fO_2, and [SO_4]. These conditions cannot lead to inorganic sulphate reduction or precipitation of the observed sulphide minerals. A more complex fluid evolution model is required to explain the wide range of $\delta^{34}S$ values, +4.5‰-+14.7‰, differences in primary and secondary pyrites; and some novel, unusually heavy, $\delta^{34}S$ values.

The heaviest values quoted for Core 58 are associated with primary pyrite. Textures of primary pyrite and chalcopyrite are consistent with precipitation from diffuse high temperature flow at or near to the mound surface, close to black smoker chimneys (e.g. Hannington et al., 1995b; Tivey et al., 1995; Knott et al., 1998; Chapter 4). To produce the observed values of $\delta^{34}S$ sulphate reduction in the near surface is required. One potential mechanism for this is in situ sulphate reduction or anhydrite replacement during chimney growth and near surface sulphide precipitation. However, reaction modelling indicates that reduction of seawater sulphate within chimney structures is limited (Janecky and Shanks, 1988) and although replacement reactions have been shown to be an important control on isotopic variation of chimney sulphides, the associated fractionations are small, typically <2‰ (e.g. Styrt et al., 1981; Zierenberg et al., 1984; Woodruff and Shanks, 1988).

Under the conditions operating at, and/or near to the surface of the *Alvin* mound during high temperature activity, bacterial sulphate reduction is one of the most efficient means for causing large fractionations between H_2S and SO_4^{2-} (e.g. Ohmoto and Rye, 1979; Canfield, 2001a; Habicht and Canfield, 2001 and references there in). The upper temperature limit for DSR is ~80-100°C (Machel, 1989; Jorgensen et al., 1992; Stackebrandt et al., 1995) and optimum growth temperatures for heterotrophic S-reduces are 38-68°C, this range includes conditions at the periphery of active chimneys and the mound surface (e.g. Tivey et al., 1995; Schultz et al., 1996). However, at the temperatures calculated by simple mixing of seawater and hydrothermal fluid for the heaviest $\delta^{34}S$ values (~162-176°C) and precipitation of chalcopyrite and pyrite during paragenetic stage 2 (Figure 4.18 & 5.14), from insulated high temperature fluids, precludes ASR, DSR and associated Rayleigh Fractionation as a means of producing heavy $\delta^{34}S$ since the temperature greatly exceeds that at which the bacteria can operate (e.g. Machel, 1989; Stackebrandt et al., 1995).

Precipitation of stage 2 pyrite and chalcopyrite with $\delta^{34}S$ values >+10‰ requires inorganic reduction of seawater sulphate. The early collomorphic pyrite crusts which insulate hydrothermal fluid leading to precipitation of high temperature sulphides do so by restricting permeability and therefore contact with cold (2°C) seawater. This restriction of permeability may lead to closed system SO_4^{2-} behaviour and abiotic sulphate reduction. Experimental work has shown that during partial reduction of seawater sulphate at temperatures <250°C a kinetic isotopic effect may occur resulting in S isotopic fractionations of ~15‰ at 150°C and ~10‰ at 200°C (Marchel et al., 1995). Thus, mixing of hydrothermal fluid which has already been modified during reactions within the subsurface, and which has $\delta^{34}S$ ~+8‰, with seawater sulphate which has undergone partial inorganic reduction at temperatures <250°C in areas where the permeability is locally restricted, could explain the heaviest primary $\delta^{34}S$ values of +10‰ to +14.7‰. Relatively heavy $\delta^{34}S$ values (>10‰) like those reported here, generated in restricted permeability conditions close to black smoker vents, are not observed in the TAG ODP drilling $\delta^{34}S$ dataset, this is because the mound surface close to the BSC was not sampled by the ODP drilling.

Whilst the heaviest $\delta^{34}S$ values can be explained in this way the question of validity of the heavy data means that such fractionation may not be necessary. Heavy $\delta^{34}S$ values within the range observed here are however, reported from the Guaymas Basin (max $\delta^{34}S$ =+11.1‰: Shanks and Niemitz, 1981) and Middle Valley (max $\delta^{34}S$ =+17.6‰: Goodfellow and Blaise, 1988; Goodfellow and Franklin, 1993) hydrothermal sites. In both cases these highly positive $\delta^{34}S$ values are attributed to abiotic reduction of seawater sulphate either during recharge to the hydrothermal system or under closed system conditions where the seawater is trapped in overlying sediments (Shanks and Niemitz, 1981; Goodfellow and Blaise, 1988; Goodfellow and Franklin, 1993).

The range of $\delta^{34}S$ observed for secondary sulphide in Core 58 (including sphalerite measured by conventional methods) (+4.5‰ - +10.0‰; mean =+6.7‰ (1σ) n=17) reflects a change in the style of sulphide precipitation from high temperature diffuse flow close to an active black smoker chimney, to precipitation beneath the mound surface from lower temperature fluids (Chapter 4; Figure 5.14). All secondary sulphide $\delta^{34}S$ values are <+10‰, this is within the range predicted for mixing of an end-member fluid with $\delta^{34}S$ =+5.5‰ with inorganically reduced seawater sulphate. The $\delta^{34}S$ values of secondary sulphide measured here can therefore, be attributed to such mixing; this is consistent with a model for S isotopic evolution in the active TAG mound proposed by Knott et al. (1998). The heaviest secondary $\delta^{34}S$ values close to +10‰ may also reflect reaction of the upwelling hydrothermal fluid with previously formed sulphides within the mound and the underlying stockwork which leads to further modification of the fluid to slightly ^{34}S enriched $\delta^{34}S$ values; modelling suggests that under optimum conditions this will increase $\delta^{34}S$ values by a maximum of 2‰ (Janecky and Shanks, 1988).

Whilst the range in secondary $\delta^{34}S$ values can be explained by simple mound mixing processes, some of the secondary pyrite textures, particularly collomorphic pyrite crusts parallel to sedimentary laminae, indicate in situ precipitation during diagenetic alteration (Chapter 4), the S isotopic signature of these sulphides is not controlled by mound processes but by diagenetic conditions, in particular pyrite oxidation and remineralisation.

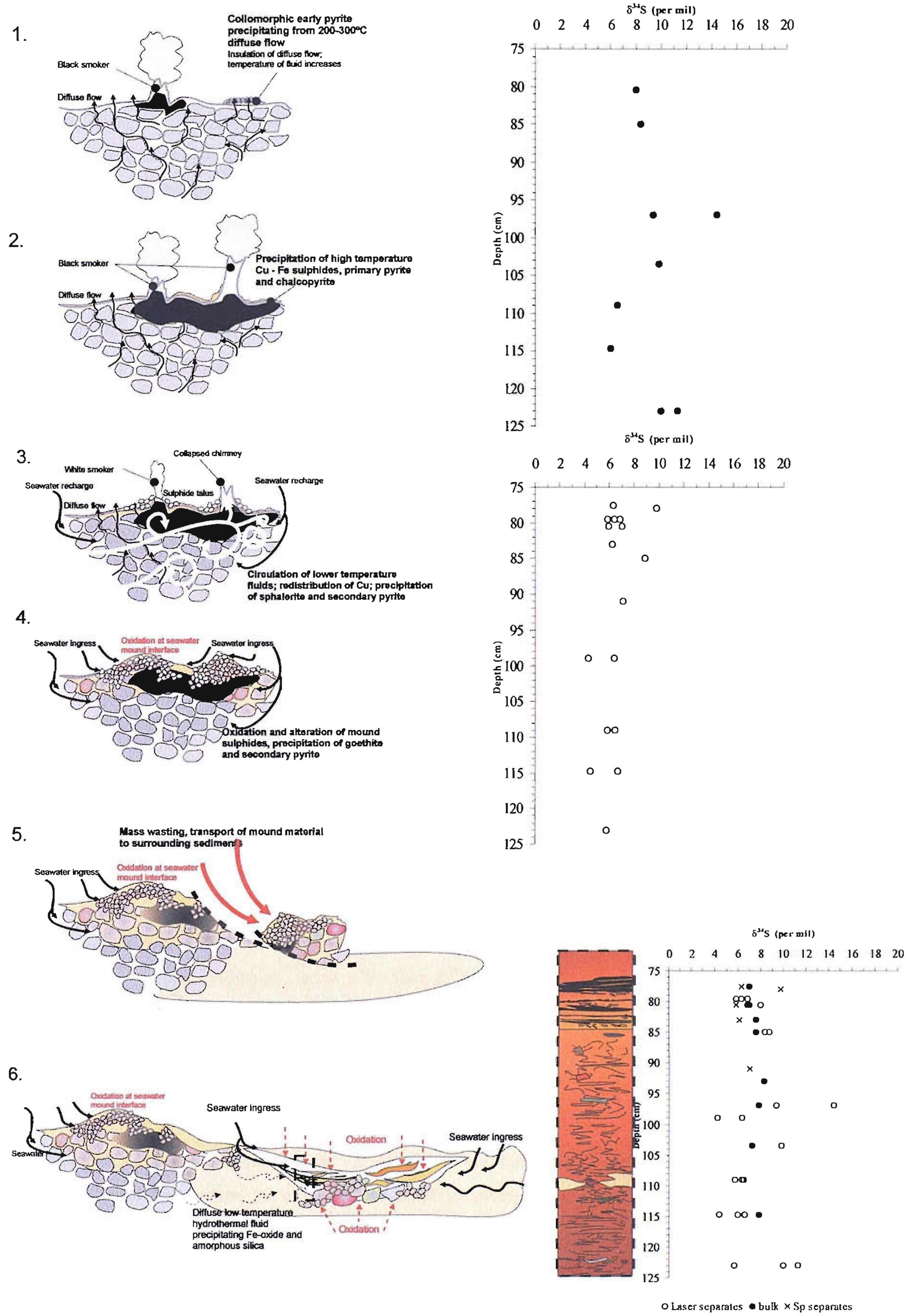

Figure 5.14: Schematic representation of sulphide paragenesis, oxidation and alteration of the *Alvin* core, CD102/58, and evolution of the sulphur isotope signature. Paragenetic stages are described in Chapter 4: Figure 4.18. Heavy $\delta^{34}S$ values for primary sulphide precipitated during stage 1 and 2 result from mixing of hydrothermal sulphur with seawater within the mound and from inorganic sulphate reduction under closed system conditions during pyrite and chalcopyrite precipitation from high temperature fluid. The lighter $\delta^{34}S$ values for secondary sulphides precipitated during stage 3 and during oxidative alteration during stage 6 result from a combination of adiabatic mixing of high temperature fluid with $\delta^{34}S$ of +5.5 per mil with reduced seawater sulphate from seawater entrainment, dissolution and remineralisation of mound derived sulphides and bacterial mediation of oxidation.
Note diagrams are not to scale.

The large $\Delta\ \delta^{34}S_{primary}$- $\delta^{34}S_{secondary}$ =max 10.2‰ cannot be explained by straight forward sulphide oxidation and remineralisation given that the oxidation rate is not controlled by the metal sulphur bond rupture and kinetic isotopic effects are negligible (e.g. Ohmoto and Rye, 1979 Canfield, 2001a). In addition, the isotopic fractionation associated with remineralisation, i.e. pyrite formation from aqueous sulphide, is <1‰ (Price and Shieh, 1979). However, chemical experiments have shown that pyrite oxidation rarely occurs as a straight forward reaction, but most commonly proceeds via intermediate sulphur and Fe species (e.g. Nordstrom, 1982; Schippers and Sand, 1999; Schippers and Jorgensen, 2001; Canfield, 2001a; Habicht and Canfield, 2001). Equation 4.4 shows a two step oxidation mechanism for pyrite via a thiosulphate intermediate (Schippers and Sand, 1999). Bacterial disproportionation of the thiosulphate intermediate can result in considerable fractionation with $\Delta\ \delta^{34}S_{thiosulphate}$-$\delta^{34}S_{H2S\ and\ sulphate}$=~-13-+12‰ (e.g. Cypionka et al., 1998; Habicht et al., 1998). This encompasses the range of $\Delta\ \delta^{34}S_{primary}$- $\delta^{34}S_{secondary}$ observed in Core 58. Bacterial pyrite oxidation however is extremely slow in anaerobic conditions (Schippers and Jorgensen, 2002), this may indicate locally oxygenated conditions within the core. This agrees with Fe-oxidation and gypsum precipitation models discussed in Chapter 6 which indicate the existence of locally important micro-geochemical environments where, for example, there are significant changes in E_h and pH.

Thus the isotopic composition of secondary pyrite is controlled by both precipitation under white smoker style conditions and oxidation and dissolution processes during sedimentary diagenesis.

5.5.2 CD102/60: The *Mir* core

These data are also considerably enriched in heavy $\delta^{34}S$ compared to $\delta^{34}S$ at other sediment free mid-ocean ridge hydrothermal sites and the active TAG mound. Assuming the $\delta^{34}S$ value of the end-member hydrothermal fluid at the *Mir* mound is +5.5‰ and that the maximum theoretical increase in $\delta^{34}S$ due to mixing with inorganically reduced seawater sulphate is 4.5‰ (Janecky and Shanks, 1988) the heaviest expected $\delta^{34}S_{sulphide}$ = +10‰. However, some of the laser $\delta^{34}S$ data from this study have values in excess of +10‰, and all of these are associated with the primary sulphide assemblage. Therefore, simple mixing of the hydrothermal and seawater sulphur reservoirs cannot directly explain the observed $\delta^{34}S$ data. Assuming simple mixing of a hydrothermal fluid with the same $\delta^{34}S_{H2S}$ of currently venting fluids at the TAG mound ($\delta^{34}S_{H2S}$ =+6.6-+7.5‰: Knott et al., 1998; Shanks, 2001) and entrained seawater, the heaviest $\delta^{34}S$ value (+13.0‰) requires a seawater contribution of ~40-43%, this results in a fluid with a temperature range of 205-216°C. Such a fluid cannot sustain the conditions required for inorganic sulphate reduction (≥250°C), nor are they appropriate for bacterial mediation of the sulphur isotopic composition. The optimum temperature for sulphate reducing bacteria is ~80°C: (Machel, 1989; Stackebrandt et al., 1995). In addition, it has been demonstrated that DSR in hydrothermal environments is electron donor limited, i.e. the common electron donors utilized by sulphate reducing bacteria, including CH_2O or H_2, are not available in sufficient concentrations to drive the significant amounts of DSR that would be required to account for the heaviest $\delta^{34}S$ values (Severmann et al., in review). Therefore, reduction of aqueous sulphate and/or anhydrite is required in the deep reaction zone.

The sulphide layer of Core 60 is inferred to have originated from a pyrite-silica breccia formed within the stockwork zone at depth in the *Mir* mound (Chapter 4). Similar pyrite-silica breccias within the active TAG mound are thought to have formed as collapse breccias during hydrothermal hiatuses, which were originally cemented by anhydrite that is then cumulatively replaced by silica with renewed activity (e.g. Humphris et al., 1995; Hannington et al., 1998; You and Bickle, 1998). Radiometric dating of sulphide from the *Mir* mound indicates at least three episodes of sulphide precipitation at ~100kya, ~50kya, and ~20kya (Lalou et al., 1995), this is consistent with intermittent activity at this site and the formation of collapse breccias which are re-cemented by subsequent high temperature activity If anhydrite is retained at depth in the system during hydrothermal inactivity, when high temperature fluid flow is reactivated seawater sulphate, in the form of anhydrite, which may then be reduced by reaction with ferrous iron and incorporated into the hydrothermal fluid, is available as an additional source of sulphide sulphur (e.g. Janecky and Shanks, 1988; Chiba et al., 1998). Modelling of stockwork alteration reactions under conditions of focused, high temperature (~350°C) flow, where hydrothermal fluid is reacted with fayalite + anhydrite, with ferrous Fe as the reducing agent and magnetite precipitation is not inhibited, have shown that in an open system, under disequilibrium sulphate-sulphide isotopic exchange, $\delta^{34}S_{H2S}$ increases to >+15‰ as the reaction progresses (Janecky and Shanks, 1988). Thus, reduction of pre-existing anhydrite, from a previous high temperature phase, within the stockwork zone at depth in the *Mir* mound can account for heavy δ^{34}S values of the primary sulphides (Figure 5.15).

The δ^{34}S values of secondary sulphides reflect precipitation under slightly different conditions. Secondary sulphide from the Core 60 has lighter δ^{34}S with no secondary sulphide samples with δ^{34}S in excess of +10‰. Assuming that all the anhydrite was replaced by silica during the precipitation of the primary sulphide phases this additional source of seawater sulphate, and heavy δ^{34}S, is no longer available for incorporation to later sulphide. This is consistent with secondary sulphide textures which, in contrast to primary sulphides, do not show any evidence for silica replacement or encroachment at grain boundaries (Chapter 4). Assuming an end-member hydrothermal fluid with δ^{34}S =+5.5‰ all of the observed δ^{34}S values for secondary sulphides can be explained by adiabatic mixing of this fluid with inorganically reduced seawater sulphate (Janecky and Shanks, 1988) and reaction of the upwelling hydrothermal fluid with previously formed sulphides within the mound and the underlying stockwork leading to a modified fluid slightly enriched in ^{34}S; modelling suggests that under optimum conditions this can increase δ^{34}S values by a maximum of 2‰ (Janecky and Shanks, 1988).

5.6 Conclusions

For both Core 58 and Core 60 the bulk sulphide δ^{34}S values measured by conventional means are consistent with previously reported values for the TAG hydrothermal field and may be explained by existing S isotope models which predict maximum δ^{34}S values of +10‰. However, whilst accepting the laser δ^{34}S data with caution, some of the δ^{34}S values of sulphide separates measured by the in situ laser combustion technique exceed this theoretical maximum. The sensitivity of the in situ laser technique utilized in this study has significantly extended the range of δ^{34}S at the TAG hydrothermal field to ~+3.4-+14.7‰ and has important implications for existing sulphur isotope models within the TAG hydrothermal field and suggests that reduction of seawater sulphate is much more important than previously recognised. The upper end of this

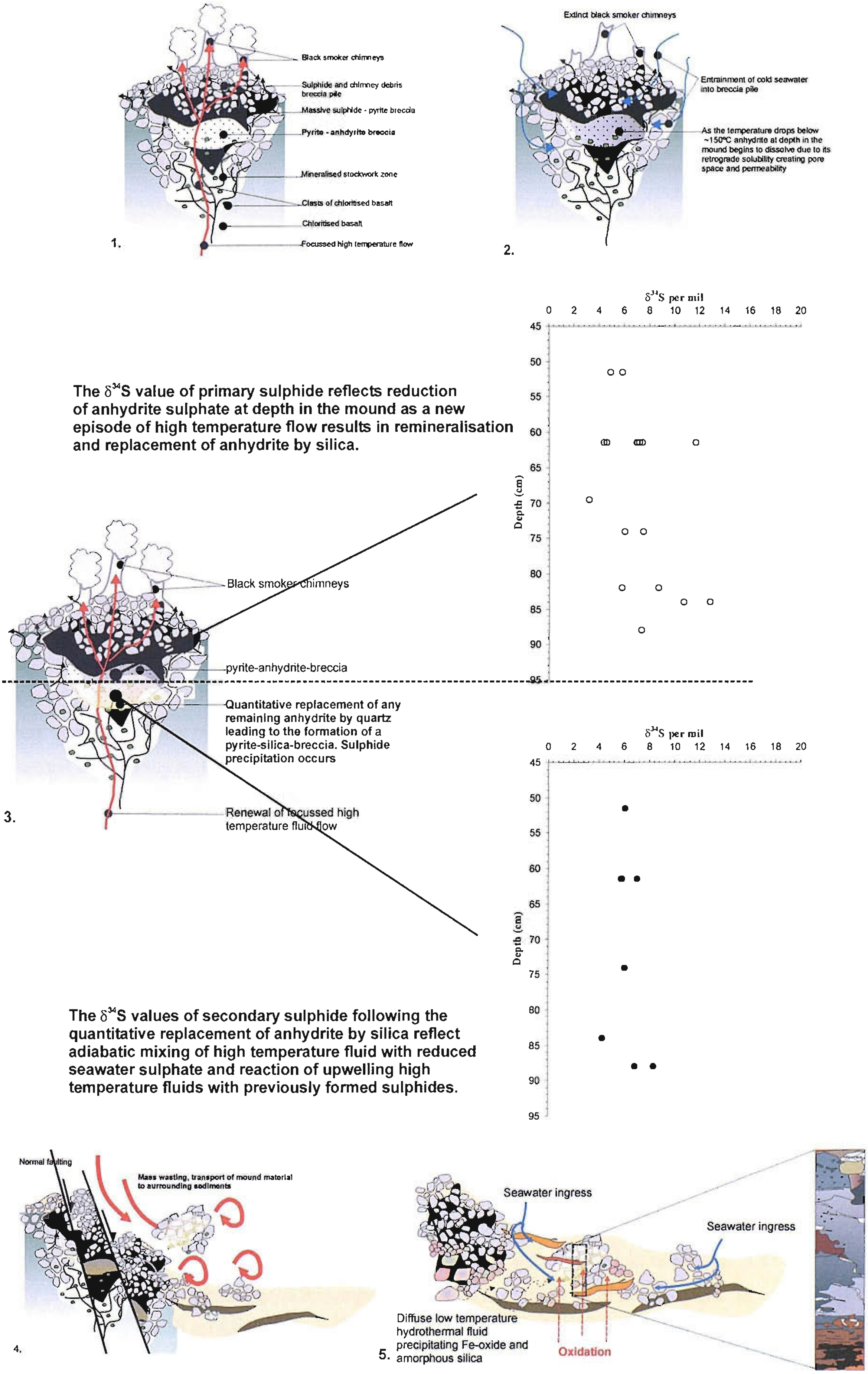

The δ^{34}S value of primary sulphide reflects reduction of anhydrite sulphate at depth in the mound as a new episode of high temperature flow results in remineralisation and replacement of anhydrite by silica.

The δ^{34}S values of secondary sulphide following the quantitative replacement of anhydrite by silica reflect adiabatic mixing of high temperature fluid with reduced seawater sulphate and reaction of upwelling high temperature fluids with previously formed sulphides.

Figure 5.15: Schematic representation of sulphide precipitation, transport to sediment and alteration of the sulphide layer of the *Mir* core, CD102/60 and evolution of the sulphur isotope signature. Paragenetic stages are described in Chapter 4: Figure 4.19. Primary δ^{34}S values result from reaction of anhydrite sulphate in the stockwork zone. Secondary sulphides are precipitated following quantitative replacement of anhydrite by silica producing a pyrite-silica breccia and δ^{34}S indicative of mixing of hydrothermal fluid with seawater and reaction with previously formed sulphides. Note diagrams not to scale.

range is considerably heavier than values of $\delta^{34}S$ from other sediment free mid ocean ridge hydrothermal sites. The range and distribution of $\delta^{34}S$ values in both Core 58 and Core 60 reflects a complex mixture of sulphur sources and multiple controls on isotopic fractionation at the *Alvin* and *Mir* mounds:

- The heavy primary sulphide $\delta^{34}S$ values from the *Alvin* mound indicate precipitation from a high temperature fluid in the near surface with S contributions from reduced seawater sulphate. The S isotopic composition of the earliest, collomorphic pyrite precipitated during stage 1 (Figure 5.14) and the relatively heavy S isotopic composition of the sulphides precipitated during stage 2 (Figure 5.14) are most probably related to kinetic isotopic effects occurring during partial, inorganic seawater sulphate reduction in a closed system with restricted permeability close to high temperature vents and the mound surface.
- $\delta^{34}S$ values of secondary sulphide from the *Alvin* mound reflect precipitation from (a) lower temperature fluids in which the S isotopic composition is controlled by adiabatic mixing of the end-member hydrothermal fluid with $\delta^{34}S$ =+5.5‰ and reduced sulphate from seawater entrainment into the mound leading to maximum $\delta^{34}S$ of +10‰. There may also be some reaction of upwelling hydrothermal fluids with pre-existing sulphides within the mound and underlying stockwork; and (b) oxidative dissolution, which may be bacterially mediated, and remineralisation of mound derived sulphides within the sediment.
- The heavy $\delta^{34}S$ of primary sulphide from the *Mir* mound result from reaction of anhydrite sulphate in the stockwork zone (which was precipitated during an earlier episode of high temperature venting) with hydrothermal fluid during replacement of the anhydrite and re-cementation of the breccia by silica. Generation of heavy $\delta^{34}S$ in Core 60 as a result of DSR is not possible due to the high temperature conditions operating within the stockwork zone during sulphide precipitation and the limited availability of suitable electron donors. However, some partial, local abiotic seawater sulphate reduction like that inferred for Core 58 stage 1& 2 primary sulphides could be occurring.
- Secondary sulphide from the *Mir* mound is precipitated following complete replacement of the anhydrite cement by silica. Like some of the secondary sulphide from Core 58 the S isotopic composition is controlled by adiabatic mixing of the end-member hydrothermal fluid ($\delta^{34}S$ =+5.5‰) and reduced sulphate from seawater entrainment into the mound leading to maximum $\delta^{34}S$ of +10‰; and reaction with previously precipitated sulphides, which can increase the $\delta^{34}S$ value by a further 2‰. Precipitation of the *Mir* sulphides at depth within the mound, and the relatively unoxidised state of the sulphide layer (Chapter 4) precludes a major biogenic influence on the S isotopic composition.

These new data demonstrate the importance of micro-scale mineralogical and textural S isotope studies in unravelling the complex paragenetic sequences of sulphide precipitation and alteration, in order to gain a full understanding of the processes controlling the S isotope composition at seafloor hydrothermal sites. In addition, they highlight the need for further micro-scale S isotope studies within the TAG field, and elsewhere, to assess the significance of heavy primary $\delta^{34}S$ and the implications for fluid evolution and the influence of bacterial processes in the shallow subsurface and at depth in large long lived deposits with intermittent high temperature activity.

Chapter 6:

Fe oxidation and bio-mineralisation in metalliferous sediments from the *Alvin* relict high temperature zone.

Some of the content of this chapter is published as: Four hundred and ninety million year record of bacteriogenic iron oxide precipitation at sea-floor hydrothermal vents: Little, CS; Glynn, SEJ and Mills RA. 2004, Special Issue of the Journal of Geomicrobiology, vol: 21, 415-429.

6.1 Introduction

Fe-oxides and oxyhydroxides are a major component of the hydrothermal deposits found at seafloor vents sites (e.g. Alt, 1988b; Binns et al., 1993; Bogdanov et al., 1998; Metz et al., 1988) Previous studies have shown that abiogenic processes that lead to Fe-oxide formation include: sedimentation from overlying hydrothermal plumes (e.g. Mills et al., 1993; Barrett et al., 1987); in situ precipitation from diffuse low temperature hydrothermal fluids (e.g. Koski et al., 1985; Alt et al., 1987), typically 20-100°C (e.g. Mills et al., 1996; Severmann et al., 2004; Bau and Dulski, 1999); material derived from mass wasting of low temperature (typically 2-50°C) Fe-Si chimneys, (e.g. Alt et al., 1987; Herzig et al., 1988; James and Elderfield, 1996a); and the products of Fe-rich sulphide oxidation in mass wasted material undergoing alteration at the seafloor (e.g. Binns et al., 1993; Hannington, 1993; Mills et al., 1993). In addition to inorganic processes, microbial activity is thought to play a role in the formation of hydrothermal Fe-oxide deposits (e.g. Alt et al., 1987; Juniper and Fouquet, 1988; Hannington and Jonasson, 1992; Juniper and Sarrazin, 1995; Emerson and Moyer, 2002; Edwards et al., 2003b & c).

Submarine hydrothermal environments are host to unique ecosystems where primary biomass is dominated by chemolithoautotrophic micro-organisms which utilise reduced chemical species as an energy source (e.g. Jannasch and Mottl, 1985; Wirsen et al., 1986). Such microbes are capable of influencing the growth and dissolution of a number of minerals by exerting control over reaction kinetics and pathways. However, relationships between Fe-oxide deposits and extant microbial populations are poorly constrained because of difficulties in distinguishing authigenic microfossils from abiogenic artefacts, as the effects of diagenesis can lead to the loss of biogenic signatures. Although Fe-oxidising bacteria are inferred to be ubiquitous in hydrothermal environments (e.g. Parkes et al., 2000) where there are sharp pH, redox and temperature gradients, and a fresh supply of Fe in dissolved and particulate forms (e.g. Juniper and Tebo, 1995; Edwards et al., 2003b; Severmann et al., in review), their impact on Fe-oxidation at vent sites and their role in the formation of Fe oxide deposits remains largely unquantified (Severmann et al., in review).

6.1.1 Biologically mediated Fe(II) oxidation

Bacterial leaching and bio-oxidation of metal sulphides to soluble metals sulphates and sulphuric acid is affected by specialised bacteria which utilise the energy gained from mineral dissolution or precipitation for cell growth and/or respiration where the oxygen supply is limited. In addition, bacteria may incorporate dissolved mineral constituents into cellular compounds as protection or to fulfil metabolic trace element requirements (e.g. Ehrlich, 1999; Ehrlich, 1996a; Ferris et al., 1988; Ghiorse, 1984). Previous investigations of bacterially mediated Fe(II) oxidation have been largely concerned with the formation and conditions of acid mine drainage (AMD) and the role of the bacterium *Thiobacillus ferrooxidans* in acid generation at these sites (e.g. Toran and Harris, 1989; Kirby et al., 1999; Dold and Fontbote, 2001; Marchand and Silverstein, 2003), whilst microbial studies at hydrothermal vents sites have focussed on chemolithoautotrophs, some of which are Fe oxidisers, which gain energy from dissolved, reduced chemical species (e.g. Jannasch and Mottl, 1985; McCollom and Shock, 1997; Wirsen et al., 1986). Only a few studies have investigated microbial utilisation of mineral surfaces as metabolic substrates (e.g. Wirsen et al., 1993; Emerson and Moyer, 2002; Edwards et al., 2003b).

AMD arises from the oxidation of sulphide minerals, principally pyrite, in mining and metallurgical processing waste. The result is acid production and contamination of adjacent water courses and ground waters which is the foremost environmental problem facing the mining industry today (e.g. Dold and Fontbote, 2002; Kirby and Elder Brady, 1998; Kirby et al., 1999; Bain et al., 2000). Whilst the oxidation of sulphide waste may occur abiotically, laboratory simulations of acidic mine conditions have shown that micro-organisms can dramatically increase reaction rates. For example *Thiobacillus ferrooxidans* (an acidophilic species with an optimum growth pH<3; e.g. Trafford et al., 1973) can increase Fe(II) oxidation rates under laboratory conditions by a factor of 10^6 (Singer and Strumm, 1970; (Nordstrom, 1985)). However, the impact of this microbe on natural Fe(II) oxidation rates has not yet been quantified (Kirby et al., 1999). The dissolution of sulphide minerals is controlled by the electrochemical conditions present at the mineral-solution interface, in particular charge transfer processes (e.g. Nicol et al., 1975; Nicol, 1993). As such the rate of microbial Fe(II) oxidation, with respect to pyrite, is affected by the concentration of ferric ions and the pH of the system (e.g. McKibben and Barnes, 1986; Fowler et al., 1999). Experimental work by Fowler et al (1999), has shown that the rate of pyrite dissolution in the presence of *T. ferrooxidans* at relatively low pH and high aqueous Fe(II) concentration is comparable to abiotic dissolution.

Bacterially catalysed oxidation of pyrite, under acidic conditions, can take place either: directly or indirectly. Direct catalysis occurs where there is contact between the bacterial cell and the mineral surface. In this case both solubilisation and Fe(II) oxidation are mediated by the microbe. This might occur through extracellular secretion of an enzyme or by sulphide mineral specific enzymes present in the cell wall with a generalised reaction (Silverman and Ehrlich, 1964):

$$FeS_2 + H_2O + \frac{7}{2}O_2 \xrightarrow{Bacteria} Fe^{2+} + 2SO_4{}^{2-} + 2H^+ \tag{6.1}$$

Indirect oxidation occurs where the microbe oxidises Fe(II) produced during abiotic pyrite oxidation (Equation 6.2; 6.3). The net reaction produces Fe(III), sulphate and acidity (Equation 6.4) (e.g. Silverman and Ehrlich, 1964; Silverman, 1967; Nordstrom, 1982). Hydrolysis of the Fe(III) produced in the net reaction results in the precipitation of Fe oxides via Equation (6.5) and generation of protons

$$FeS_{2(s)} + 14Fe^{3+} + 8H_2O \rightarrow 15Fe^{2+} + 2SO_4{}^{2-} + 16H^+ \tag{6.2}$$

$$15Fe^{2+} \Downarrow + 3.75O_2 + 15H^+ \xrightarrow{Bacteria} 15Fe^{3+} + 7.5H_2O \tag{6.3}$$

Net Reaction:

$$FeS_{2(s)} + 3.75O_2 + 0.5H_2O \rightarrow Fe^{3+} + 2SO_4^{2-} + H^+ \qquad (6.4)$$

Fe(III) Hydrolysis:

$$Fe^{3+} + 3H_2O \rightarrow Fe(OH)_3 + 3H^+ \qquad (6.5)$$

Because Fe(III) hydrolysis and subsequent goethite or hematite precipitation proceeds more rapidly than Fe(II) oxidation , microbial Fe(II) oxidation is the rate determining step in the dissolution of pyrite and precipitation of Fe-oxides in AMD environments (e.g. Singer and Strumm, 1970; McKibben and Barnes, 1986; Kasama and Murakami, 2001).

Although it is often useful to consider sulphide oxidation as a simple net reaction, e.g. Equation 6.5, experiments have shown that pyrite oxidation, in natural systems rarely occurs as a straight forward reaction, but most commonly proceeds via intermediate sulphur and Fe species (e.g. Nordstrom, 1982 Schippers and Sand, 1999; Schippers and Jorgensen, 2001; Habicht and Canfield, 2001; Canfield, 2001a) e.g. Equations 4.4 which shows the extended mechanism, via a thiosulphate intermediate, for Equation 6.2 (e.g. Schippers and Sand, 1999)

Most of the intermediate sulphur compounds formed during sulphide oxidation are unstable and therefore do not accumulate in the environment. However, experimental work by Schippers and Sand (1998) and Schippers and Jørgensen (2001) has shown that the presence of sulphur intermediates, e.g. thiosulphate, during bioleaching processes can have a significant impact on sulphide dissolution rates. Bacterial disproportionation and oxidation of sulphur species generates additional acidity (e.g. Equation 6.7; e.g. Johnson and Hallberg, 2003) which supplies protons for hydrolysis sulphide attack.

$$S_2O_3^{2-} + 2O_2 + H_2O \xrightarrow{Bacteria} 2H^+ + 2SO_4^{2-} \qquad (6.6)$$

The role of microbes in enhancing Fe(II) oxidation rates at neutral pH is less clear. Inorganic Fe(II) oxidation is inferred to dominate at neutral pH; oxidation rates from field studies (e.g. Kirby and Elder Brady, 1998) are consistent with those calculated from inorganic rate laws (Strumm and Lee, 1961). Despite this a variety of neutrophilic Fe-oxidising bacterium, including: *Leptothrix ochracea*; and *Gallionella ferruginea*; have been observed in neutral pH environments such as Fe(II) bearing groundwater seeps (e.g. Hallbeck et al., 1993; Emerson and Moyer, 1997; Ehrlich, 1996a). In these conditions *G. ferruginea* can grow autotrophically and mixotrophically with Fe(II) as the electron donor (Hallbeck et al., 1993), however, there is no equivocal evidence for enzymatic Fe oxidation by *G. ferruginea* or other Fe-oxidising bacteria at circumneutral pH (Ehrlich, 1996a). Although there is no evidence for a direct link between Fe oxidation and metabolic processes at neutral pH, field studies of ferrihydrite stalactites in caves have demonstrated fast Fe(II) oxidation and precipitation rates that are approximately 10^4 times those inferred from inorganic rate laws (Kasama and Murakami, 2001). In this instance increased reactions rates are inferred to be related to mineral templating on microbe surfaces (Kasama and Murakami, 2001; Edwards et al., 2003b & c).

6.1.2 Mechanisms of bio-mineralisation

The mechanisms of bio-mineralisation can be broadly divided into two groups: (1) direct, intracellular mineral deposition, i.e. within the cell, and at the surface of the cell; and (2) indirect, extracellular mineral deposition, i.e. formation of minerals in the external bulk phase. In both cases mineral growth may result from either active metabolic, enzymatic processes and/or more passive processes. Passive processes include reaction of positively charged ions with functional groups on the bacterial surface, or where inorganic ions involved in metabolism, such as sulphide, are excreted from the cell leading to stoichiometric excess in the bulk phase and mineral precipitation. Distinctions can be made between biologically controlled precipitation, i.e. direct mediation, and biologically induced mineralisation, i.e. indirect processes. Figure 6.1 summarises the most common sites of intracellular mineral deposition and the mechanisms responsible for mineralisation. Figure 6.2 summarises common processes involved in extracellular microbial metal mineralisation. Preservation of bacterial structures in the fossil record is largely the result of mineral templating of the bacterial structure via bio-mineralisation within the cell envelope and at the cell surface. There are two basic mechanisms by which mineral templating of microbial surfaces and cells may take place. In the first mechanism, templating arises from passive or active uptake of inorganic ion species into the cell which are then converted to oxides and salts for cellular protection, the microbe serves as a template by specifying the structural arrangement of the mineral e.g. $CaCO_3$ as foraminiferal tests (e.g. Ehrlich, 1996b; Ehrlich, 1999). Mineral templating of bacterial cells in this way is advantageous for some micro-organisms, including foraminifera, as it can provide protection from physical damage. In addition, intracellular fixation and immobilisation of metals allows some bacteria to survive by in environments where the level of toxicants is high by converting them to less or non-toxic forms (e.g. Beveridge et al., 1983; Ferris et al., 1986; Ehrlich, 1999).

The second mechanism is concerned with extracellular and epi-cellular processes. Because almost all bacterial surfaces have a net electronegative charge (e.g. Beveridge, 1989; Ehrlich, 1999) they are effective sorption interfaces for metal complexation. Once a metal has complexed to the cell surface the metal itself then provides a nucleation site for further complexation resulting in the formation of mineral precipitates around the cell, these precipitates are initially amorphous, in the case of Fe ferrihydrite is the initial precipitate, converting to more crystalline phases over time, ferrihydrite converts to hematite (e.g. Schultze-Lam et al., 1996; Ferris et al., 1986; Ehrlich, 1996b). In addition to metal complexation with the negatively charge cell surface, Fe oxidising bacteria can accumulate Fe oxide in extracellular polymeric substances (EPS). EPS mediate the contact between the cell wall and the surface of the mineral from which Fe(II) is obtained (e.g. Gehrke et al., 1995; Kinzler et al., 2003). Deposition of Fe oxides in the EPS layer surrounding a cell can lead to preservation of the microbial structure e.g. *L. ochracea, L. discophora,* and *Leptospirillum ferrooxidans*, which form sheaths of Fe oxide around the cell (e.g. Emerson and Revsbech, 1994). When Fe oxides completely cover the surface of bacterial cells access of nutrients into the cell and expulsion of cellular waste is prevented which may ultimately lead to cell death. Some bacteria can avoid this problem, for example *G. ferruginea*, which limits Fe oxide deposition to its stalk from which the cell can detach (e.g. Ehrlich, 1999). *Bacillus subtilis* solves the problem by restricting the number of negatively charged sites at the cell surface by occupying some of these sites with the protons produced during respiration, thereby restricting the number of metal binding sites. As a consequence of this live *B. subtilis* cells have a lower metal-binding capacity than dead cells (e.g. Schultze-Lam et al., 1996; Urrutia et al., 1992).

Mineral deposition in the cytoplasm

The mechanism of CaCO$_3$ precipitation is unknown. It may result from spontaneous reaction of aqueous Ca^{2+} taken into the cell with metabollically produced CO$_2$ under conditions of stoichiometric excess (e.g. Erhlich, 1999).

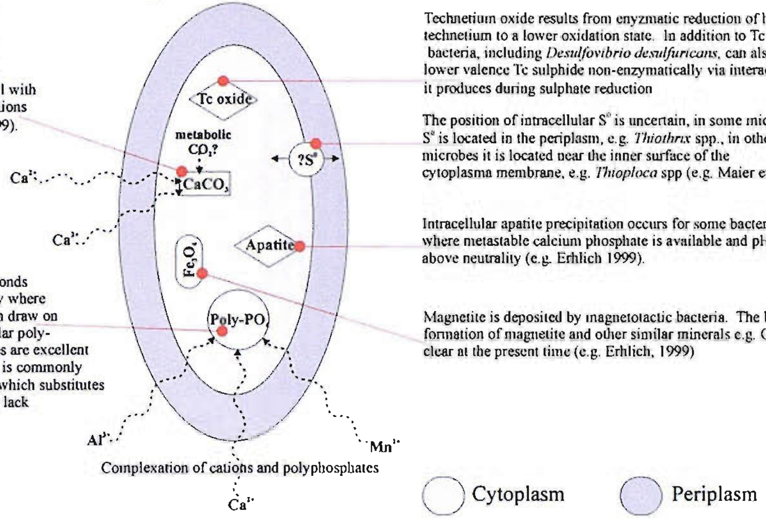

Technetium oxide results from enyzmatic reduction of heptavalent technetium to a lower oxidation state. In addition to Tc oxides some bacteria, including *Desulfovibrio desulfuricans*, can also precipitate a lower valence Tc sulphide non-enzymatically via interaction with the H$_2$S it produces during sulphate reduction

The position of intracellular S^0 is uncertain, in some microbes S^0 is located in the periplasm, e.g. *Thiothrix* spp., in other microbes it is located near the inner surface of the cytoplasma membrane, e.g. *Thioploca* spp (e.g. Maier et al., 1990).

Intracellular apatite precipitation occurs for some bacteria (e.g. *E.coli*) where metastable calcium phosphate is available and pH is slightly above neutrality (e.g. Erhlich 1999).

Poly phosphates are linked by anhydrite bonds which store metabolically available energy where new energy sources are scarce bacteria can draw on this stored energy, if this occurs intracellular poly-phosphates are dissolved. Poly-phosphates are excellent ligands for certain cations. Complexation is commonly species specific e.g. Mn^{2+} in *Lactobacilli*, which substitutes functionally for the catalase these bacteria lack (e.g. Kornberg, 1995).

Magnetite is deposited by magnetotactic bacteria. The bacterial formation of magnetite and other similar minerals e.g. Greigite is not clear at the present time (e.g. Erhlich, 1999)

Sites of intracellular mineral deposition in prokaryotic microbes. Eukaryotes are only known to deposit poly-phosphate intracellularly. Microbial involvement in intracellular mineral deposition is enzymatic driven by metabolic and trace element requirements.

Mineral deposition in the cell envelope (periplasm)

Te^0 is deposited in the periplasm and in the plasma membrane following enzymatic reduction of Tellurite which acts as a terminal electron acceptor in respiratory processes (e.g. Gerrard et al., 1974; Erhlich, 1999).

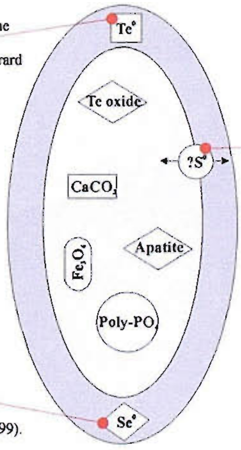

As above, position of S^0 is uncertain, newer studies suggest it is found in both the cytoplasm and the periplasm because of an association with the plasma membrane. Sulphur in the periplasm is formed from either S$_2$O$_3^{2-}$ or H$_2$S (e.g. Erhlich 1999, and references therein).

Se^0 is deposited in the periplasm following enzymatic reduction of Selenite and/or Selenate which both act as terminal electron acceptors in respiratory processes. All bacteria assimilate at least some Se^0 into the cell because it is an essential nutrient (e.g. Gerrard et al., 1974; Erhlich, 1999).

Sites of mineral deposition in the cell envelope in prokaryotic microbes. Eukaryotes are not known to deposit minerals in these sites. Mineral deposition is principally enzymatic however some non-enyzmatic reations may result in similar mineral formation.

Epi-cellular Mineral deposition

Ca^{2+} passively bound to the cell surface forms calcite or aragonite with CO$_2$ derived from cell respiration, providing that the surrounding water contains enough carbonate. CaCO$_3$ bound to the cell surface prevents access of nutrients and expulsion of waste, this will ultimately lead to cellular death. Calcite encrusted cells then act as nuclei for further abiotic calcite deposition in supersaturated conditions (e.g. Greenfield, 1963). In contrast, some organisms actively induce CaCO$_3$ precipitation and exert controls on the resulting crystal structure e.g. Coccoliths and Foraminifera (Erhlich, 1999 and references therein). Since the morphology of foraminiferal tests is species specific the mechanisms controlling CaCO$_3$ deposition are also species specific.

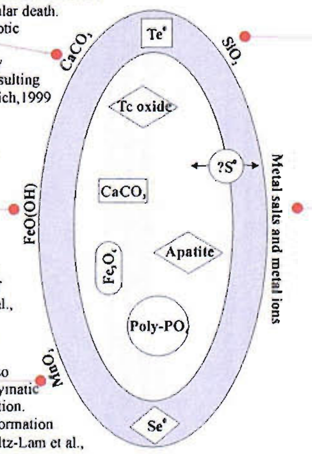

Electropositive amine groups within the cell wall provide effective sorption surfaces for silicate ions at circumneutral pH. There are not enough amine groups to account for the large amounts of epicellularly bound silicate observed in nature; ' extra' silicate is deposited through metal ion bridging in which multi-valent metal ions e.g. Fe^{3+} form electrostatic bonds with SiO$_4^{2-}$ (Urrutia and Beveridge, 1993). Laboratory simulations have shown recognisable preservation of bacterial structures via silicification at low temperature, particularly at ~60°C (e.g. Oehler, 1976).

Almost all bacterial surfaces have an overall electronegative charge (e.g. Beveridge, 1989) this makes them effective sorption surfaces for metal ion complexation. The bound metal ions may than form metal salts and oxides which provide further nucleation sites for further deposition of metals and resulting in mineral growth. In this way bacteria can cause the immobilisation of aqueous metal ions.

Fe-oxidising bacteria accumulate ferric oxides in extracellular polymeric substances (EPS). EPS mediate the contact between the bacterial cell proper and the surface of minerals from which Fe(II) is obtained, Fe(III) complexed EPS has a positive charge and this allows the bacterium to attach to the surface of minerals in a reduced state, e.g. Pyrite (e.g. Kinzler et al., 2003). Fe(II) can be used as an electron donor in heterotrophic respiration, fermentation and hydrolysis reactions (e.g. Sorensen et al., 1981). In addition to Mn(II) oxidisers several Fe oxidising bacteria are also able to deposit Mn oxides at the cell surface where enzymatic processes affect the redox state resulting in immobilisation. Incorporation of OH$^-$, HCO$_3^-$, SO$_4^{2-}$, etc, results in the formation of hydrated metal compounds e.g. FeO(OH) (e.g. Schultz-Lam et al., 1996; Erhlich, 1999, and references therein).

Epi-cellular sites of mineral deposition. Both enzymatic and non-enzymatic processes are involved in the precipitation of minerals at the cell surface.

Figure 6.1: Summary of the common sites and deposition mechanisms of intracellular microbial mineralisation. Adapted from Erhlich, 1999.

Metal sulphide formation is the result of passive processes where inorganic anions e.g. HS- utilised for metabolic processes are excreted from the cell and interact with aqueous metal cations e.g. Fe^{2+}, Cu^{2+}, in the surrounding environment, under conditions of stoichiometric excess this will lead to mineral precipitation. Precipitation of sulphide minerals in this way is particularly important in environments where sulphate reducing bacteria e.g. *Desulfovibrio desulfuricans* are present.

Metal sulphide e.g. FeS_2

Microbially mediated growth of Fe oxides and carbonates in the bulk phase (in contrast to intracellular Fe oxide precipitation, which is largely carried out by Fe oxidising bacteria) most commonly results from the action of Fe reducing bacteria, e.g. bacterial reduction of ferric iron with acetate results in the precipitation of magnetite in the bulk phase. Environmental conditions, principally the redox state, are the main control on whether the organically reduced iron accumulates as Fe(II), magnetite, hematite or siderite (e.g. Bell et al., 1987; Erhlich, 1999).

Fe_3O_4, Fe_2CO_3

Bulk phase accumulation of microbially produced S^0 is uncommon, most of the sulphur excreted by microbes is in a reduced, e.g. HS^-, H_2S, or oxidised form, e.g. $S_2O_3^{2-}$, SO_4^{2-}. However some bacterial strains, most notably green sulphur bacteria excrete S^0 to the bulk phase when oxidising HS^- during anaerobic photosynthesis (e.g. Pfennig et al. 1977).

S^0

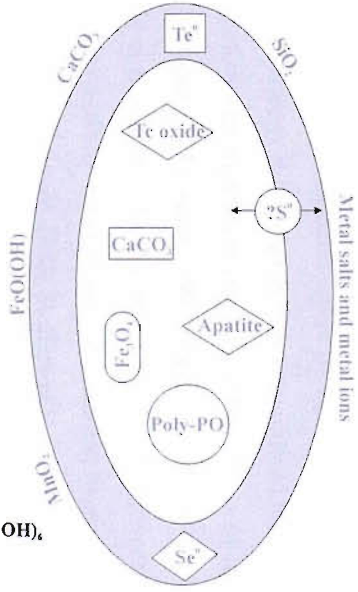

Some bacteria e.g. *Bacillus* spp, are able to limit the toxicity of chromate by reduction of Cr(VI) to Cr(III) under pH conditions close to neutrality (e.g. Wang and Xiao, 1995), the Cr(III) produced may then be precipitated as an oxide in the bulk phase.

CrOOH

Uranium (IV) oxide in the bulk phase may be precipitated either via reduction of UO_2^{2+} by HS^- released by sulphate reducing bacteria, and/or via enzymatic reduction of UO_2^{2+} by sulphate and metal reducing bacteria under anaerobic conditions (e.g. Lovely and Philips, 1992).

UO_2

MnO_2

MnO_2 precipitation in the bulk phase results from the action of Mn(II) oxidising bacteria. which utilise Mn2+ as electron acceptor in respiration. Oxidation of Mn(II) to Mn(III) is enzymatic, Erhlich, (1990) proposed that the resulting Mn(III) remains bound to the enzyme which then catalyses conversion of Mn(III) to Mn(IV) and produces MnO_2. In bacteria where MnO_2 accumulation is not possible, the MnO_2 is excreted from the cell to the bulk phase and may become incorporated in pre-exisiting manganese oxides or ferromanganese or added to certain clays (e.g. Erhlich, 1999; 1996).

Acidophilic Fe oxidising bacteria, e.g. *Thiobacillus ferrooxidans* may precipitate jarosite during bio-alteration of sulphide material at low pH.

$(K, Na)Fe_3(SO_4)_2(OH)_6$
(Jarosite)

Au^0

Microbial deposition of Au in the bulk phase arises from liberation of Au which was originally located intracellularly during autolysis. This liberated gold forms pseudotrigonal and hexagonal-octahedral crystals which may then form aggregates leading to the formation of gold nuggets. The valence state of the gold when it is inside the cell is not known, the reduction from auric to metallic gold may take place intracellularly or in the bulk phase (e.g. Southam and Beveridge, 1994).

$Ca_5(PO_4)_3(F,Cl,OH)$(apatite) / $Mg(NH_4)PO_4.6H_2O$ (struvite) /
$FePO_4.2H_2O$ (strengite) / $Fe_3(PO_4)_2.8H_2O$ (vivianite) / $AlPO_4.2H_2O$ (variscite)

Phosphate minerals form authigenically from dissolved species of which one or more is microbial in origin; microbial metabolic processes mobilise organically bound phosphate which can then react authigenically with cations in the surrounding environment, e.g. interaction with Ca2+ results in precipitation of phosphorite and ultimately apatite deposition.

Figure 6.2: Summary of common epicelluar microbially mediated and microbially induced mineralisation. Adapted from Erhlich, 1999.

Bacterial walls are also effective sorption surfaces for silicate ions, although cell walls have a net electronegative charge, the presence of free electropositive amine groups promotes interaction with SiO_3^{2-} (Urrutia and Beveridge, 1994). The amount of silica that can be bound to the cell wall is increased by metal-ion bridging, where a multivalent metal ion, e.g. Fe^{3+}, cross-links SiO_3^{2-} to COO^- or PO_4^{3-} by electrostatic interaction (Urrutia and Beveridge, 1994). Structural preservation is enhanced by the binding of metal ions (which inactivate autolytic enzymes that degrade cell walls following death) prior to silicification (Ferris et al., 1988). Binding of silicate to bacterial surfaces has a positive feedback on the overall capacity for metal sorption, since silicate minerals bound to the cell surface provide additional metal sorption sites (e.g. Urrutia and Beveridge, 1994; Schultze-Lam et al., 1996). Fossilisation of recognizable microbial structures can be achieved via silicification in this way (Oehler and Schopf, 1971; Oehler, 1976; Urrutia and Beveridge, 1994; Schultze-Lam et al., 1996).

6.1.3 Microbial bio-mineralisation at seafloor hydrothermal sites

Extensive sampling of hydrothermal vent sites over the last few decades has led to many observations of Fe-oxide and silicified filamentous textures in low temperature Fe oxide rich deposits adjacent to vent sites (Table 6.1 summaries the seafloor sampling of putative biogenic structures) and also in vent fluids (Halbach et al., 2001). Many of these observations are from seamounts where pervasive diffuse flow is the dominant venting style (e.g. Alt, 1988b). The mineralogy is dominated by poorly ordered Fe oxyhydroxides (Two-XRD-line ferrihydrite and goethite), often with significant amounts of amorphous silica (up to 73wt%) and Mn (up to 14wt%) (e.g. Alt, 1988b; Juniper and Fouquet, 1988; Hekinian et al., 1993; Boyd and Scott, 2001; Emerson and Moyer, 2002; Kennedy et al., 2003b). The filaments are usually between 1 and 5µm in diameter, and 10s to 100s µm long, and many have distinctive morphologies, including twisted ribbons, hollow sheaths, and dendritic forms (Alt, 1988b; Juniper and Fouquet, 1988; Stoffers et al., 1993; Thorseth et al., 2001; Boyd and Scott, 2001; Emerson and Moyer, 2002; Kennedy et al., 2003b). Several authors have noted the similarity of these morphologies with structures formed by neutrophilic Fe oxidising bacteria, including *G. ferruginea*, which grows Fe encrusted twisted stalks (e.g. Hanert, 2002), and *L. ochracea*, which forms Fe oxide encrusted sheaths (e.g. Emerson and Revsbech, 1994). Although neither of these bacterial taxa have been conclusively identified (by culture or molecular analysis) from marine hydrothermal Fe oxide deposits, a novel strain of Fe oxidising bacterium (PV-1) has been cultured from the Loihi Seamount vent site (Emerson and Moyer, 2002). PV-1 grows slender (<1µm diameter) Fe oxide filaments which are comparable to filaments in natural samples from the seamount. Very similar sheathed and helical Fe oxide filaments have also been observed to form on sulphide surfaces at a low temperature vent within the Endeavour Vent Field, Juan de Fuca Ridge (JdFR) during in situ incubation experiments (Edwards et al., 2003b & c).

Mineral templating of cell surfaces appears to be important for preservation at hydrothermal sites. Most hydrothermal Fe oxide deposits are intermixed with clay minerals, principally nontronite, which form in the suboxic conditions associated with sulphide weathering (e.g. Severmann et al., 2004). The nontronite is often intimately associated with Fe oxide filaments (e.g. Alt, 1988b) and nontronitic filaments, tubes and sheaths have been observed in white smoker chimneys, these structures are inferred to arise from templating of the clays around biogenic structures (Kohler et al., 1994). TEM and epiflourescence imaging has shown that some of the filaments described in the literature are cylindrical casts of Fe oxyhydroxides formed around

Area	Location	Depth	Bulk mineralogy	Observation	Reference
Explorer Ridge Philosopher Vent	NE Pacific		Amorphous silica and Fe-oxide	Hyphae-like filament networks, long branching filaments, hollow filaments 1-2μm diameter	Juniper and Fouquet, 1988
Main Endeavour segment	Juan de Fuca Ridge (JdFR) NE Pacific		Various metal sulphides	Irregularly twisted branching filaments, coiled and vibroid-shaped cells, and chains of nano-spheres.	Edwards et al. 2003a
Middle Valley segment	JdFR		Metal sulphide unspecified	Twisted, dendritic Fe-oxides, straight bundles of filaments, braided filaments	Edwards et al. 2003b
Axial Volcano	Juan de Fuca Ridge 46°N, 130°W	1500m	Fe-oxides unspecified	Spirals, sheaths, PV-1	Kennedy et al., 2003
	21° 30'N EPR		Fragment of inactive oxide chimney	Hollow filaments	Juniper and Fouquet. 1988
Red Sea Mount	EPR, 21°N	1940m	Not specified; soft oxide muds	Fe-oxide spirals, flat twisted ribbons; Short multi branching filaments	Alt, 1988; Juniper and Fouquet, 1988
Mariana Trough	18°N, 144°W	3610m	Nontronite	Filaments, tubes and sheaths.	Kohler et al., 1994
Seamount 5	EPR, 13°N	1000m	amorphous Fe oxides and nontronite	Twisted filaments	Alt, 1988
	EPR, 12° 50'N		Chimney fragment not specified	Branching filaments	Juniper and Fouquet 1988
Galapagos Rift	0°N, 85°W	2550m	Nontronite	Filaments, tubes and sheaths.	Kohler et al., 1994
Loihi Seamount	Hawaii	1200m		Sheaths, filaments, extensive bacterial mats	Emerson and Moyer, 2002
Coriolis Trough	SW Pacific	1100-1500m	Fe-Si oxyhydroxides	Filamentous web like networks. Hollow tubes	Iizasa et al. 1998
Knipovich Ridge	MAR, 76°N			Twisted filaments	Thorseth et al., 2001
FAMOUS	MAR, 36° 57'N		From oxide mound unspecified	Clustered branching filaments	Juniper and Fouquet, 1988
TAG	MAR, 26°N	3650m	Red and gray chert, not specified	Thread like cellular masses, chains of nano-spheriods	Al-Hanbali and Holm, 2002; Al-Hanbali et al. 2001
TAG	MAR, 26°N	3650m	Moss agate	Branching dendritic Fe-oxides (assigned an inorganic origin)	Hopkinson et al. 1998

Table 6.1: Summary of seafloor sampling of putative biogenic structures (from Little, Glynn and Mills., 2004).

bacterial cells (Fortin et al., 1998; Emerson and Moyer, 2002; Hanert, 2002; Kennedy et al., 2003a, b & c) and are thus indisputably biogenic. However most identification of microbial structures in natural samples is based entirely on similarities in the morphology of filaments and sheaths; the twisted helical structure of *G. ferruginea* being one of the most compelling examples cited as evidence for Fe oxidising bacteria (e.g. Alt, 1988b; Ghiorse, 1984), and there are problems associated with recognition of bacterial structures based on morphology alone (e.g. Reysenbach and Cady, 2001; Garcia-Ruiz et al., 2002; Garcia-Ruiz et al., 2003). For example, Hopkinson et al., (1998) propose an alternative, abiogenic mechanism to explain the formation of dendritic Fe-oxysilicates embedded in amorphous Si in the upper TAG hydrothermal mound. Diffusion limited growth of branching Fe-aggregates within a silica gel at the dissolution-redox front associated with pyrite weathering, are invoked to explain the filamentous structures sampled.

The extent to which precipitation and mediation of iron, silica and sulphate minerals at seafloor hydrothermal sites, is the result of metabolic activity of the bacteria, or more passive processes where functional groups on the bacterial surfaces interact with positively charged ions, is unclear (Konhauser et al., 2002; Glasauer et al., 2001; Emerson and Moyer, 2002; Kennedy et al., 2003a, b & c).

6.1.4 Filamentous textures in ancient Fe oxide deposits

The jasper beds which are commonly associated with terrestrial massive sulphide deposits are inferred to be the ancient analogues of modern seafloor Fe oxide deposits (e.g. Duhig et al., 1992; Davidson et al., 2001; Little and Thorseth, 2002; Greene and Slack, 2003). Although most authors suggest that the jaspers formed from diffuse, low temperature Fe-Si-rich hydrothermal fluids filaments in the jaspers differ from seafloor filamentous Fe oxides in two respects: (1) the filaments are usually composed of hematite rather than ferrihydrite or goethite and silica is present in crystalline form, either as chalcedony and/or quartz, rather than amorphous silica. This reflects the greater thermal maturity of terrestrial jasper deposits and the change from metastable highly hydrated mineral forms to more stable, crystalline minerals (e.g. Schultze-Lam et al., 1996; Boyd and Scott, 2001); (2) silica is much more abundant accounting for 80-95vol% (Table 6.2. and references therein).

The filamentous Fe oxides sampled from terrestrial jasper deposits commonly have distinctive morphologies, including: dendritic and branching forms; twisted ribbons; hollow rod-like cylinders and; interlocking meshes (Table 6.2 summaries the sampling of jaspers with filamentous textures). Some of these textures, such as twisted ribbons, have been directly compared to Fe oxidising bacteria such as *Gallionella* spp. (e.g. Juniper and Fouquet, 1988; Duhig et al., 1992; Little et al., 1999; Little and Thorseth, 2002). Other morphologies such as large dendritic masses, for example those described from Ballynoe (Ireland) (Table 6.2) cannot be attributed to any specific microbial morphology (e.g. Little and Thorseth, 2002; Boyce et al., 2003). Although the jasper filaments share many morphological characteristics with bacterial forms, and with seafloor filamentous Fe oxides; some of which are unquestionably biogenic (Fortin et al., 1998; Emerson and Moyer, 2002; Hanert, 2002; Kennedy et al., 2003a, b & c) there is no definitive proof for biogenic origins. While most authors support a biogenic formation mechanism for the filaments, abiogenic mechanisms which have also been proposed deserve some comment (e.g. Garcia-Ruiz et al., 2002; Garcia-Ruiz et al., 2003). In laboratory simulations, Garcia-Ruiz et al (2002; 2003) were able to grow twisted filaments of barium

Jasper deposit	Location	Age	Host rocks	Palaeotectonic setting	Bulk mineralogy	Filament mineralogy	Reference
Juniper and Fouquet terrestrial sample 2	Luzon, Philippines	Late Eocene	Zambales Ophiolite; jasper associated with Barlo VMS deposit	Supra-subduction zone	'Pyritic chert' (not specified)	'Fe oxide' (not specified)	Juniper and Fouquet 1988
Kambia	Cyprus	Late Cretaceous (~91 Ma)	Basaltic pillow lavas of Troodos Ophiolite; jasper assocaited with Kambia VMS deposit	Supra-subduction zone	Quartz, chalcedony, Haematite	Haematite	Little and Thorseth 2002
Juniper and Fouquet terrestrial sample 1	Cyprus	Late Cretaceous (~91 Ma)	Interpillow chert from Troodos Ophiolite	Supra-subduction zone	'Chert' (not specified)	'Fe oxide' (not specified)	Juniper and Fouquet 1988
Juniper and Fouquet terrestrial sample 3	California, USA	Late Jurassic	Interpillow chert from Coast Range Ophiolite	Supra-subduction zone fore-arc basin	'Brecciated chert' (not specified)	'Fe oxide' (not specified)	Juniper and Fouquet 1988
ODP Core 129-801C-4R	Pigafetta Basin, Western Pacific	Mid Jurassic (~165 Ma)	Pillow basalts	Mid-ocean ridge and ocean island	Quartz, Fe oxyhydroxide	Fe oxyhydroxide	Alt et al. 1992
Figueroa	California, USA	Early Jurassic (~190 Ma)	Basaltic pillow lavas of Franciscan Complex; jasper associated with Figueroa VMS deposit	Mid-ocean ridge or ocean island	Quartz, Haematite	Haematite	Little et al. 1999; Little and Thorseth 2002
Ballynoe	Ireland	Early Carboniferous (~352 Ma)	Carbonates; jasper occurs within Ballynoe barite deposit	Intracratonic basin	Quartz, Haematite, barite	Haematite	Little and Thorseth 2002; Boyce et al. 2003
Alexandrinka	Chelyabinsk district, Southern Urals, Russia	Mid Devonian (~390 Ma)	Rhyodacites; jasper associated with Alexandrinka VMS deposit	Island-arc	Quartz, Haematite	Haematite	Little and Thorseth 2002
Several different jasper lenses in Mt. Windor Fmn.	Queensland, Australia	Early Ordovician (481-485 Ma)	Felsic volcanics of Mount Windsor Formation; some jaspers associated with Thalanga VMS deposit	Back-arc basin	Quartz, Haematite	Haematite	Duhig et al. 1992a,b
Løkken	Trondheim region, Norway	Early Ordovician (~490 Ma)	Basaltic pillow lavas of Løkken ophiolite; jaspers associated with Løkken and Høydal VMS deposits	Back-arc basin	Quartz, Haematite; minor goethite and carbonate	Haematite	Grenne and Slack 2003, in press

Table 6.2: **Jaspers with filamentous textures (from Little, Glynn and Mills., 2004).**

carbonate (witherite) in alkaline silica-rich solutions, and hollow helical silica filaments by acid etching of the witherite filaments. These structures, grown abiogenically, superficially resemble the Fe oxide filaments described from jasper deposits and have led Garcia-Ruiz et al (2002; 2003) to question the biogenicity of natural samples. However, there are three important differences between these 'biomorphs' and the jasper filaments:

1. The 'biomorphs' are composed of witherite; the jasper filaments of Fe oxide. In addition, the initial witherite filaments are solid whereas the jasper filaments are typically hollow cylinders.
2. The witherite filaments, in contrast to the Fe oxide jasper filaments, have variable not constant diameters; in addition, they are commonly an order of magnitude larger than the Fe oxide filaments.
3. None of the synthetic filaments are septate, some filaments from the Figueroa jaspers have internal septae and/or terminal knobs (Little et al., 1999; Little and Thorseth, 2002); nor are there any looped or branching forms such as those reported for Ballynoe and Kambia filaments (e.g. Little and Thorseth, 2002; Boyce et al., 2003).

In the absence of definitive evidence either for or against a biogenic origin, the circumstantial evidence suggests that a biogenic origin for jasper filaments is the most likely (e.g. Juniper and Fouquet, 1988; Little and Thorseth, 2002; Little et al., in press 2004).

Abiogenic processes are inferred to dominate oxidation of Fe(II) in the circumneutral pH conditions found in hydrothermal plumes and at the seafloor (McCollom, 2000) where Fe(II) has a half life of ~2-3 minutes (Millero et al., 1987) and oxidation proceeds rapidly. However, inorganic oxidation of Fe(II) proceeds extremely slowly in the lower pH (pH ~6), low oxygen (O2 ~1 ml/l) environment present in the upper 10s of centimetres of hydrothermal deposits (Fe(II) half life >5 days; Millero et al., 1987). This environment potentially provides the conditions for significant biological mediation of Fe(II) oxidation (Emerson and Moyer, 2002). Although the presence of Fe oxide and silica coated filaments is of great potential as a biomarker for Fe oxidising bacteria in modern hydrothermal vent deposits, without definitive evidence of organic matter, identification, and the biogenicity of these structures remains uncertain. Demonstrating an association between bacteria and Fe oxidation is the key to quantifying their role in the alteration of Fe-rich hydrothermal deposits.

6.1.5 Aims and objectives

This study investigates Fe-oxide filaments and associated minerals in hydrothermal sediments from the *Alvin* relict high temperature zone at TAG and examines their relationship to sediment diagenesis with an aim to discriminate between abiogenic and biogenic formation processes. The trace metal geochemistry and strontium and sulphur isotopic compositions of associated gypsum were examined in order to identify potential biogeochemical tracers of microbially mediated Fe oxidation. Qualitative X-ray spot microanalyses of filament meshes were carried out in order to check for biogenic remnants. In addition to the investigation of Fe oxide filaments, a biogenic origin for the larger sulphide and Fe oxide tubes discovered during hand picking of mineral separates for sulphide S isotope analysis (Chapter 5) was investigated.

6.2 Materials and Methods

All samples are taken from the sulphide layer (76-138.5cm depth) of CD102/58: the *Alvin* core. The bulk geochemistry of the sulphide layer sediment is given in Chapter 3; sulphide paragenesis and alteration are discussed in Chapter 4; and sulphide mineral S isotope variation in Chapter 5.

6.2.1 Sample preparation

Three polished thin sections 30μm thick were prepared for transmitted light microscopy and SEM analysis from the resin impregnated laminated section at 76-87cm depth, from the top of the sulphide layer, details of the impregnated section are given in Chapter 4. Sulphide and Fe oxide tubes for SEM and X-ray spot microanalyses were hand picked from 6 sub samples at 1cm depth intervals between 76-86cm depth downcore.

Gypsum separates for ICP-AES, $^{87}Sr/^{86}Sr$ and sulphur isotopic analysis were hand picked from 1-2cm depth sub-samples at depths of 76-100cm downcore. The surfaces of the gypsum crystals were cleaned by ultra sonic agitation in 0.5M HCl for 30 minutes following which the samples were washed with Milli-Q water and dried overnight at ~50°C. Samples were then hand ground to a fine powder in an agate pestle and mortar. Total dissolution of 0.01-0.09g of ground gypsum separates was achieved using 0.6M HCl. Samples were reacted with ~10ml of 0.6M HCl in sealed 15ml Teflon beakers and refluxed at ~70°C for 72 hours. 1ml aliquots of the resulting solution were reserved for ICP-AES and Sr isotope analyses. The remaining solution was converted to $BaSO_4$ via reaction with BaCl solution in stoichiometric excess, dried overnight at ~70°C and hand ground to a fine powder in an agate pestle and mortar for use in conventional S isotope analysis.

6.2.2 Optical microscopy

The polished thin sections were examined and photographed in transmitted and reflected light on a binocular polarising microscope.

6.2.3 Scanning Electron Microscopy (SEM)

Method for polished thin sections is given in Chapter 4. Prior to SEM analysis the sulphide and Fe-oxide tubes were attached to carbon discs on 12mm diameter aluminium stubs. The tubes were then coated with gold (~20nm thick) under vacuum in an Ar atmosphere using a HUMMER VI A with an applied voltage of 10mA. Subsequent SEM examination of the tube structures and X-ray spot microanalysis follows the method given in Chapter 4.

6.2.4 Thermal Ionisation Mass Spectrometry (TIMS): Strontium isotopes

0.1-0.2ml aliquots of the 0.6M HCl gypsum solutions were evaporated to incipient dryness and taken up in 300μl of 3M HNO_3. Sr was separated from the mineral solution in 2ml columns with 30mm Sr spec resin bed volume (mesh 100-150 microns); eluted with 3M HNO_3; and loaded on to out-gassed tantalum single filaments using a Ta activator solution. $^{87}Sr/^{86}Sr$ ratios were then measured on a V.G. Sector 54 TIMS. External precision and accuracy were monitored by simultaneous analysis of standard reference material; NBS 987. The average value of NBS 987 on this instrument is 0.71025±19 (2σ standard error (SE)) (M. Cooper, Pers. Comm.).

6.2.5 Sulphur isotopes

~10mg of $BaSO_4$ were mixed with ~200mg Cu_2O and 600mg SiO_2 and roasted under vacuum conditions at 1075°C in a furnace for ~20 minutes. The resulting SO_2 from the high temperature furnace is open to a secondary Cu furnace at ~700°C on the vacuum distillation line prior to the slush trap. The SO_2 was then cryogenically purified by vacuum distillation. Sulphur isotopes analyses were carried out following the conventional S isotope method given in Chapter 5. One sub-sample of sulphide tubes from 80-81.5cm depth was also run for S isotopes following the conventional S isotope method given in Chapter 5.

6.2.6 Inductively Coupled Plasma-Atomic Emission Spectroscopy (ICP-AES)

0.1-0.2ml aliquots of the 0.6M HCl gypsum solutions were diluted ~4700-fold. The resulting solutions and reagent blanks were then analysed for Ca, Sr, Mg, Fe and Mn by ICP-AES on a Perkin Elmer Optima 4300DV. Measurements were calibrated using a range of 5 matrix matched, multi element standards (standard concentrations are listed in Appendix B), the analytical accuracy was monitored by simultaneous analysis of these standard solutions. Analytical precision was calculated from 10 repeat analyses of standard 1, expressed as a coefficient of variation, the precision of all measurements is better than 0.3% (1σ).

6.3 Results

The results of ICP-AES analyses of gypsum crystals are listed in Table 6.3a & b; $^{87}Sr/^{86}Sr$ ratios of gypsum separates are given in Table 6.4; and the S isotope composition of gypsum separates are given in Table 6.5.

6.3.1 Fe oxide Filaments

Filament occurrence

All the filaments described in this study come from the laminated section at 76-87cm depth (Figure 4.6) at the top of the *Alvin* core (CD102/58) sulphide layer (76-138.5cm depth downcore). XRD traces and optical microscopy of bulk samples indicate that the black layers are dominated by pyrite, with smaller quantities of chalcopyrite and sphalerite with minor covellite. Orange layers are predominantly composed of goethite with amorphous silica and quartz, with minor gypsum and clay phases (the mineralogy and geochemistry of this section is discussed in detail in Chapter 3 and Chapter 4). Well preserved hematitc and goethitic filaments were observed in all goethite and quartz dominated layers and are associated with the secondary mineral assemblage of silica, gypsum, secondary pyrite, covellite, atacamite and goethite. The filaments show a range of diameters between ~0.5-10μm and are typically 50-100μm long but can be up to 250μm in length. They are observed cemented within gypsum (Figure 6.3a-c) and amorphous silica and quartz phases (Figure 6.4a-g), as non-cemented meshes and as nets associated with and surrounding corroded pyrite grains (Figure 6.5a & b; Figure 6.6a & b).

Filament Morphologies

Dendritic branching structures dominate the morphology of filaments cemented in gypsum. In some instances, the filaments radiate from dense masses in the centre of euhedral gypsum crystals forming branching, dendritic structures (Figure 6.3a). Other gypsum cemented examples show coiling and bundled filaments (Figure 6.3b) and more rarely, rod-like, layered filaments with apparent directed growth parallel to

Sample ID	Depth (cm)	Ca ppm	Fe ppm	Mg ppm	Sr ppm	Mn ppm	% dissolution of solid	Comments
89G	76.25	100641	27926	465	377	85	43.23	Black sulphide rich laminae
90.5G	77.50	196575	38619	555	653	133	84.44	Orange oxide rich laminae
91G	78.00	183790	35426	501	662	132	78.95	Mix of fine black and orange laminae
93G	79.50	98975	18201	264	378	50	42.52	Black sulphide rich Laminae with some oxide material
94G	80.75	41009	6626	109	137	16	17.62	Black sulphide rich Laminae with clearly visible fresh pyrite
96G	83.00	193664	49376	618	657	147	83.19	Orange oxide rich laminae
Mean		135776	29362	419	477	94	58.325	
1σ (SE)		24108	5692	72	80	20	10	
Precision		**0.18**	**0.24**	**0.29**	**0.15**	**0.17**		

Table 6.3a: ICP-AES results for gypsum separates. % dissolution was calculated from the Ca concentration assuming that the solid was pure, stoichiometrically matched gypsum ($CaSO_4.2H_2O$). All of the calculated dissolutions indicate incomplete dissolution of the solid. The best dissolutions are related to gypsum picked from oxide-rich laminae and the lowest dissolutions are related to gypsum picked from sulphide-rich laminae. The majority of gypsum crystals from the laminated section contain sulphides; incomplete dissolution therefore, is inferred to be the result of sulphide inclusions which are not dissolved by 0.6M HCl.

Sample ID	Depth (cm)		Sr/Ca mmol/mol	Mg/Ca mmol/mol	Fe/Mn molar ratio
89G	76.25		1.71	7.62	325
90.5G	77.50		1.52	4.65	287
91G	78.00		1.65	4.49	265
93G	79.50		1.75	4.40	356
94G	80.75		1.53	4.39	416
96G	83.00		1.55	5.26	330
Mean			1.62	5.14	330
1σ (SE)			0.04	0.47	20
Precision			**0.05**	**0.29**	**0.14**

Table 6.3b: Calculated molar ratios for gypsum separates. The precision was calculated as the coefficient of variation from 10 repeat analyses of standard solution 5 (Appendix A).

Table 6.3a & b: ICP-AES analysis of gypsum separates. Table 6.3a shows raw data; Table 6.3b shows molar ratios.

Sample ID	Depth (cm)	^{87}Sr/^{86}Sr	2σ	Hydrothermal fluid %	Seawater %	Inferred temperature °C
89-91.5-G	76.25	0.709145	0.000013	0.5	99.5	3.8
90.5-92.5-G	77.5	0.709165	0.000012	0.2	99.8	2.8
91-93-G	78	0.709157	0.000018	0.3	99.7	3.2
94-95.5-G	80.75	0.708069	0.000017	16.1	83.9	60.2
95-96-G	81.5	0.708570	0.000028	8.7	91.3	33.5
96-97-G	82.5	0.708452	0.000031	10.5	89.5	39.8
96-98-G	83	0.709150	0.000011	0.4	99.6	3.5
98-100-G	85	0.709142	0.000010	0.5	99.5	3.9
104-106-G	91	0.709154	0.000012	0.4	99.6	3.4
106-108-G	93	0.709090	0.000050	1.3	98.7	6.6
112-114-G	99	0.709166	0.000011	0.2	99.8	2.7
Mean		**0.708933 ±0.00012**		**3.6 ±1.6**	**96.4 ±1.6**	**14.9 ±5.8**

Table 6.4a

Parameter	Hydrothermal fluid	Seawater
[Sr] ppm	9.025[a]	7.622
^{87}Sr/^{86}Sr	0.70319[b]	0.70916[c]
Temperature °C	363[a]	2

Table 6.4b References: [a] – Edmond et al., 1995 [b] – Elderfield et al., 1993 [c] – Hodell et al., 1991

Table 6.4: A) Results of Sr isotope TIMS analyses for gypsum separates. Depth is given as the mid-sampling interval. Calculated end-member hydrothermal fluid and seawater strontium contributions are shown, from these a temperature for the mineralising fluid is inferred (equations 6.8). Mean is shown ± 1 standard error calculated at 1σ. B) end member data for TAG hydrothermal fluid and North Atlantic seawater used in equation 6.8 to calculate the temperature of precipitation and the proportions of hydrothermal fluid and seawater Sr in the gypsum separates.

Sample ID	Depth (cm)	Line number	Gas yield %	$\delta^{34}S_{CDT}$‰
Gypsum				
89-91.5-Ba	76.25	SA9353	85	10.4
90.5-92.5-Ba	77.5	SA9351	82	9.7
93-94-Ba	79.5	SA9346	81	10.0
96-98-Ba	83	SA9343	86	9.9
98-100	85	SA9344	79	9.9
104-106-Ba	91	SA9349	82	9.6
112-114-Ba	99	SA9348	79	10.6
			Mean	**10.0±0.14**
SulphideTubes				
94-95.5-T	80.75	SA9358	83	5.8

Table 6.5: Summary of S isotope analyses of gypsum separates and one sulphide tube sample. Depth is given as the mid-sampling interval. Mean is shown ± 1 standard error calculated at 1σ.

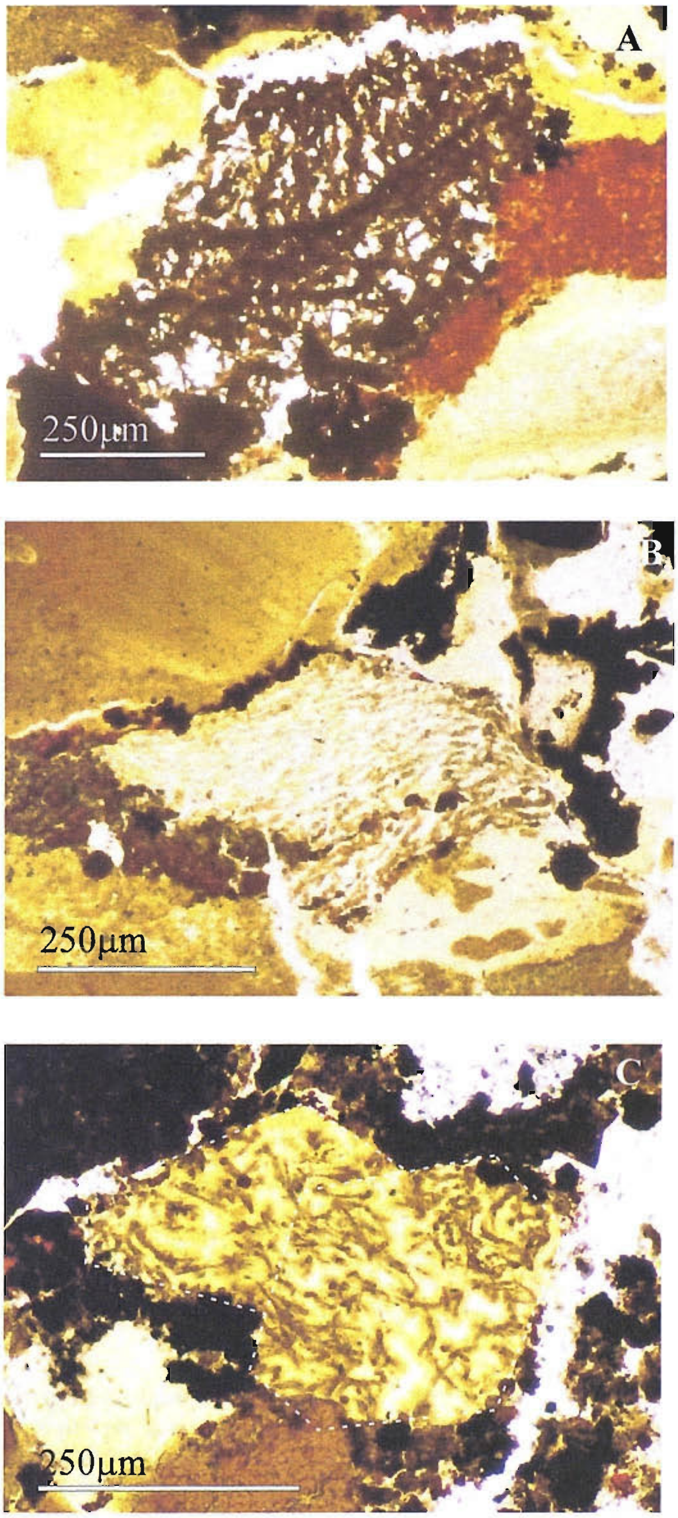

Figure 6.3: Transmitted light photomicrographs of filamentous structures cemented by gypsum. A) Dendritic mass of Fe oxide filaments within euhedral gypsum crystal; B) Goethite filaments showing directed growth lengthwise parallel to sedimentary layering; C) Rod-like goethite filaments variably encrusted with hematite cemented by twinned euhedral gypsum crystals. White dashed lines indicate the crystal boundaries. In all three images the filaments do not extend beyond the gypsum crystal boundaries.

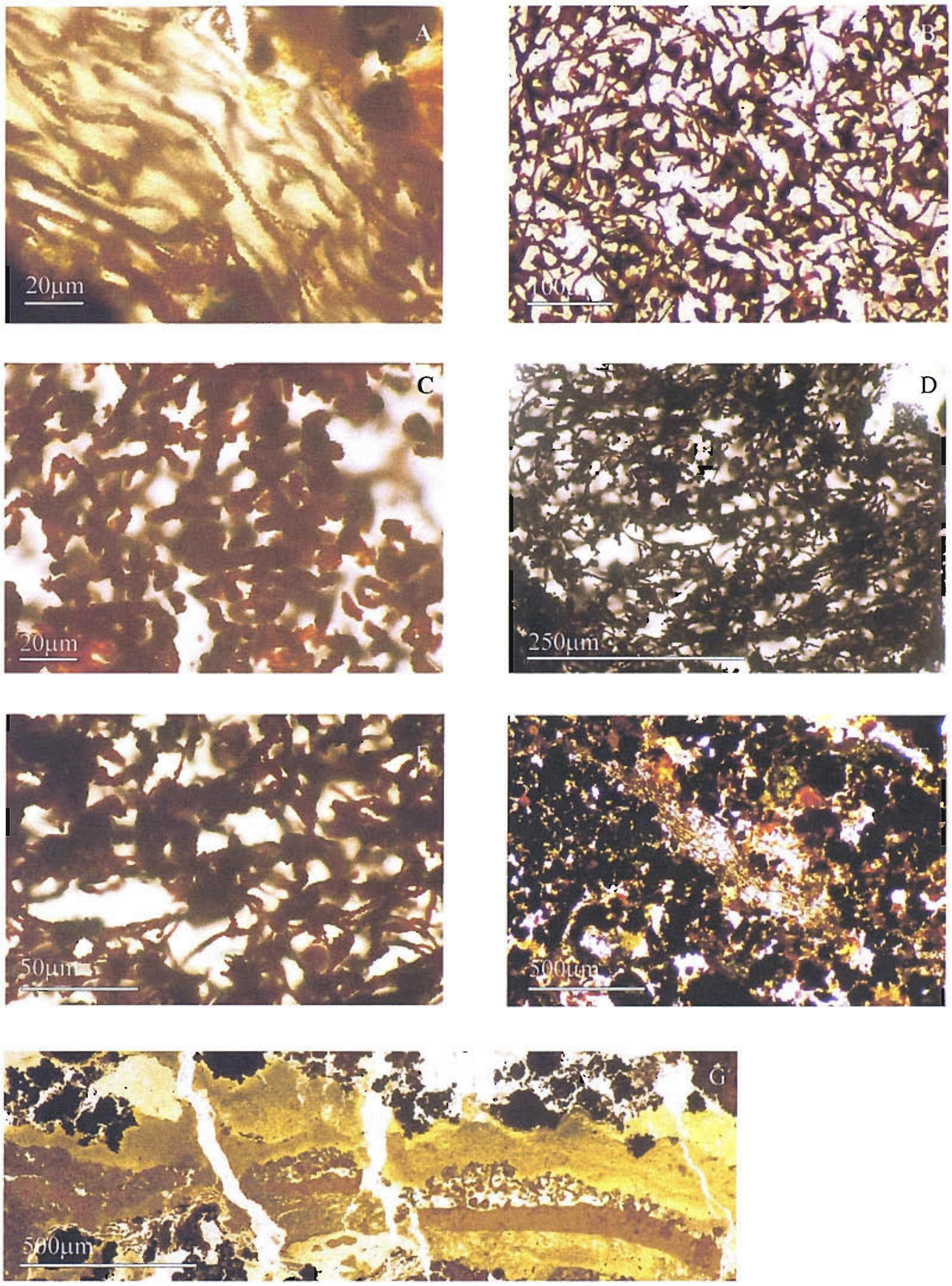

Figure 6.4: Transmitted light photomicrographs of filamentous structures cemented by silica. A) long twisted goethite filaments showing directed growth lengthwise parallel to sedimentary layering; B) Rod-like hematite filaments; C) Bundled twisted filaments; D) and E) Mesh of twisted and rod-like filaments some show branching; F) Long twisted hematite filaments showing directed growth; G) Rod-like and bundled goethite filaments in a band parallel with sedimentary layers.

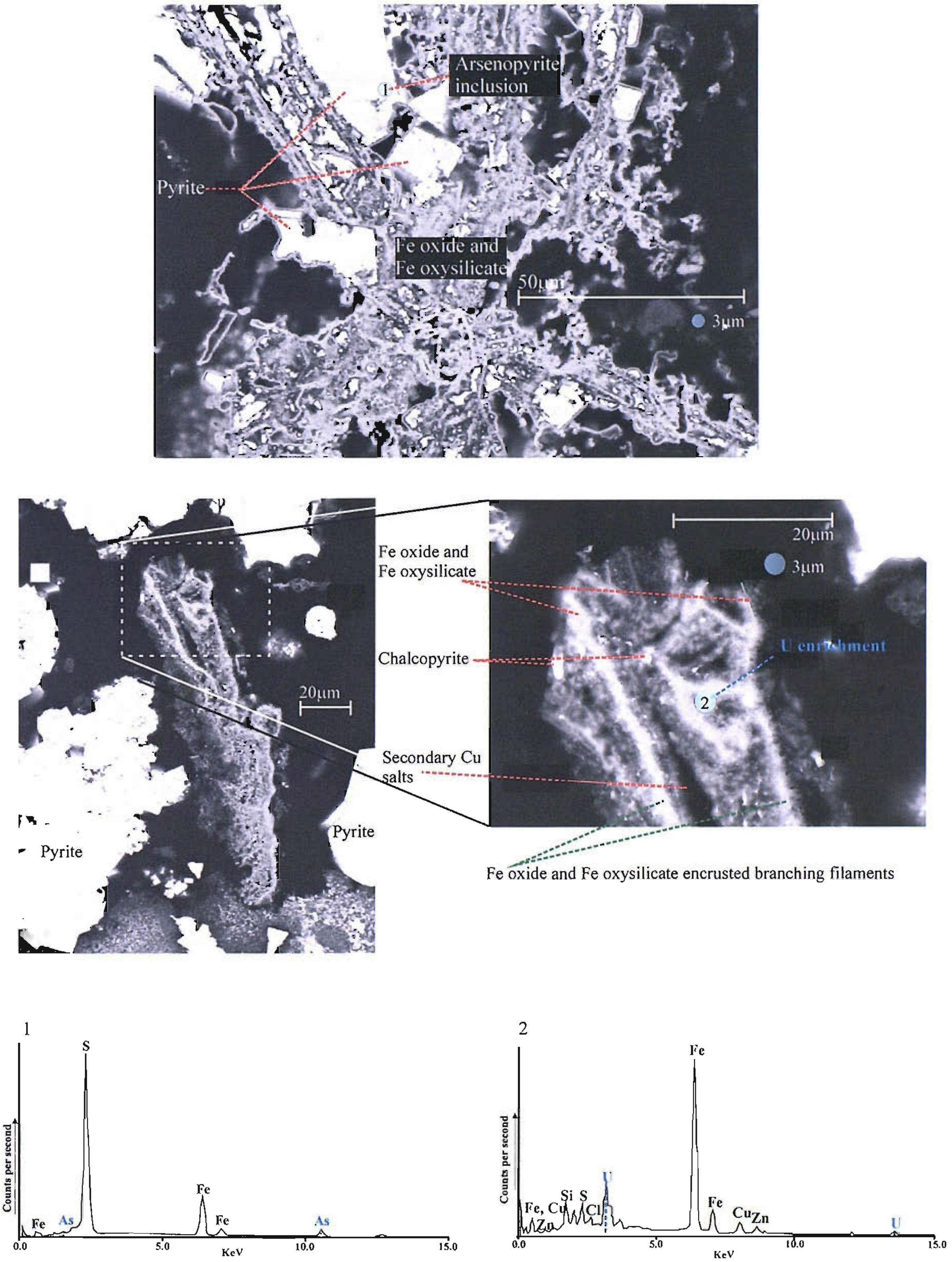

Figure 6.5: SEM images of Fe oxide filaments encrusted by Fe silicates and amorphous silica which are associated with sulphides. A) shows a branching filament network which appears to be growing around sub-euhedral pyrite grains. The large pyrite grain in the centre top of the image contains an arsenopyrite inclusion. B) shows slightly branched, sheath-like filaments encrusted in Fe oxides and amorphous silica. Small chalcopyrite inclusions a few microns in size occur at the edges of the filaments and these contain U enrichments. In a previous study of hydrothermal sediment from the TAG area U enrichment in pyrite grains was attributed to microbial fixation (Mills et al., 1994).

sedimentary laminae (Figure 6.3c). Sulphide minerals are often found within the gypsum crystals adjacent to the filaments. The morphology and occurrence of quartz-cemented filaments differs from those within gypsum in several respects. Branching forms are less frequent and commonly less densely packed (Figure 6.4a and b). The filament morphology is dominated by short, rod-like filaments (Figure 6.4c and d) and longer twisted forms many of which show directed growth where the apparent growth direction is lengthwise parallel to the sedimentary laminae (Figure 6.4d and f). Some of the filaments are in bands where the filament growth is perpendicular to the sedimentary laminae (Figure 6.4g). In some cases the quartz-cemented filaments are associated with chalcedony spherules that appear to have nucleated on the filaments, in some cases the filaments cross-cut the spherules. At high magnification, under transmitted light, some of the quartz-cemented, rod-like hematite filaments appear to be tubes of hematite with blebs of goethite or colloform goethite overgrowths along their length.

The non-cemented filaments are extremely fragile. Optical microscopy shows that these non-cemented meshes and are always composed of hematite. They form dense nets of interlocking, branched and dendritic filaments, and are always closely associated with sulphide minerals.

SEM imaging has revealed nets of Fe oxide filaments surrounding corroded pyrite grains (Figure 6.5; Figure 6.6a and b). These filaments are short, ~5-15µm long, rods, some of which are sinuous, of Fe oxide. Some of these rod-like filaments are in bunched masses perpendicular to the pyrite surface and appear to have nucleated on the sulphide grain. The shorter, straighter rods are lengthwise parallel to the pyrite surface and form cross-links to the perpendicular bundles (Figure 6.6a & b).

6.3.2 Sulphide and Fe oxide Tubes

Tube occurrence and morphology

All the sulphide and Fe oxide tube structures described in this study also come from the laminated section (76-87cm depth) of Core 58. The tube structures are found in both the sulphide dominated and the goethite dominated layers. They are composed of either Fe oxides or poly-metallic sulphides. The majority of these structures are hollow cylinders (Figure 6.7c, d and e) however, many of those composed of Fe oxide are solid (Figure 6.7a and b). Some of the tubes have relatively smooth, even surfaces whilst others are lumpy and uneven (Figure 6.7f). The diameter of the tubes range from 158-459µm with a mean diameter of 320µm ±79 (1σ) (n=40). The difference between the minimum and maximum diameters for the whole data set (301µm) is much larger than the range within each sub-sample depth (mean max-min =171µm). The sub-sample depth mean is within error of the total mean for all depths except 82.5cm where the sub sample mean is 406.3µm diameter (Figure 6.8). The length of the tubes is highly variable (Figure 6.9) but is typically 1-2mm, this variability in length arises because the tubes have fragmented ends and many appear to have been broken off larger structures or snapped in two. Whether this is a direct result of sampling or due to sedimentary processes is unclear, it is most likely the result of a combination of both.

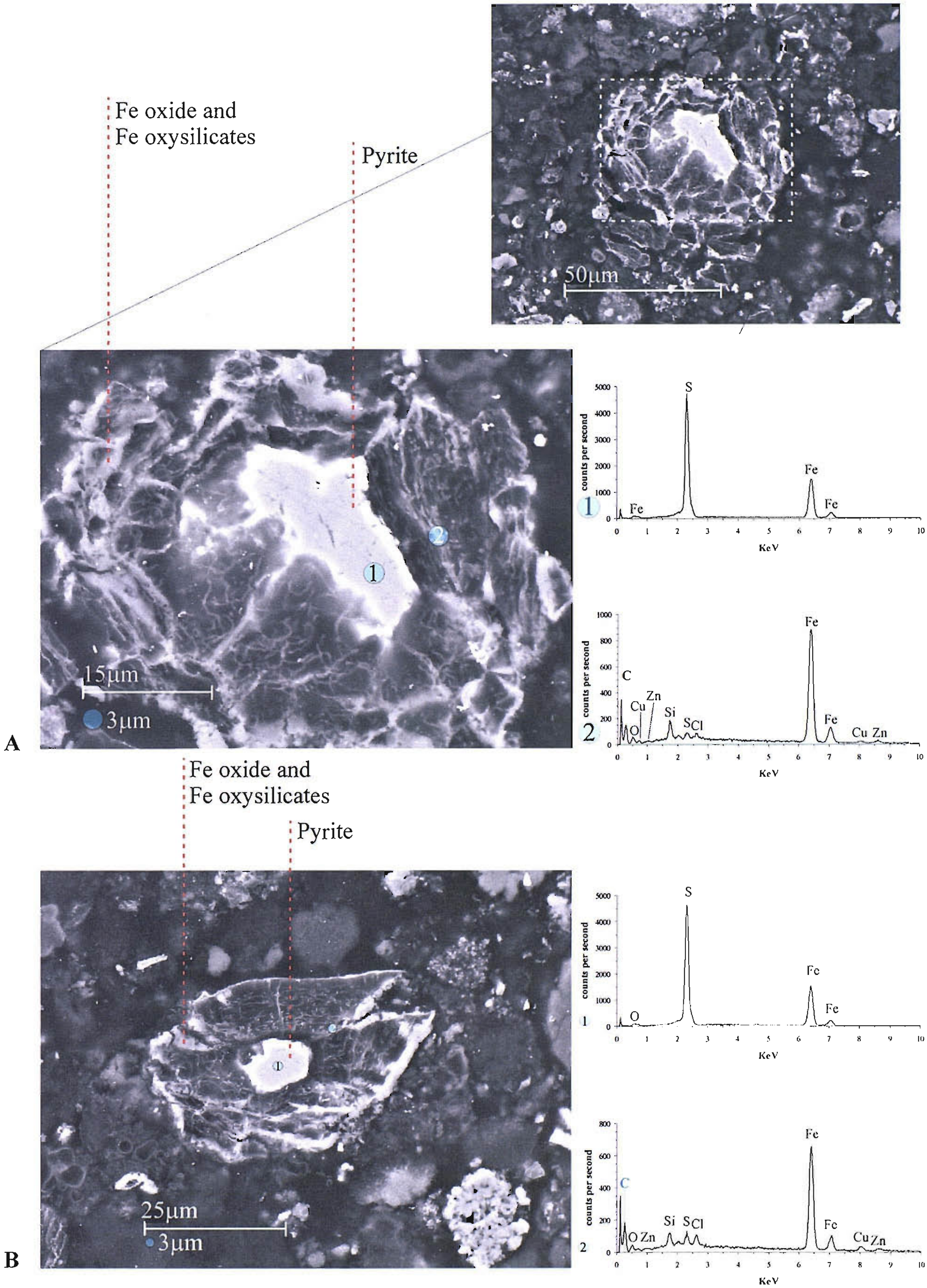

Figure 6.6: SEM images of corroded pyrites surrounded by Fe oxide filament networks. The filaments are short rod-like forms, and sinuous rods that appear to be nucleated on the pyrite surfaces
Typical qualitative X-ray spot microanalyses of the filaments, pyrite and surrounding matrix are shown.

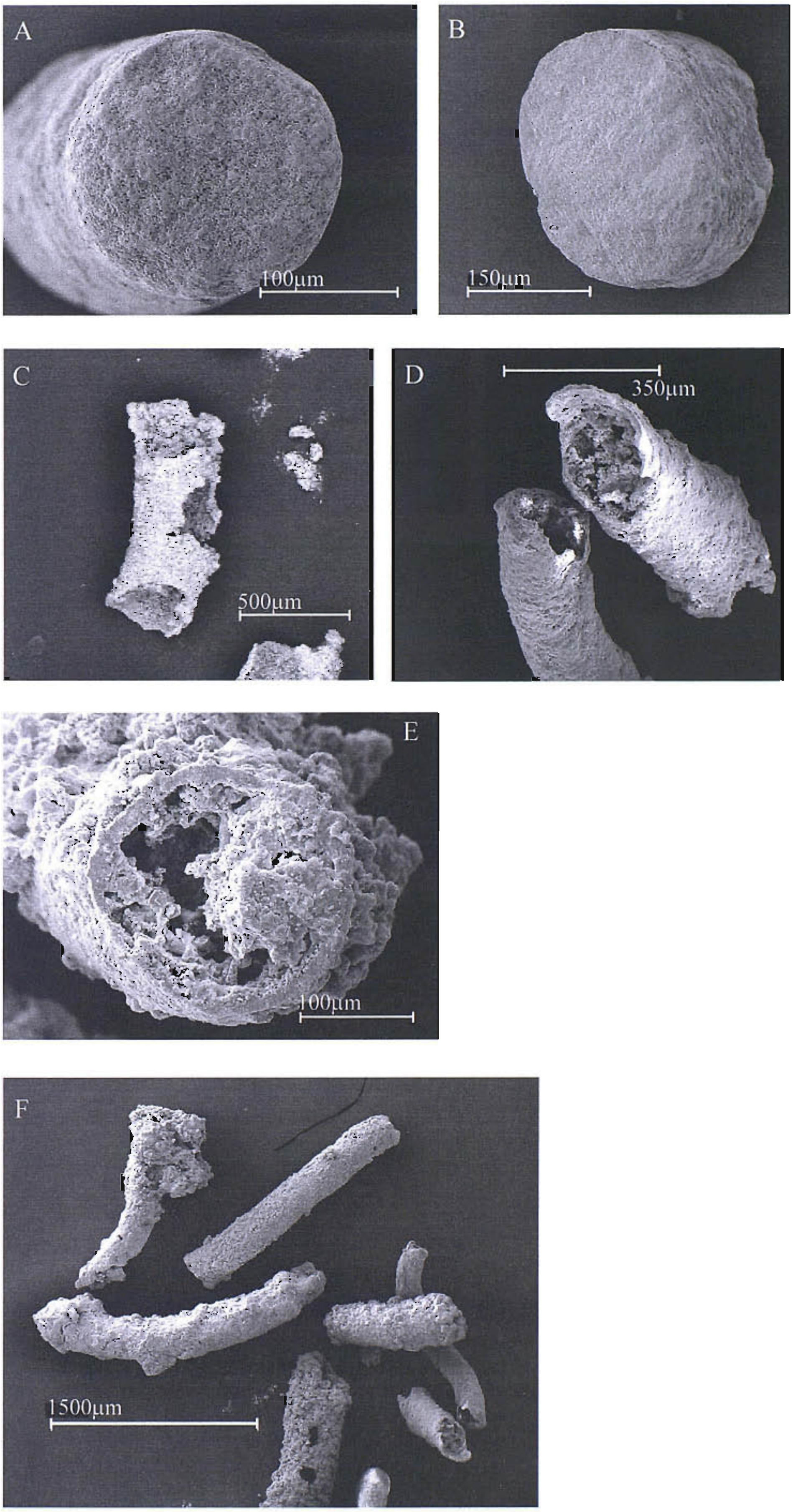

Figure 6.7: SEM images of sulphide and Fe oxide tubes from the laminated section (76-87cm) at the top of the sulphide layer core 58. A & B) Solid Fe oxide cylinders; C) Hollow sulphide tube; D & E) Hollow sulphide tubes partially in filled and overgrown by Fe oxide; F) Smooth and lumpy tube and cylinder structures from 82cm depth.

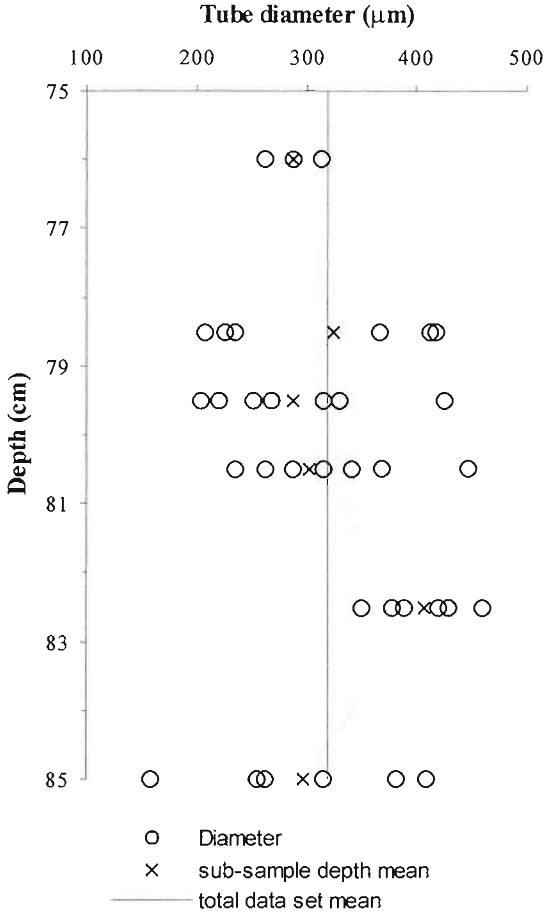

Figure 6.8: Downcore variation in tube and cylinder diameter. Excepting structures from 82.5cm depth sub-sample mean values downcore are within error of the total data set mean.

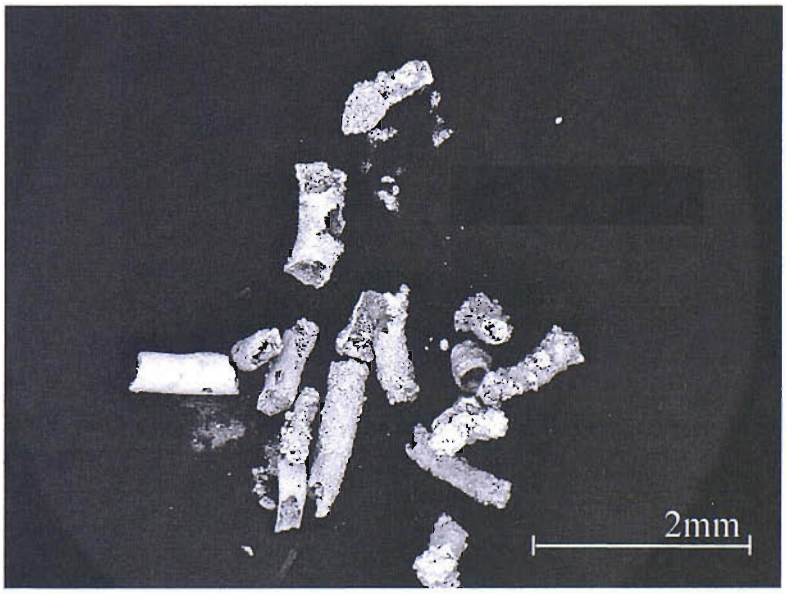

Figure 6.9: Sulphide and Fe oxide tube and cylinder structures from 82.5cm depth downcore showing variable length.

Tube mineralogy

Solid in-filled tube structures (e.g. Figure 6.7a & b) are always composed of fine-grained and amorphous Fe oxides, in some cases amorphous silica is also present. In contrast, the sulphide tubes show a range in mineralogy. SEM imaging and X-ray spot microanalyses of cross sections through tube walls have shown that many of the sulphide tubes are mineralogically zoned. The most common sequence consists of a thin layer of chalcopyrite at the inner wall surface with the bulk of the tube wall composed of pyrite followed by sphalerite at the outer tube surface (Figure 6.10). Other, less common, zonation sequences show changes from pyrite dominated interior walls to chalcopyrite, pyrite and Fe oxide dominated exterior walls (Figure 6.11), pyrite interiors to Fe oxide exteriors or from a thin layer of chalcopyrite at the inner wall to pyrite at the outer wall (Figure6.13a & c). Sulphide tubes which do not show zoning of sulphide minerals are always composed solely of pyrite (Figure 6.12). These monomineralic pyrite tubes are constructed of euhedral cubic pyrite which is typically porous at the inner wall and pristine at the outer wall (Figure 6.13 b & d).

The sulphide dominated tubes are always coated with amorphous Fe oxides, these coatings are typically collomorphic (Figure 6.14a) but some are seen as 'dusty coatings on pyrite cubes (Figure 6.14b), and/or as irregular masses and plate-like stacks (Figure 6.14c). Fe oxide pseudomorphs of cubic pyrite are also common at the outer surfaces of partially oxidised sulphide tubes (Figure 6.14d). At high magnification rod-like Fe oxide filaments were observed at the outer surface of oxidising sulphide tubes (Figure 6.14e). These filaments are much smaller than those described above observed within gypsum and silica; the filaments are typically 1-2μm in length and ~85nm in diameter.

Sprays of euhedral gypsum crystals are frequently observed overgrowing the tube surfaces (Figure6.15a-c). The gypsum is found on both oxide and sulphide dominated tubes but is always spatially associated with oxide and silica phases and appears to be nucleated on Fe oxides. In rare cases barite is also observed and seems to be nucleated on the gypsum (Figure 6.15a), it is never observed where gypsum is absent.

6.3.3 Gypsum major element geochemistry

Molar Sr/Ca ratios also show very little variation with depth and cover a restricted range of $1.52\text{-}1.75\times10^{-3}$ (mean =1.62 ±0.041 (n=6)) (Figure 6.16a). Downcore Mg/Ca ratios have a peak value of 7.62×10^{-3} at 76.25cm but remain fairly constant below this with a mean value of 5.14 ±0.47 (n=6) (Figure 6.16b). Fe/Mn molar ratios range from 265-416 (Figure 6.16c). The maximum Fe/Mn value is from 80.75cm depth and corresponds to the downcore minimum concentrations of each of the individual elements measured.

Correlations

A correlation matrix for all the gypsum sub-samples (Table 6.6a) indicates linear correlations between all the elements measured. The excellent correlations between Ca and Mg (r =0.91) and Ca and Sr (r =0.99) (Figure 6.17a & b) reflects the ability of Mg and Sr to substitute for Ca in the gypsum crystal lattice. Ca also shows an excellent correlation to Fe with r =0.94 (Figure 6.17d), as do Sr and Mg (r =0.93 & 0.98 respectively) (Figure 6.17c & e). Assuming that all the Fe is present as oxide filaments, these correlations strongly suggest that gypsum precipitation is related to the occurrence of Fe oxide filaments. A correlation matrix for Sr/Ca,

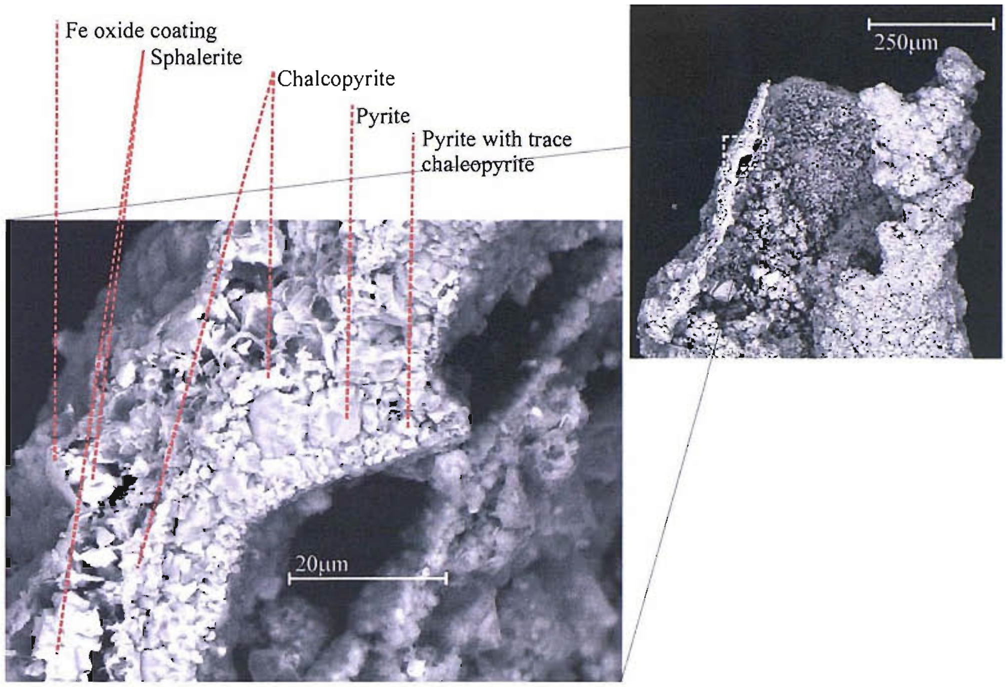

Figure 6.10: Section through a sulphide tube wall from 80.5cm depth showing compositional zoning of sulphide minerals from pyrite at the interior edge, to chalcopyrite and then sphalerite at the outer surface which is coated with Fe oxide.

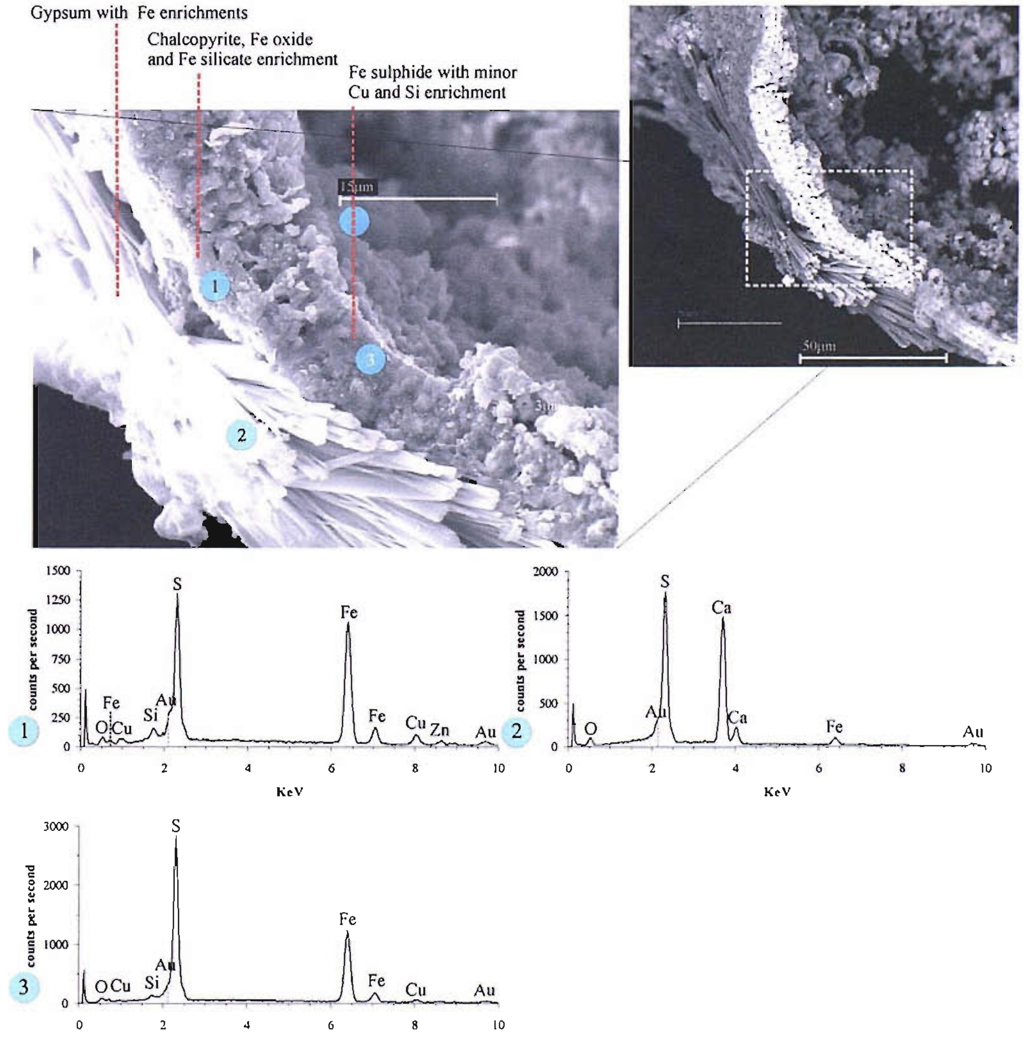

Figure 6.11: Section through a sulphide/oxide tube from 79.5cm depth. Typical X-ray spot microanalyses are shown, these indicate that the inner tube wall is composed chiefly of Fe sulphide, and that the outer tube wall contains oxide and silicate in addition to sulphide. The outer tube wall is encrusted by euhedral gypsum laths which appear to have nucleated on the oxide material.

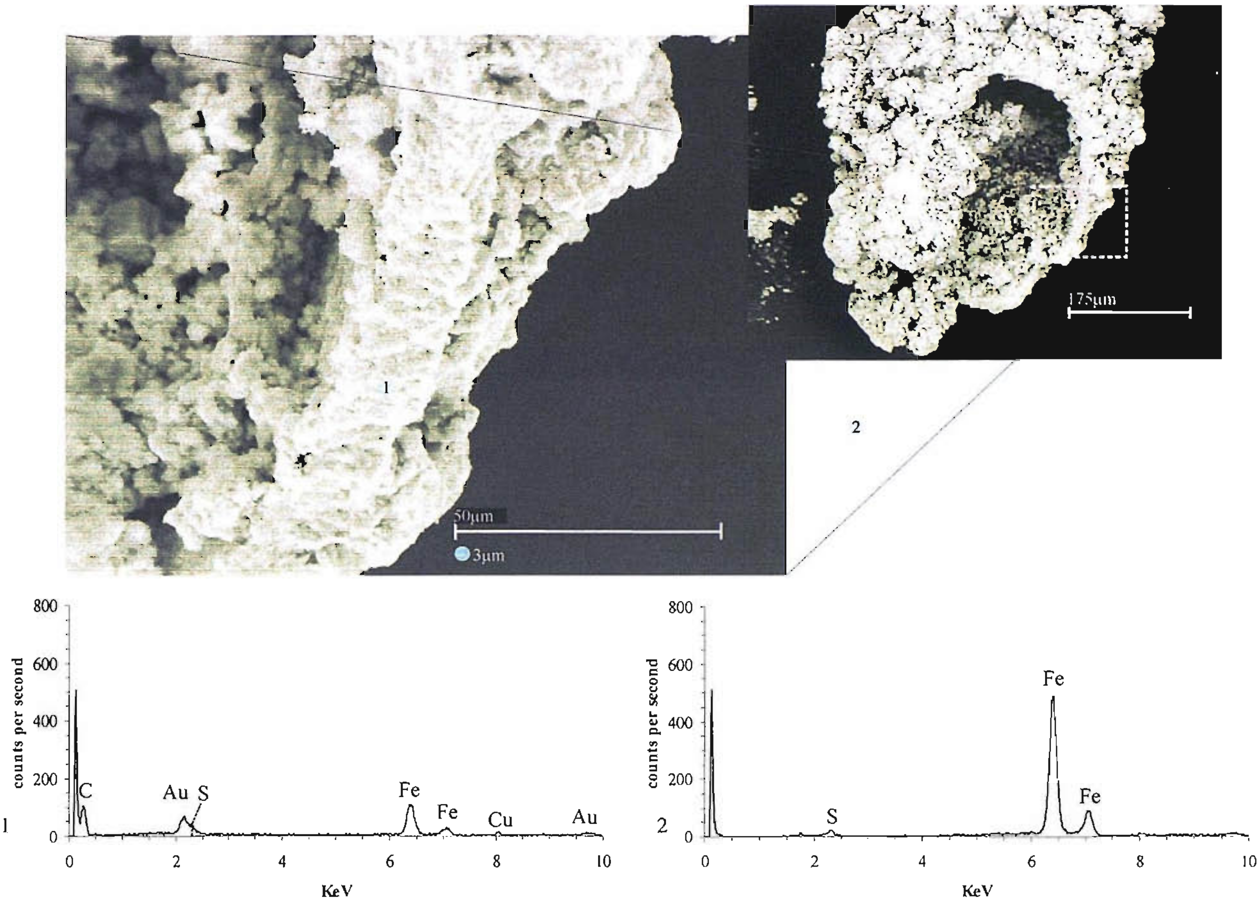

Figure 6.12: Secondary SEM images: section through pyrite tube wall from 79.5cm depth. Typical x-ray spot microanalyses are shown for the tube wall (1) and the outer tube surface (2).

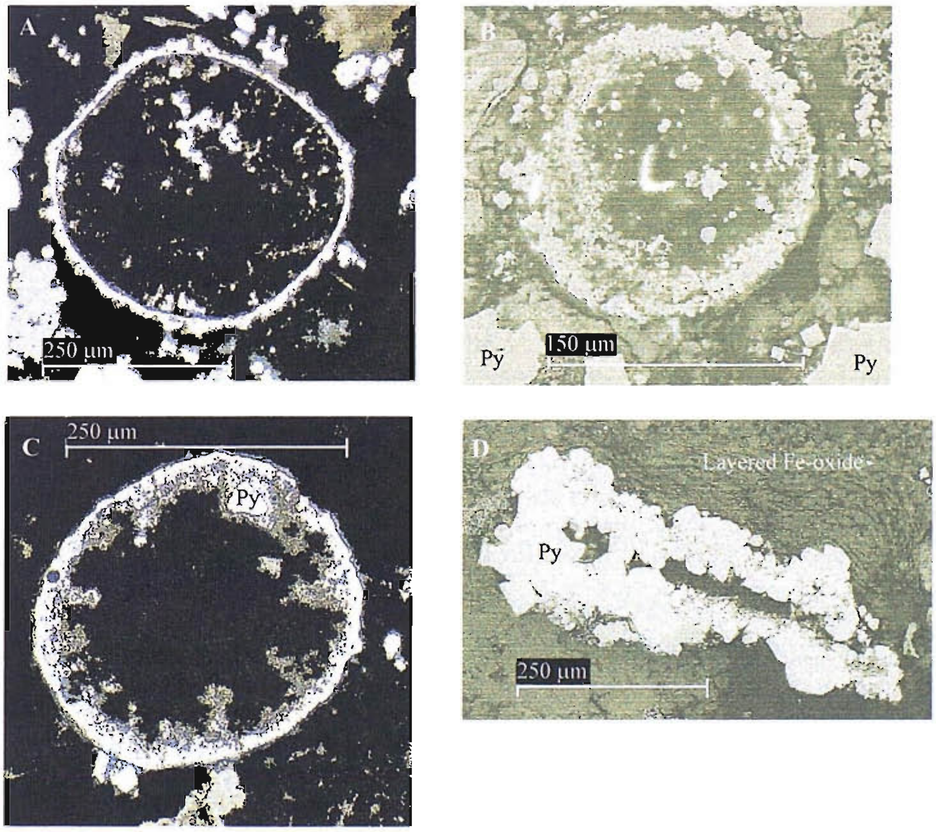

Figure 6.13: Reflected light photomicrographs (A & C) and back scatter SEM images (B & D) of sulphide tubes. A) Cross section through pyrite tube, within the tube are subhedral chalcopyrite and pyrite crystals; B) Cross section through pyrite tube, the inner wall is composed of porous anhedral pyrite, the outer wall is composed of an amalgamation of cubic pyrite; C) Cross section through sulphide tube. Pyrite dominates the outer tube wall whilst the inner wall is composed of a thin layer of chalcopyrite; D) Lateral cross section through a pyrite tube fragment. The tube is composed of euhedral pyrite cubes.

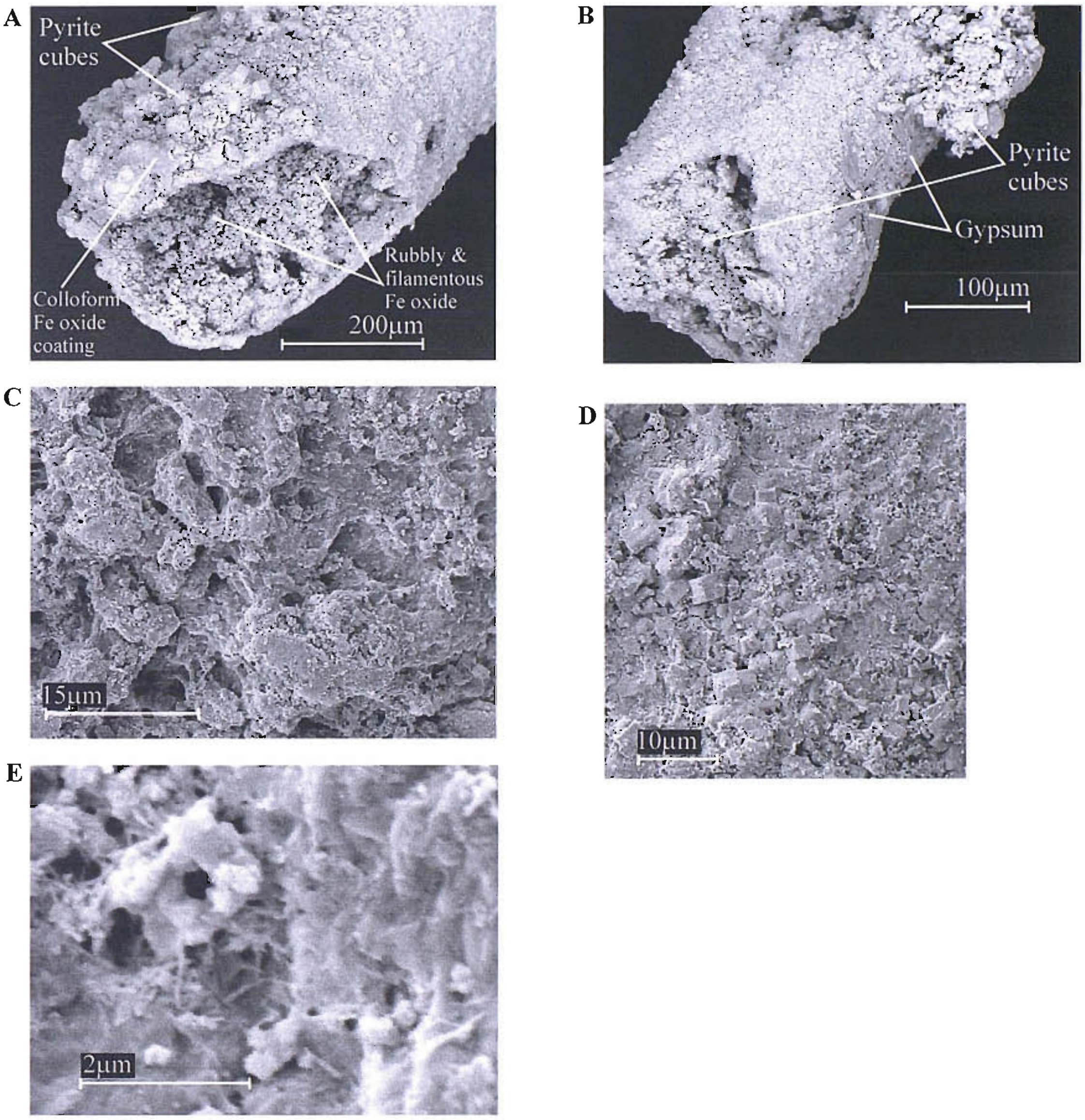

Figure 6.14: Secondary SEM images of outer tube surface mineralogy and textures. A) tube from 82.5cm depth, the outer surface is composed of pyrite cubes and Fe oxides, some of the Fe oxide occurs as a collomorphic coating over the pyrite cubes; B) tube from 78.5cm depth outer surface is composed of pyrite cubes and Fe oxide, some areas are overgrown by euhedral gypsum crystals; C) part of the outer surface of a tube from 76cm depth composed of amorphous Fe oxide in plate-like stacks; D) the outer surface of a tube from 85cm depth predominantly composed of cubic pyrite, Fe oxide pseudomorphs of cubic pyrite and some amorphous Fe oxide; E) Highly magnified view of an outer tube surface from 76cm depth showing rod-like Fe oxide filaments and amorphous Fe oxide.

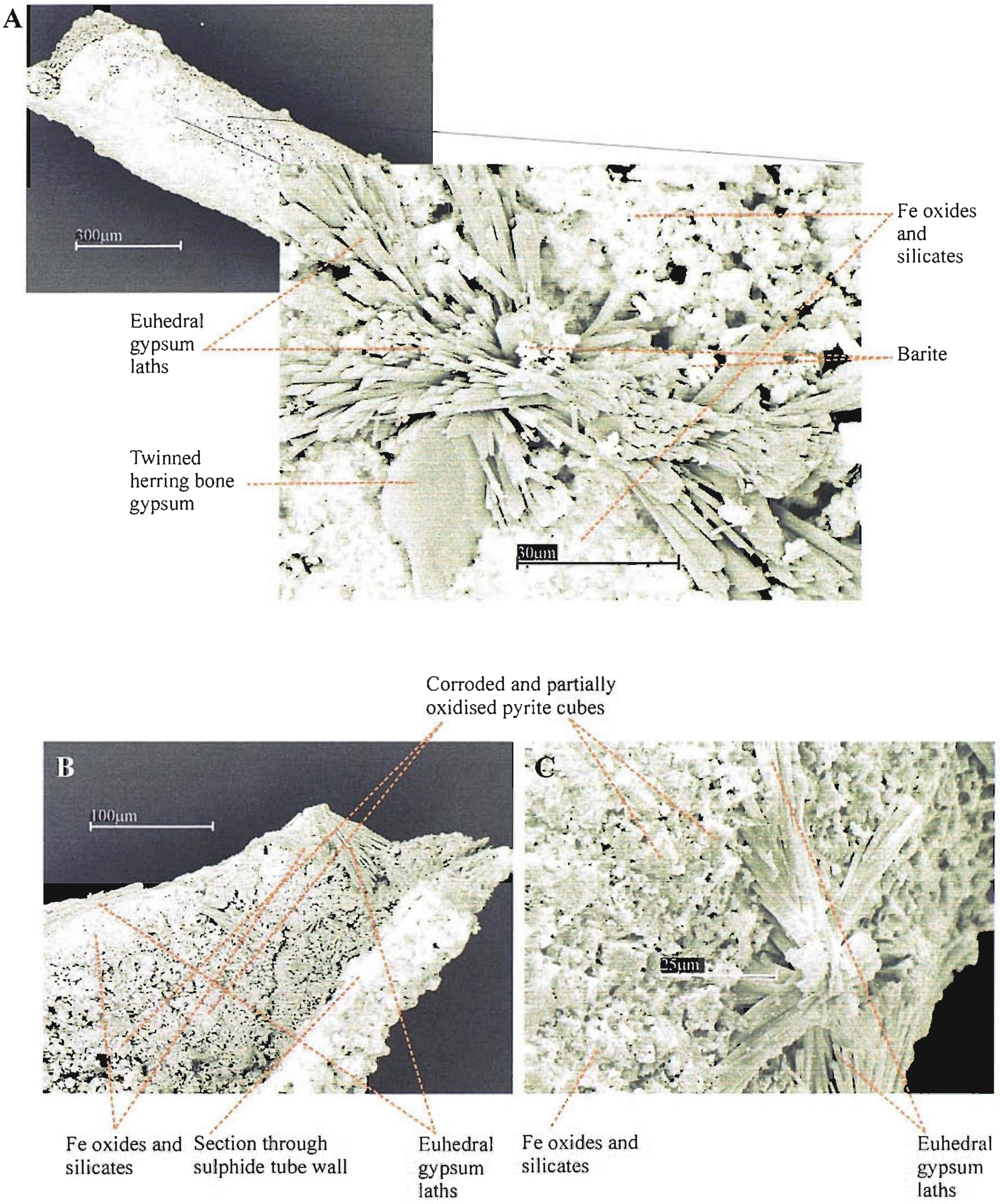

Figure 6.15: Secondary SEM images of gypsum associated with tube structures.
Gypsum occurs as euhedral lath-like crystals with occasional herring bone twins. The gypsum is a late feature and is always associated with oxidised areas of the tube surfaces. A) shows herring bone twinned gypsum on the surface of a partially oxidised sulphide tube from 82.5cm depth. Rare occurrences of subhedral barite are also observed on this tube and these are associated with the gypsum. B) Fragment of sulphide tube from 82.5cm depth showing patchy growth of euhedral gypsum laths over all surfaces. The gypsum is nucleated on Fe oxide and amorphous silicate phases which form a collomorphic coating over the sulphide tube structure. Pyrite cubes are observed on the inner surface of this fragment and some of these have been oxidised producing Fe oxide, pyrite cube pseudomorphs. C) Surface of partially oxidised sulphide tube from 78.5cm depth. The tube surface is composed of variously oxidised cubic pyrite which is overgrown by euhedral gypsum laths and has a patchy coating of amorphous Fe oxide and silicate.

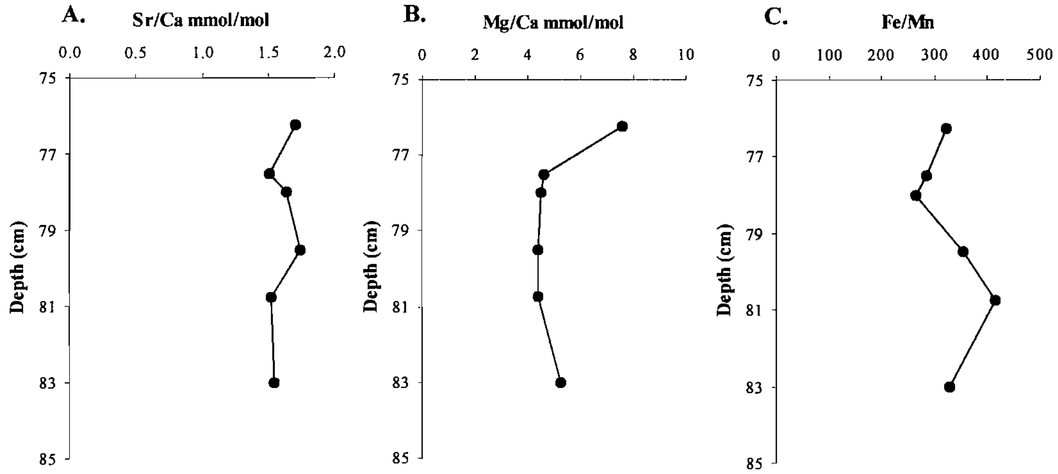

Figure 6.16: Downcore variation in A.) Sr/Ca; B.) Mg/Ca and C). Fe/Mn, molar ratios for gypsum separates.

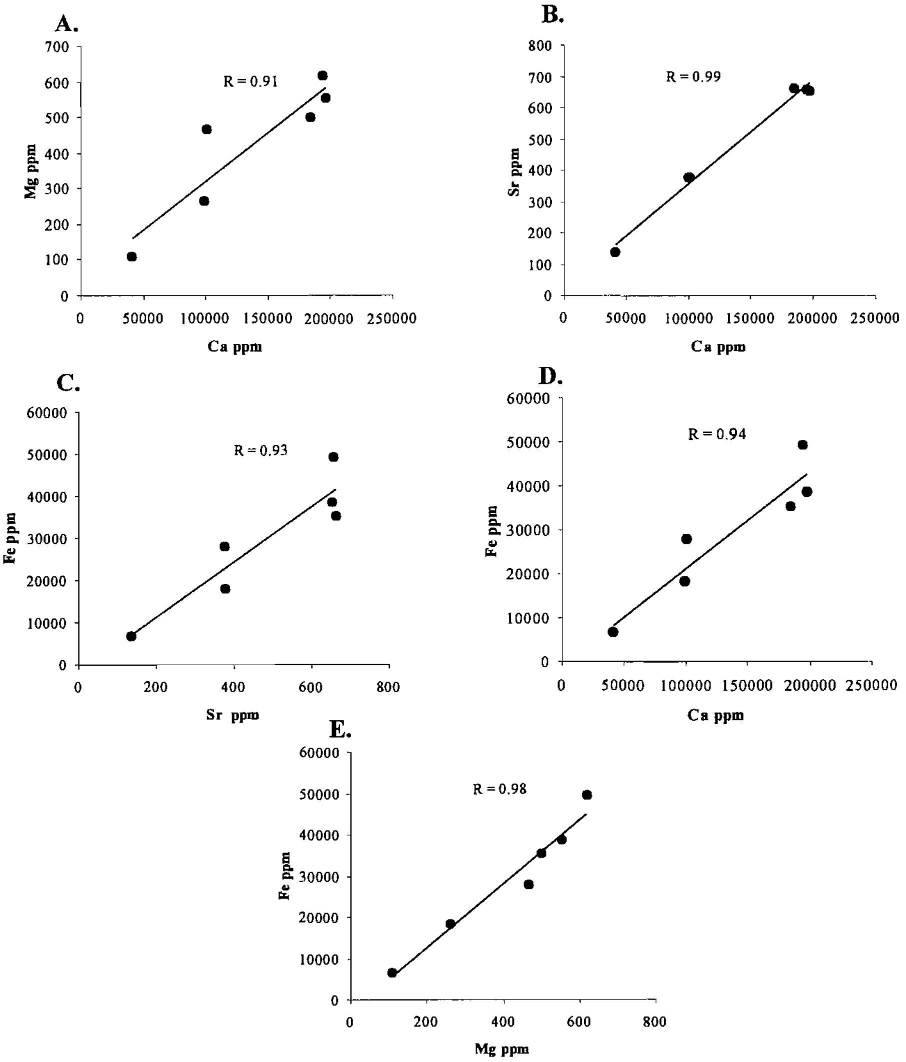

Figure 6.17: Scatter plots of A.) Ca vs. Mg; B.) Ca vs. Sr; C). Fe v.s Sr; D). Fe vs. Ca and E). Fe vs. Mg for gypsum separates.

	Ca ppm	**Fe ppm**	**Mg ppm**	**Sr ppm**	**Mn ppm**
Ca ppm	1.00				
Fe ppm	0.94	1.00			
Mg ppm	0.91	0.98	1.00		
Sr ppm	0.99	0.93	0.91	1.00	
Mn ppm	0.97	0.98	0.97	0.97	1.00

Table 6.6a: Correlation matrix of elemental concentrations in gypsum separates

	Sr/Ca	**Mg/Ca**	**Fe/Mn**
Sr/Ca	1.00		
Mg/Ca	-0.36	1.00	
Fe/Mn	0.10	0.10	1.00

Table 6.6b: Correlation matrix of molar ratios in gypsum separates

Table 6.6a & b: Elemental and molar ratio correlations in ICP-AES gypsum separates data.

	Measured solid (*Alvin* gypsum)		**Calculated fluid**
Depth cm	**$^{87}Sr/^{86}Sr$**	**Sr/Ca mmol/mol**	**Sr/Ca mmol/mol**
76.25	0.709145	1.71	6.848
77.5	0.709165	1.52	6.08
78	0.709157	1.65	6.588
79.5	~	1.75	6.992
80.75	0.708069	1.53	6.1
83	0.70915	1.55	6.204

Table 6.7: Measured $^{87}Sr/^{86}Sr$ and Sr/Ca ratios for *Alvin* gypsum and predicted Sr/Ca for the precipitating fluid calculated assuming D_{Sr} =0.25 (Burns, 1979).

Mg/Ca and Fe/Mn ratios (Table 6.6b) indicates that there are no significant linear correlations between these parameters.

6.3.4 Strontium isotopic composition of Gypsum

Strontium isotopic compositions were measured for gypsum separates from 75-100cm depth, the measured $^{87}Sr/^{86}Sr$ ratios are given in Table 6.4a. The different Sr isotope compositions of seawater (0.70916: (Hodell et al., 1991)) and TAG hydrothermal fluid (0.70319: (Elderfield et al., 1993)) and similar Sr concentrations (~90μM: Edmond et al., 1995) make Sr a useful tracer of hydrothermal fluid and seawater interaction. Sr isotopic systematics are also important in the study of primary mineral alteration (e.g. (Teagle et al., 1998c)). Since there is no fraction of Sr isotopes during mineralisation, the $^{87}Sr/^{86}Sr$ composition of gypsum will record the extent of mixing between hydrothermal fluid and seawater. The relative proportions of hydrothermal fluid to seawater in these precipitates can be calculated by mass balance:

$$X_{SW} = \frac{[Sr]_{HT}[(^{87}Sr/^{86}Sr)_{HT} - (^{87}Sr/^{86}Sr)_{mix}]}{[Sr]_{SW}[(^{87}Sr/^{86}Sr)_{mix} - (^{87}Sr/^{86}Sr)_{SW}] + [Sr]_{HT}[(^{87}Sr/^{86}Sr)_{HT} - (^{87}Sr/^{86}Sr)_{mix}]} \qquad (6.7)$$

Where subscripts SW and HT correspond to seawater and hydrothermal fluid respectively. Assuming that the measured value is a mixture of these two end members it can be substituted into the equation as $(^{87}Sr/^{86}Sr)_{mix}$. Values for each parameter are listed in Table 6.4b and calculated proportions in Table 6.4a. Assuming conservative mixing of the two end member fluids with temperatures of 2°C (NADW) and 363°C (TAG black smoker fluid) (Edmond et al., 1995) an inferred temperature of precipitation for the gypsum separates can be calculated, the results of these calculations are listed in Table 6.4a.

All the gypsum sub-samples from this study give seawater dominated $^{87}Sr/^{86}Sr$ ratios (Figure 6.18). Sr contributions from end member hydrothermal fluid are typically <1%, except between 80-83cm depth where $^{87}Sr/^{86}Sr$ ratios indicate hydrothermal contributions of 8.7-16.1%, this is indicative of precipitation from a fluid produced from subsurface mixing of hydrothermal fluid and seawater. The $^{87}Sr/^{86}Sr$ ratios of gypsum from Core 58, although close to the seawater end member, are within the range reported for anhydrite ($CaSO_4$) (0.705038-0.709128) (Figure 6.19) from the TAG active mound which is precipitated during high temperature activity (e.g. Mills and Tivey, 1999; Mills et al., 1998; Teagle et al., 1998a). They are also consistent with similar $^{87}Sr/^{86}Sr$ values (1-14% hydrothermal component) observed for hydrothermal clays precipitated during diagenesis, from core CD102/43 (collected in close proximity to CD102/58) (Severmann et al., 2004), pore fluids from sediments surrounding the active TAG mound (Mills et al., 1996), and diffuse low temperature fluids sampled from the surface of the active TAG mound (James and Elderfield, 1996a; Mills et al., 1996). Gypsum precipitation in situ from a mixed low temperature fluid is also consistent with the silica and quartz mineralogy of Core 58, which also indicates in situ precipitation from a low temperature mixed fluid (Chapter 3). No correlation is observed between either Sr/Ca or Mg/Ca ratios and $^{87}Sr/^{86}Sr$. However, Fe and Ca contents do show a linear correlation to $^{87}Sr/^{86}Sr$ with $r = 0.77$ in both cases.

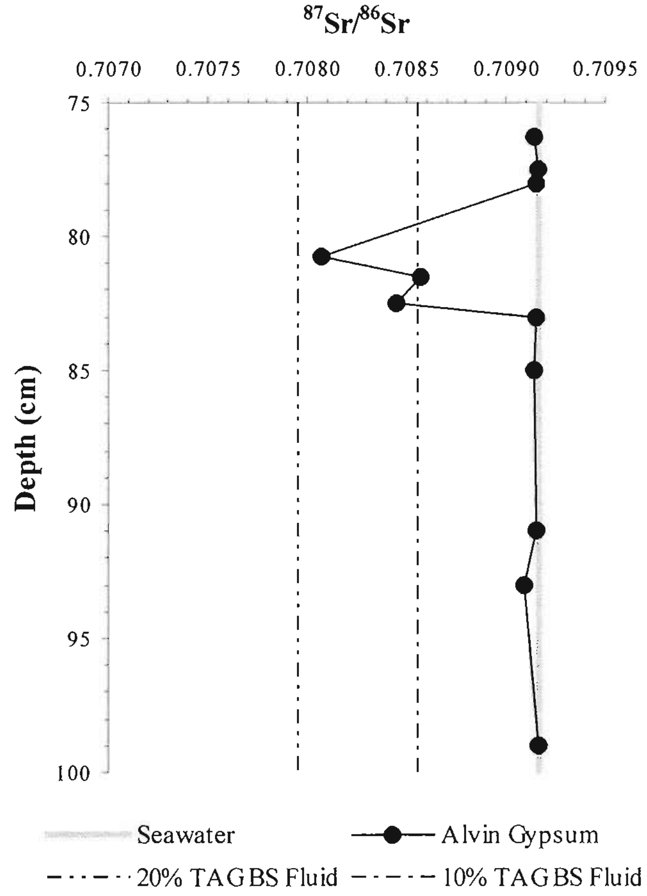

Figure 6.18: Variation in strontium isotopic composition with depth. The value of seawater Sr is shown for comparison. The Sr isotopic composition of mixed seawater and hydrothermal fluids with hydrothermal contributions of 10 and 20% are also shown.

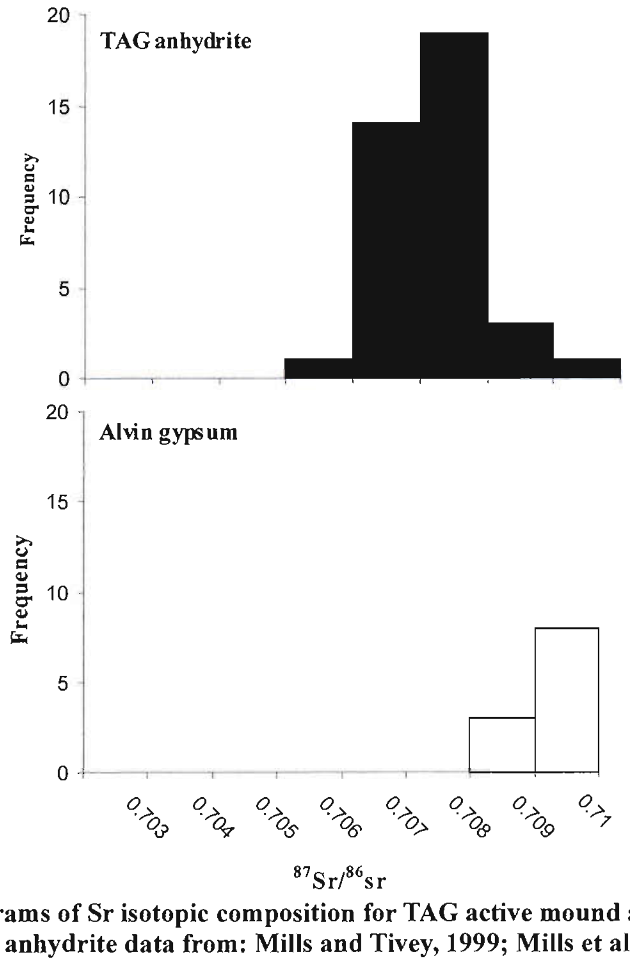

Figure 6.19: Histograms of Sr isotopic composition for TAG active mound anhydrite and *Alvin* gypsum. (TAG anhydrite data from: Mills and Tivey, 1999; Mills et al., 1998; Teagle et al., 1998a).

6.3.5 Sr/Ca Partition Coefficient for *Alvin* Gypsum

The partitioning of trace elements between the solid and solution phase during unidirectional mineralisation is controlled by the partition coefficient (e.g. Shikazono and Holland, 1983). The Sr/Ca partition coefficient, D_{Sr}, is calculated using Equation 6.8:

$$D_{Sr} = \frac{(Sr / Ca)_{solid}}{(Sr / Ca)_{fluid}} \qquad (6.8)$$

The experimentally predicted range of D_{Sr} for anhydrite ($CaSO_4$) is 0.27-0.73 (Shikazono and Holland, 1983; Berndt et al., 1988). Most of the anhydrite from the TAG active mound falls within this range (e.g. Mills et al., 1998; Teagle et al., 1998a; Mills and Tivey, 1999). Figure 6.20 shows measured $^{87}Sr/^{86}Sr$ ratios vs. measured Sr/Ca molar ratios for the *Alvin* gypsum and TAG active mound anhydrite. Calculated curves show predicted mineral compositions for precipitation from mixtures of TAG hydrothermal fluid and seawater over a range of arbitrary partition coefficients calculated using Equation 6.8. The *Alvin* gypsum separates show apparent D_{Sr} close to 0.2, assuming precipitation from simple mixtures of hydrothermal fluid and seawater; this is much lower than the D_{Sr} of TAG anhydrite assuming the same precipitation conditions (Teagle et al., 1998a). However, unlike TAG anhydrite, which is precipitated during high temperature activity, the *Alvin* gypsum was not precipitated under high temperature conditions but during alteration within the sediment pile at an inactive mound. As such the mineralising fluid is unlikely to be a simple mixture of hydrothermal fluid and seawater.

Using an experimentally determined partition coefficient for seawater gypsum (D_{Sr}=0.25 at 30°C: Burns, 1979) the Sr/Ca ratio of the mineralising fluid can be calculated (Table 6.7; Figure 6.21). These calculations give Sr/Ca fluid ratios that are lower than those predicted by simple mixing models. This implies that in addition to basaltic and seawater derived Sr/Ca, further mixing with a fluid which has a lower Sr/Ca ratio has occurred. The most likely source of additional Sr/Ca is the overlying carbonate cap. Dissolution of the carbonate cap can occur as a result of the acidic pore fluids produced during sulphide oxidation reactions (e.g. Severmann, 2000; Severmann et al., 2004; Chapter 3). The Sr/Ca ratio of carbonate at the top of Core 58 is 2.75×10^{-3}, this is lower than the Sr/Ca ratio of both seawater (Sr/Ca $=8.53 \times 10^{-3}$) and end member hydrothermal fluid (Sr/Ca $=3.34 \times 10^{-3}$). The calculated Sr/Ca fluid ratios of *Alvin* gypsum are consistent with mixing of Sr/Ca from quantitative dissolution of the carbonate cap with Sr/Ca from hydrothermal fluid and seawater (Figure 6.21).

Mg/Ca ratios are significantly higher than those predicted from simple mixing of hydrothermal fluid and seawater (Figure 6.22). Despite this, Mg and Ca contents are much lower than those expected from a simple mixed fluid (Figure 6.23). The elevated Mg/Ca ratios may reflect the presence of minor amounts of talc. The low Mg content may reflect the preferential partitioning of Sr over Mg in the gypsum crystal lattice; the general order of cation partitioning in gypsum is Sr » Na-K › Mg › Cl (e.g. Chang et al., 1996).

6.3.6 Sulphur isotopic composition of Gypsum

The $\delta^{34}S$ values were measured for 7 gypsum separates from depths of 75-100cm. Gypsum $\delta^{34}S$ values have a restricted range of +9.6-+10.6‰, with a mean value of +10.0‰ (n=7) ±0.14 (1SE) (Figure 6.24). This is ~2.5‰ heavier than both the mean bulk and laser sulphide $\delta^{34}S$ values for this core (+7.6‰ and +7.5‰

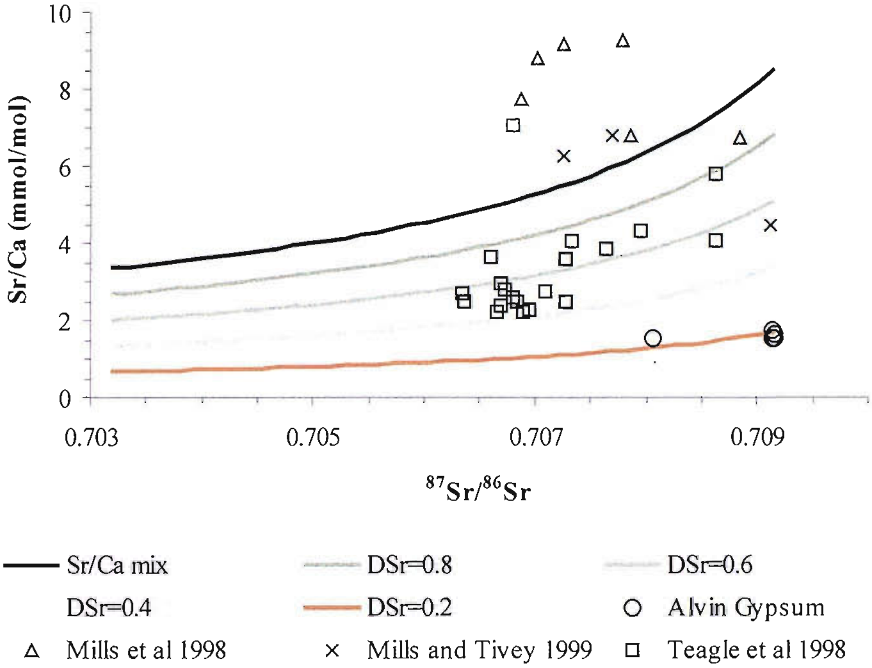

Figure 6.20: Measured $^{87}Sr/^{86}Sr$ vs. Measured Sr/Ca ratios of *Alvin* gypsum and TAG active mound anhydrite. Calculated curves show the predicted range of gypsum and anhydrite compositions precipitated from simple mixtures of hydrothermal fluid and seawater for an arbitrary range of Sr/Ca partition coefficients. All *Alvin* gypsum samples have apparent D_{Sr} close to 0.2.

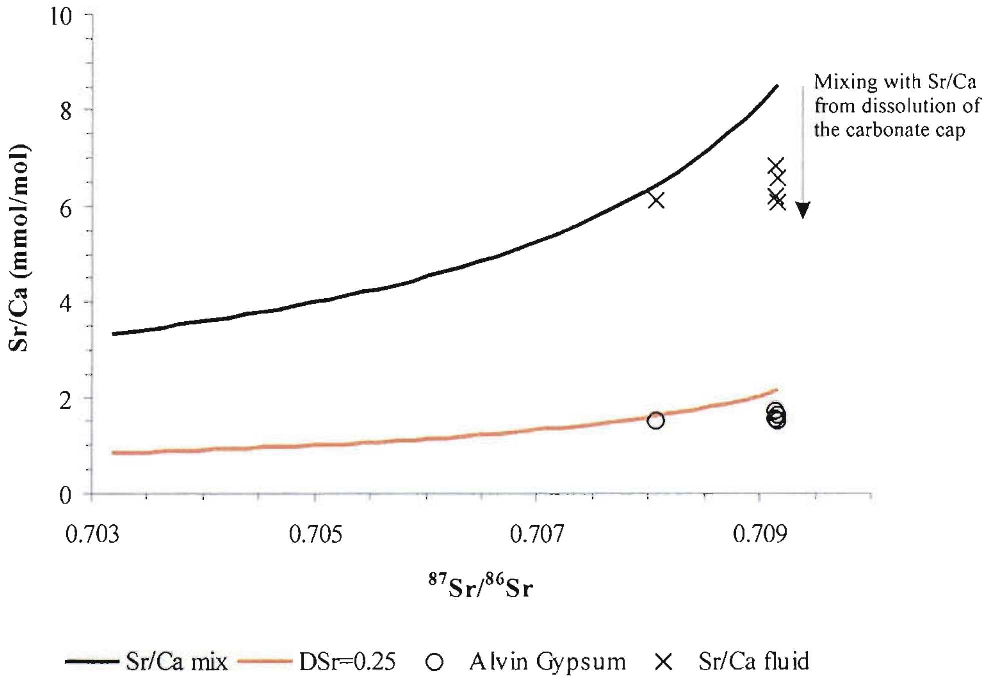

Figure 6.21: Measured $^{87}Sr/^{86}Sr$ vs. Measured Sr/Ca ratios of *Alvin* gypsum and calculated Sr/Ca ratios of the mineralising fluid assuming $D_{Sr}=0.25$ for seawater gypsum at 30°C (Burns, 1979). Calculated fluid Sr/Ca is lower than that predicted for a fluid produced by simple mixing of hydrothermal fluid and seawater. An additional source with lower Sr/Ca is required. Partial dissolution of the overlying carbonate cap with a Sr/Ca ratio of $2.75x10^{-3}$ is inferred to be the additional Sr/Ca source.

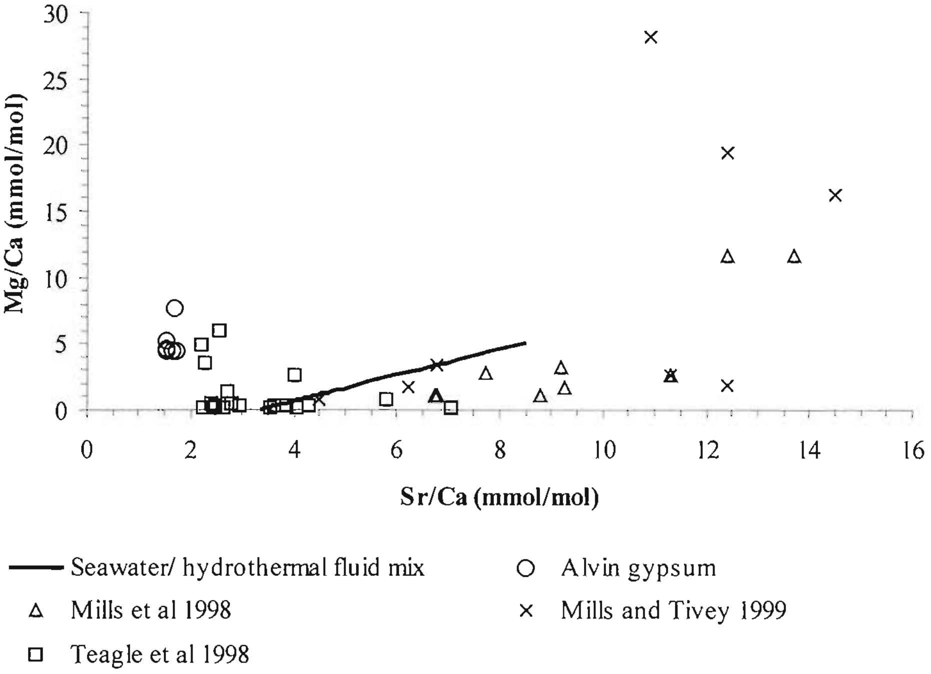

Figure 6.22: Sr/Ca vs. Mg/Ca molar ratios of *Alvin* gypsum. The predicted range of Sr/Ca and Mg/Ca ratios for a simple mixture of hydrothermal fluid and seawater, and for TAG active mound anhydrite are shown for comparison.

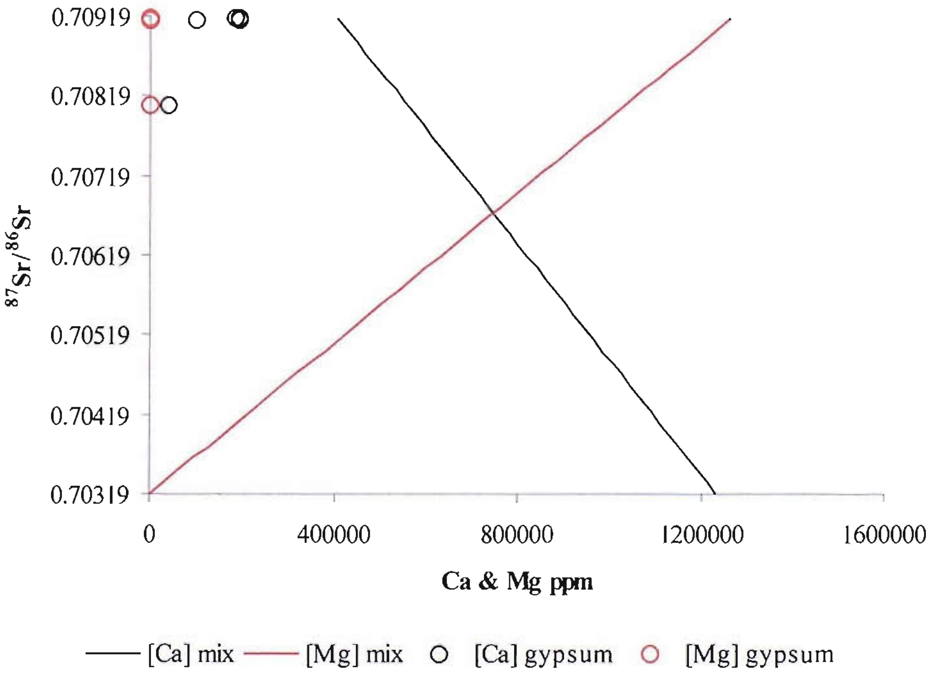

Figure 6.23: 87Sr/86Sr ratios vs. Ca & Mg contents of *Alvin* gypsum. Mixing lines for the predicted range of Ca and Mg contents for a simple mixture of hydrothermal fluid and seawater are shown for comparison.

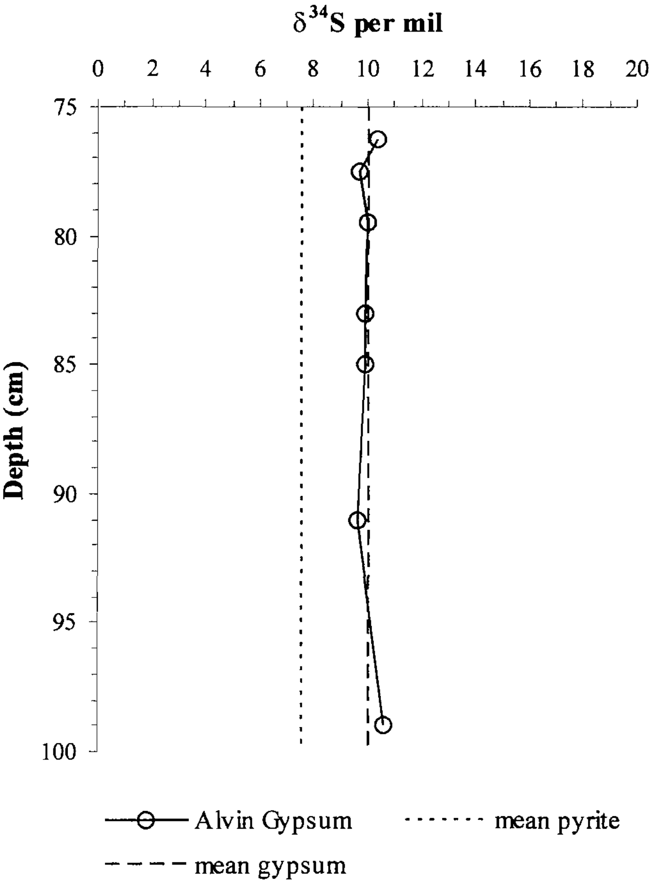

Figure 6.24: Variation in gypsum sulphur isotopic composition with depth. The mean $\delta^{34}S$ value of *Alvin* pyrite is shown for comparison.

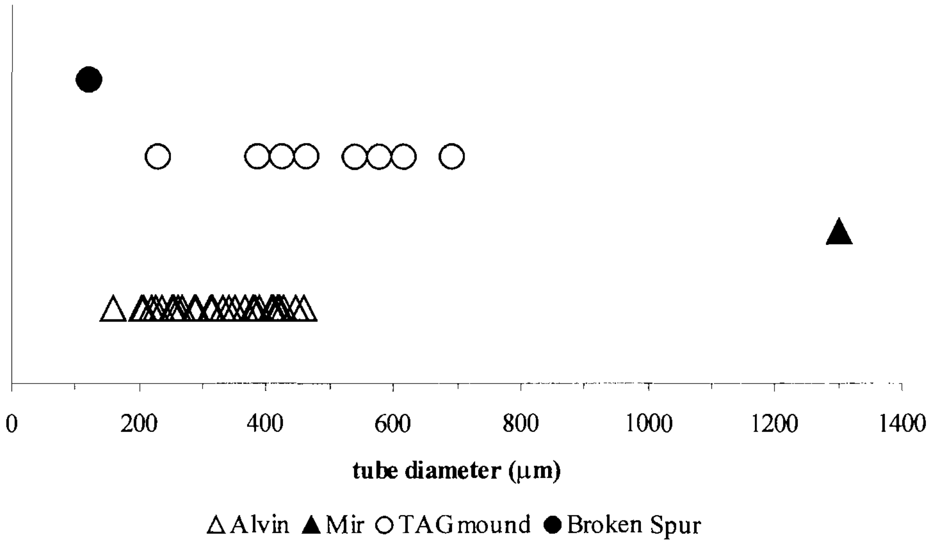

Figure 6.26: Comparison of the diameters of sulphide tubes from the *Alvin* sediments with similar tubular structures described from the Mir zone (Rona et al., 1993); the TAG mound (Hannington et al., 1995) and the Broken Spur hydrothermal vent site at 29°N MAR (Butler et al., 1998).

respectively). Whilst the $^{87}Sr/^{86}Sr$ ratios of the gypsum samples are comparable to those of anhydrite from the active TAG mound, the $\delta^{34}S$ values of the gypsum separates are significantly lighter than those of the TAG anhydrite which have $\delta^{34}S$ close to seawater values ($\delta^{34}S_{seawater\ sulphate}$ =+20.9‰: Rees et al., 1978) (e.g. Chiba et al., 1998). Because the $\delta^{34}S$ values of the gypsum samples cover such a narrow range downcore variation is minimal. The $\delta^{34}S$ values do not correlate with either $^{87}Sr/^{86}Sr$ or any of the major elements and elemental ratios.

6.4 Discussion

6.4.1 Biogenicity of the *Alvin* Fe oxide filaments

6.4.1.1 Morphological evidence

The *Alvin* filaments share many morphological characteristics with Fe oxide filaments described from previous studies of seafloor hydrothermal deposits (Table 6.1) and are also very similar to filaments within terrestrial jasper deposits (Table 6.2):

- they have similar sizes
- they are formed of hematite and goethite
- they are concentrated in discrete laminae or domains
- they show a range of morphologies including straight, twisted, dendritic and branching forms
- some examples show directed growth patterns parallel to sedimentary structures

Some of the *Alvin* filament morphologies can be directly compared to known Fe oxidising microbes. For example the twisted filaments are almost identical to Fe oxide filaments which have been attributed to the Fe oxide encrusted twisted stalks of *Gallionella* spp. in deep water (e.g. Alt, 1988b; Boyd and Scott, 2001; Emerson and Moyer, 2002; Kennedy et al., 2003a, b & c) and shallow water (e.g. Hanert, 2002), at seafloor hydrothermal vents sites, and weathered sulphide mineral surfaces (e.g. Edwards et al., 2003b). Other morphologies common in the *Alvin* samples can be compared to the Fe oxide encrusted sheaths of *Leptothrix* spp. (e.g. Alt, 1988b; Emerson and Revsbech, 1994; Boyd and Scott, 2001; Emerson and Moyer, 2002; Kennedy et al., 2003a, b & c), and to the filamentous structures formed by the novel bacterial strain PV-1 (Emerson and Moyer, 2002). Branching filaments which are common in the *Alvin* samples may record true branching of filamentous microbes, or 'false-branching' where there is successive budding of separate microbial cells; a phenomenon known to produce bifurcating stalks in *Gallionella* spp. (e.g. Heldal and Tumyr, 1983) and sheaths in *Sphaerotilus natans* (e.g. Ghiorse, 1984).

The large dendritic *Alvin* filaments are comparable to dendritic Fe oxide filamentous textures described from Fe oxide-silica deposits in the Indian Ocean (Halbach et al., 2002), on the East Pacific Rise (EPR) (Juniper and Fouquet, 1988) and from the active TAG mound (Hopkinson et al., 1998), none of which have been attributed to specific microbial strains and morphologies. Whilst Juniper and Fouquet (1998) invoke a microbial origin, suggesting that they represent dense Fe oxide deposition on filaments in the most oxidised areas of microbial mats, other authors have attributed these dendritic structures to abiotic processes where they result from diffusion limited growth of branching Fe oxide aggregates in a silica gel at the dissolution-redox front associated with pyrite weathering (Hopkinson et al., 1998). Two lines of evidence are used by Hopkinson et al. (1998) to support their model for the formation of the TAG dendritic textures in highly viscous silica gels: 1) there are no cavities between the Fe oxyhydroxide dendrites, these being filled entirely with silica; and 2) that the dendrites do not project beyond the silica cement into free space. However, the occurrence of un-cemented dendritic filament meshes and dendrites cemented by both silica and gypsum observed in this study do not conform to this model of abiogenic filament growth in a silica gel. In addition, the dendritic textures described by Hopkinson et al. (1998), unlike some of the *Alvin* filaments, are not cylinders of Fe oxides. This suggests that the *Alvin* filaments are not diffusive structures and are more likely to have a biogenic origin. Furthermore some of the large dendritic masses are composed of both short and long filaments, similar size transitions have been observed in seafloor Fe oxide dendrites from the EPR (Juniper and Fouquet, 1988) and from the terrestrial Ballynoe Fe oxide deposit (Little et al., 2004 in press). These transitions from long to short, or short to long forms may represent some secondary abiogenic Fe oxide growth onto preformed biogenic Fe oxides (e.g. Emerson and Moyer, 2002; Little et al., 2004 in press).

6.4.1.2 Isotopic and Geochemical evidence – the origin of *Alvin* gypsum

The $\delta^{34}S$ values (+9.6-+10.6‰) of the gypsum which cements some of the *Alvin* Fe oxide filaments are close to the average $\delta^{34}S$ of bulk sulphide samples (+7.6‰ (n=8)) and pyrite separates from these sediments (+7.6‰ (n=20)). This suggests that the gypsum SO_4^{2-} is derived from sulphide oxidation rather than seawater ($\delta^{34}S$ =+20.9‰: Rees et al., 1978). This is consistent with porewater studies of an adjacent core; CD102/43, where average porewater SO_4^{2-} concentrations (29.0 ±3 mM) are within the error of bottom seawater SO_4^{2-} (28 mM) but which show elevated concentrations in a lower sulphide layer (32.1 mM) which are attributed to oxidation of sulphides (Severmann et al., in review). Due to the high solubility of sulphate in seawater the presence of sulphide derived gypsum sulphate is unexpected and requires precipitation of the sulphate before mixing and dilution by sediment porewaters can occur. Furthermore, gypsum is assumed to be highly undersaturated in the sediment porewaters, and inorganic homogeneous precipitation of gypsum is unlikely. However, meshes of bacterial filaments growing directly from oxidation of mineral dissolution products on sulphide surfaces (e.g. Figure 6.6) could create a geochemical microenvironment at the mineral/porewater interface where free advective and diffusive exchange with bulk porewaters are restricted (e.g. Thompson and Ferris, 1990; Schultze-lam et al., 1992). In these conditions, the saturation level of gypsum could be increased by continual addition of SO_4^{2-} from sulphide decay to the bacterial mesh, where filament surfaces act as nucleation sites. This type of precipitation via heterogeneous nucleation on bacterial filaments requires a lower saturation level than that required for homogeneous, abiogenic nucleation from a fluid. Effectively, bacterially promoted nucleation is energetically favoured over abiogenic precipitation (Warren and Ferris, 1998).

The Sr isotope data indicate that some of the gypsum is precipitated from an evolved fluid produced by mixing of end member hydrothermal fluid with seawater in the subsurface. Estimates of the mineralising fluid temperature, calculated assuming simple mixing of hydrothermal fluid at 363°C and north Atlantic bottom water at 2°C (Table 6.4a), lie in the range 2.7-60.2°C which is within the optimum growth temperature range for most Fe oxidising bacteria (e.g. Staley, 1973; Edwards et al., 2003c). Sr/Ca ratios however, indicate that the mineralising fluid was not a simple mixture of hydrothermal fluid and seawater, but also contained Sr/Ca from the overlying carbonate cap. It appears that this low temperature, seawater dominated, evolved fluid percolated through the sediment during early diagenesis providing the Ca, Sr and Mg for authigenic gypsum precipitation. Such a fluid may also be rich in Si, Mn and Fe; low temperature evolved fluids (10-15°C) similar to this are thought to be responsible for many of the filamentous textures in both ancient jaspers and seafloor Fe oxide deposits (e.g. Alt, 1988b; Juniper and Fouquet, 1988; Duhig et al., 1992)

SEM X-ray spot microanalyses of filament nets around corroded pyrite grains (Figure 6.6) which show accumulation of O, Fe, S, Si, Cu, and Zn are also suggestive of a microbial origin for the filament structures. A similar ESEM microprobe study of cell-like structures from the active TAG mound revealed comparable elemental accumulations in thread-like cellular masses (Al-Hanbali et al., 2001; Al-Hanbali and Holm, 2002). In addition, SEM X-ray spot microanalyses have identified submicron scale U enrichments at the edges of pyrite grains associated with Fe oxide filament meshes (Figure 6.5). Localised U enrichment in pyrite grains has previously been reported in other sulphide-rich sediments from the TAG area (Mills et al., 1994) and from an adjacent core, CD102/43 (Severmann et al., in review). In both cases enrichment is attributed to fixation via microbial U(VI) reduction. The sub-micron scale U enrichment close to the surface of pyrite associated with Fe oxide filaments in this core is consistent with microbial mediation and fixation of U.

Precipitation of *Alvin* gypsum via nucleation on Fe oxide filaments is also supported by the major element geochemistry. The excellent correlation between Ca and Fe (r =0.94) (Figure 6.17d) indicates that gypsum and Fe oxide precipitation are intimately linked. Whilst Fe oxide filaments are observed cemented in silica and as un-cemented meshes as well as within gypsum, gypsum is always associated with Fe oxide filaments. This suggests that the correlation between Ca and Fe reflects a control on gypsum precipitation rather than Fe oxide precipitation. This is consistent with filament controlled nucleation of gypsum as described above and links the construction of filamentous textures with Fe oxidation which supports a biogenic origin for these structures.

6.4.2 Microbial filament fossilization processes in the *Alvin* sulphide layer

Based on the observations of filament morphologies, gypsum geochemistry and published work on biogenic Fe oxide precipitation the following fossilization processes are inferred:

1. Nucleation of nanometric-scale Fe oxide particles occurs within the cell envelope and at the cell/stalk surface of Fe oxidising bacteria (e.g. *Leptothrix* spp. and *Gallionella* spp.). The oxidation of Fe(II) to Fe(III) requires oxic conditions and circumneutral pH. Nucleation occurs as a direct result of metabolic oxidation of Fe(II) to Fe(III) during sulphide alteration, and/or by sorption of preformed Fe(III) colloids (e.g. Fortin et al., 1998; Warren and Ferris, 1998; Glasauer et al., 2001). This early Fe oxide is likely to occur as poorly ordered Fe oxyhydroxides e.g. Ferrihydrite.
2. The initial Fe oxide uptake of the cell is sparse, but with increasing Fe oxide production the coatings thickened to enclose whole cells/stalks in a cylinder of Fe oxide. Fe oxidising bacteria such as *Gallionella* spp. which are able to detach themselves from the Fe oxide coating do so, leaving mineralised casts which may then provide nucleation sites for subsequent abiotic Fe oxide precipitation (e.g. Emerson and Moyer, 2002; Little et al., 2004 in press). Bacteria which are not able to detach from the Fe oxide coating may die. The Fe oxide casts produced by such bacteria are then able to act as nucleation sites for further abiotic Fe(III) precipitation e.g. the blebs and collomorphic coatings of goethite observed along some cylindrical hematite casts in the *Alvin* sediments. Alternatively they may provide 'budding sites' for

growth of new bacterial cells. The formation of the observed dendritic structures, which are cannot be assigned a specific bacterial morphology, most likely result from this type of secondary, abiotic Fe oxide precipitation following initial biogenic precipitation.

3. The Fe oxide fossilised filament networks may then act as nucleation sites for colloidal silica gels producing the silica encased examples described above. Or they may induce gypsum precipitation by provision of nucleation sites and by creating a micro-geochemical environment where SO_4^{2-} derived from sulphide oxidation is able to accumulate to stoichiometric excess (Figure 6.25). Later thermal maturation of amorphous silica and the poorly ordered bacteriogenic Fe oxides produces minerals such as quartz, goethite and hematite.

6.4.3 Sulphide and Fe oxide tubes – a biogenic origin (?)

The sulphide and Fe oxide tubes and cylinders described in this study are very similar to tubular sulphide structures reported from the Mir zone (Rona et al., 1993b; Rona et al., 1993a), the active TAG mound (Hannington et al., 1995a) and from the Broken Spur hydrothermal vent site at 29°N MAR (Butler et al., 1998):

- In all cases the tubular structures are predominantly composed of pyrite and/or marcasite
- The structures are associated with high temperature sulphide debris
- They have comparable sizes, tube diameters for each site fall within the range ~150-1500µm (Figure 6.26)

While little attention has been paid to the pyrite tubes described from the Mir, TAG and Broken Spur sites, in each case these structures are inferred to represent fossilised polychaete worm tubes (Rona et al., 1993b; Hannington et al., 1995a; Butler et al., 1998).

Polychaetes, vestimentiferans and other unidentified tubeworms are the most common hydrothermal vent fossils reported from ancient massive sulphide deposits (e.g. Oudin and Constantinou, 1984; Haymon et al., 1984; Little et al., 1997; Little et al., 1999). All of these fossils are preserved as pyrite moulds with no remaining shell or organic matter (Little et al., 1998). The fossilization process is thought to take place rapidly with mineralisation resulting from sulphide, elemental sulphur and trace metal accumulation in the biogenic mucus coatings secreted by the tubeworms (e.g. Juniper et al., 1986). However, the exact mechanisms of mineralisation are not clearly understood (e.g. Little et al., 1998; Maginn et al., 2002). Investigations of deep sea tubeworms at modern vent sites have shown a variety of mineralisation styles, e.g. vestimentiferans tubes from the JdFR are initially replaced by barite and amorphous silica which are then replaced by Fe, Zn and Cu sulphides (Cook and Stakes, 1995) whereas alvinellid polychaetes from the EPR are replaced by layers of silica and pyrite and/or marcasite (e.g. Zbinden et al., 2003) or by Fe and Zn sulphides (e.g. Maginn et al., 2002). In some cases the worms tubes are mineralogically zoned (e.g. Maginn et al., 2002; Zbinden et al., 2003). However, the tubes of alvinellid worms from the EPR are significantly larger (several cm's in diameter; e.g. Cook and Stakes, 1995; Zbinden et al., 2003) than the tubes described here.

Although the tube structures from the *Mir*, TAG and Broken Spur hydrothermal sites (MAR) are attributed to polychaete fossilisation there is no direct evidence for this and studies of vent fauna from the MAR (e.g. Van Dover, 1995) have not identified a suitable live candidate. Furthermore, the tube structures described here are too small to have been formed by any known polychaete worm (J. Copley. Pers. Comm.) These structures

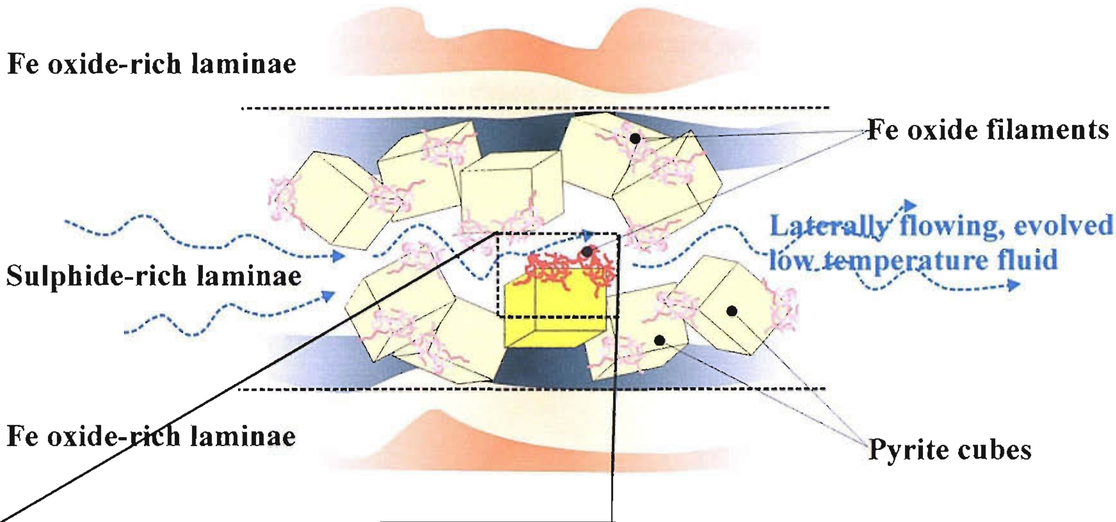

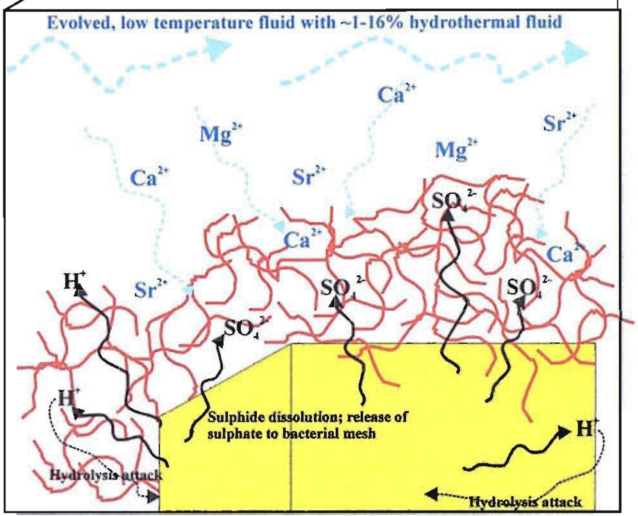

Oxidation and dissolution of pyrite cubes in the sulphide-rich laminae during low temperature fluid flow as diagenetic alteration takes place is mediated by Fe oxidising microbes. Microbially controlled precipitation of Fe oxide leads to the formation of filament meshes and/or branching/ dendritic filament networks. These filament network restrict advective and diffusive exchange of sulphide decay products (sulphate and Fe(II)), with the seawater dominated porewaters.

Accumulation of sulphate from sulphide decay and Ca from the adjacent porewaters leads to local stoichiometric excess of gypsum in the filament network. Gypsum is then precipitated following heterogeneous nucleation on the Fe oxide filaments. Nucleation in this way requires a lower saturation level than homogeneous nucleation and such microbially induced mineralisation of gypsum is energetically favoured over abiogenic precipitation. The end result is fossilization of the Fe oxide filaments in euhedral gypsum crystals. The sulphur and strontium isotopic compositions of these gypsum crystals indicate that they precipitated from a mixed fluid in which sulphate was sourced from sulphide decay ($\delta^{34}S$ is the same as sulphide values) and strontium, calcium and magnesium from an evolved, low temperature, seawater dominated fluid similar to other previously describe fluids responsible for diagenetic hydrothermal clay formation (Severmann et al., 2004) and diffuse low temperature fluids from the surface of the TAG mound (James and Elderfield, 1996).

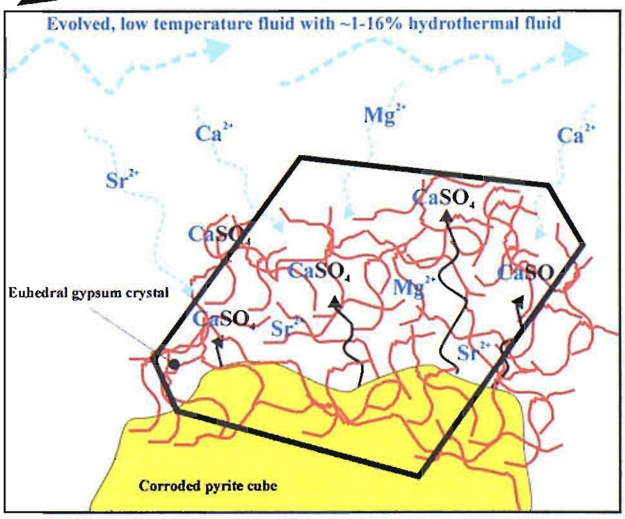

N.B. Not to scale

Figure 6.25: Schematic representation of microbially induced gypsum precipitation,leading to Fe oxide filament preservation in the laminated section (76-87cm depth) at the top of the sulphide layer in the Alvin core (CD102/58).

may not in fact be biogenic at all. The presence of chalcopyrite indicates precipitation under high temperature (>250°C) conditions; in addition, the observed mineralogical zonation (chalcopyrite/ pyrite/ sphalerite) is typical of black smoker chimneys. Furthermore, the $\delta^{34}S$ value of +5.8‰ is close to the predicted $\delta^{34}S$ value of end member hydrothermal fluid entering the TAG system at depth: $\delta^{34}S$ =+5.5‰ (Knott et al. 1998), and measured the $\delta^{34}S$ =+6.6-+7.5‰ (Knott et al., 1998; Shanks, 2001) of vent fluids currently emanating from the black smoker complex. Therefore, the tube structures could represent small, high temperature fluid conduits rather than worm casts. While the exact provenance of the tube structures remains ambiguous, their precipitation under high temperature conditions is clear.

6.5 Conclusions

6.5.1 Fe oxide and oxyhydroxide filaments

- Based on morphological similarities with structures formed by Fe oxidising bacteria direct biogenic mineralisation is invoked for some of the Fe oxide and oxyhydroxide filaments described here. Passive, microbially induced mineralisation also appears to be important for some filament textures and for precipitation of authigenic gypsum and silica phases.
- The S isotopic composition of authigenic gypsum, which acts as a cement for filament networks and is precipitated under micro-geochemical conditions, links the filament structures to sulphide oxidation. Mean gypsum $\delta^{34}S$ of +10.0‰ (n=7) indicates that the *Alvin* gypsum SO_4^{2-} is derived from sulphide oxidation and not from seawater ($\delta^{34}S$ =+20.9‰: Rees et al., 1978). The filament meshes growing directly from oxidation of mineral dissolution products on sulphide surfaces restrict free advective and diffusive exchange with bulk porewaters trapping sulphide derived SO_4^{2-}, they then act as nucleation sites for gypsum precipitation.
- Sr isotopes and Sr/Ca ratios indicate that the Sr, Ca and Mg for gypsum precipitation were provided by an evolved low temperature fluid representing a mixture of sources: seawater, hydrothermal fluid and dissolution of the overlying carbonate cap.
- Filament networks also provide nucleation sites for colloidal silica gels, this accounts for silica cemented filament samples.

Although a biogenic origin for the Fe oxide/ oxyhydroxide filaments is identified here it should be noted that these filaments only constitute a small percentage (<5%) of the total volume of Fe oxide in Core 58. The rest of the Fe oxide in this core is precipitated abiogenically. The exact proportions of biogenic and abiogenic Fe oxide precipitation are difficult to estimate since it is likely that the metabolic activity of even volumetrically small microbial colonies will alter local physiochemical conditions enough to substantially increase precipitation of Fe oxides over that which would occur by abiogenic precipitation alone (e.g. Sobolev and Roden, 2001; Emerson and Moyer, 2002; Kennedy et al., 2003a, b & c).

6.5.2 Sulphide and Fe oxide Tubes

Although similar tubes have previously been described from the TAG and Broken Spur hydrothermal sites and attributed to polychaete fossilisation there is no evidence to support this. Instead, the tube structures described here are inferred to represent small, high temperature fluid conduits which have been transported to the sediment during mass wasting of high temperature mound material. This is supported by S isotopic compositions: $\delta^{34}S$ of tube sample =+5.8‰, $\delta^{34}S$ of TAG black smoker fluids =+6.6‰-+7.5‰ (Knott et al., 1998; Shanks, 2001); and by the observed sequence of mineral zonation (chalcopyrite/ pyrite/ sphalerite). As such these structures have an inorganic rather than biogenic origin.

Chapter 7:

Conclusions

7.1 Sediment formation and diagenetic alteration

7.1.1 The *Alvin* core: CD102/58

The downcore mineralogy and geochemistry of Core 58 reflects deposition from a complex mixture of sources and subsequent physical and chemical alteration. Variation in sulphide mineralogy and textures indicate that initial sulphide precipitation occurred at the surface of the *Alvin* mound close to actively venting black smokers. The sulphur isotopic composition of the earliest collomorphic pyrite reflects a mixture of basaltic and seawater sulphur sources. Insulation of hydrothermal fluid by these early collomorphic crusts led to the precipitation of high temperature (>250°C) Cu-Fe sulphides e.g. chalcopyrite. The heaviest $\delta^{34}S$ values (up to +14.7‰) associated with the high temperature sulphides are the result of partial inorganic reduction of seawater sulphate in a closed system with restricted permeability. The earliest oxidation and alteration of sulphide minerals was contemporaneous with high temperature activity. Mound sulphides and their oxidation products were transported to the surrounding sediments during a mass wasting event. The laminations at the top of the sulphide layer are a sedimentalogical feature relating to settling following mass wasting and represent small turbidite sequences.

Oxidation and alteration of mound material continued within the sediment pile. Downcore metal distributions reflect the relative proportions of sulphides and oxides as well as remobilisation due to oxidative dissolution (e.g. Cr and Cu), secondary mineralisation (e.g. atacamite and covellite), redox cycling (important for redox sensitive elements e.g. Mn, and for Ni which is not redox active but appears to be scavenged by MnO_2), precipitation from diffuse low temperature fluids (e.g. opaline silica, nontronite and gypsum) and scavenging from seawater (V and P). The secondary mineralogy indicates that supergene processes have been important in the modification of this material. The mechanisms of authigenic sulphide precipitation and secondary metal enrichment resemble sub-aerial supergene reactions. Submarine supergene processes appear to be locally important controlled by grain scale remobilisation and enrichment rather than the large scale (tens of metres), downward migrating zones of oxidation and secondary enrichment observed in sub-aerial deposits. Remobilisation appears to be driven by acid leaching and the pH gradients produced during sulphide oxidation reactions. Microbial mediation of sulphide oxidation and dissolution within the sediment leads to secondary authigenic sulphides the S isotopic signature of these sulphides is controlled by the prevalent diagenetic conditions, in particular pyrite oxidation and remineralisation.

Microbes are also involved in Fe oxide precipitation. Filamentous Fe oxide textures cemented within authigenic gypsum and silica, and as non-cemented meshes result from fossilisation of Fe oxidising microbes. The geochemistry and isotopic composition of the gypsum which cements some filaments links the Fe oxide filaments with sulphide oxidation. $\delta^{34}S$ values indicate that the gypsum SO_4^{2-} is derived from sulphide oxidation rather than seawater. Filaments growing directly from oxidation of mineral dissolution products on sulphide surfaces create a micro-geochemical environment at the mineral/ porewater interface where free advective and diffusive exchange with seawater dominated bulk porefluids are restricted. Accumulation of sulphide SO_4^{2-} within the filament mesh and Ca, Sr and Mg contributions from the porefluids leads to gypsum precipitation where the filaments act as nucleation sites. The Sr/Ca and $^{87}Sr/^{86}Sr$ ratios of this gypsum indicate that the porefluids are a complex mix of sources dominated by seawater but with small contributions from low temperature diffuse hydrothermal fluids and the products of dissolution of the overlying carbonate cap.

7.1.2 The *Mir* core: CD102/60

The downcore mineralogy and geochemistry of Core 60 also reflects deposition from a complex mixture of sources and subsequent physical and chemical alteration. Mineralogical and textural variations indicated that the sulphide layer is derived from a pyrite-quartz breccia formed at depth in the *Mir* mound during high temperature activity. Textural and geochemical evidence suggests that primary sulphides were precipitated during reaction of hydrothermal fluid with anhydrite deep in the hydrothermal stockwork zone. The heaviest $\delta^{34}S$ values result from mixing of sulphide from the hydrothermal fluid with reduced anhydrite SO_4^{2-} under high temperature (>250°C) conditions. Secondary sulphide was precipitated following complete replacement of the earlier anhydrite by silica. $\delta^{34}S$ values during secondary sulphide precipitation are controlled by adiabatic mixing of hydrothermal fluid and reduced sulphate from seawater entrainment into the *Mir* mound at depth. The inner mound pyrite-quartz breccia was transported to the surrounding sediment during a mass wasting event. Mass wasting of a pyrite-quartz breccia formed at depth in the *Mir* mound was probably the result of movement on the axis parallel and obliquely oriented faults which dissect the *Mir* mound (Rona et al., 1996).

Alteration of the mound material within the sediment pile is driven by oxidation and acid leaching processes which like Core 58 resemble sub-aerial supergene reactions. Grain scale remineralisation and secondary enrichment are important. However, extensive quartz and cristobalite cement in the upper portions of the sulphide layer appears to have limited the oxidation of primary mound material by restricting permeability and therefore fluid flow. Downcore metal distributions and enrichments predominantly reflect the primary mineralogical composition rather than large scale remobilisation. However, there is evidence for redox cycling (e.g. Mn), secondary mineralisation (e.g. covellite and atacamite) and precipitation from low temperature diffuse fluids (e.g. opaline silica, minor nontronite and collomorphic Fe oxides).

7.1.3 Comparison to other Metalliferous Sediments from the TAG site

Both Core 58 and 60 are broadly similar to other metalliferous sediment cores from the TAG hydrothermal field which have also been attributed to mass wasting of sulphidic mound material (e.g. Metz et al., 1988; German et al., 1993; Mills et al., 1993; Severmann, 2000; Severmann et al., 2004). However, Cores 58 and 60 are significantly less altered than the sediments of previous studies and the geochemistry of the sulphidic layers of Cores 58 and 60 is predominantly controlled by the mineralogy rather than dissolution, re-mobilisation and seawater scavenging processes with minimal plume inputs. The occurrence of Fe oxides and oxyhydroxides in Cores 58 and 60, and other sulphide dominated sediments from the TAG field can be variously attributed to the oxidation of sulphide phases, which are thermodynamically unstable in ambient seawater, and precipitation from diffuse low temperature fluids circulating within the sediment pile (Thompson et al., 1985; Metz et al., 1988; German et al., 1993; Mills et al., 1993; Severmann, 2000; Severmann et al., 2004). The complexity of mineralogical associations and variations in the bulk geochemistry of Cores 58 and 60 and other similar metalliferous sediments from the TAG site reflects the extreme heterogeneity in the extent of alteration and preservation of primary features across the TAG hydrothermal field.

7.1.4 The Global Context of TAG Metalliferous Sediments

The TAG field exhibits the most extensive metalliferous sediments in the Atlantic (e.g. Shearme et al., 1983; Metz et al., 1988; German et al., 1993; Mills, 1995). The occurrence of distinct, relatively thick sulphide layers within TAG near field sediments, like those described for Core 58 and 60, appears to be related to the longevity of high temperature hydrothermal activity at this site. Large, mature sulphide mounds like those of the TAG field, where lots of mass wasting can occur, result in transport of a significant amount of sulphidic material to the surrounding sediments. Thus the occurrence of sulphide dominated near field sediments at Atlantic hydrothermal sites, and only minimal, often admixed sulphide inputs to sediments at Pacific hydrothermal sites reflects the fact that Pacific sites are typically composed of many small mounds and chimney clusters whereas Atlantic sites commonly comprise much larger massive sulphide mounds which are stable over longer periods. The distinct sulphide layers of Cores 58 and 60 can be related to the occurrence of the large, mature, relict mounds of the *Alvin* and *Mir* zones which reflect the longevity and stability of hydrothermal activity at the TAG site. In particular, the pyrite-quartz breccia assemblage of the Core 60 sulphide layer requires a mature mound where there have been multiple episodes of high temperature activity. In this respect, the type of sulphide sediment, and the formation of Core 60 maybe unique to the TAG field.

7.2 Wider Implications

7.2.1 Sulphur Isotopes

The new data presented in this thesis have extended the range of $\delta^{34}S$ at the TAG hydrothermal site to +3.2‰-+14.5‰. The upper end of this range is substantially heavier than values of $\delta^{34}S$ from other sediment free mid ocean ridge hydrothermal sites and suggests that sulphur contributions from reduction of seawater sulphate are much more important than previously recognised. The use of the laser combustion technique has shown that micro-scale mineralogical and textural sulphur isotope studies are essential in unravelling the complex paragenetic sequences, and conditions, of sulphide precipitation and alteration mechanisms. In order to fully assess the extent and significance of heavy primary $\delta^{34}S$ values and the implications for fluid evolution and the influence of bacterial processes in the shallow subsurface and at depth in long lived hydrothermal systems with intermittent high temperature activity further micro-scale sulphur isotope studies are needed.

7.2.2 Microbial Interactions

The biogenic origin of the Fe oxide filaments from the laminated section of Core 58 inferred from morphological similarities with structures formed by Fe oxidising bacteria is supported by the geochemistry of the *Alvin* gypsum which for the first time has directly linked these structures to sulphide oxidation. These filament morphologies can therefore be used as biomarkers for bacteriogenic Fe oxide precipitation. However, earlier suggestions that Fe oxidising bacteria are an important control on Fe oxide precipitation within hydrothermal sediments appear to be overestimated (e.g. Alt et al., 1987; Juniper and Fouquet, 1988; Hannington and Jonasson, 1992; Wirsen et al., 1993; Emerson and Moyer, 2002). Fe oxide filaments in Core 58 only make up a minor percentage of the total volume of Fe oxide and are restricted to oxic layers in the upper portion of the core where circumneutral pH conditions are inferred and there are steep redox gradients (inferred from mineralogy). This is consistent with the findings of a recent study by Severmann et al (in review, 2004) which suggests that the role of bacteria in the weathering of seafloor deposits is only important in the upper tens of centimetres of these deposits which are directly exposed to circumneutral pH conditions and seawater. Although abiogenic Fe oxide precipitation appears to dominate over biogenic precipitation in both Core 60 and Core 58 the relative importance of abiogenic vs. biogenic processes is difficult to estimate. This is because even volumetrically small colonies of Fe oxidising bacteria will alter the local physiochemical conditions enough to substantially increase the precipitation of Fe oxide than would otherwise occur by abiogenic precipitation alone (e.g. Sobolev and Roden, 2001; Emerson and Moyer, 2002; Kennedy et al., 2003a, b & c).

7.2.3 Sulphide Alteration

The precipitation of secondary and late sulphides within Cores 58 and 60, including covellite and sphalerite, as a consequence of acid leaching processes resemble sub-aerial supergene reactions. However, in contrast to the much larger scale, downward migrating zones of oxidation and secondary enrichment observed in sub-aerial deposits, submarine supergene processes appear to be dominated by locally important, grain-scale re-mineralisation and secondary enrichments. The end products of alteration in Cores 58 and 60 are dominated by goethite and are similar to gossans overlying sub-aerial massive sulphides (e.g. Constantinou and Govett, 1973; Scott et al., 2001), and other submarine Fe-oxide rich deposits which have also been compared to sub-aerial gossanous material (e.g. Oudin et al., 1981; Alt et al., 1987; Hannington et al., 1988; Metz et al., 1988; Herzig et al., 1991; Hannington and Jonasson, 1992; Hannington, 1993; Dill et al., 1994; Hannington et al., 1995b; Goulding, 1998). Since goethite and hematite are the ultimate result of supergene reactions in seafloor metalliferous sediments the Cu and Zn of primary phases must be lost to the oceans. These sediments therefore are unlikely to act as long term sinks for hydrothermally derived metals, but as sources.

7.3 The Way Forward

The sediment record at large seafloor hydrothermal sites, such as TAG, provides information about the genesis of these deposits and their evolution in space and time. Although this study has contributed to our understanding of sediment formation and diagenesis, in particular the fate of sulphide minerals during early seafloor alteration, our understanding of low temperature processes and gossan production at seafloor hydrothermal sites is far from complete. In order to unravel the complex record of sedimentation and the history of hydrothermal venting at individual vent sites a more complete understanding of sediment genesis and evolution is required. This can only be achieved by combined petrological and geochemical studies.

APPENDIX A

Sampling

CD102/58 Sampling Notes

Section 1/2		**CD102/58 Sampling**
Sampling Depth (cm)	**True Depth (cm)**	**Comments**
14-17	0-3	Homogeneous moderate brown clay
17-19	3-5	Transition from clay into darker brown rubbly material, some gritty clasts.
19-21	5-7	Dark red brown rubbly material
21-23	7-9	Moderate brown muddy material with some rubbly pieces
23-25	9-11	Moderate brown clay
25-27	11-13	Lighter brown clay
27-29	13-15	Light tan clay
29-31	15-17	Light tan clay
31-32	17-18	Pelagic to sulphides boundary
32-34	18-20	Sulphide and oxide rubble
34-36	20-22	Sulphide and oxide rubble - boundary with pelagics at 36cm
36-38	22-24	Light tan pelagics containing some upper sulphides
38-40	24-26	Pelagics with some red patches
40-42	26-28	Pelagics with red and brown clasts
42-44	28-30	Moderate brown silty clay with red and brown clasts
44-46	30-32	Moderate brown silt containing black, red, olive green and brown clasts
46-47	32-33	Gradational boundary pelagics into Fe-oxides and hydroxides
47-49	33-35	Red brown silt with black and red clasts
49-51	35-37	Red brown silt with black and red coarse clasts, crumbly
51-53	37-39	Red brown, very crumbly and coarse grained
53-54	39-40	Boundary - red brown into moderate brown, very crumbly
54-56	40-42	Finer silty material brown with orange patches
56-57	42-43	Sulphide finger layer, very coarse grained clasts occur
57-59	43-45	Clay into a second finger of sulphide clasts
59-61	45-47	Moderate brown pelagics admixed with sulphide clasts
61-63	47-49	Moderate brown pelagics admixed with sulphide clasts
63-65	49-51	Moderate brown pelagics admixed with sulphide clasts
65-67	51-53	Moderate brown pelagics admixed with sulphide clasts
67-69	53-55	Darker moderate brown pelagics admixed with sulphide clasts
69-71	55-57	Darker moderate brown pelagics admixed with sulphide clasts
71-73	57-59	Coarser and darker pelagics admixed with sulphide clasts, very crumbly
73-75	59-61	Rubbly material with black, orange, olive green and red clasts
75-77	61-63	Rubbly material with black, orange, olive green and red clasts
77-79	63-65	Rubbly material with black, orange, olive green and red clasts
79-81.5	65-67.5	Rubbly material with black, orange, olive green and red clasts
Section 2/2		
81.5-83.5	67.5-69.5	Dark orange brown clay
83.5-85.5	69.5-71.5	Orange brown clay
85.5-87.5	71.5-73.5	Orange brown clay very crumbly
87.5-89.5	73.5-75.5	Orange brown clay very crumbly
89.5-91	75.5-77	Orange brown clay very crumbly to boundary with black and red/orange layers
91-93	77-79	black/orange silt boundary contains some fresh sulphides
94-95.5	80-81.5	Top of striped layer, visable atacamite and fresh sulphides black
95.5-96.5	81.5-82.5	red-orange laminae coarser grained than the black above
96.5-97.5	82.5-83.5	Black laminae
97.5-99	83.5-85	Black and orange laminae, laminae to thin to sample separately
99-100.5	85-86.5	Black with red patches
100.5-102	86.5-88	more homogeneous dark orange brown finer grained material
102-104	88-90	Orange/brown medium grained
104-106	90-92	Orange/brown medium grained
106-108	92-94	Orange/brown medium grained
108-110	94-96	Orange/brown medium- coarse grained
110-112	96-98	Orange/brown medium-coarse grained
112-114	98-100	Orange brown coarse grained material with olive green clasts
114-116	100-102	Orange brown coarse grained material with olive green clasts
116-118	102-104	Orange brown coarse grained material with olive green clasts
118-120	104-106	Orange brown coarse grained material with olive green clasts
120-122	106-108	Orange brown coarse grained material with olive green clasts
122-124	108-110	Orange brown coarse grained with olive green clasts, bright red in core centre
124-126	110-112	Orange brown coarse grained material with olive green clasts
126-128	112-114	Orange brown coarse grained with olive green clasts, very rubbly and crumbly
128-130.5	114-116.5	Orange brown coarse grained material with olive green clasts, very rubbly and crumbly contains a pebble
130.5-132.5	116.5-118.5	Dark brown, coarse and crumbly
132.5-134.5	118.5-120.5	Dark brown, very coarse with pebbles
134.5-136	120.5-122	Very coarse and crumbly
136-138	122-124	Contains large pebble very coarse and crumbly

Section 2/2		**CD102/58 Sampling Continued**
Sampling Depth (cm)	**True Depth (cm)**	**Comments**
138-140	124-126	Very coarse and crumbly
140-142	126-128	Dark brown coarse and crumbly material
142-144	128-130	Dark brown coarse and crumbly material
144-146	130-132	Dark brown coarse and crumbly material
146-148	132-134	Dark brown coarse and crumbly material
148-150	134-136	Becoming less coarse, dark brown orange material
150-152.5	136-138.5	Becoming less coarse, dark brown orange material
152.5-154	138.5-140	Boundary between orange clay and brown crumbly material, material is redder in this sample than above and below
154-156	140-142	Orange brown clay with occasional medium clasts
156-158	142-144	Orange clay with dark olive green grey clay in the centre of the core
158-160	144-146	Orange clay with dark olive green grey clay in the centre of the core
160-162	146-148	Orange clay with dark olive green grey clay in the centre of the core
162-163	148-149	End of orange clay layer
163-165	149-151	Orange brown crumbly material
165-167	151-153	Orange brown crumbly material
167-169	153-155	Orange brown crumbly material
169-171	155-157	Orange brown crumbly material
171-173	157-159	Orange brown crumbly material
173-175	159-161	Orange brown crumbly material
175-177	161-163	Orange brown crumbly material
177-179	163-165	Orange brown crumbly material
179-181	165-167	Boundary into orange clay with the centre of the core as olive green grey
181-183	167-169	Orange clay with dark olive grey centre and clasts
183-185	169-171	Orange clay with dark olive grey centre and clasts
185-187	171-173	Orange clay with dark olive grey centre and clasts
187-189	173-175	Orange clay with dark olive grey centre and clasts
189-191	175-177	Orange clay with dark olive grey centre and clasts with a bright green patch
191-193	177-179	Orange clay with dark olive grey centre and clasts
193-195	179-181	Orange brown clay with dark olive grey centre
195-197	181-183	Orange brown clay with dark olive grey centre
197-199	183-185	Orange brown clay with dark olive grey centre
199-201	185-187	Orange brown clay with dark olive grey centre
201-202.5	187-188.5	Orange brown clay with dark olive grey centre

CD102/60 Sampling Notes

Section 1/1		**CD102/60 Sampling**
Sampling Depth (cm)	**True Depth(cm)**	**Comments**
11-14	0-3	Dark tan pelagics
14-16	3-5	Dark tan pelagics
16-18	5-7	Dark tan pelagics
18-20	7-9	Dark tan pelagics with sand sized black and cream clasts
20-22	9-11	Dark tan pelagics with sand sized black and cream clasts
22-24	11-13	Similar to above but with a lense of light tan material
24-26	13-15	Dark tan pelagics with sand sized black and cream clasts
26-28	15-17	Darker brown tan pelagics containing sand sized clasts
28-30	17-19	Dark brown material containing sand sized clasts
30-32	19-21	Dark brown material containing sand sized clasts
32-34	21-23	Dark brown material containing sand sized clasts
34-36	23-25	Becoming redder with larger clasts
36-38	25-27	Becoming redder with larger clasts
38-40	27-29	Becoming redder with larger clasts
40-42	29-31	Becoming redder with larger clasts
42-44	31-33	Becoming redder with larger clasts, crumbly texture
44-46	33-35	Dark red brown and crumbly
46-48	35-37	Dark red brown
48-50	37-39	Dark erd brown
50-52	39-41	Dark red brown slightly crumbly
52-54	41-43	Dark red brown slightly crumbly
54-56	43-45	Dark red brown with pea green and orange specks
56-58	45-47	Transition into sulphide layer
59-61	47-49	Dark grey sulphide rubble, contains fresh sulphide crystals
60.5-64.5	**48.5-52.5**	**Sulphide nugget**
61-63	49-51	Dark grey sulphide rubble, contains fresh sulphide crystals
63-65	51-53	Dark grey sulphide rubble, contains fresh sulphide crystals
65-67	53-55	Dark grey sulphide rubble, contains fresh sulphide crystals
67-69	55-57	Dark grey sulphide rubble, contains fresh sulphide crystals
69-71	57-59	Dark grey sulphide rubble, contains fresh sulphide crystals
71-74	59-62	Dark grey sulphide rubble, contains fresh sulphide crystals
69-74	**57-62**	**Sulphide nugget**
74-76	62-64	Sulphide rubble
76-78	64-66	Sulphide rubble
78-80	66-68	Sulphide rubble
80-82	68-70	Sulphide rubble admixed with oxide rubble
78.5-82.5	**66.5-70.5**	**Sulphide nugget**
82-84	70-72	Sulphide rubble
84-86	72-74	Sulphide rubble
86-88	74-76	Sulphide rubble
88-90	76-78	Sulphide rubble and pale grey clasts
90-92	78-80	Sulphide rubble and pale grey clasts
92-94	80-82	Sulphide rubble admixed with oxide rubble
94-96	82-84	Sulphide rubble admixed with oxide rubble
96-98	84-86	Sulphide rubble admixed with oxide rubble
98-100	86-88	Sulphide rubble admixed with oxide rubble
100-102	88-90	Dark red/black contains red and black clasts, some of the black clasts have a pale green edge
102-105	90-93	Red oxides admixed with sulphides, rubbly
105-107	93-95	Dark red brown material with some sulphide material
107-109	95-97	Red and olivey green grey clay material with some clasts
109-111	97-99	Red and olivey green grey clay material with some clasts
111-113	99-101	Red and olivey green material as above however more consolidated
113-115	101-103	Red and olivey green material as above however more consolidated
115-117	103-105	Red and olivey green material as above however more consolidated
117-119	105-107	Red brown mud with some black clasts
119-121	107-109	Red brown mud with some black clasts
121-123	109-111	Red brown mud with some black and green/black clasts
123-125	111-113	Red brown mud with some black and green/black clasts
125-127	113-115	Red brown mud with some black and green/black clasts
127-130	115-118	Olive tan layer containing a clast of sulphide
130-132	118-120	Red brown with assorted clasts
132-134	120-122	Red brown with assorted clasts
134-137	122-125	Red brown with dark brown clasts

Petrophysics

CD102/58 Graphical Summary of Petrophysical Analyses:

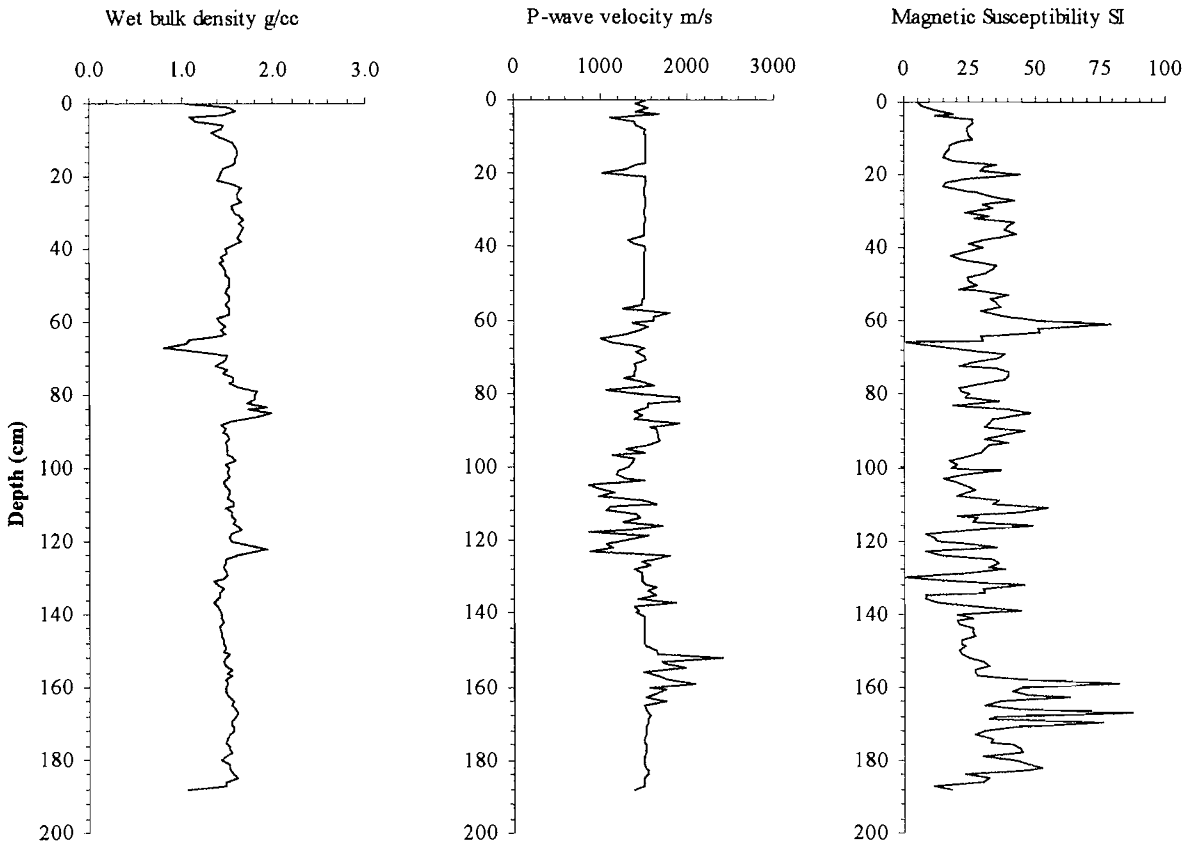

CD102/60 Graphical Summary of Petrophysical Analyses:

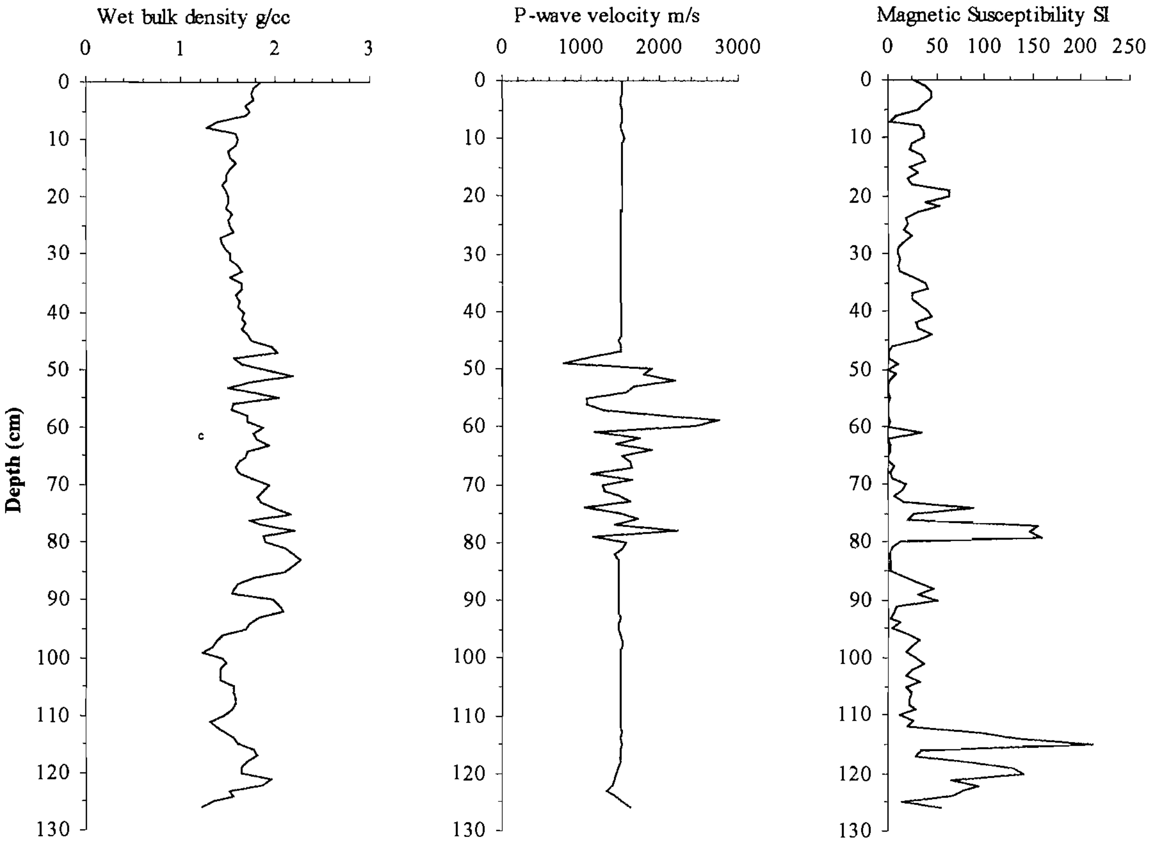

APPENDIX B

ICP-AES:

Bulk sediment samples

Multi-Element Standard Concentrations:

Element	**S1**	**S2**	**S3**	**S4**	**S5**
			All concentrations in ppm		
Fe	245.14	187.81	131.58	29.68	8.05
Ca	133.87	82.60	51.58	15.78	5.16
Zn	94.95	79.35	74.88	25.14	5.03
Cu	81.73	51.56	25.72	10.36	5.16
Al	32.45	25.01	16.70	7.60	2.12
Na	20.64	15.91	10.62	4.84	1.35
Mg	16.72	12.89	8.60	3.92	1.09
Mn	9.93	7.66	5.11	2.33	0.65
P	10.23	7.88	5.26	2.40	0.67
K	5.06	3.90	2.61	1.19	0.33
Sr	1.08	0.51	0.30	0.16	0.10
Ni	1.06	0.50	0.30	0.15	0.10
V	0.53	0.25	0.15	0.08	0.05
Ba	0.42	0.20	0.12	0.06	0.04
Cr	0.32	0.15	0.09	0.05	0.03
Co	0.16	0.08	0.04	0.02	0.02
TIS std	**S1**	**S2**	**S3**	**S4**	**S5**
S	172.18	88.90	44.45	12.83	4.39
Ti	3.50	1.81	0.90	0.26	0.09
K	5.10	2.64	1.32	0.38	0.13
Na	20.65	10.66	5.33	1.54	0.53
Al	32.00	16.52	8.26	2.38	0.82

Machine running order for bulk sediment samples:

Run position	Solution ID DM = drift monitor	Sample depth (cm)	Run position	Solution ID DM = drift monitor	Sample depth (cm)
1	0.6M HCl (reagent blank)	Multi-element standards	**56**	58-91-94	78
2	S5		**57**	60-102-105	92.5
3	S4		**58**	58-65-67	52
4	S3		**59**	60-82-84	72
5	S2		**60**	60-11-14	1.5
6	S1		**61**	60-40-42	30
7	TiS5		**62**	60-74-76	64
8	TiS4		**63**	58-95.5-96.5	82
9	TiS3		**64**	0.6M HCl (reagent blank)	
10	TiS2		**65**	S3 DM	
11	TiS1		**66**	TiS3 DM	
12	0.6M HCl (reagent blank)		**67**	58-114-116	101
13	S3 DM		**68**	60-132-134	122
14	TiS3 DM		**69**	HCl 2 (digest blank)	
15	9	58/117.5	**70**	58-87.5-89.5	74.5
16	18	58/31	**71**	58-175-177	162
17	3	58/60	**72**	58-51-53	38
18	1	60/16	**73**	58-100.5-102	87.25
19	17	Blank 2	**74**	HCl 1 (digest blank)	
20	6	58/111	**75**	60-111-113	101
21	14	58/143	**76**	58-195-197	182
22	5	58/19	**77**	0.6M HCl (reagent blank)	
23	10	58/172	**78**	S3 DM	
24	4	60/78	**79**	TiS3 DM	
25	0.6M HCl (reagent blank)		**80**	S5	Replicates of standard 5 for precision checks
26	S3 DM		**81**	S5	
27	TiS3 DM		**82**	S5	
28	12	58/186	**83**	S5	
29	16	Blank 1	**84**	S5	
30	13	58/154	**85**	S5	
31	15	58/105	**86**	S5	
32	2	60/46	**87**	S5	
33	11	60/97	**88**	S5	
34	8	58/66.25	**89**	S5	
35	7	60/111	**90**	0.6M HCl (reagent blank)	
36	HNO_3 1 (digest blank)		**91**	S3 DM	
37	HNO_3 2 (digest blank)		**92**	TiS3 DM	
38	0.6M HCl (reagent blank)		**93**	58-97.5-99	84.25
39	S3 DM		**94**	58-99-100.5	85.75
40	TiS3 DM		**95**	58-97.5-99	84.25
41	60-67-69	57	**96**	60-59-61	49
42	HF 2 (digest blank)		**97**	60-67-69	57
43	58-160-162	147	**98**	0.6M HCl (reagent blank)	
44	58-14-17	1.5	**99**	S3 DM	
45	58-96.5-97.5	83	**100**	TiS3 DM	
46	TAG in house mix		**101**	0.6M HCl (reagent blank)	
47	58-140-142	127	**102**	0.6M HCl (reagent blank)	
48	60-48-50	38	**103**	0.6M HCl (reagent blank)	
49	60-59-61	49	**104**	0.6M HCl (reagent blank)	
50	HF 2 (digest blank)		**105**	0.6M HCl (reagent blank)	
51	0.6M HCl (reagent blank)		**106**	0.6M HCl (reagent blank)	
52	S3 DM		**107**	0.6M HCl (reagent blank)	
53	TiS3 DM		**108**	0.6M HCl (reagent blank)	
54	60-127-130	117.5	**109**	Milli-Q water	
55	60-96-98	86			

Accuracy and Precision:

Element		Fe	Ca	Zn	Cu	Al	Na	Mg	Mn	P	K	Sr	Ni	V	Ba	Cr	Co		Ti
		µg/g								ng/g									ng/g
Measured concentrations	**S5**	9.10	5.50	5.78	5.65	2.21	1.40	1.16	0.71	0.74	343	112	108	54.6	43.7	34.5	17.8	**S3**	953
	S5	9.40	5.68	5.98	5.79	2.26	1.44	1.19	0.73	0.80	352	115	112	58.1	45.2	35.7	18.6	**S3**	925
	S5	9.53	5.76	6.07	5.86	2.29	1.45	1.21	0.74	0.82	352	117	113	58.9	45.7	36.1	18.8	**S3**	895
	S5	9.07	5.48	5.76	5.63	2.21	1.40	1.16	0.70	0.77	341	112	108	55.2	43.7	34.4	17.9	**S3**	913
	S5	8.99	5.41	5.71	5.60	2.20	1.40	1.15	0.70	0.77	337	111	107	54.4	43.4	34.0	17.6	**S3**	921
	S5	8.94	5.37	5.64	5.61	2.19	1.40	1.16	0.69	0.75	335	111	106	53.7	43.5	33.6	17.5	**S3**	939
	S5	8.94	5.38	5.63	5.59	2.19	1.39	1.16	0.69	0.73	336	111	106	54.1	43.5	33.9	17.2	**S3**	942
	S5	9.14	5.52	5.82	5.62	2.21	1.39	1.17	0.70	0.77	339	112	109	55.2	43.8	34.9	17.9	**S3**	935
	S5	9.13	5.53	5.83	5.60	2.20	1.39	1.15	0.70	0.78	337	111	108	55.3	43.5	34.9	17.7	~	~
	S5	9.04	5.46	5.75	5.59	2.19	1.38	1.15	0.70	0.76	335	111	107	54.1	43.3	34.3	17.7	~	~
Mean		**9.13**	**5.51**	**5.80**	**5.66**	**2.22**	**1.40**	**1.16**	**0.71**	**0.77**	**341**	**112**	**109**	**55.4**	**43.9**	**34.6**	**17.9**		**928**
2σ		**0.37**	**0.24**	**0.26**	**0.18**	**0.06**	**0.04**	**0.04**	**0.03**	**0.05**	**12.16**	**3.89**	**4.27**	**3.31**	**1.55**	**1.46**	**0.91**		**34.54**
Precision		**0.67**	**0.73**	**0.75**	**0.53**	**0.48**	**0.49**	**0.52**	**0.62**	**1.11**	**0.59**	**0.58**	**0.66**	**1.00**	**0.59**	**0.70**	**0.85**		**0.66**
True standard concentration		**8.05**	**5.16**	**5.03**	**5.16**	**2.12**	**1.35**	**1.09**	**0.65**	**0.67**	**331**	**103**	**101**	**50.7**	**40.3**	**x**	**15.2**		**903**
% difference between measured and standard concentrations		**13.4**	**6.8**	**15.3**	**9.7**	**4.7**	**3.7**	**6.4**	**9.2**	**14.9**	**3.0**	**8.7**	**7.9**	**9.3**	**8.9**	**14.2**	**17.8**		**2.8**

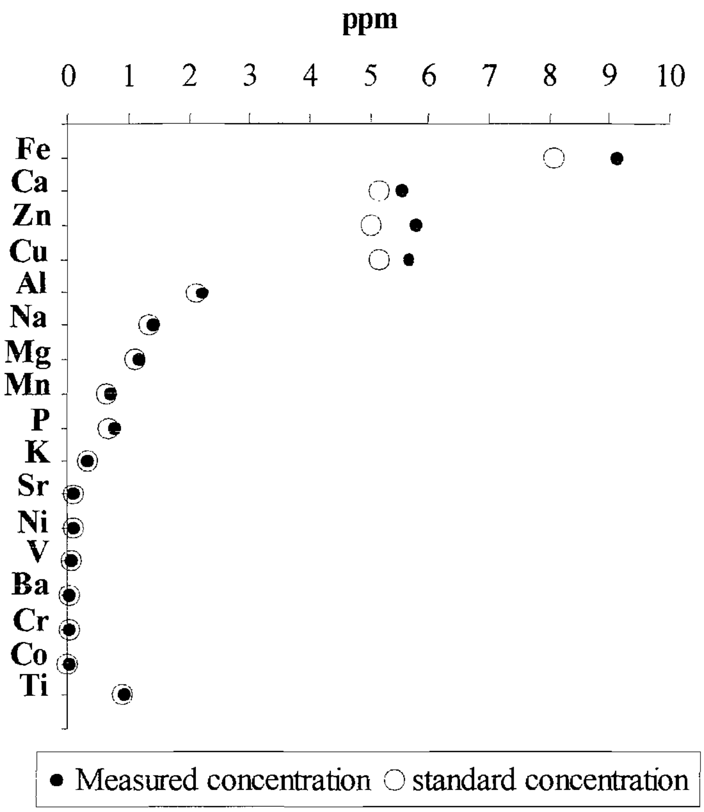

Figure 1: Comparison of measured concentrations for bulk ICP-AES samples with known standard concentrations.

Gypsum sub-samples

Multi-Element Standard Concentrations:

Element	S1	S2	S3	S4	S5
Ca ppm	1.34	2.64	5.22	7.99	10.7
Fe ppb	13.7	26.9	53.3	81.6	109
Mg ppb	6.92	13.6	27.0	41.3	55.2
Sr ppb	4.03	7.94	15.7	24.0	32.1
Mn ppm	0.06	0.13	0.25	0.51	1.03

Machine running order for gypsum samples:

Run position	Solution ID DM = drift monitor	Sample depth (cm)
1	0.6M HCl (reagent blank)	Multi-element standards
2	S1	
3	S2	
4	S3	
5	S4	
6	S5	
7	0.6M HCl (reagent blank)	
8	S3 DM	
9	G96	83
10	G91	78
11	G93	79.5
12	G90.5	77.5
13	G94	80.75
14	G89	76.25
15	0.6M HCl (reagent blank)	
16	S3 DM	
17	S5	Replicates of standard 5 for precision checks
18	S5	
19	S5	
20	S5	
21	S5	
22	S5	
23	S5	
24	S5	
25	S5	
26	S5	
27	0.6M HCl (reagent blank)	
28	S3 DM	
29	Milli-Q water	

Accuracy and precision:

	Element	Ca	Fe	Mg	Sr	Mn
		µg/g		ng/g		µg/g
Measured concentrations	S5	10.6	109	54.9	31.7	1.01
	S5	10.5	108	54.6	31.5	1.01
	S5	10.4	106	53.8	31.3	1.00
	S5	10.4	108	55.6	31.3	1.01
	S5	10.4	108	54.3	31.3	1.02
	S5	10.4	108	54.0	31.2	1.02
	S5	10.4	109	54.5	31.3	1.01
	S5	10.4	108	54.5	31.4	1.02
	S5	10.4	108	54.4	31.4	1.01
	S5	10.5	108	54.7	31.5	1.01
	Mean	**10.5**	**108**	**54.5**	**31.4**	**1.01**
	2σ	**0.12**	**1.57**	**0.96**	**0.29**	**0.01**
	Precision	**0.19**	**0.23**	**0.28**	**0.16**	**0.20**
True standard concentration		**10.7**	**109**	**55.2**	**32.1**	**1.03**
% difference between measured and standard concentrations		**1.87**	**0.92**	**1.27**	**2.18**	**1.94**

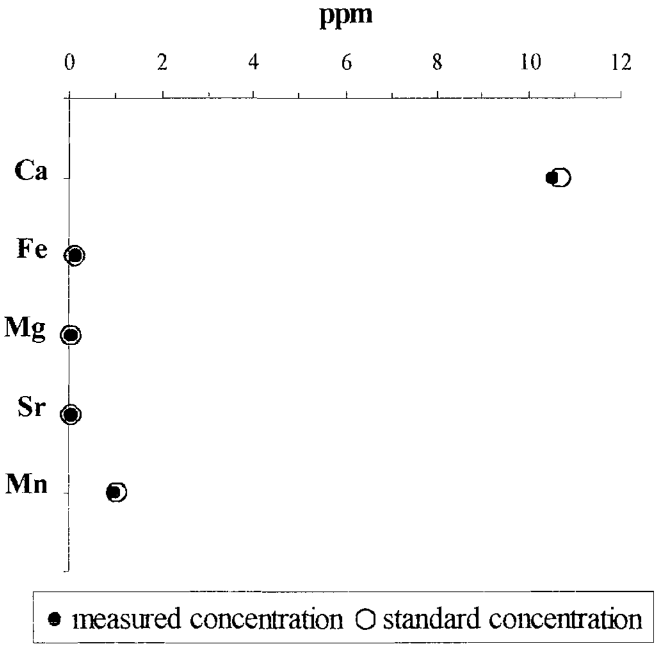

Figure 2: Comparison of measured concentrations for gypsum ICP-AES samples with known standard concentrations.

Equations used in calculations:

Arithmetic mean: $\tilde{x} = \frac{\sum_{i=1}^{n} x_i}{n}$

Standard deviation: $\sigma = \sqrt{\frac{\sum_{i=1}^{n} (x_i - \mu)^2}{n}}$

Precision is calculated as the coefficient of variation and expressed as a percentage: $\left(SE/\tilde{x}\right) \times 100$

Where standard error (SE) is: $\sigma/\sqrt{n}$

APPENDIX C

XRD

CD102/58 Summary of XRD analyses

True depth (cm)	Pyrite	Sphalerite	Chalcopyrite	Goethite	Atacamite	Paratacamite	Gypsum	Quartz	Calcite	Clay	Hematite	Halite	Smectite	Chlorite	Kaolinite	Mica	Illite
0-3				X					X			X	X	X	X	X	X
3-5																	
5-7																	
7-9																	
9-11																	
11-13																	
13-15																	
15-17																	
17-18																	
18-20				X				X	X			X					
20-22																	
22-24																	
24-26																	
26-28																	
28-30																	
30-32				X				X	X			X					
32-33				X				X	X			X	X	X	X	X	X
33-35																	
35-37				X								X					
37-39																	
39-40																	
40-42																	
42-43				X				X				X					
43-45																	
45-47																	
47-49				X				X	\	X		X					
49-51				X			\		X			X					
51-53				X				X	X			X	X	X	\	X	X
53-55																	
55-57				X				X	\			X					
57-59																	
59-61				X								X					
61-63																	
63-65																	
65-67.5				X								X	X	X	\		
67.5-69.5				X				X				X					
69.5-71.5				X				X				X					
71.5-73.5				X				X				X					
73.5-75.5				X			\	X					X	\	\	\	X
75.5-77																	
77-79	X	X	X	X	X	\	X	X				X					
80-81.5	X	X	X	X	X	\	X	X				X					
81.5-82.5	X		X			X		X									
82.5-83.5	X	X	X		\			X			\						
83.5-85																	
85-86.5	X	X	X	\		\					\						
86.5-88																	
88-90	X	X	\	X								X	X			\	\
90-92																	
92-94																	
94-96																	
96-98	X	\		X			X	X				X					
98-100																	
100-102																	
102-104																	
104-106													X			\	\
106-108																	
108-110																	
110-112	X			X			X	X			X						
112-114																	
114-116.5																	
116.5-118.5	X	X	X	X				X			X	X	X			\	\
118.5-120.5																	
120.5-122																	

Continued.	Pyrite	Sphalerite	Chalcopyrite	Goethite	Atacamite	Paratacamite	Gypsum	Quartz	Calcite	Clay	Hematite	Halite	Smectite	Chlorite	Kaolinite	Mica	Illite
122-124																	
124-126																	
126-128																	
128-130	X	X		X				X				X					
130-132																	
132-134																	
134-136																	
136-138.5																	
138.5-140																	
140-142																	
142-144				X				X				X					
144-146																	
146-148																	
148-149				X								X					
149-151																	
151-153																	
153-155				X				X				X	X			X	X
155-157																	
157-159																	
159-161																	
161-163				X								X					
163-165																	
165-167																	
167-169																	
169-171																	
171-173				X				X				X					
173-175																	
175-177																	
177-179																	
179-181																	
181-183													X			X	X
183-185																	
185-187				X								X					
187-188.5																	

CD102/60 Summary of XRD analyses

True depth (cm)	Pyrite	Sphalerite	Chalcopyrite	Goethite	Atacamite	Plagioclase	Cristobalite	Quartz	Amorphous Si, Opal CT?	Calcite	Clay	Hematite	Halite	Smectite	Chlorite	Kaolinite	Mica	Illite
0-3								X	X	X			X	X	X	X	X	X
3-5																		
5-7																		
7-9																		
9-11																		
11-13																		
13-15																		
15-17				X				X		X			X					
17-19																		
19-21																		
21-23																		
23-25																		
25-27																		
27-29																		
29-31								X		X		X	X					
31-33																		
33-35																		
35-37																		
37-39				X	X		X	X				X	X	X				
39-41																		
41-43																		
43-45																		
45-47				X	X		X	X	X			X	X					
47-49	X	X						X					X					
48.5-52.5																		
49-51																		
51-53																		
53-55	X	X					X	X					X					
55-57																		
57-59																		
59-62	X	X					X	X					X	X	X		X	
57-62	X		X				X	X					X					
62-64																		
64-66	X	X	X				X	X										
66-68																		
68-70																		
66.5-70.5																		
70-72	X	X				X		X										
72-74																		
74-76																		
76-78	X	X	X		X	X		X										
78-80																		
80-82																		
82-84	X	X	X	X	X	X	X											
84-86	X	X	X	X	X		X	X					X	X	X			
86-88																		
88-90																		
90-93	X	X	X	X	X		X						X					
93-95																		
95-97				X		X		X	X			X	X					
97-99																		
99-101														X	X	X		
101-103																		
103-105																		
105-107																		
107-109																		
109-111				X				X					x					
111-113																		
113-115																		
115-118																		
118-120				X				X				X	X	X	X	X	X	X
120-122																		
122-125								X	X			X						

References:

Al-Hanbali, H. and Holm, N., (2002). Evidence for fossilized subsurface microbial communities at the TAG hydrothermal mound. *Journal of Geomicrobiology*, **19**: 429-438.

Al-Hanbali, H., Sowerby, S. and Holm, N., (2001). Biogenicity of silicified microbes from a hydrothermal system: relevance to the search for evidence of life on earth and other planets. *Earth and Planetary Science Letters*, **191**: 213-218.

Alt, J., (1988a). The chemistry and sulfur isotope composition of massive sulfide and associated deposits on Green Seamount, Eastern Pacific. *Economic Geology*, **83**: 1026-1033.

Alt, J., (1995). Subseafloor processes in mid-ocean ridge hydrothermal systems. In: Seafloor hydrothermal systems: physical, chemical, biological and geological interactions. S. Humphris, R. Zierenberg, L. Mullineaux and R. Thomson (Editors) *American Geophysical Union*, Washington, pp. 85-114.

Alt, J., Anderson, T. and Bonnel, l., (1989). The geochemistry of sulfur in a 1.3km section of hydrothermally altered oceanic crust, DSDP hole 504B. *Geochimica et Cosmochimica Acta*, **53**(2): 1011-1023.

Alt, J., Honorez, J., Laverne, C. and Emmermann, R., (1986). Hydrothermal alteration of a 1 km section through the upper ocean crust, deep sea drilling program hole 504B: Mineralogy, chemistry and evolution of seawater basalt interactions. *Journal of geophysical research*, **91**(B10): 10309-10335.

Alt, J., Lonsdale, P., Haymon, R. and Muehlenbachs, K., (1987). Hydrothermal sulfide and oxide deposits on seamounts near 21°N, East Pacific Rise. *Geological Society of America Bulletin*, **98**: 157-168.

Alt, J. and Teagle, D., (1998). Probing the TAG mound and stockwork: oxygen-isotopic profiles from deep ocean drilling. *Proceedings of the ODP, scientific results*, **158**: 285-295.

Alt, J. et al., (1996). Ridge Flank alteration of upper ocean crust in the eastern pacific: synthesis of results for volcanic rocks of holes 504B and 896A. *Proceedings of the ODP, scientific results*, **148**: 435-450.

Alt, J.C., (1988b). Hydrothermal oxide and nontronite deposits on seamounts in the Eastern Pacific. *Marine Geology*, **81**: 227-239.

Arnold, M. and Sheppard, S., (1981). East Pacific Rise at latitude 21° N: isotopic composition and origin of the hydrothermal sulphur. *Earth and Planetary Science Letters*, **56**: 148-156.

Ault, W. and Jensen, M., (1963). Summary of sulfur isotope standards. In: *Biogeochemisty of Sulfur Isotopes*. M. Jensen (Editor), National Science Foundation., Symposium Proceedings., Yale University.

Baes, C. and Mesmer, R., (1976). *The hydrolysis of cations*. Wiley, New York, 489 pp.

Bain, J., Blowes, D., Robertson, W. and Frind, E., (2000). Modeling of sulfide oxidation with reactive transport at a mine drainage site. *Journal. Contam. Hydrol.*, **41**: 23-47.

Bak, F. and Cypionka, H., (1987). A novel type of energy metabolism involving fermentation of inorganic sulphur compounds. *Nature*, **326**: 891-892.

Bak, F. and Pfennig, N., (1987). Chemolithotrophic growth of *Deulfovibrio sulfodismutans* sp. nov. by disproportionation of inorganic sulfur compounds. *Arch. Microbiol*, **147**: 184-189.

Baker, E., German, C. and Elderfield, H. (1995). Hydrothermal plumes over spreading centre Axis: Global distributions and geological inferences. In *Physical, Chemical, Biological and Geological interactions Within Submarine Hydrothermal Systems*. SE, Humphris; Mullineaux, L; Zierenberg, RA; Thomson, R (Editors). *Geophysical Monographs*, **91**: 47-71

Balashova, V., Vedenina, I., Markosyan, G. and Zavarzin, G., (1974). *Leptospirillum* ferrooxidans and peculiarities of its autotrophic growth. *Mikrobiologya*, **43**: 581-585.

Banfield, J., Welch, S., Zhang, H., Thomsen Ebert, T. and Lee Penn, R., (2000). Aggregation based on crystal growth and microstructure development in natural iron oxyhydroxide biomineralisation products. *Science*, **289**: 751-754.

Barrett, T. and Friedrichsen, H., (1982). Elemental and isotopic compositions of some metalliferous and pelagic sediments from the Galapagos Mounds area, DSDP leg 170. *Chemical Geology*, **36**: 275-298.

Barrett, T. and Jarvis, I., (1988). Rare-earth element geochemistry of metalliferous sediments from DSDP leg 92: The East Pacific Rise transect. *Chemical Geology*, **67**: 243-259.

Barrett, T., Jarvis, I., Longstaffe, F. and Farquhar, R., (1988). Geochemical aspects of hydrothermal sediments in the Eastern Pacific Ocean: An update. *Canadian Mineralogist*, **26**(3): 841-858.

Barrett, T., Taylor, P. and Lugowski, J., (1987). Metalliferous sediments from DSDP leg 92: The East Pacific Rise Transect. *Geochimica et Cosmochimica Acta*, **51**: 2241-2253.

Barton, B.J. and Skinner, B., (1979). Sulphide mineral stabilities. In: *Geochemistry of hydrothermal ore deposits*. H. Barnes (Editor). Wiley-Interscience, New York, pp. 278.

Barton, P. and Bethke, P., (1960). Thermodynamic properties of some synthetic zinc and copper minerals. *American Journal of Science*, **258**: 21-34.

Bau, M. and Dulski, P., (1999). Comparing yttrium and rare earths in hydrothermal fluids from the Mid-Atlantic Ridge: implications for Y and REE behaviour during near-vent mixing and for the Y/Ho ratio of Proterozoic seawater. *Chemical Geology*, **155**: 77-90.

Bawden, T., Einaudi, MT., Bostick, BC., Meibom, A., Wooden, J., Norby, JW., Orobona, MJT.,
Chamberlain, CP, (2003). Extreme ^{34}S depletions in ZnS at the Mike gold deposit, Carlin Trend, Nevada: Evidence for bacteriogenic supergene sphalerite. *Geology*, **31**: 913-916.

Bear, L., (1963). The mineral resources and mining industry of Cyprus. *Cyprus Geological Survey Bulletin*, **1**: 208.

Bender, M., Broecker, W., Gornitz, V., Middel, U., Kay, R., Sun, S., Biscaye, PE (1971).
Geochemistry of three cores from the East Pacific Rise. *Earth and Planetary Science Letters*, **12**: 425-433.

Berndt, M., Seyfried, W. and Beck, J., (1988). Hydrothermal alteration processes at mid-ocean ridges: experimental and theorectical constraints from Ca and Sr exchange reactions and Sr isotope ratios. *Journal of Geophysical Research*, **93**: 4573-4583.

Bettermann, P. and Liebau, F., (1975). The transformation of amorphous silica to crystalline silica under hydrothermal conditions. *Contributions to mineralogy and petrology*, **53**: 25-36.

Beveridge, T., (1989). Metal ions and bacteria. In: *Metal ions and bacteria*. T. Beveridge and R. Doyle (Editors). Wiley, New York, pp. 1-29.

Beveridge, T., Meloche, J., Fyfe, W. and Murray, R., (1983). Diagenesis of metals chemically complexed to bacteria - laboratory formation of metal phosphates, sulfides and organic condensates in artificial sediments. *Appl. Environ. Microbiol*, **45**: 1094-1108.

Binns, R., Scott, SD., Bogdanov, YA., Lisitsyn, AP., Gordeev, VV., Gurvich, EG., Finlayson, EJ.,
Boyd, T., Dotter, LE., Wheller, GE., Muravyev, KG (1993). Hydrothermal oxide and gold-rich sulfate deposits of Franklin Seamount, West Woodlark Basin, Papua New Guinea. *Marine Geology*, **142**: 99-117.

Bischoff, J. and Pitzer, K., (1985). Phase relations and adiabats in boiling seafloor geothermal systems. *Earth and Planetary Science Letters*, **75**: 327-338.

Bischoff, J. and Rosenbauer, R., (1984). The critical point and two phase boundary of seawater, 200-500°C. *Earth and Planetary Science Letters*, **68**: 172-180.

Bischoff, J. and Rosenbauer, R., (1987). Phase separation in seafloor geothermal systems: experimental study of the effects on metal transport. *American Journal of Science*, **287**: 953-978.

Bischoff, J., Rosenbauer, R., Aruscavage, P., Baedecker, P. and Crock, J., (1983). Sea-floor massive sulphide deposits from 21°N, East Pacific Rise; Juan de Fuca Ridge; and Galapagos Rift: bulk chemical composition and economic implications. *Economic Geology*, **78**: 1711-1720.

Bischoff, J. and Seyfried, W., (1978). Hydrothermal chemistry of seawater from 25° to 350°C. *American Journal of Science*, **278**: 838-860.

Blount, C., 1977. Barite solubilities and thermodynamic properties up to 300°C and 1400 bars. *American Mineralogist*, **62**: 942-957.

Blount, C. and Dickson, F., (1969). The solubility of anhydrite (CaSO4) in NaCl-H2O from 100 to 450°C and 1 to 1000 bars. *Geochimica et Cosmochimica Acta*, **33**: 227-245.

Blum, N. and Puchelt, H., (1991). Sedimentary-hosted polymetallic massive sulfide deposits of the Kebrit and Shaban Deeps, Red Sea. *Mineral. Deposita*, **26**: 217-227.

Bluth, G. and Ohmoto, H., (1988). Sulfide-sulfate chimenys on the East Pacific Rise, 11° and 13°N latitudes. Part II: Sulfur isotopes. *Canadian mineralogist*, **26**(3): 505-515.

Bogdanov, Y., Gorshov, A., Bogdanova, O., Gurvich, E. and Sivtsov, A., (1998). Composition of low temperature Fe-Mn minerals in metalliferous sediments of the TAG area (Mid-Atlantic Ridge). *Okeanologiya*, **38**: 11-121.

Bosecker, K., 1997. Bioleaching: metal solubilization by microorganisms. *FEMS microbiol. Rev.*, **20**: 591-604.

Bostrom, K., Peterson, M.N.A., Joensuu, O., and Fisher, D.E., (1969). Aluminium-Poor Ferromanganoan Sediments on Active Oceanic Ridges. *Journal of Geophysical Research*, **74**(12): 3261-3270.

Bottcher, M., (2001). Sulfur isotope fractionation in the biogeochemical sulfur cycle of marine sediments. *Isotopes in Environmental and health studies*, **37**: 97-99.

Bowen, H., (1979). *Environmental chemistry of the elements*. Academic Press, 333 pp.

Bowers, T.S., (1989). Stable isotope signatures of water-rock interaction in Mid-Ocean Ridge hydrothermal systems: sulfur, oxygen and hydrogen. *Journal of Geophysical Research*, **94**(B5): 5775-5786.

Boyce, A., Little, C. and Russel, M., (2003). A new fossil vent biota in the Ballynoe barite deposit, Silvermines, Ireland: evidence for intracratonic seafloor hydrothermal activity about 352Ma. *Economic Geology*, **98**: 649-656.

Boyd, T. and Scott, S., (2001). Microbial and hydrothermal aspects of ferric oxyhydroxides and ferrosic hydroxides: the example of the Franklin Seamount, Western Woodlark Basin, Papua New Guniea. *Gechemical Transactions*, **7** [Internet Journal].

Boyle, R., (1979). The geochemistry of gold and its deposits. *Canada Geological Survey Bulletin*, **280**: 584.

Broecker, W. and Peng, T.-H., (1982). How fast does the mill grind? Rates of verticle mixing and sediment accumlation., Tracers in the Sea. Eldigion Press, pp. 236-271.

Burns, R., (1979). Marine Minerals. Reviews in Mineralogy, 6. *Mineralogical Society of America*, Washington D.C., 380 pp.

Butler, I., Fallick, A. and Nesbitt, R., (1998). Mineralogy, sulphur isotope geochemistry and the development of sulphide structures at the Broken Spur hydrothermal vent site, 29°10'N, Mid-Atlantic Ridge. *Journal of the Geological Society*, London., **155**: 773-785.

Butterfield, McDuff, RE., Mottl, MJ., Lilley, MD., Lupton, JE., Massoth, ET (1994). Gradients in the composition of hydrothermal fluids from the Endeavour segment vent field: Phase separation and brine loss. *Journal of Geophysical Research*, **99**: 9561-9584.

Campbell, A. et al., (1988). Chemistry of hot springs on the Mid-Atlantic Ridge. *Nature*, **335**: 514-518.

Campbell, A.C., (1991). Mineralogy and chemistry of marine particles by synchotron X-ray spectrometry, Mossbauer spectrometry and plasma-mass spectrometry. In: *Marine particles: analysis and characterisation*. D.C. Hurd, Spencer, D.W. (Editors). American geophysical union, Washington, pp. 375-390.

Campbell, B., Jeanathon, C., Kostka, J., Luther, G. and Cary, S., (2001). Growth and phylogenetic properties of novel bacteria belonging to the epsilon subdivision of the Proteobacteria enriched from Alvinella pompejana and deep-sea hydrothermal vents. *Appl. Environ. Microbiol*, **67**: 4566-4572.

Canfield, D., (2001a). Biogeochemistry of sulfur isotopes. In: Valley J W and C.D. R (Editors), Stable Isotope Geochemistry. Reviews in mineralogy and geochemistry. *Mineralogical Society of America*, pp. 607-636.

Canfield, D., (2001b). Isotope fractionation by natural populations of sulfate reducing bacteria. *Geochimica et Cosmochimica Acta*, **65**: 1117-1124.

Canfield, D. and Teske, A., (1996). Late proterozoic rise in atmospheric oxygen concentration inferred from phylogenetic and sulfur isotope studies. *Nature*, **382**: 127.

Canfield, D., Thamdrup, B. and Fleisher, S., (1998). Isotope fractionation and sulfur metabolism by pure and enrichment cultures of elemental sulfur-disproportionating bacteria. *Limnology and Oceanography*, **43**: 253-264.

Cave, R., German, C., Thomson, J. and Nesbitt, R., (2002). Fluxes to sediments underlying the Rainbow hydrothermal plume at 36°14'N on the Mid-Atlantic Ridge. *Geochimica et Cosmochimica Acta*, **66**(11): 1905-1923.

Chambers, L., Trudinger, P., Smith, J. and Burns, M., (1975). Fractionation of sulfur isotopes by continuous cultures of *Desulfovibrio desulfuricans*. *Canadian Journal of Microbiology*, **21**: 1602-1607.

Chang, L., Howie, R. and Zussman, J., (1996). Rock forming minerals, Non-silicates. In: *Rock forming minerals, 5B: Non-silicates*. Longman Group Limited, London, 382 pp.

Chen, C. and Marshall, W., (1982). Amorphous silica solubilities IV., Behavior in pure water and aqueous sodium chloride, sodium sulfate, magnesium chloride, and magnesium sulfate solutions up to 350°C. *Geochimica et Cosmochimica Acta*, **46**: 279-287.

Cherkashev, G., (1995). Hydrothermal input into sediments of the Mid-Atlantic Ridge. In: *Hydrothermal Vents and Processes*. L. Parson, C. Walker and D. Dixon (Editors). Geological Society, London, pp. 223-229.

Chiba, H., Uchiyama, N. and Teagle, D., (1998). Stable isotope study of anhydrite and sulfide minerals at the TAG hydrothermal mound, Mid-Atlantic Ridge, 26°N. *Proceedings of the ODP, scientific results*, **158**: 85-90.

Constantinou, G. and Govett, G., (1973). Geology, Geochemistry, and Genesis of Cyprus Sulfide Deposits. *Economic Geology*, **68**: 843-858.

Cook, T. and Stakes, D., (1995). Biogeological mineralisation in deep-sea hydrothermal deposits. *Science*, **267**: 1975-1979.

Corliss, J.B., Dymond, J., and 9 others, (1979). Submarine hydrothermal springs on the Galapagos Rift. *Science*, **203**: 1073-1083.

Cornell, R. and Schwertmann, U., (1996). *The iron oxides: structure, properties, reactions, occurrence and uses*. Germany VHC: 573.

Cronan, D., (1983). Metalliferous sediments in the CCOP/SOPAC region of the southwest Pacific, with particular reference to geochemical exploration for the deposits. *CCOP/SOPAC Tech. Bull.*, **4**: 55.

Cronan, D., Hodkinson, R., Harkness, D., Moorby, S. and Glasby, G., (1986). Accumulation rates of hydrothermal metalliferous sediments in the Lau basin, SW Pacific. *Geo-Marine Letters*, **6**: 51-56.

Cypionka, H., Smock, A. and Bottcher, M., (1998). A combined pathway of sulfur compound disproportination in *Desulfovivrio desulfuricans*. *FEMS Microbiol. Letts*, **166**: 181-186.

Davidson, G., Stolz, A. and Eggins, S., (2001). Geochemical anatomy of silica iron exhalatives: evidence for hydrothermal oxyanion cycling in response to vent fluid redox and thermal evolution (Mt Windsor Subprovince, Australia). *Economic Geology*, **96**: 1201-1226.

Delaney, J., McDuff, R. and Lupton, J., (1984). Hydrothermal fluid temperatures of 400°C on the Endeavour segment, northern Juan de Fuca Ridge. (abstract) *EOS Transactions, AGU*, **65**: 973.

Deloule, E., Allegre, C. and Doe, B., (1986). Lead and sulphur isotope microstratigraphy in galena crystals from Mississippi Valley-type deposits. *Economic Geology*, **81**: 1307-1321.

Detrick and Onboard Scientific Party, (1986). Drilling the Snake Pit hydrothermal sulphide deposit on the Mid-Atlantic Ridge, Lat 23°22'N. *Geology*, **14**: 1004-1007.

D'Hondt, S., Rutherford, S. and Spivak, A., (2002). Metabolic activity of subsurface life in deep sea sediments. *Science*, **295**: 2067-2070.

Dill, H., G, Siegfanz, and V, Marchig. (1994). Mineralogy and chemistry of Metalliferous Muds forming the Topstratum of a massive sulfide-metalliferous sediment sequence from East Pacific rise 18S: its origin and implications concerning the formation of ochrous sediments in Cyprus-type deposits. *Marine Georesources and Geotechnology*, **12**: 159-180.

Dill, H., Pollmann, H., Bosecker, K., Hahn, L. and Mwiya, S., (2002). Supergene mineralisation in mining residues of the Matchless cupreous pyrite deposit (Namibia) - a clue to the origin of modern and fossil duricrusts in semiarid climates. *Journal of Geochmical Exploration*, **75**: 43-70.

Dold, B. and Fontbote, L., (2001). Element cycling and secondary mineralogy in porphyry copper tailings as a function of climate, primary mineralogy, and mineral processing. *Journal of Geochmical Exploration*, **74**: 3-55.

Dold, B. and Fontbote, L., (2002). A mineralogical and geochemical study of element mobility in sulfide mine tailings of Fe-oxide Cu-Au deposits from the Punta del Cobre belt, Northern Chile. *Chemical Geology*, **189**: 135-163.

Drummond, S. and Ohmoto, H., (1985). Chemical evolution and mineral deposition in boiling hydrothermal systems. *Economic Geology*, **80**: 126-147.

Duckworth, R., Falick, A. and Rickard, D., (1994). Mineralogy and sulfur isotopic composition of the Middle Valley massive sulfide deposit, northern Juan de Fuca Ridge. *Proceedings of the ODP, scientific results*, **139**: 373-385.

Duckworth, R. Knott, R., Fallick, AE., Rickard, D., Murton, BJ., Van Dover, C (1995). Mineralogy and sulphur isotope geochemistry of the broken spur sulphides, 29°N, Mid-Atlantic Ridge. In: W.C.L. Parson. L. M., Dixon. D. R. (Editor), *Hydrothermal vents and processes*. Geological Society Special Publications. The Geological Society, London, pp. 175-189.

Duhig, N., Stolz, J., Davidson, G. and Large, R., (1992). Cambrian microbial and silica gel textures in silica iron exhalites from the Mount Windsor Volcanic Belt, Australia; Their petrography, chemistry and origin. *Economic Geology*, **87**: 764-784.

Dymond, J., (1981). Geochemistry of Nazca Plate surface sediments: An evaluation of hydrothermal, biogenic, detrital and hydrogenous sources. *Geological Society of America Mem*, **154**: 133-170.

Dymond, J. Corliss, JB., Heath, GR., Field, CW., Dasch, EJ., Veeh, HH, (1973). Origin of metalliferous sediments from the Pacific Ocean. *Geol Soc of America*, **84**: 3355-3372.

Dymond, J. and Veeh, H., (1975). Metal accumulation rates in the southeast Pacific and the origin of metalliferous sediments. *Earth and Planetary Science Letters*, **28**: 13-22.

Eberhart, G., Rona, P. and Honnorez, J., (1988). Geologic controls of hydrothermal activity in the Mid-Atlantic Ridge valley: Tectonics and Volcanics. *Marine Geophysical Research*, **10**: 233-239.

Edmond, J. Campbell, AC., Palmer, MR., German, CR., Klinkhammer, GP., Edmonds, HN., Elderfield, H., Thompson, G., Rona, PA (1995). Time-series of vent fluids from the TAG and MARK sites (1986, 1990): Mid-Atlantic Ridge: A new solution chemistry model and a mechanism for Cu/Zn zonation in massive sulphide ore bodies. In: *Hydrothermal vents and processes*, W.C.L. Parson. L. M., Dixon. D. R. (Editors). Geological Society Special Publication, London, pp. 77-86.

Edmond, J. Measures, C., Mangum, B., Grant, B., Sclatter, FR., Collier, R., Hudson, A., Gordon, LI., Corliss, JB (1979a). On the formation of metal-rich deposits at ridge crests. *Earth and Planetary Science Letters*, **46**: 19-30.

Edmond, J. Measures, C., McDuff, RE., Chan, LH., Collier, R., Grant, B (1979b). Ridge crest hydrothermal activity and the balances of the major and minor elements in the ocean: the Galapagos data. *Earth and Planetary Science Letters*, **46**: 1-18.

Edmond, J., Von Damm, K., McDuff, R. and Measures, C., (1982). Chemistry of hot springs on the East Pacific Rise and their effluent dispersal. *Nature*, **297**: 187-191.

Edmonds, H., German, CR., Green, DRH., Huh, Y., Gamo, T., Edmond, JM (1996). Continuation of the hydrothermal fluid chemistry time series at TAG, and the effects of ODP drilling. *Geophysical Research Letters*, **23**(23): 3487-3489.

Edwards, K., Bach, W. and Rogers, D., (2003a). Geomicrobiology of the ocean crust: a role for chemoautotrophic Fe-Bacteria. *Biological Bulletin*, **204**(2): 180-185.

Edwards, K., McCollom, T., Konishi, H. and Buseck, P., (2003b). Seafloor biomineralisation of sulfide minerals: Results from insitu incubation studies. *Geochimica et Cosmochimica Acta*, **67**(15): 2843-2856.

Edwards, K., Rogers, D., Wirsen, C. and McCollom, T., (2003c). Isolation and characterisation of novel psychrophilic, neutrophilic, Fe-oxidising, chemolithautotrophic α–and γ-proteobacteria from the deep sea. *Appl. Environ. Microbiol*, **69**(5): 2906-2913.

Ehrlich, H., (1981). Geomicrobiology. Marcel Dekker, New York, 393 pp.

Ehrlich, H., (1996a). Geomicrobiology of iron. H. Ehrlich (Editor), In: *Geomicrobiology*. Marcel Dekker, New York, pp. 312-388.

Ehrlich, H., (1996b). How microbes influence mineral growth and dissolution. *Chemical Geology*, **132**: 5-9.

Ehrlich, H., (1999). Microbes as geologic agents: their role in mineral formation. *Journal of Geomicrobiology*, **16**: 135-153.

Elderfield, H., Mills, R. and Rudnicki, M., (1993). Geochemical and thermal fluxes, high temperature venting and diffuse flow from the mid-ocean ridge systems: the TAG hydrothermal field, Mid-Atlantic Ridge 26°N. *Geological Society Special Publication*, London, **76**: 295-307.

Elderfield, H. and Schultz, A., (1996). Mid-Ocean Ridge Hydrothermal Fluxes and the Chemical Composition of the Ocean. *Annu. Rev. Earth and Planetary Science Letters*, **24**: 191-224.

Emberly, R., Jonasson, IR., Perfit, MR., Franklin, JM., Tivey, MA., Malahoff, A., Smith, MF., Frances, TJG (1988). Submersible investigations of an extinct hydrothermal system on the Galapagos Ridge; sulphide mounds, stockwork zone, and differentiated lava. *Canadian Mineralogist*, **26**: 517-539.

Emerson, D. and Moyer, C., (1997). Isolation and characterisation of novel iron-oxidising bacteria that grow at circumneutral pH. *Appl. Environ. Microbiol*, **63**: 4784-4792.

Emerson, D. and Moyer, C., (2002). Neutrophilic Fe-oxidising bacteria are abundant at the Loihi Seamount and Hydrothermal vents and play a major role in Fe oxide deposition. *Appl. Environ. Microbiol*, **68**: 2906-2913.

Emerson, D. and Revsbech, N., (1994). Investigation of an iron-oxidising microbial mat community lacated near Aarhus, Denmark: feild studies. *Appl. Environ. Microbiol*, **60**: 4022-4031.

Evans, R., (1996). A seafloor gravity profile across the TAG hydrothermal mound. *Geophysical Research Letters*, **23**(23): 3447-3450.

Feely, R., Massoth, ET., Baker, JP., Cowen, JP., Lamb, MF., Krogslund, KA (1990). The effect of hydrothermal processes on midwater Phosphorus distributions in the northeast Pacific. *Earth and Planetary Science Letters*, **96**: 305-318.

Feely, R., Trefry, J., Massoth, G. and Metz, S., (1991). A comparison of the scavenging of phosphorus and arsenic from seawater by hydrothermal iron oxyhydroxides in the Atlantic and Pacific Oceans. *Deep-Sea Research*, **38**(6): 617-623.

Ferris, F., Beveridge, T. and Fyfe, W., (1986). Iron-silica crystallite nucleation by bacteria in a geothermal sediment. *Nature*, **320**: 609-611.

Ferris, F., Fyfe, W. and Beveridge, T., (1988). Metallic ion binding by *bacillus subtilis*: implications for the fossilisation of microorganisms. *Geology*, **16**: 149-152.

Fleet, A. and Robertson, A., (1980). Ocean-ridge metalliferous sediments and pelagic sediments of the Semail nappe, Oman,. *Journal of the Geological Society*, London., **137**: 403-422.

Fortin, D., Ferris, F. and Scott, S., (1998). Formation of Fe-silicates and Fe oxides on bacterial surfaces in samples collected near hydrothermal vents in the Southern Explorer Ridge in the northeast Pacific Ocean. *American Mineralogist*, **83**: 1399-1408.

Fouquet, Y., (1997). Where are the large hydrothermal sulphide deposits in the oceans? *Phil. Trans. R. Soc. Lond.*, **355**: 427-441.

Fouquet, Y., Henry, K., Knott, R. and Cambon, P., (1998). Geochemical section of the TAG hydrothermal mound. *Proceedings of the ODP, scientific results*, **158**: 363-387.

Fouquet, Y. Von Stackelberg, JL., Charlou, J., Erzinger, PM., Herzig, PM., Muhe, R., Wiedicke, M, (1993a). Metallogenesis in back arc environments: The Lau Basin example. *Economic Geology*, **88**: 2154-2181.

Fouquet, Y., Wafik, A., Cambon, P., Mevel, C., Meyer, G., Gente, P (1993b). Tectonic setting and mineralogical and geochemical zonation in the Snake Pit sulfide deposit (Mid-Atlantic Ridge at 23°N). *Economic Geology*, **88**: 2018-2036.

Fowler, T., Holmes, P. and Crundwell, F., (1999). Mechanism of pyrite dissolution in the presnce of *Thiobacillus ferrooxidans*. *Appl. Environ. Microbiol*, **65**: 2987-2993.

Fox, C., (1990). Consequences of phase separation on the distribution of hydrothermal fluids at ASHES Vent Field, Axial Volcano, Juan de Fuca Ridge. *Journal of Geophysical Research*-Solid Earth and Planets, **95**: 12923-12926.

Gamo, T., Chiba, H., Masuda, H., Edmonds, HN., Fujioka, K., Kodama, Y., Nanba, H., Sano, Y (1996). Chemical characteristics of hydrothermal fluids from the TAG mound of the Mid-Atlantic Ridge in August 1994: implications for spatial and temporal variability of hydrothermal activity. *Geophysical Research Letters*, **23**(23): 3483-3486.

Garcia-Ruiz, J., Hyde, ST., Carnerup, AM., Christy, AG., Van Kranendonk, MJ., Welham, NJ (2002). Morphology: an ambiguous indicator of biogenicity. *Astrobiology*, **2**: 353-369.

Garcia-Ruiz, J., Hyde, ST., Carnerup, AM., Christy, AG., Van Kranendonk, MJ., Welham, NJ (2003). Self-assembled silica-carbonate structures and detection of ancient microfossils. *Science*, **302**: 1194-1197.

Gehrke, T., Hallmann, R. and Sand, W., (1995). Importance of extracellular polymeric substances from *Thiobacillus ferrooxidans* and *Leptospirillum ferroxidans* for bioleaching. In: C. Jerez, T. Vargas, H. Toledo and J. Wiertz (Editors), In: *Biohydromettallurgical Processing*. University of Chile, Santiago, pp. 1-11.

Gemmell, J. and Sharpe, R., (1998). Detailed sulfur isotope investigation of the TAG hydrothermal mound and stockwork zone, 26°N, Mid-Atlantic Ridge. *Proceedings of the ODP, scientific results*, **158**: 71-84.

German, C., Baker, E. and Klinkhammer, G., (1995). Regional setting of hydrothermal activity. In: *Hydrothermal vents and processes*, L. Parson, C. Walker and D. Dixon (Editors). Geological Society Special publication, London, pp. 3-15.

German, C., Briem, J., Chin, C., Danielson, M., Holland, S., James, R., Jonsdottir, A., Ludford, EM., Moser, C., Olafson, J., Palmer, MR.,Rudnicki, MD (1994). Hydrothermal activity on the Reykjanes Ridge: the Steinaholl vent-field at 63°06'N. *Earth and Planetary Science Letters*, **121**: 647-654.

German, C., Campbell, A. and Edmond, J., (1990). Hydrothermal scavenging of rare earth elements in the ocean. *Nature*, **316**: 516-518.

German, C., Campbell, A. and Edmond, J., (1991). Hydrothermal scavenging at the Mid-Atlantic Ridge Modification of trace element dissolved fluxes. *Earth and planetary Science Letters*, **107**: 101-114.

German, C., Hergt, J., Palmer, M. and Edmond, J., (1999). Geochemistry of a hydrothermal sediment core from the OBS vent-field, 21N East Pacific Rise. *Chemical Geology*, **155**: 65-75.

German, C., Higgs, NC., Thomson, J., Mills, RA., Elderfield, H., Blusztajn, J., Fleer, AP., Bacon, MP (1993). A Geochemical Study of Metalliferous Sediment From the TAG Hydrothermal Mound, 26deg 08'N, Mid-Atlantic Ridge. *Journal of Geophysical Research*, **98**(B6): 9683-9692.

German, C., Klinkhammer, G. and Rudnicki, M., (1996). The Rainbow hydrothermal plume 36°N15'N, Mid-Atlantic Ridge. *Geophysical Research Letters*, **23**: 2979-2982.

Ghiorse, W., (1984). Biology of iron and manganese depositing bacteria. *Annual Reviews in Microbiology*, **38**: 515-550.

Glasauer, S., Langley, S. and Beveridge, T., (2001). Sorption of Fe (hydr)oxides to the surface of *Shewanella putrefaciens*: cell-bound fine-grained minerals are not always formed de novo. *Appl. Environ. Microbiol*, **67**: 5544-5550.

Godfrey, L., Mills, R., Elderfield, H. and Gurvich, E., (1994). Lead behaviour at the TAG hydrothermal vent field, 26degN, Mid-Atlantic Ridge. *Marine Chemistry*, **46**: 237-254.

Goldfarb, M., Converse, D., Holland, H. and Edmond, J., (1983). The genesis of hot spring deposits on the East Pacific Rise, 21°N. In: *The Kuroko and related volcanigenic massive sulphide deposits*, H. Ohmoto and B. Skinner (Editors),. Economic geology publishing monographs, Duluth, pp. 184-197.

Goodfellow, W. and Blaise, B., (1988). Sulphide formation and hydrothermal alteration of hemiplagic sediment in Middle Valley, Northren Juan de Fuca Ridge. *Canadian Mineralogist*, **26**: 675-696.

Goodfellow, W. and Franklin, J., (1993). Geology, Mineralogy, and Chemistry of sediment-hosted clastic massive sulfides in shallow cores, Middle Valley, Northern Juan de Fuca Ridge. *Economic Geology*, **88**: 2037-2068.

Goulding, H., (1998). Genesis and Preservation of metalliferous sediments, Southampton, Southampton, 207 pp.

Goulding, H., Mills, R. and Nesbitt, R., (1997). Genesis and preservation of metalliferous sediments from TAG and Oman. BRIDGE Newsletter, 13: 52.

Goulding, H., Mills, R. and Nesbitt, R., (1998). Precipitation of hydrothermal sediments on the active TAG mound: implications for ochre formation. In: *Modern Ocean Floor Processes and the Geological Record*, R. Mills and K. Harrison (Editors). Geological Society, London, pp. 201-216.

Graham, U., Bluth, G. and Ohmoto, H., (1988). Sulfide-sulfate chimenys on the East Pacific Rise, 11° and 13°N latitudes. Part 1: Mineralogy and Paragenesis. *Canadian Mineralogist*, **26**(3): 487-504.

Grenne, T. and Slack, J., (2003). Paleozoic and Mesozoic silica-rich seawater: evidence from hematitic chert (jasper) deposits. *Geology*, **31**(4): 319-322.

Habicht, K. and Canfield, D., (2001). Isotope fractionation by sulfate-reducing natural population and the isotopic composition of sulfide in marine sediments. *Geology*, **29**(6): 555-558.

Habicht, K., Canfield, D. and Rethmeimer, J., (1998). Sulfur isotope fractionation during bacterial reduction and disproportionation of thiosulfate and sulfite. *Geochimica et Cosmochimica Acta*, **62**: 2585-2595.

Halbach, M., Halbach, P. and Luders, V., (2002). Sulfide-impregnated and pure silica precipitates of hydrothermal origin from the Central Indian Ocean. *Chemical Geology*, **182**: 357-375.

Halbach, M., Koschinsky, A. and Halbach, P., (2001). Report on the discovery of *Gallionella ferruginea* from an active hydrothermal field in the deep sea. *InterRidge News*, **10**: 18-20.

Hall, J., Walls, C. and Young, J.-S., (1989). Constructional features of the Troodos ophiolite and implications for the distribution of ore bodies and the generation of oceanic crust. *Canadian Journal of Earth Science*, **26**: 1172-1184.

Hallbeck, L., Stahl, F. and Pedersen, K., (1993). Phylogeny and phenotypic characterisation of the stalk-forming and iron-oxidising bacterium *Gallionella ferruginea*. *Journal of General Microbiology*, **139**: 1531-1535.

Hanert, H., (1973). Rezente marine eisenerze auf Santorin, Griechenland II. Bakterogenese von eisenhydroxidesedimenten. *Geol Rund*, **62**: 803-812.

Hanert, H., (2002). Bacterial and chemical iron oxide depostion in a shallow bay on Palaea Kameni, Santorini, Greece: Microscopy, Electron probe Microanalysis, and Photometry of insitu experiments. *Journal of Geomicrobiology*, **19**: 317-342.

Hannington, M., (1993). The formation of atacamite during weathering of sulphides on the modern seafloor. *The Canadian Mineralogist*, **31**: 945-956.

Hannington, M., Galley, A., Herzig, P. and Petersen, S., (1998). Comparison of the TAG mound and stockwork complex with cyprus-type massive sulphide deposits. *Proceedings of the ODP, scientific results*, **158**: 389-415.

Hannington, M., Herzig, P., Scott, S., Thompson, G. and Rona, P., (1991). Comparitive mineralogy and geochemistry of gold bearing sulphide deposits on the mid-ocean ridges. *Marine Geology*, **101**: 217-248.

Hannington, M. and Jonasson, I., (1992). Fe and Mn oxides at seafloor hydrothermal vents. *Catena Supplement*, **21**: 351-370.

Hannington, M., Jonasson, I., Herzig, P. and Petersen, S., (1995a). Physical and chemical processes of seafloor mineralization at mid-ocean ridges. In *Seafloor Hydrothermal Systems: Physical, Chemical, Biological and Geological interactions, Geophysical Monograph*, **91**: 115-157

Hannington, M. and Scott, S., (1988). Mineralogy and geochemistry of a hydrothermal silica-sulfide-sulfate spire in the caldera of Axial Seamount, Juan de Fuca Ridge. *Canadian Mineralogist*, **26**: 6.03-625.

Hannington, M., Thompson, G., Rona, P. and Scott, S., (1988). Gold and native copper in supergene sulphides from the Mid-Altantic Ridge. *Nature*, **333**: 64-66.

Hannington, M., Tivey, M., Larocque, A., Petersen, S. and Rona, P., (1995b). The occurrence of gold in sulfide deposits of the TAG hydrothermal field, Mid-Atlantic Ridge. *Canadian Mineralogist*, **33**: 1285-1310.

Harder, H., (1976). Nontronite synthesis at low temperatures. *Chemical Geology*, **18**: 169-180.

Hawkins, J. and Helu, S., (1986). Polymetallic sulphide deposit from 'black smoker' chimney: Lau basin. *EOS, Trans. Am. Geophys. Union*, **67**: 378.

Haymon, R., (1983). Growth history of hydrothermal black smoker chimneys. *Nature*, **301**(24 Feb): 695-698.

Haymon, R. and Kastner, M., (1981). Hot spring deposits on the East Pacific Rise at 21N: preliminary description of mineralogy and genesis. *Earth and Planetary Science Letters*, **53**: 363-381.

Haymon, R., Koski, R. and Sinclair, C., (1984). Fossils of hydrothermal vent worms from Cretaceous sulphide ores of the Samail ophiolite, Oman. *Science*, **223**: 1407-1409.

Hekinian, R., Heoffert, M., Larque, P., Cheminee, JL., Stoffers, P., Bideau, D (1993). Hydrothermal Fe and Si Oxyhydroxide deposits from South Pacific Intraplate Volcanoes and East Pacific Rise Axial and Off-axial Regions. *Economic Geology*, **88**: 2099-2121.

Heldal, M. and Tumyr, O., (1983). Gallionella from metalimnion in a eutrophic lake: morphology and X-ray energy dispersive microanalysis of the apical cells and stalks. *Canadian Journal of Microbiology*, **29**: 303-308.

Herzig, P., Becker, K., Stoffers, P., Backer, H. and Blum, N., (1988). Hydrothermal silica chimney fields in the Galapagos Spreading Center at 86°W. *Earth and Planetary Science Letters*, **89**: 73-86.

Herzig, P., Hannington, M. and Arribas, A., (1998a). Sulfur isotopic composition of hydrothermal precipitates from the Lau back-arc: implication for magmagtic contributions to seafloor hydrothermal systems. *Mineralium Deposita*, **33**: 226-237.

Herzig, P., Hannington, MD., Scott, SD., Maliotis, G., Rona, PA., Thompson, G (1991). Gold-rich sea-floor gossans in the Troodos Ophiolite and on the Mid-Atlantic Ridge. *Economic Geology*, **86**: 1747-1755.

Herzig, P., Peterson, S. and Hannington, M., (1998b). Geochemistry and sulfur isotopic composition of the TAG hydrothermal mound, Mid-Atlantic Ridge, 26°N. *Proceedings of the ODP, scientific results*, **158**: 47-70.

Hodell, D., Muellar, P. and Garrido, J., (1991). Variation in the strontium isotopic composition of seawater during the Neogene. *Geology*, **19**: 24-27.

Hodkinson, R. and Cronan, D., (1991). Geochemistry of recent hydrothermal sediments in relation to tectonic environment in the Lau Basin, southwest Pacific. *Marine Geology*, **98**: 353-366.

Hodkinson, R., Cronan, D., Glasby, G. and Moorby, S., (1986). Geochemistry of marine sediments from the Lau basin, Havre Trough, and Tonga-Kermadec Ridge. *N.Z. Journal of Geology and Geophysics*, **29**: 335-344.

Honnorez, J., Alt, J. and Humphris, S., (1998). Vivisection and autopsy of actvie and fossil hydrothermal alterations of basalt beneath and within the TAG hydrothermal mound. *Proceedings of the ODP, scientific results*, **158**: 231-245.

Hopkinson, L., Roberts, S., Herrington, R. and Wilkinson, J., (1998). Self-organisation of submarine hydrothermal siliceous deposits: evidence from the TAG hydrothermal mound, 26N Mid-Atlantic Ridge. *Geology*, **26**(4): 347-350.

Hopkinson, L., Roberts, S., Herrington, R. and Wilkinson, J., (1999). The nature of crystalline silica from the TAG submarine hydrothermal mound, 26N Mid Atlantic Ridge. *Contributions to Mineralogy and Petrology*, **137**: 342-350.

Humphris, S., Herzig, PM., Miler, DJ., Alt, JC., Becker, K., Brown, D., Brugmann, G., Chiba, H., Fouquet, Y., Gemmel, JB., Guerin, G., Hannington, MD., Holm, NG., Honnorez, JJ., Iturrino, GJ., Knott, R., Ludwig, R., Nakamura, K., Petersen, S., Reysenbach, AL., Rona, PA., Smith, S., Sturz, AA., Tivey, MK., Zhoa, X. (1995). The internal structure of an active seafloor massive sulphide deposit. *Nature*, **377**: 713-716.

Humphris, S. and Kleinrock, M., (1996). Detailed morphology of the TAG active hydrothermal mound: Insights into its formation and growth. *Geophysical Research Letters*, **23**(23): 3443-3446.

James, R. and Elderfield, H., (1996a). Chemistry and ore-forming fluids and mineral formation rates in an active hydrothermal sulphide deposit on the Mid-Atlantic Ridge. *Geology*, **24**(12): 1147-1150.

James, R. and Elderfield, H., (1996b). Dissolved and particulate trace metals in hydrothermal plumes at the Mid-Atlantic Ridge. *Geophysical Research Letters*, **23**(23): 3499-3502.

Janecky, D. and Seyfried, W., (1984). Formation of massive sulphide deposits on oceanic ridge crests: incremental reaction models for mixing between hydrothermal solutions and seawater. *Geochimica et Cosmochimica Acta*, **48**: 2723-2738.

Janecky, D. and Shanks, W., (1988). Computational modelling of chemical and sulfur isotopic reaction processes in seafloor hydrothermal systems: chimneys, massive sulphides and subjacent alteration zones. *Canadian Mineralogist*, **26**: 805-825.

Jannasch, H. and Mottl, M., (1985). Geomicrobiology of deep sea hydrothermal vents. *Science*, **229**: 717-725.

Jenkins, W., Rona, P. and Edmond, J., (1980). Excess ^{3}He in the deep water over the Mid-Atlantic Ridge at 26°N: evidence of hydrothermal activity. *Earth and Planetary Science Letters*, **49**(1): 39-44.

Johnson, D. and Hallberg, K., (2003). The microbiology of acidic miner waters. *Research in Microbiology*, **154**: 466-473.

Jorgensen, B., (1990). A thiosulfate shunt in the sulfur cycle of marine sediments. *Science*, **249**: 152-154.

Jorgensen, B., Isaksen, M. and Jannasch, H., (1992). Bacterial sulphate reduction above 100°C in deep sea hydrothermal vent sediments. *Science*, **258**: 1756-1757.

Juniper, S. and Fouquet, Y., (1988). Filamentous iron-silica deposits from modern and ancient hydrothermal sites. *Canadian Mineralogist*, **26**(3): 859-869.

Juniper, S. and Sarrazin, J., (1995). Interaction of vent biota and hydrothermal deposits: present evidence and future experimentation. In: *Seafloor Hydrothermal Systems: Physical, Chemical, Biological and Geological Interactions*, S. Humphris, R. Zierenberg, L. Mullineaux and R. Thompson (Editors). Geophysical Monographs. American Geophysical Union, Washington DC, pp. 178-193.

Juniper, S. and Tebo, B., (1995). Microbe-metal interactions and mineral deposition at hydrothermal vents. In: *The Microbiology of Deep-Sea Hydrothermal Vents*, D. Karl (Editor). CRC Press, Boca Raton, pp. 219-253.

Juniper, S., Thompson, J. and Calvert, S., (1986). Accumulation of minerals and trace elements in biogenic mucus at hydrothermal vents. *Deep Sea Research*, **33**: 339-347.

Kadko, D., (1993). An assessment of the effect of chemical scavenging within submarine hydrothermal plumes upon ocean geochemistry. *Earth and Planetary Science Letters*, **120**: 361-374.

Kaplan, I. and Rittenberg, S., (1964). Microbiological fractionation of sulphur isotopes. *Journal of General Microbiology*, **34**: 195-212.

Kasama, T. and Murakami, T., (2001). The effect of microorganisms on the Fe-precipitation rates at neutral pH. *Chemical Geology*, **180**: 117-128.

Kase, K., Yamoamoto, M. and Shibata, T., (1990). Copper-rich sulfide deposit near 23°N, Mid-Atlantic Ridge: chemical composition, mineral chemistry, and sulphur isotopes. *Proceedings of the ODP, scientific results*, **106/109**: 163-177.

Kelley, S. P., and Fallick, A. E., (1990). High precision spatially resolved analysis of δ^{34}S in sulphidesusing a laser extraction technique. *Geochim. Cosmochim. Acta* **54:** 883-888.

Kemp, A. and Thode, H., (1968). The mechanism of the bacterial reduction of sulphate and sulphite from isotope fractionation studies. *Geochimica et Cosmochimica Acta*, **32**: 71-91.

Kennedy, C., Martinez, R., Scott, S. and Ferris, F., (2003a). Surface chemistry and reactivity of bacteriogenic iron oxides from Axial Volcano, Juan de Fuca Ridge, Northeast Pacific Ocean. *Geomicrobiology*, **1**: 59-69.

Kennedy, C., Scott, S. and Ferris, F., (2003b). Characterization of Bacteriogenic Iron Oxide Deposits from Axial Volcano, Juan de Fuca Ridge, Northeast Pacific Ocean. *Journal of Geomicrobiology*, **20**: 199-214.

Kennedy, C., Scott, S. and Ferris, F., (2003c). Ultrastructure and potential sub-seafloor evidence of bacteriogenic iron oxides from axial volcano, Juan de Fuca Ridge, Northeast Pacific Ocean. *Fems Microbiology Ecology*, **43**: 247-254.

Kinzler, K., Gehrke, T., Telegdi, J. and Sand, W., (2003). Bioleaching - a result of intrafacial processes caused by extracellular polymeric substances (EPS). *Hydrometallurgy*, **71**: 83-88.

Kirby, C. and Elder Brady, J., (1998). Field determination of Fe2+ oxidation rates in acid mine drainage using a continuously-stirred tank reactor. *Applied Geochemistry*, **13**: 509-520.

Kirby, C., Thomas, H., Southam, G. and Donald, R., (1999). Relative contributions of abiotic and biological factors in Fe (II) oxidation in mine drainage. *Applied Geochemistry*, **14**: 511-530.

Kleinrock, M. and Humphris, S., (1996). Structural asymmetry of the TAG rift valley: Evidence from a near-bottom survey for epsiodic spreading. *Geophysical Research Letters*, **23**(23): 3439-3442.

Klinkhammer, G., Elderfield, H., Greaves, M., Rona, P. and Nelsen, T., 91986). Manganese geochemistry near high-temperature vents in the Mid-Atlantic Ridge rift valley. *Earth and Planetary Science Letters*, **80**: 230-240.

Klinkhammer, G., Elderfield, H. and Hudson, A., (1983). Rare earth elements in seawater near hydrothermal vents. *Nature*, **305**: 185-188.

Klinkhammer, G. and Hudson, A., (1986). Dispersal patterns for hydrothermal plumes in the South Pacific using manganese as a tracer. *Earth and Planetary Science Letters*, **79**: 241-249.

Knott, R., Fallick, A., Rickard, D. and Backer, H., (1995). Mineralogy and sulpur isotope characteristics of a massive sulphide boulder, Galapagos Rift, 8555'W. In: *Hydrothermal vents and processes*,. Parson. L. M., Walker. C., Dixon. D. R. (Editor). Geological Society Special Publication. The Geological Society, London, pp. 207-222.

Knott, R., Fouquet, Y., Honnorez, J., Petersen, S. and Bohn, M., (1998). Petrology of hydrothermal mineralisation: a vertical section through the TAG mound. *Proceedings of the ODP, scientific results*, **158**: 5-26.

Kohler, B., Singer, A. and Stoffers, P., (1994). Biogenic nontronite from marine white smoker chimneys. *Clays and Clay Mineralogy*, **42**: 689-701.

Kong, L., Solomon, S. and Purdy, G., (1992). Microearthquake characteristics of a mid-ocean ridge along axis. *Journal of Geophysical Research*, **97**: 1659-1685.

Konhauser, K., Schiffman, P. and Fisher, Q., (2002). Microbial mediation of authigenic clays during hydrothermal alteration of basaltic tephra, Kilauea Volcano. *Geochemistry, Geophysics, Geosystems*, **3**(12).

Koski, R., Clague, D. and Oudin, E., (1984). Mineralogy and chemistry of massive sulfide deposits from the Juan de Fuca Ridge. *Geological Society of America Bulletin*, **95**: 930-945.

Koski, R., Jonasson, I., Kadko, D., Smith, V. and Wong, F., (1994). Compositions, growth mechanisms, and temporal relations of hydrothermal sulphide-sulphate-silica chimneys at the northern Cleft segment Juan de Fuca Ridge. *Journal of Geophysical Research*, **99**(B3): 4813-4832.

Koski, R., Lonsdale, P., Shanks, W., Berndt, M. and Howe, S., (1985). Mineralogy and geochemisrty of a sediment hosted hydrothermal sulfide deposit from the Southern Trough of the Guaymas Basin, Gulf of California. *Journal of Geophysical Research*, **90**: 6695-7607.

Krasnov, S., Pokrovski, G. and Cherkashev, G., (1995). Geological setting of high temperature hydrothermal activity and massive sulphide formation on fast and slow spreading ridges. In:, *Hydrothermal vents and processes*, L. Parson, C. Walker and D. Dixon (Editors). Geological Society Special Publication, London, pp. 17-32.

Kusakabe, M., Chiba, H. and Ohmoto, H., (1982). Stable isotopes and fluid inclusion study of anhydrite from the East Pacific Rise at 21°N. *Journal of Geochemistry*, **16**: 89-95.

Lacey, D. and Lawson, F., (1970). Kinetics of the liquid-phase oxidation of acid ferrous sulfate by the bacterium *Thiobacillus ferrooxidans*. *Biotechnology and Bioengineering*, **12**: 29-50.

Lalou, C., Brichet, E. and Lange, J., (1989). Fossil hydrothermal sulfide deposits at the Galapagos spreading centre near 85° West: geological setting, mineralogy and chronology. *Oceanologica Atca*, **12**(1): 1-8.

Lalou, C., Reyes, J-L., Brichet, E., Arnold, M., Thompson, G., Fouquet, Yves., Rona, PA (1993). New age data for Mid-Atlantic Ridge hydrothermal sites: TAG and Snake Pit chronology revisited. *Journal of Geophysical Research*, **98**(B6): 9705-9713.

Lalou, C., Reyss, J., Brichet, E., Rona, P. and Thompson, G., (1995). Hydrothermal activity on a 10^5 - year scale at a slow-spreading ridge, TAG hydrothermal field, Mid-Atlantic Ridge 26°N. *Journal of Geophysical Research*, **100**: 17,855-17,862.

Lalou, C., Thompson, G., Arnold, M., Brichet, E., Druffel, E., Rona, PA (1990). Geochemistry of TAG and Snakepit hydrothermal fields, Mid-Atlantic Ridge: witness to a long and complex hydrothermal history. *Earth and Planetary Science Letters*, **97**: 113-128.

Lambert, C., Bishop, J., Biscaye, P. and Chesselet, R., (1984). Particulate aluminium, iron, and manganese chemistry at the deep Atlantic boundary layer. *Earth and Planetary Science Letters*, **70**: 237-248.

Langmuir, C., Humphris, S., Fornari, D., Van Dover, C., Von Damm, K., Tivey, MK., Colodner, D.,Charlou, J-L., Desonie, D., Wilson, C., Fouquet, Y., Klinkhammer, G., Bougault, H (1997). Hydrothermal vents near a mantle hot spot: the Lucky Strike vent field at 37°N on the Mid-Atlantic Ridge. *Earth and Planetary Science Letters*, **148**: 69-91.

Large, R., (1977). Chemical evolution and zonation of massive sulphide deposits in volcanic terrains. *Economic Geology*, **72**: 549-572.

Large, R., Huston, D., McGoldrick, P., Ruxton, P. and McArther, G., (1989). Gold distribution and genesis in Australian volcanogenic massive sulphide deposits and their significance for gold transport models. *Economic Geology Monograph*, **6**: 520-536.

Lein, A., Ul'yanova, N., Grinenko, V. and Lisitsyn, A., (1991). Geochemistry of the hydrothermal sulphide ores of the Mid-Atlantic Ridge (26°N). *Geochem. Int*, **28**: 1-13.

Lisitsyn, A., Bogdanov, Y., Zonenshain, L., Kuzmin, M. and Sagalevitch, A., (1989). Hydrothermal phenomena in the Mid-Atlantic Ridge at latitude 26°N (TAG hydrothermal field). *International Geology Reviews.*, **31**: 1183-1198.

Little, C., Glynn, S. and Mills, R., (2004). Four hundred and ninety million year record of bacteriogenic iron oxide precipitation at sea-floor hydrothermal vents. *Special Issue of the Journal of Geomicrobiology*, **21**: 415-429.

Little, C., Herrington, R., Haymon, R. and Danelian, T., (1999). Early Jurassic hydrothermal vent community from the Franciscan Complex, San Rafael Mountains, California. *Geology*, **27**: 167-170.

Little, C., Herrington, R., maslennikov, V., Morris, N. and Zaykov, V., (1997). Silurian hydrothermal vent community from the Southern Urals of Russia. *Nature*, **385**: 146-148.

Little, C., Herrington, R., Maslennikov, V. and Zaykov, V., (1998). The fossil record of hydrothermal vent communities. In: *Modern Ocean Floor Processes and the Geological Record*, R. Mills and K. Harrison (Editors). Geological Society, Special Publication, London, pp. 259-270.

Little, C. and Thorseth, I., (2002). hydrothermal vent microbial communities: a fossil perspective. *Cah. Biol. Mar.*, **43**: 317-319.

Lowell, R. and Rona, P., (1985). Hydrothermal models for the generation of massive sulphide ore deposits. *Journal of Geophysical Research*, **90**(B10): 8769-8783.

Ludford, E., Plamer, M., German, C. and Klinkhammer, G., (1996). The geochemistry of Atlantic hydrothermal particles. *Geophysical Research Letters*, **23**(23): 3503-3506.

Lupton, J., (1995). Hydrothermal Plumes: Near and Far Field. *Geophysical monograph*, **91**: 317-343.

Lupton, J. and Craig, H., (1981). A major Helium-3 source at 15degS on the East Pacific Rise. *Science*, **214**: 13-18.

Lydon, J., (1984). Some observations on the mineralogy and chemical zonation patterns of volcanogenic sulphide deposits of Cyprus. *Papers of the Geological Survey of Canada*, **84**(1A): 611-616.

Lydon, J., (1988). Volcanogenic massive sulphide deposits, Part 2: Genetic models. *Geoscience Canada*, **15**: 43-65.

MacGregor, L., Sinha, M. and Constable, S., (2001). Electrical resistivity structure of the Valu Fa Ridge, Lau Basin, from marine controlled-source electromagnetic sounding. *Geophysical Journal International*, **146**: 217-236.

Machel, H., (1989). Relationships between sulphate reduction and oxidation of organic compounds to carbonate diagenesis, hydrocarbon accumulations, salt domes and metal sulphide deposits. In: *Carbonates and Evaporites*, S. Mazzullo and J. Gregg (Editors). North Eastern Science Foundation, New York, pp. 137-151.

Magenheim, A. and Gieskes, J., (1992). Hydrothermal discharge and alteration in near surface sediments from the Guaymas Basin, Gulf of California. *Geochimica et Cosmochimica Acta*, **56**: 2329-2338.

Maginn, E., Little, C., Herrington, R. and Mills, R., (2002). Sulphide mineralisation in the deep sea hydrothermal vent polychaete, *Alvinella pompejana*: implications for fossil preservation. *Marine Geology*, **181**: 337-356.

Mann, A., (1984). Mobility of Gold and Silver in lateritic weathering profiles: Some observations from Western Australia. *Economic Geology*, **79**: 38-49.

Marchand, E. and Silverstein, J., (2003). The role of enhanced hetertrophic bacterial growth on iron oxidation by *Acidithiobacillus ferrooxidans*. *Journal of Geomicrobiology*, **20**: 231-244.

Marchel, H., Krous, H. and Sassen, R., (1995). Products and distinguishing criteria of bacterial and thermochemical sulfate reduction. *Applied Geochemistry*, **10**: 373-389.

Marchig, V., Gundlach, H., Moller, P. and Schley, F., (1982). Some geochemical indicators for discrimination between diagenetic and hydrothermal metalliferous sediments. *Marine Geology*, **50**: 241-256.

Marchig, V., Puchelt, H., Rosch, H. and Blum, N., (1990). Massive sulphides from ultra-fast spreading ridge, East Pacific Rise at 18-21° S: A geochemical stock report. *Marine Mining*, **9**: 459-493.

McClain, J., Begnaud, M., Wright, M., Fondrk, J. and Von Damm, G., (1993). Seismicity and tremor in a submarine hydrothermal field. The Northern Juan de Fuca Ridge. *Geophysical Research Letters*, **20**: 1883-1886.

McCollom, T., (2000). Geochemical constraints on primary productivity in submarine hydrothermal vent plumes. *Deep Sea Research*, **I.47**.

McCollom, T. and Shock, E., (1997). Geochemical constraints on chemolithoautotrophic metabolism by microorganisms in seafloor hydrothermal systems. *Geochimica et Cosmochimica Acta*, **61**: 4375-4391.

McGowan, R., Roberts, S., Foster, R., Boyce, A. and Coller, D., (2003). Origin of the copper-cobalt deposits of the Zambian Copperbelt: An epigenic view from Nchanga. *Geology*, **31**: 497-500.

McGregor, B., Harrison, C., Lavelle, J. and Rona, P., (1977). Magnetic anomaly patterns on Mid-Atlantic Ridge crest at 26°N. *Journal of Geophysical Research*, **82**(2): 231-238.

McKenzie, D., (1967). Some remarks on heat flow and gravity anomalies. *Journal of Geophysical Research*, **72**: 6261-6173.

McKibben, M. and Barnes, H., (1986). Oxidation of pyrite in low temperature acidic solution: rate laws and surface textures. *Geochimica et Cosmochimica Acta*, **50**: 1509-1520.

McKibben, M. and Eldridge, C., (1995). Microscopic sulfur isotope variations in ore minerals from the Viburnum Trend, Southeast Missouri: a SHRIMP study. *Economic Geology*, **90**: 228-245.

Mehra, O. and Jackson, M., (1960). Iron oxide removal from soild and clays by a dithionite-citrate system buffered with sodium bicarbonate. *Clays and Clay Mineralogy*, **7**: 317-327.

Metz, S., Trefry, J. and Nelsen, T., (1988). History and geochemistry of a metalliferous sediment core from the Mid-Atlantic Ridge at 26 degrees N. *Geochimica et Cosmochimica Acta*, **52**: 2369-2378.

Millero, F., Sotolongo, S. and M, I., (1987). The oxidation-kinetics of Fe(II) in seawater. *Geochimica et Cosmochimica Acta*, **51**(4): 793-801.

Mills, R., (1995). Hydrothermal deposits and metalliferous sediments from TAG 26degN Nid-Atlantic Ridge. *Geological Society Special Publication*, **87**: 121-132.

Mills, R., Clayton, T. and Alt, J., (1996). Low-temperature fluid flow through sulfidic sediments from TAG: modification of fluid chemistry and alteration of mineral deposits. *Geophysical Research Letters*, **23**(23): 3495-3498.

Mills, R. and Elderfield, H., (1995a). Hydrothermal Activity and the Geochemistry of Metalliferous Sediments. *Geophysical Monographs*, **91**: 392-407.

Mills, R. and Elderfield, H., (1995b). Rare earth element geochemistry of hydrothermal deposits from the active TAG mound, 26°N Mid-Atlantic Ridge. *Geochimica et Cosmochimica Atca*, **59**(17): 3511-3523.

Mills, R., Elderfield, H. and Thomson, J., (1993). A Dual Origin for the Hydrothermal Component in a Metalliferous Sediment Core from the Mid-Atlantic Ridge. *Journal of Geophysical Research*, **98**(B6): 9671-9681.

Mills, R., Teagle, D. and Tivey, M., (1998). Fluid mixing and anhydrite precipitation within the TAG mound. *Proceedings of the Ocean Drilling Program, Scientific Results.*, **158**: 119-127.

Mills, R., Thomson, J., Elderfield, H., Hinton, R. and Hyslop, E., (1994). Uranium enrichment in metalliferous sediments from the Mid-Atlantic Ridge. *Earth and Planetary Science Letters*, **124**: 35-47.

Mills, R. and Tivey, M., (1999). Seawater entrainment and fluid evolution within the TAG hydrothermal mound: evidence from analyses of anhydrite, Mid Ocean Ridges: dynamics of processes associated with creation of new ocean crust. *The Royal Society*, London, pp. 225-248.

Mills, R., Wells, D. and Roberts, S., (2001). Genesis of ferromanganese crusts from the TAG hydrothermal field. *Chemical Geology*, **176**: 283-293.

Miroshnichenko, M. et al., (2002). Nautilia Lithotrophica, gen. nov., sp nov., a thermophilic sulfur-reducing epsilon-proteobacterium isolated from a deep-sea hydrothermal vent. International *Journal of Systematic and Evolutionary Microbiology*, **52**: 1299-1304.

Morton, J., ML, H. and RA, K., (1987). Volcanism and massive sulphide fromation at a sedimented spreading centre, Escanaba Trough, Gorda Ridge, Northeast Pacific Ocean. *Geophysical Research Letters*, **14**(7): 769-772.

Mottl, M., (1983). Metabasalts, Axial Hot Springs, and the Structure of Hydrothermal Systems at Mid-Ocean Ridges. *Geological Society of America Bulletin*, **94**: 161-180.

Mottl, M. and McConachy, T., (1990). Chemical processes in buoyant hydrothermal plumes on the East Pacific Rise near 21deg N. *Geochimica et Cosmochimica Acta*, **54**: 1911-1927.

Mottl, M. and Wheat, C., (1994). Hydrothermal circulation through mid-ocean ridge flanks: Fluxes of heat and magnesium. *Geochimica et Cosmochimica Acta*, **58**: 2225-2237.

Murowchick, J. and Barnes, H., (1986). Formation of cubic FeS. *American Mineralogist*, **71**: 1243-1246.

Murray, J. and Renard, A., (1891). Deep sea deposits. *Report from 'Challenger' Expedition (1873-1876), London.*

Nicol, M., (1993). Plenary lecture: the role of eletrochemistry in hydrometallurgy. In: Hydrometallurgy, fundamentals, technology and innovation, J. Hiskey and G. Warren (Editors). Society for Mining, Metallurgy and Exploration, Inc, Littleton, Colorado, pp. 43-62.

Nicol, M., Needes, C. and Finkelstein, N., (1975). Electrochemical model for the leaching of uranium dioxide. In: *Leaching and Reduction in hydrometallurgy*, A. Burkin (Editor). Institute of Mining and Metallurgy, London, pp. 1-11.

Nordstrom, D., (1982). Aqueous pyrite oxidation and the consequent formation of secondary minerals. In: *Acid sulphate weathering: Pedogeochemistry and relationship to manipulation of soil materials*, J.A. Kittrick, Fanning, D.S. and Hossner, L.R. (Editor). Soil. Sci. Soc. Am. Press, Madison, Wisconsin, pp. 37-56.

Nordstrom, D., (1985). The rate of ferrous iron oxidation in a stream recieving acid mine effluent, *Selected papers in the Hydrologic Sciences*. U.S.G.S., Washington D.C., pp. 113-119.

Oehler, J., (1976). Experimental studies in precambrian paleontology: structural and chemical changes in blue-green algae during simulated fossilisation in synthetic chert. *Geological Society of America Bulletin*, **87**: 117-129.

Oehler, J. and Schopf, J., (1971). Artificial microfossils: experimental studies of permineralisation of blue green algae in silica. *Science*, **260**: 640-646.

Ohmoto, H. and Goldhaber, M., (1997). Sulfur and Carbon isotopes. In: *Geochemistry of hydrothermal ore deposits*, H. Barnes (Editor). J Wiley and Sons, New York, pp. 517-612.

Ohmoto, H. and Lasage, A., (1982). Kinetics of reactions between aqueous sulfates and sulfides in hydrothermal systems. *Geochimica et Cosmochimica Acta*, **46**: 1727-1745.

Ohmoto, H., Mizukami, M., Drummond, SE., Eldridge, CS., Pisutha-Arnond, V., Lenagh, TC (1983). Chemical processes of Kuroko formation. *Economic Geology Monograph*, **5**: 570-567.

Ohmoto, H. and Rye, R., (1979). Isotopes of sulfur and carbon. In: *Geochemistry of hydrothermal ore deposits*, H. Barnes (Editor). John Wiley, New York, pp. 509-567.

Olivarez, A. and Owen, R., (1989). REE/Fe variations in hydrothermal sediments: implications for the REE content of seawater. *Geochimica et Cosmochimica Acta*, **53**: 757-762.

Oudin, E. and Constantinou, G., (1984). Black smoker chimney fragments in Cyprus sulphide deposits. *Nature*, **308**: 349-353.

Oudin, E., Picot, P. and Pouit, G., (1981). Comparison of sulphide deposits from the East Pacific Rise and Cyprus. *Nature*, **291**: 404-407.

Palmer, M. and Edmond, J., (1989). The strontium isotope budget of the modern ocean. *Earth and Planetary Science Letters*, **92**: 11-26.

Palmer, M. and scientific party CD102, (1996). The interaction of microbial activity and diagenesis in hydrothermal sediments at the Mid Atlantic Ridge at 26°N. *Cruise Report CD102*, Univeristy of Bristol, Department of Geology.

Paradis, S., Jonasson, I., Le Cheminant, G. and Watkinson, D., (1988). Two Zn-rich chimneys from the Plume site, Southern Juan de Fuca Ridge. *Canadian Mineralogist*, **26**: 637-654.

Parkes, R., Cragg, B. and Wellbury, P., (2000). Recent studies on bacterial populations and processes in subseafloor sediments: A review. *Journal of hydrogeology*, **8**: 11-28.

Peevler, J., Mostafa, F., Misra, K. and Riciputi, L., (2003). Sulphur isotope microanalysis of sphalerite by SIMS: constraints on the genesis of Mississippi valley-type mineralisation, from the Mascot-Jefferson City district, East Tennessee. *Journal of Geochemical Exploration*, **80**: 277-296.

Peter, J. and Shanks, W., (1992). Sulfur, carbon and oxygen isotope variations in submarine hydrothermal deposits of Guaymas Basin, Gulf of California, USA. *Geochimica et Cosmochimica Acta*, **56**: 2025-2040.

Pitwell, L., (1973). Some coordination effects in orebody formation. *Chemical Geology*, **12**: 39-49.

Price, F. and Shieh, Y., (1979). Fractionation of sulfur isotopes during laboratory synthesis of pyrite at low temperatures. *Chemical Geology*, **27**: 245-253.

Purdy, G., Sempere, J.-C., Schouten, H., Dubois, D. and Goldsmith, R., (1990). Bathymetry of the Mid-Atlantic Ridge, 24° - 31°N: A map series. *Marine Geophysical Research*, **12**: 247-252.

Rees, C., (1973). A steady state model for sulphur isotope fractionation in bacterial reduction processes. *Geochimica et Cosmochimica Acta*, **37**: 1141-1162.

Rees, C., Jenkins, W. and Monster, J., (1978). The sulphur isotopic compostion of ocean seawater sulphate. *Geochimica et Cosmochimica Acta*, **42**: 377-381.

Reich, V. and Marchig, V., (1990). Hydrothermal and volcanic input in sediments of the Lau back-arc basin, SW Pacific. *Marine Mineralogy*, **9**: 183-203.

Reysenbach, A.-L. and Cady, S., (2001). Microbiology of ancient and modern hydrothermal systems. *Trends in Microbiology*, **9**: 79-86.

Robertson, A. and Boyle, J., (1983). Tectonic setting and origin of metaliferous sediments in the Mesozoic Tethys ocean. In: *Hydrothermal processes at seafloor spreading centres*, P. A. Rona., K., Luabier, L., K. L. Smith., (Editor), pp. 595.

Robigou, V., Delaney, J. and Stakes, D., (1993). Large massive sulfide deposits in a newly discoved active hydrothermal system, the High-Rise Field, Endeavour Segment, Juan de Fuca Ridge. *Geophysical Research Letters*, **20**: 1887-1890.

Rohr, K., (1994). Increase of seismic velocities in upper oceanic crust and hydrothermal circulation in the Juan de Fuca plate. *Geophysical Research Letters*, **21**: 2163-2166.

Rona, P., (1985). Black smokers and massive sulphides at the TAG hydrothermal field, Mid-Atlantic Ridge, 26deg N. *EOS (American Geophysical Union Transactions)*, **66**: 936.

Rona, P., (1988). Hydrothermal mineralisation at oceanic ridges. *Canadian Mineralogist*, **26**: 431-465.

Rona, P., Bogdanov, YA., Gurvich, EG., Rimski-Korsakov, NA., Sagalevitch, AM., Hannington, MD., Thompson, G (1993a). Relict hydrothermal zones in the TAG Hydrothermal field, Mid-Atlantic Ridge 26°N, 45°W. *Journal of Geophysical Research*, **98**: 9715-9730.

Rona, P., Hannington, MD., Raman, CV., Thompson, G., Tivey, MK., Humphris, SE., Lalou, C., Petersen, S. (1993b). Active and Relict Seafloor Hydrothermal Mineralisation at the TAG Hydrothermal Field, Mid-Atlantic Ridge. *Economic Geology*, **88**: 1989-2017.

Rona, P., Klinkhammer, G., Nelsen, T., Trefry, J. and Elderfield, H., (1986). Black Smokers, Massive Sulphides and Vent Biota at the Mid-Atlantic Ridge. *Nature*, **321**(1 May): 33-37.

Rona, P., McGregor, B., Betzer, P., Bolger, G. and Krause, D., (1975). Anomalous water temperatures over Mid-Atlantic Ridge crest at 26° North Latitude. *Deep Sea Research*, **22**: 611-618.

Rona, P., Petersen, S., Becker, K., Von Herzen, RP., Hannington, MD., Herzig, PM., Naka, J., Lalou, C., Thompson, G. (1996). Heat flow and mineralogy of TAG relict high-temeprature hydrothermal zones: Mid-Atlantic Ridge 26 deg N, 45 deg W. *Geophysical Research Letters*, **23**(23): 3507-3510.

Rona, P and Trivett, D., (1992). Discrete and diffuse heat tmasfer at ASHES vent field, axial volcano, Juan de Fuca Ridge. *Earth and Planetary Science Letters*, **109**: 51-71.

Rose, A., (1976). The effect of cuprous chloride complexes on the origin of red-bed copper and related deposits. *Economic Geology*, **71**: 1036-1048.

Rudnicki, M. and Elderfield, H., (1993). A chemical model of the buoyant and neutrally buoyant plume above the TAG vent field, 26 deg N, Mid-Atlantic Ridge. *Geochimica et Cosmochimica Acta*, **57**: 2939-2957.

Sakai, H., Des Marais, D., Ueda, A. and Moore, J., (1984). Concentrations and isotope ratios of carbon, nitrogen and sulfur in ocean-floor basalts. *Geochimica et Cosmochimica Acta*, **48**: 2433-2441.

Schippers, A. and Jorgensen, B., (2001). Oxidation of pyrite and iron sulpfide by manganese dioxide in marine sediments. *Geochimica et Cosmochimica Acta*, **65**: 915-922.

Schippers, A. and Sand, W., (1999). Bacterial leaching of metal sulfides proceeds by two indirect mechanisms via thiosulfate or via polysulfides and sulfur. *Appl. Environ. Microbiol*, **65**: 319-321.

Schultz, A., Dickson, P. and Elderfield, H., (1996). Temporal variations in diffuse hydrothermal flow at TAG. *Geophysical Research Letters*, **23**(23): 3471-3474.

Schultze-Lam, S., Fortin, D., Davis, B. and Beveridge, T., (1996). Mineralisation of bacterial surfaces. *Chemical Geology*, **132**: 171-181.

Schultze-lam, S., Harauz, G. and Beveridge, T., (1992). Participtation of a cyanobacterial S-Layer in fine grain mineral formation. *Journal of Bacteriology*, **174**: 7971-7981.

Scott, K., Ashley, P. and Lawie, D., (2001). The geochemistry, mineralogy and maturity of gossans derived from volcanogenic Zn-Pb-Cu deposits of the eastern Lachlan Fold Belt, NSW, Australia. *Journal of Geochmical Exploration*, **72**: 169-191.

Scott, M., Salter, P. and Barnard, L., (1979). Chemistry of Ridge Crest Sediments from the North Atlantic Ocean. Deep Drilling results in the Atlantic Ocean: Ocean Crust. *American Geophysical Union*, Washington DC, 403-428 pp.

Scott, R., Rona, P., McGergor, B. and Scott, M., (1974). The TAG hydrothemal field. *Nature*, **251**: 301-302.

Scott, S., (1997). Submarine hydrothermal systems and deposits. In: *Geochemistry of Hydrothermal Ore Deposits*, H.L. Barnes (Editor). John Wiley and Sons Inc, pp. 797.

Scott, S. and Barnes, H., (1972). Sphalerite-wurtzite equilibria and stoichiometry. *Geochimica et Cosmochimica Acta*, **36**: 1275.

Scott, S., Chase, RL., Hannington, MD., Michael, PJ., McConachy, TF., Shea, GT (1990). Sulphide deposits, tectonics and petrogenesis of Southern Explorer Ridge, Northeast Pacific Ocean. In: Ophiolite-Oceanic Crustal Analogues, Proceedings of Troodos '87, J. Malpas, E. Moores, A. Panayiotou and C. Xenophontos (Editors). Geological Survey Department, Nicosia, Cyprus, pp. 719-733.

Seewald, J. and Seyfried, W., (1990). The effect of temperature on metal mobility in subseafloor hydrothermal systems: constraints from basalt alteration experiments. *Earth and Planetary Science Letters*, **101**: 388-403.

Severmann, S., (2000). The geochemistry and geomicrobiology of relict hydrothermal sulphide deposits, Southampton, Southampton, pp 223.

Severmann, S., Mills, R., Palmer, M. and Fallick, A., (2004). The origin of clay minerals in active and relict hydrothermal deposits. *Geochimica et Cosmochimica Acta*, **68**: 73-88.

Severmann, S., Mills, RA., Palmer, MR., Parkes, RJ., Cragg, BA., Telling, JP in review. Pore fluid -sediment - microbe interactions in hydrothermal sediments.

Severmann, S., Mills, RA., Parkes, RJ., Palmer, MR., Cragg, BA., Rhodes, J., Telling, JP (1998). Microbially mediated mobilisation of redox-sensitive metals in relict hydrothermal sulphide deposits. *Mineralogical Magazine*, **62**: 1367-1368.

Seyfried, W. and Janecky, D., (1985). Heavy metal and sulfur transport during subcritical and supercritical hydrothermal alteration of basalt: influence of fluid pressures and basalt composition and crystallinity. *Geochimica et Cosmochimica Acta*, **49**: 2545-2560.

Shanks, W., (2001). Stable isotopes in seafloor hydrothermal systems: Vent fluids, hydrothermal deposits, hydrothrmal alteration, and microbial processes. In: *Stable isotope Geochemistry*. Reviews in Mineralogy and Geochemistry, V.J. W and D. Cole (Editors). Mineralogical society of America, pp. 470-525.

Shanks, W., Bischoff, J. and Rosenbauer, R., (1981). Seawater sulphate reduction and sulfur isotope fractionation in basaltic systems: Interaction of seawater with fayalite and magnetite at 200-350°C. *Geochimica et Cosmochimica Acta*, **45**: 1977-1995.

Shanks, W., Bohlke, J. and Seal, R., (1995). Stable isotopes in mid-ocean ridge hydrothermal systems: interactions between fluids, minerals and organisms. In: *Seafloor hydrothermal systems: physical, chemical, biological and geological interactions*, S. Humphris, R. Zierenberg, L. Mullineaux and R. Thompson (Editors). Geophysical Monographs, pp. 194-221.

Shanks, W. and Niemitz, J., (1981). Sulphur Isotope Studies of Hydrothermal Anhydrite and Pyrite, Deep Sea Drilling Project Leg 64, Guaymas Basin, Gulf of California. *Initial Reports DSDP*, **64**.

Shanks, W. and Seyfried, W., (1987). Stable isotope studies of vent fluids and chimney minerals , Southern Juan de Fuca Ridge: sodium metasomatism and seawater sulfate reduction. *Journal of Geophysical Research*, **92**(B11): 11387-11399.

Shearme, S., Cronan, D. and Rona, P., (1983). Geochemistry of Sediments from the TAG hydrothermal field, MAR at latitude 26 deg N. *Marine Geology*, **51**: 269-291.

Shikazono, N. and Holland, H., (1983). The partitioning of strontium between anhydrite and aqueous solutions from 150° to 250°C. *Economic Geology, Monograph* **5**: 320-328.

Shimmield, G. and Price, N., (1988). The scavenging of U, 238Th and 231Pa during pulsed hydrothermal activity at 20°S EPR. *Geochimica et Cosmochimica Acta*, **52**: 669-677.

Sillen, L. and Martell, A., (1964). Stability constants of metal-ion complexes. *Chemistry Society London special publication*, **17**.

Sillen, L. and Martell, A., (1971). Stability constants of metal-ion complexes. *Chemical Society of London specail publication*, **25**(Supplement 1).

Silverman, M., (1967). Mechanisms of bacterial pyrite oxidation. *Journal of Bacteriology*, **94**: 1046-1051.

Silverman, M. and Ehrlich, H., (1964). Microbial formation and degradation of minerals. *Adv. Appl. Microbiol*, **6**: 181-183.

Singer, A. and Stoffers, P., (1987). Mineralogy of a hydrothermal sequence in a core from the Atlantis II Deep, Red Sea. *Clays and Clay Mineralogy*, **22**: 251-267.

Singer, A., Stoffers, P., Heller-Kallai, L. and Szafranek, D., (1984). Nontronite in a deep-sea core from the South Pacific. *Clays and Clay Mineralogy*, **32**(375-383).

Singer, P. and Strumm, W., (1970). Acidic mine drainage: the rate determining step. *Science*, **167**: 1121-1123.

Sobolev, D. and Roden, E., (2001). Suboxic deposition of ferric iron by bacteria in opposing gradients of Fe(II) and oxygen at circumneutral pH. *Appl. Environ. Microbiol*, **67**: 1328-1334.

Sorensen, J., Christensen, D. and Jorgensen, B., (1981). Volitile fatty acids and hydrogen as substrates for sulfate-reducing bacteria in anaerobic marine sediments. *Appl. Environ. Microbiol*, **42**: 5-11.

Spiess, F., Macdonald, KC., Atwater, T., Ballard, R., Caranze, A., Cordoba, D., Cox, C., Diaz Garcia, VM., Francheteau, J., Guerrero, J., Hawkins, JW., Haymon, R., Hessler, R., Juteau, T., Kastner, M., Larson, R., Luyendyk. B., Macdougall, JD., Miller, S., Normark, W., Orcutt, J., Rangin, C (1980). East Pacific Rise hot springs and geophysical experiments. *Science*, **207**: 1421-1433.

Stackebrandt, E., Stahl, D. and Devereux, R., (1995). Taxonomic relationships. In: *Sulfate-Reducing Bacteria*, L. Barton (Editor). Plenum, New York, pp. 49-87.

Staley, J., (1973). Bacteria with acellular appendages. In: *Handbook of microbiology*, A. Laskin and H. Lechevalier (Editors). CRC Press, Cleveland, Ohio, pp. 51-55.

Stein, C. and Stein, S., (1994). Constriants on hydrothermal heat flux through the oceanic lithosphere from global heat flow. *Journal of Geophysical Research.*, **99**: 3081-3095.

Stepanova, T., Krasnov, S. and Cherkashev, G., (1996). Mineralogy, chemical composition and structure of the MIR mound, TAG hydrothermal field. *Geophysical Research Letters*, **23**(23): 3515-3518.

Stoffers, P., Glasby, GP., Stuben, D., Pierre, TG., Webb, J., Cardile, CM (1993). Comparative mineralogy and geochemistry of hydrothermal iron-rich crusts from the Pitcairn Teahitia-Mehetia, and Macdonald hot spot areas of the S.W. Pacific. *Marine Georesources and Geotechnology*, **11**: 45-86.

Strens, M. and Cann, J., (1986). A fracture-loop thermal balance model of black smoker circulation. *Tectonophysics*, **122**(3/4): 307-324.

Strumm, W. and Lee, G., (1961). Oxygenation of ferrous iron. *Industrial and Engineering Chemistry*, **53**: 143-146.

Strumm, W. and Morgan, J., (1981). Aquatic Chemistry. John Wiley and Sons, London, 780 pp.

Stuart, F., Duckworth, R., Turner, G. and Schofield, P., (1994). Helium and sulfur isotopes of sulfide minerals from Middle Valley, Northern Juan De Fuca Ridge. *Proceedings of the ODP, scientific results*, **139**: 387-392.

Styrt, M., Brackman, AJ., Holland, HD., Clark, BC., Pisutha-Arnond, V., Eldridge, CS., Ohmoto, H (1981). The mineralogy and the isotopic composition of sulfur in hydrothermal sulfide/sulfate deposits on the East Pacific Rise, 21N Latitude. *Earth and Planetary Science Letters*, **53**: 382-390.

Teagle, D., Alt, J., Chiba, H., Humphris, S. and Halliday, A., (1998a). Strontium and oxygen isotopic constraints on fluid mixing alteration and mineralization in the TAG hydrothermal deposit. *Chemical Geology*, **149**: 1-24.

Teagle, D., Alt, J. and Halliday, A., (1998b). Tracing the chemical evolution of fluids during hydrothermal recharge: Constraints from anhydrite recovered in ODP hole 504B. *Earth and Planetary Science Letters*, **155**: 167-182.

Teagle, D., Alt, J., Humphris, S. and Halliday, A., (1998c). Dissecting an active hydrothermal deposit: The strontium and oxygen isotopic anatomy of the TAG hydrothermal mound - whole rock and silicate minerals. In: *Proceedings of the ODP, scientific results*. College Station TX (Ocean Drilling Program), P. Herzig, S. Humphris, D. Miller and R. Zierenberg (Editors). pp. 297-309.

Thompson, G., Humphris, S., Schroeder, B., Sulanowska and Rona, P., (1988). Active vents and massive sulphides at 26 deg N (TAG) and 23 deg N (Snake Pit) on the Mid-Atlantic Ridge. *Canadian Mineralogist*, **26**: 697-711.

Thompson, G., Mottl, M. and Rona, P., (1985). Morphology, mineralogy and chemistry of hydrothermal deposits from the TAG area, 26N Mid-Atlantic Ridge. *Chemical Geology*, **49**(1/3): 243-257.

Thompson, J. and Ferris, F., (1990). Cyanobacterial precipitation of gypsum, calcite and magnesite from natural alkaline lake water. *Geology*, **18**: 995-998.

Thornber, M., (1985). Supergene alteration of sulphides VII. Distribution of elements during the gossan-forming process. *Chemical Geology*, **53**: 279-301.

Thornber, M. and Wildman, J., 1984. Supergene alteration of sulphides, VI. The binding of Cu, Ni, Zn, Co and Pb with iron bearing gossan minerals. *Chemical Geology*, **44**: 399-434.

Thorseth, I., Torsvik, T., Torsvik, V., Daae, FL., Pedersen, RB., Keldysh-98 Scientific party (2001). Diversity of life in ocean floor basalt. *Earth and Planetary Science Letters*, **194**: 31-37.

Tivey, M. and Delaney, J., (1986). Growth of large sulfide structures on the Endevour segment of the Juan de Fuca Ridge. *Earth and Planetary Science Letters*, 77: 303-317.

Tivey, M., Humphris, S., Thompson, G., Hannington, M. and Rona, P., (1995). Deducing patterns of fluid flow and mixing within the TAG active hydrothermal mound using mineralogical and geochemical data. *Journal of Geophysical Research.*, **100**: 12,527-12,555.

Tivey, M. and McDuff, R., (1990). Mineral Precipitation in the Walls of Black Smoker Chimneys: A Quantitative Model of Transport and Chemical Reaction. *Journal of Geophysical Research*, **95**: 12617-12637.

Tivey, M., Rona, P. and Kleinrock, M., (1996). Reduced crustal magnetization beneath relict hydrothermal mounds: TAG hydrothermal field, Mid-Atlantic Ridge, 26°N. *Geophysical Research Letters*, **23**(23): 3511-3514.

Toran, L. and Harris, R., (1989). Interpretation of sulfur and oxygen isotopes in biological and abiological sulfide oxidation. *Geochimica et Cosmochimica Acta*, **53**: 2341-2348.

Trafford, B., Bloomfield, C., Kelso, W. and Pruden, G., (1973). Ochre formation in field drains in pyritic soils. *Journal of soil science*. **24**: 453-460.

Trefry, J. and Metz, S., (1989). Role of hydrothermal precipitates in the geochemical cycling of Vanadium. *Nature*, **342**: 531-533.

Trefry, J., Trocine, R., Klinkhammer, G. and Rona, P., (1985). Iron and copper enrichment of suspended particles in dispersed hydrothermal plumes along the Mid-Atlantic Ridge. *Geophysical Research Letters*, **12**(8): 506-509.

Trocine, R. and Trefry, J., (1988). Disribution and chemistry of suspended particles from an active hydrothermal vent site on the Mid-Atlantic Ridge at 26°N. *Earth and Planetary Science Letters*, **88**: 1-15.

Trudinger, P., Chambers, L. and Smith, J., (1985). Low-temperature sulphate reduction: biological versus abiological. *Canadian journal of Earth Science*, **22**: 1910-1918.

Urrutia, M. and Beveridge, T., (1994). Formation of fine-grained silicate mineral and metal precipitates by a bacterial surface (Bacillus subtilis) and the implications in the global cycling of silicon. *Chemical Geology*, **116**: 261-280.

Urrutia, M., Kemper, M., Doyle, R. and Beveridge, T., (1992). The membrane-induced proton motive force influences in the metal-binding ability of *Bacillus subtilis* cell walls. *Appl. Environ. Microbiol*, **58**: 3837-3844.

Vidal, P. and Clauer, N., (1981). Pb and Sr isotope systematics of some basalts and sulfides from the East Pacific Rise at 21 N (project RITA). *Earth and Planetary Science Letters*, **55**: 237-246.

Von Damm, K., (1988). Systematics of and postulated controls on submarine hydrothermal solution chemistry. *Journal of Geophysical Research*, **93**: 4551-4561.

Von Damm, K., (1990). Seafloor hydrothermal activity: black smoker chemistry and chimneys. *Annual Review, Earth and Planetary Science Letters*, **18**: 173-205.

Von Damm, K. (Editor), (1995). Controls on the chemistry and temporal variability of seafloor hydrothermal fluids. Seafloor Hydrothermal Systems, *Geophysical monographs, 91*. American Geophysical Union, 222-247 pp.

Von Damm, K., Bray, A., Buttermore, L. and Oosting, S., (1998). The geochemical controls on vent fluids from the Lucky Strike vent field, Mid-Atlantic Ridge. *Earth and Planetary Science Letters*, **160**: 521-536.

Van Dover, C., (1995). Ecology of Mid-Atlantic Ridge hydrothermal vents. In: *Hydrothermal Vents and Processes*, L. Parson, C. Walker. and D. Dixon (Editors). Geological Society Special Publication, London, pp. 257-294.

Von Stackelberg, U., (1985). Hydrothermal sulphide deposits in back arc spreading centres in the southwest Pacific. *B.G.R. circ.*, **2**: 14.

Wagner, T., Boyce, A. J., and Fallick, A. E. (2002). Laser combustion analysis of $\delta^{34}S$ of sulfosalt minerals: determination of the fractionation systematics and some crystal-chemical considerations. *Geochim. Cosmochim. Acta* **66**: 2855-2863.

Walsh, A. and Mitchell, R., (1972). An acid-tolerant iron-oxidising Metallogenium. *Journal of General Microbiology*, **72**: 369-376.

Walter, P. and Stoffers, P., (1985). Chemical characteristics of metalliferous sediments from eight areas on the Galapagos Rift and East Pacific Rise between 2 deg N and 42 deg S. *Marine Geology*, **65**: 271-287.

Warren, L. and Ferris, F., (1998). Continuum between sorption and precipitation of Fe(ii) on microbial surfaces. *Environ. Sci. Technol*, **32**: 2331-2337.

Wiersma, C. and Rimstidt, J., (1984). Rates of reaction of pyrite and marcasite with ferric iron at pH 2. *Geochimica et Cosmochimica Acta*, **48**: 85-92.

Williams, L., Parks, G. and Crerar, D., (1985). Silica diagenesis I. Solubility controls. *Journal of sedimentary petrology*, **55**(3): 301-311.

Wirsen, C., Jannasch, H. and Molyneaux, S., (1993). Chemosynthetic microbial activity at Mid-Atlantic Ridge Hydrothermal vent sites. *Journal of Geophysical Research*, **98**: 9693-9703.

Wirsen, C., Tuttle, J. and Jannasch, H., (1986). Activity of sulfur oxidising bacteria at the 21°N East Pacific Rise vent site. *Marine Biology*, **92**: 449-456.

Woodruff, L. and Shanks, W. (1988). Sulphur isotope study of chimney minerals and vent fluids from 21°N, East Pacific Rise: Hydrothermal sulphur sources and disequilibrium sulphate reduction. *Journal of Geophysical Research*, **93**(B5): 4562-4572.

You, C.-F. and Bickle, M., (1998). Evolution of an active seafloor massive sulphide deposit. *Nature*, **394**: 668-670.

Zbinden, M., Le Bris, N., Compere, P., Martinez, I., Guyot, F., Gaill, F (2003). Mineralogical gradients associated with alvinellids at deep-sea hydrothermal vents. *Deep Sea Research*, **50**: 269-280.

Zierenberg, R., Koski, R., Morton, J., Bouse, R. and Shanks, W., (1993). Genesis of massive sulphide deposits in a sediment-covered spreading center, Escanaba Trough, Southern Gorda Ridge. *Economic Geology*, **88**: 2069-2098.

Zierenberg, R. and Schiffman, P., (1990). Microbial control of silver mineralisation at the seafloor hydrothermal site on the northern Gorda Ridge. *Nature*, **348**: 155-157.

Zierenberg, R., Shanks, W. and Bischoff, J., (1984). Massive sulphide deposits at 21°N, EPR: chemical composition, stable isotopes, and phase equilibria. *Geological Society of America Bulletin*, **95**: 922-929.

Zierenberg, R., Shanks, W., Seyfried, W., Koski, R. and Strickler, M., (1988). Mineralisation, alteration, and hydrothermal metamorphism of the ophiolite-hosted Turner-Albright sulfide deposit, South Western Oregon. *Journal of Geophysical Research.*, **93**(B5): 4657-4674.